8th Large Engine Symposium 2024
The Future of Large Engines VIII

Novel Technology and Fuel Options: The Route to Clean Shipping

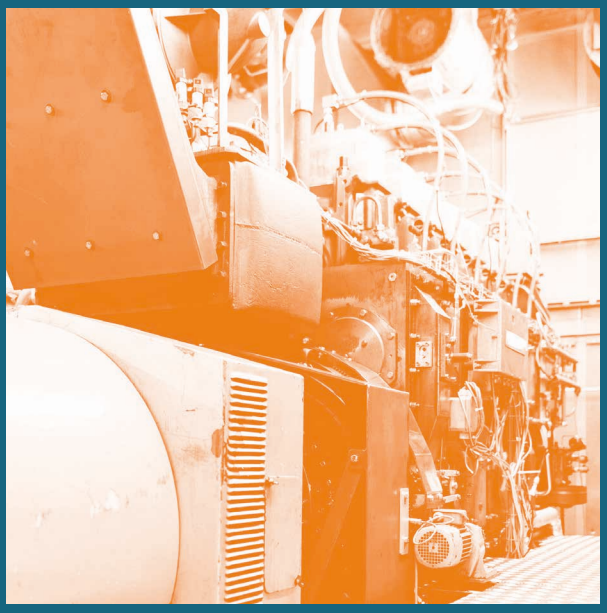

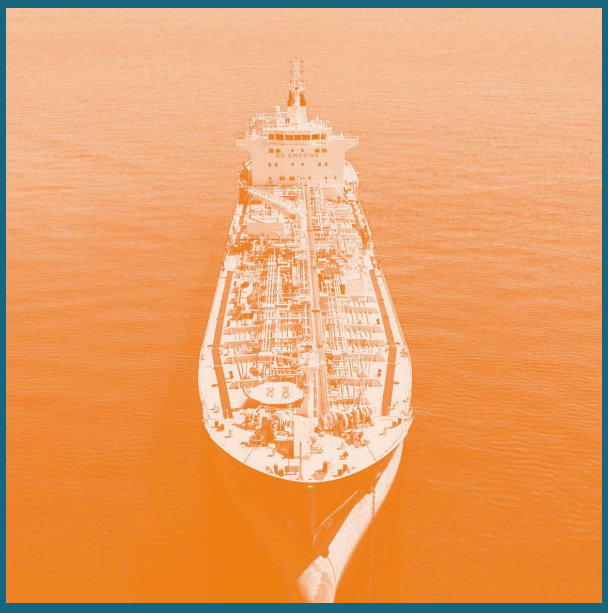

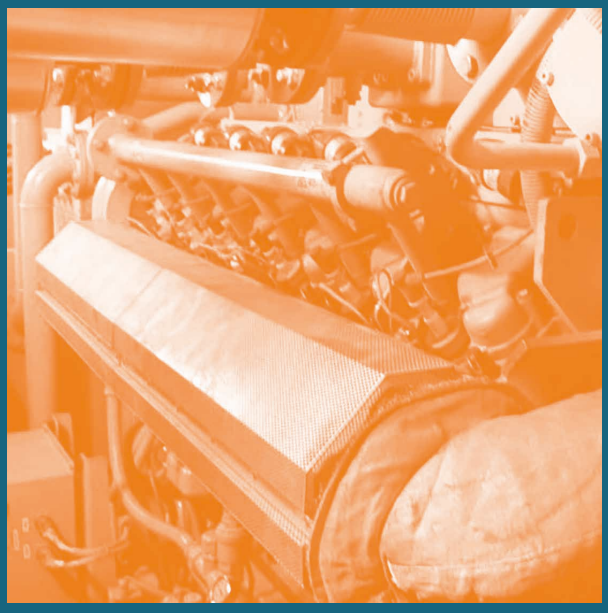

Bert Buchholz (Editor)
and 103 co-authors

Prof. Dr.-Ing. Bert Buchholz (Editor)

and 103 co-authors

8th Rostock Large Engine Symposium 2024

The Future of Large Engines VIII

Technology Concepts and Fuel Options:

The Route to Clean Shipping

with 284 figures und 46 tables

FVTR textbook series

The Future of Large Engines VIII

1st edition

Rostock, September 2024

FVTR textbook series

FVTR Forschungszentrum für Verbrennungsmotoren und Thermodynamik Rostock GmbH
Joachim-Jungius-Str. 9, D-18059 Rostock, Germany
Tel.: +49 381-4059650

Fax: +49 381-4059657

E-mail: office@fvtr.de

Web: https://fvtr.de/

https://doi.org/10.18453/rosdok_id00004630

Foreword:

This year's conference, the 8th Rostock Large Engine Symposium, is taking place in very exciting times. The progress in the marine industry towards the implementation of new, climate neutral fuels has been tremendous since our last conference two years ago. The IMO revised its Greenhouse Gas Strategy in 2023, the ETS system has been extended to shipping within the EU (2024) and the first real GHG legislation will commence with the implementation of the FuelEU Maritime regulation in 2025, defining mandatory targets for reduced greenhouse gas intensity of the fuels used on board. In 2027, the IMO will hopefully follow suit with comparable regulations.

Research has also moved forward. The major candidates for future viable, climate-neutral marine fuels have been characterised as well as their basic, engine related physical and chemical properties. The resulting requirements for tailored fuel injection strategies and combustion processes have been investigated further. These issues were already broadly discussed at the 7th RGMT in 2022. Two years on, much more detailed analyses of specific combustion requirements are presented, efficiency goals, emission reduction challenges as well as reliability issues are discussed. Methanol and ammonia are in the focus of many presentations at the 8th RGMT in 2024. Potentials and challenges of premixed combustion systems and direct injection diffusion-controlled combustion concepts are analysed for both fuels. Special attention is paid to emissions and emission abatement technologies as well as design changes brought about by these new fuels. In addition, practical issues related to the use of marine biofuels are shown at the conference as these fuels are becoming increasingly available in the marine sector and already offer significant GHG reductions today.

I am sure that the presentations, the papers and all the information shared during the various discussions will give input and impulses for the current and future work of all conference attendees.

The technical programme is always the most important part of any conference. My very special thanks are due to all authors and presenters of conference papers. The success of this year's conference is very much linked to your effort in writing the papers

and preparing the presentations. I also wish to thank the companies Robert Bosch GmbH, Schaller Automation Industrielle Automationstechnik GmbH & Co. KG, AVL Deutschland GmbH and Winterthur Gas & Diesel Ltd. for their support in sponsoring the participation of 11 students at the conference. And thanks to the session chairs and all attendees for joining the conference and for their contributions to lively scientific exchange.

Just like the previous conferences, the 8th Rostock Large Engine Symposium is jointly organised by the University of Rostock's Department of Piston Machines and Internal Combustion Engines and FVTR GmbH. Organising a conference requires many hard-working hands at many different levels and in many different places. My special thanks therefore go to all employees of the Department of Piston Machines and Internal Combustion Engines (LKV, University of Rostock) and of FVTR GmbH who were involved in the preparation and implementation of this symposium. Thank you for your dedication, creativity and optimism in the many organisational and administrative tasks required for the symposium. Without your commitment, the 8th RGMT – Rostock Large Engine Symposium in September 2024 would never have been possible.

Rostock, September 2024, Bert Buchholz

Table of Contents

The Partners ot the 8th Large Engine Symposium in Rostock

Media partners:

HANSA
INTERNATIONAL MARITIME JOURNAL

Schiff&Hafen

Diesel & Gas Turbine
WORLDWIDE
COVERING LARGE ENGINE AND GAS TURBINE MARKETS SINCE 1969

POWER
SOURCING GUIDE

THE MOTORSHIP
MARINE TECHNOLOGY

The Partners ot the 8th Large Engine Symposium in Rostock

Student sponsoring:

Keywords: biofuels, marine fuels, pyrolysis oil, hydrothermal liquefaction oil, biodiesel, renewable diesel

Biofuels as Heavy Fuel Oil Substitutes in the Maritime Sector: Findings and Potential Pathways

Dr. Michael Kass[1], Dr. Brian Kaul[1], Mr. Timothy Theiss[1], Mr. Joshua Messner[2], Dr. Eric Tan[3], Mr. Abhijit Dutta[3], Dr. Shuyun Li[4], Dr. Karthikeyan Ramasamy[4], Dr. Farhad Masum[5], Dr. Lívia Benvenutti[5], Dr. Troy Hawkins[5]

[1] Oak Ridge National Laboratory, [2] United States Department of Energy, [3] National Renewable Energy Laboratory, [4] Pacific Northwest National Laboratory, [5] Argonne National Laboratory

https://doi.org/10.18453/rosdok_id00004632

Abstract

The United States Department of Energy has commissioned four national laboratories to evaluate the feasibility of biofuels in the maritime sector. This effort is briefly described including the overall project goals, structure, and aims. The large two-stroke crosshead engines used to power large merchant vessels were of particular interest since they can burn lower combustion quality fuels relative to four-stroke engines. This characteristic allows for consideration of pyrolysis oils and hydrothermal liquefaction (HTL) oils, which are feedstock agnostic and—without further upgrading such as hydrotreating—are more economical compared to distillate drop-in fuels. Pyrolysis and HTL oils are collectively known as bio-intermediates since they require additional processing for use in distillate fuel systems.

The key limiting feature is that these bio-intermediate fuels will cause asphaltene precipitation when blended with heavy fuel oils (HFOs) such as very low sulfur fuel oil (VLSFO) unless the bio-intermediates are upgraded to remove water and oxygenates. Economics is the key driver for scalability, and preliminary techno-economic analyses (TEAs) indicate that bio-intermediates have potentially lower costs relative to other biofuels such as biodiesel and renewable diesel; blending limits and the cost of upgrading bio-intermediates to enable blend stability needs further study to fully

understand the economic outlook. Additionally, life cycle analyses (LCAs) of feedstocks and pathways show significant life cycle carbon reduction benefit relative to HFOs or marine diesel oils (MDOs). In addition to TEA and LCA results, we also present on the technical feasibility of these fuels. These studies have focused on the properties of biofuel blends with VLSFO that are critical to the fuel systems of maritime vessels fueled with HFOs. These properties include the compatibility with fuel system metals, viscosity, and blend stability. Aging studies with blends of VLSFO with biodiesel, HTL, and pyrolysis oils are also presented. Future efforts are being planned to conduct additional biofuel testing, including the use of biofuels as pilot fuels in zero carbon shipping options fueled with ammonia and methanol, ship-based demonstrations, and bioresource competition studies.

1. Introduction

Marine transportation is a key driver of global economies, carrying over 80% of internationally traded goods [1]. At present, marine shipping is powered almost exclusively by fossil fuels [2], leading to a significant greenhouse gas (GHG) impact: in 2022, CO_2 emissions from shipping totaled 706 Mt [3], which accounts for about 2% of the global total and if ranked as a nation would be the 6th leading emitter, ahead of the national impact of, e.g., Germany or South Korea, as shown in Figure 1; this estimate is only expected to increase over the coming decades with projected economic growth and increased maritime shipping activities.

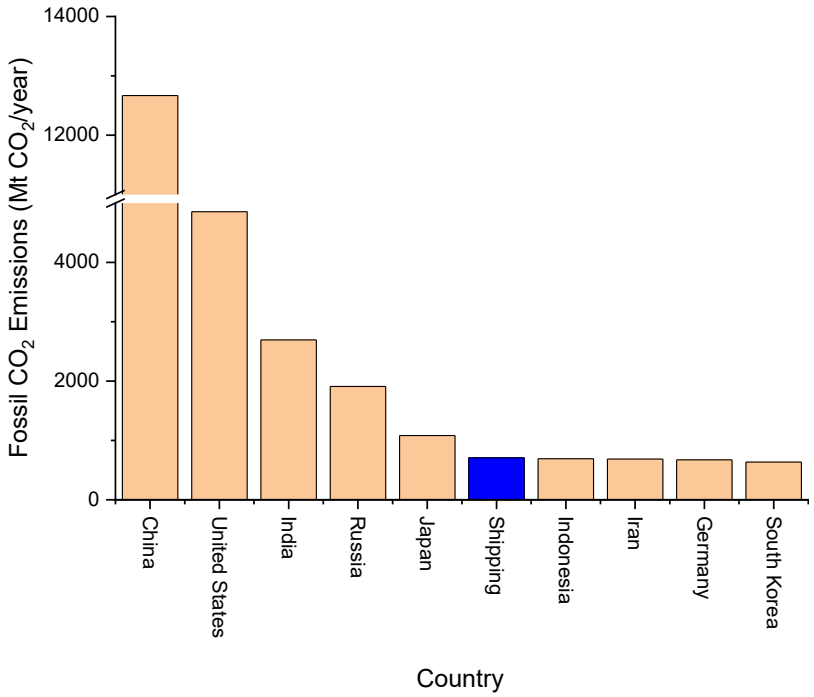

Figure 1: Annual CO_2 emissions from fossil fuel combustion ranked by country. Country data from Emissions Database for Global Atmospheric Research (EDGAR) [4]; shipping data from International Energy Agency [3].

Unlike national economies that include major impacts from electricity generation and industrial use, the energy use in marine shipping is exclusively the long-distance, high-load transportation use case that is among the most difficult to decarbonize. At the same time, there is a mandate from the International Maritime Organization (IMO) to cut GHG emissions from shipping by 70–80% by 2040 and reach net-zero emissions by or around 2050 [5]. This will require new low-lifecycle-carbon fuels (LLCF) and engines, and substantial efforts are underway to explore ammonia, methanol, and other novel fuels in the marine sector in pursuance of this goal. These novel fuels will have an increasing impact over time as new ships designed to operate with them come online, but with the long lifespan of ships and marine engines, much of the current fleet will still be at sea when these emissions reduction targets come due. Biofuels are thus an attractive LLCF—especially in the near term—due to their suitability as a drop-in fuel that can reduce GHG in the existing fleet. They also offer a potential path to achieve net-zero carbon when used in dual-fuel approaches, displacing petroleum-based fuel oils as the pilot fuel alongside other alternative fuels.

Biofuels including alcohols (e.g., ethanol and methanol) and fatty acid methyl ester (FAME) biodiesels have a long history in the market, typically as blending agents with gasoline or diesel fuels. These traditional biofuels will continue to play a role in the future, and the latest ISO standard for marine fuels now accounts for the use of FAME biodiesel at blends of up to 100% [6], up from the previous maximum of 7%. Methanol can also be sourced as a biofuel in addition to the synthetic e-fuel pathways being considered for green methanol. In addition to these traditional biofuels, there is growing interest in biofuels made from fast pyrolysis and hydrothermal liquefaction (HTL) processes, which can convert biomass and wet wastes, respectively, that are difficult and expensive to use for production of traditional biofuels like FAME biodiesel, bio-alcohols, or renewable diesel fuel.

Approximately two-thirds of global marine fuel usage is in ships powered by large low-speed 2-stroke engines [7], as shown in Figure 2. These engines are currently primarily operated on VLSFO and are both highly efficient and tolerant of low-quality fuels. This presents a significant opportunity for use of HTL and pyrolysis oil derived biofuels directly in these engines rather than as feedstocks to refineries to produce higher-quality fuels, saving on the energy usage and cost of upgrading them.

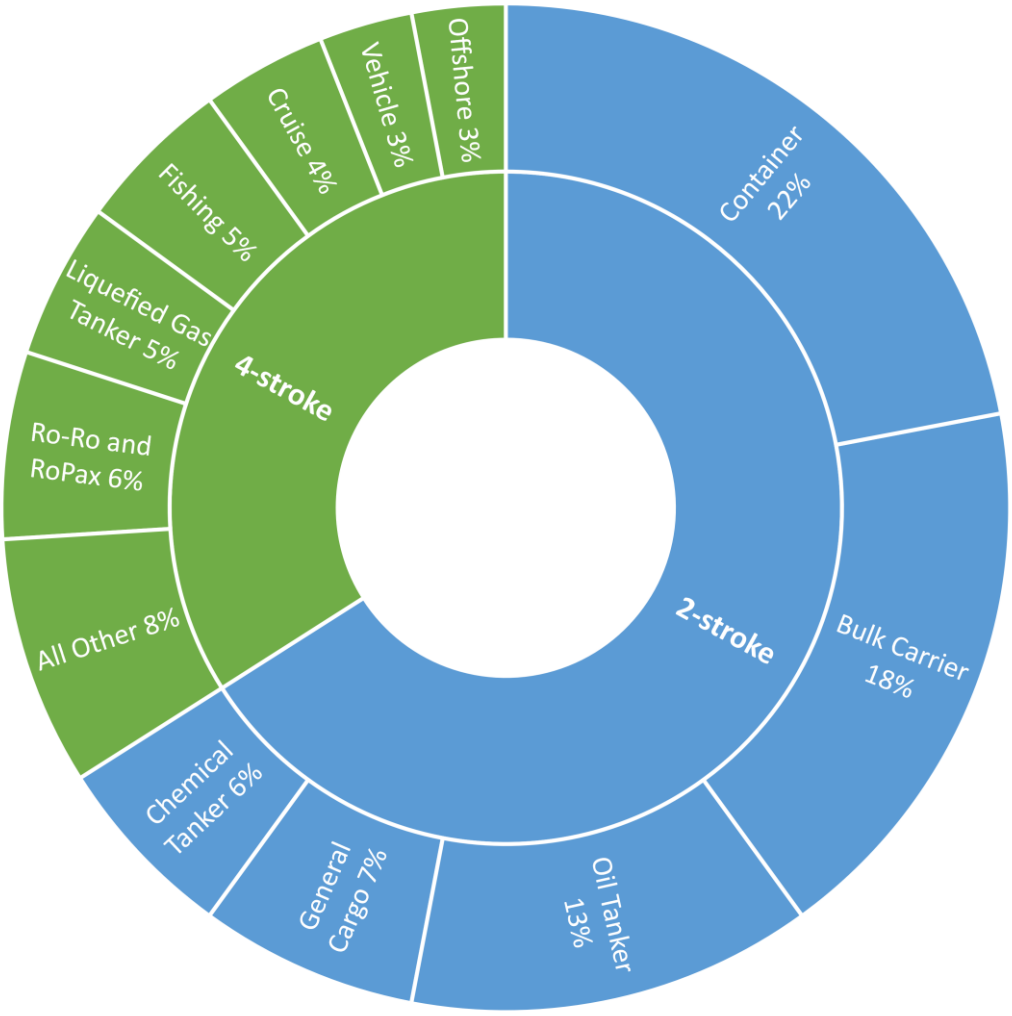

Figure 2: Fuel consumption by ship main engine type. Reproduced from Curran et al. [8]. Data from Concawe [7].

Biofuel use in the marine sector is growing rapidly, with the fuel testing company VPS reporting having tested over 500,000 Mt of biofuels (mostly FAME) in 2023, up from 230,000 Mt in 2022 [9]. A recent

study by the Oil and Gas Climate Initiative (OGCI) [10] shows that while under current conditions biomass supply for the marine market is likely to be constrained by 2050, with increased legislative support there is "more than enough biomass available for marine fuel use, even accounting for sector competition." Similarly, the 2023 Billion-Ton Report from the United States Department of Energy (DOE)'s Bioenergy Technologies Office (BETO) indicates that 1.1–1.5 billion tons of sustainable biomass production potential would exist in a mature market [11].

A key challenge that must be addressed for the adoption of new biofuels in the marine sector is blending compatibility with existing market fuels. This is important not only as a pathway to ramp up blend levels as production capacities increase, but also for switching between fuels onboard the vessel as different fuels are available in different ports. The primary concern is the presence in heavy fuel oils of asphaltenes, which are high-molecular-weight polymers in a colloidal dispersion that exist in chemical equilibrium with the surrounding fuel [7]. The solubility properties of these molecules with the surrounding liquid are important to prevent them from falling out of solution as a precipitate, which can cause filter plugging, fouling, and flow difficulties in residual fuels [12]. Regulatory emissions compliance must also be maintained, and the impact of novel fuels on emissions profiles is not yet well understood.

The DOE's Bioenergy Technologies Office initially sponsored a study conducted jointly by Oak Ridge National Laboratory (ORNL), Argonne National Laboratory (ANL), Pacific Northwest National Laboratory (PNNL), and the National Renewable Energy Laboratory (NREL) to evaluate the opportunities and feasibility of using biofuels in ocean-going marine vessels. This study provided an initial favorable assessment and highlighted existing research needs [13]. Based on this initial assessment, a follow-up study was launched to conduct preliminary techno-economic analysis (TEA) and lifecycle analysis (LCA) along with key technical feasibility efforts [14]. This effort has grown into a study intended to provide the foundational information and demonstrations that will lead to future ship-based engine demonstrations of advanced biofuel blends. The scope includes determining the minimum level of upgrading and treatment necessary to successfully blend HTL and fast pyrolysis derived biofuels with heavy fuel oils, as well as updated techno-economic and lifecycle analyses of their impacts and evaluation of both the physical properties of the fuels and the impact on engine emissions in dynamometer testing. The project aims to address barriers to biofuel use in marine engines and ultimately conduct a sea trial demonstration.

2. Economic Feasibility and Greenhouse Gas Emissions Impact

In order to assess the potential opportunity for biofuels for decarbonization of the marine sector, it is important to understand both the economic feasibility of using these fuels and the potential lifecycle GHG impact of doing so. To address these questions, TEA and LCA of various pathways were conducted. This section briefly summarizes some of the results of these studies.

2.1. Techno-economic analysis

A detailed TEA was previously conducted and reported in Li *et al.* [15]. This study compared four conversion pathways: HTL of wet wastes such as sewage sludge and manure, fast pyrolysis of woody biomass, landfill gas Fischer-Tropsch synthesis, and lignin-ethanol oil from a lignocellulosic ethanol biorefinery using reductive catalytic fractionation. The fuels were modelled to have minimum fuel selling prices between $1.68 and $3.98 per HFO gallon equivalent in 2016 U.S. dollars, based on a mature plant assessment. For comparison, VLSFO ranged in price from approximately $0.50 to $1.50 per HFO

gallon equivalent over the 2-year period considered in the study. While these prices are not competitive in today's market, all decarbonization solutions will be more expensive than the status quo, and the difference is small enough to consider some of these fuels as plausible options for marine transportation.

Since that study, pathways for both HTL and pyrolysis oils have been updated—in particular, considering catalytic fast pyrolysis (CFP) oils, which have better blending compatibility properties than non-catalytic fast pyrolysis oils. With these updated pathways—and considering two catalyst technologies for the CFP oils (ZSM-5 zeolite and Pt-TiO_2)—minimum fuel selling prices in 2020 U.S. dollars are shown in Figure 3 and are estimated for non-hydrotreated CFP oils using conceptual scaleup of bench scale results. Here, waste pathways include feedstock credits in the form of tipping fees (fees that would have otherwise been charged for landfill disposal). For comparison, VLSFO prices for the first half of 2024 have ranged globally from $1.82 to $2.07 per HFO gallon equivalent in 2020 U.S. dollars [16]. Hence, the overall conclusion is similar: both CFP and HTL oils are expected to require a modest price premium over today's market fuel prices to be economically viable, which is plausible given existing mandates for decarbonization and is in line with proposed carbon taxes and similar incentive policies being considered.

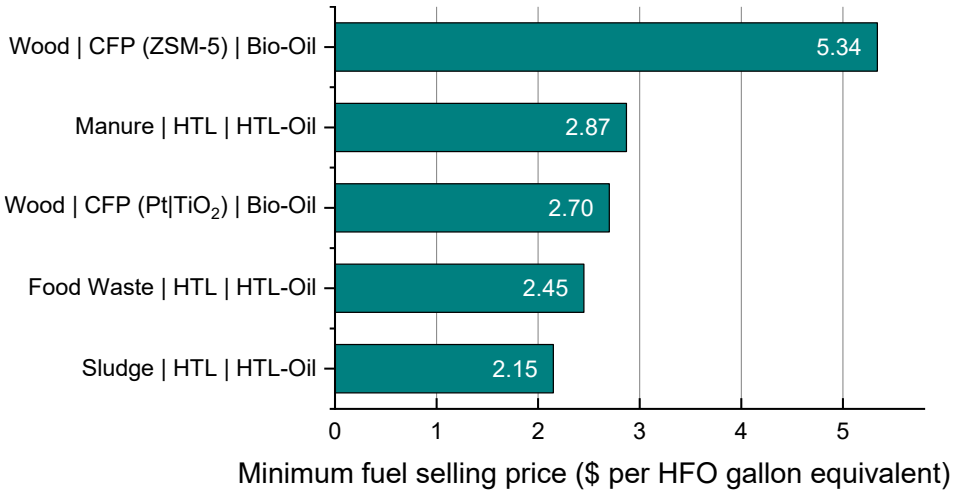

Figure 3: Updated TEA results showing minimum fuel selling price for several HTL and CFP pathways

2.2. Lifecycle GHG analysis

A comprehensive LCA of the GHG emissions impacts of a variety of biofuels for marine applications was also previously conducted and reported by Masum *et al.* [17]. This study considered eleven total biofuel pathways via four conversion processes, including HTL from wastewater sludge and manure, CFP of woody biomass, diesel produced via Fischer-Tropsch synthesis from landfill gas, and lignin ethanol oil from reductive catalytic fractionation of poplar. Results showed lifecycle GHG emissions ranging from -60–56 gCO_2e/MJ, which is a reduction of 41–163% compared to conventional VLSFOs. Waste pathways, in particular, showed net-negative carbon emissions with over 100% reduction due to offsetting the default waste management methods that would result in decomposition and methane emissions.

The earlier LCA was also updated with the new CFP and HTL pathways. The GREET lifecycle assessment model was used to conduct the GHG emissions estimation [18]. Figure 4 shows the

updated results, with lifecycle GHG emissions ranging from approximately -81–16 gCO_2e/MJ; again, waste pathways show net-negative carbon emissions. This analysis only includes biomass production (farming), landing processing (which includes cutting down shorter limbs, cutting logs to transportable lengths, and sometimes debarking on site), transportation, receiving & handling, and storage, and transportation from the farming site to the biorefinery. In Figure 4, Natural gas, Electricity, and Diesel are categories representing energy inputs consumed during the conversion process. The Material & Chemicals and Catalysts categories are inputs considered in the conversion process to produce the biofuel. The T&D category relates to the emissions from transporting fuel to distribution sites and, in case of the HTL pathways, emissions due to transporting HTL-biosolids to the carbon sequestration site 100 km away. The Combustion category captures end-use emissions of products and includes CO_2 (which is biogenic in this case), CH_4, N_2O, volatile organic compounds (VOC), black carbon (BC), and organic carbon (OC). The C Sequestration category captures credits from the biosolids generated in the process of conversion: these were viewed as potential means of carbon sequestration, and hence credits were applied. Displacement credits are due to electricity and sulfur production that displaces U.S.-based grid electricity and conventional sulfur. Counterfactual credits are generated by avoiding the conventional waste management practices and diverting the waste for fuel generation. Conventional waste management results in the decomposition of waste materials and therefore methane emissions from sludge, manure, and food waste to the air. Finally, the LCA provides the numbers of the life cycle assessment from farming through end use of the product. In all cases, a significant benefit is seen, with reductions of 83–188% compared to petroleum-based marine fuels (see marine diesel oil, MDO, 0.1% sulfur).

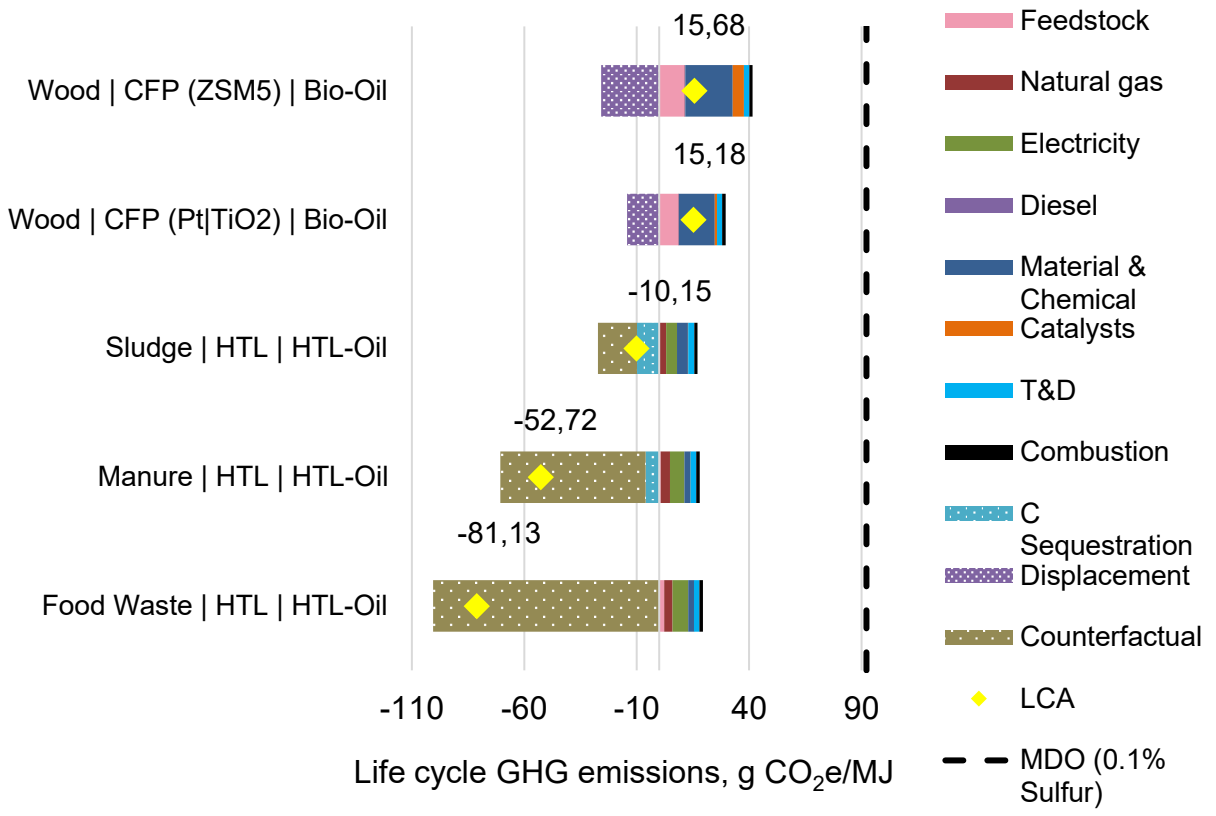

Figure 4: Updated LCA results showing lifecycle GHG emissions for several HTL and CFP pathways

3. End-use Technical Feasibility

In addition to understanding the economic feasibility and GHG impact of potential biofuels, it is also important to understand the impacts of new biofuels in end-use situations in order to enable their use. This includes effects of the physical properties of the fuels (viscosity, fuel system materials compatibility, blending compatibility, etc.) that will have a direct impact on infrastructure and ship hardware as well as impacts on engine combustion and regulated emissions, including NO_x. This section briefly summarizes the results of studies into these effects.

3.1. Physical properties and compatibility

In order to be effectively used for GHG reduction in the existing fleet, novel biofuels must be compatible with infrastructure and fuel system components. To enable transition away from petroleum-derived fuels, the new fuels must also have good blend compatibility with existing market fuels. Viscosity is also a key property, as VLSFO requires heating to meet particular viscosity targets for pumping and fuel injection. These effects have been studied in both neat biofuels and blends.

The most important factor for blend compatibility with existing market fuels is avoiding asphaltene precipitation. CFP oils have shown good blend stability up to at least 50% mass concentration in some instances [19], while HTL oils are more challenging, with precipitation occurring at blend levels as low as 5%. Initial results indicate commercially available additives can allow blending of HTL oils beyond 20% [14], and hydrotreating can also be used to improve the blending properties of CFP, FP, and HTL oils.

Raw (unprocessed) pyrolysis oils (also known as bio-oil) have relatively high concentrations of organic acids and water. They are corrosive to carbon steels, though type 430F and type 316 stainless steels perform reasonably well [20, 21]. Compatibility with fuel system elastomers and plastics has also been evaluated, with raw pyrolysis oils causing significant elastomer swell for most relevant elastomers relative to diesel fuel [22]. Hydrotreating and co-processing with petroleum-derived oils can reduce the acid content and abate the corrosion concerns [20]. Synergistically, this is the same processing needed to ensure blend compatibility with petroleum-based heavy fuel oils.

Biofuels generally have a beneficial impact on viscosity in blends with VLSFO, with a nonlinear impact even at low blend levels, as shown in Figure 5 for HTL and FAME biodiesel blends, where both exponential curve fits have an R^2 of 0.998. The significant reduction in viscosity implies a reduction in heating energy input to achieve operational viscosity targets for fuel injection.

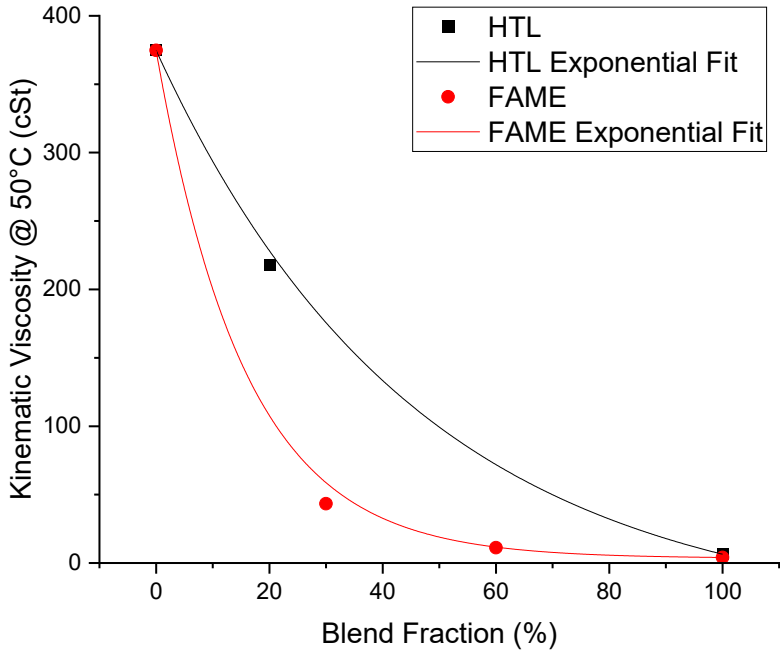

Figure 5: Viscosity blending effects of HTL and FAME biofuels with VLSFO

Polymerization is also a concern with pyrolysis-derived bio-oils, as this can cause issues in the fuel system. If polymerization occurs at relatively low temperatures, filter plugging and similar obstructions can occur; more critically, the higher temperatures experienced in fuel injector tips during engine operation can cause injector fouling and loss of power. An initial study of viscosity aging effects with 10% blends of HTL and CFP oils into VLSFO shows that CFP oils are prone to this, as illustrated in Figure 6: even when aged at 50 °C for extended periods, a notable increase in viscosity is observed for the 10% CFP blend; when aged at 90 °C , the 10% CFP viscosity rapidly surpasses that of the base VLSFO and continues to increase with time. A more detailed viscosity aging analysis will be reported in future publications. Avoidance of polymerization is in pyrolysis-derived bio-oils is an area of active research, with various additives and processing methods being evaluated for their effectiveness in avoiding this effect. The HTL blend did not show signs of polymerization, with aging stability approximately the same as that of the base VLSFO.

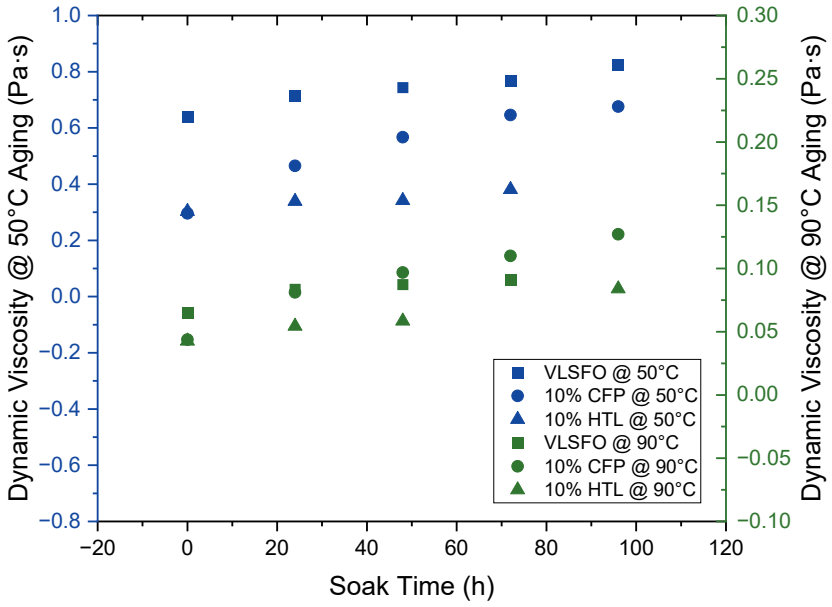

Figure 6: Viscosity aging effects at 50 °C and 90 °C for VLSFO and 10% blends of CFP and HTL oils

3.2. Engine combustion and emissions impacts

A number of studies have been completed examining the impact of FAME biodiesel on NO_x and particulate matter (PM)/black carbon (BC) emissions. The results are generally consistent in that NO_x increases and BC decreases with increasing biodiesel content, though for blend levels < 30%, the NO_x increase is typically within testing repeatability [23–25]; for higher blend levels, adjusting the fuel injection timing can compensate for the increase in NO_x emissions [26]. There is less historical experience with the use of HTL and CFP bio-oils and blends, and thus a lack of data in the literature on their emissions impacts.

An initial study within this project tested 10% blends of both CFP and HTL bio-oils splash-blended into a VLSFO in the Enterprise single-cylinder marine diesel research engine. This is a reduced-scale 2-stroke crosshead research engine designed to replicate many of the key features of full-scale low-speed 2-stroke marine diesel engines with significantly reduced fuel and lubricant requirements. Table 1 lists the primary specifications of the engine, which is designed with a high-swirl flow field two hydraulic electronic unit injector (HEUI) fuel injectors with an asymmetrical spray pattern, as illustrated in Figure 7. The engine is approximately 1:10 scale relative to typical low-speed 2-stroke marine engines, and while boundary conditions are duplicated to the greatest extent possible, time-scales and rotational speeds do vary. In order to maintain a realistic mean piston speed (which sets the boundary condition for the cylinder lubricant at the piston ring/liner interface), the rotational speed scales inversely with the stroke. This means that while thermodynamic conditions in the cylinder can be matched, the time-scales will be reduced relative to the full-scale engines. Emissions impacts from fuel changes will be directionally correct, but either model-based scaling studies or full-scale testing would be necessary to precisely quantify expected emissions from a full-scale engine. A detailed description of the engine design can be found in Kaul, *et al.* [27].

Table 1. Enterprise engine specifications

Cylinder bore	107.95 mm
Piston stroke	432 mm
Stroke/bore ratio	4:1
Displacement	3.95 l
Geometric compression ratio	13:1
Mean piston speed	8 m/s @ 556 rpm

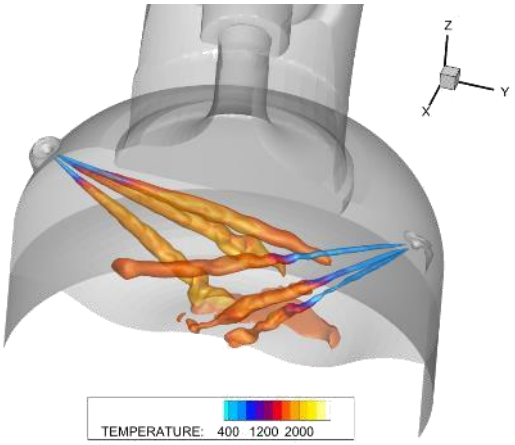

Figure 7: CFD simulation of combustion in the Enterprise engine, showing fuel injection spray patterns.

Samples of mildly hydrotreated CFP and HTL oils produced by NREL and PNNL were blended at 10% by volume into a base VLSFO and run in the engine at several steady-state speed/load operating conditions (shown in Table 2) with no changes to the engine calibration. NO_x emissions were measured using a Fourier transform infrared analyzer (FTIR), and PM emissions concentrations were measured using an AVL Micro Soot Sensor. Results showed no notable impact for the 10% blend levels tested, as indicated in Figure 8. There was similarly no notable impact to combustion phasing or duration for these low-level blends, though prior operation on this engine with high-level bio-diesel blends has shown a strong correlation between combustion phasing and NO_x emissions like that observed in the literature. Operation with higher blend levels (or potentially neat bio-fuels) is planned in the upcoming months, with larger fuel quantities becoming available from commercial vendors.

Table 2. Engine operating conditions

Operating condition	**Speed, rpm (% rated)**	**BMEP, bar**
Full steaming	545 (98%)	14.1
Slow steaming	400 (72%)	9.8
Maneuvering	280 (50%)	3.9

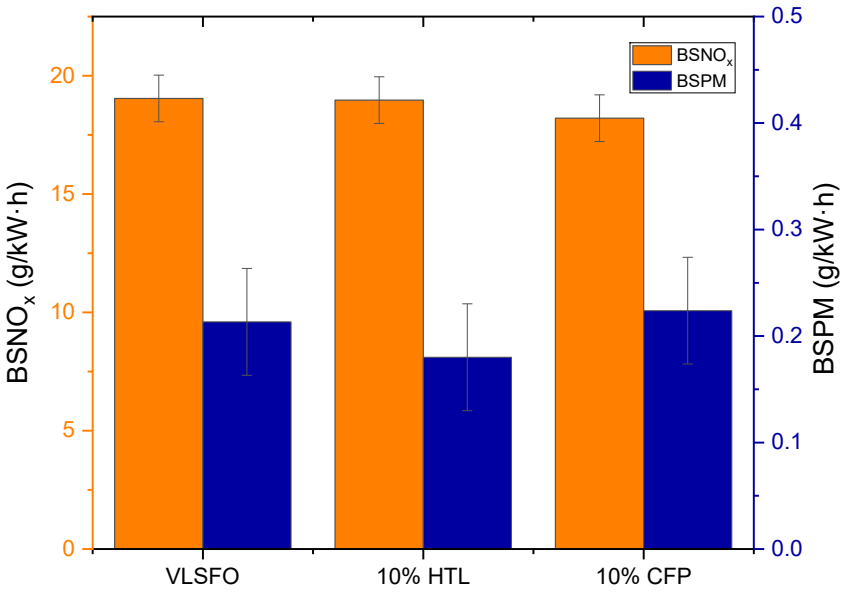

Figure 8: Brake-specific NO_x ($BSNO_x$) and brake-specific PM (BSPM) emissions at full steaming operation for VLSFO and 10% blends of HTL and CFP fuels in the Enterprise research engine. Error bars represent the standard deviation of 8 repeats of the baseline VLSFO fuel.

4. Future Plans

Research to address remaining barriers to engine demonstrations, both in the laboratory and the field, is ongoing. High blend levels (potentially up to 100%) of mildly hydrotreated CFP and HTL bio-oils will be tested in the upcoming year to evaluate the blending compatibility and thermal stability (i.e., resistance to polymerization) of blends exceeding 50% biofuel, and mitigation measures, including additives to prevent polymerization will be explored to address remaining challenges. High blend levels will be tested in the Enterprise research engine to gain further confidence of suitability for engine operation as well as data on emissions impacts. In parallel with these efforts, planning is underway for a ship-borne demonstration, including fuel sourcing and partnerships with operators to enable sea trials.

5. Conclusion

The U.S. Department of Energy's Bioenergy Technologies Office (BETO) has sponsored a project comprising four national laboratories to evaluate the opportunities for the use of biofuels to decarbonize marine transportation, with a particular focus on HTL and CFP oils for the displacement of heavy fuel oils in ocean-going vessels. This project spans from TEA and LCA evaluations of the high-level impacts and economics to end-use challenges, including material compatibility, blend stability, and engine emissions impacts. Results to date show significant potential, with a few remaining challenges to implementation that are the subject of ongoing studies. Fuels are being systematically evaluated for suitability for engine testing and eventual sea trials, and barriers are being identified and addressed.

Acknowledgments

This research was supported by the DOE Office of Energy Efficiency and Renewable Energy (EERE), Bioenergy Technologies Office and used resources at the National Transportation Research Center, a DOE-EERE User Facility at Oak Ridge National Laboratory. The authors would like to thank Josh Messner at BETO for supporting this work. The views expressed in this article do not necessarily represent the views of the DOE or the U.S. Government.

Literature

[1] Organisation for Economic Co-operation and Development (OECD). "Ocean Shipping and Shipbuilding," [Online], 2022 [cited 2024 July 1]. Available from: https://www.oecd.org/ocean/topics/ocean-shipping/

[2] International Energy Agency (IEA). "International Shipping," [Online].; 2022 [cited 2024 July 1]. Available from: https://www.iea.org/energy-system/transport/international-shipping

[3] International Energy Agency (IEA). "CO_2 Emissions from International Shipping in the Net Zero Scenario, 2000–2030," [Online], 2023 [cited 2024 July 1]. Available from: https://www.iea.org/data-and-statistics/charts/co2-emissions-from-international-shipping-in-the-net-zero-scenario-2000-2030-3

[4] Crippa M, Guizzardi D, Schaaf E, Monforti-Ferrario F, Quadrelli R, Risquez Martin A, *et al.* "GHG Emissions of All World Countries," European Commission, Joint Research Centre, 2023. doi:10.2760/953322

[5] International Maritime Organization (IMO). "2023 IMO Strategy on Reduction of GHG Emissions from Ships (MEPC 80 Annex 15)," 2023.

[6] International Organization for Standardization. "ISO 8217:2024 Products from Petroleum, Synthetic and Renewable Sources — Fuels (class F) — Specifications of Marine Fuels," [Online], 2024 [cited 2024 July 1]. Available from: https://www.iso.org/standard/80579.html

[7] CONCAWE. "Marine Fuel Facts," [Online], 2017. Available from: https://www.concawe.eu/wp-content/uploads/2017/01/marine_factsheet_web.pdf

[8] Curran S, Onorati A, Payri R, Agarwal AK, Arcoumanis C, Bae C, *et al.* "The Future of Ship Engines: Renewable Fuels and Enabling Technologies for Decarbonization," *International Journal of Engine Research 25(1),* 2023. doi:10.1177/14680874231187954

[9] VPS. "2023 Marine Bunker Fuels Review," [Online].; 2023 [cited 2024 July 25]. Available from: https://www.vpsveritas.com/knowledgecentre/articles/2023-marine-bunker-fuels-review

[10] Oil and Gas Climate Initiative. "Economically Viable and Sustainable Biomass for Marine Fuel Use," OGCI, 2023.

[11] U.S. Department of Energy. *Billion-Ton Report: An Assessment of U.S. Renewable Carbon Resources.* Langholtz MH (Lead). Oak Ridge, TN: Oak Ridge National Laboratory, 2024. ORNL/SPR-2024/3103 doi:10.23720/BT2023/2316165

[12] McKay JF, Amend PJ, Cogswell TE, Harnsberger PM, Erickson RB, Latham DR. "Petroleum Asphaltenes: Chemistry and Composition," in Uden PC, Siggia S, Jensen HB, Editors. *Analytical Chemistry of Liquid Fuel Sources.* p. 128–142. Washington, DC: American Chemical Society, 1978. doi:10.1021/ba-1978-0170.ch009

[13] Kass M, Abdulla Z, Biddy M, Drennan C, Hawkins T, Jones S, *et al.* "Understanding the Opportunities of Biofuels for Marine Shipping," ORNL Report ORNL/TM-2018/1080. Oak Ridge National Laboratory, 2018.

[14] Kass M, Tan E, Ramasamy K, Hawkins T, Theiss T, Abdullah Z, *et al.* "Biofuel Viability for the Ocean-Going Marine Sector," ORNL Report ORNL/TM-2022/2373. Oak Ridge National Laboraotry, 2022. doi:10.2172/2278927

[15] Li S, Tan ECD, Dutta A, Snowden-Swan LJ, Thorson MR, Ramasamy KK, *et al.* "Techno-Economic Analysis of Sustainable Biofuels for Marine Transportation," *Environmental Science & Technology* 56(23): p. 17206–17214, 2022. doi:10.1021/acs.est.2c03960

[16] Ship & Bunker. "VLSFO Bunker Prices," [Online], 2024 [cited 2024 July 1]. Available from: https://shipandbunker.com/prices/am/nampac/us-lax-la-long-beach#VLSFO

[17] Masum FH, Zaimes GG, Tan ECD, Li S, Dutta A, Ramasamy KK, *et al.* "Comparing LIfe-Cycle Emissions of Biofuels for Marine Applications: Hydrothermal Liquefaction of Wet Wastes, Pyrolysis of Wood, Fischer-Tropsch Synthesis of Landfill Gas, and Solvolysis of Wood," *Environmental Science & Technology* 57(34): p. 12701–12712, 2023. doi:10.1021/acs.est.3c00388

[18] Wang M, Elgowainy A, Lee U, Baek K, Balchandani S, Benavides P, *et al.* "Greenhouse Gases, Regulated Emissions, and Energy use in Technologies (GREET) Model ® (2023 Excel)," 2023. doi:10.11578/GREET-Excel-2023/dc.20230907.1

[19] Kass MD, Armstrong BL, Kaul BC, Connatser RM, Lewis S, Keiser JR, *et al.* "Stability, Combustion, and Compatibility of High-Viscosity Heavy Fuel Oil Blends with a Fast Pyrolysis Bio-Oil," *Energy & Fuels* 34(7): p. 8403–8413, 2020. doi:10.1021/acs.energyfuels.0c00721

[20] Keiser JR, Brady MP, Jun J, Sulejmanovic D, Kass MD. "Performance of Structural Alloys in Bio-oil Production, Upgrading, and Storage Systems," *Energy & Fuels* 37(2): p. 1104–1115, 2023. doi:10.1021/acs.energyfuels.2c02018

[21] Jun J, Su YF, Keiser JR, Wade JEI, Kass MD, Ferrell JRI, *et al.* "Corrosion Compatibility of Stainless Steels and NIckel in Pyrolysis Biomass-Derived Oil at Elevated Storage Temperatures," *Sustainability* 15(1), 2022. doi:10.3390/su15010022

[22] Kass MD, Janke CJ, Lobodin VV, Bras W, Keiser JR, Sulejmanovic D, *et al.* "Compatibility of Fuel System Elastomers and Plastics with a Fast-Pyrolysis Oil (Bio-oil) at Room Temperature," *Energy & Fuels* 36(16): p. 9158–9170, 2022. doi:10.1021/acs.energyfuels.2c01878

[23] Chountalas TD, Founti M, Hountalas DT. "Review of Biofuel Effect on Emissions of Various Types of Marine Propulsion and Auxiliary Engines," *Energies* 16(4647), 2023. doi:10.3390/en16124647

[24] Noor CWM, Noor MM, Mamat R. "Biodiesel as Alternative Fuel for Marine Diesel Engine Applications: A Review," *Renewable and Sustainable Energy Reviews* 94: p. 127–142, 2018. doi:10.1016/j.ser.2018.05.031

[25] Renaud P, Heyberger B, Griffaton B. "Comparison of Exhaust Gas Emissions of a Marine Engine Burning Different Blends of Bio-VLSFO," Paper No. 373 in *Proceedings of the 30th CIMAC World Congress,* 2023; Busan, Korea.

[26] Ko J, Seo J, Kim B, Choi K, Park J, Kim K. "Investigation of Bio-Fuel on Engine Performance, Emissions and Durability of the HiMSEN Diesel Engine," Paper No. 039 in *Proceedings of the 30th CIMAC World Congress,* 2023; Busan, Korea.

[27] Kaul B, Nafziger E, Kass M, Givens W, Crouthamel K, Fogarty J, *et al.* "Enterprise: A Reduced-Scale, Flexible Fuel, Single-Cylinder Crosshead Marine Diesel Research Engine," Paper No. 326 in *Proceedings of the 29th CIMAC World Congress,* 2019; Vancouver, Canada.

Keywords: Large Two-Stroke Engine, Ammonia, Methanol, Combustion, IC Engine, Experimental, Optical Investigation, Simulation

Experimental investigations and simulation validation regarding future fuel combustion systems of low-speed two-stroke engines using WinGD's spray and combustion chamber

Dr. Beat von Rotz, Pascal Süess, Martin Bohnenblust, Dr. Christophe Barro, Dr. Omar Seddik, Juan Reina Martinez, Dr. Andrea Schirru, Dr. Andreas Schmid, Dr. German Weisser

WinGD

https://doi.org/10.18453/rosdok_id00004634

Abstract

In pursuit of the International Maritime Organization's (IMO) ambitious targets for substantial reductions in the carbon intensity and overall greenhouse gas emissions of the shipping industry, a rigorous shift from conventional fossil fuels to alternative, sustainable options are imperative. Among these alternatives, methanol and ammonia have been identified as promising candidates, offering economically viable pathways for decarbonization due to their potential for CO_2-neutral production. Recognizing their significance, WinGD is expanding its product portfolio to include engine technology tailored for ammonia and methanol applications. A prerequisite for a deliberate technology development for future fuel combustion systems is the fundamental understanding of the in-cylinder processes which is established through various experimental studies and numerical investigations.

WinGD's spray and combustion chamber (SCC) is a unique experimental test facility to carry out investigations regarding the injection behaviour and spray/fuel admission characteristics as well as ignition/combustion behaviour and subsequent emission formation at engine-relevant conditions for low-speed two-stroke combustion systems. Optical accessibility allows the application of various (laser-) optical and advanced measurement techniques to examine the in-cylinder processes and their underlying phenomena.

The SCC is equipped to handle the injection and combustion of a wide range of fuels and their combinations. Dedicated fuel conditioning and supply systems have been designed and installed allowing for various operating principles and enabling investigations with a broad variety of fuels, such as standard (distillate and residual) fuel oils as well as alternative liquid/gaseous fuel types especially including alcoholic fuels (e. g. methanol) and ammonia. When operating with such hazardous substances, appropriate safety concepts need to be in place and installations of additional safety measures such as gas detection and ventilation systems are required.

Exemplary results from the high-pressure injection of methanol and ammonia, showcasing the diesel pilot-ignited combustion process under realistic engine conditions with full-scale hardware,

demonstrate the fundamental investigations and studies contributing to a reference database for validating and calibrating WinGD's simulation toolbox. In this respect, the experimentally obtained data from the SCC regarding combustion characteristics and emissions is compared to numerical results derived from 0/1-D models and/or 3-D CFD simulations.

The contribution shall summarize WinGD's dedicated approach for the future fuel combustion system technology development incorporating the pioneering research at engine-like conditions and size from the spray combustion chamber and its utilization for the calibration/validation of numerical models and simulations. The methodology enables a high degree of confidence before engine concepts are implemented at full engine scale for testing and allows well-founded statements regarding the anticipated engine performance.

1. Introduction

The International Maritime Organization (IMO) has set ambitious targets for reducing carbon intensity and greenhouse gas emissions in the shipping industry, necessitating a significant transition from traditional fossil fuels to sustainable alternatives. Methanol and ammonia have emerged as promising options for decarbonization, offering economically viable pathways due to their potential for CO_2-neutral production [1].

The IMO's 2023 revised GHG Strategy includes a reduction of the total annual GHG emissions from international shipping by at least 20%, striving for 30%, by 2030 compared to 2008 levels. Furthermore, the strategy aims for net-zero GHG emissions from international shipping by or around 2050. These targets demand for major technological advancements and adoption of alternative fuels in the maritime sector [2].

WinGD's existing dual-fuel and diesel engine product portfolio already offers the potential for a significant reduction of GHG emissions by being fully capable of using drop-in fuels such as liquid biofuel types and methane from either biogenic sources or synthesis. But such drop-in fuel types will not be available in sufficiently large amounts to cope with the demands of international shipping.

The transition to alternative fuels like methanol and ammonia aligns with the IMO's goal of increasing the uptake of zero or near-zero GHG emission technologies, fuels, and energy sources. The strategy aims for these alternatives to represent at least 5%, endeavouring for 10% of the energy used by international shipping by 2030. This shift is crucial for achieving the long-term objectives of decarbonizing the shipping industry and contributing to global climate change mitigation efforts.

The importance of alternative fuels has been recognized and engine manufacturers are expanding their product portfolios to include technology specifically designed for ammonia and methanol applications. Well noting that WinGD committed itself towards decarbonization and implemented dedicated strategic actions to considerably invest into alternative fuel technologies years before IMO's revised GHG reduction strategy was adopted [3-4].

This did not only involve the commitment to put substantive efforts into such activities but also feature a considerable extension of workforce as well as infrastructure, especially in our global testing & validation facilities [5], for the validation of the technologies under development.

1.1. WinGD's Future Fuel Technology Development Approach

The rapid and successful development of novel technologies to apply methanol and ammonia with a large two-stroke marine diesel engine combustion system requests for fundamental understanding of the phenomena regarding fuel injection and spray formation, ignition behaviour and combustion characteristics as well as emission formation. WinGD's dedicated spray combustion chamber (SCC) is allowing detailed investigations of key components and parameters already in the early stages of the technology development process.

The project timeline for the methanol and ammonia engine development program was exceptionally tough, with initial deliveries scheduled for early 2025. This ambitious aim drastically reduced the window for traditional testing and concept validation. To address this challenge, the team implemented a robust frontloading strategy, heavily emphasizing on numerical development tools which have been validated and calibrated by experimental data from SCC investigations (see Figure 1). This approach enabled rapid iteration and verification of design concepts, allowing the project to maintain its

ambitious timeline while still ensuring thorough evaluation of all critical components. By leveraging advanced simulation technologies, the team aimed to mitigate the risks associated with the tight development plan and meet the unprecedented engine delivery targets.

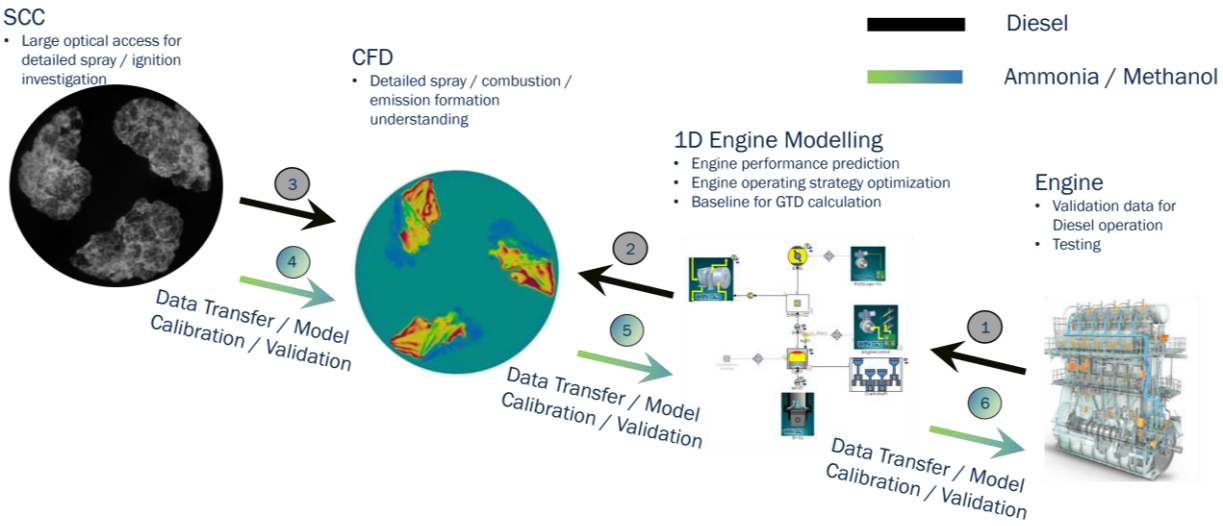

Figure 1: Illustration of WinGD's methanol and ammonia engine development approach highlighting the main process steps (1-6).

The simulation toolbox applied for investigating the combustion system behaviour and ultimately predicting the key performance parameters consist of a 1-D engine model using GT-POWER and 3-D Computational Fluid Dynamics (CFD) simulation by means of CONVERGE CFD, in combination with a variety of enhancements and specifically tailored sub-models such as chemical reaction kinetics.

Besides data from various lab engines, also measurement sets acquired for the complete portfolio in the course of prototype tests as well as series engine confirmation trials have been incorporated into the simulation tool development (Figure 1: step 1). The resulting model was further validated by applying it to the specific conditions and domain of the SCC. This step ensured accurate predictions of initial conditions for spray, ignition, combustion, and emission simulation results using CFD in diesel operations. Additionally, it confirmed the transferability of combustion characteristics obtained through CFD to 1-D engine simulations. (Figure 1: step 2).

The subsequent validation effort then consisted in the assessment of the CFD results against the experimental data obtained on the SCC for a large range of key parameter variations, first for operation on conventional diesel type fuels, then followed by a similar exercise for the methanol/ammonia combustion (Figure 1: step 3/4). This requires an iterative process between experiment and simulation in order to make sure that the modelling approaches used for all relevant processes properly reflect the effects and characteristics inside the SCC and its subsystems.

The successful validation/calibration of the underlying models of the CFD simulation with the obtained data from the SCC paved the way for the next steps along the designated development approach. This phase involved creating a parametric model of the combustion system with methanol/ammonia serving as a primary fuel and diesel as pilot source (Figure 1: step 5). To validate this 1-D model, simulations with the SCC domain were utilized and subsequently, the resulting tool was employed to forecast engine performance parameters for the laboratory test engine platforms where the X-DF-A as well as X-DF-M combustion concepts are tested and validated (Figure 1: step 6).

Furthermore, the agreeing results gave high confidence in applying the developed models to design the combustion system for the first production engines along the announced portfolio program. This proactive approach allows for concurrent development and refinement, optimizing the timeline from concept to production.

2. Experimental Setup

2.1. Spray Combustion Chamber SCC

This unique experimental research test facility enables comprehensive investigations into injection behavior, spray/fuel admission characteristics, ignition/combustion dynamics, and subsequent emission formation. The versatile setup allows for experiments under engine-like conditions, with peak firing pressures up to 20 MPa, relevant for large marine engine combustion systems representative of smaller-size two-stroke and larger four-stroke engine configurations.

To achieve the high pressure and temperature conditions of the gas prior to fuel injection, two pressurized vessels are filled with air or a desired gas mixture (e.g. non-reactive, EGR). By precisely controlling the filling time of the two main valves, pressurized gas from the pressure vessels enters the regenerator and is heated to a temperature comparable to that after the compression stroke. A specially designed intake system between the regenerator and SCC reproduces the strong gas swirl motion within the combustion chamber, mimicking conditions in real engines from WinGD [6-10].

The fuel injection system at the SCC has been further refined and developed with dedicated conditioning and supply systems installed for various fuels [5]. As illustrated in Figure 2, the SCC is capable of investigating high-pressure injected fuels (e.g. methanol, ammonia). To ignite these future fuels, an upstream injector delivers a small amount of diesel to initiate and enhance the subsequent combustion of the downstream main injection.

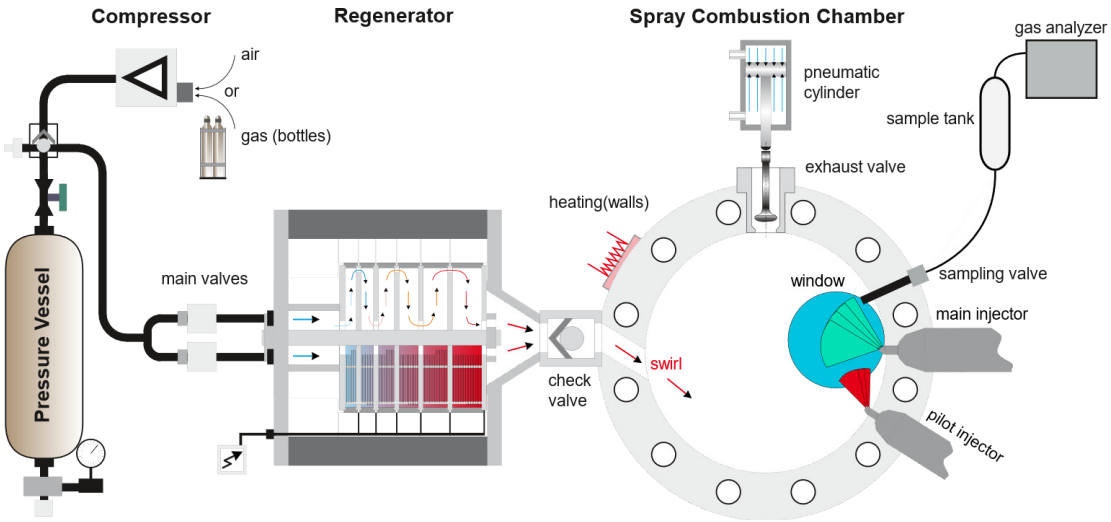

Figure 2: Schematic of the spray and combustion chamber test rig with the associated devices for charge conditioning (pressure, temperature) as well as piloted high-pressure fuel injection setup and emission sampling system.

A specially designed exhaust gas sampling system enables the precise collection of exhaust gas during or after combustion, which can then be analysed using advanced emission measurement devices to accurately quantify the concentrations of individual chemical species present in the exhaust. This system allows for real-time sampling and high-precision collection methods, ensuring the integrity of the

samples throughout the analysis process. With the aforementioned fuels, formaldehyde, nitrous oxide, and ammonia are of particular interest due to their significant environmental impact and role as indicators of combustion efficiency. The ability to accurately measure these compounds provides valuable insights for emissions research and the development of cleaner combustion technologies.

Optical accessibility is provided through sapphire windows with diameters up to 180 mm, offering exceptional clarity and durability for visual observations. The combustion chamber is equipped with eccentric window holders and fixed window positions in a rotatable cover, enabling comprehensive visual access to any location within the chamber.

2.2. Optical Diagnostics and Data analysis

The optical setup used for the experiments on the SCC consists of four high-speed CMOS cameras (3x Photron NOVA S16, 1x Photron HSS6) together with a lens-coupled image intensifier (LaVision IRO) and a pulsed diode laser as a light source (Cavitar Cavilux).

The schematics of the optical setup used for various injection and combustion studies are depicted in Figure 3. Camera 1 captures the Mie-scattering from the fuel spray, which is illuminated by an expanded diode laser beam. A tele-zoom lens attached to the camera provides magnification, enhancing the spatial resolution and allowing for detailed visualization of the spray's structure, atomization, and evaporation. Cameras 2 and 3 cover an identical field of view, but the light is separated by a dichroic mirror. The visible part is transmitted and directed by a second mirror towards Camera 2, which acquires colour images of the flame luminosity. These images enable detailed study of flame propagation and characteristics. The light with a wavelength below 400 nm is reflected by the aforementioned dichroic mirror and used for OH*-chemiluminescence imaging. For this purpose, Camera 3 is equipped with a band-pass filter at 310 nm, an UV-lens, and a lens-coupled image intensifier. This optical technique enables the detection of spatial initiation of ignition and combustion in the intensified, non-visible wavelength range. Moreover, a newly developed ultra-wide angle high-speed imaging setup (camera 4) is implemented to record not only the flame characteristics near the nozzle but also its propagation through the entire combustion chamber. This setup provides unique and unprecedented insights into the combustion system of a large two-stroke Diesel engine.

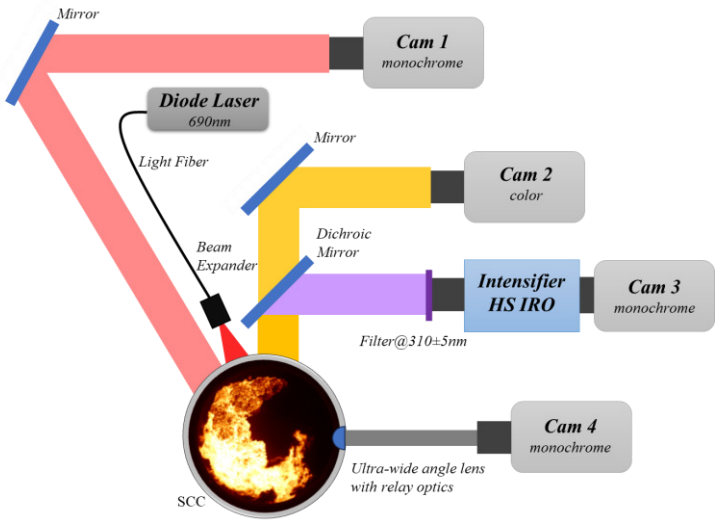

Figure 3: Schematic of optical measurement setup applied at the SCC with simultaneous Mie-scattering, OH-chemiluminescence and flame-luminosity in both, near nozzle and ultra-wide angle view.*

The heat release rate (HRR) is calculated via the pressure and temperature trace measured in the SCC. In order to consider the heat losses for the rate of heat release, which are additionally increased due to the high swirl velocities present during filling and combustion, the derivative of the pressure signal before and after the combustion is analysed. Hence, the heat losses before start of combustion as well as after its ending are calculated and corrected, accordingly. As a simplification, the heat losses during the combustion are linearly approximated.

3. Combustion Visualization and Characteristics

The SCC played a pivotal role in developing WinGD's methanol and ammonia engines by facilitating the first-ever combustion of both fuels in a large two-stroke combustion system environment. Its unique capability to optically study ignition and combustion processes at these length scales provided highly valuable reference data for CFD validation, complementing conventional engine data such as heat release calculated from in-cylinder pressure as well as emission characteristics provided by the advanced exhaust gas sampling system. Example data of a single pilot/main injection configuration and detailed analyses will be explained in the following sections.

3.1. Methanol

The methanol combustion characteristics are described via an exemplary experiment conducted at a typical engine operating condition of 50% load with pressure and temperature before the injection being 116 bar and 860 K, respectively. For this experiment, the fuel flexibility of the SCC [5] allowed a rapid exploration of a new fuel as without changing the standard (diesel) injector positions, one injector could be converted to methanol operation, while its upstream counterpart was operated with diesel for piloting. For subsequent measurements, the position of the pilot injector was brought closer to an engine-like setup with a shorter distance between the two injectors.

The timing of the pilot injector was set to ensure the pilot flame reaches the methanol spray way before conditions allowed a self-ignition of methanol. In the first image in Figure 4 at 5.4 ms after start of pilot injection, the pilot flame is approaching the position of the main injector, which just has started injecting liquid methanol. The second image (at 7.4 ms) captures the moment where the diesel pilot flame first contacts the methanol spray. An instant ignition of the methanol fuel occurs at this time and location. Subsequent images (at 8.4 and 11.4 ms) show the propagation of the methanol flame throughout the spray, eventually reaching a stable lift-off length from the injector.

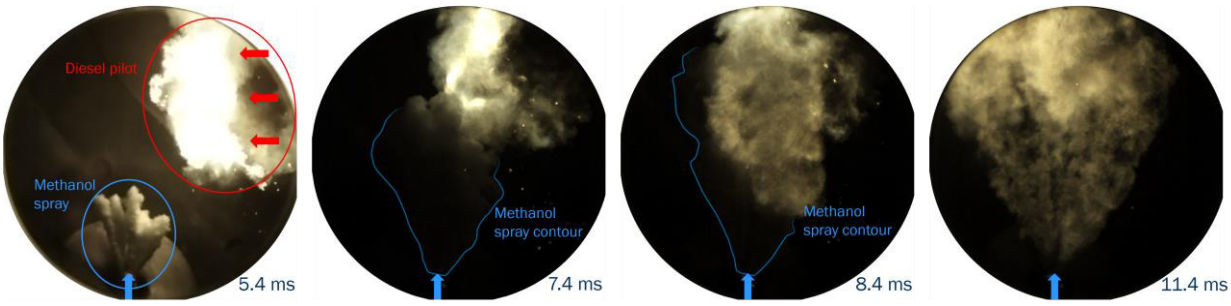

Figure 4: Flame luminosity image sequence showing the diesel piloted (red) high-pressure methanol (blue) injection and combustion process (near main injector view).

Besides the high-speed image acquisition, also relevant pressures and temperatures are recorded in the combustion chamber. From these signals the rate of heat release can be derived, which is a key

parameter for the characterization of combustion phenomena and provides valuable insights into the combustion process. Figure 5 is showing the HRR and the corresponding cumulative heat release in relation to the aforementioned experiment.

For this measurement configuration and pilot/main timing, the added heat from the pilot combustion as well as the exact ignition time can be clearly recognized in the graph. Following the methanol ignition, the initial peak is attributed to the premixed part of the combustion which occurs until a stable flame is established. After this premixed peak, the combustion is followed by a transition to fuel-air mixing controlled phase, resulting in a distinctive diesel-like heat release rate shape.

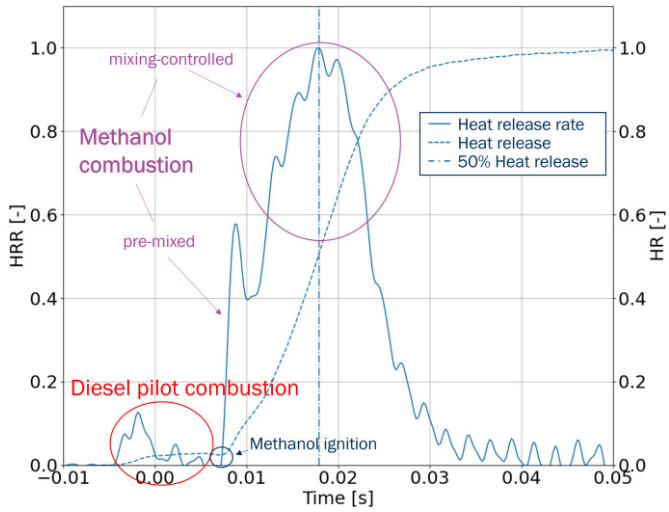

Figure 5: Heat release characteristics of a diesel pilot-ignited high-pressure injected methanol combustion.

During these comprehensive investigations of methanol combustion, a large variety of different conditions including variations in injection pressure, gas temperature/pressure, pilot and main energising time and timing, atomizer execution, pilot-to-main setup and main injector temperature were examined. Under each condition the before mentioned signals as well as the derived heat release rate were explored, exhaust emissions and high-speed images were analysed. The resulting dataset served as basis for validating and calibrating our 0/1-D and 3-D simulation models, which are described in subsequent sections.

3.2. Ammonia

Hereafter, the experiments from the first-ever ammonia combustion in a large two-stroke engine combustion system environment are presented. The optical data was acquired using an ultra-wide-angle camera inserted into center of the combustion chamber cover, enabling comprehensive investigations of the pilot ignition/combustion, and subsequent ignition of the liquid-injected, atomized, and evaporated ammonia throughout the entire combustion chamber. As with the methanol case, this experiment was conducted at the same operating condition with pressure and temperature before the injection being 116 bar and 860 K, respectively.

In Figure 6, the first image (at 5 ms after start of main injector energising) captures the diesel pilot flame directed towards the main injection. The intense luminosity of the soot from the diesel flame leads to a very high exposure signal of the pilot spray in the recordings but also illuminates the liquid ammonia injection. In order to visualize the various characteristics of the diesel piloted high-pressure ammonia combustion, the images have been individually intensity corrected. The not yet fully ignited

ammonia spray can be clearly distinguished in the second image (at 10 ms) as a dark cloud within the bright diesel pilot flame. As the combustion of the ammonia proceeds, the turbulences increase, causing the pilot flame to become fragmented and dimming the overall exposure (image 3 at 15 ms). The heavily intensified images 4-6 (20 - 30 ms) reveal the propagation of the ammonia flame through the combustion chamber as the overall illumination by the remaining diesel pilot rapidly decreases.

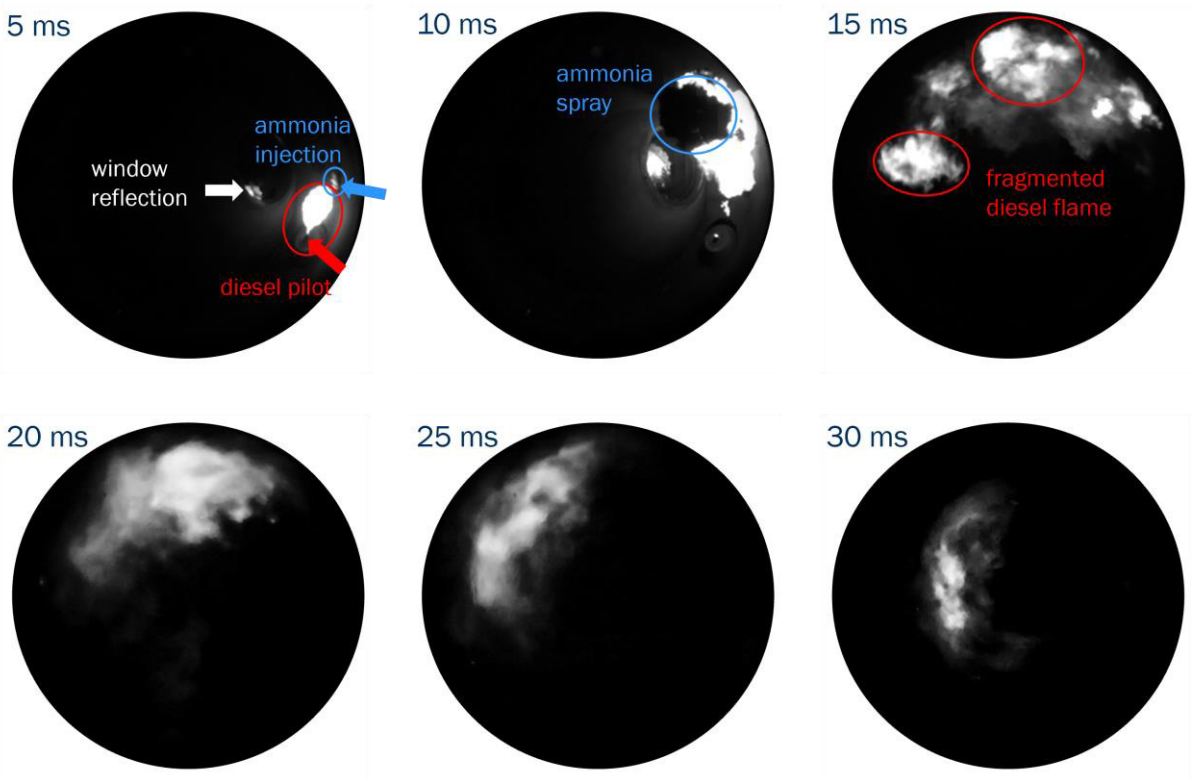

Figure 6: Flame luminosity image sequence of a diesel piloted (red) ammonia (blue) ignition and combustion process between 5 ms and 30 ms after start of main injector energizing (ultra wide-angle view).

Figure 7 shows the derived rate of heat release for the ammonia combustion. With the pilot/main injector setup and timing for this experiment, the diesel pilot combustion is directly followed by the ammonia combustion and thus no distinct separation in the HRR plot can be recognized. The HRR for a piloted ammonia combustion related to a large two-stroke engine system can be divided into two distinct phases: The first phase, starting with the ignition of the ammonia by the diesel pilot flame, is mainly governed by the premixed combustion of the injected ammonia. After a short transition phase where the HRR decreases significantly, the second phase of the ammonia combustion can be observed. At this stage the HRR is generally governed by the mixing rate but also significantly superimposed with (comparably slow) chemical reaction rate of ammonia. As the gas pressure and temperature are rising during the combustion, the chemical reaction rate accelerates, leading to a steady increase in HRR until fuel availability decreases (the ammonia injection has stopped slightly before the peak in the second phase, ca. at 40 ms) and the HRR slowly drops to zero.

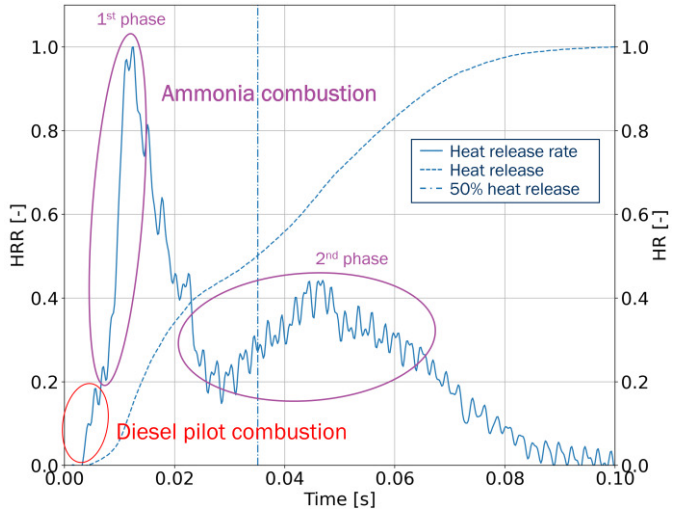

Figure 7: Heat release characteristics of a diesel pilot-ignited high-pressure injected ammonia combustion.

In a similar manner, to gather a vast data set for the validation and calibration of our simulation models, different variations were studied, such as injection pressure, compression pressure and temperature, energising time, pilot timing, main injector temperature, main injector configuration, swirl and a variety of different piloting strategies.

In this contribution for each fuel (methanol and ammonia) only the flame luminosity high-speed visualizations are exemplarily shown (colour camera and ultra-wide angle camera setup). It is worth noting that for the vast majority of experiments conducted under this experimental campaign, all available imaging systems were used for both fuels. Furthermore, the presented results show a single pilot/main in order to focus on the validation and calibration of the main phenomena such as the injection and spray formation as well as combustion model adjustments where these data already generate a highly valuable reference data set. Subsequently, experiments with multiple single pilot/main injector setups have been performed and are under evaluation.

4. Simulation Toolbox: Validation and Calibration

CFD simulations are invaluable tools for both design-oriented and research-oriented activities, as they enable the exploration of new designs - such as injectors with different features or changes in engine geometry - without the high costs and long lead times associated with manufacturing new parts or operating the engine. These simulations can quickly deliver results and provide detailed local information about what occurs inside the cylinder with very fine resolution. This capability is crucial for our application, as the operating costs for testing a two-stroke engine are exceptionally high and many tests can be efficiently conducted in a virtual environment using CFD. However, to ensure the accuracy of CFD models, they must be validated against real-world data by comparing results from simulations with experimental data. In our case, we compare performance parameters such as pressure, apparent heat release rate (AHRR) and emissions, as well as the morphology of the flame. These comparisons are challenging and expensive to perform directly on the engine, particularly in the early stages of development where design and manufacturing of most of the components is still not consolidated. Furthermore, safety precautions can be considered within a much smaller framework, and it results in an environmental benefit when comparing with full size engine testing. Therefore, the initial step in validating our models occurs within the SCC, where the geometrical characteristics and

ambient conditions (pressure, temperature and swirl) closely resemble those of the engine. This controlled setup allows us to compare simulations and experiments while accessing detailed information, such as flame and spray features, that would not be available in engine tests.

For this numerical campaign, 3-D CFD simulations were conducted using CONVERGE, which offers a range of combustion and spray models as well as meshing features specifically designed for simulating internal combustion engines. The combustion process was modelled using the SAGE combustion model [11] which relies on detailed kinetics. The simulations covered both the filling process of the SCC and the combustion phase, using time-varying boundary conditions and initial conditions derived from experiments. This approach ensured an accurate description of the flow field inside the SCC at the start of injection (SOI).

The computational grid employed for the simulations had a base size of 2.5 mm, with local refinements in the regions near the diesel and ammonia/methanol injectors. An adaptive mesh refinement (AMR) technique, based on velocity, temperature, and species gradients, was used to more precisely describe the ignited jet, achieving a minimum mesh size of approximately half the injector nozzle diameter. This mesh resolution is crucial for maintaining contained void fraction values, which are essential for the KH-RT breakup model used in this investigation to accurately predict spray morphology and evaporation. Lastly, turbulence was modelled using the RANS approach with the well-known two-equation k-ε model.

4.1. Methanol Simulation Results

In this section, the main results for the comparison and validation of the CFD model to experimental results for methanol will be presented. In Figure 8, a comparison between the normalized experimental and CFD AHRR is shown for the three energizing times (15, 20 and 25 ms) at 50% load conditions (116 bar and 860 K before start of main injection). The normalization was done on the basis of the maximum experimental HRR. In general, the pilot ignition delay is well captured, with just a slight overprediction by the CFD in comparison to the experiment, and the peaks of the pilot combustion are well matched. Additionally, it can be observed, especially from the CFD AHRR curves, that there is a small premixed portion of the combustion. A small peak can also be seen in the experimental HRR but it is less pronounced as in the simulation curve which partly can be attributed to the signal processing of the experimental raw data of the pressure measurement. The transition from premixed combustion to mixing controlled is slightly slower in the CFD than the AHRR computed from the experiment. However, the overall combustion duration, heat release peak and fall off are in good agreement with the experiment, the last being a critical factor in NO_x formation prediction.

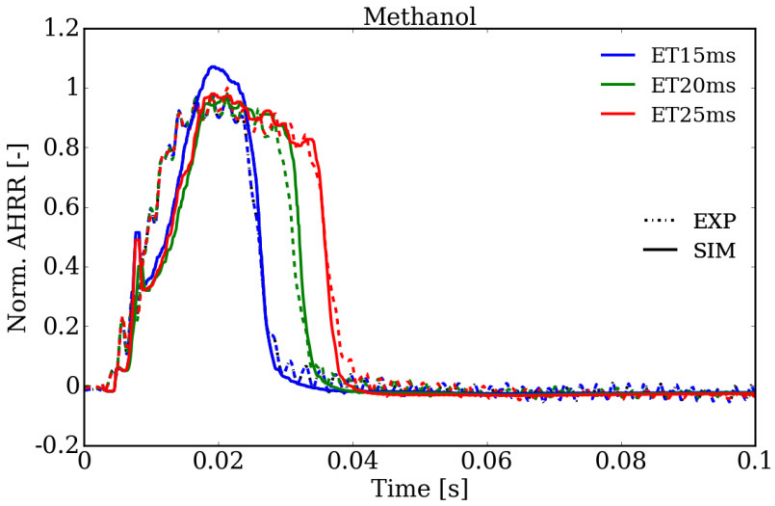

Figure 8: Normalized Apparent Heat Release Rate for methanol combustion at different main injector energising times.

In Figure 9, a comparison of the temporal evolution of the flame is shown at intervals of 5 ms after start of main injector energizing. The top row depicts the CFD results, represented by iso volumes of temperature, while the bottom row shows the experimental images at the same time step, accordingly. The swirl effect of the SCC can also be recognized in the images and generally, the agreement between CFD and experiment in terms of overall shape and location of the tip is very reasonable.

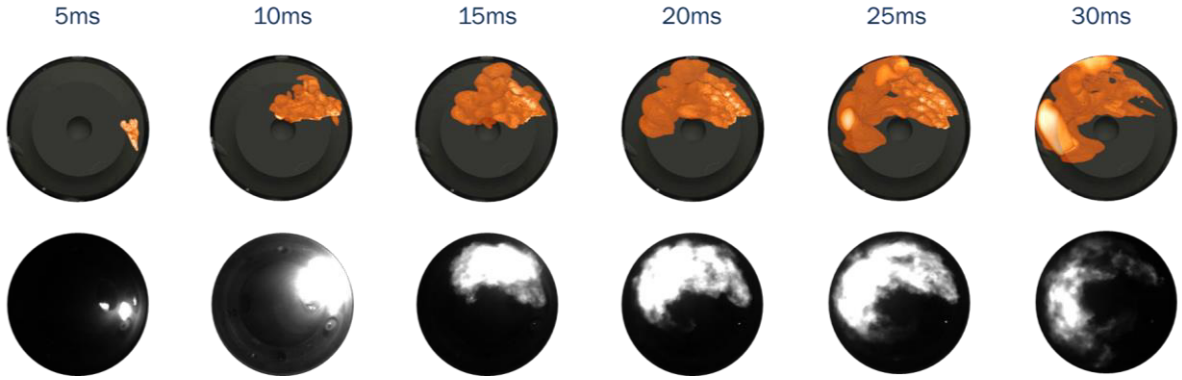

Figure 9: Comparison of the temporal evolution of the methanol flame within the combustion chamber between CFD (top) and experiment (bottom).

Figure 10 presents a bar graph of the NO_x emission comparison between CFD and experiment at the three energising times. An error bar is indicated for the experimental data which was measured as the maximum variation measured for a given condition during multiple instances of the same test. The values are normalized by taking as reference the maximum value from experiments. NO_x of CFD is calculated using an extended Zeldovich mechanism as there is no NO_x path in the used chemical mechanism. Generally, CFD slightly over-predicts NO_x emissions, but the overall trend is well matched as the NO_x increases with longer injection durations.

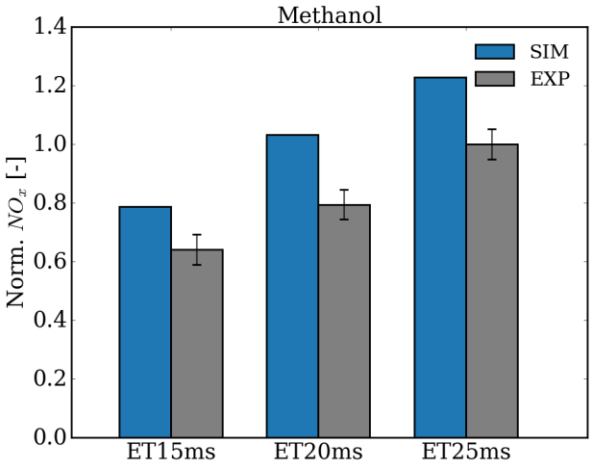

Figure 10: Comparison of normalized NO_x emissions between simulations and experiments at different main injector energising times.

4.2. Ammonia Simulation Results

Figure 11 presents a comparison between the simulated and experimental AHRR curves for an ET variation at 50% load conditions (116 bar and 860 K before start of main injection), with values normalized to the maximum experimental AHRR across all conditions. Qualitatively, the numerical setup successfully reproduces the main characteristics observed in the experiments. The simulations accurately capture ignition delay times for both pilot and main, indicating that the chemical scheme and the interaction between pilot and main injection are well-represented. Additionally, the model accurately identifies the AHRR drop characteristic of conditions with an ET ranging from 30 to 50 ms. This decrease in the AHRR signifies a transition from the first combustion phase, governed by a mostly premixed regime, to a second phase where the prolonged chemical timescales characteristic of ammonia combustion additionally influences the rate at which heat is released. This superimposing phenomenon is due to the significantly longer chemical ignition delay compared to evaporation and mixing times, preventing the ammonia flame from stabilizing under the selected ambient conditions.

The overall combustion duration and the second AHRR peak at the end of injection are also well predicted by the model, demonstrating sensitivity to variations in ET. However, the simulations tend to overestimate the premixed peak, likely due to the underlying assumptions of the combustion model. While the SAGE model provides detailed chemical predictions, it does not fully account for the effects of the turbulence field on the chemical evolution of the combustion. This simplification can lead to a slightly faster ignition of the mixture, resulting in an overestimation of the heat release rate during the premixed phase. Consequently, this overestimation impacts the predicted NO_x emissions, which are generally higher in the simulations, as shown in Figure 12a (values are normalized by taking as reference the maximum value from experiments). Despite this, the model accurately predicts the trend of NO_x emissions variation with energizing time, indicating higher NO_x emissions for longer injections.

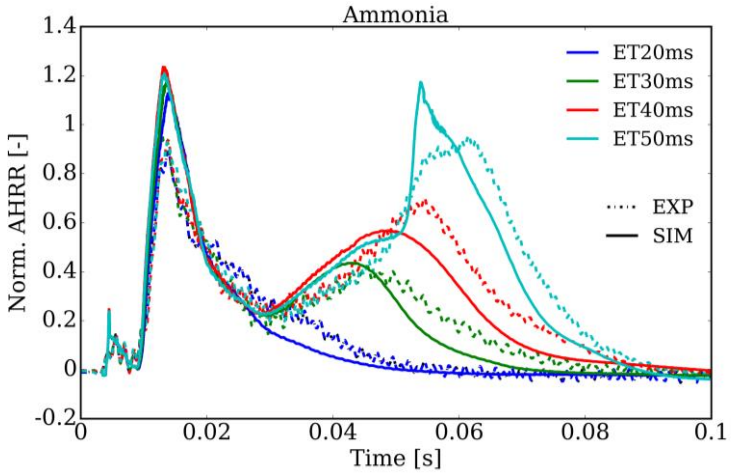

Figure 11: Normalized Apparent Heat Release Rate for ammonia combustions at different main injector energising times.

Figure 12b illustrates that NO_x production occurs in two phases: an initial phase during the premixed combustion event, followed by stabilisation during the transition phase between combustion regimes and a second production phase.

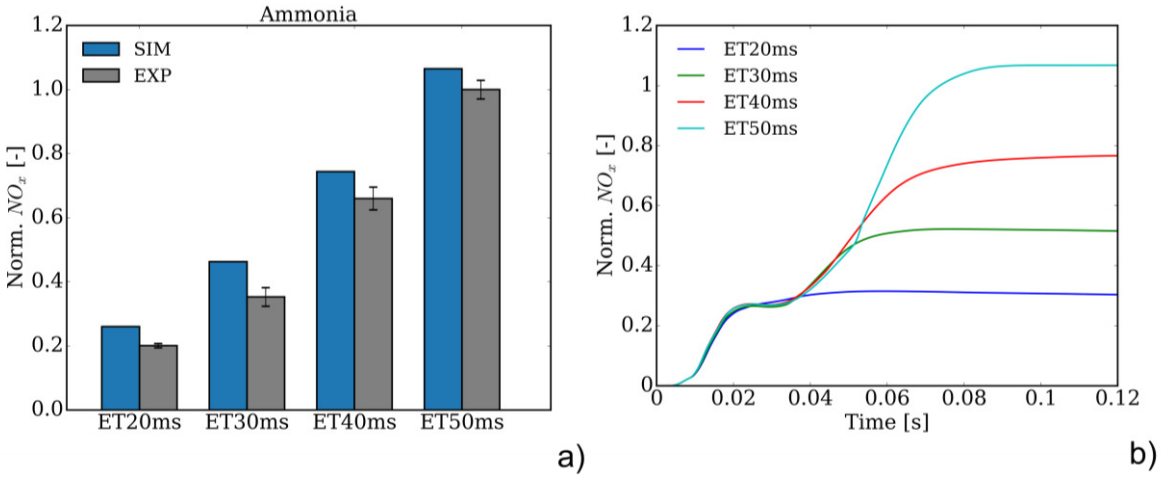

Figure 12: Comparison of normalized NO_x emissions between simulations and experiments at different main injector energising times (b) as well as time-resolved NO_x simulation values (a).

In Figure 13, temperature, NO mass fraction and equivalence ratio are shown on a slice cutting through the main ammonia jet. The ignition of a largely lean ammonia-air mixture is evident, leading to the initial production of NO_x in the ignited region of the ammonia jet. The figure also illustrates the inability of the ammonia flame to stabilize, causing the lift-off length to increase steadily during the combustion process. Consequently, combustion occurs far from the nozzle tip, while, in the vicinity of the injector, a significant amount of ammonia is left to mix with the surrounding air without participating to this stage of the combustion. The process is then largely governed by ammonia's chemical timescales, which control the rate of fuel consumption. As pressure and temperature rise within the SCC, the mixture's reactivity increases, enhancing the fuel's burning rate and causing the second peak shown in Figure 10. Following this peak, the scarcity of ammonia in the SCC leads to a gradual decrease in AHRR until the combustion process is complete.

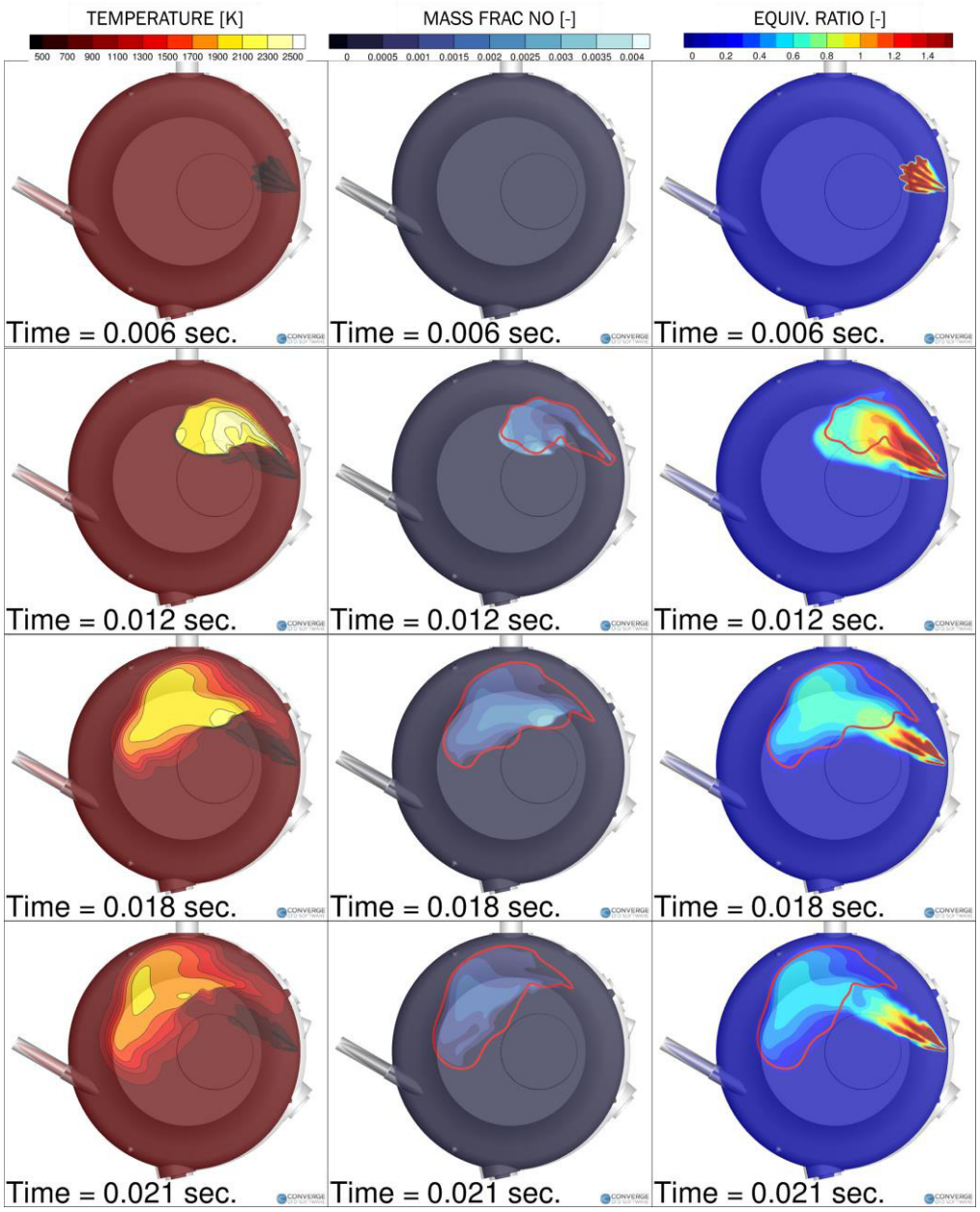

Figure 13: CFD results for ammonia combustion showing temperature (left), NO mass fraction (middle) and equivalence ratio (right) fields. The highlighted red line represents an iso-line of temperature at 1200 K. The condition showed here is that with ET of 30 ms for the main injection.

When discussing ammonia combustion, one significant concern is the production of nitrous oxide (N_2O) emissions. N_2O is a potent greenhouse gas with a global warming potential of 298 times that of CO_2 over a 100-year period [12]. In Figure 14, a comparison between experimental and simulated values of N_2O emissions is presented (values are normalized by taking as reference the maximum value from experiments.). It is observed that the CFD model consistently overestimates the production N_2O compared to experimental data. While this indicates that there is a potential for further improvement in the chemical mechanisms used in the simulation, it also provides a conservative estimate when applied to real engine scenarios. This conservative nature of the CFD model ensures that any predictions made will likely overestimate the actual emissions, providing a safer margin for engine performance considerations.

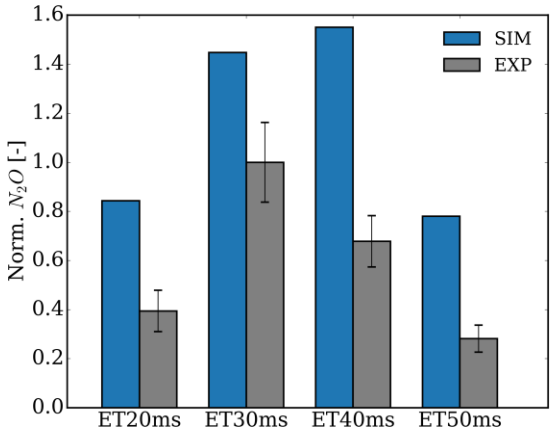

Figure 14: Comparison of normalized N_2O emissions between simulations and experiments at different main injector energising times.

4.3. Methanol 0/1-D Modelling Results

The prediction of engine performance and emissions is a necessity in the development of marine engines, since the number of engines with the exact same configuration is small and engines with new configurations or fuels are potentially sold way before they are built. For this reason, a combustion and emission model methodology has been developed for integration into a one-dimensional engine simulation environment. According to the presented approach in this contribution, the methodology has been adapted for the methanol as well as ammonia combustion system development. Hereafter, the corresponding considerations are exemplarily described for the methanol application.

The CFD investigation showed along with the measurements, that for diesel as well as for methanol, the majority of the fuel is converted in a mixing controlled manner. Therefore, a simplified combustion model has been developed, which was calibrated using the measured heat release rate from the spray combustion chamber. The combustion model describes only the mixing controlled combustion phase. It uses an underlying spray model and nozzle characteristics to estimate the turbulent kinetic energy and dissipation rate from the fuel spray. In addition, the combustion chamber background turbulence level is estimated. The goal of the spray-based combustion model is to reproduce the characteristic mixing rate. The characteristic mixing rate ν_{mix} is defined as follows:

$$\nu_{mix} = \frac{HRR(t)}{Q_{avail}(t)} = \frac{HRR(t)}{\int_0^t \left(\dot{q}_{inj}(t) - HRR(t)\right) dt} \tag{1}$$

This simplified definition of the characteristic mixing rate follows the assumptions that the ignition delay is insignificant in contrast to the injection duration and the evaporation time of the fuel is insignificant in contrast to the mixing of the air and the fuel. The injected energy (blue, diesel), the heat release rate (red) and the according characteristic mixing rate (black) are depicted in Figure 15. The figure shows three operating conditions with a variation in injection duration: a short (dashed), a medium (solid), and a long injection duration (dash-dotted). The mixing rate during injection is increasing due to the increase of pressure during combustion. This effect is particularly strong in the spray combustion chamber due the absence of an expanding volume. The small drop in mixing rate after injection indicates a high background turbulence level, which is originating from the spray combustion chamber filling process.

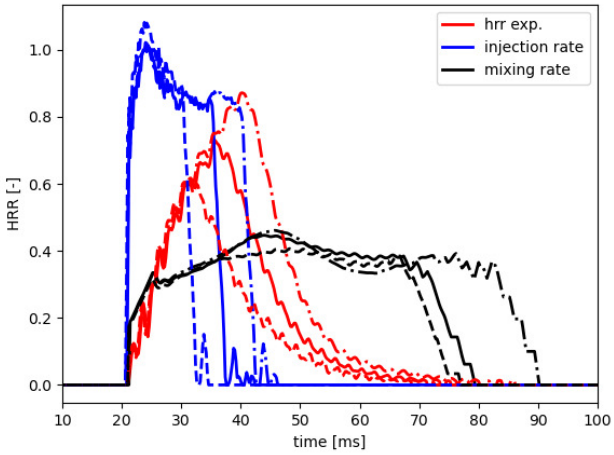

Figure 15: Injected energy rate (blue), heat release rate (red) and mixing rate (black) of three different diesel injection durations (dashed, solid, dash-dotted).

Figure 16 shows the measured versus modelled heat release rates after calibrating the turbulence parameters in the combustion model. The injection and the heat release rate are equally coloured as in the previous figure, the modelled heat release rate is plotted in black. The modelled heat release rate shows a very high accuracy to the measured one.

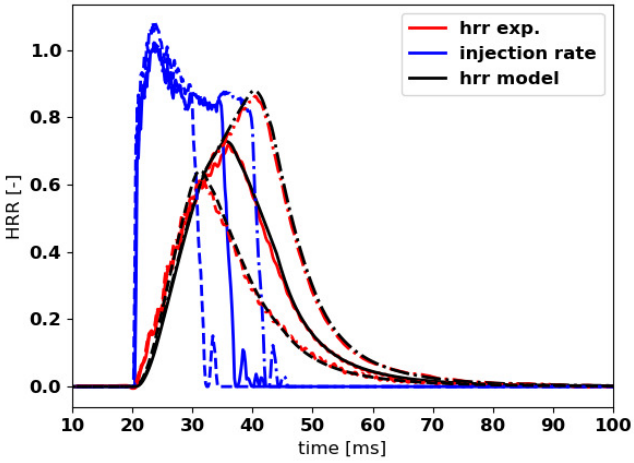

Figure 16: Injected energy rate (blue), measured heat release rate (red) and modelled heat release rate (black) of three different diesel injection durations (dashed, solid, dash-dotted).

The model calibration has been minorly adapted and applied to three different operating conditions using methanol as a fuel (and a small percentage of diesel to support the ignition). Figure 17 shows the injected energy rate (blue, methanol), the measured heat release rate (red) and the modelled heat release rate (black) for three different injection durations (solid, dash-dotted and dashed). In contrast to diesel, methanol shows a significantly reduced lower heating value. In addition, due to the oxygen content of methanol, the stoichiometric air-to-fuel-ratio is lower. As a consequence, the required time to mix to stoichiometry is shorter for similar spray conditions. Consequently, the combustion rate is higher and the heat release rate is closer to the profile of the injection rate. The results show that this type of model is very well capable to reproduce this combustion behaviour.

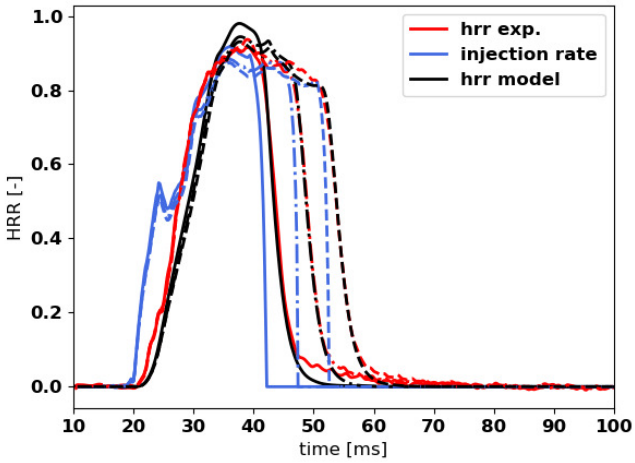

Figure 17: Injected energy rate (blue), measured heat release rate (red) and modelled heat release rate (black) of three different methanol injection durations (dashed, solid, dash-dotted).

This combustion modelling methodology was then transferred to an engine simulation environment, where the combustion model could also be calibrated using inputs from CFD. This setup allowed engine simulations with broad variations in operating conditions at minimum computational costs and experimental effort, which have been used for determining the best selection of injection system layout as a basis for the subsequent optimisation of the associated parameters.

5. Conclusions

The rapid development of methanol and ammonia technologies for large two-stroke marine diesel engines has indeed required a fundamental understanding of fuel injection, spray formation, ignition behaviour, combustion characteristics, and emission formation. WinGD's dedicated spray combustion chamber enables detailed investigations of key components and parameters early in the technology development process. The exemplary visualizations and characteristics of the diesel-piloted high-pressure injected methanol and ammonia combustion provide an insight into the investigations for an in-depth understanding of the underlying phenomena. This is especially important when focusing on the unique behaviour of the onset of combustion by the pilot as well as the subsequent heat release of methanol and, in particular, ammonia.

Generating this highly valuable reference data set enabled the application of a robust frontloading strategy. It includes information on hydraulic injector performance, injection behaviour and spray formation as well as important characteristics of the piloted main ignition and combustion process at various cell conditions and configurations (e.g. pilot/main energizing time and timing, injection pressure, injector temperature and atomizer configurations). Furthermore, the investigations were complemented with essential insights into emission formation and characteristics.

The presented approach heavily emphasizes numerical development tools, validated and calibrated by a comprehensive set of measurements from SCC experiments. For methanol as well as ammonia a selection of CFD simulations is shown, highlighting the validation and calibration procedure to further develop or adjust the sub-models for the spray formation, the combustion model and subsequent emission formation. These detailed investigations revealed the similarities of the methanol combustion process with diesel but even more interesting the peculiarities of a not mainly mixing-controlled combustion phase when operating ammonia at the conditions found in a large two-stroke engine

combustion system. The simulation outcomes demonstrate excellent concordance with the experimental findings, accurately reflecting the main characteristics of combustion for both methanol and, notably, ammonia. The models' performance in capturing these processes enables a high degree of confidence in the related results.

Finally, the successful validation and calibration of the underlying models paved the way for creating a parametric 1-D model of the combustion system in an engine simulation environment with methanol/ammonia as the primary fuel source. The combined efforts of CFD investigations and experimental measurements gave a detailed insight into the combustion processes of both diesel and future fuels. These findings have important implications for understanding and modelling the combustion dynamics in large two-stroke marine engines which has been exemplarily demonstrated for the methanol combustion in this contribution.

In addition to the simulation toolbox development, the application of the presented approach resulted in identifying challenges of the methanol/ammonia injection and combustion process at an early stage of the technology development. For instance, the injection behaviour or the detection of possible locations of unburnt (e.g. NH_3 slip) or not completely burnt fuel such as N_2O, when referring to ammonia. Furthermore, this methodology is very cost-efficient and agile allowing for quick iterations between experiments and simulations.

The confidence gained from these numerical tools has allowed WinGD to apply the developed models to design combustion systems for the first production engines in their announced future fuel portfolio program.

Literature

[1] International Maritime Organization, "Resolution MEPC.377(80) – 2023 IMO Strategy on Reduction of GHG Emissions from Ships", 2023

[2] Global Maritime Forum, "The implications of the IMO Revised GHG Strategy for shipping", July 2023

[3] Schneiter, D., Goranov, S., Krähenbühl, P., Schäpper, D., Spahni, M., Weisser, G., "WinGD's X-act initiative: A holistic approach towards sustainable shipping", 18th Symposium "Sustainable Mobility, Transport and Power Generation", 2021

[4] Weisser, G., Goranov, S., Krähenbühl, P., Holtbecker, R., Zagorskiy, A., Schneiter, D., "Outlook on a decarbonised future of international shipping and how WinGD can contribute", 19th Symposium "Sustainable Mobility, Transport and Power Generation", 2023

[5] Hensel S., Gerber P., Karrer I., Schleppe Th., Schmidle M., Süess P., von Rotz B., Liu Bo: "Preparing for future demands – the CSSC Global 2-stroke Test Center", CIMAC 2023, Busan

[6] von Rotz B., Herrmann K., Weisser G., Cattin M., Bolla M. and Boulouchos K., "Impact of evaporation, swirl and fuel quality on the characteristics of sprays typical of large 2-stroke marine diesel engine combustion systems", ILASS-Europe, 2011.

[7] Herrmann K., Kyrtatos A., Schulz R. and Weisser G., von Rotz B., Schneider B. and Boulouchos B., "Validation and Initial Application of a Novel Spray Combustion Chamber Representative of Large Two-Stroke Diesel Engine Combustion Systems", ICLASS, 2009.

[8] Schmid A., von Rotz B., Bombach R., Weisser G., Herrmann K., and Boulouchos K., "Ignition Behaviour of Marine Diesel Sprays", COMODIA, 2012.

[9] von Rotz B., "Experimental Investigation of Spray Characteristics and Ignition Processes at Conditions representative of Large Two-Stroke Marine Diesel Engines", PhD thesis, No. 22968, ETH Zurich, 2015.

[10] von Rotz B., Herrmann K. and Boulouchos K., "Experimental Investigation on the Characteristics of Sprays Representative for Large 2-Stroke Marine Diesel Engine Combustion Systems", JSAE 20159074, 2015.

[11] Senecal P. K., "Multi-Dimensional Modeling of Direct-Injection Diesel Spray Liquid Length and Flame Lift-off Length using CFD and Parallel Detailed Chemistry", SAE, 2003-01-1043, 2003.

[12] Solomon, S., Qin D., Manning M., Chen Z., Marquis M., Averyt K.B., Tignor M., "Fourth Assessment Report of the Intergovernmental Panel on Climate Change", 2007, Cambridge University Press, Cambridge, United Kingdom and New York, NY, USA.

Keywords: CFD, Simulation, Combustion, Methanol, Dual Fuel

Development of dual fuel methanol engine using CFD techniques for PFI and HPDI injection strategies

Dr. Bhuvaneswaran Manickam, Dr. Cornelius Wagner, Dominik Krnac, Dr. Eric Lauer, Peter Holand, Dr. Matthias Auer

MAN Energy Solutions SE

https://doi.org/10.18453/rosdok_id00004635

Abstract

The shipping industry plays a significant role in the global economy, responsible for 90% of world commerce. Moreover, it also accounts for 2 to 3% of global CO_2 emissions. There is increasing pressure on the marine sector to reduce its carbon footprint, and the net CO_2 emissions should reach zero by the end of 2050. The usage of carbon-free fuels such as hydrogen and ammonia are under development and not fully mature yet. Methanol can be a carbon-neutral fuel when produced using green hydrogen and captured CO_2, thus bringing the net CO_2 emissions to zero. It can act as a transition fuel due to easy handling and existing infrastructure for bunkering. Since the ship engines are in operation for up to 40 years, CO_2 neutrality should be achieved for the existing engines in the fleet, as replacing old engines with new ones is uneconomical. Therefore, the retrofit solutions can be an effective and economical way to reduce the net GHG emissions of the maritime industry. Furthermore, when it comes to new engine concepts fueled with methanol, their performance is of utmost importance.

MAN-ES has been working on the development of dual-fuel methanol engines for retrofit solutions and newbuilds. The retrofit solution for the existing engine is achieved by incorporating minor modifications in the intake port and other engine components. The methanol injectors are installed in the intake port, called port fuel injection (PFI), operated at low injection pressure. This reduces not only GHG emissions but also costs for customer. Another approach to bring the methanol into cylinder is the high-pressure direct injection (HPDI) technique, in which methanol is burned in diffusion combustion manner. Pilot fuel is used for igniting methanol in both port fuel and direct injection conditions.

CFD technique can be employed to evaluate the preliminary design of injector and cylinder components and their influence on mixture formation and combustion for PFI and HPDI conditions. Since it is used for the design analysis, it is vital to validate the CFD simulation method. Two experimental configurations are considered for validation, and the results obtained are presented in this paper. The first set of HPDI measurements was conducted at TUM using a Rapid Compression and Expansion Machine (RCEM), and the second at WTZ using PFI methanol injection on a 32/44DF single-cylinder engine (SCE).

The first part presents the CFD simulation results of the RCEM for spray characteristics and methanol combustion. The high-pressure methanol injection is modeled using Huh and Reitz-Diwakar breakup model: The predicted spray angle, penetration length, and shape are compared against experimental data. Two modeling approaches, Extended Coherent Flamelet Model (EFCM) and detailed chemistry were investigated for simulating diesel-ignited methanol combustion. The results of the combustion process are in good agreement with the RCEM experimental data for the variation of methanol injection timing and the interaction angle between the methanol and diesel spray.

In the second part of the paper, the simulation results of the SCE engine for PFI methanol injection are presented for the variation of engine load and air/fuel ratio. The CFD results gave insights into methanol evaporation in the intake port, and mixture formation in the cylinder, which is vital for combustion stability and emissions. The simulation methods for HPDI and PFI methanol combustion will be further employed to facilitate the development of MAN's methanol engines for reducing GHG emissions.

1. Introduction

The shipping industry plays a significant role in the global economy, responsible for 90% of world commerce. Moreover, it also accounts for 2 to 3% of global CO_2 emissions. There is increasing pressure on the marine sector to reduce its carbon footprint, and the net CO_2 emissions should reach zero by the end of 2050 as enforced by the International Maritime Organisation (IMO). To achieve the future emission requirement, the ship engine manufacturers are focusing on using alternative fuels and drive concepts in the maritime sector. The usage of carbon-free fuels such as hydrogen and ammonia are under development and not fully mature yet. Methanol can be a carbon-neutral fuel when produced using green hydrogen and captured CO_2 or biomass, thus bringing the net CO_2 emissions to zero [1].

Methanol is considered as one of the most favourable alternative fuels due to its renewability, cost, and its combustion characteristics due to the presence of the hydroxyl group. As it has a single carbon atom, it cannot easily form particulate matter from long-chain hydrocarbons when compared to other alcohols. It has a high-octane rating and, thus has higher knock resistance and can be used at high compression ratios [2]. However, for CI engines, usage of methanol can be challenging due to its low Cetane number and latent heat of vaporization which is four times than that of diesel. Due to this high ignition temperature and being in liquid at standard temperature pressure (STP), methanol is safer to store, and transport. Considering all the mentioned properties of methanol, easy handling, and existing infrastructure for bunkering, it can act as a transition fuel before moving into carbon-free fuels in the future. Since the ship engines are in operation for up to 40 years, CO_2 neutrality should be achieved for the existing engines in the fleet, as replacing old engines with new ones is uneconomical. Therefore, the retrofit solutions can be an effective and economical way to reduce the net GHG emissions of the maritime industry. Furthermore, when it comes to new engine concepts fuelled with methanol, their performance is of utmost importance.

MAN Energy Solutions SE has been working on the development of carbon-free and carbon-neutral fuel engines, such as dual-fuel methanol/diesel engines for retrofit solutions and newbuilds [3]. Different fuel admission and combustion concepts were evaluated based on ease of retrofit, costs, time to market, and performance. PFI and HPDI injection strategies are considered for fuel injection that leads to premixed Otto-like and Diesel-like diffusion combustions respectively [4] [5]. The retrofit solution for the existing engine is achieved by incorporating minor modifications in the intake port and other engine components. The methanol injectors are installed in the intake port, called port fuel injection (PFI), operated at low injection pressure. This reduces not only GHG emissions but also costs for customers. Another approach to bringing the methanol into a cylinder is the high-pressure direct injection (HPDI) technique, in which methanol is burned in a diffusion combustion manner. Pilot fuel ignites methanol in both port fuel and direct injection conditions. The PFI technique will be implemented in MAN's 48/60 and 51/60 engine platforms and for the 21/30 genset engines. Moreover, the HPDI methanol injection method will be introduced in new builds and retrofit solutions to the newly developed 32/44 and 49/60 engine platforms [5].

CFD technique can be employed to evaluate the preliminary design of injector and cylinder components and their influence on mixture formation and combustion for PFI and HPDI conditions. Since it is used for the design analysis, it is vital to validate the CFD simulation method. Two experimental configurations are considered for validation, and the results obtained are presented in this paper. The first set of HPDI measurements was conducted at TUM using a Rapid Compression

and Expansion Machine (RCEM), and the second at WTZ using PFI methanol injection on a 32/44DF single-cylinder engine (SCE).

2. Experimental Setup and Data

2.1. Rapid Compression and Expansion Machine (RCEM)

For the HPDI methanol-diesel combustion, experiments were carried out using a RCEM setup by Scharl et al. [6], the obtained measurement data are used for the current CFD validation. The RCEM is a pneumatically driven engine that mimics the stroke motion of an internal combustion engine, particularly in the top dead center (TDC) area, and thus permits investigations under engine conditions. Figure 1 shows the schematic overview of RCEM with piston, fuel injectors, and optical measuring equipment.

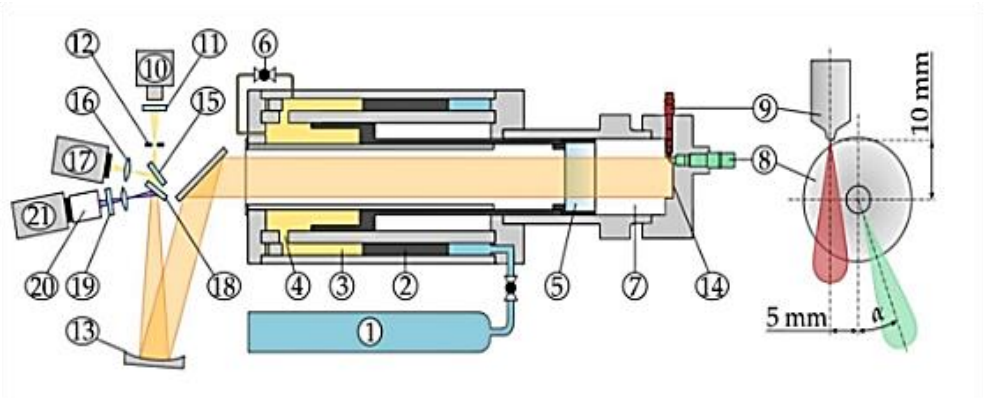

Figure 1: RCEM experimental setup with optical measurement (left), engine (middle) and injector arrangement (right). Components: (1) compressed air bottles, (2) driving piston, (3) hydraulic oil, (4) orifice holes, (5) working piston, (6) bypass valve, (7) combustion chamber, (8) methanol injector, (9) diesel injector, (10) arc lamp, (11) UV filter

For each experiment, air in the cylinder is compressed from its initial state to the required final pressure and temperature at the top dead center (TDC). Two operating conditions such as OP1 and OP4 are considered for the spray validation in which the final pressures are 75 and 125 bar as shown in Table 1. Around TDC, diesel and methanol are injected via the injectors with variable arrangement. The diesel injector (9) is a single-hole injector while the methanol injector (8) is a double-hole injector with an angle of 30° between the individual holes. The diesel injector is the pilot injector with an axially mounted nozzle with a diameter of 0.2 mm, which is designed for injections in small quantities. This is arranged at right angles to the methanol injector, which has a radial nozzle diameter of 0.94 mm so that the jets lie in an interaction plane orthogonal to the cylinder axis.

Table 1: Overview of pressure and temperature at initial and final conditions (before TDC) in RCEM

	P_Initial (bar)	T_Initial (K)	P_Final (bar)	T_Final (K)	Inert - Spray Data	HDPI – DF Combustion Data
OP1	2.37	296	75 ±1.5	780±8	at 75 bar	
OP4	2.16	296	125±2	920±10	at 125 bar	Spray Interaction angle (+7.5° / +22.5°) Injection timing (+0.5 ms, -0.5 ms)

The methanol injector can be rotated by an angle α relative to the diesel injector. Together with an electronic control system for the injections this design allows any variation in the spatial and temporal interaction of both fuels. Investigation of methanol spray has been carried out for OP1 and OP4 in which the RCEM was filled with inert gas without oxygen and pilot diesel. In addition, a series of ignition and combustion tests were conducted for OP4, carried out at full-load engine operation. The mass of injected pilot diesel in combustion test is 5 mg and the injection duration is 0.5 ms. Also, 254 mg of methanol was injected as the main fuel for the injection duration of 2.7 ms, and the injection profiles are shown in Figure 2. Two ranges of relative injection timings of +0.5 ms (diesel injected first) and -0.5 ms (methanol injected first) were varied. The interaction angle α is measured for the far side of the spray and is varied between two positions as shown in Figure 2: +7.5 (interaction with both the sprays), +22.5° (strong interaction with near side spray). The CFD simulations were carried out for evaluating spray and combustion characteristics and the results were validated using these measurement points.

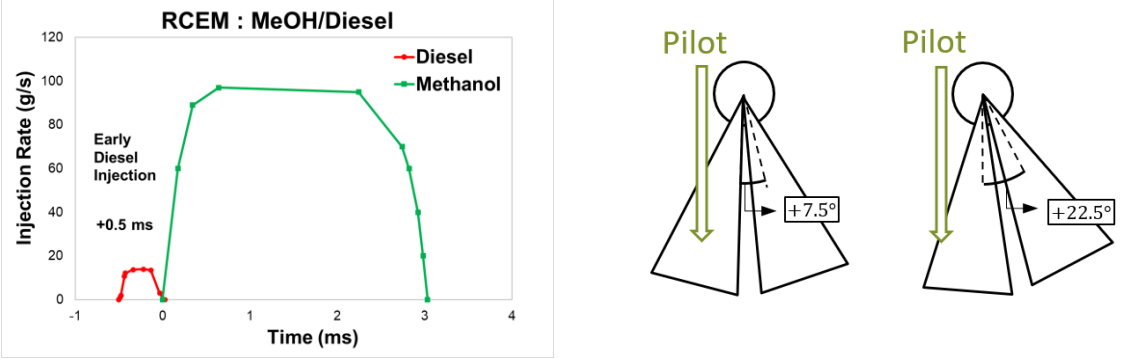

Figure 2: Injection profiles for diesel and methanol (left) and spray interaction angles of +7.5 ° and +22.5 ° between pilot-diesel and methanol (right)

The simulation geometry and mesh of the RCEM combustion chamber including the methanol and diesel injectors are shown in Figure 3. A global mesh size of 3 mm is assigned for the combustion chamber. Two levels of grid refinements were applied for better prediction of diesel and ammonia sprays. For turbulence modeling, the RNG k-epsilon model is used. The primary and secondary droplet breakups are modeled using Huh atomization and the Reitz-Diwakar models. Similarly, combustion is modeled using complex chemistry and EFCM-CLEH approaches. The CFD simulations are conducted using STAR-CCM+ 2210 [7].

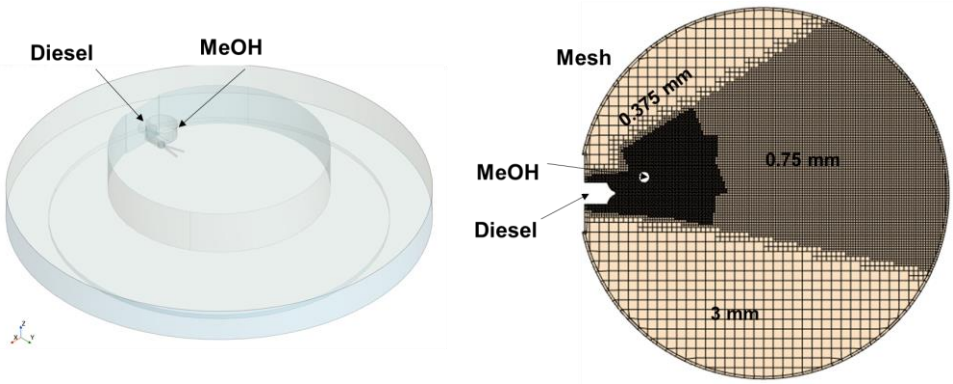

Figure 3: Simulation model of RCEM with single hole diesel injector and 2-hole methanol injectors (left), Simulation mesh for the cut sections through diesel injector plane (right), mesh size of 3 mm and two levels of refinement.

2.2. Single Cylinder Engine (SCE) Testbed

The Dual fuel combustion experiments of methanol and diesel pilot fuel were carried out in WTZ using the MAN 32/44DF-M which features a 320 mm bore diameter, and 440 mm stroke length. The single-cylinder engine uses a PFI injection strategy with two methanol injectors integrated into the intake ports through a retrofit solution, which provides an easy way to convert existing engines to dual-fuel operation mode without major design changes. The position and orientation of the methanol injector are important as they dictate the ease of installation and mixture formation in the cylinder. In the present test bench, the injectors were installed and directed towards their respective intake valves. Methanol is supplied continuously at a low pressure of 15 bar. Figure 4 shows the methanol conditioning unit and the single cylinder engine (SCE) test bench of 32/44DF-M.

Figure 4: Methanol conditioning unit (left) and the MAN-32/44DF-M SCE Engine test bench (right) at WTZ, Roßlau

The methanol-air mixture enters through the two intake valves into the cylinder. A high-pressure diesel injector sits at the head of the cylinder and injects a small amount of pilot diesel directly into the cylinder. Experiments are performed with varying intake air temperature, methanol start of injection (SOI), and two operating conditions. The simulation geometry and mesh of the SCE MAN 32/44DF-M engine is shown in Figure 5. Additional two-level mesh refinements are applied downstream of the methanol injector and cylinder head. Engine load points of 50% and 85% are considered with the intake

air temperature of 65 °C and 45 °C respectively. The methanol is injected at 45° CA and 30° CA after the intake valve opening for 50% and 85% loads respectively. The PFI methanol spray is defined using droplet size distribution and cone angle, and the breakup is modeled using the Reitz-Diwakar model.

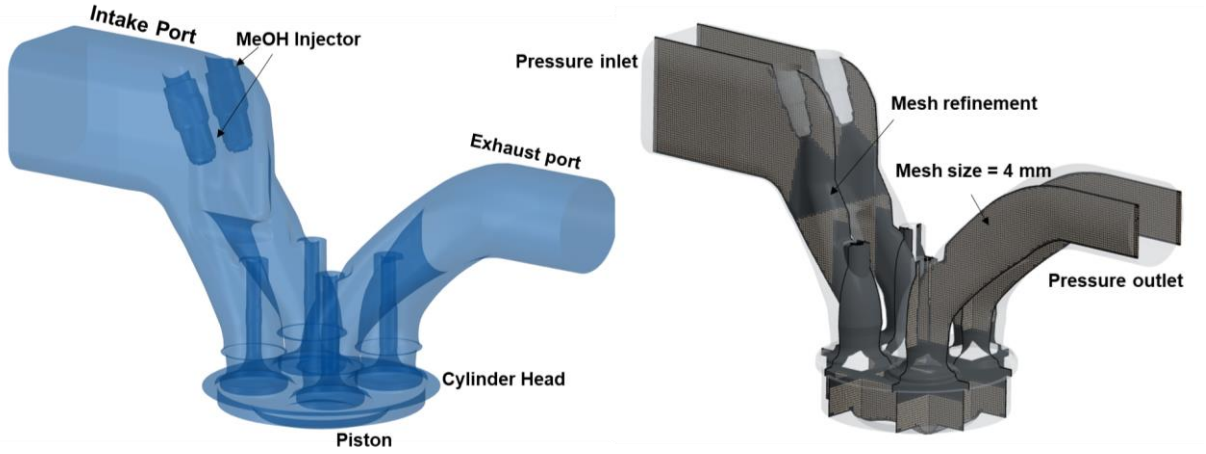

Figure 5: Simulation model of MAN-32/44DF-M SCE with two methanol injectors in intake port

3. Modelling and Simulation Approach

3.1. Spray Modelling

The liquid fuel droplets are introduced in the form of Lagrangian parcels, and the primary and secondary droplet breakups are modelled using the Huh atomization model and Reitz-Diwakar breakup model respectively. When a droplet is injected and the critical Weber number (We_{crit}) is reached, the represented droplets undergo an atomization process immediately after they leave the nozzle. In the model of Huh et al., two main factors are considered responsible for spray atomization: gas inertia and turbulence stresses generated within the nozzle. For the secondary breakup the Reitz-Diwakar model was chosen. It accounts for two different breakup regimes, 'bag'-breakup and 'stripping'-breakup. Bag breakup is caused by the droplet expanding into the low-pressure wake region behind it until it disintegrates. It is assumed to be possible when We > We_{crit}. The stable diameter is obtained when We= We_{crit}. The characteristic time scale for this breakup regime is derived to be:

$$\tau_b = \frac{C_{b2} d}{4} \sqrt{\frac{\rho_l d}{\sigma}} \quad \text{We} > \text{Wecrit} \tag{1}$$

In the stripping breakup regime, new droplets are stripped from the droplet surface by the shear forces. It is assumed to occur when We > max ($2C_{S1}Re^{0.5}$, We_{crit}). The timescale for this breakup regime is:

$$\tau_s = \frac{C_{s2}}{2} \sqrt{\frac{\rho_l}{\rho}} \frac{d}{|v_s|} \tag{2}$$

3.2. Combustion Modelling

During combustion, hundreds of reactions occur between different species resulting in new species at different rates. A reaction mechanism represents these reactions as a sequence of elementary reactions and the kinetics of the starting materials and intermediates as a function of thermodynamic conditions over a wide range. Utilizing the reaction mechanism, the combustion can be modelled by species

transport equation and a chemistry solver to solve the source terms. To achieve this, the simulation tool provides a tabulated and detailed approach for combustion modelling.

Complex Chemistry (CC)

The complex chemistry approach solves thousands of chemical reactions among various species in each computational cell in addition to continuity, momentum, and energy transport equations. The chemical reaction mechanism, thermal, and transport properties of reaction mechanisms in Chemkin format are coupled to the solver. The species transport equation is:

$$\frac{\partial}{\partial t}\rho Y_i + \frac{\partial}{\partial x_j}\left(\rho u_j Y_i + F_{k,j}\right) = \omega_i \tag{3}$$

where Y_i is the mass fraction and ω_i is the rate of production of species i, and $F_{k,j}$ is the diffusion flux component.

The species transport is solved with an explicit reaction source term ω_i for the ith species:

$$\omega_i = \rho f\left(\frac{Y_i^* - Y_i}{\tau}\right) \tag{4}$$

Simulations with detailed chemistry method results in a high computational effort, which is many times higher than that of the tabulated combustion models.

Tabulated Chemistry

To reduce computational time, the reactions representative of different thermodynamic conditions can be precomputed, and the relevant quantities can be tabulated. In the simulation tool, the Extended Coherent Flame Models (ECFM) model has been implemented which is a type of laminar flamelet model, where the turbulent flame is assumed to be composed of many thin laminar flamelet structures that are locally one-dimensional. Assuming this one-dimensional model, the reaction products can be precomputed and stored in lookup tables. The ECFM model is applicable in the region of the corrugated flames regime (Da = 1) represented in the Borghi Diagram. ECFM models are further modified to ECFM-3Z (three zones) and ECFM–CLEH (Chemical rates Limited by Equilibrium of Enthalpy) to model partially premixed combustion. In ECFM 3Z and ECFM-CLEH models, each computation cell is divided into three zones: unmixed air, mixed air, and fuel, and unmixed fuel zone. The zones are further divided into unburnt gas (u) and burnt gas zones (b). The amount of unburnt and burnt gases in the mixed zone is given by the progress variable $\bar{c}$. $\bar{c}$ is zero when it is a fresh-unburned mixture and one when all the fuel in the mixed zone has been burned.

In the ECFM-CLEH model, mean reaction rates are calculated based on four different combustion modes, such as auto-ignition (AI), premixed (PM), diffusion (DIFF), and post-oxidation (PSTOX). For example, the mean turbulent reaction rate in the premixed model is calculated using the flame surface density (Σ), and the laminar fuel consumption per unit surface (w_L). w_L is calculated from the unburned gas mixture density $\rho\left(Z_{f|PM} - Y_{f|PM}^{eq}\right)$ and laminar burning velocity (U_l). The required intrinsic properties of mixture, such as ignition delay time (IDT) of the fuel-air mixture and unstretched laminar burning velocity (U_l) is calculated for the variation of mixture temperature, pressure, equivalence ratio, concentration of each fuel, and exhaust gas concentration in fresh mixture. The IDT and U_l tables are used for predicting the reaction rate and thereby the net heat release rate in each combustion mode and they are created using different chemical reaction mechanisms.

Chemical Mechanism

Reaction mechanisms play a vital role in the prediction of single or dual-fuel combustion in both detailed and tabulated chemistry approaches. Three different reaction mechanisms have been considered for the investigation. The first mechanism (Mech1) is from Xu et al. [8] with 69 species and 389 reactions, that was developed and validated for hydrocarbon fuels and later extended for ammonia combustion. The second mechanism (Mech2) is a blended reaction mechanism of Curran et al. [9] and Ulrike et al. [10] which has 224 species and 1204 reactions that has not yet been published. The third mechanism (Mech3) is a comprehensive mechanism for n-heptane combustion by Sieser et al. [11] with 160 species and 1540 reactions. For the detailed chemistry simulation, the reaction mechanisms in CHEMKIN format can be incorporated for calculating the reaction rates. And for tabulated chemistry, the required IDT, U_l, and equilibrium tables are generated using all three reaction mechanisms.

4. CFD Simulation Results: RCEM-HPDI

Scharl et al. [6] conducted spray measurements at OP1 and OP4 conditions, in which the cylinder of RCEM was filled with inert gas, without oxygen and pilot diesel. In the inert spray experiments, only methanol was injected for a relative angle of +7.5°, and the data was used for spray model validation.

4.1. HPDI: Spray Validation

Since the HPDI combustion highly depends on fuel droplet breakup, air entrainment, and fuel-air mixing, accurate prediction of spray is essential. The properties of methanol are different from the conventional hydrocarbon fuels, the spray breakup model parameters set should be determined for methanol. For this spray investigation, three parameters such as Reitz-Diwakar stripping breakup time scale coefficient C_{s2}, discharge coefficient for injector C_d, and injector nozzle length L are varied for OP4. The obtained spray simulation results have been compared with the measured vapor penetration length, spray angle, and spray shape. In the simulation, an iso-surface of methanol vapor is created for 0.1% mass fraction to compare the spray shapes.

After varying multiple combinations of three spray parameters, one parameter set has better predicted the spray characteristics of methanol at 125 bar cylinder pressure (OP4). Using the same parameter set, for OP1 spray has been simulated. As illustrated in Figure 6, the measured and simulated vapor penetration lengths are in good agreement with specific set up spray model parameters for OP1 and OP4. Moreover, the comparison of shadowgraph images of methanol spray with iso-surfaces obtained from the simulation are closely matching, including the hot island zone in the middle of the spray. The spray angles are quantitively calculated and compared, and they are 35° for OP4 and 40° for OP1.

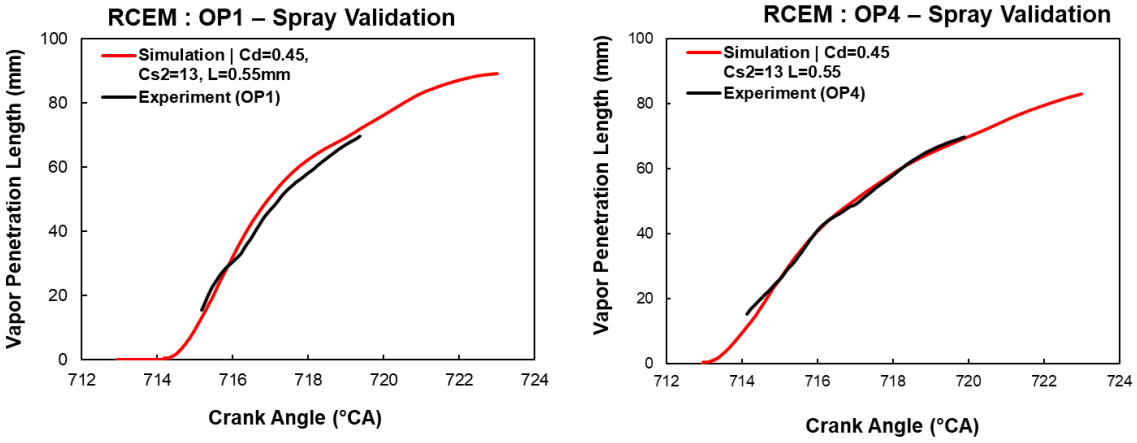

Figure 6: Simulated vapor penetration length at OP1 and OP4 conditions

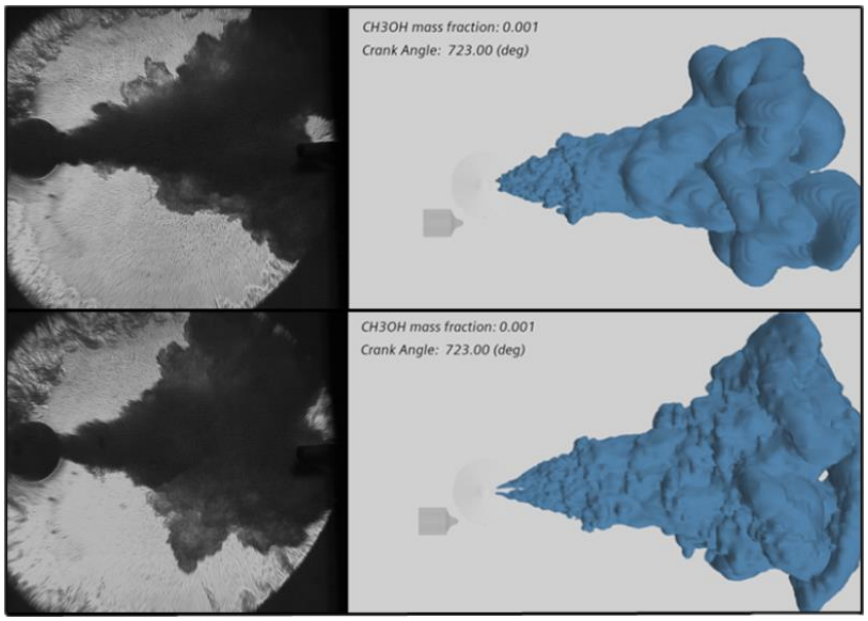

Figure 7: Shadowgraph images of methanol spray (left) at OP1 (top) and OP4 (bottom) with 0.1% methanol mass fraction from simulation (right)

4.2. HPDI: Combustion Simulation Results

In this section, simulation results of methanol-diesel combustion at OP4 for the variation of reaction mechanisms (Mech1, Mech2, Mech3) and combustion modelling (complex chemistry, ECFM-CLEH) approaches using the available experimental data as given in Table 1, for the variation of spray interaction angles (+7.5° and +22.5°) and injection timings (+0.5 ms and -0.5 ms) are presented. For the combustion simulation, the determined spray parameter set has been used.

Reaction Mechanism Variation using CC: Mech1 / Mech2 / Mech3

Figure 8 illustrates the different stages of diesel-ignited methanol combustion using the "Mech1" mechanism, spray interaction angle of +7.5°, and methanol injection timing of +0.5 ms. At first, pilot-diesel is injected into the cylinder, which is then evaporated and combusted forming the hot plume of burned products in the center of the cylinder. The injected methanol from two nozzle holes penetrates through the hot gas, thus enhancing evaporation, and igniting the methanol-air mixture. This

phenomenon can be observed on the near side of the methanol spray where the CO_2 and OH radicals formed on the outer regions of the spray at t = 0.652 ms (716.8° CA). Due to the continuous injection of methanol, the gas temperature in the inner region of the plume drops due to methanol evaporation and mixing, thus changing the flame shape, and drifting the flame position towards the cylinder wall. The concentration of CO_2 and OH radicals at t = 1.763 ms (720° CA) reveals the position of the combustion, i.e., mainly on the outer regions of the methanol spray. Since the RCEM wall temperatures were relatively lower than the gas temperature, the methanol flame at the front got quenched, leading to the flame propagation only in the radial direction. The methanol flame is anchored at a certain distance from the methanol injector and remains identical throughout the injection duration. The temperature contours of the simulation align closely well with the experimental combined SG/OH*-CL images. This alignment suggests a strong overall predictive capability of the CFD model.

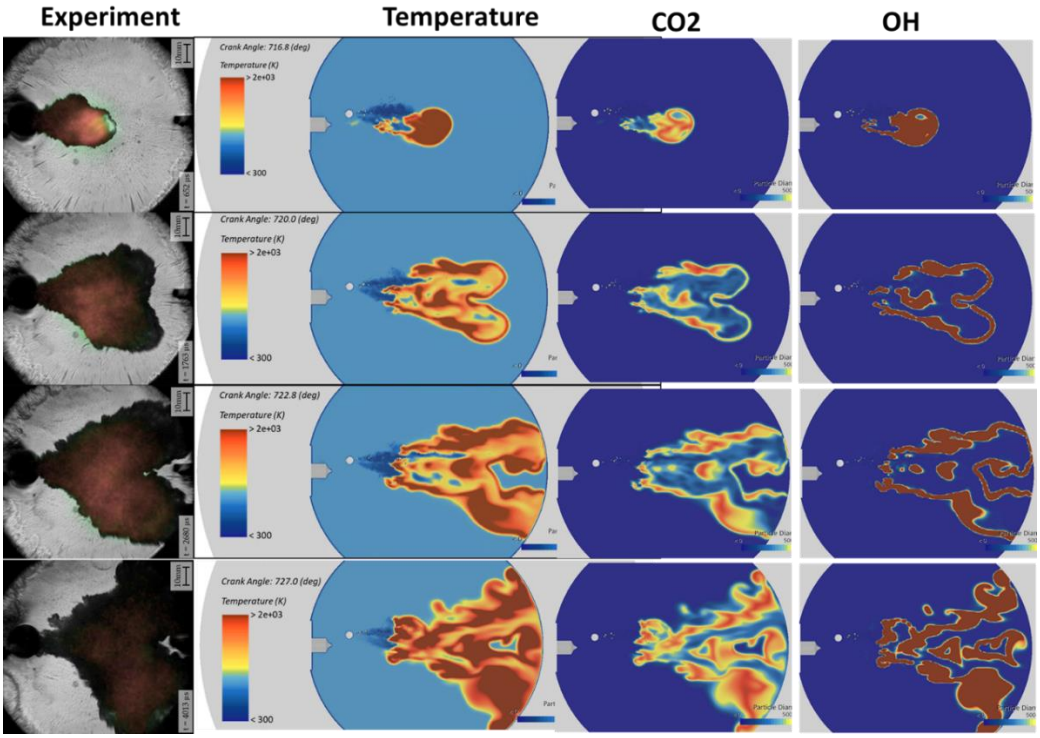

Figure 8: Combined shadowgraph (SG) and OH-Chemiluminescence (CL) images (Experiment) and simulated temperature, CO_2, and OH contours for spray interaction angles of +7.5°, injection timings of +0.5 ms, and Mech1*

In Figure 9, the heat release rates of the experiment and simulation for early diesel (+0.5 ms) and early methanol (-0.5 ms) injection results are presented. In the case of early diesel injection, it can be observed that three reaction mechanisms show nearly identical combustion characteristics. However, the Mech2 predicts diesel combustion more accurately. Mech1 and Mech3 have some delay in diesel ignition by up to 1.5° CA. For early methanol injection (-0.5 ms), diesel combustion starts relatively later, and the premixed combustion peaks are overpredicted by Mech3. The difference between the experiment and simulation after 720°CA occurs when the flame touches the wall as shown in Figure 9. In the experiment, the heat loss to the RCEM wall is calculated based on the temperature gradient. It could be possible that the calculated heat loss is relatively higher in the experiment compared to the simulations. Overall, Mech1 and Mech2 show good agreement with the experimental data for both early diesel and early methanol injection conditions.

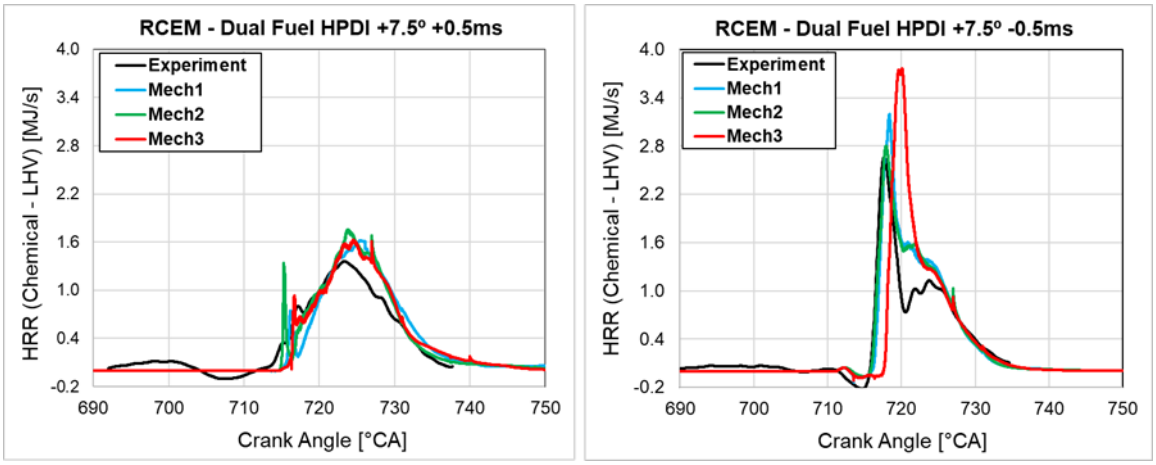

Figure 9: Experimental and Simulated HRR for spray interaction angles of +7.5° and injection timings of +0.5 ms and -0.5 ms for three reaction mechanisms

Combustion modelling - CC / ECFM-CLEH : Early methanol Injection (-0.5 ms)

Combustion simulations have been performed for OP4 conditions using complex chemistry (CC) and EFCM-CLEH modelling approaches. Using the Mech1 reaction mechanism the IDT, U_l, and equilibrium tables were generated for the ECFM-CLEH model and used in the combustion simulation. The results for the spray interaction angle of +7.5° with early diesel injection (+0.5 ms) and early methanol injection (-0.5 ms) are presented in this section. Figure 10 depicts the combustion phenomenon that occurs in early methanol injection condition (-0.5 ms). At t = 1.499 ms (716° CA), injected methanol during the early phase of injection is evaporated and forms an ignitable mixture in the cylinder. The pilot diesel ignition arises in the outer regions of the methanol spray which ignites the premixed methanol air mixture at the near end of the diesel nozzle, thus causing more heat release in a short duration. Furthermore, the methanol flame propagates further to combust the methanol from the second nozzle. After the premixed combustion at t = 3.852 ms (721° CA), the methanol burns in a diffusive combustion mode. Comparing the temperature contours between CC and ECFM-CLEH in Figure 10, one can observe that the CC model can predict the earlier diesel ignition and premixed methanol combustion well compared to the ECFM-CLEH model.

The quantitative comparison of HRR in Figure 11 concludes that the EFCM-CLEH model shows small deviation at the early phase of injection, mainly on diesel ignition. However, the difference becomes smaller at the late phase of methanol injection, followed by combustion and heat release. Overall, both complex chemistry and ECFM-CLEH combustion modelling approaches could predict well the full diffusion combustion and a combination of premixed and diffusion modes and their predictions are in good agreement with the experimental data. Since all the reactions that exist in the mechanism have to be solved for each cell in a complex chemistry method, the computational time for one simulation is 6 times longer compared to that of the ECFM-CLEH model.

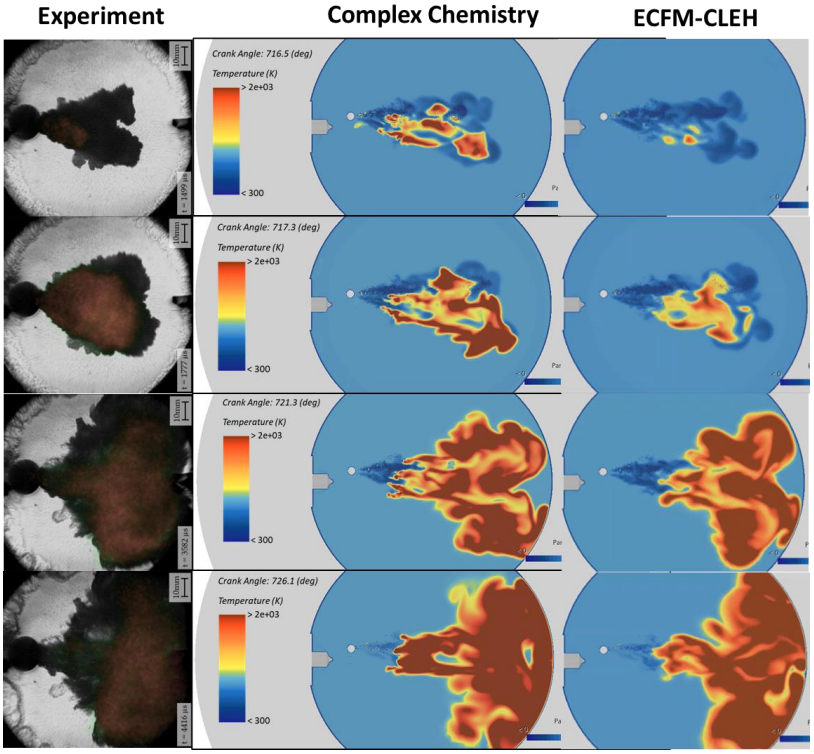

Figure 10: Combined shadowgraph (SG) and OH-CL images (Exp.) and temperature contours of Complex-Chemistry and ECFM-CLEH simulations at OP4 with +7.5° spray interaction angle, early methanol injection (-0.5 ms)*

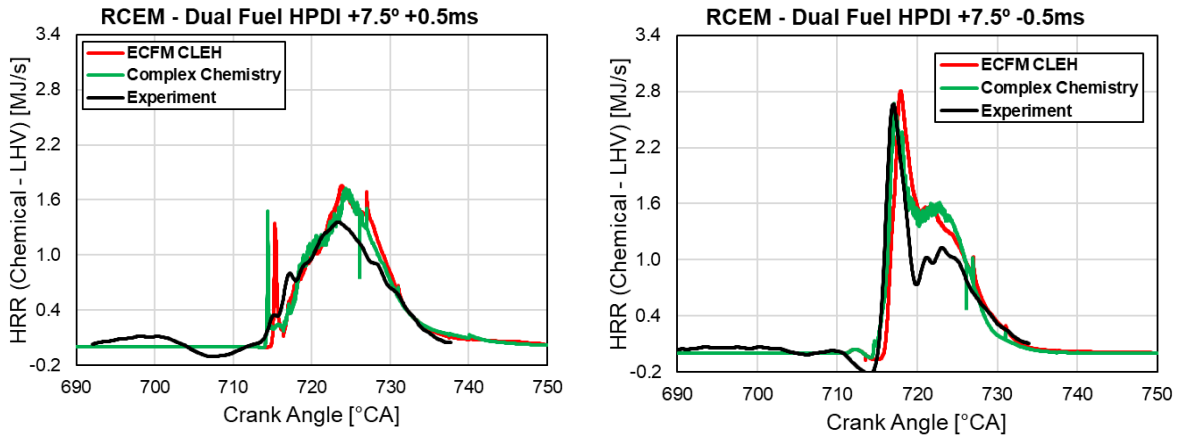

Figure 11: Experimental and Simulated HRR for spray interaction angles of +7.5° and injection timings of +0.5 ms and -0.5 ms for EFCM-CLEH and complex chemistry combustion modelling techniques

Diesel/Methanol spray interaction angle variation: 22.5 °

In a two/more needle multi-hole injector, the interaction between individual diesel and methanol sprays plays a major role in diesel ignition and methanol combustion. So, the simulation methodology has been further validated using the measurement data for the 22.5° interaction angle and early diesel injection (+0.5 ms). Figure 12 illustrates the early diesel injection, followed by the ignition of methanol and its combustion. At t = 0.986 ms (714° CA), the diesel ignites the methanol mixture at the near side of the methanol spray. And the developed flame propagates into methanol released from the nozzle hole located at the far end of the diesel injector, thus causing lower HRR compared to that of observed in

+7.5°. The methanol flame drifts towards the wall during injection and the methanol flame stabilizes at the downstream of injector. From the comparison of OH*-CL and temperature contours at various timings, one can conclude that methanol combustion is well predicted in both the early and late stages of methanol injection.

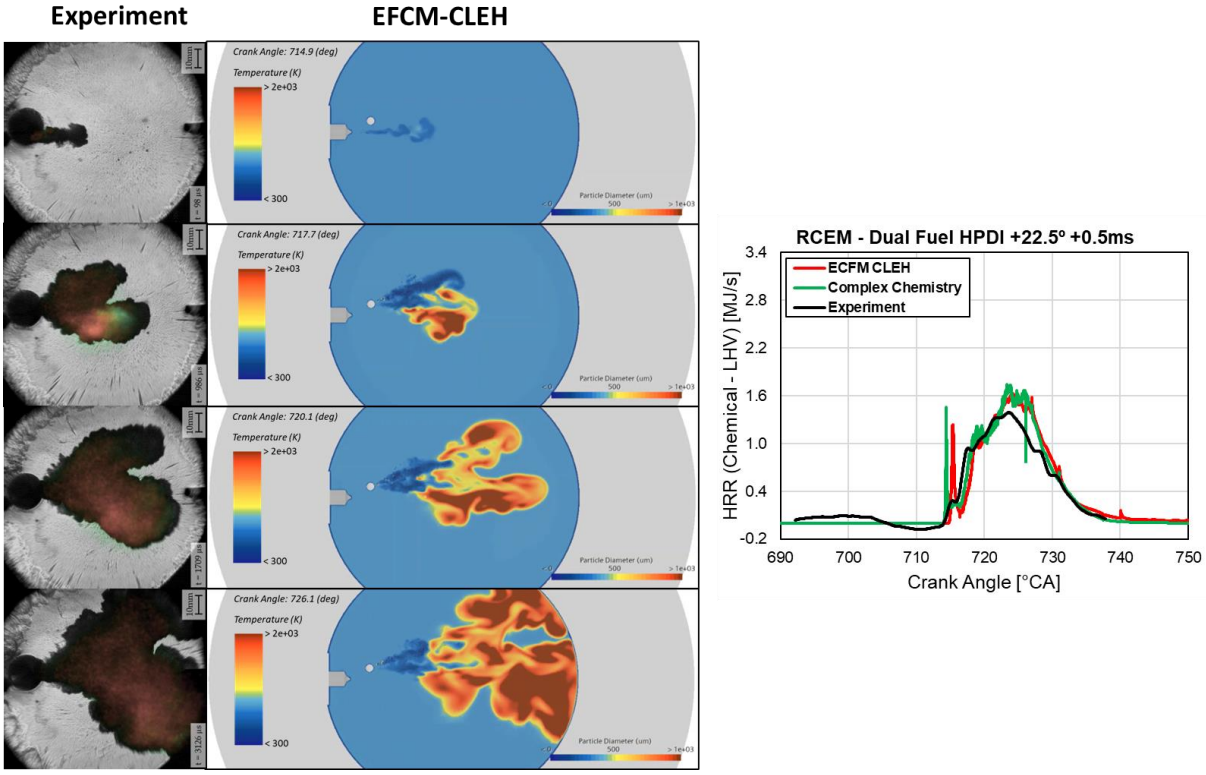

Figure 12: OH-Chemiluminescence (CL) images (Exp.) and temperature contours of ECFM-CLEH simulations at OP4 with +22.5° spray interaction angle and +0.5 ms injection timing (left) and the heat release rates comparison (right)*

5. CFD Simulation Results: Port Fuel Injection (PFI)

Retrofits of existing fleet engines can be realized by injecting methanol in the intake port, thereby a portion of the methanol is evaporated and mixed with air at the intake port. The remaining evaporation and mixing occur in the cylinder during the intake and compression stroke. The premixed methanol-air mixture is ignited by the diesel pilot fuel. Furthermore, the methanol injection, evaporation, and mixture formation play a significant role in the emission and performance behaviours of an Otto-cycle methanol engine. Achieving good methanol-air mixing in the cylinder depends on many parameters such as injector design and its position in the intake port, injection timing, and intake air conditions. The influence of injector position on mixing has been discussed in [5]. In this investigation, CFD simulations have been carried out to evaluate evaporation and mixing characteristics at two engine load points of 50% and 85% for the variation of injection timings and their results are presented in this section.

5.1. Spray and Mixing Characteristics

The simulation CAD model and mesh, that are shown in Figure 5 are used for the CFD analysis. The measured experimental data is used as initial and boundary conditions for the cylinder, intake, and exhaust ports. The injected methanol mass for both engine operating conditions corresponds to 95% of the total energy. The injection profile is defined with an initial ramp-up curve and ramp-down curve

with a constant profile in the middle. The chosen injection duration allows enough time for most of the liquid droplets to flow into the cylinder. Thus, reduces the stored methanol in intake port and its slip during valve overlap. The start of injection (SOI) of methanol, for 50% and 85% loads are IVO+45° CA, and IVO+30° CA respectively. Figure 13 shows the methanol injection from two injectors and liquid droplet distribution in the air at the intake port. At downstream of the methanol injector, the droplets start to break up and evaporate, thereby vapor is even formed at the tip of the injector. The methanol vapour and liquid droplets are flowing on the right side, this is to avoid the methanol droplet and liner collision in the cylinder. Three stages of droplet breakup were observed, i.e., immediately after the injection, in the intake port, and above the intake valve head where the gas reaches high velocity. The temperature contours in Figure 14 indicate that the gas temperature drops by up to 40 K locally due to methanol evaporation, and the low-temperature gas shows the flow path of liquid droplets. Since the injection pressure of methanol is low, conditions of intake air play a vital role in droplet breakup and evaporation.

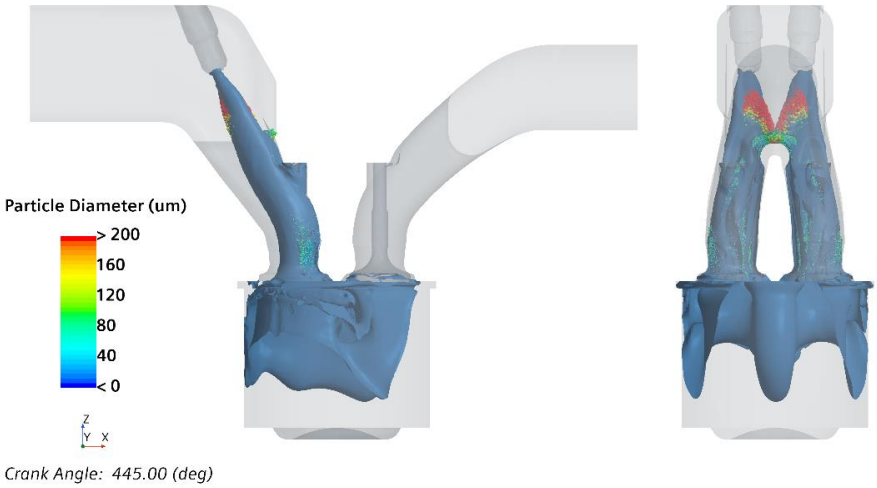

Figure 13: Iso surface of methanol vapor, mass fraction between 0.1 and 10% and methanol droplets during injection for engine load P = 50%, SOI_Methanol = IVO + 45° CA

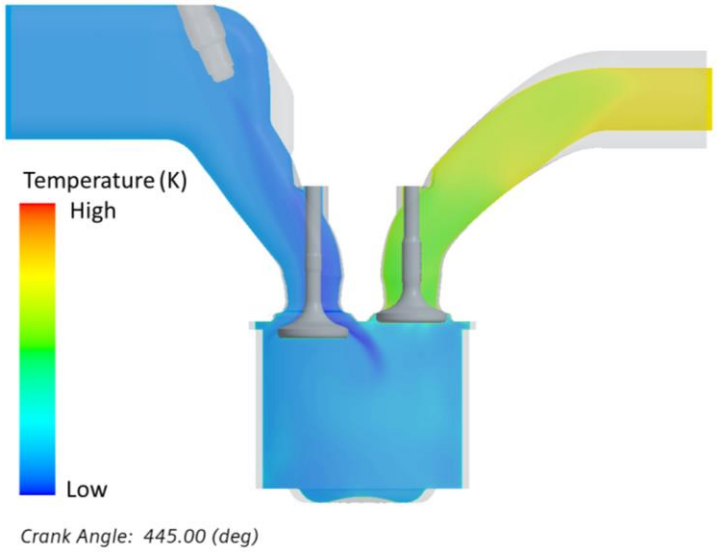

Figure 14: Contours of gas temperature during methanol injection for engine load P = 50%

The mass of methanol evaporated in the intake port is less than 20% and the remaining evaporation occurs in the cylinder. The methanol-air mixing is prominently dominated by the flow distribution and how the methanol vapour interacts with the intake air. Figure 15 depicts how the methanol vapour and its droplets flow in the cylinder for engine load of 85% and for SOI_Methanol of IVO+30° CA. One portion of the methanol vapour passes through the front section of the intake valve hit the piston directly below the exhaust valves. The remaining liquid droplets and vapour flow along the liner and mix with the air. As shown in Figure 16, most of the evaporation occurs during the intake phase of the engine cycle due to high turbulent flow in intake port and cylinder which enhances droplet breakup and mixing. During the compression phase, the remaining droplets are converted into vapour before TDC. The higher intake air temperature at 50% load facilitates methanol evaporation, thereby lowering the mass of liquid droplet at the end of compression. The contours and histogram of the air-fuel ratio in Figure 17 and Figure 18 indicate that slightly better mixing is observed in 50% load conditions compared to 85%. This could be due to slightly higher intake air temperature and later methanol injection timings, thus, enhancing droplet breakup, evaporation, and mixing. Overall, the mixing quality in both conditions is good, though there is a small deviation in the local concentrations. Finally, the comparison of the simulated pressure is well aligned with the measurement data, and the temperature shows a minor deviation at TDC which was further improved while using liquid film models in the simulation.

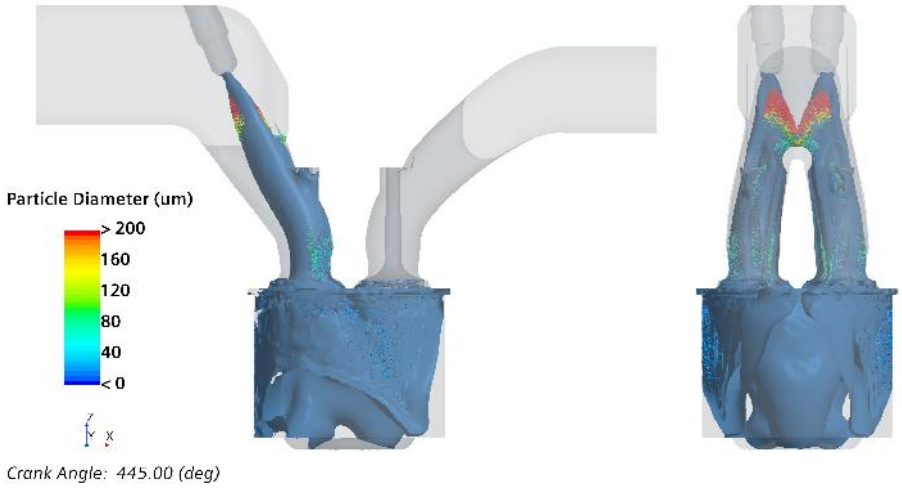

Figure 15: Iso surface of methanol vapor, mass fraction between 0.1 and 10% and methanol droplets during injection for engine load P = 85%, SOI_Methanol = IVO + 30° CA

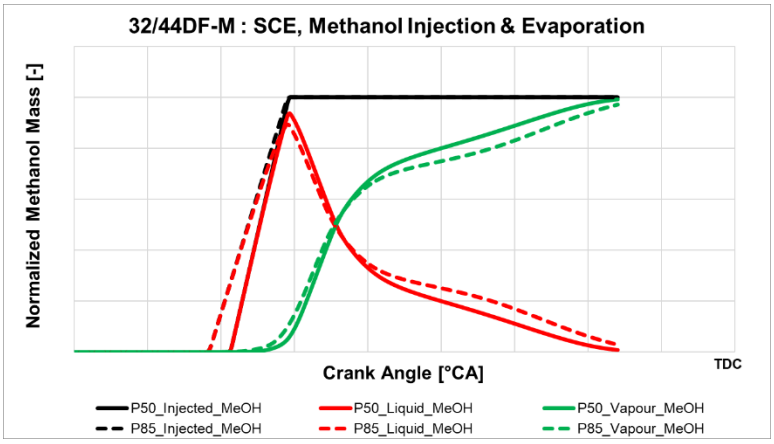

Figure 16: Methanol mass injected, in vapor phase after evaporation and the remaining mass in liquid phase

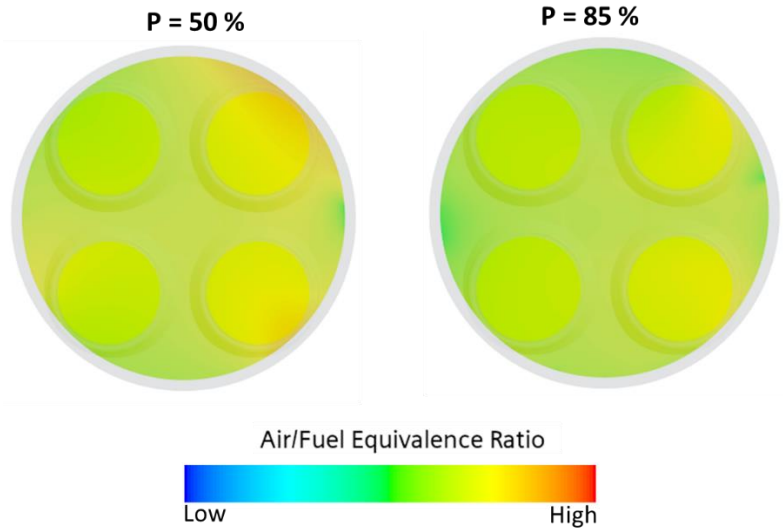

Figure 17: Contours of air/fuel equivalence ratio for engine load 50% (left) and 85% (right)

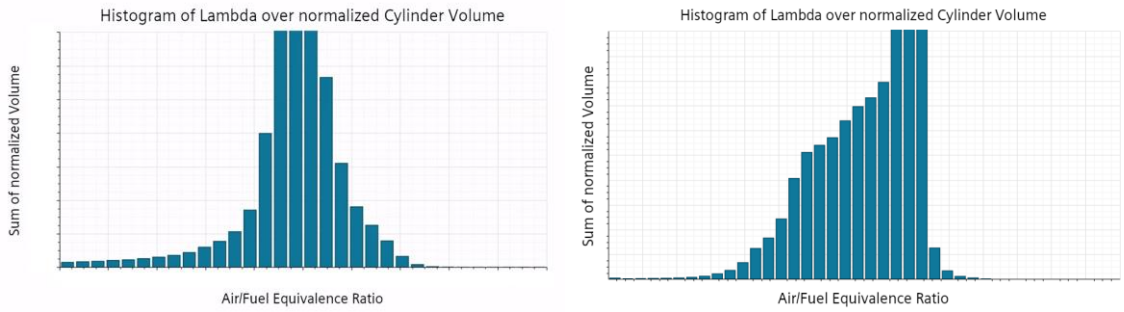

Figure 18: Histogram of air/fuel equivalence ratio vs norm. cylinder volume for engine load 50% (left) and 85% (right)

6. Conclusion

MAN Energy Solutions SE has been working on the development of carbon-free and carbon-neutral fuel engines, such as dual-fuel methanol engines for retrofit solutions and newbuilds. PFI and HPDI injection strategies are considered for fuel injection that leads to premixed Otto-like and Diesel-like diffusion combustion respectively. The PFI technique will be implemented in MAN's 48/60 and 51/60

engine platforms as well as for the 21/30 genset engines. Besides, the HPDI methanol injection method will be introduced in new builds and retrofit solutions to the newly developed 32/44 and 49/60 engine platforms.

In this CFD investigation, spray validation has been carried out using RCEM setup for 50 bar and 125 bar cylinder pressure conditions. The simulated spray shape, spray cone angle, penetration length, are in good agreement with the experimental data for certain Reitz-Diwakar model parameter sets. The combustion simulation results for the early diesel injection (+0.5 ms) case show that the diesel combustion products ignite methanol. Most of the combustion occurs in diffusive mode on the outer regions of spray where OH and CO_2 concentrations are higher. For early methanol injection (-0.5 ms), methanol forms a combustible mixture, thus releasing high heat release due to premixed combustion, followed by a diffusive combustion due to slow evaporation and mixture formation. Methanol could be ignited by the pilot for diverging sprays with +22.5° angle between diesel-methanol sprays and the combustion characteristics are nearly identical to that of predicted in +7.5°. This indicates that the methanol ignition could be secured even for diverging spray with low interaction between methanol and diesel sprays.

The predictions of Mech1 and Mech2 are aligned with the experimental data while using complex chemistry and ECFM-CLEH modelling approaches for all the simulated conditions. Mech3 shows delayed diesel ignition and faster methanol combustion, which is largely deviating from the heat release rate for both early diesel and early methanol injection conditions. Overall, the simulated temperature contours which depict the diesel and methanol flames, match well with the combined SG/OH*-CL images from the experiments, indicating a good overall predictive capability of the CFD methodology for HPDI dual fuel methanol-diesel combustion.

The PFI simulations carried out for 32/44DF-M SCE engine setup for load points 50% and 85% indicate that the intake air temperature is reduced by up to 40 K due to methanol evaporation. For the simulated conditions, less than 20% of the injected methanol is evaporated in the intake port and the remaining 80% occurs in the cylinder during intake and compression stroke. During the intake phase, a sharp increase of methanol vapour mass in the cylinder was observed due to better interaction between droplet and air. Around 40% of the droplets evaporated in the cylinder during compression phase. At the BDC, the gas temperature is low, and the movement of air is slower than that of observed in intake port. Thus, reduces the evaporation rate. At the later phase of compression, increase in gas temperature enhances the droplet evaporation. The predicted mixing quality for 50% load is better compared to 80% owing to higher intake air temperature and earlier methanol ignition timings. Using this simulation approach, the evaluation of injector design, its position, and injection timing has been completed for 51/60DF-M and 21/31DF-M engines. The combustion simulation of dual fuel premixed methanol combustion ignited by pilot diesel is currently ongoing. The developed simulation methods for HPDI and PFI methanol combustion will be further employed to facilitate the development of MAN's methanol engines for reducing GHG emissions.

Abbreviations and acronyms

GHG	Greenhouse gas
IMO	Internation maritime organisation
CC	Complex chemistry

ECFM-3Z	Extended coherent flamelet Model – 3 Zone
ECFM-CLEH	Extended coherent flamelet model – Combustion limited by equilibrium enthalpy
RCEM	Rapid compression and expansion machine
HPDI	High Pressure Direct injection
MeOH	Methanol
PFI	Port fuel injection
OH*-CL	OH*- Chemiluminescence
SG	Shadowgraphy
IVO	Intake valve open
TDC	Top dead center
BDC	Bottom dead center

Acknowledgements

The investigations on the single cylinder engine (SCE), the CFD-simulation, and the evaluation of the combustion concepts were funded by the German Federal Ministry for Economic Affairs and Climate Action based on a decision by the German Bundestag (project no. 03SX585A), which is gratefully acknowledged. In this context, the authors would like to acknowledge the collaboration and support of the CliNeR-ECo project partners WTZ-Roßlau gGmbH and the STFS/RSM-University of Darmstadt. Furthermore, the authors would like to express their sincere gratitude to Dr. Valentin Scharl and Prof. Thomas F. Sattelmayer and Mr. Utkarsh Pathak for providing the RCEM measurement data and their support.

Literature

[1] DNV Maritime Forecast 2023.

[2] S. Verhelst, J. Turner, L. Sileghem and J. Vancoillie, Methanol as a fuel for internal combustion engines, Progress in Energy and Combustion Science, vol. 70, 2019.

[3] Rektorik, P., Aabo K., Gunnar S.: Methanol as a viable fuel option to drive carbon-neutral shipping. 7th Large Engine Symposium 2022.

[4] Auer M., Markus B., Ganzer G., Sebastian S., Knafl A., Gunnar S.: Power-to-X: The key for the Maritime Energy Transition. In: 29th CIMAC Congress Vancouver, 2023.

[5] Kunkel, C., Hagl P., Manickam B., Gross C., Eppler F.: Methanol retrofit for a net-CO_2 reduction in the marine market; 13. Dessau Gas Engine Conference, Dessau-Rosslau, 2024

[6] Scharl, V., Sattelmayer, T.: Ignition and combustion characteristics of diesel piloted ammonia injections, Fuel Communications, vol. 11, 2022

[7] Simcenter STAR-CCM+ (Version 2210), Siemens Digital Industries Software, Siemens, 2022.

[8] Xu L., Chang Y., Treacy, M., Zhou Y., Jia M., Bai X.S.: A skeletal chemical kinetic mechanism for ammonia/n-heptane combustion, Fuel, Vol. 331, 2023.

[9] Curran, H. J., P. Gaffuri, W. J. Pitz, and C. K. Westbrook: A Comprehensive Modeling Study of n-Heptane Oxidation, Combustion and Flame 114:149-177, 1998

[10] Burke U., Metcalfe W. K., Burke, S. M., Heufer K. A., Dagaut P., Curran J. H.: A detailed chemical kinetic modelling, ignition delay time and jet-stirred reactor study of methanol oxidation, Combustion and Flame, Vol. 165, pp 125-136, 2016.

[11] Seiser R., Pitsch H., Seshadri K., Pitz W. J., Curran H. J.: Extinction and Autoignition of n-Heptane in Counterflow Configuration, Proc. of the Combustion Institute, Volume 28, 2000.

Keywords: Turbocharging strategies, predictive thermodynamic combustion models, Ammonia/hydrogen marine engine, Diesel-gas mode

Turbocharging strategies to enable fuel-flexibility over a full operating map in a 4-stroke marine engine

Dr. Qiyan Zhou[1], Dr. Dirk Bergmann[1], Elmar Strittmatter[1], Herve Martin[1], Prof. Dr. Gianluca D'Errico[2], Alberto Ballerini[2]

(1) Accelleron c/o Turbo Systems Switzerland Ltd, (2) Department of Energy, Politecnico di Milano

https://doi.org/10.18453/rosdok_id00004636

Abstract

The use of alternative marine fuels is considered an important strategy to reduce the environmental and climate impacts of shipping. Among all the future fuels, ammonia has been gaining attention recently thanks to its potential to be carbon-free from production to combustion. There are a lot of attempts to use ammonia in the premixed Otto cycle, where a high compression ratio is used due to its high-octane rating, and hydrogen is added to compensate for its high ignition energy and low flame speed. A fuel-flexible ammonia-Diesel engine, where depending on prices or local regulations, the operators can decide to use ammonia in the gas mode or switch to conventional Diesel mode, is of great interest for maritime decarbonization, cost reduction, and enhancing reliability. In particular, Diesel fuel also provides a backup operation in case of gas feed interruption or component failure. However, the two working modes may differ in air requirement and exhaust temperature, which might add another layer of complexity in turbo-matching. To this end, the ultimate goal of this paper is to perform a comprehensive study on turbocharging strategies and provide a solution to enable optimal engine performance in both working modes.

In this paper, simulations are performed using ACTUS (Advanced Computation of TUrbocharging Systems), the Accelleron in-house software for large-bore engine simulation, in which advanced and predictive thermodynamic combustion models for both premixed and diffusive combustion developed by Politecnico di Milano have been included recently. Details of the combustion models will be first given, and then the model validation will be performed. In particular, a premixed combustion model based on the flamelet assumption will be used to simulate the natural gas engine considering the equivalence air-fuel ratio (ϕ), spark timing and load sweeps; a constant equivalence ratio multi-zone approach for diffusion flames will be validated along the nominal operating curve in a Diesel engine. Different turbocharging strategies will be investigated and compared to optimize the air supply system, which could enable fuel flexibility in ammonia–Diesel engines.

1. Introduction

The International Maritime Organization (IMO) has proposed a reduction of at least 70% in greenhouse gas (GHG) emissions from international shipping by 2040, with the ultimate goal of achieving net-zero shipping by around 2050 [1]. As a result, replacing conventional marine fuels with near-zero or net-zero GHG alternative fuels is inevitable and is being actively researched and developed. There have been many studies comparing the application of various alternative fuels in the marine sector: Stolz et al. [2] compared various alternative fuels such as hydrogen, ammonia, methane, and methanol and concluded that ammonia is the most balanced carbon-free fuel, while methanol is the most balanced carbonaceous fuel. Kanchiralla et al. [3] compared the lifecycle costs of using hydrogen, ammonia, and methanol as alternative fuels in three ships. They found that the use of ammonia and methanol fuel has the lowest lifecycle cost for all studied cases. In [4], Zhou et al. further highlighted ammonia as an ideal alternative fuel for future international shipping due to its low storage and transportation costs, as well as its well-established infrastructures. One of the possible approaches to burn ammonia in IC engine applications is the use of the Otto cycle, either through the spark ignition or a dual-fuel approach involving a small amount of highly reactive fuel, such as diesel [5]. Recognizing the variability of operational conditions and regulatory landscapes across different maritime regions, an ammonia-Diesel dual fuel engine is preferred, where depending on prices or local regulations, the operators can decide to use ammonia in the gas mode or switch to conventional Diesel mode, similar to [6]. This is of great interest for maritime decarbonization, cost reduction, and enhancing reliability, in particular, Diesel fuel also provides a backup operation in case of gas feed interruption or component failure. However, the two working modes may differ in air requirement and exhaust temperature, which might add another layer of complexity in turbo-matching. A comprehensive assessment of the turbocharging system will be essential to determine the optimal strategy for enabling fuel flexibility in such an ammonia-Diesel dual-fuel engine.

To assess different turbocharging strategies without incurring significant costs, advanced 1D-0D computational tools are crucial, where an accurate description of the combustion process is essential for a precise and detailed turbocharging study, especially for ammonia engines with limited experimental data. Over the years, various combustion models have been developed in different computational codes to simulate combustion in IC engines, ranging from fast and simple empirical relations such as the Wiebe or semi-empirical models [7], to more complex and capable thermodynamic models [8], [9]. Accelleron has a long tradition of developing simulation tools for turbocharged large engine system [10], and in 2012, it introduced its new simulation software, ACTUS (Advanced Computation of TUrbocharging Systems). Since then, a continuous development and improvement of the modeling capability of ACTUS has been carried out, and recently the advanced and predictive thermodynamic combustion models for both premixed and diffusive combustion developed by Politecnico di Milano have been included for investigating new turbocharging concepts and their impact on engine performance.

Details of the combustion models will be first given in this paper, followed by a comprehensive model validation in different engines. In particular, a premixed combustion model based on the flamelet assumption will be used to simulate the natural gas engine considering the equivalence air-fuel ratio (ϕ), spark timing, and load sweeps; a constant Equivalence Ratio Multi-Zone Approach for diffusion flames will be validated along the nominal operating curve in a Diesel engine. Different turbocharging concepts will be investigated and compared to optimize the air supply system for Diesel mode and

ammonia gas mode to enable optimal performance in both operation modes. It is important to highlight that in ammonia gas mode, diesel-pilot ignition will be replaced with spark ignition to simplify combustion modeling. This assumption should be adequate for such preliminary assessment on turbocharging systems, especially at high loads, where the diesel energy ratio is generally kept as low as possible [4], [11].

2. Combustion models

2.1. Multi-Zone Approach for Diffusion Flames

The model is based on the solution of the mixing process of the injected fuel into the trapped mass inside the cylinder by applying the momentum jet theory developed by Musculus and Kattke [12]. The computed mixing distributions are casted into a pre-defined number of zones characterized by constant equivalence ratios in which the combustion process takes place. As a result, the model is able to predict the ignition of the charge in Diesel engines which depends on both physical aspects, such as fuel evaporation and charge distribution, and chemical kinetics. Real engine conditions and geometry sub-models are included: the geometrical details of the combustion chamber, the characteristics of the injection system, and the charge thermodynamic conditions such as in-cylinder pressure, temperature, and presence of EGR are considered.

The model can be split into two sub-models, a one-dimensional charge stratification one used to describe the direct injection of liquid fuel from which the mass and energy exchanges between the homogeneous iso-ϕ zones are computed through a 2D resolution of the reacting fuel spray. This information is later used in a zero-dimensional combustion model that computes the multi-zone properties, including combustion and emission formation processes [13].

Charge stratification model and coupled chemical-physical ignition

In the extension of the momentum jet theory developed by Musculus and Kattke [12], a conical numerical spray domain is divided into small control volumes (as shown in Figure 1) with a fixed axial width Δz, whose value can be arbitrarily chosen and is set to 0.001 m in this study. Initially, these CVs are filled by air.

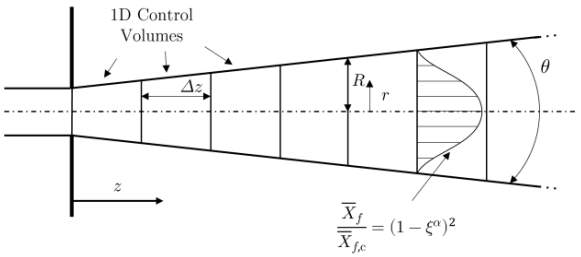

Figure 1: 1D discretization of the fuel spray in axial control volumes. Details of the spreading angle θ, iso-ϕ contours and radial distribution are illustrated.

The cone spray angle of the one-dimensional domain is computed with the formulation proposed by Naber et al in [14]:

$$\theta = 2 \cdot arctan\left[C_\theta \left(\left(\frac{\rho_a}{\rho_f}\right)^{0.19} - 0.0043\left(\frac{\rho_f}{\rho_a}\right)^{0.5}\right)\right] \quad (1)$$

Where ρ_a and ρ_f are the ambient air and liquid fuel density, C_θ is a tuning parameter specific to geometry of the injector. These quantities are determined at the Start Of Injection (SOI) and kept constant during the simulation. Following an Eulerian approach, the variation of the mass of fuel and total jet momentum at each time step for a given CV are computed with:

$$\frac{dm_f}{dt} = \dot{m}_{f,in} - \dot{m}_{f,out} \tag{2}$$

$$\frac{dM}{dt} = \dot{M}_{in} - \dot{M}_{out} \tag{3}$$

Where m_f and M are the mean axial turbulent fuel mass and jet momentum, respectively. Over-dots quantities indicate integral flux quantities, with subscripts denoting whether the contribution is entering or exiting the CV. From these equations, it is possible to obtain the fuel distribution in the iso-equivalence ratios zone by imposing a radial distribution of fuel in each CV. Further information on the application of this post-process of the 1D spray model can be found in [9], [15]. The interaction of the spray with the wall (piston or liner) is also accounted for as it greatly affects the combustion process. In particular, after the so-called POI (Point Of Impact), the cone spray angle is reduced and the radial distribution is changed to account for the "packing" of the leanest particles with the ones deviating from the core to the edge of the spray by the impact with the piston walls. This results in a lower air entrainment and the subsequent reduction of the heat released by combustion, which is typical of diffusive combustion processes. In addition, the spray model includes specific sub-models to simulate the coupled chemical-physical ignition mechanism. Indeed, the physical aspect is considered by classifying the CVs that form the 1D spray into three sub-regions, namely "liquid", "unburned vapor" and "burned vapor. The "liquid" sub-region is defined via a thermodynamic evaporation sub-model based on the hypothesis of mixing-controlled evaporation [16], [17]. With this model, it is possible to identify the Liquid Length (LL), as the one-dimensional threshold between the "liquid" and "vapor" region of the spray. Downstream the LL, the fuel is assumed to be in the "vapor" state and ready to react. To compute the actual ignition, which is delayed by chemical kinetics, the Tabulated Kinetics Ignition (TKI) approach is developed, providing a detailed and fast description of the complex reaction mechanisms [18], [19]. This approach is based on the computation of a normalized progress variable c along the axial control volumes. Ignition occurs when $c_i \geq c_{i,ign}$ in one of the CVs. After this, the status of that CV will be updated from "unburnt vapor" to "burned vapor" and combustion has started. It is also possible to identify the Flame Lift-off Length (FLOL) as the closest CV to the injector in a "burnt vapor" state. A conceptual description of the 1D spray and division in the three different sub-regions is shown in Figure 2.

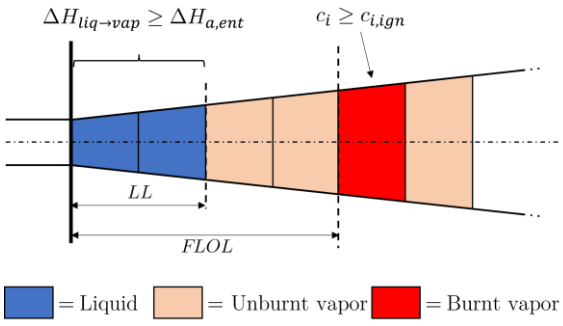

Figure 2: Scheme of the "liquid", "unburned vapor" and "burned vapor" state sub-regions in the 1D spray domain.

Computational scheme of the model

The computational scheme implemented for this model is subdivided into the following steps:

1. The conditions at IVC, including pressure, temperature, and compositions, are used as initial conditions for combustion simulation.
2. Before the SOI, a single zone containing only the fresh charge is considered. The in-cylinder pressure and temperature are computed at each iteration, taking into account only the heat exchange with the walls and the compression of the charge due to piston motion.
3. Once the injection starts, the 1D CV approach is used to determine the spatial distribution of the iso-ϕ zones. The newly created thermodynamic zones are populated, and for each zone, the mass, temperature, composition, and other thermodynamic quantities are calculated. A homogeneous pressure is assumed for the entire cylinder and all zones.
4. The evolution of the spray is performed for each CV. Each CV will contain either the liquid fuel or the "vapor" mixture in the "unburned" or "burned" state. For the CVs in the "vapor" state, the progress variable c_i is calculated to determine where the ignition occurs first and to identify the "burnt" and "unburnt" CVs.
5. If combustion has started, the thermodynamic properties are recomputed. It is necessary to consider that for each "vapor" CV two states ("burnt" and "unburnt") can coexist, so the energy balance must be written for each zone. The derivatives of the "burnt" zones need to include the heat released by the combustion of the fresh charge. Moreover, the NO emissions are calculated with a Zeldovich-extended thermal mechanism [20], [21] as described in [9].
6. Steps 2 to 5 are repeated until the Exhaust Valve Opening (EVO) is reached.

2.2. Premixed combustion model based on flamelet assumption

The objective of predictive combustion models within the 0D approaches is to sufficiently describe the influence of the main physical and chemical parameters that determine the overall burning rate, despite the simplifications introduced by the inability to resolve the flow field locally:

- at the spark timing, a high-temperature kernel of the order of 1 mm in diameter between the electrodes of the sparkplug is formed. The growth of its initial flame kernel is quasi-laminar and highly stretched with a gradual transition to a turbulent flame as the local flow increasingly distorts the flame front;
- when the flame is fully developed, turbulence wrinkles considerably the flame front, and the flame propagates throughout the combustion chamber, where the greatest part of the energy content is released. Microscopically examining the globally wrinkled and turbulent flame reveals that its structure remains laminar and its thickness consistently thin, characteristic of a corrugated flame or wrinkled flamelets combustion regime. Hence every element of the flame propagates toward the fresh gases with the laminar flame speed, so that the burning rate would depend on such a flame velocity to the contour that is referred as the turbulent flame surface (A_T). Applying the Damköhler hypothesis we can correlate the ratio of the turbulence (s_T) to laminar flame speed (s_L) to the ratio of the turbulent to the mean flame surface, a contour of a fictitious mean flame surface (A_L) assumed to be spherical:

$$\frac{s_T}{s_L} = \frac{A_T}{A_L} \tag{4}$$

- turbulent flame propagation continues until flame-wall interaction becomes significant, initiating extinction mechanisms until the flame is extinguished. During this phase, flame front wrinkling diminishes due to the impact of the flow boundary layer, increased heat losses to the cold wall, and the flame's confinement by the wall.

The proposed 0D model aims to describe all these phases of the combustion process from the kernel formation to the flame extinguishment, using several sub-models to account for laminar flame speed, flame surface, aerodynamic turbulence, turbulent flame propagation, flame-wall interaction. All length scales of aerodynamic turbulence are assumed to be larger than the flame front thickness (flamelet regime), so a global turbulent flame speed or a wrinkling factor is calculated, based on a revised version of the Eddy Burn Up model, which assumes the combustion mechanism in the SI engine depends on the entrainment of turbulent eddies in the flame front.

Modified Eddy Burn Up model

Combustion is modelled in two steps: first, the fresh gases are entrained in the flame front at a speed corresponding to the turbulent flame speed (s_T). Then, the entrained mass burns over characteristic time:

$$\frac{dm_{ent}}{dt} = \rho_u A_L s_T \tag{5}$$

$$\frac{dm_b}{dt} = \frac{m_{ent} - m_b}{\tau_b} \tag{6}$$

where τ_b is a characteristic time that physically corresponds to the time required for the turbulence eddies to be entrained into the flame front. To account for the effects of variations in the burning rate with the existing turbulence intensity as a function of the engine load and speed, a modified definition of the characteristic time τ_b has been adopted:

$$\tau_b = \frac{0.15}{C_{centr}} \frac{L_i}{u'} \tag{7}$$

Where u' is the turbulent intensity and L_i is the integral length scale. The fully turbulent flame speed S_T can be determined using Gulder's correlation [22]:

$$S_T = C_{st} S_L \left(1 + 0.62 f \sqrt{\frac{u'}{S_L} Re_\eta} \right) \tag{8}$$

where C_{st} is a tuning constant and its default value is 1.0. f is a transition function from laminar (0) to turbulence (1) condition and Re_η is the Kolmogorov Reynolds number and τ_η is the Kolmogorov time scale. These equations necessitate solving for the turbulent flow field, which will be described in the following section.

Additionally, it is necessary to account for both the initial phase of combustion, involving the transition from the laminar to the fully turbulent speed, and the final phase of combustion, involving the flame-wall interaction. The initial phase is described by the introduction of a transition parameter f ($0 \leq f \leq 1$), which is computed using the Herweg and Maly approach [23]:

$$f = \left[1 - exp\left(-\frac{r_K - S_{tay}}{C_{delay} L_i}\right)\right]^{0.5} \left[1 - exp\left(-\frac{u' + S_L}{L_i} t_{ign}\right)\right]^{0.5} \quad (9)$$

where t_{ign} is the time elapsed from sparking timing, r_K is the flame kernel radius, and S_{tay} is the Taylor micro-scale. C_{delay} is a tuning constant with a default value of 1.

The end of combustion, involving flame-wall interaction, is not described by a physical model since the mechanism depends on the local structure of the flame and flow fields. Hence a phenomenological approach is used by imposing a correction factor C_w (ranging from 0 for an undisturbed flame to 1 for a quenching flame), which is computed according to a S-shape formula:

$$C_w = 1 - exp\left(-2.908 \frac{X_b - X_{b50}}{1 - X_{b50}}\right)^{2.5} \quad (10)$$

where X_b is the burnt mass fraction and X_{b50} is the burnt mass fraction when the flame surface wetted by the cylinder walls equals to 50% of the total flame front.

For all the fuels considered by the model, the Metghalchi & Keck formula [3] [4] is adopted to determine the laminar flame speed, with specific coefficients that are fuel-dependent. This correlation uses the following form to express the influence of equivalence ratio, pressure, temperature, and residual gas content:

$$S_L(\emptyset, p, T, X_{res}) = S_{L0} \left(\frac{T}{T_0}\right)^{\alpha} \left(\frac{p}{p_0}\right)^{\beta} (1 - 2.1 X_{res}) \quad (11)$$

Where the coefficients α and β depend on the fuel and the equivalence ratio. In the case of NH_3/H_2 blends, the correlation from Pessina et al. [26] is used.

In-cylinder turbulence

Turbulence inside the cylinder is primarily formed during the intake phase when the incoming air generates flow structures with large-scale turbulent motions which then expand and transform their kinetic energy into internal energy of the surroundings. As previously described, the determination of the burning mass rate requires the knowledge of the main turbulence parameters, specifically the turbulent intensity u' and the integral length L_i. In the literature, numerous approaches have been proposed, generally involving the application of Reynolds-averaged Navier-Stokes equations in quasi-dimensional simulation to model turbulence production and dissipation. Among those, here the so-called $K - k - \varepsilon$ model proposed by Fogla et al. [27] has been adopted, which accounts for the balance equation for the mean kinetic energy $K = \frac{1}{2} U^2$ (U is the mean velocity inside the cylinder), for the turbulent kinetic energy $k = \frac{3}{2} u'^2$ and for the turbulent dissipation rate ε:

$$\frac{d(mK)}{dt} = C_{in}(1 - \alpha_{in}) E_{in} + K \dot{m}_{out} - P_k \quad (12)$$

$$\frac{d(mk)}{dt} = C_{in} \alpha_{in} E_{in} + k \dot{m}_{out} + P_k + C_{tumb} T - m\epsilon \quad (13)$$

$$\frac{d(m\varepsilon)}{dt} = C_{in} E_{in} \frac{\sqrt{k}}{L_g} + \varepsilon \dot{m}_{out} + P_\varepsilon + C_{tumb} T \frac{\sqrt{k}}{L_g} - 1.92 \frac{m\varepsilon^2}{k} \quad (14)$$

where $E_{in} = (1 - C_T)\frac{1}{2}\dot{m}_{in}v_{in}^2$, $\dot{m}_{in}$ and v_{in} are the mass flow rate and isentropic velocity of the flow entering the cylinder respectively. C_T is the tumble coefficient associated with the valves. C_{in} is the model parameter which is used to account for the actual flow velocities through the valves, α_{in} is indicative of the fraction of inflow energy that directly enters the cylinder as turbulence and is not generated by the cascade process, $\dot{m}_{out}$ is the mass flow rate of the flow exiting the cylinder, T is the production of turbulence due to the decay of the tumble macro-vortex during the compression stroke and C_{tumb} is a tuning constant that controls the intensity of this process. P_k and P_ε model the production of turbulent kinetic energy and dissipation rate from the large-scale mean flows via the energy cascade process, and L_g is the angular momentum. A detailed description of each term and the validation of the model can be found in [27]. Solutions of k and ε allow to determine the turbulence intensity u' and the integral length L_i which are required to determine the burning rate applying the previously described combustion model.

Finally, pollutant emissions are determined based on equilibrium assumptions of the main species (whose list will depend on the chosen fuel) and a kinetically controlled formation of the NOx according to the well-known thermal mechanism.

3. Experimental validation

3.1. Diesel Cycle

The validation of the diffusion combustion model was first performed in a 6-cylinder medium-speed Diesel engine with a bore size of 0.2 m for marine applications, which is of interest as a conventional propulsion system to be eventually considered as a reference baseline case. The available experimental data refer to a load sweep along the nominal engine speed of 1000 rpm. While detailed information regarding the fuel injection rate profile was not available, a profile was taken from [28], scaled based on injection pressure by keeping the same ramp-up and ramp-down slopes.

Figure 3 shows the comparison between measured and computed normalized in-cylinder pressure and apparent heat release rate (AHRR). For all conditions, the model shows a rather good accuracy in describing the evolution of the combustion process, including the initial ramp of the AHRR, its quasi-steady-state value at full load, the time of its earlier decrease at lower loads, and the burnout phase. Some differences can be observed in the initial stage of combustion where experimentally a peak of heat release rate associated with premixed combustion occurs. The lack of such detail in the model is due to the use of a simplified approach for prediction ignition instead of using the Tabulated Kinetics Ignition (TKI) approach. In this work, ignition was computed for each iso-ϕ zone using the following equation:

$$\tau_{ID,y} = C_{ID}\, p_{cyl}^{-1.02} \phi_y^{-0.2} \exp\left(-\frac{E_A}{RT_{cyl}}\right) \tag{15}$$

where C_{ID} is a frequency parameter, E_A is the energy of activation and R is the gas constant. Here: $C_{ID} = 3.45\ ms^{-1}$ and $E_A/R = 2100\ K$.

During the ignition delay time, p_{cyl} and T_{cyl} may vary due to the compression resulting from piston motion. To account for these changing conditions, the ignition delay is obtained numerically by integrating the reciprocal of the equation (15) until the following relation is satisfied:

$$\int \frac{1}{\tau_{ID,y}} dt = 1 \tag{16}$$

Equation (16) has been developed under the assumption of multi-zone/two-zone combustion, a thermodynamic model often used to simulate Diesel combustion. Under these conditions, the equivalence ratio term $\phi_y^{-0.2}$ corresponds to the global air-fuel injected ratio, but in this model, it represents the local value, and its applicability is a bit more limited. The use of a TKI overcomes these limits and allows us to consider the effect of the fuel sensitivity on the ignition process, but its application was considered beyond the scope of this work and the reader is referred to other papers for these model capacities [13].

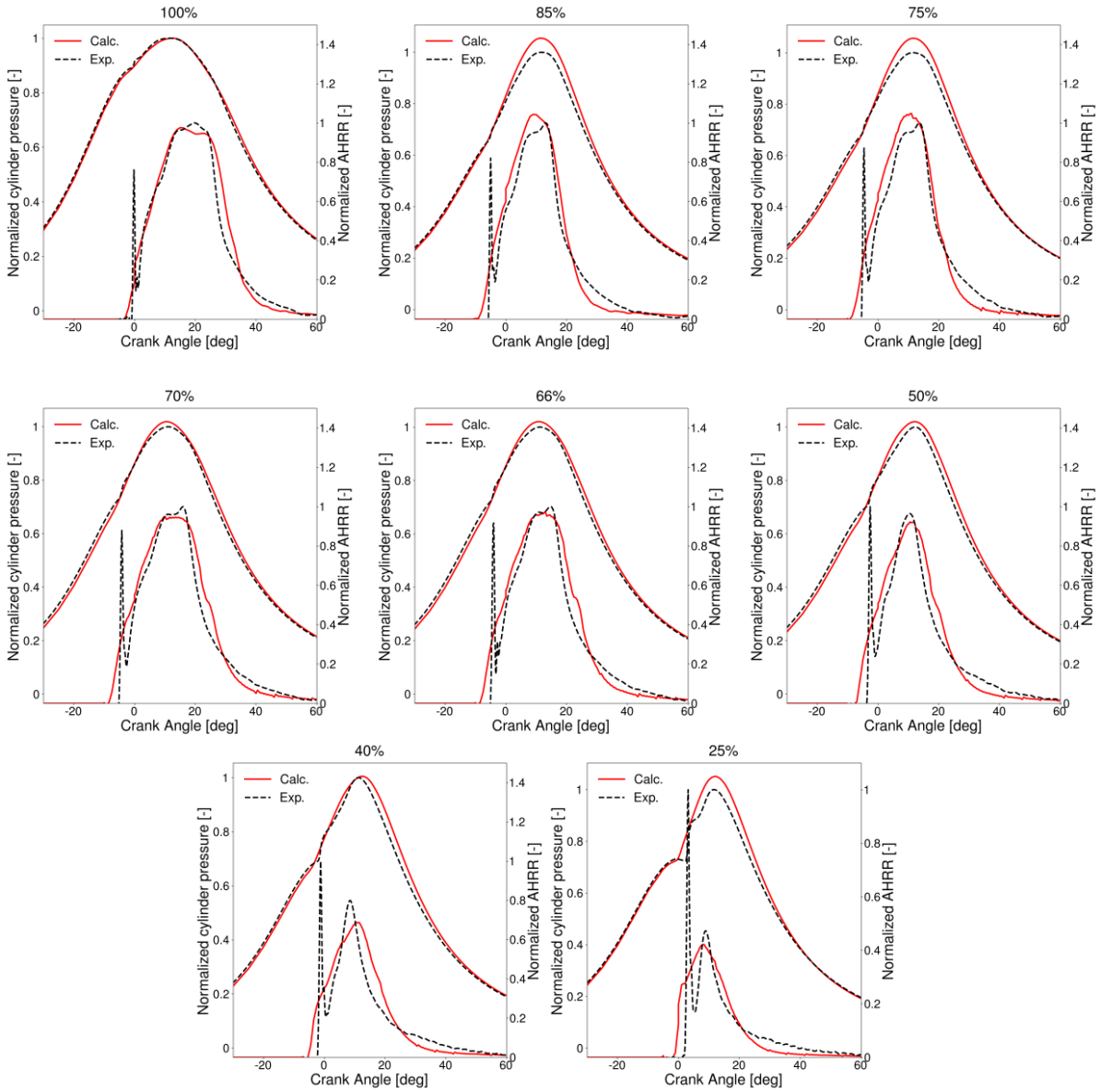

Figure 3: Comparison between experimental and computational pressure and AHRR. Results are normalized using the maximum pressure and AHRR in experiments.

Figure 4 compares the measured and computed pressure at the intake receiver on the left y-axis, while the corresponding values of the temperature at the turbine inlet are shown on the right y-axis. These

temperature values depend on the accuracy of the combustion model, and their agreement falls within an acceptable range, allowing for reliable turbocharging studies. The pressure at the intake receiver is well captured, demonstrating the accuracy of ACTUS in turbocharging simulation.

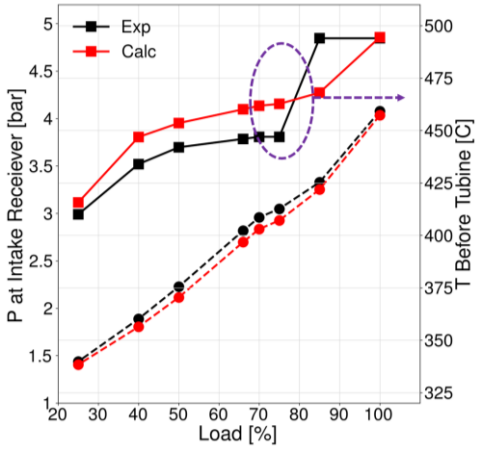

Figure 4: Comparison between measured and simulated pressure at intake receiver and temperature at turbine inlet.

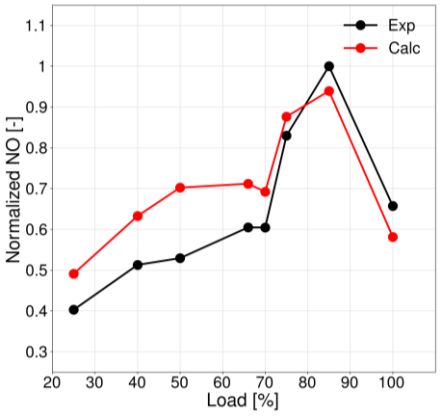

Figure 5: Comparison between measured and simulated NO_x emission. Results are normalized with respect to the maximum measured value.

Figure 5 compares the measured and simulated engine-out NO_x emissions, normalized to the maximum measured value. It demonstrates that the mode can well capture both the trend and the absolute value of NO_x emission.

3.2. Otto Cycle

The model's capabilities in describing the combustion process in spark-ignition (SI) engines were initially verified by studying a natural gas spark-ignited engine with a bore size of 0.145 m. The nominal engine speed was set at 1500 rpm, and three loads with three different spark timings (-15, -10, -5 CA aTDC) for each load and corresponding air-fuel ratio values were considered (see Table 1).

Table 1. Operating conditions

Load1	Spark Advance	λ	Load2	Spark Advance	λ	Load3	Spark Advance	λ
A1	-15 CA aTDC	1.404	**B1**	-15 CA aTDC	1.493	**C1**	-15 CA aTDC	1.518
A2	-10 CA aTDC	1.36	**B2**	-10 CA aTDC	1.418	**C2**	-10 CA aTDC	1.612
A3	-5 CA aTDC	1.305	**B3**	-5 CA aTDC	1.349	**C3**	-5 CA aTDC	1.373

Figure 6 compares the normalized measured and computed in-cylinder pressure curves and the corresponding AHRR for all three loads. For Load 1, the results show a very good agreement between measured and computed data: the model accurately predicts the compression curve, the start of combustion, the transition from laminar to turbulent combustion, the timing and value of the maximum heat release rate, and the completion of the process. The model captures the observed trend of reduced spark advance: a shift in the AHRR curves and a slight increase in their peak. Some differences between measured and computed AHRR can be observed in the last part of the combustion where the simulations show some overestimations. It is believed that in this phase of combustion, when the flame front approaches the walls, the approximations due to the sphericity of its surface become significant and the details of the occurring process cannot be completely captured due to the inherent simplifications in the approach.

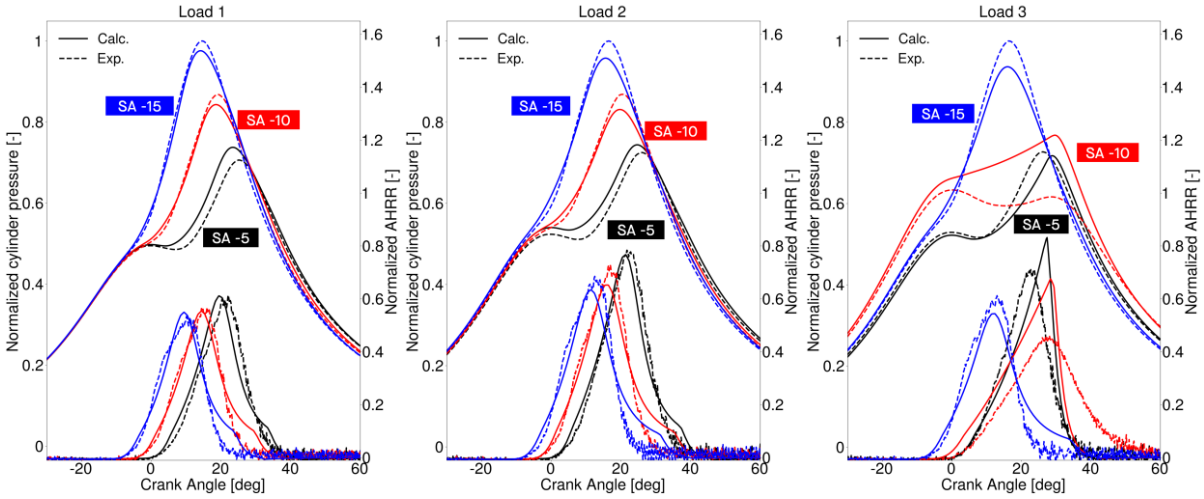

Figure 6: Comparison between measured and simulated pressure and AHRR at different loads and spark timing. Results are normalized with the maximum pressure and AHRR at different loads.

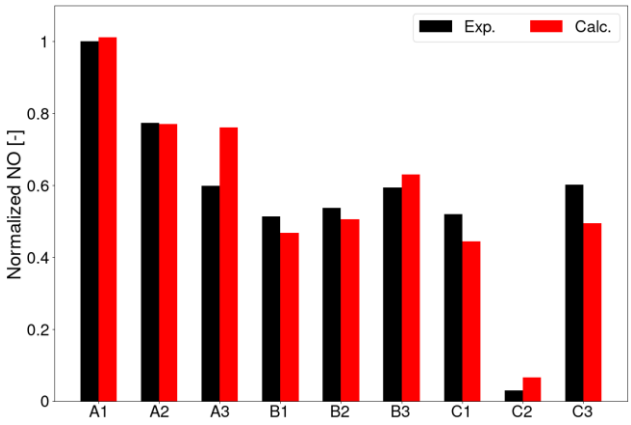

Figure 7: Comparison between measured and simulated NOx emission at different operating conditions. Results are normalized with the maximum measured value.

Similar observations can be made for Load 2, confirming the model's capabilities in this condition. At the highest load (Load 3), a good agreement in terms of the AHRR is observed for the operating points with -15 and -5 CA spark advances, with only minor differences in the computed maximum value of AHRR. However, the computed pressure curve for a spark advance of -10 CA aTDC does not align well with the measured data. Despite this, a closer examination of the AHRR profiles reveals that the model accurately captures the trend changes with varying spark advances. Specifically, the timing of the peak AHRR is delayed in the red curves (SA = -10 CA aTDC) compared to the black curve (SA = -5 CA aTDC), which is correctly represented by the model.

Figure 7 compares the measured and simulated NO_x emissions across all operating conditions. The results, normalized to the maximum measured value, show good quantitative and qualitative agreement. The model accurately predicts the observed variations at each load, attributed to combinations of spark advance and air-to-fuel ratio, as well as the changes from one load to another.

4. Turbocharging strategies

Following comprehensive validation in the previous section, these two predictive combustion models were employed in turbocharging studies to develop a concept that facilitates both Diesel and ammonia gas mode operation in a marine 4-stroke engine. To reduce computational costs, the heat release rate from the complete combustion simulation was fitted to a Wiebe function and subsequently utilized in the investigation of turbocharging concepts. Simulations were conducted along the propeller curve for a 6-cylinder engine configuration with a bore size of 0.2 m. As reported in [29], the ammonia gas engine operates within a λ range of 1.1 to 1.4, depending on the H_2 blend ratio, with 2% and 6% H_2 volume fractions considered. For this study, a λ of 1.25 with an H_2 volume fraction of 2.7% (representing 2% of the energy ratio) was selected to assess air requirements and exhaust gas, thereby determining the turbocharging requirements. The turbocharging studies will be conducted in two steps:

1. Understanding the turbocharging characteristics of ammonia gas engines, highlighting their differences from conventional gas engines, and providing guidance on identifying a suitable turbocharging system for ammonia-Diesel dual-fuel engines;
2. Assessing different turbocharging concepts for the ammonia gas mode and ensuring its compatibility with the Diesel operation mode.

4.1. Ammonia gas mode turbocharging characteristics

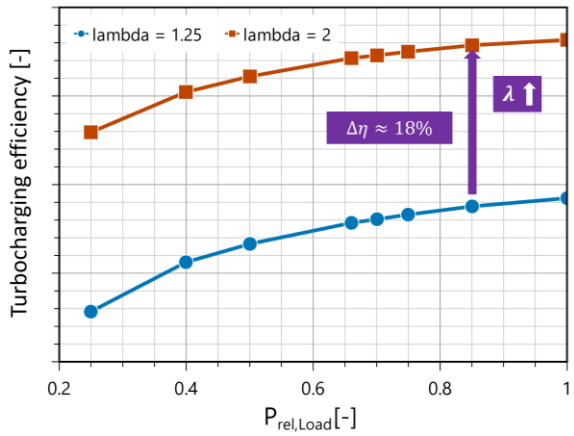

Figure 8: Turbocharging efficiency for gas engine operates at λ = 1.25 and 2.

As illustrated in Figure 8, operating under a low λ requires a lower turbocharging efficiency, which is defined by the energy ratio between the charge entering the cylinder and the exhaust gas exiting the cylinder. This is due to the high exhaust gas temperature and low inlet mass flow rate under such conditions. Compared to a commercial gas engine operating at λ ~ 2, reducing the λ to 1.25 could result in an 18% decrease in the turbocharging efficiency requirement. Consequently, a certain amount of energy must be dissipated in the turbocharging process for ammonia gas operation. Common methods to achieve this include using a wastegate and compressed air blow-off (or compressor recirculation), which will be studied and compared in the next section.

The operation lines for two fuel admission concepts—port fuel injection (PFI) and fuel admission upstream of the compressor—are illustrated in Figure 9. It is evident that under the same operating conditions, the PFI concept results in a much lower volume flow rate due to the absence of fuel in the compressed gas, which accounts for approximately 11.35% of the total mass. The fuel mass fraction is proportional to: $\frac{1}{\lambda*(stoichiometric\ AFR/LHV)}$, where stoichiometric AFR represents the stoichiometric air-fuel ratio and LHV is the low heating value. Such high fuel mass fraction in the ammonia gas engine can therefore be attributed to two factors: the low λ operation and the low stoichiometric AFR/LHV of ammonia. Specifically, ammonia has a stoichiometric AFR/LHV of 0.325, which is around 5% lower than that of methane (stoichiometric AFR/LHV ≈ 0.344). This suggests that the fuel admission approach could have a nonnegligible impact on turbo-matching, and detailed studies should be performed for each concept. In this study, the authors will focus only on the PFI concept.

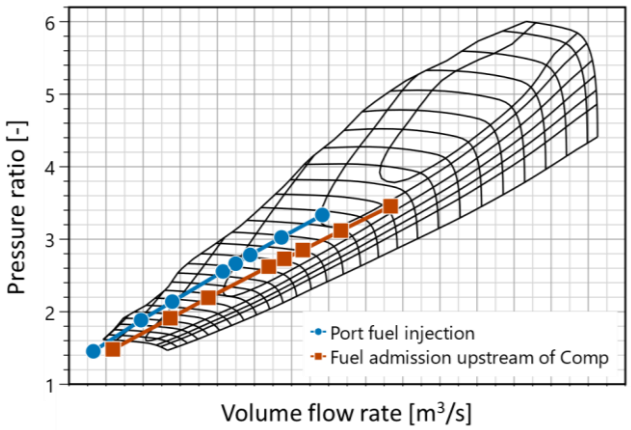

Figure 9: Operation lines for port fuel injection and fuel admission upstream of the compressor concepts.

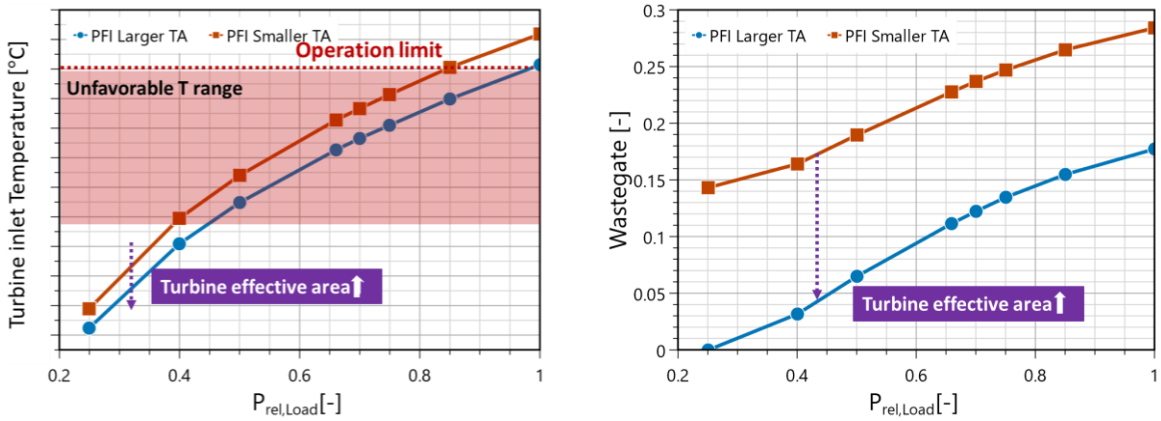

(a) Turbine inlet temperature

(b) Wastegate mass flow rate ratio

Figure 10: Effects of turbine effective area in the PFI ammonia engine.

Figure 10 illustrates the impact of increasing the turbine effective area (S_{eff}). As shown, a larger turbine can reduce the engine back pressure and improve the gas exchange phase. This results in less hot exhaust gas being trapped in the cylinder and a lower temperature at IVC, and consequently, a reduction of the turbine inlet temperature and the opening of the wastegate. However, even with the maximum feasible S_{eff}, where the wastegate is switched off at 25% load (as further increases in S_{eff} would fail to meet the low-load air requirement), the turbine inlet temperature still exceeds the component's operational limit. Most operating conditions fall within an unfavorable temperature range, where constant operation could shorten the maintenance interval. A potential solution to lower the turbine inlet temperature is to activate the engine bypass and cool the exhaust gas with air from the compressor outlet. To summarize, operating in ammonia gas mode may require:

- Compressed air blow-off or a wastegate to dissipate excess energy during the turbocharging process.
- An engine bypass to lower the turbine inlet temperature, bringing it below the component operation limit and avoiding the unfavorable temperature range.

These considerations will be studied and compared in the next section, where compatibility between Diesel and gas modes, in other words, using the same turbocharger specifications for both Diesel and gas modes, will also be taken into account.

4.2. From Diesel mode to ammonia gas mode

The turbocharger specifications were first selected for Diesel mode, where maintaining a high λ (indicative of turbocharging efficiency) is crucial to minimize soot formation. This approach leaves limited flexibility for tuning or matching the turbocharging system. In this paper, the turbine effective area was chosen to ensure the λ remains above the smoke limit at low load (λ = 1.65 at 25% load was obtained). These specifications were then applied to investigate different turbocharging concepts for ammonia gas mode. Specifically, the study assessed the wastegate with engine bypass and compressed air blow-off with engine bypass approaches, as depicted in Figure 11.

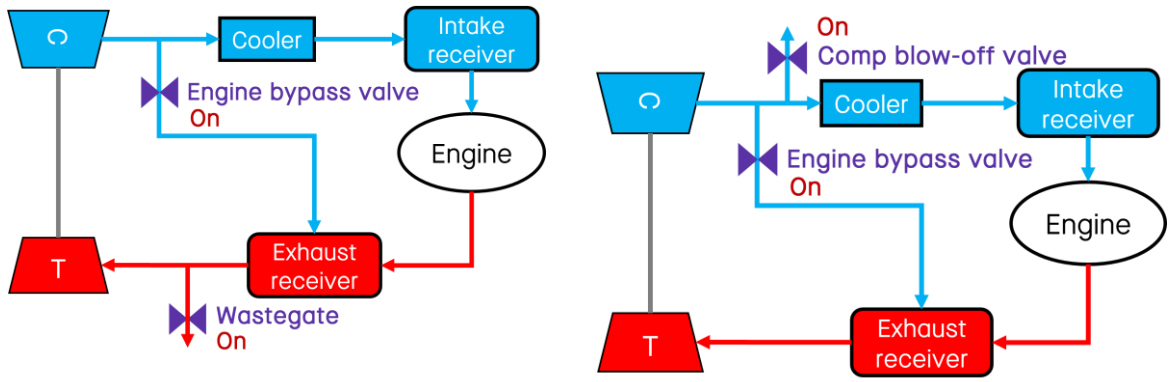

(a) Wastegate & engine bypass concept *(b) Compressed air blow-off & engine bypass concept*

Figure 11: Schematic diagram of different turbocharging concepts.

Concept 1: Wastegate & Engine bypass

Figures 12(a) and (b) respectively depict the operation lines and turbine inlet temperatures for Diesel mode and ammonia gas mode using wastegate and engine bypass turbocharging concepts, as well as the wastegate-only approach. An increase in engine bypass ratio or a wider engine bypass valve opening can result in a higher compressor volume flow rate and a lower turbine inlet temperature. Detailed operating parameters are illustrated in Figure 13: approximately 27% of the exhaust gas/energy must be dissipated through the wastegate at 100% load, with the wastegate opening reducing as the load decreases. However, the wastegate needs to remain open even at low load to maintain a low λ . As the engine bypass increases, a higher wastegate ratio becomes necessary at low loads for two reasons: the increased engine bypass elevates the energy flow in the exhaust, and the turbocharger efficiency improves (Figure 13(a)) due to the higher expansion ratio of the turbine, which shifts the operation point to a more efficient zone. An opposite trend is observed at high load (100% load), where the reduction in engine efficiency becomes more significant. This will be further discussed in Figure 14.

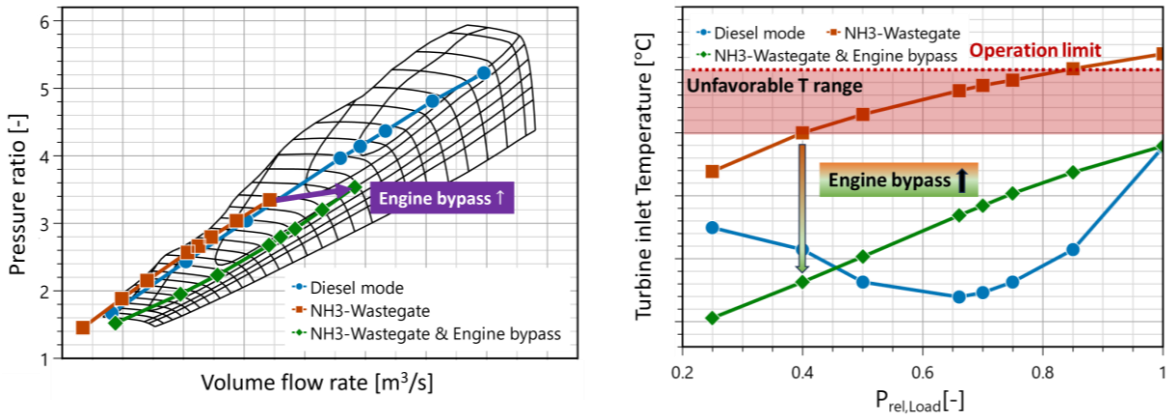

(a) Operation line *(b) Turbine inlet temperature*

Figure 12: Comparison between Diesel mode operation, and ammonia gas mode with and without engine bypass turbocharging systems.

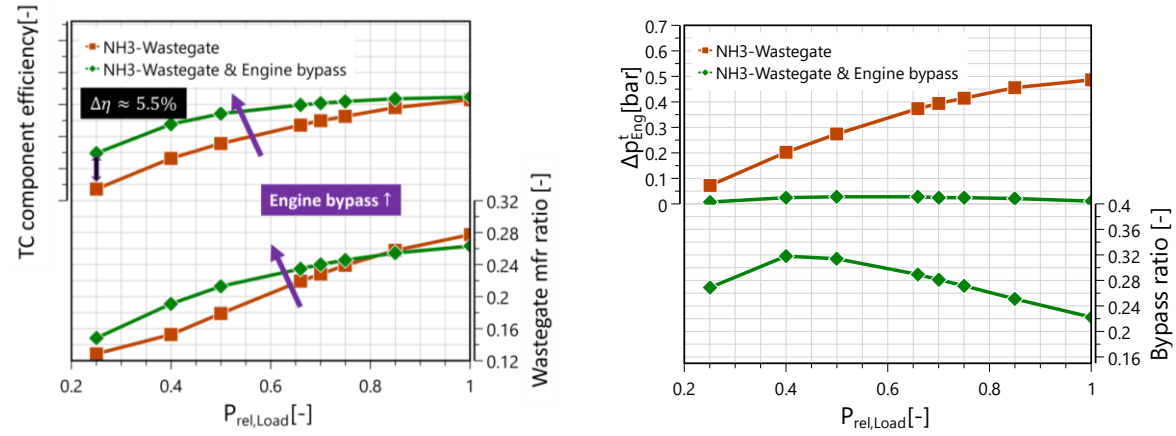

(a) Turbocharger efficiency & mass flow rate ratio *(b) Pressure difference over engine & engine bypass ratio*

Figure 13: Comparison between two turbocharging systems for ammonia gas mode operation: wastegate only vs engine bypass & wastegate.

As also shown in Figure 12(a), the operation line shifts to a more efficient zone in the compressor map. However, further increases in engine bypass may cause the operation line to approach the choke region, significantly reducing compressor efficiency, which limits the potential reduction in turbine inlet temperature. However, such an increase in engine bypass is not feasible with passive engine bypass control, as the engine bypass remains fully open at all loads, and the pressure difference across the engine (from intake to exhaust) becomes too low (around 20 mbar) to drive additional flow from intake to exhaust (Figure 13(b)). Such a small pressure difference can lead to a high gas exchange loss and consequently lower engine efficiency. As shown in Figure 14, there is approximately a 0.67%-pts loss in engine efficiency at 100% load where the pressure difference drops the most (Figure 13(b)) when changing the engine bypass opening from 0 to 100%. It is important to note that these two methods (in Figure 12(a)) represent the extreme cases, with any additional measures (e.g. pump). An intermediate option can be chosen with the appropriate wastegate ratio and bypass ratio.

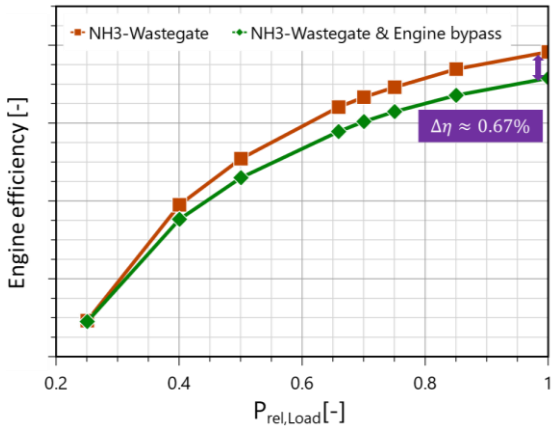

Figure 14: Comparison of engine efficiency in ammonia gas mode: wastegate only vs. engine bypass and wastegate turbocharging systems.

Concept 2: Compressed air blow-off & Engine bypass

Figure 15(a) and (b) present the operation lines and turbine inlet temperatures for Diesel mode and ammonia gas mode using the compressed air blow-off turbocharging approach. It is evident that, with compressed air blow-off alone, the turbine inlet temperature becomes too high for ammonia gas operation at most loads, necessitating the opening of the engine bypass valve. However, using compressed air blow-off results in a high volume flow rate in the compressor, and opening the engine bypass valve shifts the operation line further into the choke region. A potential solution could be the cut-in of an additional turbocharger in ammonia gas mode to facilitate the use of both compressed air blow-off and the engine bypass. The operation lines for such a turbocharger cut-in system are shown in Figure 16(a) for the main turbocharger and (b) for the additional cut-in turbocharger. The cut-in turbocharger is significantly smaller, with about 54% of the flow capacity of the main turbocharger.

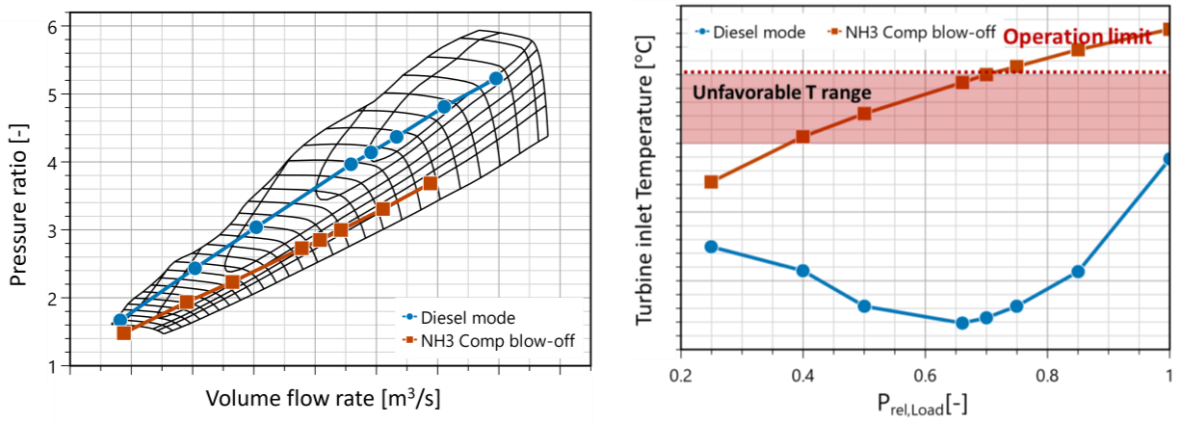

(a) Operation line

(b) Turbine inlet temperature

Figure 15: Ammonia gas mode with compressed air blow-off turbocharging system

In Figure 16(a), the operation line for the compressed air blow-off & engine bypass approach in ammonia gas mode is closer to that of the Diesel mode, indicating a more efficient compressor operation zone compared to the wastegate & engine bypass turbocharging system. Figure 17 illustrates that the turbine inlet temperatures for both Diesel and ammonia gas modes, using two different

turbocharging strategies, reveal that the compressed air blow-off with engine bypass achieves a lower turbine inlet temperature due to the higher engine bypass ratio (Figure 18(a)). As seen in Figure 16(a), there is potential for further shifting of the operation line in the compressed air blow-off & engine bypass setup, suggesting that additional adjustments to the engine bypass ratio can still be made to control the turbine inlet temperature.

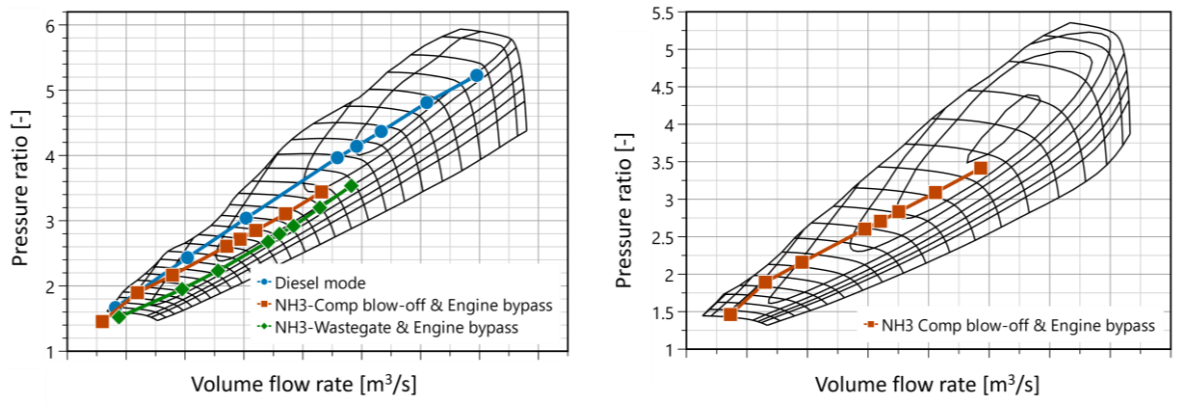

(a) Main turbocharger *(b) Cut-in turbocharger*

Figure 16: Operation lines for Diesel mode, and ammonia gas mode with two different turbocharging systems: compressed air blow-off only, and compressed air blow-off & engine bypass.

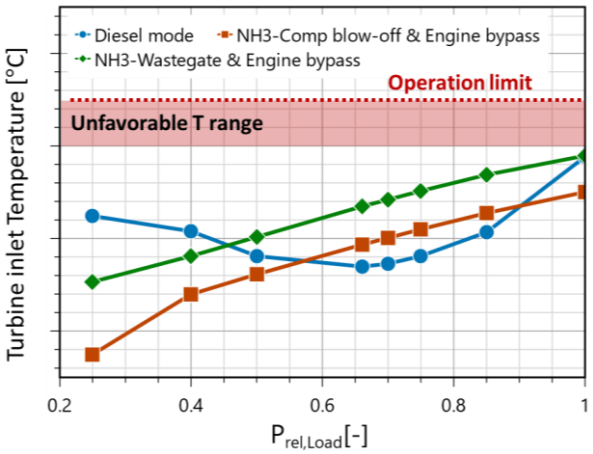

Figure 17: Temperatures at turbine inlet for Diesel mode operation, and ammonia gas mode with two different turbocharging concepts: compressed air blow-off & engine bypass and wastegate & engine bypass.

Figure 18(a) also shows that the compressed air blow-off method allows for a higher engine bypass ratio, defined by the mass flow rate through the engine bypass valve relative to the mass flow rate after the compressed air blow-off valve. This is because the turbocharger cut-in significantly reduces engine back pressure, thereby increasing the pressure difference across the engine. This results in a high mass flow rate through the bypass valve and a high bypass ratio without fully opening the bypass valve. At 25% loads, the engine bypass valve needs to be fully open to increase energy flow at the turbine inlet and achieve the target λ. Reducing the turbine effective area of the cut-in turbocharger may be beneficial at low loads, which will be investigated in future studies. Figure 18(b) presents the wastegate and compressed air blow-off ratios for each turbocharging system, showing that approximately 23% of

the compressed air or 26% of the exhaust gas needs to be dissipated at 100% load to meet the low λ requirement. Figure 19 compares the engine efficiency in ammonia gas mode using two different turbocharging systems. The compressed air blow-off approach demonstrates a slight improvement in engine efficiency due to reduced gas exchange loss resulting from higher pressure over the engine. In summary, compared to the wastegate approach, the turbocharger cut-in with compressed air blow-off has two primary functions: it provides additional control over turbine inlet temperature and converts the energy flow of exhaust gas passing through the wastegate into compressed air.

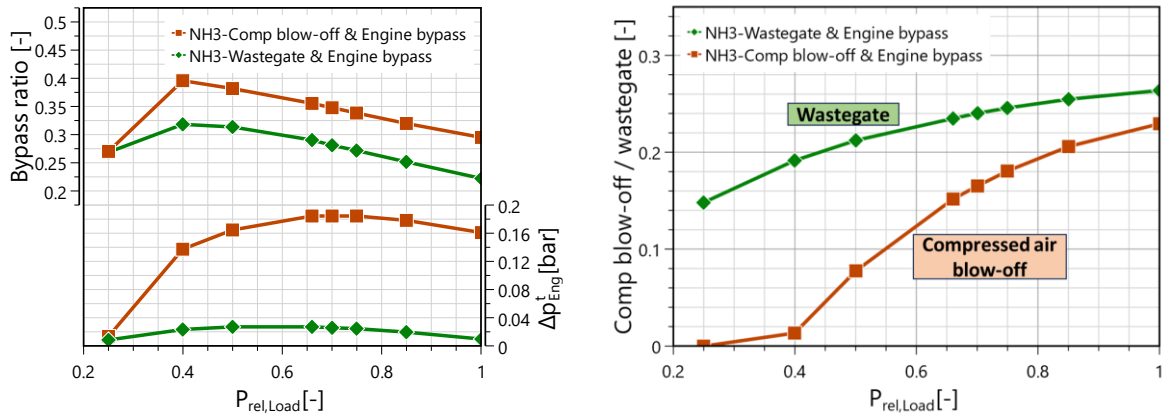

(a) Engine bypass ratio & pressure difference over engine *(b) wastegate / compressed air blow-off ratio*

Figure 18: Comparison between two turbocharging concepts for ammonia gas mode: compressed air blow-off & engine bypass vs wastegate & engine bypass.

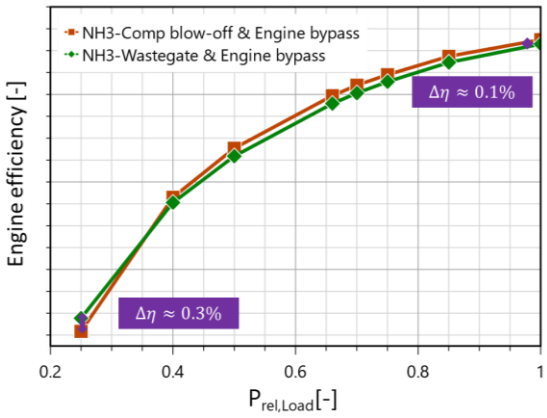

Figure 19: Comparison of engine efficiency in ammonia gas mode: compressed air blow-off & engine bypass vs wastegate & engine bypass turbocharging concepts.

5. Conclusion and outlook

This paper presents the latest development of our in-house software, which now includes advanced and predictive thermodynamic combustion models for both premixed and diffusive combustion, developed by Politecnico di Milano. A comprehensive validation was conducted to build confidence in their application for turbocharging assessments. The characteristics of ammonia gas engine turbocharging were evaluated, and various turbocharging concepts were studied and compared

considering the compatibility with Diesel mode operation. Key observations can be summarized as follows:

- The premixed and diffusion combustion models can accurately predict the combustion processes in natural gas and Diesel engines, respectively, demonstrating their reliability for turbocharging studies.
- Due to the low LHV of ammonia and the low λ operation, the fuel accounts for about 11.35% of the air-fuel mixture, indicating that the fuel admission concepts (fuel admission before or after the compressor) could have an impact on turbo-matching.
- In the ammonia gas engine, over 20% of the energy from the exhaust gas needs to be dissipated during the turbocharging process. This is necessary even using the largest feasible turbine effective area, due to the high turbine inlet temperature and low air requirement from the low λ operation and the turbine inlet temperature exceeds component limits. Wastegate or compressed air blow-off can be used to dissipate the extra energy, and the engine bypass could reduce the temperature below the operation limit of the components.
- The wastegate and engine bypass approach can enable compatibility between ammonia gas mode and Diesel mode operation, and such configuration can be found in existing gas-Diesel dual-fuel engines, making it a straightforward retrofitting solution. However, there is a trade-off between the compressor operation line and the turbine inlet temperature: a higher turbine inlet temperature brings the operation line closer to the efficient zone / Diesel mode operation line in the compressor map.
- The compressed air blow-off and engine bypass approach can also enable compatibility with Diesel mode operation and allow greater adjustment of turbine inlet temperature. However, this approach involves a turbocharger cut-in/-out process during operation, adding complexity to control, and how and where the extra compressed air can be utilized need to be explored.

Some considerations for future investigation include:

- Extending the combustion model for dual-fuel applications, incorporating the diesel pilot to achieve a more realistic turbocharging analysis for an ammonia-Diesel fuel-flexible dual-fuel engine.
- Conducting transient investigations of different control methods to facilitate a smooth transition between the two operation modes.
- Investigating the waste heat recovery in ammonia gas mode to enhance the overall energy efficiency of the ship: utilizing exhaust gas from the wastegate in the wastegate & engine bypass approach, and applying the extra compressed air in the compressed air blow-off & engine bypass approach.

Acknowledgment

The authors extend their gratitude to all colleagues within the Accelleron c/o Turbosystem Switzerland Ltd and Politecnico di Milano who contributed to the considerations and studies presented in this paper, as well as to those who participated in the discussion and revision of its content. Special thanks

to Alberto Pedrocchi, Stefan Hiltbrand, Raphael Ryser, Gilles Hardy, and Prof. Gianluca Montenegro for their significant contributions to the paper and the project.

Literature

[1] "Revised GHG reduction strategy for global shipping adopted." Accessed: Jul. 22, 2024. [Online]. Available: https://www.imo.org/en/MediaCentre/PressBriefings/pages/Revised-GHG-reduction-strategy-for-global-shipping-adopted-.aspx

[2] B. Stolz, M. Held, G. Georges, and K. Boulouchos, "Techno-economic analysis of renewable fuels for ships carrying bulk cargo in Europe," *Nat. Energy*, vol. 7, no. 2, pp. 203–212, Feb. 2022, doi: 10.1038/s41560-021-00957-9.

[3] F. M. Kanchiralla, S. Brynolf, T. Olsson, J. Ellis, J. Hansson, and M. Grahn, "How do variations in ship operation impact the techno-economic feasibility and environmental performance of fossil-free fuels? A life cycle study," *Appl. Energy*, vol. 350, p. 121773, Nov. 2023, doi: 10.1016/j.apenergy.2023.121773.

[4] X. Zhou, T. Li, N. Wang, X. Wang, R. Chen, and S. Li, "Pilot diesel-ignited ammonia dual fuel low-speed marine engines: A comparative analysis of ammonia premixed and high-pressure spray combustion modes with CFD simulation," *Renew. Sustain. Energy Rev.*, vol. 173, p. 113108, Mar. 2023, doi: 10.1016/j.rser.2022.113108.

[5] A. J. Nyongesa, J. K. Kim, and W.-J. Lee, "Investigation on the combustion of ammonia using direct high/medium-pressure-Otto injection approach in a diesel two-stroke marine slow speed engine," *J. Energy Inst.*, vol. 114, p. 101641, Jun. 2024, doi: 10.1016/j.joei.2024.101641.

[6] "Dual-fuel engines from Wärtsilä," Wartsila.com. Accessed: Jul. 22, 2024. [Online]. Available: https://www.wartsila.com/encyclopedia/term/dual-fuel-engines-from-wartsila

[7] N. Watson, A. D. Pilley, and M. Marzouk, "A Combustion Correlation for Diesel Engine Simulation," SAE International, Warrendale, PA, SAE Technical Paper 800029, Feb. 1980. doi: 10.4271/800029.

[8] V. D. Bellis, F. Bozza, D. Tufano, V. D. Bellis, F. Bozza, and D. Tufano, "A Comparison Between Two Phenomenological Combustion Models Applied to Different SI Engines," presented at the International Powertrains, Fuels & Lubricants Meeting, SAE International, Oct. 2017. doi: 10.4271/2017-01-2184.

[9] M. Tamborski, G. D'Errico, T. Lucchini, T. Cerri, and A. Onorati, "A Constant Equivalence Ratio Multi-Zone Approach for a Detailed and Fast Prediction of Performances and Emission in CI Engines," *SAE Int. J. Adv. Curr. Pract. Mobil.*, vol. 4, no. 5, Art. no. 2022-01–0381, Mar. 2022, doi: 10.4271/2022-01-0381.

[10] "Turbo boost: ACTUS is ABB's new simulation software for large turbocharged combustion engines," ResearchGate. Accessed: Jul. 22, 2024. [Online]. Available: https://www.researchgate.net/publication/296067793_Turbo_boost_ACTUS_is_ABB's_new_simulation_software_for_large_turbocharged_combustion_engines

[11] Y. Qiu *et al.*, "Ammonia fueled engine with diesel pilot ignition: Approach to achieve ultra-high ammonia substitution," *Int. J. Engine Res.*, p. 14680874241248507, Apr. 2024, doi: 10.1177/14680874241248507.

[12] M. P. B. Musculus and K. Kattke, "Entrainment Waves in Diesel Jets," *SAE Int. J. Engines*, vol. 2, no. 1, Art. no. 2009-01–1355, Apr. 2009, doi: 10.4271/2009-01-1355.

[13] M. Tamborski, G. D'Errico, T. Lucchini, and A. Onorati, "Detailed prediction of HRR and NOx emissions in CI engines via a novel thermodynamic model with constant equivalence ratio zones," *Int. J. Engine Res.*, vol. 24, no. 6, pp. 2315–2337, Jun. 2023, doi: 10.1177/14680874221128645.

[14] J. D. Naber, D. L. Siebers, J. D. Naber, and D. L. Siebers, "Effects of Gas Density and Vaporization on Penetration and Dispersion of Diesel Sprays," presented at the International Congress & Exposition, SAE International, Feb. 1996. doi: 10.4271/960034.

[15] A. Ballerini *et al.*, "Extension and Validation of a Constant Equivalence Ratio Multi-Zone Approach to DME Combustion in Vessels and CI Engines," presented at the WCX SAE World Congress Experience, SAE International, Apr. 2023. doi: 10.4271/2023-01-0193.

[16] D. L. Siebers, "Scaling Liquid-Phase Fuel Penetration in Diesel Sprays Based on Mixing-Limited Vaporization," presented at the International Congress & Exposition, SAE International, Mar. 1999. doi: 10.4271/1999-01-0528.

[17] D. L. Siebers, "Liquid-Phase Fuel Penetration in Diesel Sprays," *SAE Trans.*, vol. 107, pp. 1205–1227, 1998.

[18] Q. Zhou, T. Lucchini, G. D'Errico, G. Hardy, and X. Lu, "Modeling heavy-duty diesel engines using tabulated kinetics in a wide range of operating conditions," *Int. J. Engine Res.*, vol. 22, no. 4, pp. 1116–1132, Apr. 2021, doi: 10.1177/14680874198961 65.

[19] T. Lucchini, D. Pontoni, G. D'Errico, and B. Somers, "Modeling diesel combustion with tabulated kinetics and different flame structure assumptions based on flamelet approach," *Int. J. Engine Res.*, vol. 21, no. 1, pp. 89–100, Jan. 2020, doi: 10.1177/1468087419862945.

[20] R. Miller, G. Davis, G. Lavoie, C. Newman, and T. Gardner, "A Super-Extended Zel'dovich Mechanism for No x Modeling and Engine Calibration," *SAE Trans.*, vol. 107, pp. 1090–1100, 1998.

[21] I. B. Zeldovich, G. I. Barenblatt, V. B. Librovich, and G. M. Makhviladze, "Mathematical theory of combustion and explosions," Jan. 1985, Accessed: Jun. 17, 2024. [Online]. Available: https://www.osti.gov/biblio/6082197

[22] Ö. L. Gülder, "Correlations of Laminar Combustion Data for Alternative S.I. Engine Fuels," presented at the West Coast International Meeting and Exposition, SAE International, Aug. 1984. doi: 10.4271/841000.

[23] R. Herweg and R. R. Maly, "A Fundamental Model for Flame Kernel Formation in S. I. Engines," SAE International, Warrendale, PA, SAE Technical Paper 922243, Oct. 1992. doi: 10.4271/922243.

[24] M. Metghalchi and J. C. Keck, "Laminar burning velocity of propane-air mixtures at high temperature and pressure," *Combust. Flame*, vol. 38, pp. 143–154, Jan. 1980, doi: 10.1016/0010-2180(80)90046-2.

[25] M. Metghalchi and J. C. Keck, "Burning velocities of mixtures of air with methanol, isooctane, and indolene at high pressure and temperature," *Combust. Flame*, vol. 48, pp. 191–210, Jan. 1982, doi: 10.1016/0010-2180(82)90127-4.

[26] V. Pessina, F. Berni, S. Fontanesi, A. Stagni, and M. Mehl, "Laminar flame speed correlations of ammonia/hydrogen mixtures at high pressure and temperature for combustion modeling applications," *Int. J. Hydrog. Energy*, vol. 47, no. 61, pp. 25780–25794, Jul. 2022, doi: 10.1016/j.ijhydene.2022.06.007.

[27] N. Fogla, M. Bybee, M. Mirzaeian, F. Millo, and S. Wahiduzzaman, "Development of a K-k-∈ Phenomenological Model to Predict In-Cylinder Turbulence," *SAE Int. J. Engines*, vol. 10, no. 2, Art. no. 2017-01–0542, Mar. 2017, doi: 10.4271/2017-01-0542.

[28] K. Panagiotis, "The effects of prolonged ignition delay due to charge air temperature reduction on combustion in a diesel engine," Ph.D. dissertation, ETH Zurich, 2013. [Online]. Available: https://www.research-collection.ethz.ch/bitstream/handle/20.500.11850/70618/eth-7278-02.pdf

[29] "E-Fuels als Schlüsseltechnologie der Dekarbonisierung." [Online]. Available: https://www.jenbacher.com/images/medias/files/6376/sonderdruck_mtz_innio__2024_deutsch_final2.pdf

[30] A. Valera-Medina, H. Xiao, M. Owen-Jones, W. I. F. David, and P. J. Bowen, "Ammonia for power," *Prog. Energy Combust. Sci.*, vol. 69, pp. 63–102, Nov. 2018, doi: 10.1016/j.pecs.2018.07.001.

EVOLVE

OUR ENGINES ARE FLEXIBLE, YOUR FUTURE IS SAFE

EVOLVE INLINE ENGINES

FUTURE PROOF AND FUEL FLEXIBLE

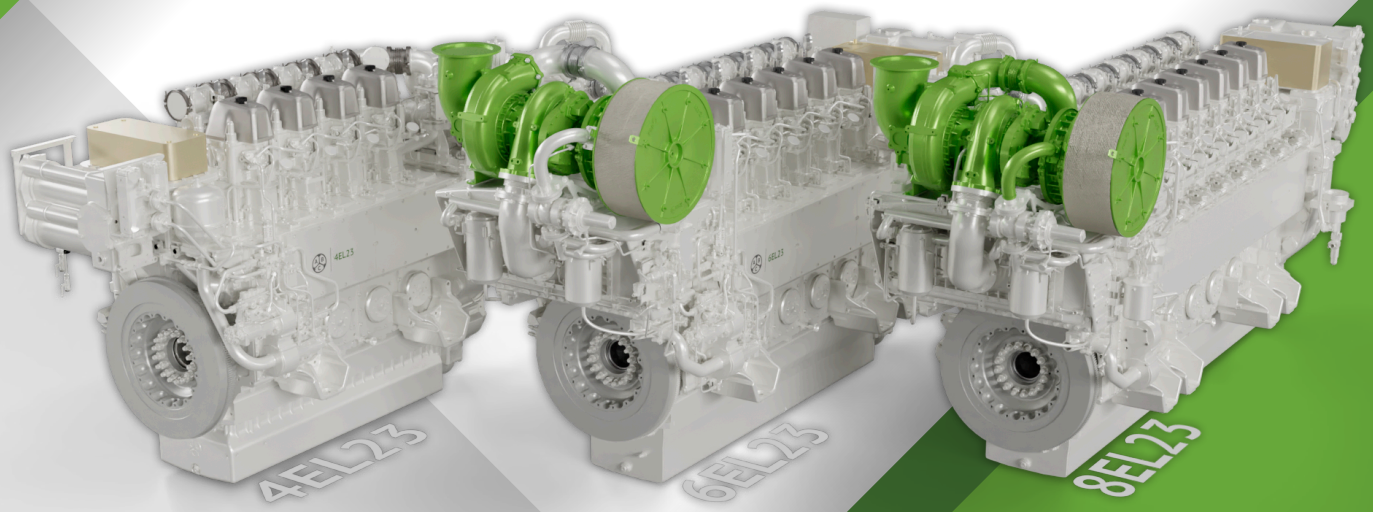

Download catalogue
Evolve Inline Engines

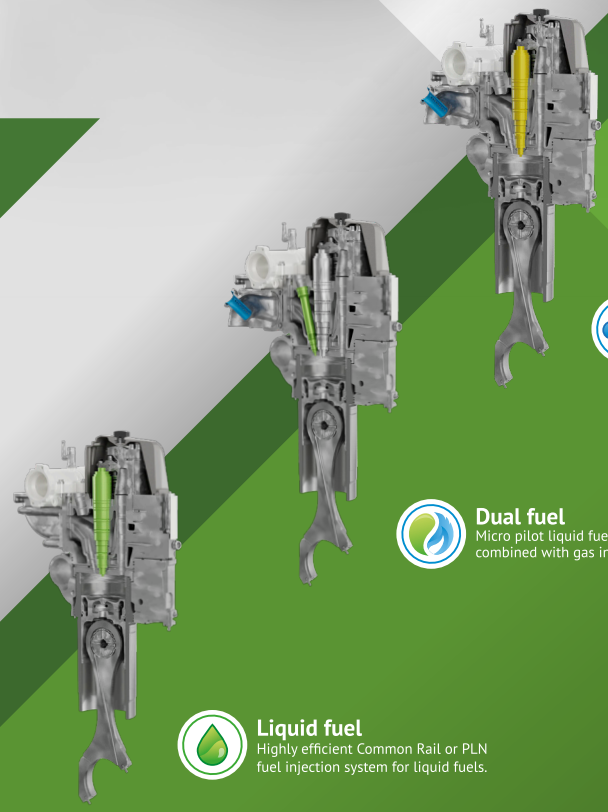

100% Gas
Gaseous fuel using a spark plug.

Dual fuel
Micro pilot liquid fuel injection combined with gas injection system.

Liquid fuel
Highly efficient Common Rail or PLN fuel injection system for liquid fuels.

Find us

Wiedauwkaai 43
9000 Gent
Belgium

Contact us

+32 9 267 00 00
info@abc-engines.com
www.abc-engines.com

Follow us

#ABCengines
#WePowerYourFuture

Keywords: shipping, decarbonization, ammonia; NO_x, N_2O, emission control, GHG

Emission Control Concepts for large two-stroke ammonia engines

Georgia Voniati, Athanasios Dimaratos, Grigorios Koltsakis, Leonidas Ntziachristos

Laboratory of Applied Thermodynamics, Department of Mechanical Engineering, Aristotle University of Thessaloniki, 54124, Thessaloniki, Greece

https://doi.org/10.18453/rosdok_id00004637

Abstract

Decarbonizing the maritime sector to meet the ambitious IMO targets requires the integration of various technologies. Among the alternative fuels, ammonia (NH_3) is a promising candidate; however, its combustion generates NO_x, NH_3, and N_2O, a potent greenhouse gas (GHG). The current study explores emissions control strategies for NH_3-fueled marine engines, employing both conventional and advanced catalytic technologies in simulated NH_3 engine exhaust to eliminate the unwanted N-species from the combustion process. Small-scale experiments are conducted on a synthetic gas bench (SGB) using three catalytic samples: two SCR technologies (vanadium-based (V-SCR) and iron-based (Fe-SCR)), and a platinum-based NH_3 oxidation catalytic (Pt-AOC). These experiments provide reaction kinetics information which are then integrated into physico-chemical models. The V-SCR reaction scheme employed commonly used reactions, whereas the Fe-SCR required specific modifications to its chemical reaction scheme. The models are then used to examine two scenarios concerning the relative engine-out concentrations of NO_x, NH_3 and N_2O: (1) low NO_x with high NH_3 and N_2O, and (2) high NO_x with lower NH_3 and N_2O levels. Simulation results indicate that NO_x could be optimized to meet the IMO limits with minimum NH_3 slip in both cases. However, high levels of NH_3 in the exhaust gas can result to significantly increased N_2O production in the exhaust aftertreatment system. In the meantime, N_2O decomposition using a cobalt-based catalyst is being examined, though the potential effects of NO_x, NH_3 and SO_2 remain to be determined.

1. Introduction

International maritime shipping plays a crucial role in the global economy and trade. Nevertheless, vessel emissions have a significant impact both on the environment and the human health. In particular, the maritime sector is responsible for almost 3% of the global Greenhouse Gas (GHG) emissions, which is expected to further increase until 2050 [1]. Apart from GHG, the maritime sector is also a source of air pollutants, such as Nitrogen Oxides (NO_x), Sulfur Oxides (SO_x) and Particulate Matter (PM) emissions [2]. In efforts to mitigate global warming and environmental impact of shipping, the International Maritime Organization (IMO) has implemented more stringent regulations on ships' emissions, aiming to at least 70% reduction in GHG by 2040, and ultimately to net-zero GHG emissions around 2050 [3]. In parallel, NO_x emissions must adhere to Tier III standards (3.4 g/kWh for vessels powered by low-speed two-stroke engines) within Emission Control Areas (ECAs), and Tier II standards (14.4 g/kWh for vessels powered by low-speed two-stroke engines) globally. Regarding SO_x emissions, the IMO has implemented a global sulfur cap, setting a maximum limit of 0.50% fuel sulfur content that decreases to 0.10% within Sulfur Emission Control Areas (SECAs) [4].

In pursuit of this goal, the introduction of alternative fuels such as liquified natural gas (LNG), methanol, ethanol, liquid petroleum gas (LPG), ammonia and hydrogen can significantly reduce emissions and minimize environmental and health risks. Among the alternative fuels, ammonia (NH_3) is one of the most promising solutions for fueling marine engines as it is carbon-free, it is easily stored in liquid form, and can be produced utilizing renewable energy sources such as wind, solar, or hydroelectric power [5]. However, the poor combustion properties of NH_3 (high autoignition temperature, low flame speed, low flammability) preclude a stable combustion with pure ammonia. Consequently, a pilot-fuel with higher cetane number (i.e., Diesel) is used to initiate the combustion of ammonia [6,7]. In addition to the poor combustion properties, it is known that ammonia combustion produces Nitrous Oxide (N_2O), unburnt NH_3 and NO_x emissions [5]. The former is one of the strongest GHG, with Global Warming Potential (GWP) over 100-year period equal to almost 300 [8]. NO_x and NH_3 (from fuel combustion and the Exhaust Aftertreatment System (EATS) respectively), are commonly targeted emissions species. Conversely, N_2O has always been treated as an unwanted product of the EATS rather as an engine emission to be targeted by a catalytic device. Therefore, the EATS of NH_3 fueled engines needs to adapt in order to simultaneously control all unwanted N-species.

The application of a Selective Catalytic Reduction (SCR) system (vanadium-based usually in marine applications) is commonly employed to reduce NO_x emissions by utilizing NH_3 or urea as the reducing agent [9]. In the case of ammonia combustion, NO_x can undergo direct reaction with the unburnt NH_3, or NH_3 can be directly injected upstream of the SCR to ensure adequate reductant availability. Ammonia slip can be minimized with an ammonia slip catalyst (ASC), however oxidation of NH_3 can promote NO_x and N_2O formation. Advanced SCR formulations are studied towards N_2O abatement. Iron-based catalysts (Fe-SCR) can be advantageous due to their ability to simultaneously reduce NO_x and N_2O by NH_3 [10,11]. It would be highly desirable to convert N_2O via catalytic thermal decomposition without the need of a reducing agent. Cobalt-based catalysts have been reported to promote such thermal N_2O decomposition [12-16], albeit only at rather high temperatures.

Based on the above, it is evident that the catalytic technologies must be developed and adopted to simultaneously reduce the unwanted N-species of NH_3 engine exhaust. However, NH_3 engines, particularly large two-stroke ones, used in the maritime sector are not yet commercially available. Consequently, the exact exhaust gas conditions for designing an emission control system are not

precisely known. Even if the exhaust gas characteristics of NH_3 engines were available from measurements, designing an emission control system through trial and error would be prohibitive due to the enormous testing costs on large two-stroke marine engines. Therefore, it is imperative to develop accurate and predictive models of the aftertreatment system that are applicable under a wide range of conditions to ensure the coverage of all possible scenarios. The development of such models is essentially the main target of the present work which is conducted within the EU-funded ENGIMMONIA project.

Exhaust aftertreatment models rely on kinetic mechanisms and rate expressions that describe the intrinsic chemical properties of the active materials. In this study, experiments are performed to derive the respective kinetic information for three catalytic formulations of interest and introduce them in integrated physico-chemical models of the transient transport and the reaction processes in monolithic catalytic reactors. The models are then used to study possible scenarios concerning the relative engine-out concentrations of NO_x, NH_3 and N_2O. The base scenario assumes an NH_3 to NO_x ratio of less than 1 (ANR<1) with low N_2O emissions, so additional NH_3 is injected upstream of the SCR, while the alternative scenario assumes low NO_x with high NH_3 (ANR>1) and higher N_2O emissions. The activity of the commonly used vanadium-based SCR (V-SCR) is compared to the Fe-SCR based technology. In the case of high NH_3 concentration in the exhaust, a dual-layer ASC is integrated to the aftertreatment system to handle the NH_3 slip. Particular emphasis is given to the formation/reduction of N_2O and the equivalent CO_2-emissions accounting for CO_2 emissions from pilot fuel as well.

2. Experimental and Modeling methods

2.1. Small-scale catalyst testing

The study of the catalyst chemistry is supported by measurements conducted on a Synthetic Gas Bench (SGB) setup (Figure 1). The flow rate and composition are regulated using the programmable mass flow controllers (MFCs). Moisture is introduced into the mixture via a pre-heated H_2O feed to avoid flue gas condensation. Subsequently, the mixture is heated to the desired temperature using a pre-heater system before traversing through the catalyst sample. The concentrations of the species at the outlet of the catalyst are quantified using an FTIR gas analyzer (AVL Sesam i60 FT SII).

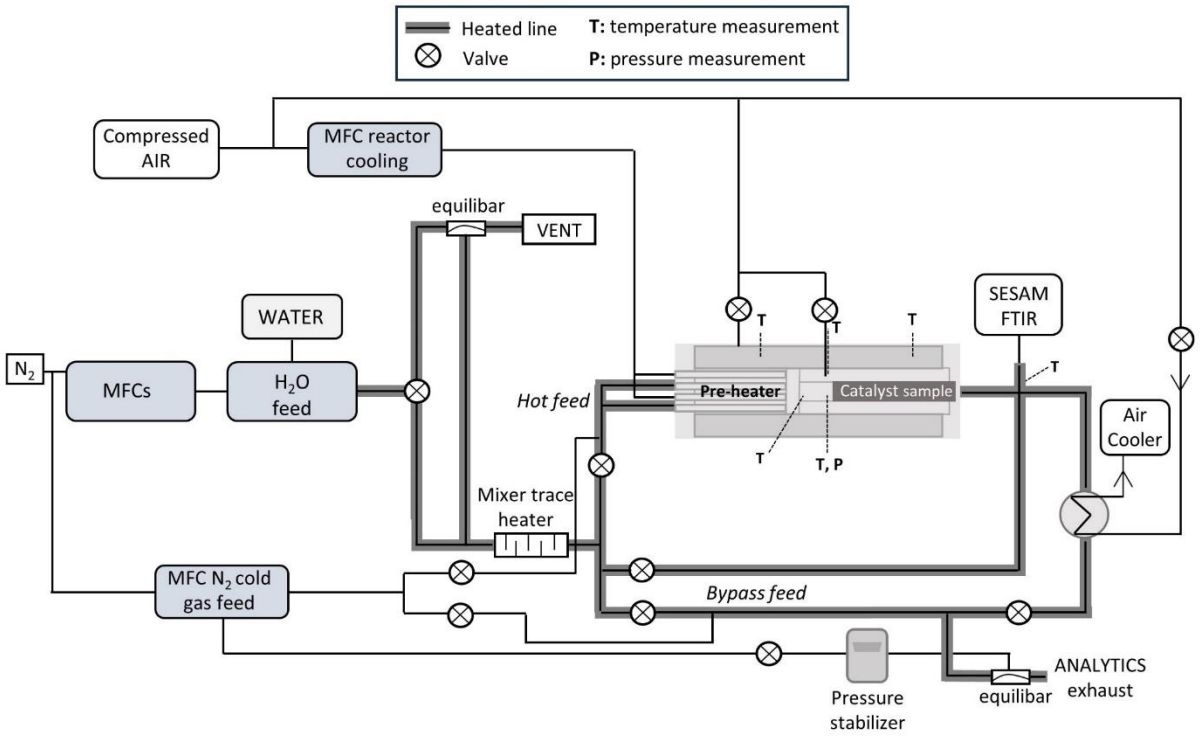

Figure 1: Synthetic Gas Bench (SGB) schematic configuration.

Three small-scale catalyst samples were tested: two diesel state-of the-art samples (a V-SCR and a Pt-AOC), and an ammonia engine tailored sample (an Fe-SCR). The characteristics of the samples are listed in Table 1. Both steady-state and light-off (temperature ramp) experiments are performed to derive kinetic information for the technologies of interest. These include NO_x reduction with NH_3, the effect of ANR on NO_x conversion, NH_3 slip and N_2O, the effect of N_2O addition in the feed gas as will be explained below.

Table 1: Properties of the tested catalyst samples.

Catalyst sample properties	**V-SCR**	**Fe-SCR**	**Pt-AOC**
Diameter x Length [mm x mm]	28 x 90	28 x 150	28 x90
CPSI [-]	100	230	200
Wall thickness [mils]	2	9	2
Substrate material [-]	metal	cordierite	metal
Cell shape [-]	triangle	square	triangle

For the purpose of marine applications, it is crucial to assess also sulfur tolerance, as SO_2 is a predictable byproduct of conventional pilot-fuel combustion, particularly when high-S fuel is used (e.g., HFO). V-SCR catalysts have demonstrated sulfur tolerance [17]; therefore, this study focuses on exclusively examining the impact of SO_2 on the Fe-SCR catalyst. Firstly, the catalyst is exposed to SO_2 until saturation. Thereafter, an SCR experiment is conducted without any further S-exposure. Finally, potential desulfation as function of temperature is examined.

2.2. Mathematical model

The present study is performed using the *ExothermiaSuite*® simulation tool [18]. The underlying models uses common assumptions to model the flow and thermophysical and chemical phenomena in the catalyst channels. These include the assumption of uniform flow, temperature, and concentration distribution at the inlet of the channels, and negligible heat losses to the ambient. Consequently, a one-dimensional (1D) representation of a single channel is adopted.

Temperature and species concentrations within the channel are determined by solving quasi-steady state balance equations for the heat (equation 1) and mass (equation 2) transfer:

$$\rho_{\mathrm{g}} C_{\mathrm{p,g}} v_{\mathrm{g}} \frac{\partial T_{\mathrm{g}}}{\partial z} = -h * \left(\frac{S_{\mathrm{F}}}{\varepsilon}\right) * \left(T_{\mathrm{g}} - T_{\mathrm{s}}\right) \tag{1}$$

$$\frac{\partial \left(v_{\mathrm{g}} y_{\mathrm{g},j}\right)}{\partial z} = -k_j * \left(\frac{S_{\mathrm{F}}}{\varepsilon}\right) * \left(y_{\mathrm{g},j} - y_{\mathrm{s},j}\right) \tag{2}$$

The wall surface temperature is calculated by the transient energy balance of the solid phase expressed as (equation 3):

$$\rho_{\mathrm{s}} C_{\mathrm{p,s}} \frac{\partial T_{\mathrm{s}}}{\partial t} = \lambda_{s,z} \frac{\partial^2 T_{\mathrm{s}}}{\partial z^2} + S \tag{3}$$

The surface concentrations are obtained by solving the concentration field inside the washcoat layer via the reaction-diffusion equation (equation 4):

$$-D_{w,j} \frac{\partial^2 y_{s,j}}{\partial w^2} = \sum_k n_{j,k} R_k \tag{4}$$

The solution of the concentration field in the washcoat layer is of particular importance for the case of technologies with multiple catalytic layers (1D + 1D). In fact, this is the case with ASCs that usually contain both a precious metal (PGM) layer, particularly an AOC layer of the oxidation of NH_3, as well as an SCR layer on top (Figure 2). This combination comes with advantages concerning NH_3 reduction and selectivity properties of the ASC, as NO_x formed in the oxidation layer diffuses through the SCR layer where it can be reduced.

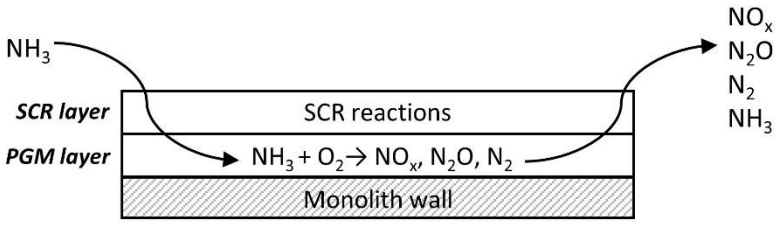

Figure 2: Dual-layer ASC schematic configuration.

2.3. Reaction Mechanisms

The SCR reactivity was described adapting commonly used SCR reaction schemes [19], including the standard, fast and NO_2 SCR reactions, as well as NH_3 and NO oxidation, and N_2O formation pathways as listed in Table 2. These reactions, commonly used in Diesel exhaust, are the starting point for developing the final models for the V- and Fe-SCR for the NH_3 engine exhaust.

Table 2; Basic SCR reaction scheme.

Reaction type	**Reaction**
NH_3 storage/release	$NH_3 \leftrightarrow NH_3$*
Standard SCR	$4\ NH_3$* + $4\ NO + O_2 \rightarrow 4\ N_2 + 6\ H_2O$
Fast SCR	$4\ NH_3$* + $2\ NO + 2\ NO_2 \rightarrow 4\ N_2 + 6\ H_2O$
NO_2 SCR	NH_3* + $3/4\ NO_2 \rightarrow 7/8\ N_2 + 3/2\ H_2O$
N_2O formation pathways	$2\ NH_3$* + $2\ NO + O_2 \rightarrow N_2 + N_2O + 3\ H_2O$ $4\ NH_3$* + $4\ NO_2 \rightarrow 2\ N_2 + 2\ N_2O + 6\ H_2O$
NO oxidation to NO_2	$NO + 1/2\ O_2 \leftrightarrow NO_2$
NH_3 oxidation	$4\ NH_3$* + $5\ O_2 \rightarrow 4\ NO + 5\ H_2O$ $2\ NH_3$* + $3/2\ O_2 \rightarrow N_2 + 3\ H_2O$ $4\ NH_3$* + $4\ O_2 \rightarrow 2\ N_2O + 6\ H_2O$

Ammonia oxidation on the Pt-AOC catalyst is approached with a simple kinetic model that gives a good representation of the overall reactions [20]. The common oxidation reactions used are listed in Table 3. These include the oxidation of NH_3 to N_2 and NO, the simultaneous oxidation of NH_3 and NO to N_2O and the oxidation of NO to NO_2.

Table 3: Basic Pt-AOC reaction scheme.

Reaction type	**Reaction**
NO oxidation to NO_2	$NO + 1/2\ O_2 \leftrightarrow NO_2$
NH_3 and NO oxidation to N_2O	$2\ NH_3 + 2\ NO + 3/2\ O_2 \rightarrow 2\ N_2O + 3\ H_2O$
NH_3 oxidation	$4\ NH_3 + 5\ O_2 \rightarrow 4\ NO + 5\ H_2O$ $2\ NH_3 + 3/2\ O_2 \rightarrow N_2 + 3\ H_2O$

3. Reaction model

3.1. V-SCR reaction model calibration

The results of the V-SCR activity tests are summarized in Figure 3 along with the respective calibrated model results. At temperatures above 300 °C, it is observed that the SCR process highly depends on the proportion of NO_x and NH_3 in the feed gas. When ANR is greater than 1, NO_x is almost fully converted, however this leads to increased NH_3 slip. When ANR is less than 1, partial NO_x conversion is achieved as expected from the SCR reaction stoichiometry (Table 2). Concerning N_2O, low selectivity (below 20 ppm) is observed in the temperature range below 500 °C. (Figure 3c). In order to examine the possible reduction of N_2O over the V-SCR catalyst, N_2O is added to the feed gas (Figure 3d). It is evident that N_2O flows through the catalyst unreacted at temperatures below 400 °C whereas N_2O is produced at 500 °C. The reaction rates of the reaction scheme listed in Table 2 are calibrated to fit the experimental determined NO_x, NH_3 and N_2O keeping the same values for the entire range of test conditions.

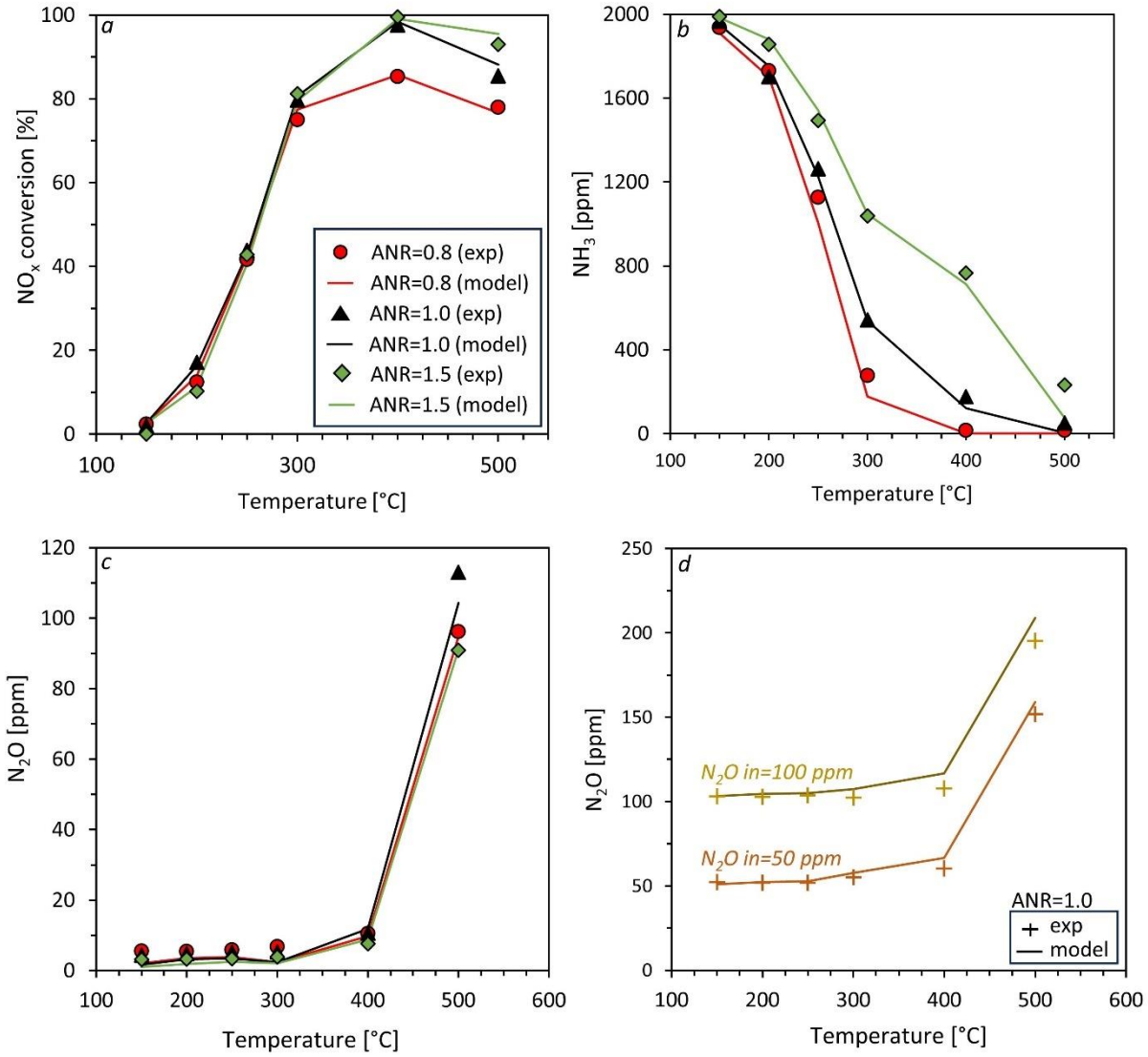

Figure 3: (a) NO_x conversion, (b) NH_3 slip, (c) N_2O without N_2O in the feed gas, under various NH_3/NO_x ratios, and (d) N_2O with 50 ppm and 100 ppm N_2O in the feed gas under ANR=1.0, over the V-SCR, based on the experimental data (symbols) and the model (solid lines) (Feed gas: 2000 ppm NO, ANR=0.8, 1.0, 1.5, 10% O_2, 15% H_2O, N_2 balance, GHSV=20,000 $^{h-1}$).

3.2. Fe-SCR reaction model calibration

For the development of the reaction kinetic model of the Fe-SCR catalyst, several modifications of the commonly used reactions in SCR technologies (Table 2) were required. Figure 4 a shows NO_x and NH_3 conversion under SCR conditions According to the standard SCR reaction (4 NO + 4 NH_3 + O_2 → 4 N_2 + 6 H_2O) equal number of moles of NO_x and NH_3 are expected to react. However, test results revealed an overconsumption of NH_3 compared to NO_x. This is also evident in Figure 4b, where $\Delta NH_3/\Delta NO_x$ is greater than 1 in the whole temperature range. This phenomenon has been documented in several previous studies [21-24]. Consequently, for the model development the stoichiometry of the typical standard SCR reaction was modified as below:

$$6\ NH_3{}^* + 5\ NO + 2\ O_2 \rightarrow 11/2\ N_2 + 9\ H_2O \qquad (5)$$

The modified standard SCR reaction is able to successfully predict the overconsumption of NH_3 (solid lines of Figure 4).

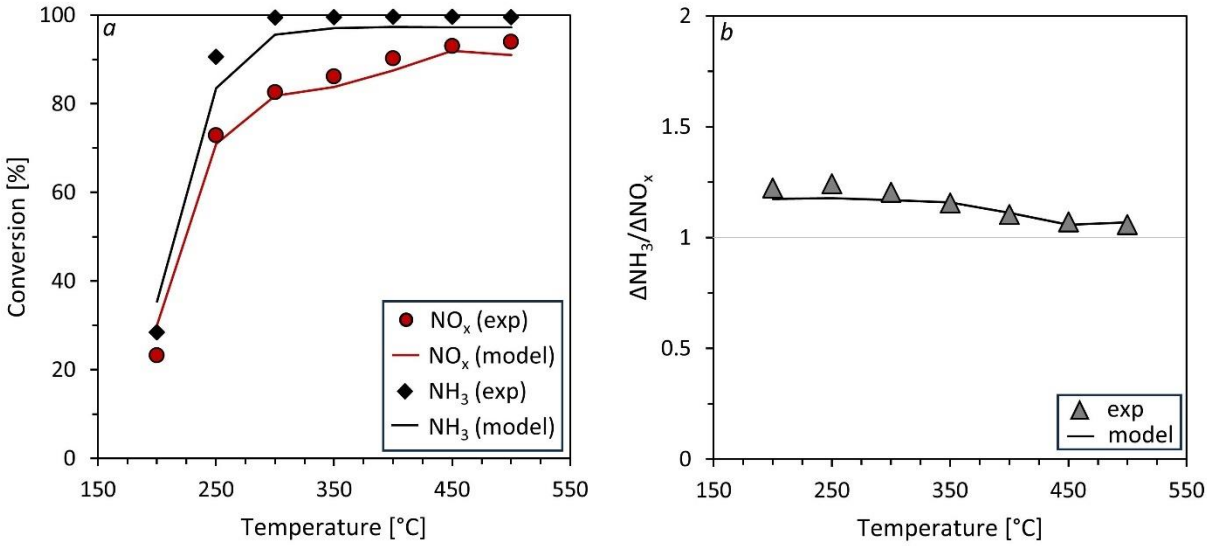

Figure 4: (a) NO_x and NH_3 conversion under Standard SCR conditions, and (b) $\Delta NH_3/\Delta NO_x$ over the Fe-SCR, based on the experimental data (symbols) and the model (solid lines) (Feed gas: 1000 ppm NO, ANR=1.0, 10% O_2, 15% H_2O, N_2 balance, GHSV=14,000 $^{h-1}$).

The experimental findings on the influence of the inlet ANR are depicted in Figure 5a with symbols. When ANR is less than 1, the catalyst performance is limited by the lack of NH_3 to further react with NO_x. When abundant NH_3 is present (ANR>1), NO_x conversion increases at temperatures above 350 °C. At temperatures below 300 °C and in excess of NH_3, NO_x conversion is significantly reduced. To capture this phenomenon in the model, it was necessary to include an inhibition term (1 + k x C_{NH3}^2) in the reaction rate of the modified standard SCR (reaction 5):

$$R = k \cdot \Psi_S \cdot \psi_{S_{NH_3}} \cdot C_{NO} \cdot C_{O_2} / (1+k \cdot C_{NH_3}{}^2) \quad (6)$$

The introduction and calibration of the inhibition term results in a good accuracy between the model and the experiment (solid lines of Figure 5a). The conversion of NO_x with and without the inhibition term for the case of ANR=3.0, is shown in Figure 5b.

Excess NH_3 leads to increased concentrations of NH_3 slip, while in the case of stoichiometric ANR or deficiency of NH_3, NH_3 completely reacts with NO_x (Figure 5c). Selectivity of N_2O is maintained at low levels (<10 ppm) and it is not affected by NH_3/NO_x ratio (Figure 5d).

In order to explain the NO_x emissions as function of temperature (Figure 6a), it was necessary to add an SCR reaction with N_2O acting as a 'promoting' species. This is realized by adding N_2O in both the reactants and products (standard SCR + N_2O):

$$NH_3{}^* + NO + ¼\ O_2 + N_2O \rightarrow N_2 + 3/2\ H_2O + N_2O \quad (7)$$

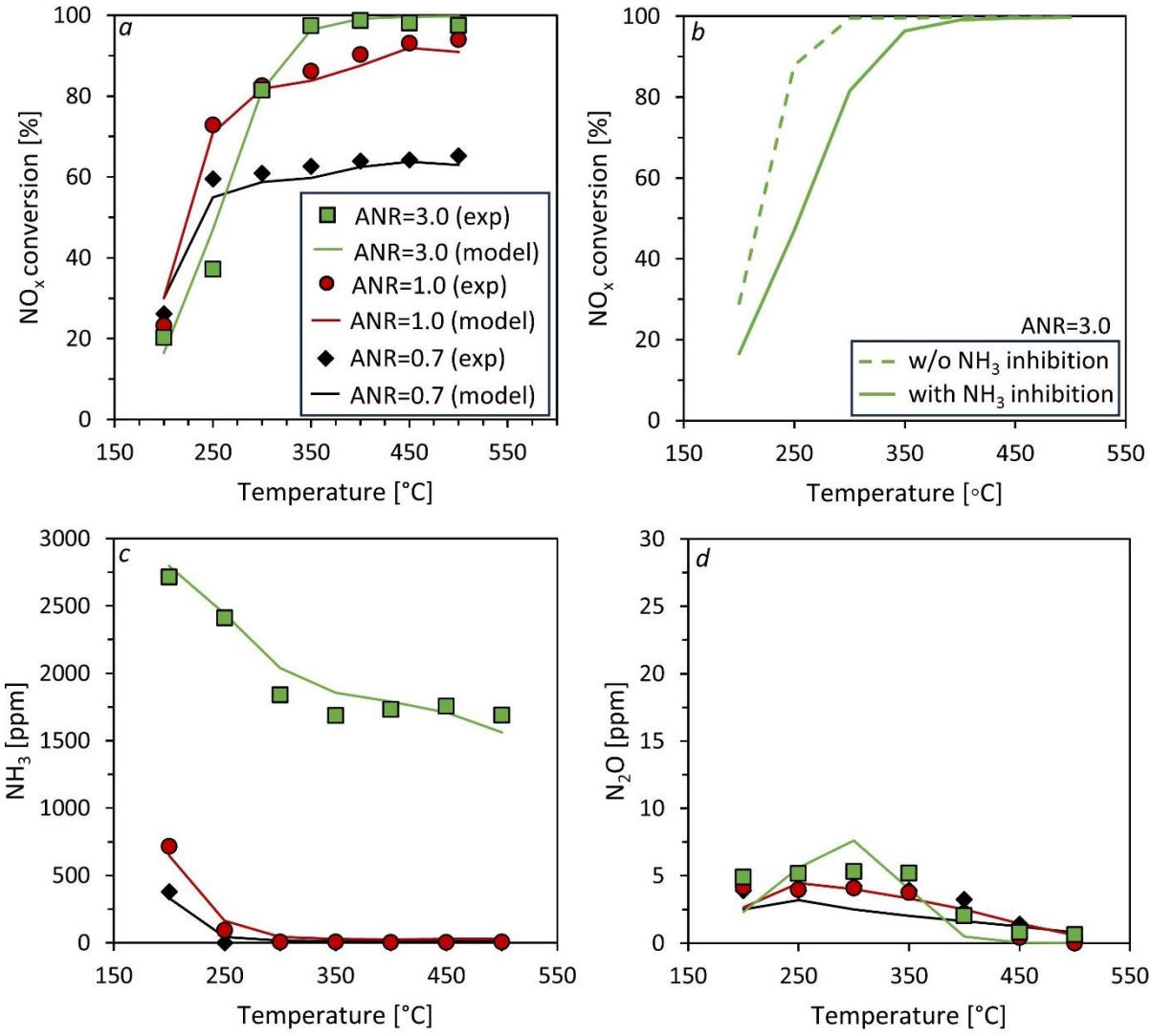

Figure 5: (a) Comparison of the experimental data and the model of (a) NO_x conversion under various ANR including the inhibition term, (b) under ANR=3.0 with and without the inhibition term, (c) NH_3 slip under various ANR ratios, and (d) N_2O selectivity under various ANR ratios, over the Fe-SCR (Feed gas: 1000 ppm NO, ANR=0.7, 1.0, 3.0, 10% O_2, 15% H_2O, N_2 balance, GHSV=14,000 $^{h-1}$).

This way, the reaction is activated only in the presence of N_2O with no effect on the N_2O concentration in the exhaust gas. The addition of this reaction resulted in very good accuracy of the model both in the presence and absence of N_2O (solid lines of Figure 6a). Figure 6b shows that in the presence of N_2O, reaction 7 is dominant while the reaction rate of the modified standard SCR (reaction 5) decreases due to competition between the two reactions.

Finally, N_2O conversion under various NH_3 concentrations is examined (Figure 7). As ANR increases, N_2O conversion also increases reaching a maximum at ANR=1.4. Further increase of NH_3 in the feed gas has a negative effect on N_2O reduction, especially at the lower temperatures (350 °C and 400 °C). To model N_2O conversion, the global reaction of direct reduction of N_2O by NH_3 (reaction 8) [25, 26] together with the global reaction of the simultaneous reduction of NO and N_2O by NH_3 (reaction 9) [27] are added to the reaction scheme:

$$2\ NH_3{}^* + 3\ N_2O \rightarrow 4\ N_2 + 3\ H_2O \qquad (8)$$

$$2\ NH_3{}^* + 2\ NO + N_2O \rightarrow 3\ N_2 + 3\ H_2O \quad (9)$$

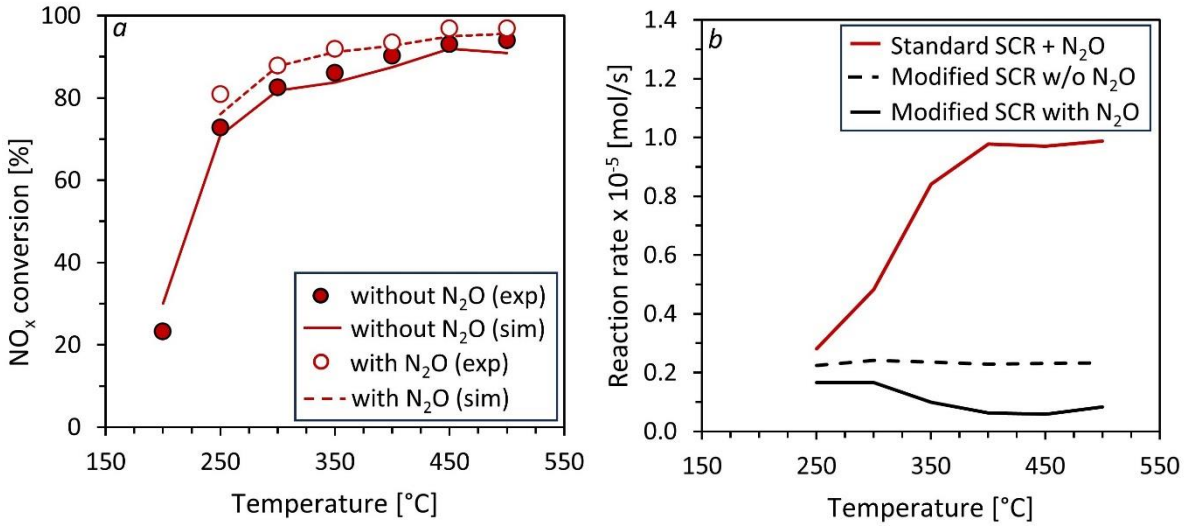

Figure 6: (a) NO_x conversion with and without N_2O and (b) reaction rates of the Standard SCR + N_2O and the modified stoichiometry SCR in the presence and absence of N_2O, over the Fe-SCR, based on the experimental data (symbols) and the model (solid lines) (Feed gas: 1000 ppm NO, ANR=1.0, 0 and 100 ppm N_2O, 10% O_2, 15% H_2O, N_2 balance, GHSV=14,000 $^{h-1}$).

For the efficient modeling of N_2O conversion in the whole range of ANR it was necessary to include an NH_3 inhibition term ($1 + k \times C_{NH3}{}^{1.5}$) to the reaction rate of the direct reduction of N_2O by NH_3 (reaction 8) as:

$$R_r = k \cdot \Psi_S \cdot \psi_{S_{NH_3}} \cdot C_{N2O} / (1+k \cdot C_{NH_3}{}^{1.5}) \quad (10)$$

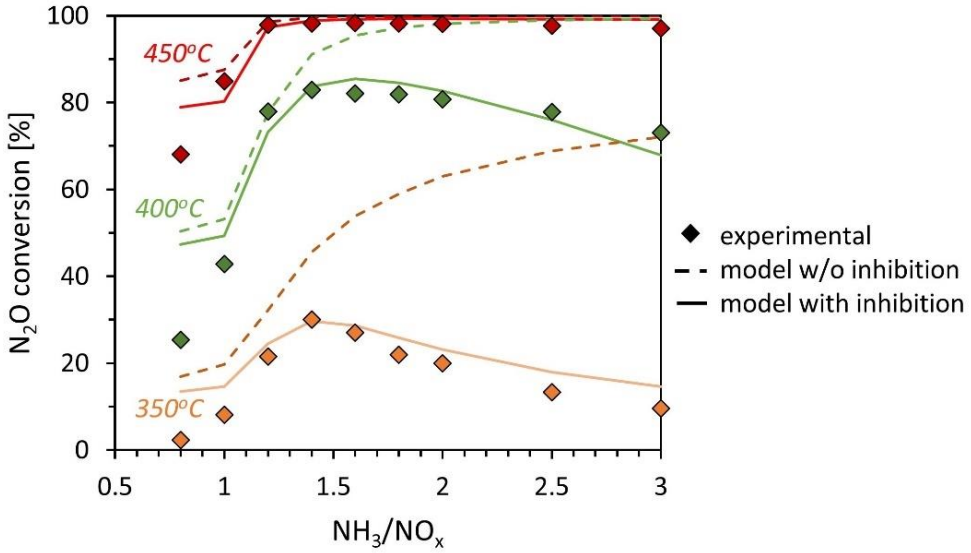

Figure 7: N_2O conversion under various NH_3/NO_x ratios, based on the experimental data (symbols) and the model without (dashed line) and with (solid line) the inhibition term, over the Fe-SCR. (Feed gas: 1000 ppm NO, variable NH_3, 100 ppm N_2O, 10% O_2, 15% H_2O, N_2 balance, GHSV=14,000 $^{h-1}$).

Considering all the necessary modifications, the final Fe-SCR reaction scheme adopted is summarized in Table 1Table 4.

Table 4: Fe-SCR reaction scheme.

Reaction type	**Reaction**
NH_3 storage/release	$NH_3 \leftrightarrow NH_3$*
Modified Standard SCR Standard SCR (+N_2O)	6 NH_3* + 5 NO + 2 O_2 → 11/2 N_2 + 9 H_2O NH_3* + NO + 1/4 O_2 + N_2O → N_2 + 3/2 H_2O +N_2O
Fast SCR	NH_3* + ½ NO + ½ NO_2 → N_2 + 3/2 H_2O
N_2O formation pathways	2 NH_3* + 2 NO + O_2 → N_2 + N_2O + 3 H_2O 2 NH_3* + 2 NO_2 → N_2 + N_2O + 3 H_2O
NO oxidation to NO_2	NO + 1/2 O_2 ↔ NO_2
NH_3 oxidation to N_2	NH_3* + 3/4 O_2 → ½ N_2 + 3/2 H_2O
N_2O reduction by NH_3	2 NH_3* + 3 N_2O → 4 N_2 + 3 H_2O
Simultaneous reduction of NO and N_2O by NH_3	2 NH_3* + 2 NO + N_2O → 3 N_2 + 3 H_2O

3.3. Pt-AOC reaction model calibration

The experimental results compared to the simulation model of the Pt-AOC catalyst are presented in Figure 8. Here the focus is not only on NH_3 reduction, but also on the formation of the unwanted NO_x and N_2O. The concentration of NH_3 decreases sharply from 200 °C to 250 °C and is completely oxidized around 300 °C. Production of N_2O is observed above 200 °C and increases significantly up to a maximum of 100 ppm at 250 °C. Above that temperature, formation of NO ad NO_2 are favored while N_2O is simultaneously decreasing. It is worth noting that the calibrated model using the common reactions of Table 3, is capable of capturing the complex trends with respect to N_2O and NO_x byproducts in the whole temperature range.

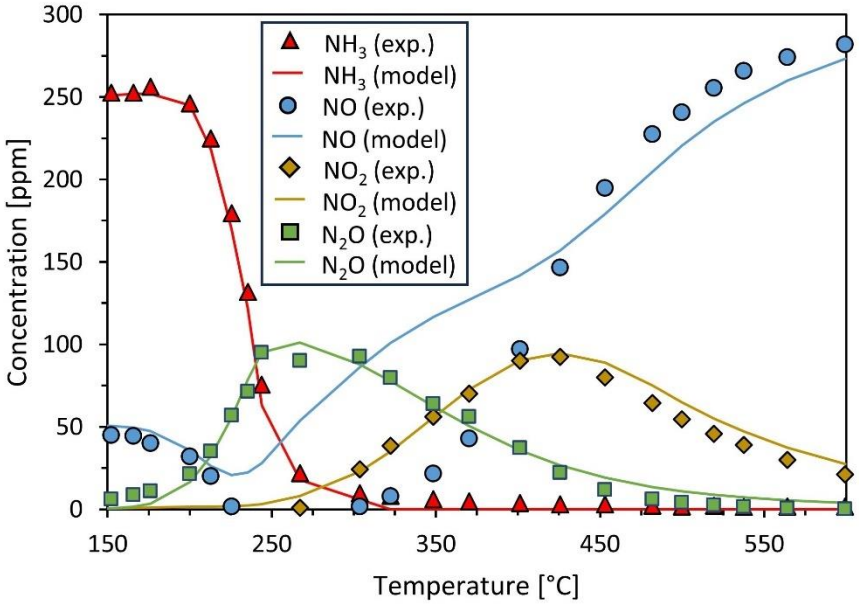

Figure 8: Comparison of the NH_3, NO, NO_2 and N_2O outlet concentrations for NH_3 oxidation over the Pt-AOC based on the experimental data (symbols) and the model (solid lines) (Feed gas: 250 ppm NH_3, 50 ppm NO, 6% O_2, 15% H_2O, 15 ppm SO_2, N_2 balance, GHSV=20,000 $^{h-1}$).

4. Sulfur saturation of the Fe-SCR

The Fe-SCR was initially exposed to 110 ppm SO_2 at 225 °C until saturation (approximately 25 minutes) as presented in Figure 9a. The maximum SO_2 stored on the catalytic sites is calculated equal to 1.13 g/l. Thereafter, an SCR experiment is conducted without any further S-exposure (Figure 9b). Compared to the fresh catalyst, reduced NO_x conversion is observed at temperatures below 300 °C. At higher temperatures, NO_x conversion efficiency was not affected by S-saturation. Concerning N_2O, the saturated catalyst shows similar activity to the fresh (Figure 9c). The desulfation at high temperatures is examined as depicted in Figure 9d. The catalyst is initially exposed at a high temperature (above 400 °C) for 30 minutes and then NO_x conversion is measured at 250 °C where NO_x conversion reduction was observed. At a desulfation temperature of 450 °C the catalyst efficiency is partially retrieved while the catalyst activity is fully recovered at 600 °C.

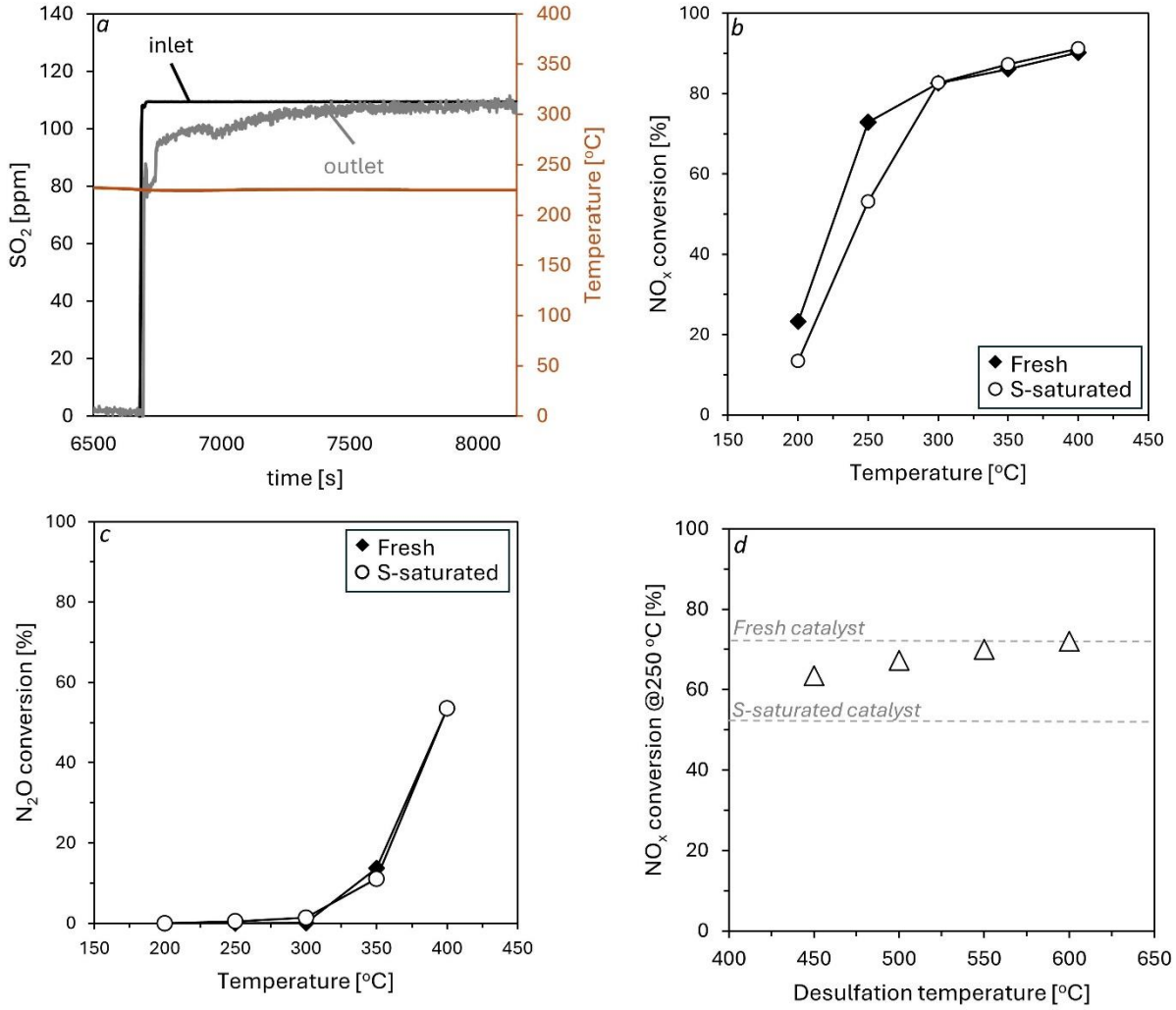

Figure 9: (a) Exposure of the Fe-BEA catalyst to SO_2, (b) NOx conversion of the fresh and s-saturated catalyst, (c) N_2O conversion of the fresh and s-saturated catalyst, (d) Desulfation of the catalyst at high temperatures (Feed gas (a): 110 ppm SO_2, 1000 ppm NO, ANR=1.0, 15% H_2O, 10% O_2, N_2 balance, GHSV=14,000 h^{-1}; Feed gas (b), (c), (d): 1000 ppm NO, ANR=1.0, 100 ppm N_2O, 15% H_2O, 10% O_2, N_2 balance, GHSV=14,000 h^{-1}).

5. Model Application in Marine Engine Exhaust

The objective of this section is to illustrate the application of modeling in the design phase of the NH_3 marine engine EATS. Given that NH_3 engines are still under development and yet commercially available, precise data on their exhaust gas conditions and emission concentrations remain unavailable. Consequently, the exhaust gas conditions of low-speed marine diesel engines are used as a basis, assuming a high-pressure (pre-turbo) EATS [28,29].

Ammonia combustion is likely to produce high levels of unburnt NH_3. It is well known that the molar ratio of NH_3/NO_x in the exhaust gas is very critical for the operation of the SCR. Recent studies [30,31] show that N_2O formation occurs in locations with significant unburnt NH_3 which is eliminated when unburnt NH_3 decreases and NO_x emissions increase. Based on these trends, two scenarios are examined: (1) high NO_x emissions with low NH_3 and N_2O (ANR<1), and (2) high unburnt NH_3 and N_2O with low NO_x emissions (ANR>1).

The simulated inlet conditions of the EATS are detailed in Table 5.

Table 5: Assumed inlet conditions of the EATS.

Engine Load [%]	**25**	**50**	**75**	**100**
Exhaust gas temperature [°C]	290	310	350	410
Exhaust gas pressure [bar]	1.4	2.1	3.1	4.0
Exhaust gas mass flow rate [kg/s]	4	9	12	15
Exhaust gas composition for ANR<1 and low N_2O	1000 ppm NO, 500 ppm NH_3, 30 ppm N_2O, 10% H_2O, 10% O_2, N_2 balance			
Exhaust gas composition for ANR>1 and high N_2O	1000 ppm NO, 3000 ppm NH_3, 100 ppm N_2O, 10% H_2O, 10% O_2, N_2 balance			

In the case of NH_3 shortage and low N_2O (ANR<1), NH_3 injection upstream of the SCR is required as shown in Figure 10a to achieve the regulated NO_x limit of 3.4 g/kWh. In the case of excessive NH_3, a dual-layer ASC is placed downstream of the SCR to treat the unreacted NH_3 of the deNO_x process (Figure 10b). The ASC is assumed to be a combination of an SCR layer and a precious metal-based layer (AOC). The composition of the SCR layer is identical to the SCR catalyst prior the ASC. In both scenarios the commonly used V-SCR is compared to Fe-SCR.

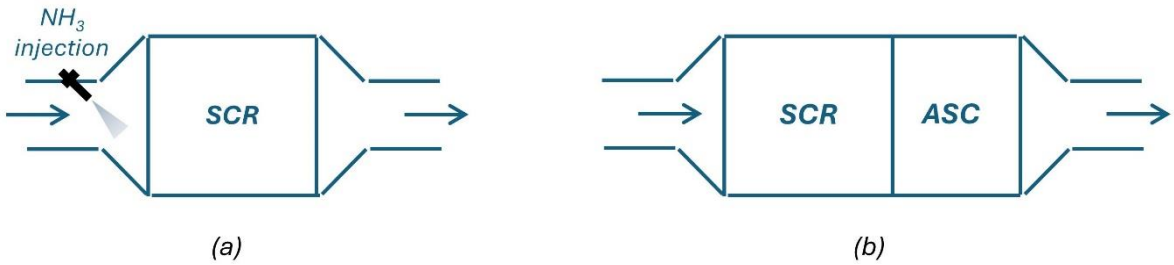

Figure 10: Model exhaust layouts for the two cases examined: (a) shortage of NH_3 with low N_2O, and (b) excess of NH_3 with high N_2O in the exhaust gas.

Besides NO_x and NH_3 control, CO_2 equivalent emissions are calculated at the system outlet, accounting for both N_2O (originating from NH_3 combustion and the EATS), and CO_2 from pilot-fuel combustion (CO_2-equivalent = N_2O x 300 + CO_2 from pilot fuel). For the latter, 5% Diesel pilot-fuel is assumed.

Based on the assumed marine engine exhaust gas conditions presented in Table 5 and the weighting factors of the legislated E3 test cycle [32], it is estimated that a NO_x conversion rate in the order of 75% is required to comply with the Tier III limit of 3.4 gNO_x/kWh.

In the scenario of NH_3 shortage (ANR<1) and low N_2O emissions, where only the SCR is utilized, the minimum deNO_x requirement is met when NH_3 is injected at a target ANR of around 0.75. The volume of each technology is chosen in order to meet both NO_x and NH_3 limits, the latter set at 10 ppm. For the V-SCR the volume is equal to 1000 liters. When the Fe-SCR is used, the volume is increased to 1400 liters.

Applying the simulation model to the four loads of the E3 test cycle under the conditions specified in Table 5, NH_3 slip, N_2O and CO_2-equivalent emissions are calculated at the system outlet as depicted in Figure 11. For the V-SCR, nearly all NH_3 is predicted to be consumed during NO_x reduction,

resulting in NH_3 slip of less than 5 ppm, with minimal N_2O formation. When the V-SCR is replaced by the Fe-SCR catalyst, NH_3 slip is reduced to the limit of 10 ppm. Notably, N_2O emissions significantly reduce at 75% and 100% engine load, benefiting from the catalyst's ability to reduce both NO_x and N_2O. Consequently, the CO_2-equivalent emissions of the Fe-SCR are lower compared to those of the V-SCR catalyst. This scenario proposes a significant reduction of GHG emissions compared to Diesel-only operation of 70% that can even reach 90% at full load when the Fe-SCR is implemented.

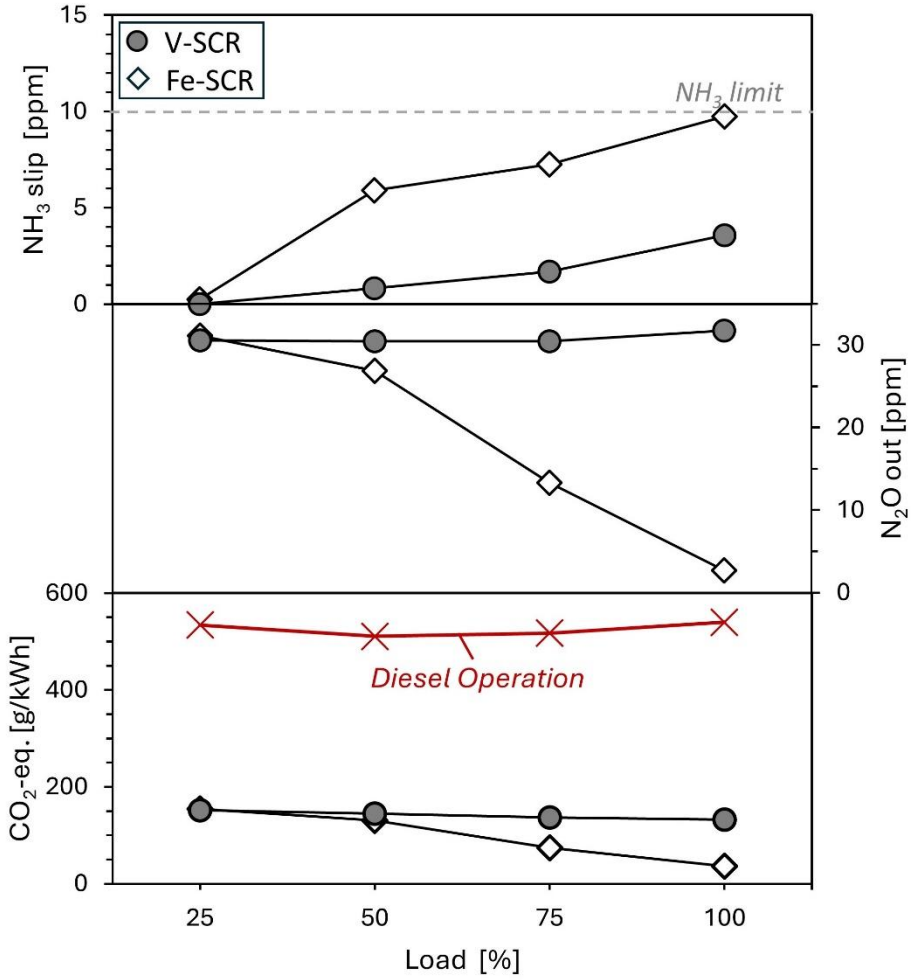

Figure 11: Model predictions for NH_3 slip, N_2O and CO_2-equivalent emissions over 100-year GWP at the SCR system outlet in the case of lack of NH_3 (ANR<1) and low N_2O in the exhaust gases. (Exhaust gas composition: 1000 ppm NO, 500 ppm NH_3, 30 ppm N_2O, 10% H_2O, 10% O_2, N_2 balance).

Figure 12 presents NO_x, NH_3, N_2O and CO_2-equivalent emissions for the case of excessive engine-out NH_3 (ANR>1) and high N_2O emissions.

For excessive NH_3 (ANR>1) and high N_2O emissions, the volume of the SCR catalysts in both technologies is assumed to be equal to 1000 liters. The volumes of the ASC catalysts are iteratively determined to reduce NH_3 below 10 ppm. For the V-SCR + ASC system, the ASC volume is 845 liters while for the Fe-SCR + ASC the respective volume is 700 liters. In this case, NO_x, NH_3, N_2O and CO_2-equivalent emissions are depicted in Figure 12. Increased ANR values lead to unreacted NH_3 at the SCR outlet, which is efficiently oxidized in the ASC (below 10 ppm). However, this oxidation process in the ASC promotes the formation of NO_x and N_2O. In the case of the Fe-SCR the N_2O emissions are significantly decreased compared to the V-SCR, especially at higher loads due to the deN_2O

capability of Fe-based catalysts. However, N_2O levels in both cases remain extremely high leading to unacceptable CO_2-equivalent emissions.

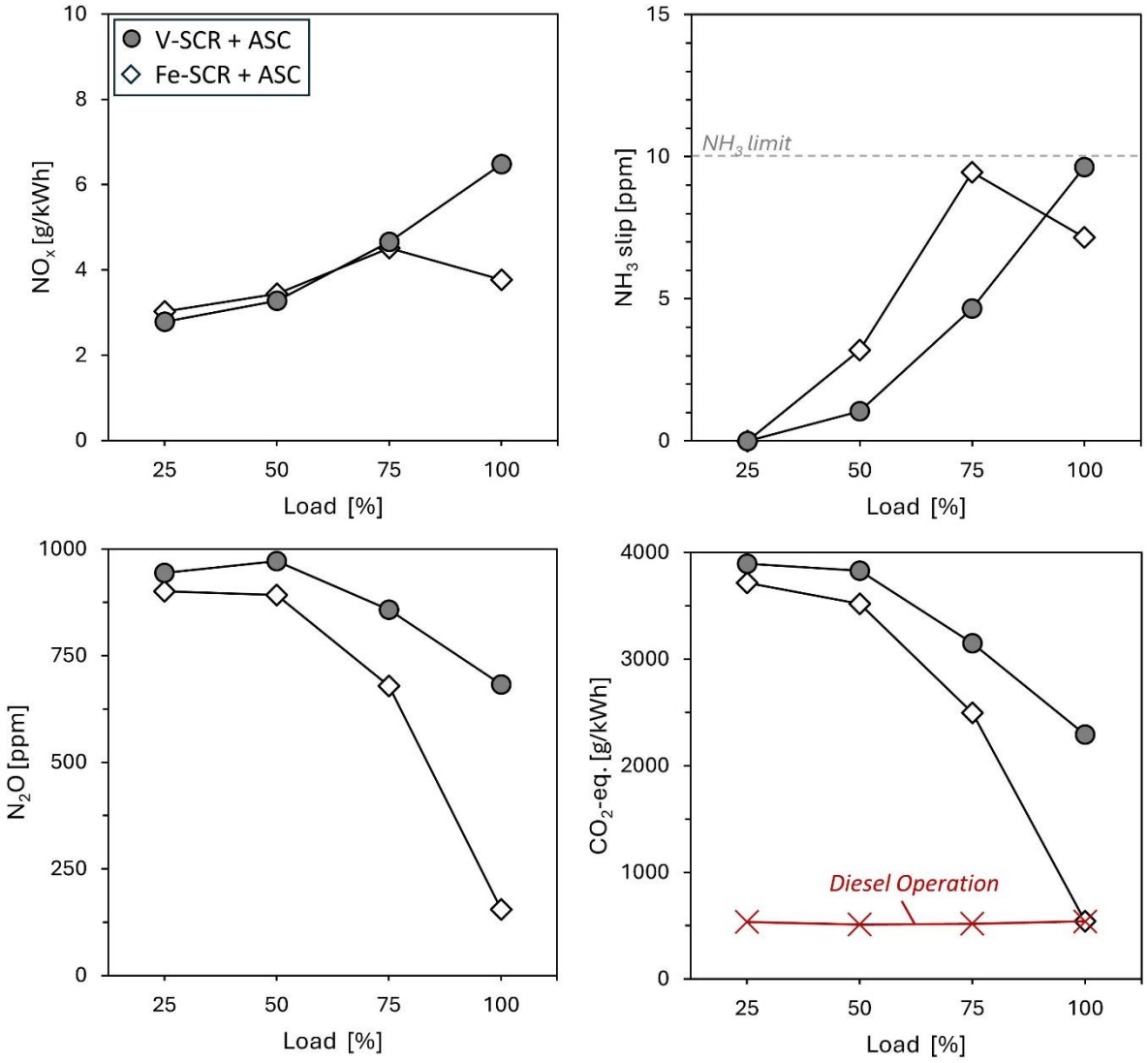

Figure 12: Model predictions for NO_x, NH_3 slip, N_2O and CO_2-equivalent emissions over 100-year GWP at the system outlet in the case of excessive NH_3 in the exhaust gases (ANR>1) (Feed gas: 1000 ppm NO, 3000 ppm NH_3, 100 ppm N_2O, 10% H_2O, 10% O_2, N_2 balance).

6. Preliminary results with Co-based deN_2O catalyst

Following the preliminary target to reduce N_2O emissions from ammonia combustion, N_2O decomposition of a cobalt-based catalyst is currently being tested and evaluated on the SGB. The preliminary experimental results are depicted in Figure 13. A first indication is that high N_2O conversion is achieved at elevated temperatures, however the effect of NO and NH_3 are yet to be determined to conclude the catalyst activity.

Thereafter, a model will be developed to be adapted in the EATS of ammonia-fueled engines.

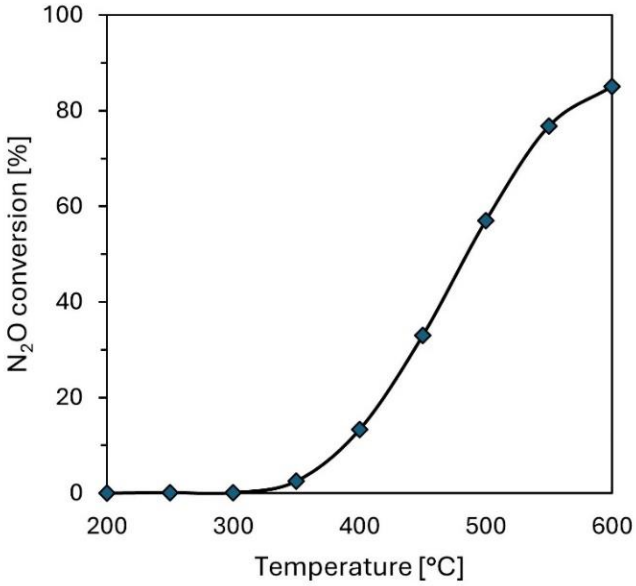

Figure 13: N_2O conversion (experimental) over the cobalt-based catalyst (Feed gas: 100 ppm N_2O, 10% H_2O, 10% O_2, 10 ppm SO_2, N_2 balance, GHSV=20,000 h^{-1}).

7. Conclusions & Future work

The main findings of the combined testing and modeling work presented here are summarized below:

- The performance of the V-SCR and the Pt-AOC catalysts are well predicted with commonly used literature reaction schemes.
- In the case of the Fe-SCR, special modifications of the chemical reaction scheme are necessary to accurately describe the occurring processes. These include the modification of the standard SCR reaction stoichiometry, inhibition of the modified standard SCR reaction by NH_3 at high NH_3 inlet concentrations and low temperatures, addition of the typical standard SCR with N_2O in both the reactants and products, and the inhibition of the direct N_2O reduction by NH_3 at high inlet concentrations of NH_3.
- Fe-SCR catalyst material was found to be sulfur tolerant in the operating range of large two-stroke marine engines.

The simulation study of the marine engine aftertreatment applications provided the following results:

- For low NH_3 and N_2O levels in the exhaust gas (ANR<1), NO_x conversion is optimized to comply with Tier III limits by NH_3 injection upstream of the SCR, resulting in low NH_3 slip levels. In addition, there is a significant reduction in CO_2-equivalent emissions by 70% to 90% (depending on the SCR technology) compared to diesel-only operation.
- For abundant NH_3 and high N_2O in the exhaust gas (ANR>1), unreacted NH_3 of the deNO_x process can be efficiently managed with an ASC. However, NH_3 oxidation promotes the formation of very high N_2O emissions, causing CO_2-equivalent emissions to reach up to 7 times the levels of diesel-only operation, rendering this configuration impractical.

Based on the above, an appropriate control strategy and optimization of the exhaust aftertreatment system, together with engine tuning of NH_3 combustion is essential to tackle both noxious and GHG

emissions. As the ultimate goal is complete decarbonization of the maritime sector, the future steps include:

- Further experimental investigation on the performance of the deN_2O cobalt-based catalyst followed by model development using the test data.
- Application of the new catalyst models in the exhaust gas stream of NH_3 engines.
- Development and optimization of the complete exhaust aftertreatment system and controls for NH_3 marine engine applications.

Funding

This work has been funded by the ENGIMMONIA project, which has received funding from the European Union's Horizon 2020 research and innovation program under grant agreement Nr. 955413.

Acknowledgments

The authors would like to acknowledge support of this work by Ecospray for providing the V-based and Pt-based catalyst samples and TOPSOE for providing the Fe-based catalyst sample and useful discussions during the experimental campaign.

Nomenclature

A. Latin letters

C_P	Specific heat capacity *J/(kg·K)*
D_w	Effective diffusivity m^2/s
h	Heat transfer coefficient *W/(m²·K)*
k_j	Mass transfer coefficient *m/s*
n	Stoichiometric coefficient -
R_k	Reaction rate *mol/(m³·s)*
S	Heat source term W/m^3
S_F	Monolith specific surface area m^2/m^3
T	Temperature *K*
v	Velocity *m/s*
w	Dimension perpendicular to wall surface -
y_j	Molar fraction -
z	Axial coordinate along monolith *m*

B. Greek letters

ε	Macroscopic void fraction -
λ	Thermal conductivity *W/(m·K)*
ρ	Density kg/m^3

C. Subscripts and Superscripts

g	Exhaust gas
j	Species index
k	Reaction index
s	Solid

Literature

[1] International Maritime Organization. Fourth IMO GHG Study Full Report; International Maritime Organization: London, UK, 2020.

[2] Liu, L.; Wu, J.; Liu, H.; Wu, Y.; Wang, Y. Investigation of combustion and emission characteristics in a low-speed marine engine using ammonia under thermal and reactive atmospheres. *Int. J. Hydrogen Energy* **2024**, 1237-1247.

[3] IMO Marine Environment Protection Committee. Eightieth Session (MEPC 80)-Summary Report; International Maritime Organization: London, UK, 2023.

[4] Ni, P.; Wang, X.; Li, H. A review on regulations, current status, effects and reduction strategies of emissions for marine diesel engines. *Fuel* **2020**, 279, 118477.

[5] Xu, L.; Xu, S.; Bai, X. S.; Repo, J. A.; Hautala, S.; Hyvönen, J. Performance and Emission Characteristics of an Ammonia/Diesel Dual-Fuel marine engine. *Renewable and Sustainable Energy Reviews* **2023**, 185, 113631.

[6] DNV GL AS Maritime. Comparison of Alternative Marine Fuels Report, SEA/LNG Ltd, Norway 2019.

[7] Rodríguez, C.G.; Lamas, M.I.; Rodríguez, J.d.D.; Abbas, A. Possibilities of Ammonia as Both Fuel and NOx Reductant in Marine Engines: A Numerical Study. *J. Mar. Sci. Eng.* **2022**, 10, 43.

[8] Wang, Q.; Yang, W.; Dang, H.; Li, L.; Wu, R.; Wang, Y.; Zhao, Y. Enhancement of N_2O Decomposition Performance by co-doping of Ni and Y to Co_3O_4 catalyst. *J. Environmental Chemical Engineering* **2024**, 12, 112463.

[9] Nova, I.; Tronconi, E. Fundamental and Applied Catalysis Urea-SCR Technology for deNO_x after Treatment of Diesel Exhausts; Springer: Berlin/Heidelberg, Germany, 2014.

[10] Han, J.; Wang, A.; Isapour, G.; Härelind, H.; Skoglundh, M.; Creaser, D.; Olsson, L. N_2O Formation during NH_3-SCR over Different Zeolite Frameworks: Effect of Framework Structure, Copper Species, and Water. *Ind. Eng. Chem. Res.* **2021**, 60, 17826–17839.

[11] Wang, A.; Wang, Y.; Walter, E.D.; Kukkudapu, R.K.; Guo, Y.; Lu, G.; Weber, R.S.; Wang, Y.; Peden, C.H.F.; Gao, F. Catalytic N_2O decomposition and reduction by NH_3 over Fe/Beta and Fe/SSZ-13 catalysts. *J. Catal.* **2018**, 358, 199–210.

[12] Zabilskiy, E. In-situ XAS Study of Catalytic N_2O Decomposition over CuO/CeO_2 Catalysts. *ChemCatChem* **2021**, 13, 1814–1823.

[13] Komvokis, V.G.; Marnellos, G.E.; Vasalos, I.A.; Triantafyllidis, K.S. Effect of Pretreatment and Regeneration Conditions of $Ru/\gamma\text{-}Al_2O_3$ Catalysts for N_2O Decomposition and/or Reduction in O_2 -rich Atmospheres and in the Presence of NO_x, SO_2 and H_2O. *Appl. Catal. B Environ.* **2009**, 89, 627–634.

[14] Hermes, A.C.; Hamilton, S.M.; Hopkins, W.S.; Harding, D.J.; Kerpal, C.; Meijer, G.; Fielicke, A.; Mackenzie, S.R. Effects of Coadsorbed Oxygen on the Infrared Driven Decomposition of N_2O on Isolated Rh^{5+} Clusters. *J. Phys. Chem. Lett.* **2011**, 2, 3053–3057

[15] Xie, P.; Luo, Y.; Ma, Z.; Wang, L.; Huang, C.; Yue, Y.; Hua, W.; Gao, Z. CoZSM-11 Catalysts for N_2O Decomposition: Effect of Preparation Methods and Nature of Active Sites. *Appl. Catal. B Environ.* **2015**, 170, 34–42.

[16] Farhan, K.M.; Thabassum, A.; Ismail, T.M.; Sajith, P.K. Theoretical Investigation into the Effect of Water on the N_2O Decomposition Reaction over the Cu-ZSM-5 Catalyst. *Catal. Sci. Technol.* **2022**, 12, 1466–1475.

[17] Busca, G.; Lietti, L.; Ramis, G.; Berti, F.; Chemical and mechanistic aspects of the selective catalytic reduction of NOx by ammonia over oxide catalysts: A review. *Applied Catalysis B: Environmental 18* **1998**, 1-36.

[18] Exothermia, S.A. Exothermia Suite User Manual, version 2022.3; Gamma Technologies, LLC: Westmont, IL, USA, 2022.

[19] Karamitros, D.; Koltsakis, G. Model-based optimization of catalyst zoning on SCR-coated particulate filters. *Chem. Eng. Sci.* **2017**, 173, 514-524.

[20] Colomb, M.; Nova, I.; Tronconi, E.; Schmeißer, V.; Brandl-Konrad, B.; Zimmermann, L.R. Experimental Modeling Study of a dual-layer (SCR + PGM) NH_3 slip monolith catalyst (ASC) for automotive SCR aftertreatment systems. Part I. Kinetics for the PGM Component and Analysis of SCR/PGM Interactions. *Appl. Catal. B Environ*. **2013**, 142–143, 861–876.

[21] Sjövall, H.; Blint, R. J.; Gopinath, A.; Olsson, L. A Kinetic Model for the Selective Catalytic Reduction of NO_x and NH_3 over an Fe-zeolite Catalyst. *Ind. Eng. Chem. Res.* **2010**, 49, 39-52.

[22] Nedyalkova, R.; Kamasamudram, K.; Currier, N. W.; Li, J.; Yezerets, A. Experimental evidence of the mechanism behind NH_3 overconsumption during SCR over Fe-zeolites. *Journal of Catalysis* **2013**, 299, 101-108.

[23] Bacher, V.; Perbandt, C.; Schwefer, M.; Siefert, R.; Pinnow, D.; Turek, T. Kinetics of ammonia consumption during the selective catalytic reduction of NO_x over an iron zeolite catalyst. *Applied Catalysis B: Environmental* **2015**, 162, 158-166.

[24] Liu, Q.; Bian, C.; Ming, S.; Guo, L.; Zhang, S.; Pang, L.; Liu, P.; Chen, Z.; Li, T. The opportunities and challenges of iron-zeolite as NH_3-SCR catalyst in purification of vehicle exhaust. *Applied Catalysis A* **2020** ,607, 117865.

[25] Aika, K.; Oshihara, K. Nitrous oxide reduction with ammonia over Co-MgO catalyst and the influence of excess oxygen. *Catalysis Today* **1996**, 29, 123-126.

[26] Zhang, X.; Shen, Q.; He, C.; Ma, C.; Chen, J.; Li, L.; Hao, Z. Investigation of Selective Catalytic Reduction of N_2O by NH_3 over an Fe-Mordenite Catalyst: Mechanism and O_2 Effect. *ASC Catal.* **2012**, 2, 512-520.

[27] Coq, B.; Mauvezin, M.; Delahay, G.; Butet, J. B.; Kieger, Stephane. The simultaneous catalytic reduction of NO and N_2O by NH_3 using an Fe-zeolte-beta catalyst. *Applied Catalysis B: Environmental* **2000**, 27, 193-198.

[28] Zhu, Y.; Xia, C.; Shreka, M.; Wang, Z.; Yuan, L.; Zhou, S.; Feng, Y.; Hou, Q.; Ahmed, S.A. Combustion and emission characteristics for a marine low-speed diesel engine with high-pressure SCR system. *Environ. Sci. Pollut. Res*. **2020**, 27, 12851–12865.

[29] Zhu, Y.; Li, T.; Xia, C.; Feng, Y.; Zhou, S. Simulation analysis on vaporizer/mixer performance of the high-pressure SCR system in a marine diesel. *Chem. Eng. Process.-Process Intensif.* **2020**, 148, 107819.

[30] Northrop, W. F. Modeling nitrogen species from ammonia reciprocating engine combustion in temperature-equivalence ratio space. *Applications in Energy and Combustion Science 17* **2024**, 100245.

[31] Reggeti, S. A.; Northrop, W. F. Lean ammonia-fueled engine operation enabled by hydrogen-assisted turbulent jet ignition. *Front. Mech. Eng.* **2024**, 10:1368717.

[32] MARPOL, Annex VI—Regulations for the Prevention of Air Pollution from Ships, Appendix II—Test Cycles and Weighting Factors (Regulation 13). Available online: http://www.marpoltraining.com/MMSKOREAN/MARPOL/Annex_VI/app2.htm

Keywords: Biofuel, Bio-Oil, Fuel Compatibility, CNSL

Cashew Nutshell Liquid Compatibility Testing – Methodology and Case Reports

Dr. Robert Bank[1], Dr. Fabian Pinkert[1], Martin Drescher[1], Dr. Martin Theile[1], Antje Hoppe[1], Dr. Fanny Langschwager[2], Dr. Ulrike Schümann[2]

(1) Forschungszentrum für Verbrennungsmotoren und Thermodynamik Rostock GmbH (FVTR), (2) Rostock University, Department of Piston Machinery and Internal Combustion Engines (LKV)

https://doi.org/10.18453/rosdok_id00004638

Abstract

Renewable fuels will have a large share in the future marine fuel mix. In addition to potential electricity-based fuels such as methanol and ammonia, which are not yet produced on an industrial scale, bio-based fuels and oils are already available today. HVO (hydrogenated vegetable oil) and FAME (fatty acid methyl ester) are the best-known representatives. While their properties in terms of engine compatibility are sufficiently well known, those of a new generation of bio-oils based on as yet unused feedstocks are still unknown. Currently, different types of pyrolysis oils and fluids derived from HTL (hydrothermal liquification) are in the focus of research. The so-called "cashew nutshell liquid" (CNSL) in particular is one of the candidates for an attractive alternative. It can be used in different stages of refinement as a blend with conventional fuels like a DMA or even VLSFO. However, every blend matrix from a bio-oil and a fossil base component is its own challenge in terms of compatibility and operability. Therefore, special test methods need to be developed to assess compatibility for marine engines and components.

In recent years, FVTR GmbH has established a test procedure to analyze the properties and effects of future bio-oils and blends, such as CNSL fuels, on engine components and combustion behavior based on laboratory tests, component tests, single-cylinder and full-engine tests. In this article, CNSL-based fuel blends of different quality and production processes are compared with regard to various chemical properties. Furthermore, their behavior in the engine fuel path and their combustion characteristics are presented. The article focuses in particular on the possible sludge formation of the fuels in fuel separators during processing the fuel blends, the impact on the deposition behavior in the fuel injection systems, e.g. the injector nozzle, and therefore the influence on fuel evaporation and finally combustion and emission behavior.

As a result, we found that possible issues in the fuel processing due to massive sludge formation can simply be avoided by adjusting the operation scheme of the separator. But knowledge of that fact as well as sensitizing the vessel crew is mandatory. The overall performance of the different bio-blends ranges from good operable and inconspicuous to clear difficulties in stable engine operation already after shortest operating time. Regarding exhaust emissions there is only minor impact for blends up to B30, containing 30% of the used bio-oil. However, this is only valid as long as there is no deposit formation in the nozzle. So, emissions are one precursor monitoring the engine state.

1. The feedstock

1.1. Usage of bio-oils

The rate of change in the maritime industry is at an all-time high. Engine and component manufacturers need to develop new products tailored to fuels that have completely different properties compared to conventional distillate and residual fuels. Ship builders face the challenge to incorporate this technology into a package while at the same time increasing their ships' efficiency through novel designs, new materials and other technological innovations. Ship operators have plenty of options at their disposal to lower their CO_2 emissions through smart monitoring, maintenance, antifouling, and CO_2 neutral fuels. The latter has gained even more importance through the Fuel EU laws demanding the usage of 2% carbon neutral fuels in the period from 2025 to 2029 and 6% from 2030 to 2034. The percentages continue to rise from there on. Until this goal can be economically achieved using carbon capture technologies, the importance of drop-in capable carbon neutral fuels - at least as a bridge technology - is drastically high.

Until recently, the usage of biofuels was mainly governed by the quotas imposed by legislation on the fuel suppliers for on-road traffic. This highly regulated usage of biofuel resulted in the addition of 7% FAME to diesel fuel, called B7. The goal here was to allow all-encompassing or at least very broad compatibility of the fuel with engines and fuel systems. With the new Fuel EU law, the responsibility for reducing the fossil fuel usage is passed on to ship owners without clear specification of the fuels and technologies to be used. As there are currently quite limited options for fuel substitution, biofuel is the easiest measure for fulfilling the quotas. Therefore, in preparation for 2025, the biofuel demand is currently rising.

The individual responsibility for fuel usage pared with the sturdiness of marine fuel system results in a significantly more flexible use of biofuels including a fast-growing range of qualities and feedstocks. So, this new generation of biofuels for shipping has a focus on the fuel price rather than broad compatibility. Many fuel producers, vendors and ship operators have turned to FVTR to help in assessing the opportunities and limits of fuels from new feedstocks, new fuel qualities and new blending recipes. One of the feedstocks that is hoped to be exploited is the cashew nut, rather the waste products from cashew nut production.

1.2. Cashew nut and CNSL

The cashew nut, as known to the end consumer, is only a small part of the whole fruit (Figure 1). The larger part of the cashew fruit is the cashew apple, which is edible, has a high nutritional value and an acquired taste. It can be hard to digest and may require special preparation, which may be the reason for its scarce usage in western countries [1]. Attached to the outside of the cashew apple is the cashew nut. It consists of a hard shell and the kernel. The kernel again is surrounded by a thin skin called testa. The shell contains within its honeycomb structure a brown viscous liquid known as cashew nutshell liquid, CNSL. The edible kernel is widely known and marketed all over the world. The testa has little use so far but is also gaining more attention as it contains bioactive compounds with functional and health-promoting benefits which may be valorized in the future. [2]

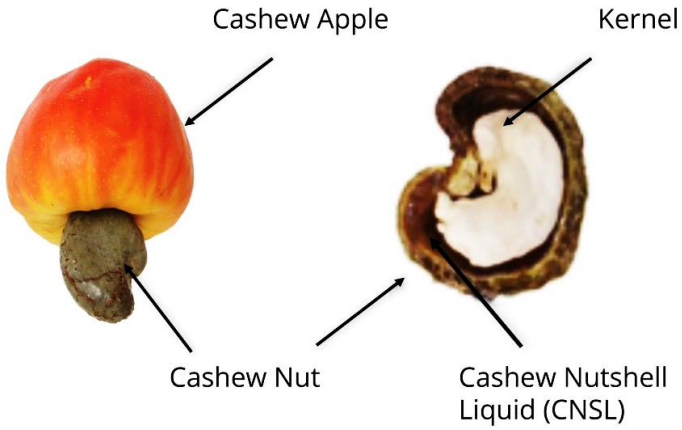

Figure 1: Cashew nut [3]

Cashew trees are grown in plantations in tropical regions like South America, Africa and Asia within the region between 23°N and 23°S of the equator. The tree can reach up to 12 m height. It is draught resistant and its sturdy root system can be used to control soil erosion and desertification. It is thus a valuable plant that can at the same time provide food and a feedstock for biofuel. The greatest perils probably lie in the creation of monocultures and in the working conditions on the farms, both of which can and should be addressed by traders and end users. Comparing the annual cashew nut production shown in Figure 2 to the country size, it becomes clear that especially Côte d'Ivoire will suffer from excessive monoculture.

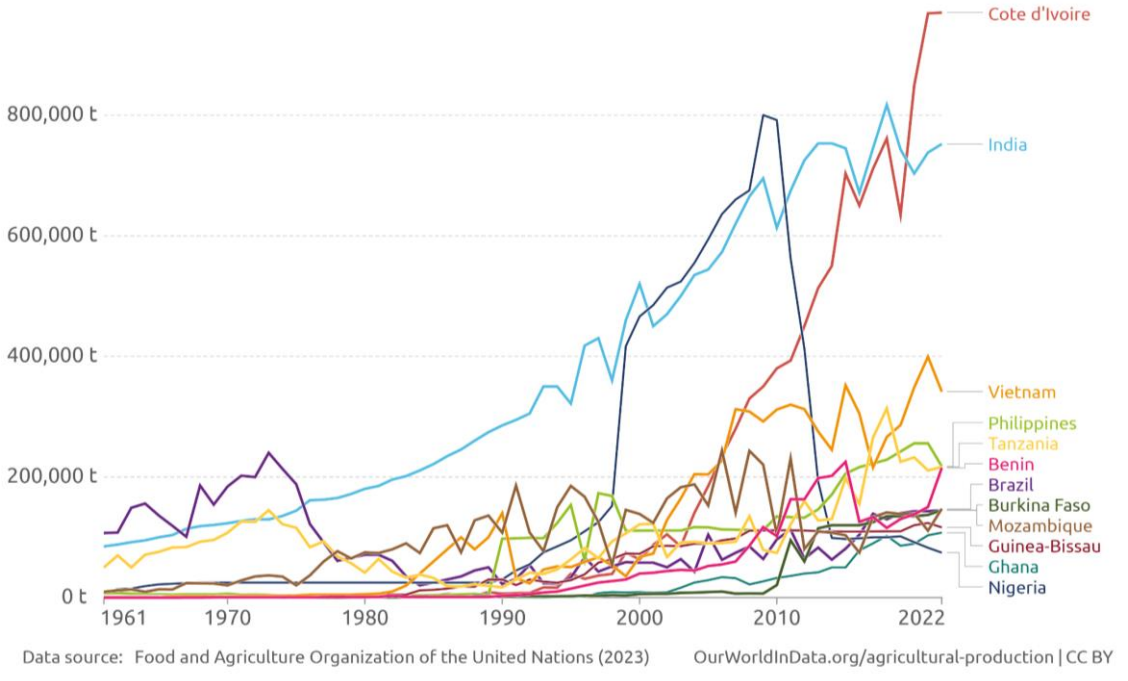

Figure 2: Cashew nut production volumes [11]

Apart from the usage of the kernel as food, the other parts of the cashew fruits have also been used in the past. Cardanol, one of the main components of the liquid, has been used for curing agents, foams, coatings and elastomers. The entire shells have also been used for their high heating value in pressed pellets. Employing this feedstock as liquid fuel for internal combustion engines will significantly increase

its value. This increased value can hopefully make an impact on wages and working conditions of the producers, which is an important issue for all biofuels that has been addressed in various reports [4].

1.3. Composition and properties of CNSL

CNSL consists of four main phenolic components, depending on the production path: Anacardic acid, cardanol, cardol and 2-methylcardanol. The C_{15} side chain of these molecules can be completely unsaturated as well as mono-, di- and tri-unsaturated. The basic chemical structures of the CNSL components are shown in Figure 3 [5][6][7][8].

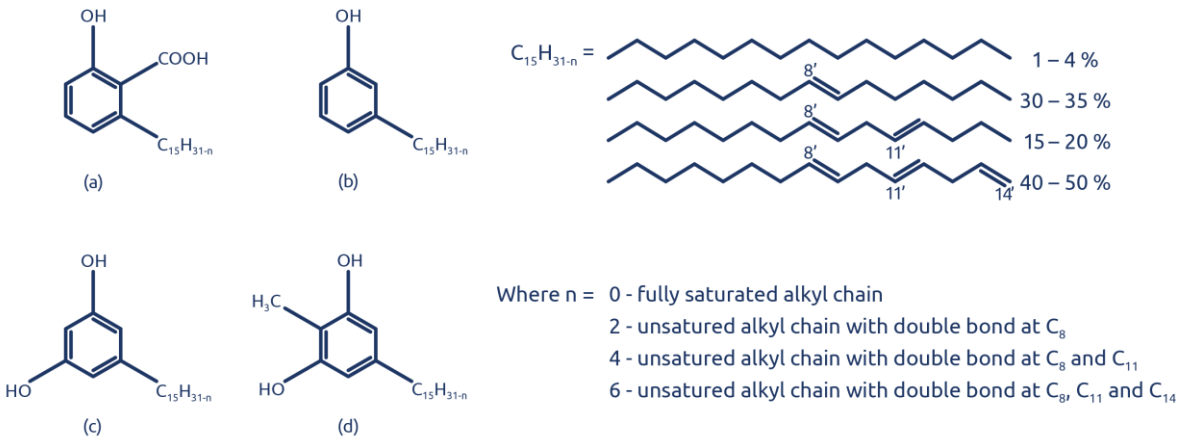

Figure 3: Chemical structures of CNSL – (a) Anacardic acid, (b) Cardanol, (c) Cardol, (d) 2-methylcardanol [5]

Technically interesting properties of CNSL include its heating value, viscosity, acidity and potassium content. The acidity of phenolic compounds varies due to the substitutions present in the phenyl ring. However, when a substantial concentration of phenolic compounds is present in the fuel, it may lead to corrosion, sludge formation and fuel injection issues. The components of CNSL typically show an elevated Acid Number ranging from 1.0 to >2.0 mg KOH/g.

All the components have polymeric properties due to their structure. The phenolic compounds in CNSL are quite reactive, due to the presence of the hydroxyl group and the unsaturated alkyl side chain with different degrees of unsaturation. This makes the reaction centers susceptible to polymerization.

Many CNSL samples have been found to contain high potassium levels. These are not native to the feedstock but might instead derive from wanted or unwanted contamination with potassium hydroxide and other alkalis used to inhibit polymerization. High levels of potassium can lead to increased post-combustion deposits. Potassium is also known to have a harmful effect on SCR (Selective Catalytic Reduction) units.

2. How to determine suitability of biofuels

FVTR and LKV have a long history and broad experience base in testing fuels. The scope here ranges from different distillate fuel qualities and determination of impurities, marine residual fuel qualities, normed biofuels and completely novel biofuels from a variety of feedstocks, blends of all the above and most recently different alternative fuels like for example methanol, ammonia and hydrogen.

The testing of these fuels depends on the application. While for on-road fuels the influence of a certain blend on the engine running characteristics at fixed engine controller settings might be of interest, other fuels might require tuning of the combustion method in various degrees using free controllers. In the case of testing biofuels for marine applications, an adaptation of the fuel system and engine control to the biofuel is not possible as the fuels are supposed to be drop-in capable. The combustion is analysed against a standard marine fuel. A big challenge arises from the high flexibility of the marine fuel system. These systems allow the usage of very low refined fuels with vastly varying properties, and the challenge is to make sure that the systems do indeed not suffer any deterioration. Generally, problems of compatibility of fuels with fuel systems can be related as shown in Figure 4.

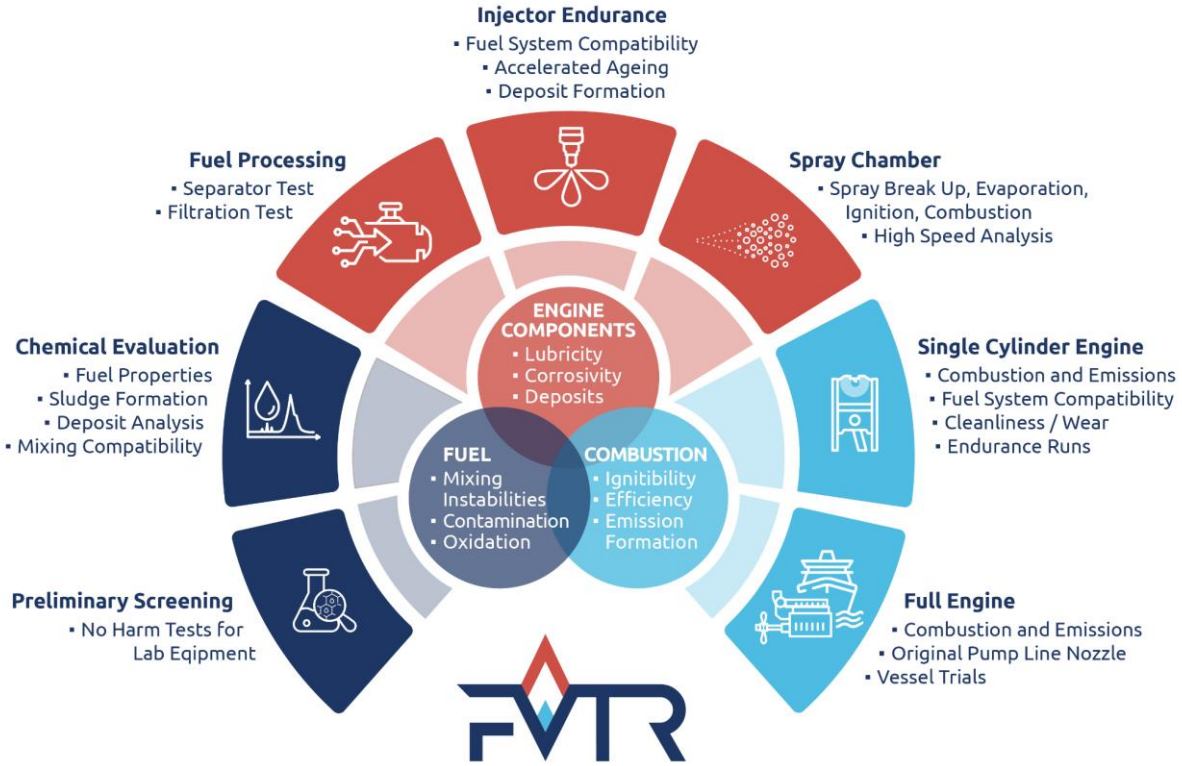

Figure 4: Compatibility issues and testing methodology for bio-oils and blends

These areas of compatibility are analyzed in a testing methodology that incorporates laboratory tests, component tests and engine tests and vary in its scope from straight forward practical orientation to a more academic focus.

2.1. Laboratory testing

ISO 8217 is meant to give minimum guarantee to ship owners that the fuel is suitable for engine use. In the case of new bio feedstocks and biofuels, the basic values of the ISO 8217 are not sufficient since the possible problems are of different nature. Therefore, additional testing or even developing new test methods seem necessary to overcome the challenges. Additional important parameters for the evaluation of biofuels are oxidative, thermal and mixing stability. In the case of oxidation and thermal stability, the aim is to examine how the fuels may change in the presence of oxygen or at higher temperatures. Oxygenated species could be formed when oxygen is incorporated. These oxygenated

species can increase the acid number, i.e. the corrosiveness of the fuel, or polymerize. Biofuels are to be used primarily as drop-in fuels, so the mixing compatibility with conventional and alternative fuels must also be tested. These tests provide information on which fuels and in which ratios may exhibit mixing instabilities or whether reactions can occur between the fuels. The influence that water can have on the fuel being tested is also important here. In addition, tests and methods are also being developed to investigate the interactions of new fuels with lubricating oils.

2.2. Purifier and injection test rig

In this stage the fuel is tested for its compatibility during the fuel handling process. Significant amounts of fuel can be lost in the separator and effort is spend on the separator operation, sludge disposal and maintenance and repair in case of a clogging of separator and subsequent filters due to excessive sludge. Especially biofuels exhibit reactions with water from the separator. This happens in purifier mode due to the liquid interface but also in clarifier mode as water is often used for automatic flushing of the bowl, which can lead to deterioration and alteration of the fuel.

The separator test bench was originally created to answer a customer's request for reproducible and realistic determination of a fuel's sludge formation tendency. The test bench is a good representation of an onboard fuel handling system and features the following main components:

- Tilted barrel representing a settling tank
- Elwa electric fuel heater
- Krohne Coriolis for exact measurement of separator flowrate
- Alpha Laval MIB 503 manual separator
- Boll Filter with different mesh sizes

The testing procedure is chosen to represent the stressing and ageing of a fuel on a vessel by including phases of heating, settling and stirring. Boundary conditions of the procedure can be set very accurately by the use of an electric heater and the Coriolis flow rate measurement.

The manual separator used in the setup has a lower rotational speed compared to large automatic separators, which is compensated by a lower feed rate and therefore a longer retention time in the centrifuge. This is outweighed however, by the small size allowing small fuel quantities and the manual emptying of the bowl allowing very accurate determination of the sludge content.

The fuel handling test bench is accompanied by a common rail injection system test rig, consisting of high-pressure pumps, rails and injectors of different sizes depending on the system to be tested. On this test bench the injector can be operated at increased injection rates, simulating an engine endurance run. Fuels that are suspected to cause deposits and wear to the injection equipment at long operation durations are ideally tested on this rig instead of the engine to reduce testing costs.

2.3. Research engine test rigs

After passing all prior tests, a final proof of usability is the engine test. Here, different options from single cylinder research engine (SCE) to full engine are possible, see Table 1.

A single-cylinder research engine (1VDS18/15CR) is used for comprehensive investigation of fuel impact on the fuel supply system, fuel injection system, engine performance, combustion, emissions and optionally exhaust gas treatment. The layout and size of the engine is representative for a maritime

medium speed engine. The SCE offers many degrees of freedom regarding all aspects of engine operation:

- Fuel handling
- High pressure generation
- Injection settings (Common Rail)
- Charge air and engine back pressure

On the SCE, the compatibility of the injection equipment is tested under severe but realistic conditions. As the common rail injector uses uncooled nozzles, the relatively high surface temperatures result in comparatively strong stress on the fuel. Because of the constant fuel pressure of the common rail system, power loss through deterioration of the nozzles is more easily detected compared to a mechanical injection system.

The engine also allows limited duration endurance runs for testing the impact of the fuel and its additives on different engine parts (auxiliary, FIE and power unit) regarding wear and cleanliness. For this purpose, new parts can be installed prior to the test, run in and stressed. Afterwards all parts of interest are rated qualitatively using charts and quantitatively using laser scanning microscopy.

The test bed is equipped with a state-of-the-art pressure-trace indication system to calculate the rate of heat release and as well as exhaust analysis using FTIR and particle analysis systems e.g. for FSN or PN/PM. Engine tests are performed at steady-state operation points at rated engine speed and varying engines loads, rail pressures and injection timing.

The final step of the fuel evaluation is a test on our full engine, a medium-speed marine research diesel engine. It's based on a Caterpillar MaK 6M20 engine block and power unit and coupled to an electric load unit, which can be tuned to allow engine operation in generator as well as in propeller mode. Apart from the injection system, which can be converted to a common rail system developed in house with support by L'Orange, all other components such as valve timing or turbocharger setup, for example, are identical to the serial production engine. Table 1 gives an overview of the engine's technical data. Combustion in all cylinders is evaluated using high speed pressure indication. Exhaust gas measuring equipment is installed to acquire the exhaust gas component concentrations and the filter smoke number (O_2, CO_2, CO, NO_X (NO + NO_2), SO_2, HC, FSN).

While the common rail system is quite useful for some test scenarios, in our case of biofuel testing, the pump-line-nozzle system is an insightful extension of the single cylinder engine with its common rail system. While the common rail system is better at detecting small changes of wear, the PLN system is more robust and the mostly used system in the field. So, this test will most closely resemble an actual field trial.

Table 1: Specification of test engines

Unit	Single Cylinder Engine	Full Engine
Engine ID	1 VDS 18/15 CR	Caterpillar MaK 6M20
Charging system	Externally charged	Turbo charger
Engine type	4-stroke	Straight six cylinder 4-stroke
Stroke / mm	180	300
Bore / mm	150	200
Compression ratio	13 (15, 16)	14.8
Rated power / kW	80	1020
Rated speed / min^{-1}	1500	1000
Fuel injection system	Common Rail, HFO capable	Pump-Line-Nozzle, HFO capable (Common Rail, distillate fuel only)

3. Results and discussion

3.1. Fuel overview and lab tests

Different candidates of CNSL and cashew-based derivates were already tested with our methodology. These bio-oils are technical, hydrotreated, distilled and refined CNSL as well as oils derived by pyrolysis processes from the cashew material. For this study five different cashew-based fuels and blends thereof are used:

CNSL base-fuels

- Technical CNSL
- Refined CNSL
- Distilled CNSL
- Hydrotreated CNSL
- Pyrolysis oil from a Cashew feedstock

The initial testing of new fuels is carried out in accordance with ISO 8217, whereby the standard parameters are determined and tested for conformity to standards. Selected results of the tests are shown in Table 2.

Table 2: Basic characterization of various cashew-based bio-oils

CNSL type	Viscosity at 50°C [mm²/s]	TAN [mgKOH/g]	K [ppm]	S [ppm]
Technical CNSL	38.21	8.3	200	120
Low-refined CNSL	35.86	8.1	33	250
Distilled CNSL	6.584	2.2	14	6
Hydrotreated CNSL	13.14	0.4	11	18
Pyrolysis oil	8.795	0.3	12	88

The viscosity of the technical and low-refined CNSL is high compared to the other three grades. The viscosity can be significantly reduced by any additional processing step. The same effect can be observed with the acid values. The technical and low-refined CNSL have very high acid numbers (limit value < 2.5 mgKOH/g) and thus limit the highest possible blend rate to < 30%. If the acid values of the fuels are too high, this can lead to corrosion of metallic components in the system. However, if the CNSL is further processed, whether by distillation, hydrotreatment or gained by alternative processes, such as pyrolysis, the limit value of the acid number parameter can be adhered to and the blend rate is therefore not limited.

It is also noticeable that the potassium content of the technical CNSL is very high. The high potassium content can, for example, lead to increased post-combustion deposits. The remaining CNSL grades have significantly lower potassium values. Therefore, a further processing step of the technical CNSL is mandatory for reducing the potassium content. The lower sulphur content of all CNSL samples should be positively highlighted here. The technical and low-refined CNSL have a rather high sulphur content compared to the other three candidates. However, this value is well below the sulphur limits. This means that blending bio-oils with conventional heavy fuel oil alone could reduce the sulphur content.

GC-MS measurements have also been carried out (data not shown). This technique allows the determination of organic chemical composition of CNSL fuels to a certain extent. The main components have been identified for technical, refined and distilled CNSL. For the hydrotreated CNSL and the pyrolysis oil, significantly more signals or compounds were detected. For the hydrotreated CNSL partially and fully hydrogenated main compounds are identified as well. For the pyrolysis oil the main components (see figure 3) are not present at all, mainly smaller molecules are identified.

Of course, the goal in fuel testing is to be able to stop using engine and component tests and replace them with cheaper and faster laboratory test methods. For newly developed fuels, however, it might be insufficient to test strictly according to the normed procedures. Failure scenarios of these fuels, as experienced in the field or on our test engines, might be specific to the fuel and therefore require specialized methods for detection and quantification. In these cases, our experts have developed new or modified test methods in many customers and public projects to help analyze test fuels. Examples of this are outlined in the following paragraphs.

Water emulsification test – simulation of purifier system

Heavy oils are pre-cleaned in a purifier system where they are exposed to water and higher temperatures. Some biofuels are not stable in the presence of water or high temperatures (acid or sludge formation). A laboratory test for the behavior of the fuels in the purifier system was developed to make it easy to understand these processes. This involves adding water to the fuel, mixing the fuel and water phases sufficiently and then centrifuging them. The results of these tests are shown in Figure 5.

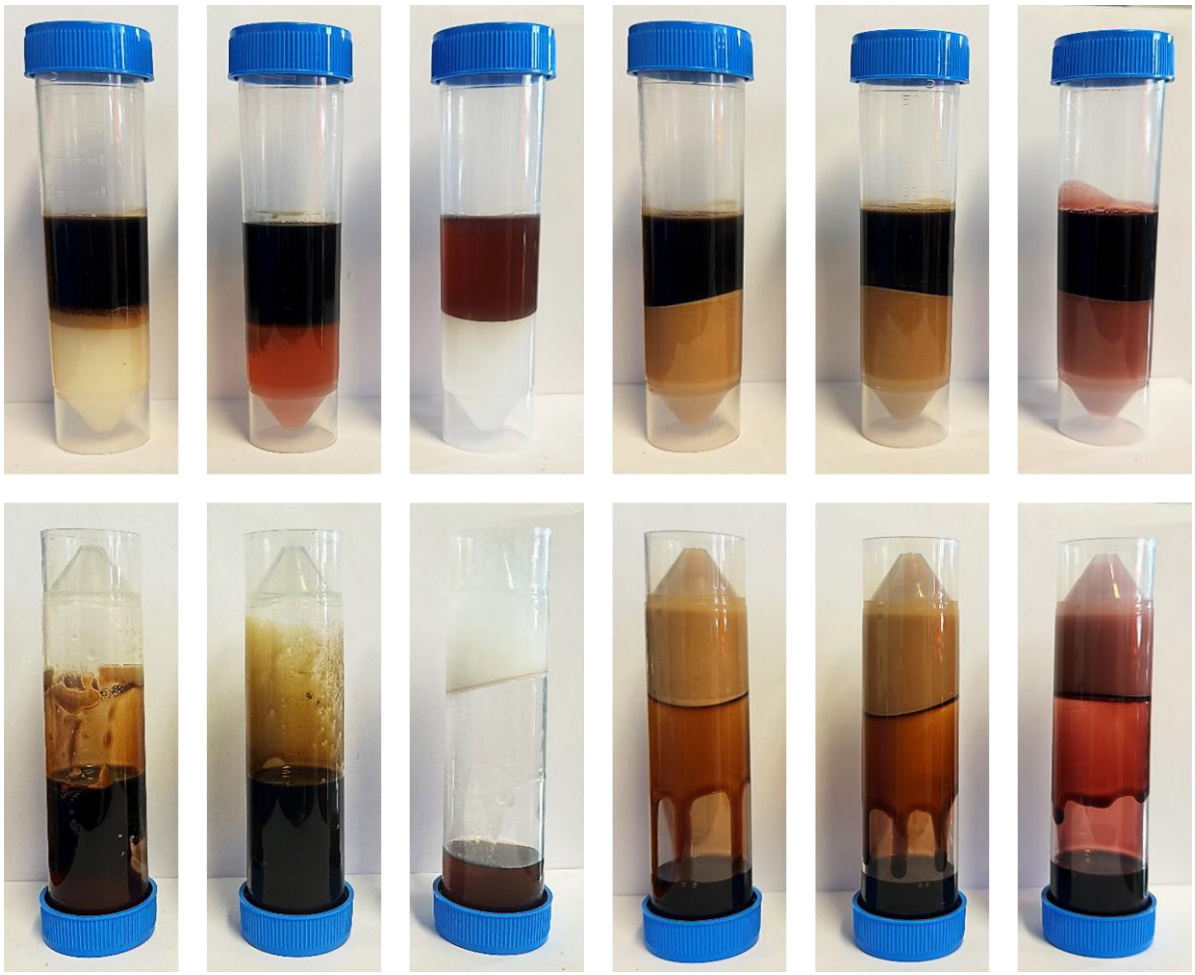

Figure 5: Water emulsification tests (left to right: technical, pyrolysis, distilled, refined, low-refined, hydrotreated CNSL)

By centrifuging the samples, the aqueous (bottom) and fuel phases (top) are separated. To check the extent of sludge or gel formation, the sample containers can be turned upside down. The figure shows that five of the CNSL fuels tested exhibit sludge formation. Only the pyrolysis oil shows no sludge formation. It has not yet been possible to clearly determine which compounds are responsible for this behavior. If these results are compared with the GC-MS measurements, it is noticeable that the pyrolysis oil is the only one that does not contain any of the basic structures of the technical CNSL already described. This suggests that the CNSL basic components could cause this behavior.

Thermal stability test – "Hot slope"

In an effort to evaluate the injector coking potential in a laboratory scale, the "hot slope" test was designed. The test addresses the processes in the injection nozzle: After an injection, fuel remains in

the sac hole until the next cycle. Draining of the sac hole through the injection orifices depends on the fuel's viscosity and surface tension. The remaining fuel has a long time to heat up to the nozzle temperature especially during the combustion phase. A part of the fuel proceeds to evaporate through the injection orifices, leaving behind heavier, longer chained fuel compounds. Thermal stress can then lead to cracking and polymerization of the fuel. Depending on the fuel, this process can leave residues which have different tendencies to be washed away and solved during the next injection or adhere to the nozzle steel and start building up firm deposits.

This process chain of heating, evaporation and resolving was combined in a test by periodically dripping fuel on a heated, sloped metal surface. This slope is heated by an underlying copper block fitted with heating cartridges. In the current CNSL tests the temperatures were varied between 230 and 310°C. Aluminium sheets were used for the slope material. A total of 10 drops of fuel were dripped onto the slope periodically every 15 seconds forming a runnel on the slope. After another 15 seconds the remaining liquid film was removed using a paper swipe. Depending on the slope temperature and the fluid characteristics a deposit was formed on the sheet metal which was rated based on its appearance. In further tests a subsequent lab analysis is intended with the aim to determine the chemical composition of the deposits.

The results for the cashew-based fuels at two slope temperatures are presented in Figure 6. The temperatures of 270 °C and 290 °C were chosen for the comparison. At 270 °C the technical and refined CNSL start to develop a discoloration on the slope. On the sides of the runnel some fuel components can be observed during the test to concentrate and start solidifying. However, these accumulating components are almost completely washed away with the subsequent drop of fuel. At 290 °C the time between the droplets is enough to allow the formation of solid deposits. In the middle of the runnel the mentioned washing effect is still active and has a visible impact on the shape of the deposits.

For the distilled CNSL the main fuel components responsible for the deposits have clearly been removed or at least reduced. Thus, almost no discoloration is seen at 270 °C. At 290 °C an accumulation on the sides of the runnel, similar to the previously described, is starting to form. Even at 310 °C the washing effect still reduces the amount of deposits in the middle of the runnel.

The hydrotreated CNSL does not form any deposits up to a temperature of 310 °C where a slight discoloration remains on the aluminium.

The pyrolysis oil starts forming discolorations at 270 °C. But unlike technical and refined CNSL the washing effect in the middle of the runnel limits the amount of deposits at 290 °C. Similar to the distilled CNSL, at 310 °C there is still a washing effect noticeable.

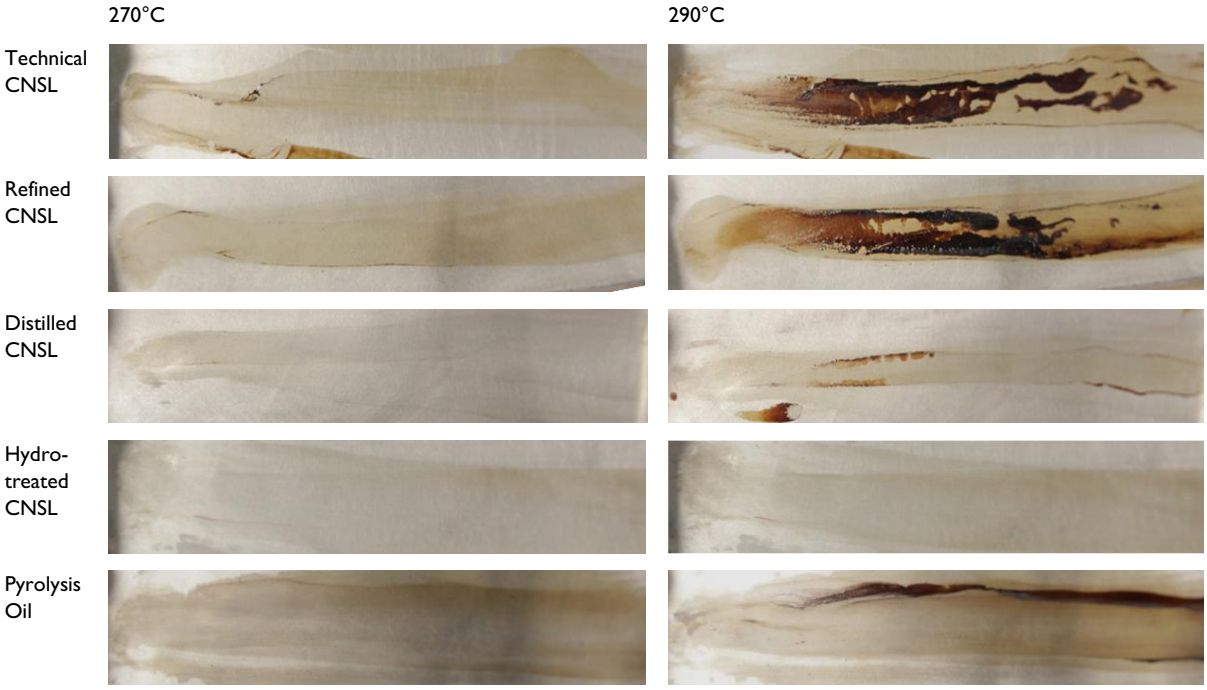

Figure 6: Resulting deposits from the hot slope test for two test temperatures

3.2. CNSL in the fuel system

For different cashew nut derived bio-oils so far, no issues regarding mixing compatibility were encountered. Heating the different blends up to typical temperatures of residual oil showed no problems, either. Therefore, the next critical step is the fuel treatment system on the vessel in term of purification.

Operating a purifier with raw or refined CNSL may cause a "gelification" of the fuel, which leads to massive sludge production on a vessel. This effect is reproduceable in the lab and was found to be caused by the interaction of the fuel with the purifier's water seal, thereby fusing all fuel components and water into a sludge-like gel. As one measure, the purifier might be operated in clarifier mode – if technically possible. This minimizes possible contact of the CNSL and water. However, even in clarifier mode some water might be present in the bowl as leftover from the automatic flushing procedure, leading to the same effect as the water seal.

Another aspect is painting and coating. Compatibility with the desired blend might be tested prior to operating. During our testing, the coating was partly damaged first and came off completely in a follow-up test. According to the manufacturer, this should not have any influence on the purifier performance.

Nonetheless, when operated with the correct conditions, particles from the production process of the cashew nut-based bio-blends and impurities are removed securely, thus facilitating further operation.

3.3. Combustion of CNSL

Single Cylinder Research Engine

Compared to a full engine, the single cylinder engine (SCE) offers much more flexibility in terms of boundary conditions. Using the Common Rail system, injection pressure as well as injection timing can be modified to optimize combustion behavior and enable operability of a vast variety of fuels.

With respect to bio-oils that would likely enter the market as drop-in fuels for fuel blends, engine operating parameters need to stay the same since an adaptation of the combustion strategy is far beyond engine operation on a vessel.

Therefore, engine operation of the SCE is started with the standard set of injection and engine operation parameters to comply with IMO Tier II limits. Regarding operability and engine safety, injection pressure and injection timing might be modified – but that is a test rig measure only.

Using the different blends at the test engines, several metrics were identified for indicating a "good" or a "poor" blend in terms of operability. Mostly, these metrics react to the quality of combustion which depends on fuel evaporation and spray quality. A bad combustion therefore shows increased CO emissions as well as an increased filter smoke number (FSN) due to incomplete combustion. This also reduces the NOx emissions due to decreasing efficiency (or increased SFOC). In case of CNSL operation, the cause for these symptoms are deposits on the inside or outside of the injector nozzle, either blocking the spray holes or interfering with the spray and thereby causing its low quality. In case of a CR system as on the SCE, the partial blocking leads to increased injection duration and therefore a shift of the center of combustion (CoC) in direction "late".

Figure 7 and Figure 8 show one bio-blend with good and one with poor operability. The engine was run consecutively at four load point. For some load points the rail pressure is also varied. The order of the load point is not of importance. The most striking marker for the degradation of the nozzle and the spray quality is the highly fluctuating CO emission in Figure 8. This can be observed to spike periodically. It is believed that these spikes correspond to the buildup and recovery of nozzle deposits which directly affect the spray quality. The center of combustion and the injection duration fluctuate roughly in accordance with the CO emissions; however, the changes are less obvious.

Comparing different blends from different bio-oils including different base fuels, the picture becomes even more complicated. Figure 9 shows test results including a reference VLSFO, marking the state-of-the-art fuel nowadays. There are combinations that seem to work well. So, technical CNSL seems to work in a larger range of admixture with distillate fuels. Since temperature is the critical point here, residual oil-based blends that need intensive pre-heating for proper injection viscosity, a direct use for engine operation leads to deposit formation.

The most interesting parameters evaluating the suitability of the different bio-oil blends in the engine test are presented in Figure 9. The pressure gradient is an indicator for the ignition delay. The worse the blend is in terms of this parameter, the harder is the combustion and may affect lifetime of the engine components. With a lower energy content of the blend an increasing injection duration occurs. But injection duration also increases with deposits in the nozzle since the narrowing causes lower flowrates at a set fuel pressure. This lower injection rate also causes a shift in the center of combustion.

The worsened spray quality is responsible for the worsened combustion which is visible in the CO signal as well as in the Filter Smoke Number. If corrected for the energy content of the blends, the injection duration is a good indicator for operability in a CR based injection system. For a poor blend which already created deposits and therefore a bad spray with a bad combustion, the maximum pressure gradient also increases. The larger droplets need more time for evaporation which adds to the physical ignition delay and results in larger premixed shares of the combustion. At low loads, the complete combustion might take place as premixed combustion due to this effect.

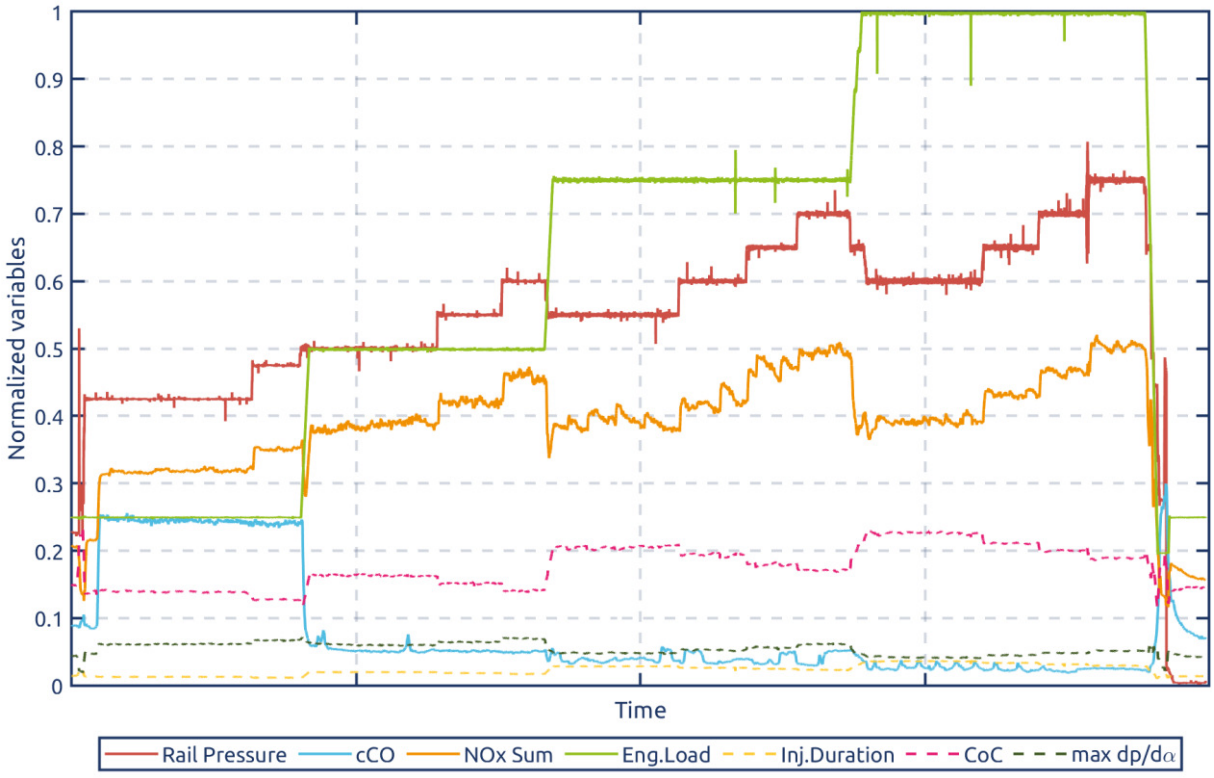

Figure 7: Test run with a promising bio-oil blend

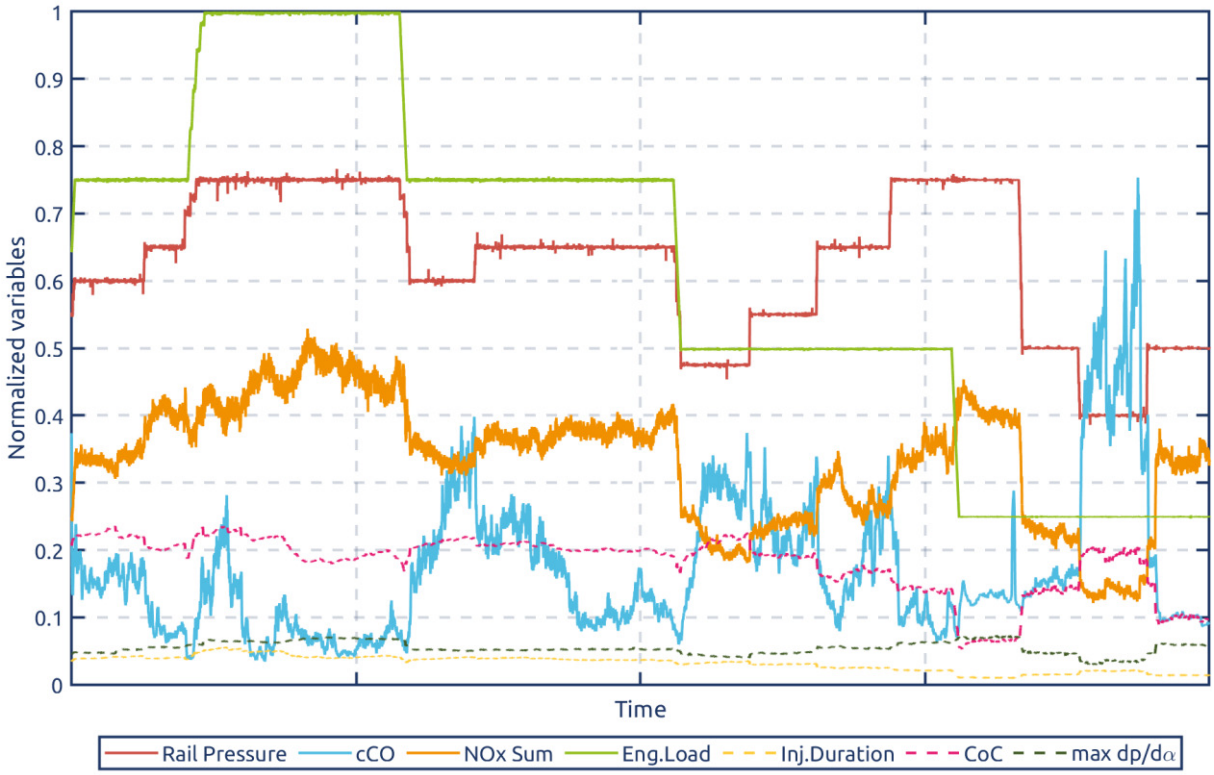

Figure 8: Test run with a problematic bio-oil blend

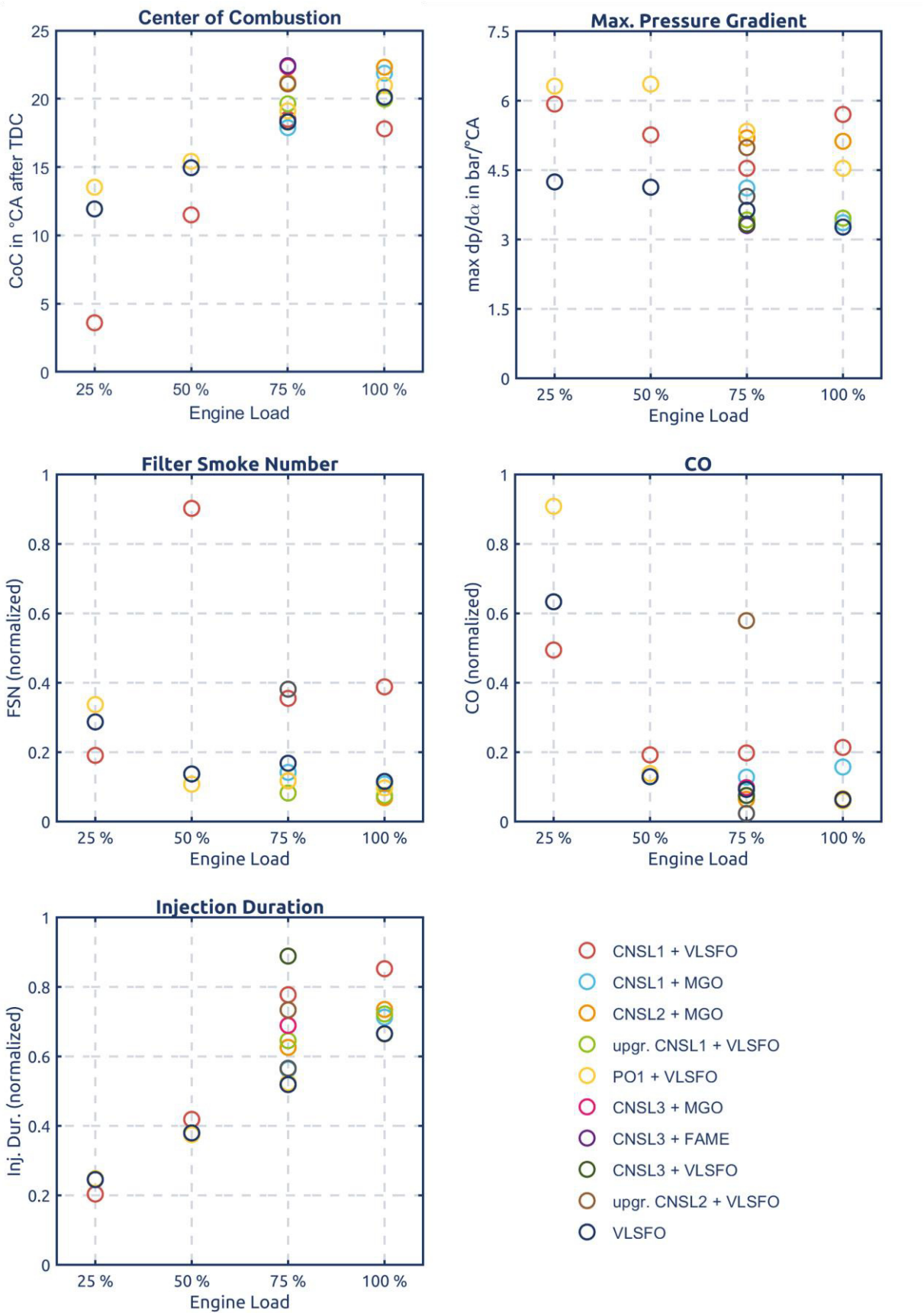

Figure 9: Comparison of engine parameters for different bio blends

In some tests with VLSFO-blends, external deposits are formed which are much firmer than typical nozzle coking from residual fuels (sometimes called "trumpets"). These external deposits can quickly deteriorate the fuel spray quality by causing larger droplet size and smaller spray angle. The external deposits however, vary in density and hardness. Figure 10 shows clearly visible deposits on the outer nozzle tip. In this case wide-opened "trumpets" are formed as the impulse of the fuel spray breaks its way through the deposits. Despite the impressive deposit formation, the corresponding test run was successful.

(a) (b)

Figure 10: (a) Nozzle tip after testing; (b) Nozzle, needle, inner parts: all clean using a proper working blend

Figure 11 shows imprints of the injector nozzle. The reference VLSFO as well as "good" blends in terms of operability show no marks of deposits in the sac hole nor the spray holes. Steady operation is the result, whilst for unsuitable blends the deposit marks inside the nozzle are clearly visible.

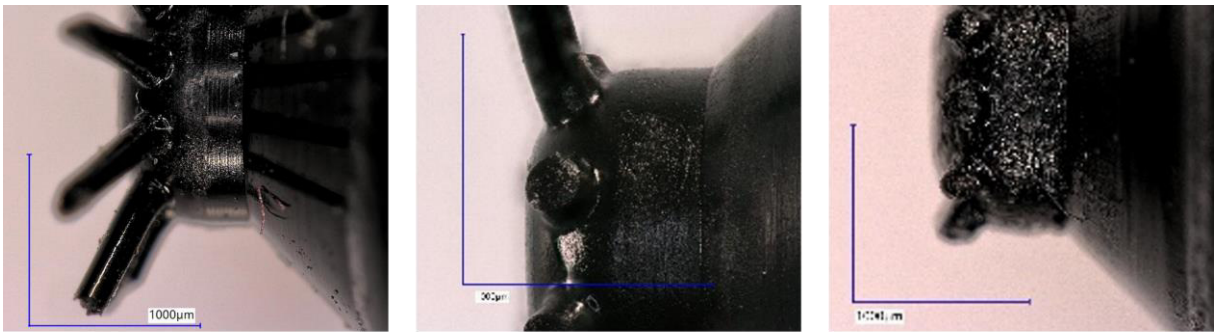

(a) (b) (c)

Figure 11: Nozzle imprints after test run with (a) Reference VLSFO, (b) a suitable bio blend and (c) a bio blend hard to operate

Full engine MaK 6M20

In case of the full engine MaK 6M20, the pump-line-nozzle injection system shows a different behavior. The injection pump is working mechanically and partial blocking or a higher resistance in the injector simply leads to pressure upbuild. Consequently, this allows better spray evaporation due to the better (smaller) droplet size of the fuel. In combination with oil-cooled nozzles, the risk of inner deposits is minimized as can be seen in Figure 12 (b) although the injector already shows deposits on the outside.

Figure 12 (c) shows a view via the injector port into the cylinder. There are deposits on the lower side of the cylinder head visible. If growing further, they might also influence the fuel spray and therefore the combustion quality. Despite these deposits one week of operation on a distillate based CNSL blend was possible.

(a) (b) (c)

Figure 12: (a) Massive coking on nozzle tip; (b) Still good state of nozzle interior; (c) Large deposits on the underside of the cylinder head in all cylinders

As a pre-cursor, again CO concentration as well as FSN can be used. Since injection duration stays constant with the mechanical injection pump, the maximum injection pressure (which increases in case of blocking in the injector) is an indicator for the onset of deposit formation.

Contrary to the SCE's CR injection system the PLN injection systems in combination with oil-cooled nozzles show a more robust behavior. The effect of deposits on the combustion was much less noticeable compared to the more sensible SCE testing. One reason for this might be the brute force injection pump pressing the fuel through the hp fuel line and the injection valve. With narrowing spray holes, the back pressure of the nozzle increases and leads to an increasing injection peak pressure. The additional stress that is caused by this for the fuel itself but also for the material of the injection system components must be considered.

4. Conclusion

The integration of renewable energy sources in marine fuels is approaching fast. As many alternative fuels require extensive infrastructural changes, currently the best option is the usage of drop-in capable biofuels. Driven by legislative pressure, previously unconsidered bio-feedstocks are entering the market. However, switching to a fuel with bio content is not straightforward. Current standards fail to guarantee operability with such fluids, as many potential issues are not covered by the required test methods.

The ultimate proof of usability of a fuel candidate is achieved through long-term engine tests that assess both performance and the condition of the engine components and peripheral systems. To minimize the risk for these long-term tests, preliminary laboratory and engine testing provides valuable support in introducing new fuel components. FVTR's methodology addresses most critical aspects of a marine fuel system, from the bunkering process to engine operation and combustion. This way, issues and potential solutions are identified early, avoiding critical situations at sea.

For cashew nut-derived biofuels, several critical scenarios have been identified in our labs. These are caused by the high temperature of fuel-contacting components as well as processing procedures like the fuel purification. In our tests, various bio-blends from the CNSL candidates and conventional base

fuels could be identified that are fit for long term sea trials. Particularly promising is the use of distillate bases, which seem to work well with most CNSL products over a wide blending range. The promising hydrotreated CNSL failed in a VLSFO blend in the engine test, a result that does not correlate with preliminary test methods. It was not tested with distillates as base fuels yet. The distilled CNSL and the pyrolysis oil are the only candidates that could be used in blends with residual fuels. This result correlates well with the deposit tendencies indicated by the hot slope test. In general, although care must be taken regarding feed stock quality and blend partners, our results encourage the further development of cashew nut related feedstocks as drop-in fuels.

In the future, our insights into bio-oils and their specific challenges for safe use in marine engines will help us develop rapid, standardizable testing methods that align and extend existing protocols. By serving the maritime industry with these advanced tools, we aim to support the successful transition to sustainable energy solutions.

Literature

[1] „The-Cashew-Conundrum-Mighty-Earth-EN.pdf“. Last access13.08.2024. https://www.mightyearth.org/wp-content/uploads/The-Cashew-Conundrum-Mighty-Earth-EN.pdf.

[2] Baron, Matthew. „Things Keep in Mind : Why Do We Not Eat Cashew Fruit?“ Wholesale Nuts and Dried Fruit, 26. Januar 2023. https://wholesalenutsanddriedfruit.com/why-do-we-not-eat-cashew-fruit/.

[3] Cardolite Corporation. „Technology“. Last access13.08.2024. https://www.cardolite.com/technology/.

[4] Sruthi, P., und M. Madhava Naidu. „Cashew nut (*Anacardium occidentale* L.) testa as a potential source of bioactive compounds: A review on its functional properties and valorization“. *Food Chemistry Advances* 3 (1. Dezember 2023): 100390. https://doi.org/10.1016/j.focha.2023.100390.

[5] David Chukwuebuka Ike, Millicent Uzoamaka Ibezim-Ezeani, Onyewuchi Akaranta, Cashe nut shell liwuid and its derivatives in oil field applications: an update, Green Chemistry Letters and Reviews (2021), 14:4, 620-633, doi: 10.1080/17518253.2021.1991485

[6] Teresinha de Jesus Aguiar dos Santos Andradea, Bruno Quirino Ara job, Antonia Maria das Graas Lopes Cit b, Juliana da Silvac, Jenifer Saf d,e, Marc Franois Richterc, Alexandre de Barros Falco Ferraz, Antioxidant properties and chemical composition of technical Cashew Nut Shell Liquid (tCNSL), Food Chemistry 126 (2011), 1044-1048, doi:10.1016/j.foodchem.2010.11.122

[7] Francisco H. A. Rodrigues, Francisco C. F. Franca, Jose R. R. Souza, Nagila M. P. S. Ricardo, Judith P. A. Feitosa, Comparison Between Physico-Chemical Properties of the Technical Cashew Nut Shell Liquid (CNSL) and those Natural Extracted from Solvent and Pressing, Polimeros vol. 21 (2011), 156-160, https://doi.org/10.1590/S0104-14282011005000028

[8] B. Deepanraj, N. Senthilkumar, D.Mala, A.Sathiamourthy, Cashew nut shell liquid as alternate fuel for CI engine—optimization approach for performance improvement, Biomass Conversion and Biorefinery (2022) 12, 1715–1728, https://doi.org/10.1007/s13399-021-01312-4

[9] Nuffield Council on Bioethics, Hrsg. *Biofuels: Ethical Issues*. London: Nuffield Council on Bioethics, 2011.

[10] VPS Veritas "Biofuels brochure", https://www.vpsveritas.com/sites/default/files/2024-03/biofuels_brochure.pdf

[11] OurWorldInData.org/agricultural-production

MET
MET Motoren- und Energietechnik GmbH

LKV ROSTOCK

Fraunhofer IGP

FVTR

IEE
Institut für Elektrische Energietechnik

Your research partners for maritime propulsion systems in

ROSTOCK

Keywords: ammonia, hydrogen

Progress and prospect of combustion technologies developed in Japan for zero-carbon fuels

Prof., Dr. Koji Takasaki[1], Dr. Satoshi Kawauchi[2], Dr. Yoichi Niki[2], Dr. Yasuhisa Ichikawa[2], Dr. Chiharu Kawakita[3], Akihiro Miyanagi[4], Koji Edo[4]

(1) Kyushu University & National Maritime Research Institute, Japan, (2) National Institute of Maritime, Port and Aviation Technology (National Maritime Research Institute), Japan, (3) New Energy and Industrial Technology Development Organization (NEDO), Japan, (4) Japan Engine Corporation

https://doi.org/10.18453/rosdok_id00004639

Abstract

In order to achieve the IMO's 2050 target of net zero GHG emissions from international shipping, the use of zero-carbon fuels such as hydrogen and ammonia is essential. In order to burn these fuels without problems, new technologies on the side of marine engines are required.

In Japan, a national project named "Green Innovation" funded by NEDO (New Energy and Industrial Technology Development Organization) is underway to develop the next generation of ships, which includes the development of technologies to burn hydrogen and ammonia in low-speed two-stroke main engines. This paper introduces the representative technologies that may be applicable to the project.

(1) The first half of the paper describes a fundamental study on the Diesel-cycle type diffusive combustion by high-pressure injection of hydrogen.

A Diesel-cycle type hydrogen-fuelled low-speed two-stroke engine for ocean-going ships is under development at Japan Engine Corporation (J-ENG.). The authors focus on the diffusive combustion by high-pressure hydrogen injection, which realizes high power and high efficiency without worrying about the back-firing, pre-ignition and knocking associated with Otto-cycle type hydrogen combustion.

As a fundamental research work for the development, visual studies on the combustion by high pressure (for example, 30 MPa) hydrogen injection including the case of 100% hydrogen without pilot fuel has been carried out.

(2) In the second half of the paper, development of the 'Stratified Injection System', which can be applied to diesel combustion of ammonia, methanol, low-grade bio-fuels, etc. is introduced.

This system was initially developed as a stratified water injection system for NO_x control. In that case, fuel, water, and fuel were injected in this order from the same injection nozzle hole during the injection duration of every cycle. Recently, this has been put to practical use for low-speed two-stroke engines by J-ENG.

Next, the following studies are introduced. Experiments using the system was conducted to apply a low-quality BFO (Bunker Fuel Oil), which had poor ignition and combustion characteristics, to a high-

speed diesel engine. In that case, MDO (Marine Diesel Oil with a good ignition and combustion characteristics like a Gas Oil), BFO, and MDO were injected in this order. Even in the case that a total mass ratio of pilot- plus post-MDO was only 10%, that meant the rest 90% was BFO, the BFO completed the combustion just as well as 100% MDO, as the pilot-MDO improved the ignition and the post-MDO mitigated the after-burning of the BFO.

In other words, this system is characterized by its ability to improve the combustion of a main fuel, which has poor ignition and combustion properties, by injecting the pilot-fuel from the same injection nozzle hole as the main fuel. If necessary, post-fuel can also be injected from the same hole.

While the engine that uses a hard-to-self-ignite fuel originally requires the two injection systems for main and pilot fuel, and the cylinder head must be equipped with two types of injection nozzles, the stratified injection requires only one injection system and simplifies the engine design.

1. Introduction

This paper introduces the two representative technologies that may be applicable to the alternative fuels.

(1) The first half of the paper focuses on the Diesel-cycle type diffusive combustion by high-pressure hydrogen injection, which realizes high power and high efficiency without worrying about the back-firing, pre-ignition and knocking associated with Otto-cycle type hydrogen combustion.

As a fundamental research work for the development, visual studies on the combustion by high pressure (for example, 30 MPa) hydrogen injection including the case of 100% hydrogen without pilot fuel has been carried out.

(2) The second half of the paper introduces the 'Stratified Injection System' technology. This system was initially developed as a stratified water injection system for NO_x control. In that case, fuel, water, and fuel were injected in this order from the same injection nozzle hole during the injection duration of every cycle. Recently, this has been put to practical use for low-speed two-stroke engines in Japan.

Next, the following studies are introduced. Experiments using the system was conducted to apply a low-quality residual fuel (BFO: Bunker Fuel Oil) to a high-speed diesel engine. In that case, BFO was sandwiched by pilot- and post-MDO (Marine Diesel Oil with a good ignition and combustion characteristics like a Gas Oil). Even in the case that a total mass ratio of pilot- plus post-MDO was only 10%, that meant the rest 90% was BFO, the BFO completed the combustion just as well as 100% MDO, as the pilot-MDO improved the ignition and the post-MDO mitigated the after-burning of the BFO.

In other word, this system is characterized by its ability to improve the combustion of a main fuel, which has poor ignition and combustion properties, by injecting the pilot-fuel from the same injection nozzle hole as the main fuel. If necessary, post-fuel can also be injected from the same hole.

While the engine that uses a hard-to-self-ignite fuel originally requires the two injection systems for main and pilot fuel, and the cylinder head must be equipped with two types of injection nozzles, the stratified injection requires only one injection system and simplifies the engine design

2. Studies on Diesel-cycle type hydrogen diffusive combustion

2.1. A Study for a high-speed 4-stroke hydrogen engine

Research on the diesel-cycle type hydrogen-burning engines in Japan dates back to 2004. MHI: Mitsubishi Heavy Industries, Ltd. conducted operational tests on a high-speed single-cylinder engine with an output of 100 kW [1].

Technical challenge of hydrogen injection engine

Comparison of properties between hydrogen and petroleum is shown in Table 1. Hydrogen has a high self-ignition temperature of over 570 °C despite its extremely high combustion speed, and its application in internal combustion engines usually requires an ignition source such as pilot diesel oil or a spark plug.

The results of this study overturned this forecast. By using a spark plug only at start-up and no ignition source at medium and high loads, and by increasing the compressed air temperature, stable hydrogen jet self-ignition operation was achieved.

The second challenge was to achieve a higher target of thermal efficiency than that of conventional diesel engines. As shown in Table 1, theoretical air quantity per heat value (L_0 /LHV) of hydrogen is smaller than that of petroleum fuels. It means that intake air pressure can be lowered in case of the same excess air ratio of petroleum fuels. Therefore, with a lower intake air pressure and a higher compression ratio, consequently higher cycle efficiency should be realized keeping the Pmax, maximum cylinder pressure constant. Furthermore, the high combustion speed of hydrogen, i.e. the short combustion duration, contributes to improve the thermal efficiency.

Apparatus for testing

The whole tests were conducted using a single cylinder test engine the specification of which was the same as engine planned to produce (Table 2). The ignition and combustion system are shown in Figure 1. For stable starting, a spark plug is set near the injection nozzle so that a hydrogen jet injected from the injector goes directly toward the electrode. Hydrogen gas is compressed to 30 MPa before the engine by a compressor.

The cross-section of a hydrogen injector is shown in Figure 2. It is controlled hydraulically and electrically. Hydrogen gas at 30 MPa is conducted from an accumulator into the needle chamber. At this time, injection does not occur because the working oil pressurized by a pump pushes the top of the needle. When the solenoid is activated, the working oil in the control chamber flows out through a small orifice. After the pressure in the control chamber gets lower and the force under the needle seat by hydrogen is higher than that on the needle, an injection starts.

Table 1: Comparison of properties between hydrogen and petroleum

Items	Hydrogen	Petroleum
Self-ignition temperature*1 [°C]	571	230
LHV [MJ/kg]	120	42.7
Stoichiometric air L_0 [kg/kg]	34.3	14.3
L_0/LHV [g/kJ]	0.271	0.334
Sonic Velocity [m/s]*2	1370	-

*1 at atmospheric pressure
*2 expansion from 300 K and 30 MPa

Table 2: Main specifications of product engine

Items	Specifications or Values
Cylinder Bore x Stroke	ϕ170mm x 220 mm
Cylinder Number	6 cylinders
Generating Output	600 kW / 1500 min^{-1}
BMEP	1.69 MPa

*Generator Efficiency 95%

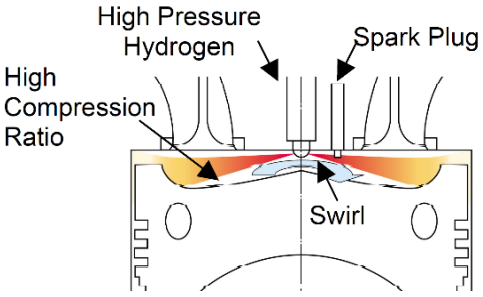

Figure 1: Combustion system of test engine

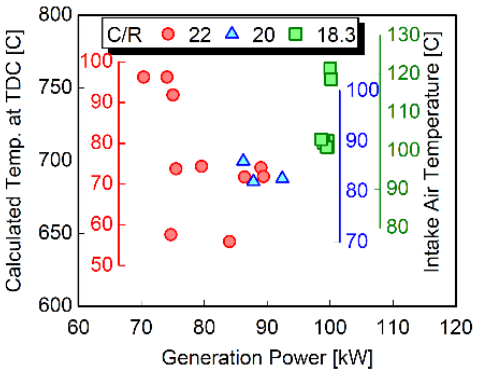

Figure 3: Estimated air temperature at TDC at higher load

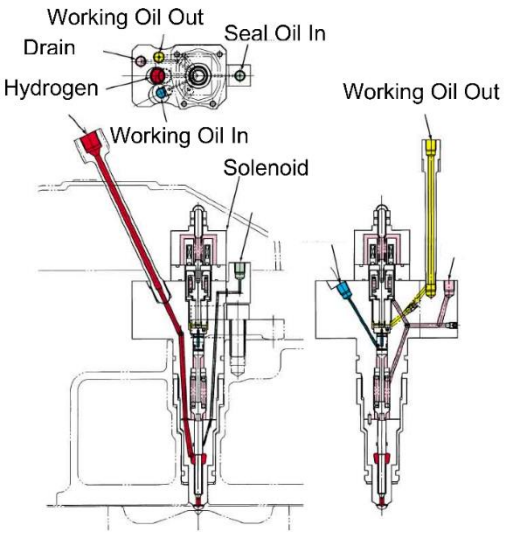

Figure 2: Cross-section of injector

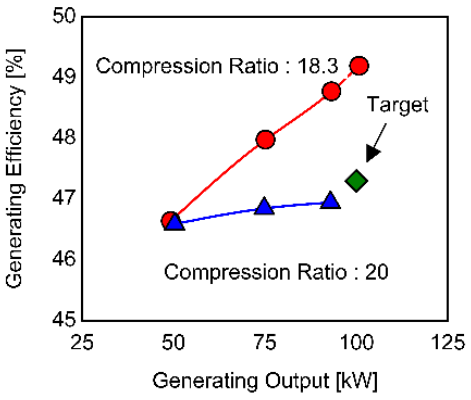

Figure 4: Measured generating efficiency

Self-ignition test at high load

As hydrogen has a higher self-ignition temperature than petroleum, stable self-ignition is supposed to be realized by enhancing the compression ratio. Therefore, tests were done with high compression ratios of 18.3, 20, and 22. At starting, intake air was heated up to the temperature at 180°C in case of 18 of compression ratio and was lowered as increasing engine output. The generated powers, intake

air temperatures, and the calculated compression temperatures that were reached at top dead center (TDC) are shown in Figure 3. Although there were some differences depending on the compression ratio, self-ignition of hydrogen was achieved at higher compression temperature than 690°C. As for the intake air temperatures, self-ignition of hydrogen was realized at higher temperature than 100°C even with the lowest compression ratio of 18.3.

As a result, the generating (thermal) efficiency of 49.2% (LHV base) was obtained as shown in Figure 4, with compression ratio of 18.3 and lower intake air pressure than conventional diesel engines, aided by the high-pressure hydrogen injection of 30 MPa.

Thermal NO_x was generated as much as that of a conventional diesel engine because of direct injection and diffusive combustion. To reduce NO_x emission, the exhaust gas re-circulation (EGR) could be adopted easily without any risk of reliability because the exhaust gas from a hydrogen engine was free from particulate matters and SO_x. In that case, the EGR gas contained no CO_2 with high specific heat, but NO_x was reduced due to the lower oxygen concentration during combustion. If the effect of EGR would be insufficient, NO_x should be deoxidized by the after-treatment apparatus. As an example, the NO emission was reduced to 835 ppm (as converted into O_2 of 0%) by EGR. Furthermore, it could be possible to be decreased to 100 ppm (likewise) by the catalytic reduction.

Reliability test

The running test for more than 50 hours was carried out to investigate the fluctuation of the engine performance and the surface condition of the fuel injection system. It was found that the movement of the parts of the fuel injection system and the engine performance did not change. After the test, the parts of fuel injection system were disassembled and it was confirmed that there was no trouble of the surface of sliding parts and gas seal parts.

As a result of measuring test of the surface temperature of combustion chamber, the temperature of burning side of piston and cylinder liner at the first ring position at TDC were similar to those of a conventional diesel engine. Therefore, it was possible that the reliability of parts composing combustion chamber for thermal load would be equivalent to that of a conventional diesel engine.

2.2. A fundamental study for a low-speed two-stroke hydrogen engine

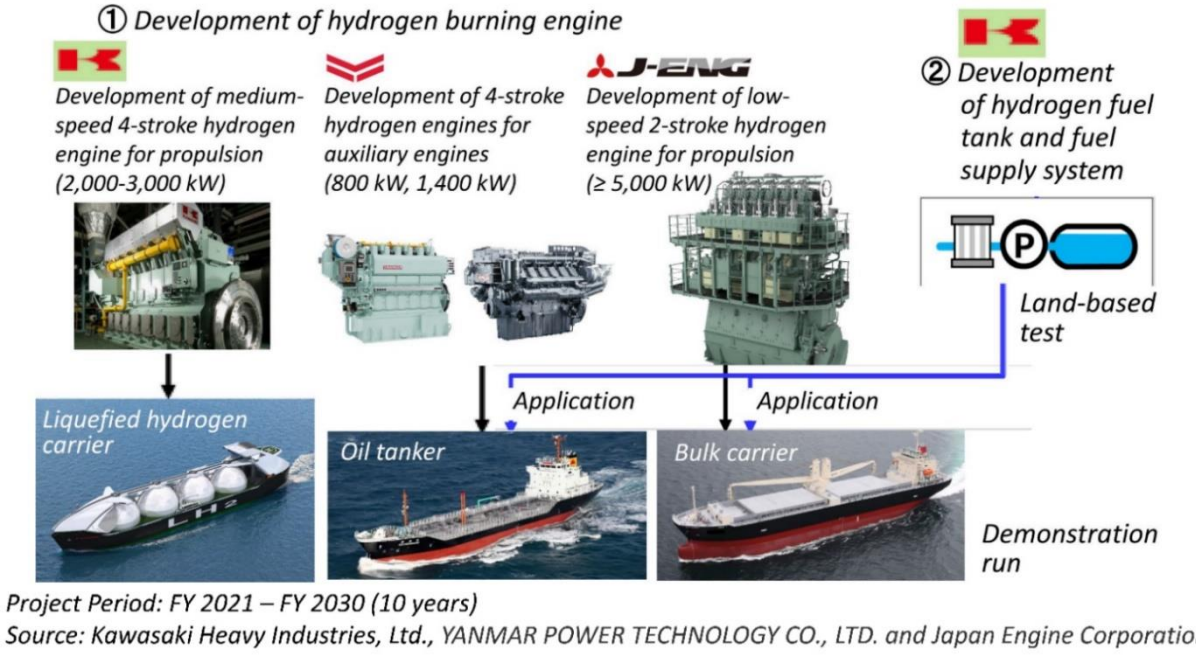

Figure 5: Green Innovation Fund project, Development of marine hydrogen engines and MHFS (Marine Hydrogen Fuel System) [2]

In Japan, the development of ocean-going vessels fuelled by green or blue hydrogen has started in 2021 under the "Green Innovation" fund by NEDO (New Energy and Industrial Technology Development Organization). An overview is given in Figure 5. As shown in this figure, three types of hydrogen engines are developed, with the low-speed, two-stroke hydrogen engine for bulk carriers on the right being a diesel cycle.

This part presents a fundamental study of high-pressure injection and diffusive combustion of hydrogen for the Diesel-cycle type hydrogen burning engine development, which has not been studied extensively compared to the premixed lean-burn (Otto-cycle) type.

Fundamental studies by Kyushu University and NMRI: National Maritime Research Institute

The properties of hydrogen are shown in Table 3 in comparison with those of methane. Based on the ratio of molecular weights of hydrogen and methane (2:16), the density of hydrogen is 1/8 of that of methane. The (lower) Calorific Value of hydrogen per mass in Table 3 is 2.4 times that of methane, but when considered per volume, hydrogen must be injected about three times the volume of methane to gain the same amount of heat.

However, the sonic velocity of hydrogen is about three times higher than that of methane, and in the case of high-pressure injection, where the initial speed of gas jet is the sonic velocity, a sufficient volume of hydrogen can be injected without extreme enlargement of injection nozzle hole.

As seen in Table 3, although hydrogen has a lower minimum ignition energy, its self-ignition temperature is much higher than that of diesel fuel oil, as already mentioned in the previous section. Therefore, at beginning of this study, pilot injection of gas oil (5% heat base) is tried to ignite the hydrogen jet. Shadowgraphs of ignited hydrogen jet taken from the side window of the RCEM (Rapid Compression

and Expansion Machine) are shown in Figure 6. As hydrogen flame cannot be visualized by the direct photography because it does not emit a luminous flame, the shadowgraph technique is applied. The white flame in the image in Figure 6 is the pilot gas oil flame and the black area is the hydrogen flame.

Figure 7 shows a comparison of heat release rate by a single spray between of methane and of hydrogen injected into the RCEM. Both sprays are ignited by a gas oil pilot injection. While both fuels are injected during almost the same injection duration and at the same injection pressure (at 30MPa into 8 MPa air), hydrogen shows the higher heat release rate and shorter combustion duration. As the injection-end timing is almost the same for the two fuels, the shorter combustion duration of hydrogen represents a faster burn-up after the end of injection, i.e., a shorter after-burning.

In this experiment, a hydrogen jet is also tried to self-ignite by further increasing the air temperature. The air temperature at hydrogen injection is raised to a higher level (estimated to be around 700°C, although unable to be measured) than normal case of diesel engines, and that allows the hydrogen to self-ignite.

From the photograph in Figure 8, it appears that the jet is self-ignited before 5.5° after the start of injection, after that the flame develops almost in proportion to the square root of the elapsed time. The penetration of flame front would be based on the momentum theory [3], just like a normal diesel fuel spray flame. This result will lead to the development of absolute zero-GHG hydrogen burning engine without any pilot fuel.

Table 3: Comparison of physical properties between hydrogen and methane

	Hydrogen	Methane
Calorific Value [kJ/g]	119.9	50.2
Maximum Adiabatic Flame Temperature [°C]	2124 (φ=1.07)	1967 (φ=1.05)
Flammable Range : vol.%	2.0-75	5.0-15.0
Equivalence Ratio (φ)	0.1-7.1	0.5-1.68
Maximum Burning Velocity[cm/s]	350 (φ=1.45)	45 (φ=1.07)
Self-Ignition Temperature [°C]	576	635
Minimum Ignition Energy [mJ]	0.015	0.29
Minimum Quenching Distance [mm]	0.51	2.03
Diffusion Coefficient [cm^2/s]	0.82	0.23
Methane Number	0	100

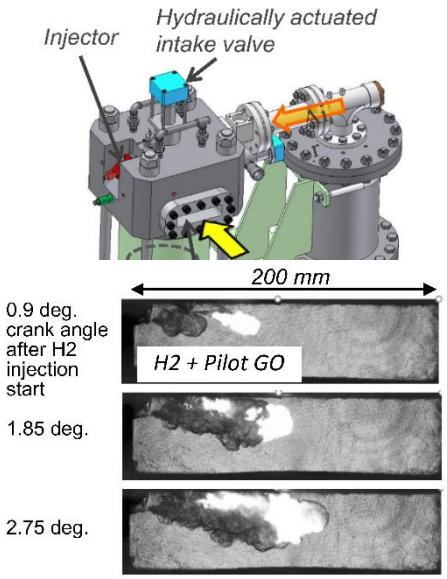

Figure 6: Upper: Side-view style RCEM, Rapid Compression and Expansion Machine

Lower: Hydrogen flame injected at 30 MPa and ignited by pilot Gas Oil

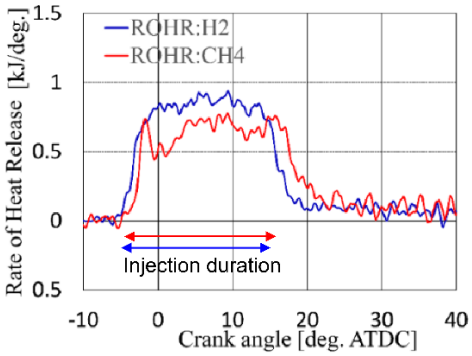

Figure 7: Comparison of heat release rate by single spray between of methane and of hydrogen, injected at 30 MPa and ignited by pilot GO. Air condition: (8 MPa, 550 ℃)

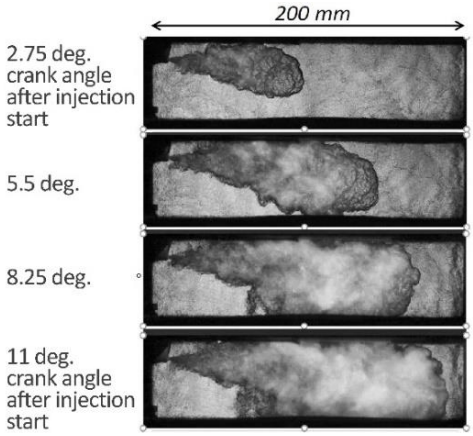

Figure 8: Hydrogen flame injected at 30 MPa and self-ignited by a higher air temperature than for Figure 6

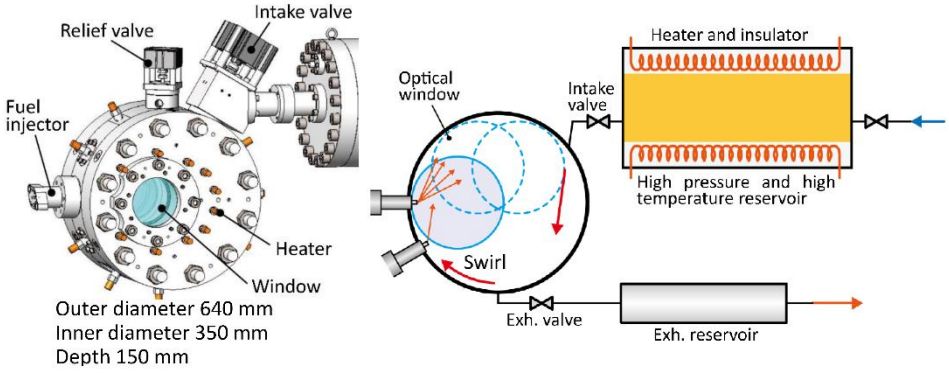

Figure 9: New visual combustion chamber for NMRI (National Maritime Research Institute in National Institute of Maritime, Port and Aviation Technology (MPAT), Japan)

Although the observation of a single flame as described above can provide some information, it is important to create the conditions close to those of the actual engine. The NMRI is currently building a visual combustion chamber as shown in Figure 9 simulating the engine to be developed. On the day of the Symposium, data taken with this equipment will be presented. CFD calculations based on this data will also be introduced.

Schedule for real engine development

As shown in Figure 5, J-ENG is developing a diesel-cycle, low-speed, two-stroke hydrogen engine with a cylinder diameter of 350 mm (UEC35LSGH). Figure 10 shows the development schedule for this engine. ClassNK has issued an Approval in Principle (AiP) for a parcel layout concept for a hydrogen-fuelled multi-purpose vessel [4]. This is the world's first AiP certification for the ship equipped with a low-speed two-stroke hydrogen-fueled engine as a main propulsion machine.

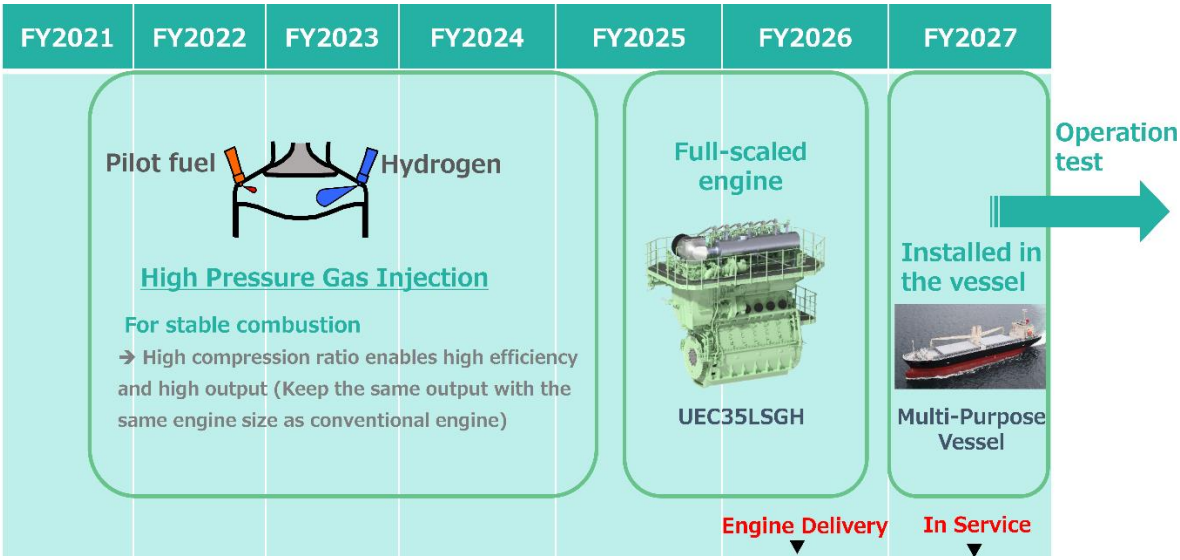

Figure 10: Schedule of hydrogen fuelled engine development by J-ENG

3. Fundamental studies on 'Stratified Injection System'

3.1. A study for a stratified fuel-water injection system

The second half of the paper introduces the 'Stratified Injection System' technology. It was initially developed as a stratified water injection system for NO_x control [5]. In that case, fuel, water, and fuel were injected in this order from the same injection nozzle hole during the injection duration of every cycle. Recently, this has been put to practical use for low-speed two-stroke engines by J-ENG [6].

Many researches were carried out in the past on the water injection into cylinder for NO_x reduction. Among them, the stratified water injection system was developed by Mitsubishi Heavy Industries, Ltd. The advantage of this system is that it does not cause a deterioration of ignitability as in the case of fuel-water emulsions. The system is also simpler than the independent water injection, where the cylinder head is equipped with an independent water injection nozzle.

Working principle of the stratified fuel and water injection

The first author analyzed the real injection rate of fuel and water injected by this system and simulated the distribution of water (water vapor) in the fuel spray [7]. As mentioned above, this system has been put into the practical use by J-ENG and its mechanism has been refined, but the function is explained at first according to Figure 11, the system used in the past study.

The whole system consists of a fuel injection pump with non-return valve (X), a fuel injection nozzle with a special water passage (including another non-return valve (Y)) connected to the fuel passage and a water supply unit, which feeds an exact quantity of water into the passage of the injection nozzle.

The working principle is as follows: Before the injection starts, water is fed into the injection nozzle with a pressure higher than the opening pressure of the non-return valve (X) in the injection pump, but lower than the opening pressure of the needle in the injection nozzle, as shown in Figure 11(a). During the period of water supply, a certain quantity of fuel pushed by water flows back to the fuel injection pump, passing through the non-return valve (X). But some fuel remains in the nozzle tip as can be seen in Figure 11(a). When injection starts, the non-return valve (Y) blocks the passage of water.

Thus, the fuel remaining in the nozzle tip is injected first as shown in Figure 11(b). Then the water in the fuel passage and lastly fuel from the injection pump is injected.

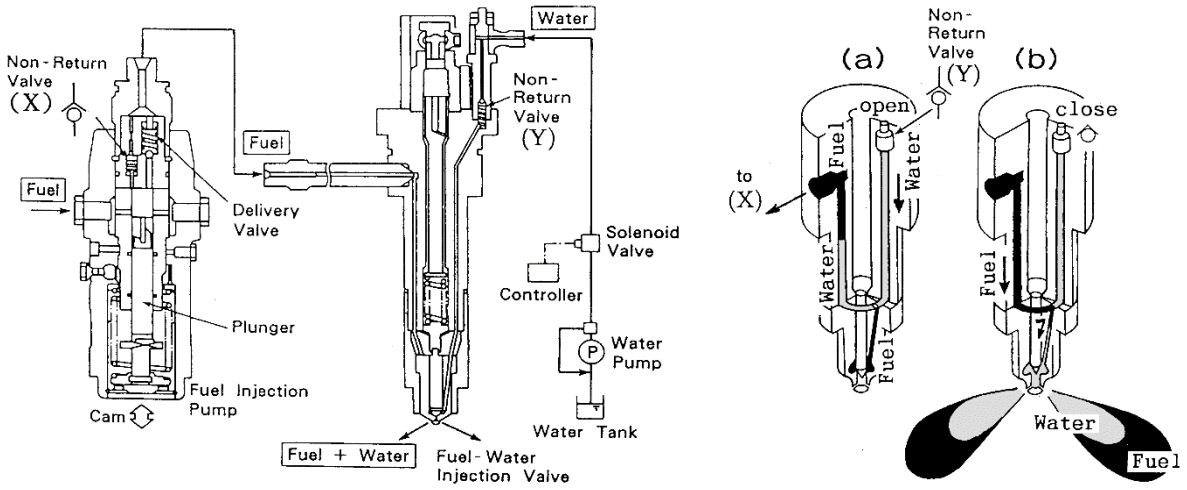

Figure 11: Stratified fuel-water injection system used in experiments by the author [7]

This method has the following advantages over the fuel-water emulsion.

- The first fuel injected does not contain water, so there is no risk of deteriorated ignitability.
- The main parts of the fuel injection pump, such as the plunger, are not exposed to water.
- The surfactant required for the emulsion is not necessary for this method.

As will be discussed later, even though fuel and water are stratified at the timing of injection, water is distributed in the fuel spray at the stage of spray forming in the air, achieving a NO_x reduction effect equivalent to that of the emulsion method.

Real injection rate of fuel and water

In order to obtain the real fuel and water injection rate by this system, a rotating slit box, Figure 12 was used. For this test, the injection system was removed from the engine and driven by an electric motor. The slit box, a vessel divided into many slits, was fixed to one end of an arm which rotated about its opposite end. The rotation of the slit box and the injection was synchronized. Only the spray of one hole of the injection nozzle was collected in the slit box. The injection rate was then obtained by measuring the height of fuel and water in each slit after many rotations.

Figure 13 shows two examples of the measured injection rate of fuel and water, the cases that 100% fuel plus 40% water are injected (left) and 100% fuel plus 50% water (right). According to the result, actually pure fuel is injected at the beginning of injection, then fuel + water and finally pure fuel again. Since the fuel quantity is the same as with the case of fuel only, the total quantity of liquid to be injected is larger when injecting fuel and water and thus the injection duration is also longer.

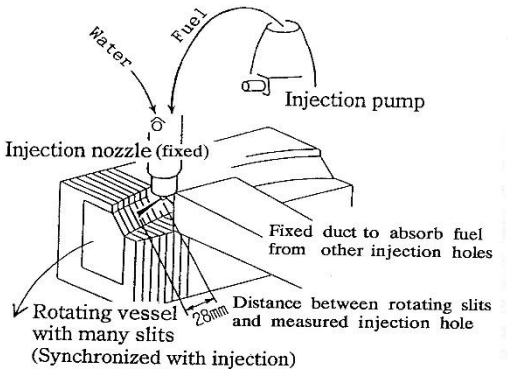

Figure 12: Fuel and water injection rate measuring apparatus

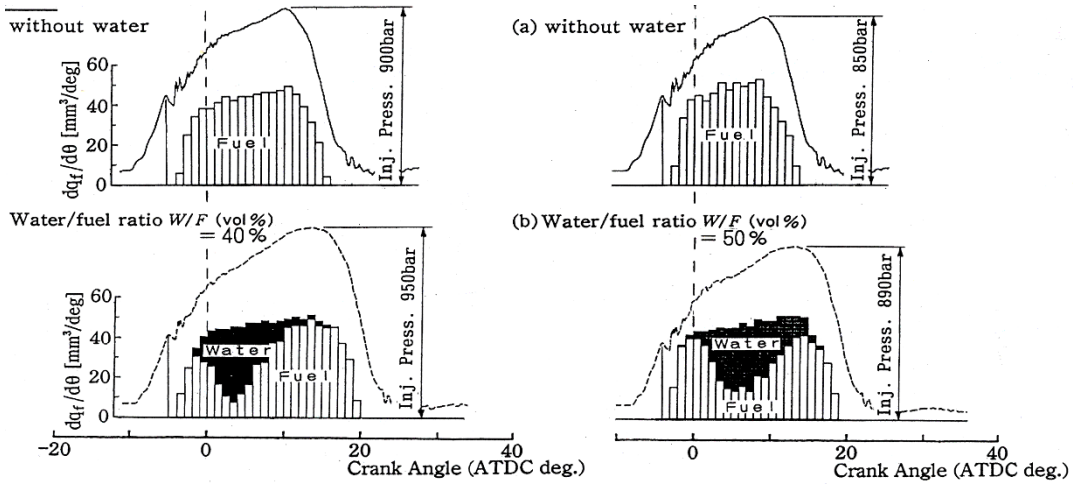

Figure 13: Measured fuel and water injection rate

Combustion with fuel/water injection

The system was tested on the 'visual test engine' in Kyushu University as follows. Figure 14 shows an example of the photographs of flames by the test engine. As can be seen in the figure, a pair of four-hole injection nozzles was used simulating a low-speed two-stroke engine. The two photographs show the spray/flame at the end of fuel injection, comparing between (a) 100% diesel fuel and (b) 100% fuel plus 50% water.

Although size of the visual test engine is small (bore: 190 mm) and it is questionable whether it is representative of the phenomenon for a real engine bore of 500 mm, the photograph shows a shorter spatial burn-up length of the flame with water than without water, that also suggests a good result of shorter after-burning with water. Though not illustrated here, despite the longer injection duration in the fuel plus water case compared to the fuel-only case, the duration of combustion determined from the measured heat release rate was remained about the same.

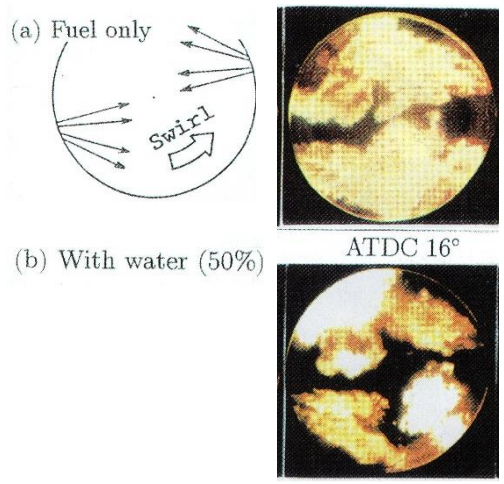

Figure 14: Visualized flame (Fuel: Marine Diesel Oil)

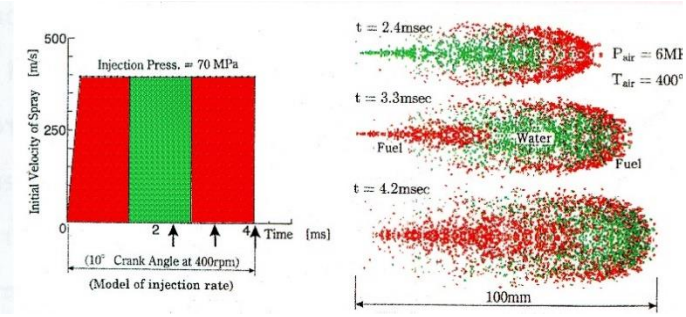

Figure 15: Calculation of fuel/water distribution in spray

Distribution of water within the spray

Reasons for the expected improvement in combustion with injected water is believed to be the improved air entrainment into the spray. In this section, this phenomenon is discussed using the results of the model calculation. The distribution of the water (vapor) in the spray was calculated using a CFD software [7]. A model injection rate as shown in the left side of Figure 15 was used as an input of the CFD. Figure 15 also shows one printout of the model calculation. The distribution of fuel is shown by red dots and that of water by green dots.

At t = 2.4 ms in the figure, the fuel spray front is decelerated by the air drag. Then the water spray penetrates the initially injected fuel spray and push and disperse the high concentration of fuel near the spray axis to the periphery. It can be seen from the graphs t = 3.3 ms and t = 4.2 ms that fuel is injected after the water again. This second fuel spray pushes the water to the front and to the side. As imaged by the photographs in Figure 14, the red dots of the initial fuel spray are already burnt and the water acts as a shield between the burnt gas of the initial fuel spray and the second fuel spray (at t = 4.2 ms). This effect prevents the second fuel spray from entraining burnt gas, which usually happens when using fuel alone.

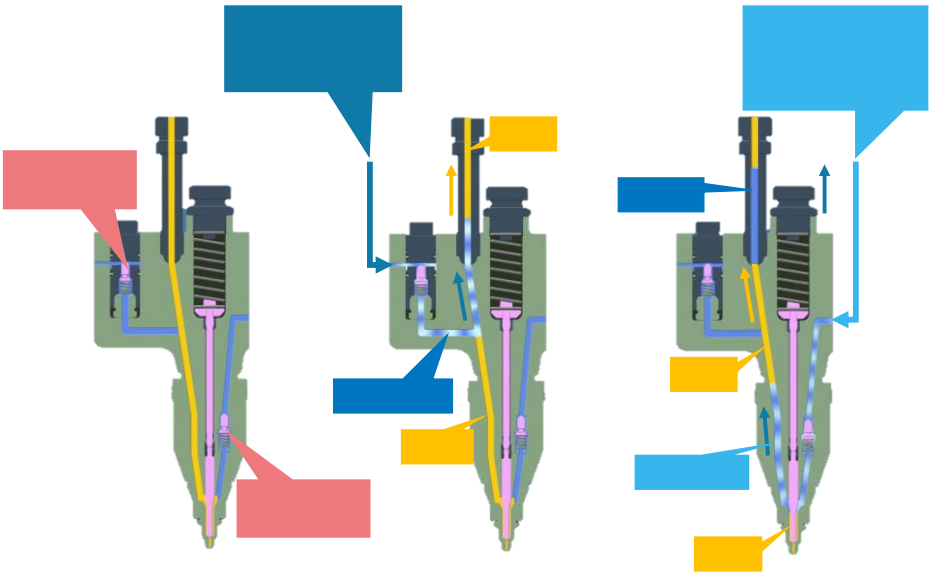

Figure 16: J-ENG's five layers stratified fuel and water injection system [6]

In any case, it can be seen that the fuel and water are not distributed in clear stratified layers in the spray, but are mixed close to homogeneously during forming the spray. Thanks to this phenomenon, NO_x reduction due to a uniform decline in flame temperature similar to that by the fuel-water emulsion can be achieved. Moreover, a spray with a higher momentum by added water entarains more air into the spray/flame, which may activate the diffusive combustion.

In the practical system by J-ENG, water is injected twice during fuel injection, in five layers: fuel, water, fuel, water and fuel. The mechanism is shown in Figure 16 [6]. This system will provide a more uniform water distribution and greater NO_x reduction with less amount of water.

3.2. A study for a stratified low-grade fuel injection system

With this system, if another fuel is provided instead of above-mentioned water, two different kinds of fuels can be injected without mixing from the same injection nozzle. MHI conducted an experiment using the system to apply a low-grade heavy fuel oil, which has poor ignition and combustion characteristics, to a high-speed diesel engine [8]. For such a small bore (170 mm), high-speed diesel engine used in these experiments, it is usually not possible to burn heavy fuel oil containing petroleum refining residues. Use of the stratified fuel injection system suggested a solution to this issue.

The following studies are introduced. Experiments using the system was conducted to apply a low-quality residual fuel (BFO: Bunker Fuel Oil) to a high-speed diesel engine. In this case, BFO was sandwiched by pilot- and post-MDO (Marine Diesel Oil with a good ignition and combustion characteristics like a Gas Oil) and injected. Even in the case that a total mass ratio of pilot- plus post-MDO was only 10%, that meant the rest 90% was BFO, the BFO completed the combustion just as well as 100% MDO, as the pilot-MDO improved the ignition and the post-MDO mitigated the after-burning of the BFO.

Test engine and working principle of the stratified fuel injection system

A supercharged single-cylinder engine with 170 mm bore (H-170 engine) was used for the test runs. The specifications of this engine are given in Table 4. The working principle of the stratified fuel injection system is shown in Figure 17. The whole system consists of a MDO injection pump, a fuel

injection nozzle and a BFO supply unit. The MDO injection pump is equipped with the non-return valve (X) and the fuel injection nozzle with the non-return valve (Y). The fuel injection nozzle has a special BFO passage, which is connected to the MDO passage. The BFO supply unit feeds the required quantity of BFO into the passage of the injection nozzle. In other words, BFO is injected instead of water of the previous section and BFO is sandwiched between MDO.

Experimental results using the stratified fuel injection system

Figure 18 shows the results obtained with the H-170 engine equipped with the stratified fuel injection system at full load. The abscissas in (a)～(c) represent the percentage of MDO added to the BFO. 0% MDO means 100% pure BFO.

(a) shows that adding even only 10% of MDO leads to an ignition delay which is close to that of pure MDO.

(b) shows the measurement of particulate matter (PM) in the exhaust gas. As expected, BFO emits much more PM than MDO. This (b) data means the following. With an addition of total 10% of pilot- and post-MDO using the system, the PM from BFO is reduced to the same value as from pure MDO.

c) shows the change in specific fuel consumption (SFC) with MDO%. Each SFC data is converted to the heat value of MDO. It also shows that 10% addition of MDO improves the SFC drastically.

According to these results, it is concluded that the system is highly effective. Even though the percentage of MDO is relatively low, good combustion characteristics, almost equal to those of pure MDO, can be obtained, as the pilot-MDO improves the ignition and the post-MDO mitigates the after-burning of BFO.

Table 4: Specification of test engine (H-170)

Engine Type	1 Cylinder, 4 Stroke, D.I., Super-charged
Bore × Stroke	170 × 180 mm
Stroke Volume	4086 cm^3
Compression Ratio	16.3
Rated Power	110 kW/1500 rpm
max. Pme	2.15 MPa
Nozzle Holes	ϕ 0.35 mm × 10

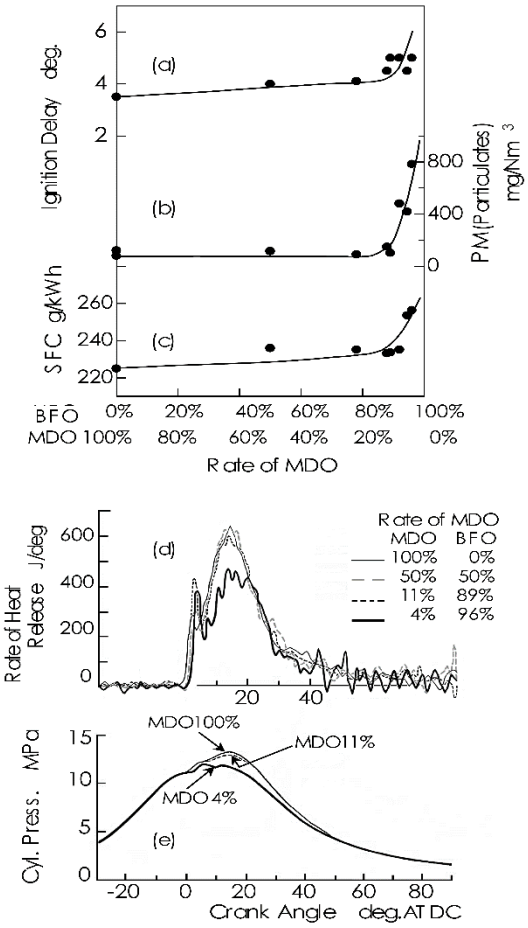

Figure 18: Effects of stratified fuel injection system

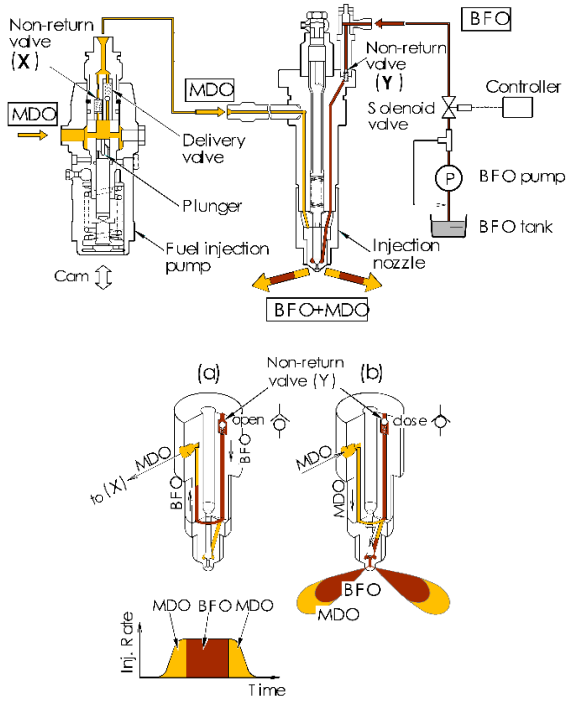

Figure 17: Working principle of stratified fuel injection system

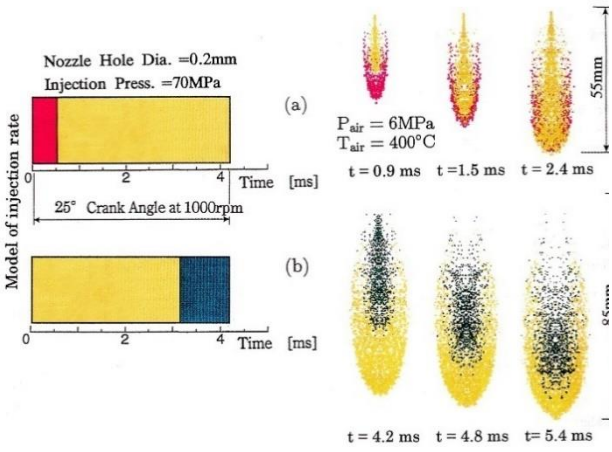

Figure 19: Numerical results of spray characteristics

Figure 18 (d) and (e) show the heat release rate and the cylinder pressure. With regard to the cost of the fuel, a smaller percentage of MDO is desirable. Therefore, a further reduction in the amount of MDO to 4% was examined. Comparing the addition rates of 11% and 4% MDO, the 11% addition shows almost the same combustion characteristics as pure MDO, whereas the 4% addition shows a much lower heat release rate during the main combustion duration. The maximum cylinder pressure becomes much lower. It is concluded that 4% of MDO is not sufficient.

Explanation of the effectiveness of the system through fuel spray simulation

To understand the characteristics of the fuel spray in detail, 2D numerical simulation was performed using a CFD software [8]. The calculation conditions and the results are shown in Figure 19. The

purpose of this simulation is to examine the distribution of the fuel particles injected at the beginning and those injected at the end of the injection duration within the spray.

In Figure 19 (a), the distribution of the fuel particles injected at the beginning of the injection duration is examined. On the left, the model injection rate is shown, on the right the resulting distribution of the particles. The red dots of the spray represent the fuel injected at the beginning (first 1/8 of the injection duration). They are marked in red in the model injection rate. The other particles are marked in yellow.

The fuel particles injected at the beginning of the injection duration are first located at the tip of the spray (t=0.9 ms). These particles are slowed down by the air drag. The later injected yellow particles penetrate the earlier injected red ones at a high velocity and push them to the side (t=1.5 ms). At t=2.4 ms, all the red particles have been pushed to the side of the spray.

In Figure 19 (b), the distribution of the fuel particles injected at the end of the injection duration is examined; the blue dots represent the fuel particles injected at the end (last 1/4 of the injection duration). Blue dots, in contrast to the red particles in (a), remains in the center of the spray (t=4.2 ms to t=5.4 ms), because no spray is following to push it to the side.

The results from this calculation explain the high level of effectiveness of the stratified fuel injection system. If the red particles of the spray in Figure 19 (a) represent a good fuel like MDO, then the early igniting MDO flame surrounds the yellow particles representing the low-grade fuel. Then the temperature of the low-grade fuel will soon rise and the evaporation and ignition of the low-grade fuel droplets is accelerated.

As mentioned above, the fuel particles injected last remain in the center of the spray, where the air supply is not sufficient. This difficulty would be the reason for the after-burning and the long combustion duration of low-grade fuel. If the fuel injected last is a good fuel like MDO, this problem would be much less severe.

3.3. Further Suggestions

As mentioned above, the stratified fuel injection system paves the way for the use of fuels with poor ignition or combustion characteristics. As an example, the effect of sandwiching ammonia with pilot- and post- gas oil has been presented by J-ENG and NMRI, National Maritime Research Institute at CIMAC 2023 [9]. On the other hand, the post-fuel is not necessary for fuels with poor ignition properties but good combustion characteristics like methanol [2]. For such a fuel, the stratified injection with pilot-injection but without post-injection is proposed as in Figure 20.

In this case, a nozzle tip with two passages is prepared as shown in the figure. The left passage is fed with methanol (yellow) from a methanol injection pump. On the other hand, the right-hand passage is fed with pilot fuel (red) like diesel oil. A non-return valve is fitted upstream of the right-hand passage.

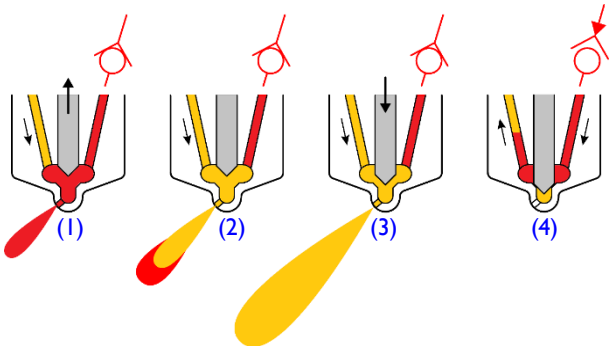

Figure 20: A propose of stratified injection with pilot injection and main injection (without post-injection)

The function is described as (1) to (4) in Figure 20.

(1) corresponds to the timing of the start of fuel injection, the main fuel pump is activated and methanol (yellow) is supplied at a high pressure to the left-hand passage. However, the space surrounding the needle (needle chamber) is filled with diesel oil (red) and the needle opens to inject the pilot diesel oil.

(2) shows that the methanol is injected as main fuel following the pilot diesel oil. During this time, the diesel oil in the right-hand passage stays there because the non-return valve is closed.

(3) is the timing at needle valve is just closing. then methanol injection ends without post-injection.

(4) is preparation for the next pilot injection, during which the diesel oil supply system is activated to charge the diesel oil from the right passage until the condition before (1) is reached for the next injection. The methanol equal to that amount of diesel oil is pushed back to the main injection pump.

4. Conclusion

This paper has introduced the two representative technologies that may be applicable to the alternative fuels and the following conclusions have been confirmed.

The first half of the paper has explained on the diffusive combustion by high-pressure hydrogen injection quoting the following studies, which realize high power and high efficiency without worrying about the back-firing, pre-ignition and knocking associated with Otto-cycle type hydrogen combustion.

- Research on the diesel-cycle type hydrogen-burning engines through the operational tests of a high-speed single-cylinder engine with an output of 100 kW has been successfully conducted by MHI: Mitsubishi Heavy Industries, Ltd.
- As a fundamental research work for the development, visual studies on the combustion by high pressure (for example, 30 MPa) hydrogen injection including the case of 100% hydrogen without pilot fuel has been conducted by Kyushu University and the National Maritime Research Institute, Japan.
- The second half of the paper has introduced the 'Stratified Injection System' technology.
- As a kind of the stratified injection system, the stratified water injection system has been developed for NO_x control. The mechanism by which water is sandwiched between fuels and injected from the same injection hole and why NO_x reduction and combustion improvement can be achieved simultaneously has been explained.

- With a stratified fuel injection system, which injects a small amount of good fuel before and after the main injection of a low-grade fuel, the whole combustion process can be improved. The effectiveness of stratified injection has been explained with the help of fuel spray simulation. In other word, this system is characterized by its ability to improve the combustion of a main fuel, which has poor ignition and combustion properties, by injecting the pilot-fuel and post-fuel from the same injection nozzle hole as the main fuel.
- A stratified injection system with pilot-injection but without post-injection has been proposed for the case that the post-fuel is not necessary for fuels with poor ignition properties but good combustion characteristics such as methanol.

Literature

[1] Osafune, S. et al., Development of Hydrogen Injection Clean Engine, CIMAC Congress 2004, Kyoto, Paper No. 207 (2004).

[2] Takasaki, K. et al., Progress and prospect of combustion studies on low- and zero-carbon fuels, CIMAC Congress 2023, Busan, Paper No. 103 (2023).

[3] Wakuri, Y., et al., Studies of the Penetration of Fuel Spray in a Diesel Engine, Bul. of JSME Vol.3 No.9 (1960) pp. 123.

[4] ClassNK Press release, 19. Oct. 2023

https://www.classnk.or.jp/hp/en/hp_news.aspx?id=10422&type=press_release&layout=1

[5] Miyano, H. et al., Development of Stratified Fuel-Water Injection System for Low-NO_x Diesel Combustion, CIMAC 1993, London (1993).

[6] Matsuda, Ch., Miyanagi, A. and Edo, K., The Latest Technologies of J-ENG UE Engine, CIMAC Congress 2019, Vancouver, Paper No.137 (2019).

[7] Takasaki, K., Verbesserung der Verbrennung in Dieselmotor durch geschichtete Wassereinspritzung (Improvement of Diesel Combustion with Stratified Fuel/Water Injection System), MTZ (Motor Technische Zeitschrift) 59. Nr.4, April 1998.

[8] Osafune, S., Takaishi T., Takasaki, K. et al., Study on Stratified Injection System, COMODIA 2001, July 2001.

[9] Oba, H. et al., Fundamental study of the effect of stratified NH3 injection system for nitrogen compounds reduction, CIMAC 2023, Busan, Paper No. 101 (2023).

Keywords: ammonia combustion concepts, ammonia high-pressure direct injection

High-pressure ammonia-diesel dual fuel combustion in medium-speed engines

Prof. Nicole Wermuth[1,2], Dr. Maximilian Malin[1], Markus Roßmann[1], Prof. Andreas Wimmer[1,2], Dr. Marco Coppo[3]

(1) LEC GmbH – Large Engines Competence Center, (2) Graz University of Technology, (3) Officine Meccaniche Torino SpA

https://doi.org/10.18453/rosdok_id00004640

Abstract

Ammonia combustion in internal combustion engines has been the focus in many research projects in recent years. One of the drawbacks of many applications with gaseous ammonia admission is the high level of pollutant emissions, nitric oxide and unburned ammonia in particular. The use of high-pressure liquid ammonia injection has the potential to reduce the level of these harmful emissions. This article presents the application of a fuel-actuated common rail injector prototype developed by OMT in a large-bore medium speed single cylinder research engine at the LEC GmbH. Building on initial insights from the fuel spray characterization in an optically accessible constant volume chamber, the injector was integrated into a cylinder head in a dual-fuel configuration with a diesel pilot injector. The focus of the test campaign was the investigation of different fuel injection strategies and operating parameters and their impact on engine combustion performance and emissions. The combustion concept allowed operation with an ammonia fuel fraction up to 90% and showed robust operation even at moderate injection pressures of around 60 MPa. A wide operating window with regard to excess air ratio and combustion phasing could be achieved and will be the foundation for further load increases and performance improvements.

1. Introduction

The global carbon dioxide (CO_2) concentration in the atmosphere has already passed the 420-ppm mark in the last couple of years [1]. According to the Copernicus Climate Change Service global temperatures reached exceptionally high levels in 2023, making it the warmest year on record – overtaking by a large margin 2016, the previous warmest year [2].

In order to limit global warming to 1.5 K above pre-industrial levels [3], a goal that was agreed on at the UN Climate Change Conference [4] the emission of CO_2 and other gases with a high global warming potential (GWP) must be reduced quickly. Governments worldwide put forward ever more ambitious greenhouse gas (GHG) emission reduction targets. The 2030 Climate Target Plan of the European Commission sets the European Union on a path to becoming climate neutral by 2050 and proposed to reduce GHG emissions at least by 55% of the 1990 levels by 2030 [5]. In February 2024 the European Commission deemed it necessary to accelerate the previous plans and recommended a 90% net GHG emission reduction by 2040 [6] as illustrated in Figure 1. The International Maritime Organization (IMO) first established targets to reduce CO_2 emissions in 2018 [7] and set even more ambitious goals in 2023 to achieve net-zero GHG emissions by 2050, with indicative intermediate points of 40% CO_2 reduction per transport work in 2030 and a total GHG emission reduction of 70% by 2040 compared to 2008.

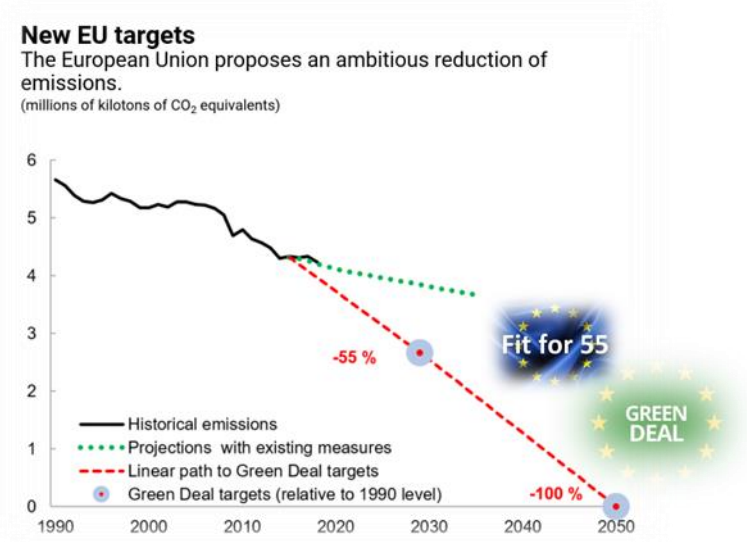

Figure 1: European Union targets for greenhouse gas emission reduction

Achieving these ambitious goals requires a global transition from fossil fuels to renewable energy sources. The volatility of these sources and the fact their production and their consumption will to a large extent take place in different regions of the world will make it necessary to store and transport energy on a large scale. Storage in the form of chemicals offers large storage capacities over long periods of time and even seasonal storage (Figure 2).

These secondary energy carriers can be used as e-fuels to decarbonize transportation, such as aviation, shipping and heavy duty on- and off-road applications. DNV GL's scenario for the path to net-zero emissions [9] shows a diverse future energy mix for the maritime sector and projects ammonia (NH_3) to be the dominant fuel in the maritime sector by 2050. The projected use of ammonia as a hydrogen

carrier and as a fuel in maritime transport and power generation is expected to drive a three to four-fold increase of global ammonia consumption by 2050. As of 2024 several engine OEMs already announced future product offerings.

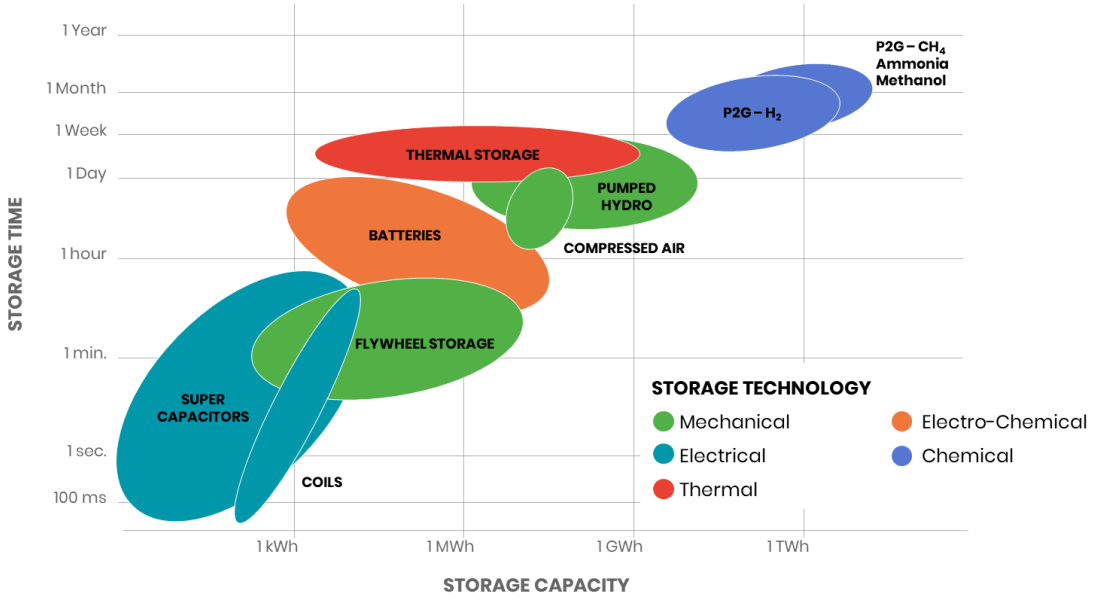

Figure 2: Energy storage options [8]

This article presents experimental results of research work on the use of liquefied high-pressure ammonia injection in a combustion concept for medium-speed large-bore compression ignition engines. The focus of study was the impact of engine operating parameters on the engine performance and exhaust gas emissions. Based on the properties of ammonia, the advantages and challenges for engine combustion systems are discussed. The selected combustion system and the operating procedures are described and experimental measurement results are presented. Finally, a comparison of the most important parameters with a diesel combustion system is shown and further possibilities for improvement are discussed.

2. Ammonia engine combustion concepts

The physical and chemical properties of ammonia differ significantly from those of fossil fuels typically used in large-engine applications and also from those of other e-fuels. Table 1 provides an overview of properties for several carbon-based and carbon-free fuels relevant for large-engine applications. Especially the low laminar flame speed and the high minimum ignition energy of ammonia in comparison to other e-fuel options are often considered to be detrimental for use in an internal combustion engine.

To overcome the challenges posed by the ammonia ignition and combustion properties, admixing of a more reactive fuel was proposed [10]. For marine applications where redundancy requirements are usually adhered to by providing diesel engine operation capability, diesel fuel is used in ongoing research as the reactive fuel component. For spark ignition applications hydrogen is a suitable high reactivity fuel.

Table 1: Fuel properties of selected e-fuels

Fuel	Lower heating value (gravimetric) [MJ/kg]	Lower heating value (volumetric) [MJ/kg]	Laminar flame speed (stoichiometric) [m/s]	Min. ignition energy [mJ]	Autoignition temperature [K]
Drop-in e-fuel (diesel-like)	43	36	0.87	0.23	483
e-methane	50	36	0.38	0.29	868
e-methanol	19	15	0.36	0.14	712
e-ammonia (liquid, - 33 °C)	20	14	0.07	8.000	930
e-hydrogen (liquid, - 253 °C)	120	9	3.50	0.017	858

There a various fuel admission and ignition concept that are feasible for ammonia-fueled engines. An overview of currently considered concepts is shown schematically in Figure 3.

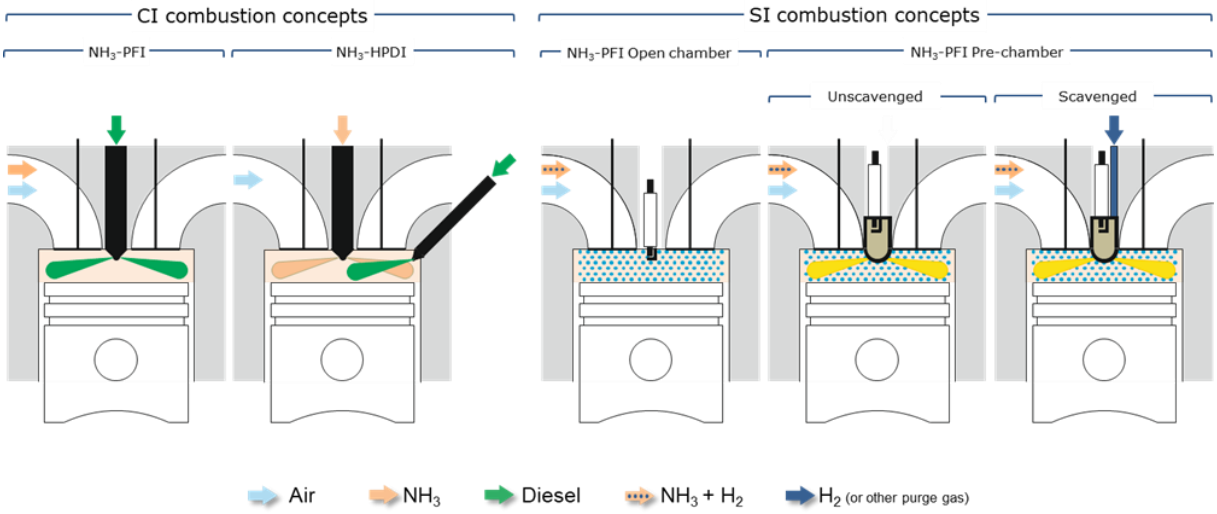

Figure 3: Compression ignition and spark ignition combustion concepts

Spark ignition (SI) concepts span the range from direct ignition concepts with a centrally mounted spark plug in the main combustion chamber (NH_3-PFI Open chamber) to pre-chamber ignition concepts with different scavenging variants (NH_3-PFI Pre-chamber). The pre-chamber concept enables mixture stratification with a fuel-rich mixture in the pre-chamber or additional hydrogen supply directly into the pre-chamber to enhance the ignition conditions at the spark plug location. These engine concepts predominantly use external mixture formation of gaseous ammonia and air either upstream of the turbocharger or via port fuel injection.

Ammonia compression ignition (CI) concepts are typically designed as dual fuel combustion concepts with diesel pilot injection. Gaseous low-pressure ammonia admission (NH_3-PFI) can be realized with

either central mixing of ammonia with air upstream of the turbocharger or the introduction of ammonia via port fuel injection. Diesel is injected directly into the combustion chamber at the end of the compression stroke to initiate the combustion process which relies on flame propagation in the ammonia-air mixture. The combustion process of liquid high-pressure ammonia injection (NH_3-HPDI) is similar to typical diesel combustion where the combustion is controlled by fuel-air mixing. This concept uses either two fuel injectors in the combustion chamber or a two-needle injector.

The pollutant emission formation of ammonia combustion is dominated by the fuel-bound nitrogen and often associated with the emission of nitrous oxide (N_2O) which, according to the IPCC has a GWP 273 times that of CO_2 for a 100-year timescale [11].

The authors previously investigated combustion concepts using gaseous ammonia admission via port fuel injection or central mixture formation in four-stroke engines [12, 13]. In those experiments considerable concentrations of unburned ammonia in the order of 5000 ppm were measured in the exhaust gases. One mitigation measure was a reduction of the excess air ratio compared to diesel or natural gas engine operation. Ammonia spray combustion has the potential to reduce the ammonia emissions and nitrogen oxide (NO_X) formation while also maintaining a high excess air ratio.

3. Experimental test set-up

3.1. Single cylinder research engine

The engine investigations were carried out on a medium-speed 4-stroke single cylinder research engine (SCE) with a displacement volume of approximately 15 liters that was modified for dual fuel operation. For the investigation of the diesel-ammonia operation, a non-reentrant piston bowl and a compression ratio (CR) of 17:1 were chosen.

The low-swirl cylinder head was equipped with two intake and two exhaust valves. Exchanging the cam shaft lobes allowed a modification of the valve lift curves. Additionally, the valve timing could be adjusted individually for the intake and the exhaust valves. For this investigation, an intake valve lift profile with early intake valve closing (IVC) before bottom dead center was selected. The engine configuration is summarized in Table 2.

Table 2: Engine specification

Parameter	**Value**
Rated speed	750 rpm
Bore	250 mm
Stroke	320 mm
Compression ratio	17:1
Valve timing	Early IVC
No. of intake/exhaust valves	2/2
Charge air	Provided by external compressors with up to 1 MPa boost pressure

The cylinder head used on the single cylinder research engine was based on the serial configuration but was modified for the dual fuel operation. The ammonia injector was located centrally in the combustion chamber, replacing a conventional diesel injector, and a second injector was integrated into the cylinder head to deliver the diesel pilot injection.

The design of the cylinder head did not allow for a vertical positioning of the diesel pilot injector but rather a lateral, inclined positioning was required. The positioning and orientation of the diesel injector nozzle in the combustion chamber required a special spray hole configuration. An illustration of the fuel jet interaction of the diesel spray and the ammonia spray is shown in Figure 4.

Additionally, the cylinder head was modified to provide two separate fuel return passages from the ammonia injector. While one of the fuel return streams was maintained at atmospheric pressure, the second stream was maintained at 5 MPa to avoid two-phase flow conditions in the injector control valve.

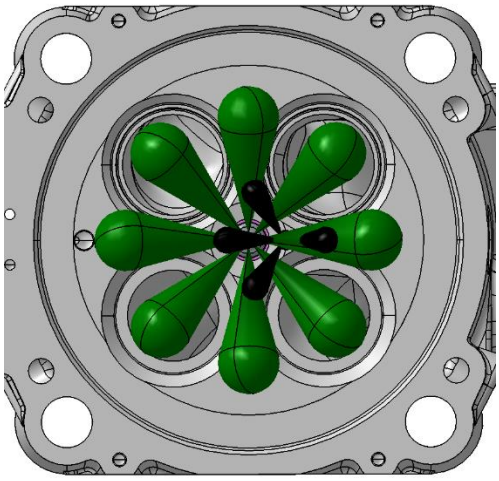

Figure 4: Illustration of diesel pilot (black) and ammonia (green) fuel jet interaction

The injector basic architecture was chosen to be a common rail (CR) arrangement, with a two-way, solenoid actuated control valve cooperating with two calibrated orifices to modulate pressure in a control chamber realized on top of the nozzle needle to actuate its opening and closing motion, an

integrated fuel accumulator and flow limiter valve, and a nozzle with zero static leakage, as described in [14] and [15].

All engine fluids including cooling water, lubricating oil, and charge air were controlled to ensure well-defined and reproducible testing conditions. Instead of a turbocharger, an air compressor upstream of the engine and a flap in the engine exhaust system were used to adjust intake and exhaust manifold pressures. A flush mounted piezoelectric cylinder pressure transducer enabled real-time calculation of the indicated mean effective pressure of each cycle.

The excess air ratio (EAR) is defined in Equation 1 and is taking the mass of ammonia m_{NH3}, the mass of diesel m_{diesel} and the mass of air m_{air} as well as the stoichiometric air-fuel ratios of ammonia $AFR_{stoich,NH3}$ and diesel $AFR_{stoich,diesel}$ into account.

$$EAR = \frac{m_{air}}{m_{NH_3} * AFR_{stoich,NH_3} + m_{diesel} * AFR_{stoich,diesel}} \quad (1)$$

In order to acquire highly reliable and reproducible exhaust gas measurements, an FTIR system was used to cover the whole range of exhaust gas components of interest. Table 3 summarizes the SCE measurement instrumentation.

Table 3: Overview engine instrumentation

Quantity	Instrumentation	Accuracy	Range
Air mass flow	Emerson Micro Motion CMF100	+/-0.35%	0 – 300 kg/h
Diesel mass flow	AVL Fuel Exact MF 150KG SF	+/-0.1%	0 – 150 kg/h
Ammonia mass flow	Emerson Micro Motion CMFS025	+/-0.1%	10 – 180 kg/h
Charge air temperature	PT 100	+/- 0.15 K * 0.002 * (t)	223 – 773 K
Charge air pressure	AVL piezoelectric transducer GU21C	+/-0.3%	0 – 8 MPa
Cylinder pressure	AVL piezoelectric transducer QC34C	+/-0.2%	0 – 25 MPa
Exhaust gas temperature	Thermocouple type K	0.004 * (t)	max. 1370 K
Exhaust gas pressure	AVL piezoelectric transducer GU21C	+/-0.3%	0 – 8 MPa

3.2. High-pressure fuel injection systems

A dedicated ammonia high-pressure fuel supply and injection systems was built for the test campaign. The main challenges in designing the system were to avoid ammonia evaporation under all operating conditions and to fulfill minimum inlet pressure requirements of the high-pressure fuel pump.

Table 4: Fuel injection equipment

Component	**Specification**
Diesel pump	Bosch
Diesel pilot injector	DUAP
Diesel pilot nozzle configuration (holes / flow rate / reference pressure)	4-hole, 1.6 l/min, 120 MPa
Ammonia fuel pump	Hammelmann HAMPRO 23
Ammonia injector	OMT common rail injector
Ammonia nozzle configuration (drilling / flow rate / reference pressure)	8 x 0.54 mm, 14 l/min, 131 MPa

Two independent high-pressure fuel systems were built for the diesel pilot and the ammonia injection. The diesel pilot injection system was capable of operating up to 120 MPa, and the pilot nozzle used had a nominal flow rate of 1.6 l/min. The pilot fuel flow rate was measured via an AVL Fuel Exact. The ammonia injector was equipped with an 8-hole nozzle with a nominal flow rate of 14 l/min. The nozzle was designed for 131 MPa and the maximum operation pressure of the injector was set at 150 MPa. The fuel injection equipment specification is summarized in Table 4.

The high-pressure fuel system for ammonia included a pump designed for a maximum injection pressure of 150 MPa. The high-pressure fuel system also included the fuel conditioning, the fuel mass flow rate measurement and the actuators and controls to maintain the desired pressure in the injector leakage return line. A schematic of the ammonia high-pressure system is depicted in Figure 5.

In addition to the dual-fuel combustion concept the SCE could also be equipped with a centrally mounted diesel injector to allow pure diesel operation. The diesel engine operation was tested with a different injector and nozzle set-up that resembled the serial production configuration.

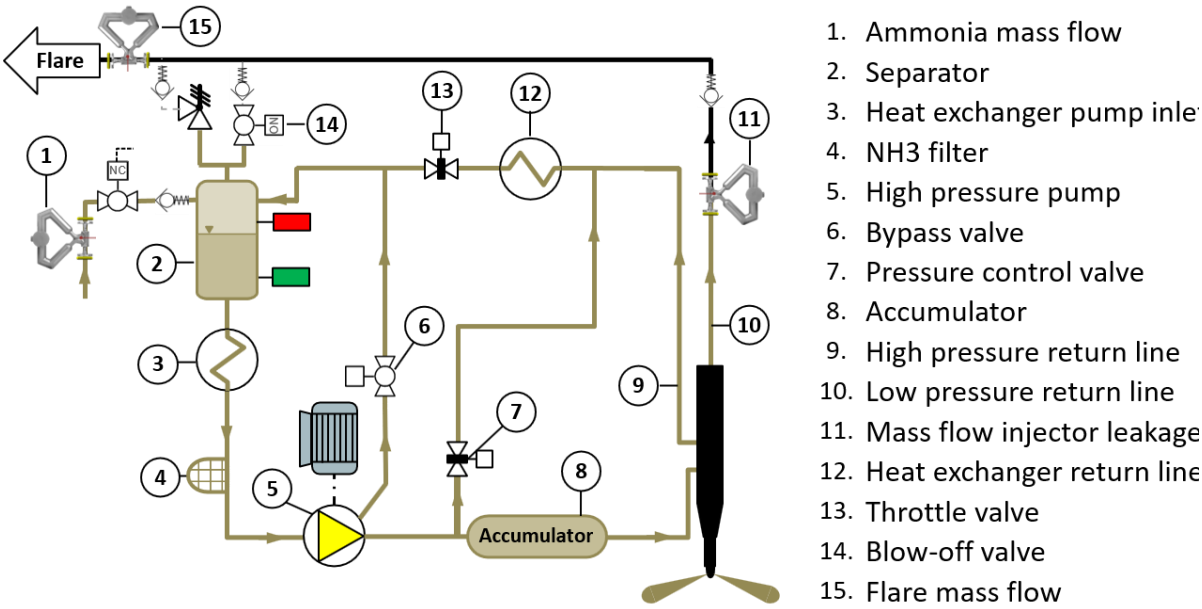

Figure 5: Ammonia high-pressure supply system

4. Experimental investigations

4.1. Test procedures

The goal of the experimental investigations with ammonia direct injection was to assess the impact of fuel injection strategies and operating parameters such as excess air ratio and combustion phasing. During the SCE investigations the key operating parameters, e.g. excess air ratio, diesel fraction, injection timing, were varied for a fixed load of 1.2 MPa brake mean effective pressure (BMEP) at a constant engine speed of 750 rpm. The excess air ratio was determined from the measured air and fuel mass flow rates and the stoichiometric air-to-fuel mass ratio for the selected share of diesel and ammonia fuel. Adjustment of the excess air ratio was achieved via boost pressure adjustment. Exhaust gas pressure was adjusted to achieve a desired ratio of boost pressure to exhaust gas pressure.

The dual fuel combustion concept with separate injectors for diesel and ammonia allows an independent adjustment of the dwell between the injection of the two fuels. Figure 6 illustrates the definition of the dwell which describes the crank angle duration from the start of the diesel injector current signal to the start of the ammonia injector current signal. Due to the hydraulic delay the injection starts later than the injector current signal which is indicated by the rail pressure drop (shown for ammonia in Figure 6). The hydraulic delay of the diesel injector amounts to only a few degrees crank angle while the ammonia injector hydraulic delay is longer (around ten degrees crank angle) and varies with the rail pressure. Since the detection of the start of injection is subject to a higher uncertainty than the injector current signal, the dwell timing will be calculated based on the injector current signals throughout the article.

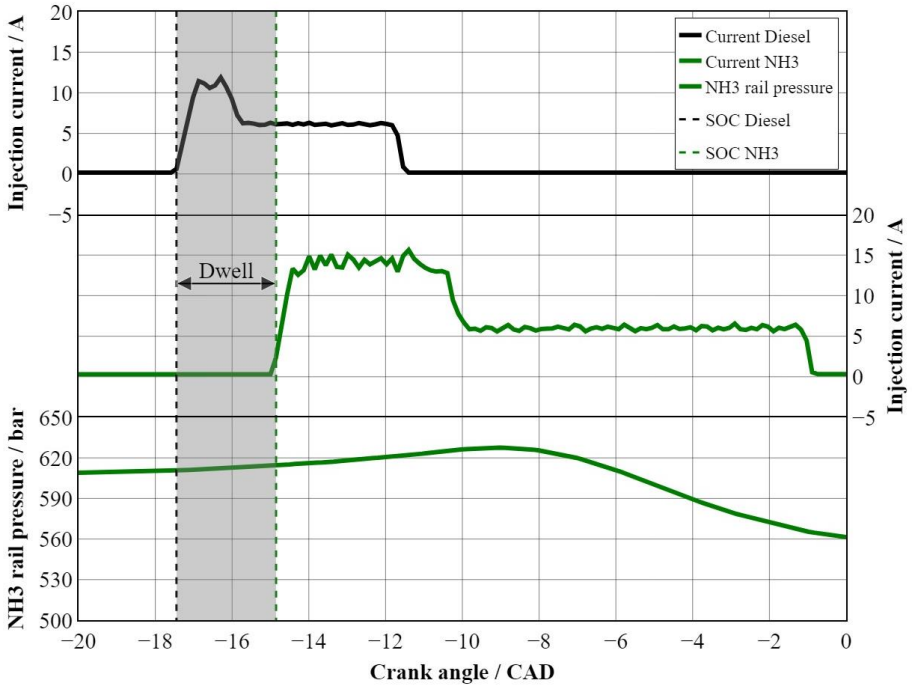

Figure 5: Definition of dwell, injector current signals and ammonia rail pressure trace

4.2. Excess air ratio variation

An excess air ratio variation between 1.2 and 1.8 was performed at a fixed combustion phasing – defined as the crank angle where 50% of the fuel energy has been released (CA50). Both the ammonia and the diesel rail pressures were maintained at a constant value of 60 MPa and 120 MPa, respectively. The diesel energetic fraction was maintained at 10% and the dwell duration was fixed at 2.5 degree crank angle (CAD) throughout the test. The injection timing that is required to achieve the desired combustion phasing is shown on the bottom of Figure 7. Towards lower excess air ratios, the start of the injector energization (start of current – SOC) had to be advanced by approximately 1 CAD which is mainly driven by a longer ignition delay time and the early part of the combustion process. The time when 5% of the fuel energy has been released (CA05) is nearly constant for the whole excess air ratio variation. A larger variation can be observed in the timing of 90% heat release (CA90). While there is only a small change between EAR = 1.8 and 1.4 there is an observable shift to later timings of CA90 for the lowest EAR = 1.2.

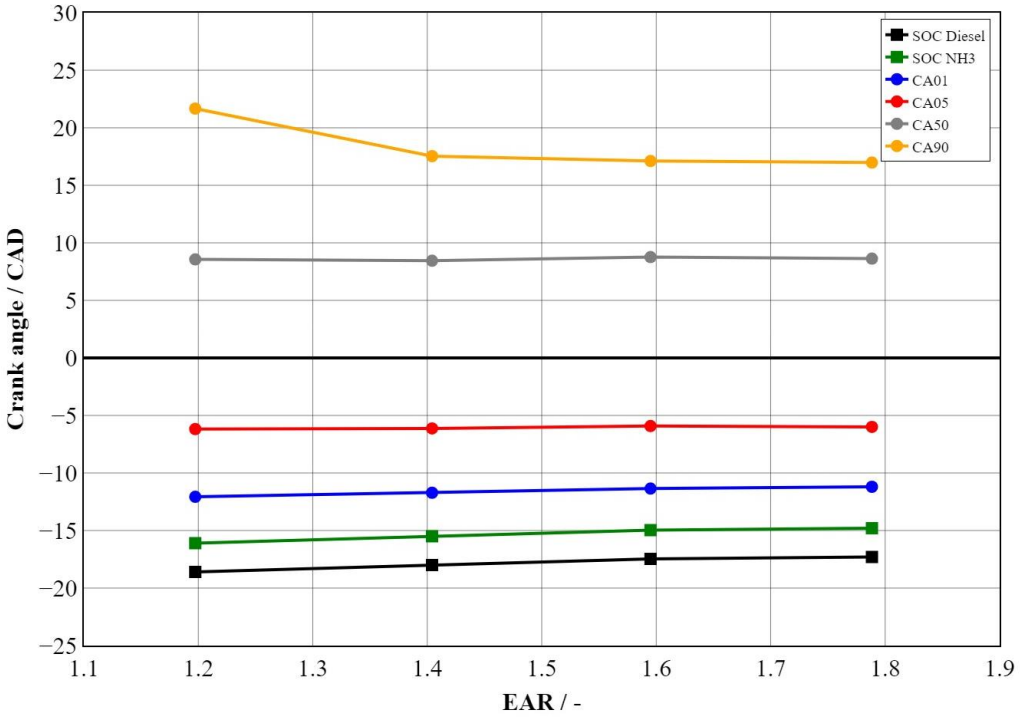

Figure 6: Injection timing and combustion progress for an EAR variation at constant BMEP

The impact of the excess air ratio on the combustion process is depicted in Figure 8 and Figure 9. In the upper part of both figures the injection timings for both the ammonia and the diesel injection are displayed. The small difference in the lengths of the injections for different excess air ratios is reflecting the efficiency benefit of the higher excess air ratios. In Figure 8 the normalized heat release rates for the early combustion phase are shown. It can be observed that the time delay between the start of the diesel injection and the first rise of the heat release rate decreases with increasing excess air ratio. Due to the long hydraulic delay of the ammonia injector the ammonia injection started only after the first heat release was observed and it is assumed that the variance in ignition delay is caused by oxygen availability. Similar to the behavior that is familiar from diesel combustion processes the fuel-air mixture that is formed within the ignition delay time is burned rapidly when the combustion starts, resulting in the well-known pre-mixed peak in the heat release rate. It is assumed that no ammonia is present in the combustion chamber at this point in time and the small differences in the height of the pre-mixed peaks are the result of different ignition delay times.

Figure 9 depicts the cumulative heat release for the same four operating conditions. Up to approximately 80% of total heat release the combustion process is nearly identical for all excess air ratios. Beyond this point the combustion proceeds considerably faster with higher excess air ratios, likely determined by the local availability of oxygen.

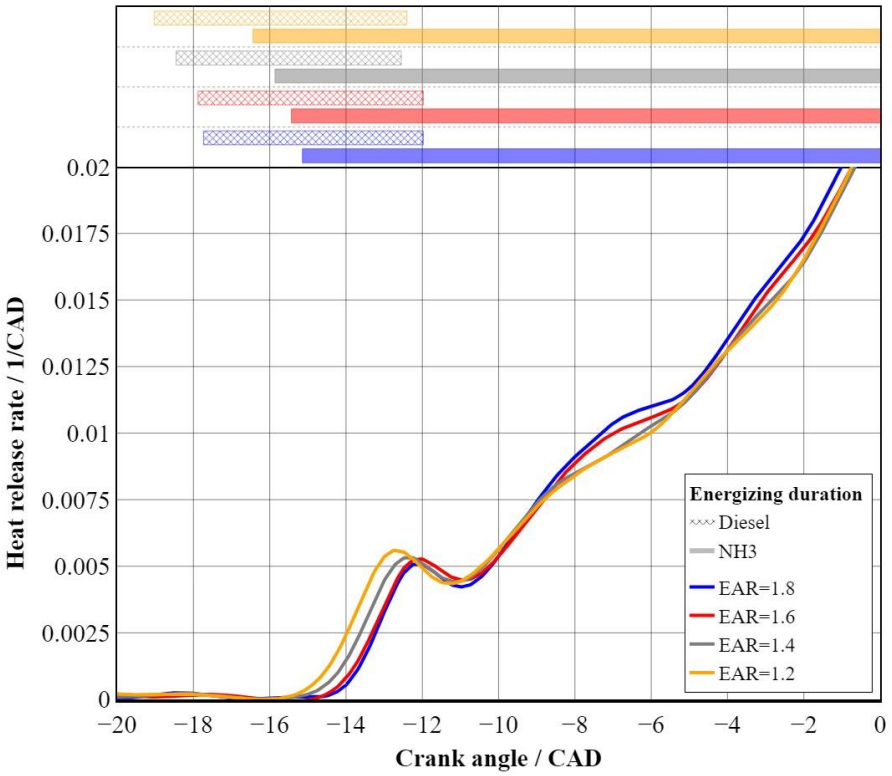

Figure 7: Heat release rate during ignition and early combustion phase for different EAR at constant BMEP

The process for the lower excess air ratio is not just characterized by a delayed heat release but also by a less complete combustion as can be seen in the emissions of unburned ammonia that are displayed in the top graph of Figure 10.

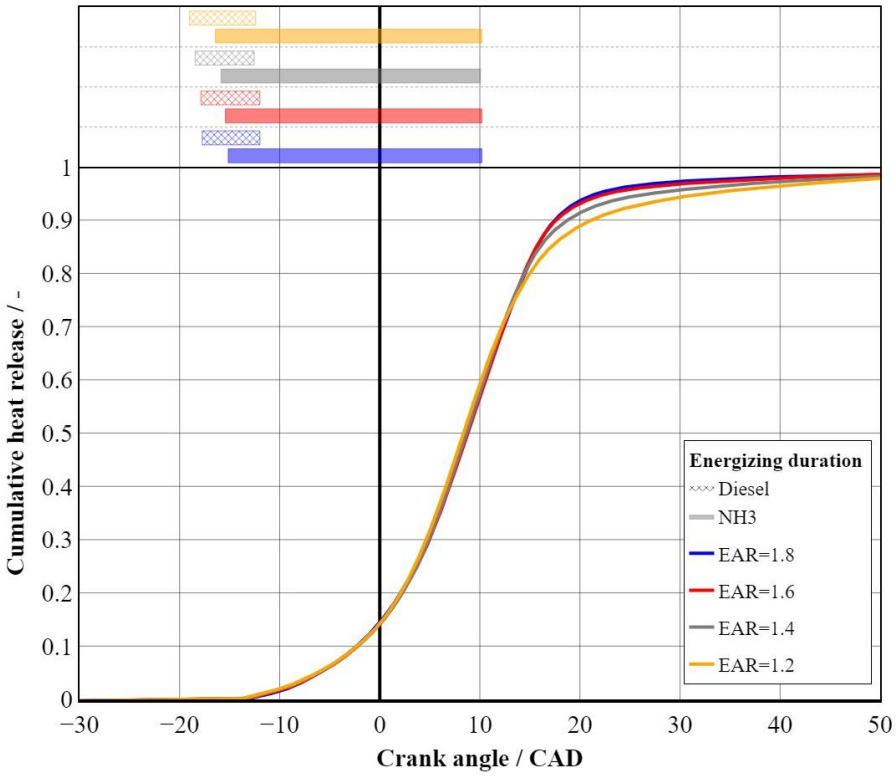

Figure 8: Cumulative heat release for different EAR at constant BMEP.

While the measured NH_3 concentrations in the exhaust gas are nearly constant between EAR = 1.4 and 1.8 there is a significant increase for EAR = 1.2. The opposite is observed for the emissions of nitrogen oxides that are lower for EAR =1.2 than for the higher excess air ratios. While the retarded and less complete combustion might contribute to this behavior, oxygen availability is likely the dominating factor. This is in line with the trends reported in the literature for (partially) premixed combustion where maximum nitrogen oxide emissions were found to occur at approximately EAR = 1.35 [16]. Taking the changing efficiency and exhaust gas mass flow rates for different excess air ratios into account the NO_X emission intensity for EAR = 1.2 was found to be approximately 40% of that for the higher excess air ratios shown in Figure 10.

The nitrous oxide emissions are on a relatively low level below 50 ppm. Due to the high global warming potential of nitrous oxide a further reduction via exhaust gas aftertreatment is still required to achieve the zero-impact emission levels. The nitrous oxide concentrations are decreasing with decreasing excess air ratio from 1.8 – to 1.4 as was found in experiments with homogeneous ammonia-air mixtures [12, 13]. For EAR = 1.2 an unexpected increase of the nitrous oxide emissions was observed. Since this increase is occurring in conjunction with a strong increase of the ammonia concentration it is possible that the nitrous oxide (or at least some share) is not formed during the main combustion phase but rather in the expansion and exhaust stroke when the unburned ammonia is reacting with nitrogen oxides at low temperature in a reaction known as selective non-catalytic reduction [17].

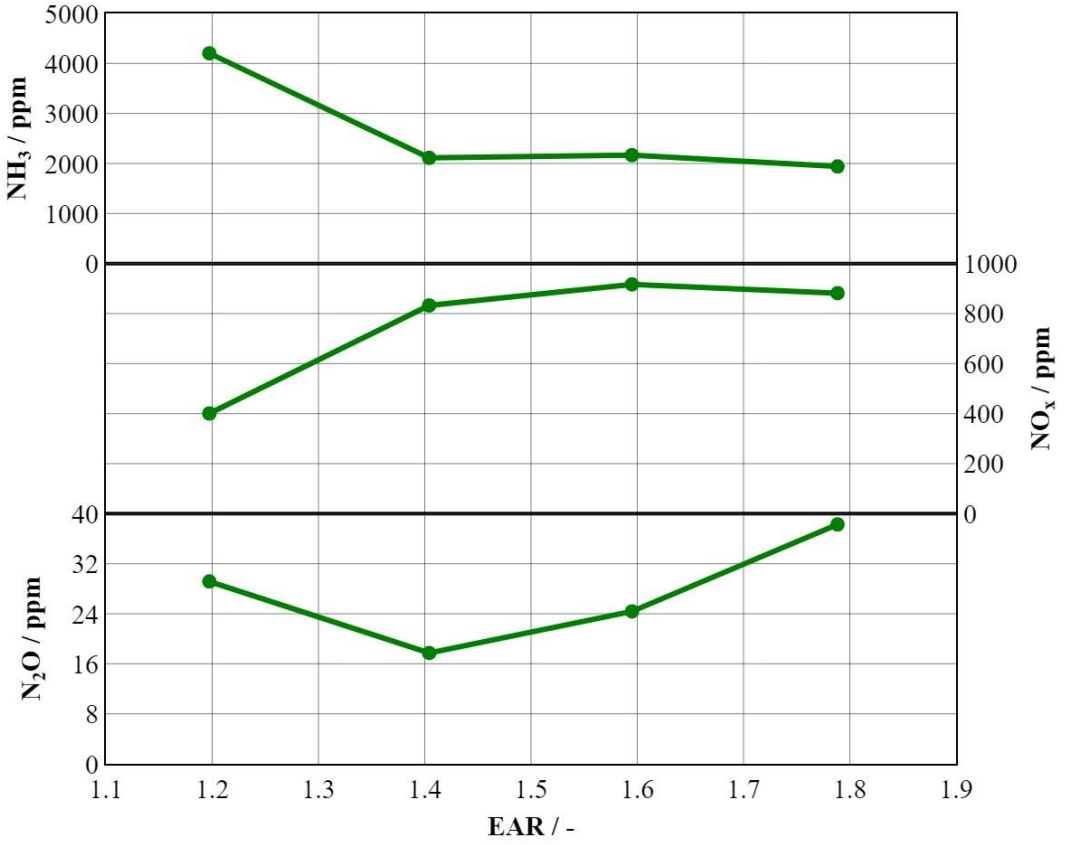

Figure 9: NH_3, NO_X and N_2O emission concentrations for an EAR variation at constant BMEP

The results show that the excess air ratio for ammonia-diesel dual fuel operation can be varied in a wide range and that an excess air ratio similar to values for typical diesel engines is feasible.

4.3. Combustion phasing variation

A combustion phasing variation between CA50 = 4 CAD after top dead center (aTDC) and 16 CAD aTDC was performed for an excess air ratio of 1.8. Both the ammonia and the diesel rail pressures were maintained at a constant value of 60 MPa and 120 MPa, respectively. The diesel energetic fraction was maintained at 10% and the dwell duration was fixed at 2.5 CAD throughout the test. The injection timing that is required to achieve the desired combustion phasing is shown on the bottom of Figure 11. In contrast to what would be expected, i.e., disproportionally advanced injection timing to achieve the earlier combustion phasing due to the increasing ignition delay time, it was observed that the injection timing had to be advanced less than the respective target combustion phasing.

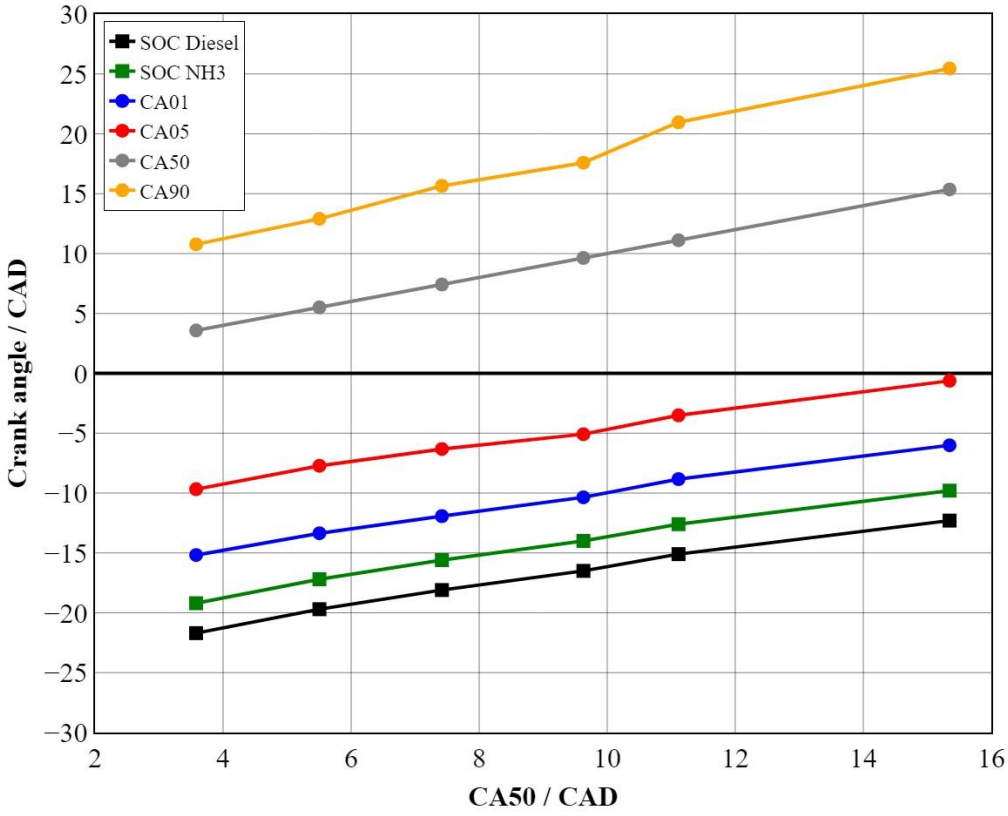

Figure 10: Injection timing and combustion progress for a combustion phasing variation at constant BMEP

A potential explanation for this unexpected trend can be seen in Figure 12 where the normalized heat release rates for the early combustion phase are shown. It can be observed that the time delay between the start of the diesel injection and the first rise of the heat release rate decreases with later injection timing, as expected due to the increasing pressures and temperatures later in the compression stroke. Again, due to the long hydraulic delay of the ammonia injector it is assumed that ammonia is not affecting this initial phase of the combustion. It can be observed, however, that with later injection timing the pre-mixed peak is reduced and the subsequent rapid increase of the heat release rate is retarded. It is hypothesized that two effects contribute to this behavior. On one hand, the shorter ignition delay time could reduce the spatial overlap of the ammonia and the diesel sprays and therefore the ignition of the ammonia spray. On the other hand, the reduced cylinder volume close to top dead center might impact the spray propagation and air entrainment.

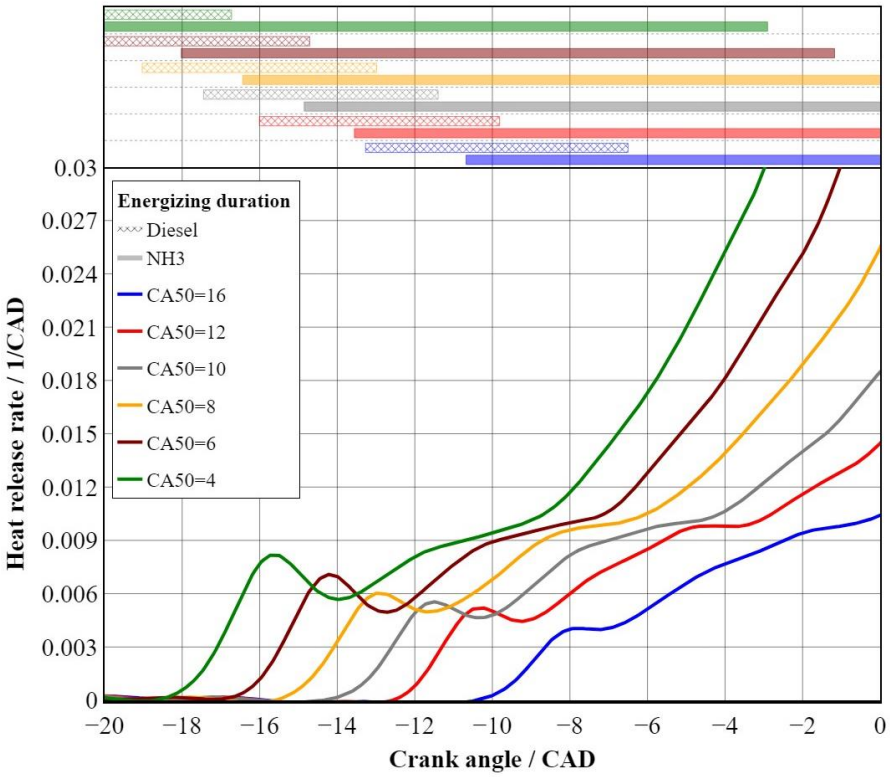

Figure 11: Heat release rate during ignition and early combustion phase for different combustion phasing

The impact of the slow increase in the heat release rate can be seen in the cumulative heat release in Figure 13. While the start of combustion shows a small spread only, the timing for CA50 shows a much higher spread from the earliest to the latest combustion phasing. This trend differs significantly from the behavior of a pure diesel combustion (with a centrally mounted diesel injector) that is shown in the bottom part of Figure 13. The cumulative heat release rates of the diesel combustion show less of a change in the shape but more a parallel shift of the curves. Apart from the interaction of the diesel and the ammonia sprays the fuel evaporation, especially the ammonia evaporation, could further impact the combustion process. Due to the significantly higher heat of vaporization the impact on combustion chamber temperature is expected to be significantly higher. The development of evaporation models and their integration into the heat release analysis tools is currently in progress and will allow a more detailed analysis of the ammonia combustion process in the future.

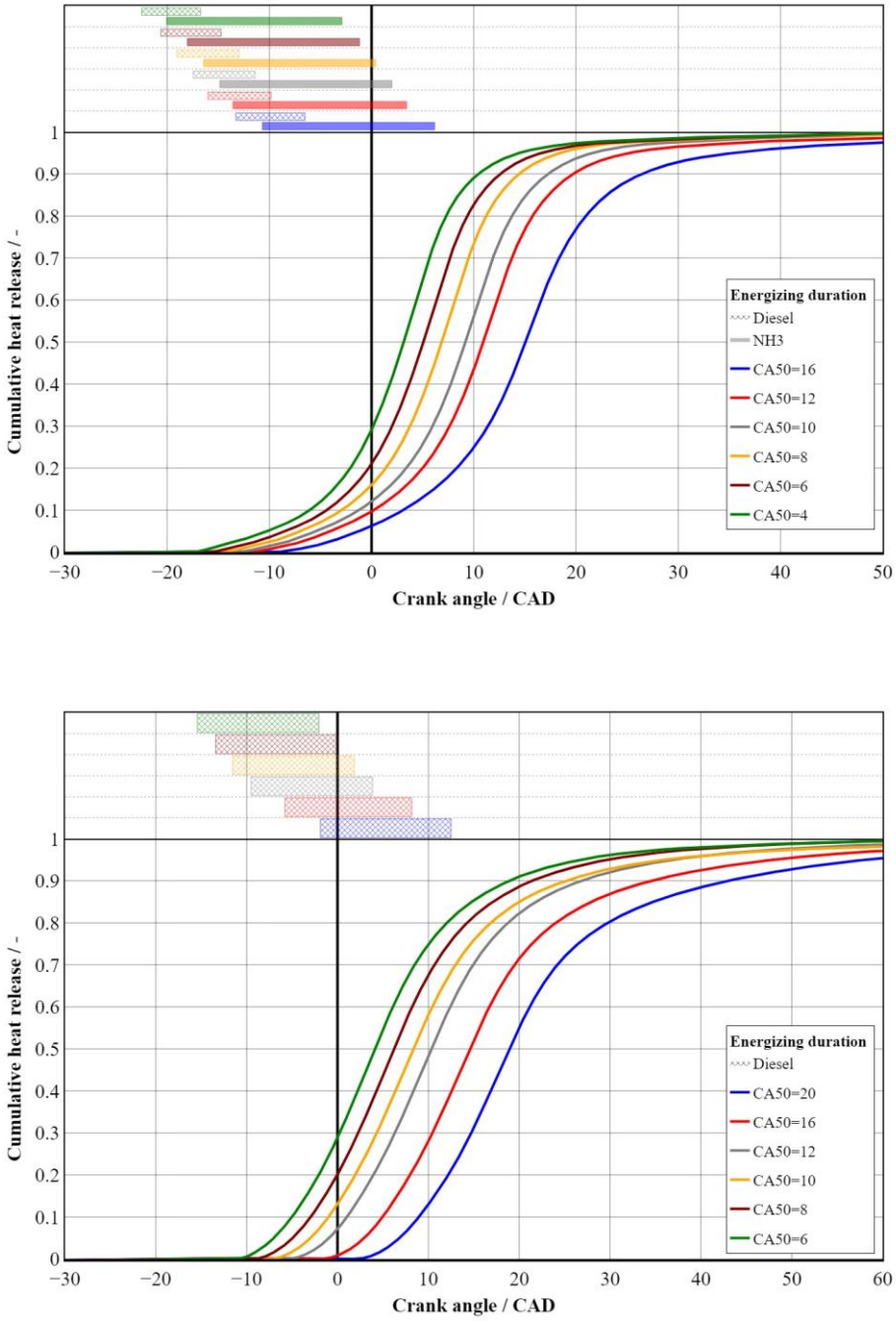

Figure 12: Cumulative heat release for different combustion phasing for ammonia (top) and diesel (bottom)

4.4. Comparison to diesel operation

The effect of the evaporative cooling can also explain some of the differences observed for a comparison of key parameters for ammonia and diesel combustion (Figure 14). The measured exhaust gas temperature for ammonia operation is approximately 100 K lower than for diesel operation with the same excess air ratio and combustion phasing. Reiter and Kong [18] performed thermodynamics calculations for the adiabatic flame temperature as a function of the fuel share between diesel and ammonia and the excess air ratio. They found that the adiabatic flame temperature for stoichiometric

conditions was reduced from 2320 K for diesel to 2100 K for ammonia and indicated the impact on the overall in-cylinder temperature level when ammonia is used as a fuel. The differences in the heat of vaporization between the fuels is exacerbating this effect. This impact on the in-cylinder temperature strongly affects the thermal NO_X formation that is typically the dominant share in hydrocarbon fuels. For ammonia combustion this temperature-driven effect is combined with the nitrogen oxide formation from fuel-bound nitrogen. The combined effect can be seen in the bottom of Figure 14 where the ammonia operation showed significantly lower nitrogen oxide emissions than the diesel combustion. The cyclic variability of the ammonia operation was higher than for diesel operation throughout the combustion phasing variation. Up to CA50 = 12 CAD aTDC the coefficient of variation of the indicated mean effective pressure (COV) could be maintained below 1.5%. For the latest combustion phasing of CA50 = 16 CAD aTDC the cyclic variability increased significantly which might be explained by the weak combustion initiation.

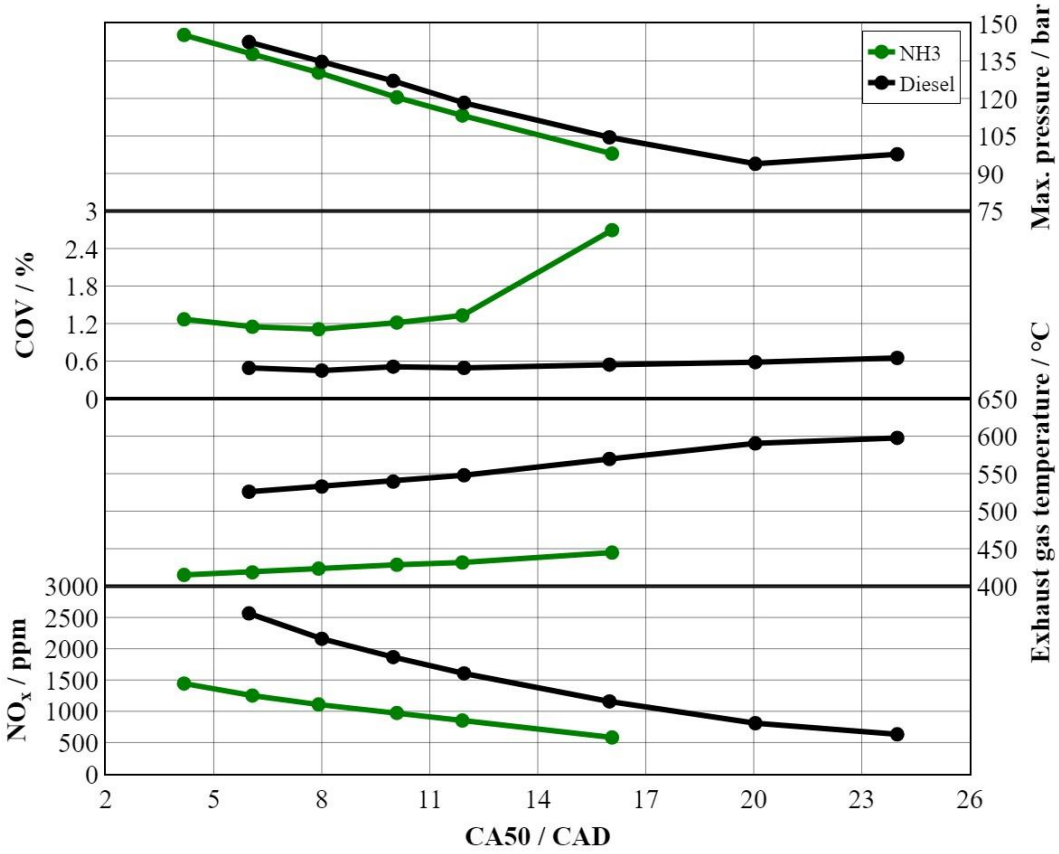

Figure 13: Selected performance parameter for the comparison of ammonia and diesel operation during a combustion phasing variation

Further analysis of the heat release rate of ammonia operation revealed that the cyclic variability is caused by the later part of the combustion. In Figure 15 the normalized heat release rates for a diesel operating point and an ammonia-diesel operating point with 10% diesel fraction are displayed. For both operating points the mean cycle (solid lines) as well as the standard deviation (shaded areas) are shown. For pure diesel operation the cyclic variability is very small and hardly visible in the diagram. For the ammonia combustion the early combustion phase has the same low cyclic variability that the diesel operation is showing. Only in the later part of the combustion where ammonia is burned the cyclic

variability increases significantly. Future work will have to determine the root cause and mitigation measures. At this point it is not entirely clear if some of the variability might originate from the fuel supply rather than the in-cylinder processes.

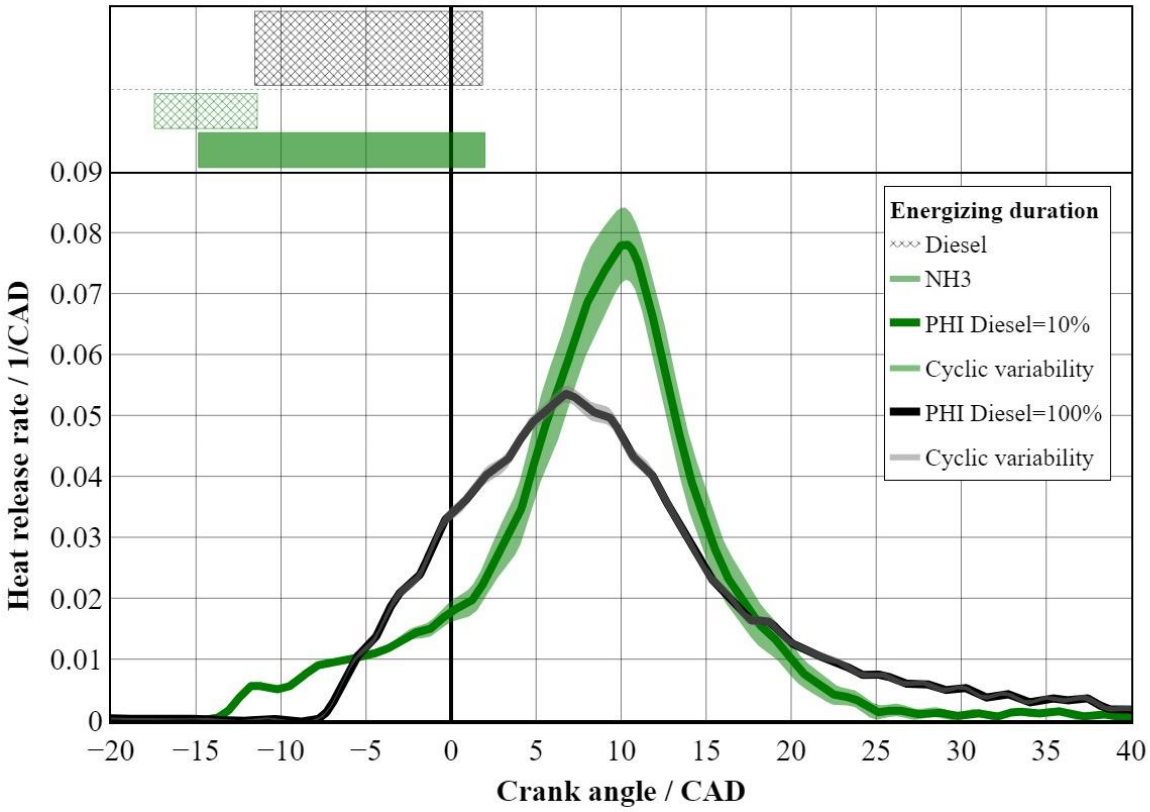

Figure 14: Illustration of cyclic variability of the heat release rate for ammonia and diesel operation

5. Conclusions

Ammonia is widely considered to be a strong candidate to serve an energy carrier for large-scale energy storage and transportation as the world transitions from a fossil fuel-based energy system to a system based on renewable energy. Although based on its physical and chemical properties ammonia does not seem to lend itself to direct use in internal combustion engines, recent progress has shown that ammonia is a suitable fuel for many applications. Different ammonia fuel admission and combustion concepts are currently under investigation to assess potential and limitations. In order to fulfill future stringent emission legislation exhaust gas aftertreatment will have to be an integral part of ammonia-based propulsion or power generation systems.

In this article an NH_3-HPDI combustion concept with a centrally mounted ammonia injector was experimentally evaluated on a medium-speed single cylinder research engine. Robust engine operation with ammonia energy shares up to 90% could be demonstrated and it was shown that moderate ammonia injection pressures of 60 MPa were sufficient to allow a wide operating range. Compared to previously published ammonia combustion investigations using port fuel injection or central mixture formation the use of high-pressure direct injection enabled a reduction of NH_3 emissions. NH_3 concentrations were mostly in the 1000 – 2000 ppm-range and for the best nozzle configuration concentrations of approximately 600 ppm were feasible even with excess air ratios typical for diesel

combustion concepts. The boost pressure demand does not increase compared to diesel operation such that existing turbocharger systems can potentially be modified to fulfill the needs of ammonia operation. The final excess air ratio selection will also have to take the exhaust gas temperature and its impact on the exhaust gas aftertreatment into account. In contrast to LNG dual fuel combustion concepts no combustion anomalies such as knocking have been observed for ammonia combustion, enabling the use of early combustion phasing. The benefits of the high excess air ratios and combustion phasing options support a favorable efficiency vs. NO_X trade-off that is illustrated in Figure 16. In comparison to the diesel operation a higher engine efficiency could be achieved with the NH_3-HPDI concept at a given NO_X intensity.

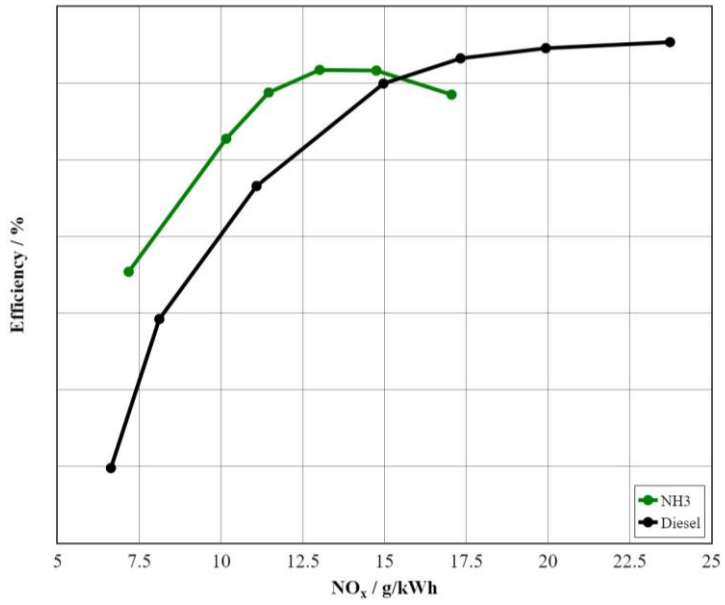

Figure 15: Efficiency vs. NO_X emission trade-off for ammonia and diesel operation

Future research on NH_3-HPDI combustion will focus on the optimization of the spray-spray and spray-piston bowl interaction as well as exhaust gas aftertreatment. Furthermore, the long-term impact of ammonia and ammonia combustion products on materials and lubricants will have to be subject to detailed investigations.

Literature

[1] Global Monitoring Laboratory, Trends in Atmospheric Carbon Dioxide, https://gml.noaa.gov/ccgg/trends/gl_gr.html, accessed: August 2023.

[2] Copernicus: 2023 is the hottest year on record, with global temperatures close to the 1.5°C limit, https://climate.copernicus.eu/copernicus-2023-hottest-year-record, accessed on April 6, 2024

[3] IPCC, 2022, Climate Change 2022: Mitigation of Climate Change. Contribution of Working Group III to the Sixth Assessment Report of the Intergovernmental Panel on Climate Change [P.R. Shukla, J. Skea, R. Slade, A. Al Khourdajie, R. van Diemen, D. McCollum, M. Pathak, S. Some, P. Vyas, R. Fradera, M. Belkacemi, A. Hasija, G. Lisboa, S. Luz, J. Malley, (eds.)].

Cambridge University Press, Cambridge, UK and New York, NY, USA. doi: 10.1017/9781009157926E.

[4] UNFCCC, Report of the Conference of the Parties on its twenty-first session, held in Paris from 30 November to 13 December 2015. Addendum. Part two: Action taken by the Conference of the Parties at its twenty-first session, https://unfccc.int/documents/909, accessed: August 2023.

[5] European Commission: "2030 Climate Target Plan". https://ec.europa.eu/clima/policies/eu-climate-action/2030_ctp_en#:~:text=With%20the%202030%20Climate%20Target,target%20of%20at%20least%2040%25, accessed on January 28th, 2021.

[6] European Commission: Recommendations for 2040 targets to reach climate neutrality by 2050, https://commission.europa.eu/news/recommendations-2040-targets-reach-climate-neutrality-2050-2024-02-06_en?prefLang=de, accessed on February 11, 2024.

[7] IMO: "Resolution MEPC.304(72) – Initial IMO Strategy on Reduction of GHG Emissions from Ships", https://wwwcdn.imo.org/localresources/en/KnowledgeCentre/IndexofIMOResolutions/MEPCDocuments/MEPC.304(72).pdf, accessed on December 29th, 2020.

[8] S. Laiminger, K. Payrhuber, N. Wermuth, A. Wimmer, The role of gas engines in a future energy market with sustainable fuels, presented at 30th CIMAC World Congress 2023: Meeting the Future of Combustion Engines, Busan, June, 2023.

[9] DNV Pathway to net zero emissions, 2023

[10] A. Valera-Medina, F. Amer-Hatem, A. K. Azad, I. C. Dedoussi, M. de Joannon, R. X. Fernandes, P. Glarborg, H. Hashemi, X. He, S. Mashruk, J. McGowan, C. Mounaim-Rouselle, A. Ortiz-Prado, A. Ortiz-Valera, I. Rossetti, B. Shu, M. Yehia, H. Xiao, M. Costa, Energy & Fuels, DOI: 10.1021/acs.energyfuels.0c03685.

[11] IPCC, The Earth's Energy Budget, Climate Feedbacks, and Climate Sensitivity. In Climate Change 2021: The Physical Science Basis. Contribution of Working Group I to the Sixth Assessment Report of the Intergovernmental Panel on Climate Change", https://www.ipcc.ch/report/ar6/wg1/, accessed: July, 2023.

[12] N. Wermuth, M. Malin, C. Schubert-Zallinger, M. Engelmayer, A. Wimmer, H. Schlick, T. Kammerdiener, Decarbonization of high-power systems: ammonia-hydrogen and ammonia-diesel combustion in HS engines (Paper No. 667), presented at 30th CIMAC World Congress 2023: Meeting the Future of Combustion Engines, Busan, June, 2023.

[13] N. Wermuth, C. Gumhold, A. Wimmer, M. Url, S. Laiminger, Energy Technology, DOI: /10.1002/ente.202301008

[14] M. Coppo, N. Wermuth, 2022. Powering a greener future: the OMT injector enables high-pressure direct injection of ammonia and methanol, pp. 68-81, Proceedings of the 7th RGMT, Rostock, Germany.

[15] M. Coppo et al., Detailed characterization and service experience of OMT injectors for dual-fuel medium- and low speed engines (Paper No. 267), presented at 29th CIMAC World Congress 2019, Vancouver, June, 2019.

[16] Westlye, F.R., Ivarsson, A. and Schramm. 2013. Experimental investigation of nitrogen-based emissions from an ammonia fueled SI engine, Fuel, 111: 239-247

[17] Miller, J.A., Glarborg, P. 1996. Modelling the Formation of N2O and NO2 in the Thermal De-NOx Process. In: Wolfrum, J., Volpp, HR., Rannacher, R., Warnatz, J. (eds) Gas Phase Chemical Reaction Systems. Springer Series in Chemical Physics, vol 61. Springer, Berlin, Heidelberg. https://doi.org/10.1007/978-3-642-80299-7_25

[18] Reiter, A.J., Kong, S.C. 2008. Demonstration of compression-ignition engine combustion using ammonia in reducing greenhouse gas emissions, Energy Fuels, 22, 5, 2963 – 2971

Galí complete Starting Solutions

we supply all our products in ATEX–IECEx version

Air Starter

Powerful **high pressure starters** to start Engines up to 7.000 kw and more.

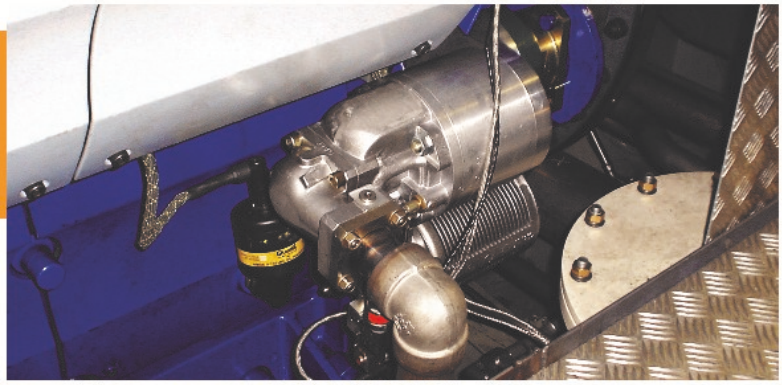

Turning Mechanism

For **engine build-up** and **service work.**

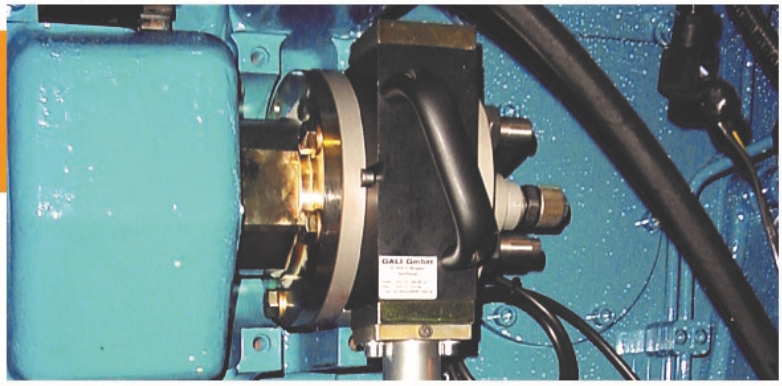

Shut off Valve

Immediate emergency stop of the engine in case of safety reasons.

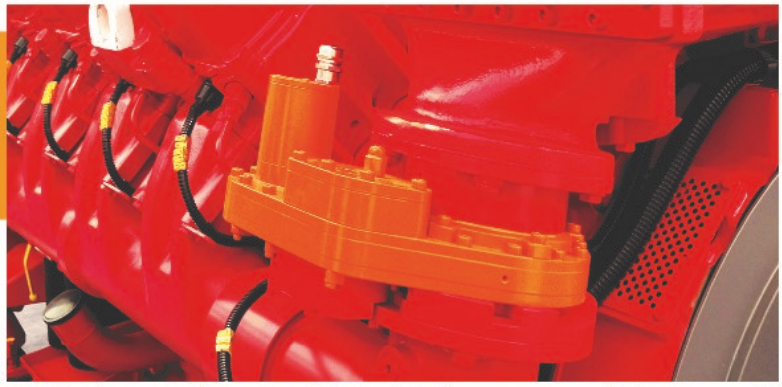

Hydraulic Starter

For **special application** and **emergency sets** (black start).

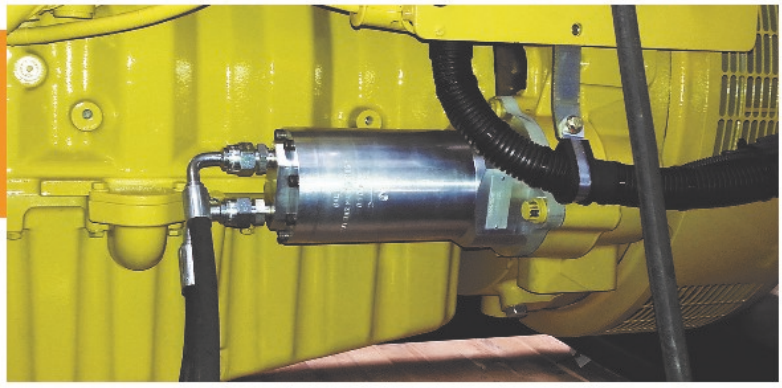

gali | Technical Solutions since 1951

SPAIN gali@galigrup.com
GERMANY info@gali.de
FRANCE comexp@gali-france.fr
ITALY gali@gali-italia.it
CHINA china@galigrup.com

www.galigrup.com

Keywords: ammonia, engine, combustion, lubricant, oil, marine, off-road, tribology

Impact of ammonia combustion on lubricant performance and engine durability

Bruno Griffaton[1], Alix Noca[2], Nicolas Obrecht[1], Oscar Lacrois-Andrivet[1], Maria Rappo[1], Dr. Bouzid Seba[2]

(1) TotalEnergies OneTech, (2) Liebherr Machine Bulle

https://doi.org/10.18453/rosdok_id00004650

Abstract

Ammonia as a fuel has been studied since the middle of the twentieth century. This technology has found renewed interest in recent years as a way to decarbonize large powertrain applications. The maritime sector will reveal its first commercial applications within the next 2 years in order to provide practical solutions to decarbonize large energy consumers (especially maritime transportation) in compliance with different legislations and greenhouse gas reduction objectives from IMO and European Council. Ammonia does not produce any direct carbon emissions during its combustion; it can be stored in liquid phase at a pressure of approximately 15 bar at ambient temperature; and it benefits from mature supply and storage infrastructures across the globe. Nevertheless, its use involves challenges such as safety linked to ammonia toxicity and combustion management, particularly for emission control, stability and engine durability. TotalEnergies, as a lubricant manufacturer, aims at identifying the ammonia combustion impacts on lubricant performance and aging, with the objective to provide technical solutions that meet the requirements of ammonia applications in a sustainable manner.

This study investigates the influence of ammonia combustion on lubricant performance, particularly its role on engine durability. The results are based on experimental studies carried out on large an off-road engine in collaboration with Liebherr Machine Bulle and a laboratory bench test comparing tribological behavior under air and ammonia atmosphere. The results of these investigations provide lessons on:

- The evolution of lubricant behavior during a durability test using an ammonia Dual Fuel combustion engine
- wear and corrosion phenomena observed on disassembled engines parts and solutions to mitigate them through lubricant formulation
- The relationship between metal surfaces alteration and the tribofilm structure in the presence of ammonia.

1. Lubricant aging during ammonia combustion endurance test

A durability engine test has been developed to study the lubricant behavior under severe ammonia combustion conditions along an extended period of time. The goal of this test is to evaluate the capacity of the engine oil to maintain its performance and the ageing intensity. The test was carried out on a prototype engine whose characteristics are described in the table 1.

Table 1: Test engine specification

Number of Cyl.	4
Displacement	9 dm3
Bore	135 mm
Stroke	157 mm
Rated Power	300 kW @ 1700-2100 rpm
Max. Torque	1739 Nm

Liebherr Machine Bulle pre-development teams modified a series Diesel engine in order to operate in Dual Fuel ammonia combustion, i.e. the combustion of the air-ammonia mixture is ignited by a Diesel pilot injection. This prototype engine uses the standard configuration of the Diesel engine in terms of turbocharging system and combustion chamber. No specific change in components material was done on this prototype engine.

1.1. Engine setup and operating conditions

Prior to the endurance test, Liebherr Machine Bulle pre-development teams investigated different strategies and hardware configurations of ammonia injection: gas or liquid phase injection, single-point or multi-point injection, adaptations of the intake line for mixture optimization. For this endurance test, the authors jointly selected a single-point liquid phase ammonia injection to ensure homogeneous air-ammonia mixture cylinder-to-cylinder and a good combustion stability over long duration tests. The injection setup is presented in figure 1.

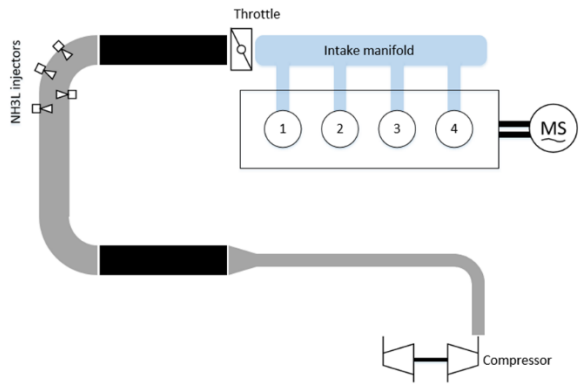

Figure 1: ammonia injection setup for endurance test

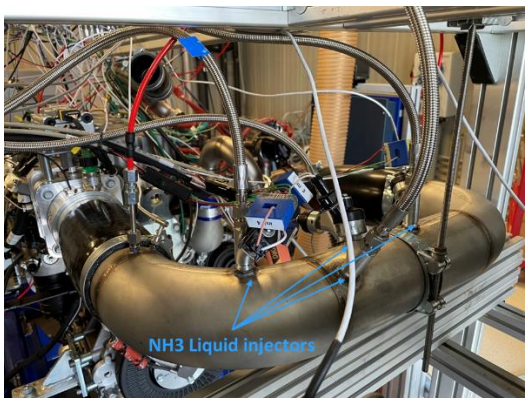

Figure 2: ammonia injectors location

The concept of the durability test was designed on a on a single operating point run for a period of 250 hours. To ensure sufficient severity and stress on the lubricant, several requirements were considered for the calibration of the operating point. A low rotational speed and high load generates high thermal and blow-by gas stress in the oil film around the piston – liner assembly on lubricated

contacts. The engine calibration allowed to reach 22.5 bar of BMEP at 1100 rpm which was considered sufficiently representative of high load conditions in field applications. The injection parameters in dual fuel mode were set to operate at the maximum cylinder pressure used by the series engine under Diesel combustion as illustrated in Figure 3. Finally, the ammonia / Diesel fuel energy ratio was optimized to maximize the exposure of the lubricant to ammonia, while allowing a stable combustion throughout the endurance run. That energy ratio was set at 90% after calibration. The summary of engine operating characteristics is presented in Table 2.

Table 2: operating point definition

Engine speed	1100 rpm
BMEP	22,5 bar
Diesel pilot injection energy ratio	10%
Ammonia fuel injection energy ratio	90%
Engine efficiency (delta with reference Diesel engine)	+3%
Max. cylinder pressure vs. Diesel engine max cylinder pressure	1:1

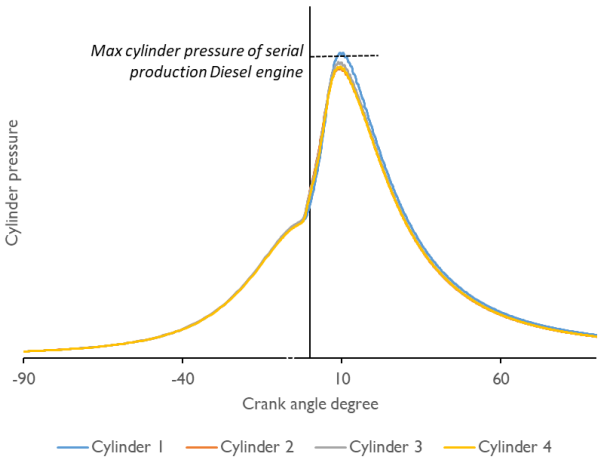

Figure 3: Cylinder pressure measurement on endurance operating point

The entire endurance test lasted 250 hours during which the engine ran on the operating point described above for 8 to 10 hours per day. Throughout the test, the engine lubricant was sampled regularly for analysis to assess its aging. Lubricants technologies were developed by TotalEnergies to ensure proper engine lubrication under ammonia combustion and used in this study. After 150 hours of operation, observing that the analysis showed regular and predictable behavior, a change from Lubricant A to Lubricant B was decided in order to test the impact of engine oil formulation on ageing pattern. Both lubricants used in that study are SAE 40 engine oils sharing the exact same base oil blend technology based on classical API group I, group II base oil slates. Except for the antiwear, different additive technologies were used between lubricant A and lubricant B leading to different total base number (TBN) values as detailed in Table 3.

Table 3: Engine oil characteristics

Name	Base oil blend technology	Antiwear additive	Additive technology	Kinematic Viscosity at 100°C	Kinematic Viscosity at 40°C	VI	TBN
				ASTM D7279	ASTM D7279	ISO 2909	ASTM D2896[1]
Units				mm^2/s	mm^2/s	-	mg KOH/g
Lubricant A	Blend 1	AW 1	ADD 1	14.44	134.0	107	12,5
Lubricant B	Blend 1	AW 1	ADD 2	14.33	132.9	107	20.0

At the start, in the middle and at the end of the endurance test, a measurement of NH_3 concentration was carried out in the crankcase ventilation circuit to quantify ammonia concentration to which the lubricant is exposed. Finally, at the end of the endurance test, the engine was disassembled for inspection. The objective was to analyze the condition of the different components to evaluate potential impacts of ammonia combustion on their integrity.

1.2. Lubricant A samples analysis

The following figures present the evolution of lubricant properties when using Lubricant A for the first 150 hours. Figure 4 shows the evolution of the acidity number (TAN) and the basicity number (TBN) of the lubricant. Unlike lubricants in Diesel or gas engines where the TAN increases and the TBN decreases with respect to the neutralization of acids, in this study, both parameters remain stable. Nitrogen oxides remain the main products of ammonia combustion, however, samples analysis does not reveal any trace of nitroxidation within the lubricant.

On the other hand, lubricant kinematic viscosities at 40 °C or 100 °C remains stable throughout the 150 hours hence showing no signs of significant oil ageing. Considering no viscosity increase and quite stable TAN and TBN values over the initial 150 h, it can be assumed that the thermal and chemical conditions do not meet oxidative alteration limits for the lubricant, despite severe operating conditions. It should also be noted that lubricant samples do not reveal presence of soot and no water was detected in the samples either, despite water vapor being a main product of ammonia combustion. This is explained by high load engine operation and therefore continually high engine coolant temperature (87 °C) and high oil temperature (95 °C).

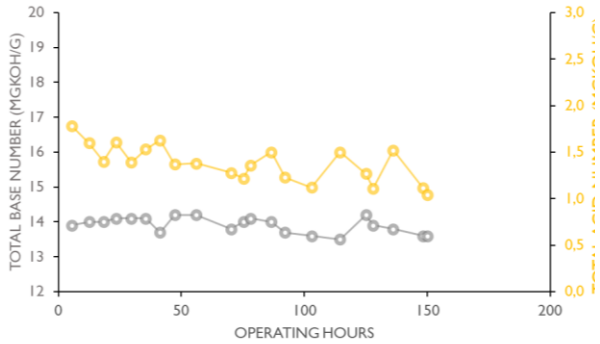

Figure 4: TBN and TAN monitoring of Lubricant A

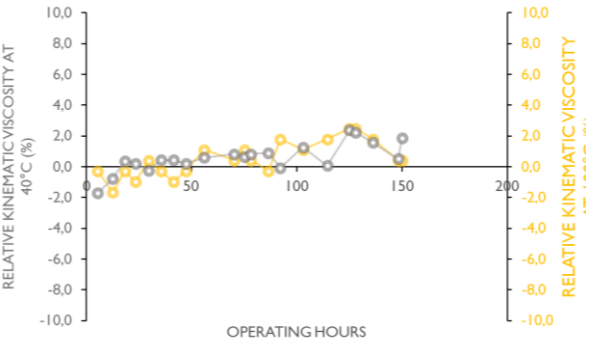

Figure 5: Relative kinematic viscosities at 40°C and 100°C monitoring of Lubricant A

Figures 6 and 7 show the evolution of metal contents concentrations in lube oil. Interestingly, a clear increase in the concentrations of copper and iron can be observed. The progressions of these concentrations are regular and greater than those found in conventional diesel or gas combustion engines.

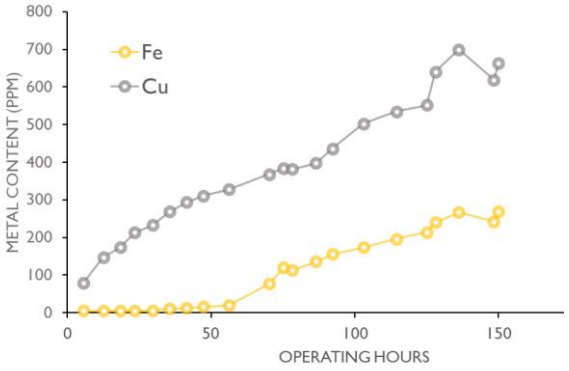

Figure 6: Copper and iron concentrations monitoring of Lubricant A

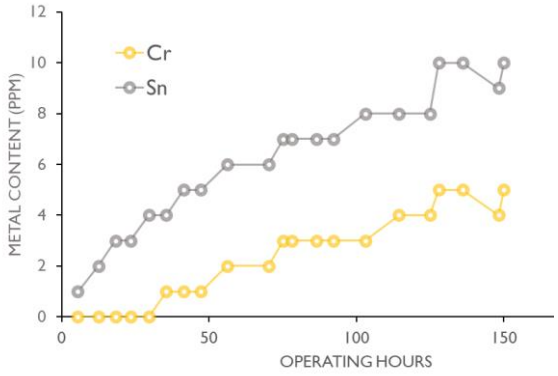

Figure 7: Chromium and tin concentrations monitoring of Lubricant A

In the case of copper, the concentration progresses quite regularly from the start of the tests. The presence of copper in the oil had been observed in a study carried out by Obrecht et al. in 2022 [1] and is expected given the corrosive nature of ammonia towards copper. Iron is present in several engine parts made of different steels. Iron in the lubricant is not immediate but appears after about fifty hours, thereby suggesting a degradation of the lubricating protection performance over time. The lack of resilience of the tribofilm under ammonia operating conditions is a potential hypothesis leading to a lower protection of the lubricated metal surfaces in motion.

Other metals such as tin and chromium also show a significant progression even if the concentrations remain moderate. Like copper, the tin concentration increases from the beginning of the tests, suggesting wear of the bearings. The chromium concentrations are significantly lower but nevertheless higher than a wear threshold considered significant at 3 ppm. Chromium is present on the fire rings. Its presence in the oil suggests wear at the ring-liner contact. In the case of ammonia combustion engines, the greater quenching distance is likely to generate ammonia accumulation area in the top land, without combustion. We can then question the impact of the presence of ammonia on the ring-liner contact at the top-ring level.

Since metal concentration progressions are regular and ageing properties are relatively constant, operating an additional 100 hours with the same lubricant would certainly not provide any new information. A change of lubricant was decided to test the impact of a new additive technology ADD 2 in the formula of lubricant B. The new additive technology ADD 2 aims to protect lubricated surfaces, having noted attacks of several metals.

1.3. Lubricant B samples analysis

Over the remaining 100 h of the endurance test, the lubricant B oil samples show kinematic viscosity profiles quite similar to Lubricant A sample during the initial 150h of the test as illustrated by Figures 8 and 9. This observation confirms that additivation B does not affect its viscosity performance of the engine oil.

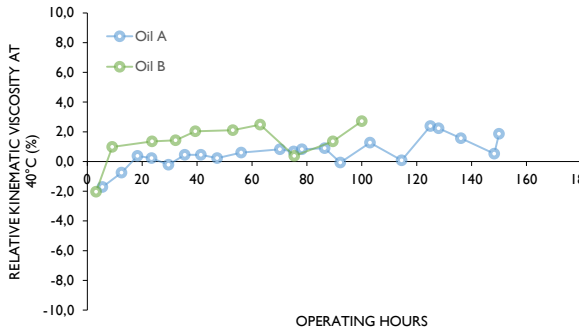

Figure 8: Relative kinematic viscosity at 40 °C of Oil A and Oil B

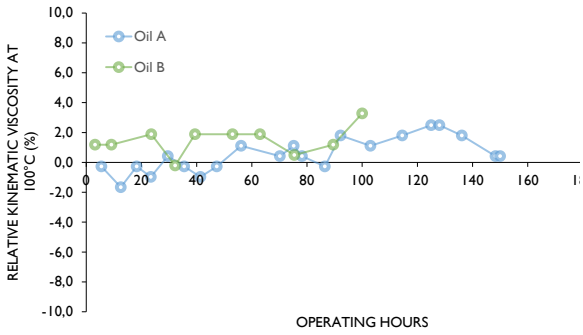

Figure 9: Relative kinematic viscosity at 100 °C of Oil A and Oil B

Figures 10 and 11 compares the evolution of acidity and basicity during the engine test for lubricants A and B. Whereas, no significant evolution of the acidity number is observed on Lubricant B oil samples, a regular decrease in the total based number is observed for Lubricant B. This behavior differs from Lubricant A and can be explained by the difference in the chemical nature of additives technologies used in both lubricants. Considering the higher initial TBN of Lubricant B, the decrease is considered quite reasonable and does not generate any increase in acidity number as emphasized previously. Considering chemical composition of Lubricant B, it is very likely that beyond the first 100 hours the TBN would continue to decrease to stabilize at 14 like lubricant A, maintaining its alkalinity reserve. Nevertheless, this hypothesis shall be verified thank to additional tests.

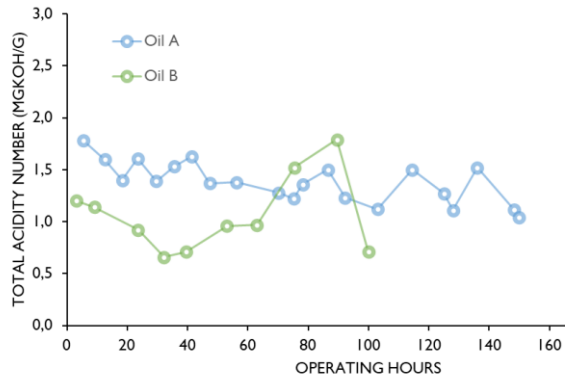

Figure 10: Total acidity number (TAN) comparison of Oil A and Oil B

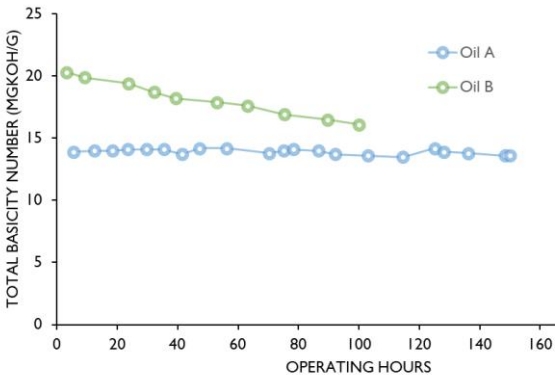

Figure 11: Total basicity number (TBN) comparison of Oil A and Oil B

Wear metal elements measured during the engine test on lubricants A and B oil samples are reported on Figures 12a, b, c and d. We clearly observe a slower progression of copper and iron concentrations with lubricant B compared to lubricant A. Additionally, the progression of the chromium concentration is also lower with lubricant B which therefore seems to ensure a more resistant tribofilm for ring-liner contact. Finally, after 100 h of operation on both oils, lubricant B shows twice as less tin concentration than with lubricant A. This suggests that the additive technology of the lubricant B allows an improved wear phenomena mitigation compared to lubricant A additive system.

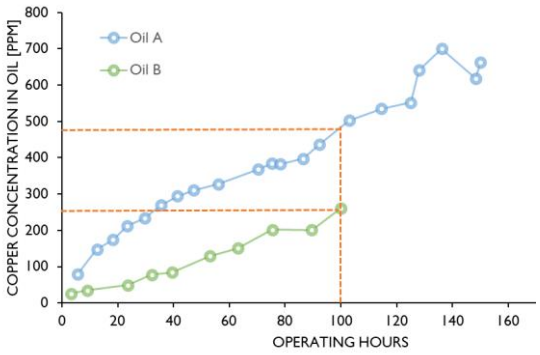

Figure 12a: Copper concentrations comparison of Oil A and Oil B

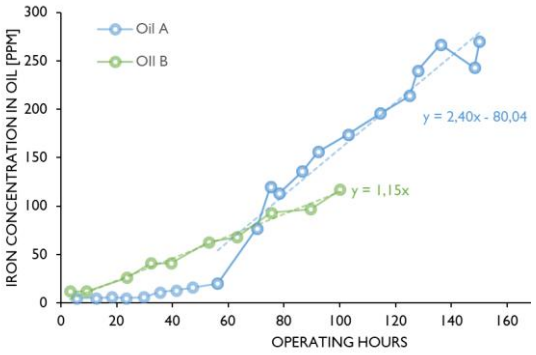

Figure 12b: Iron concentrations comparison of Oil A and Oil B

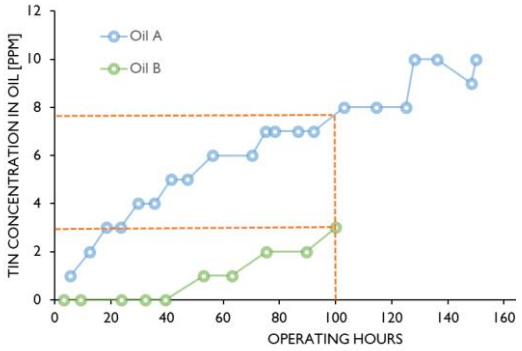

Figure 12c: Tin concentrations comparison of Oil A and Oil B

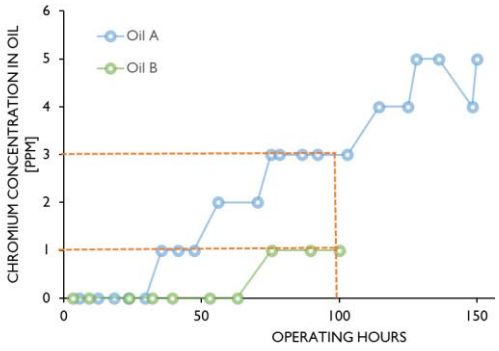

Figure 12d: Chromium concentrations comparison of Oil A and Oil B

1.4. Ammonia concentration measurements of crankcase gases

In order to know what concentration of ammonia the lubricant is exposed to in the crankcase, a specific measurement setup was installed for these tests. The ammonia concentration measurement was carried out at the start of the test, after 125 hours, and at the end of the test. Figure 13 shows the ammonia concentrations measurements for the 3 samples.

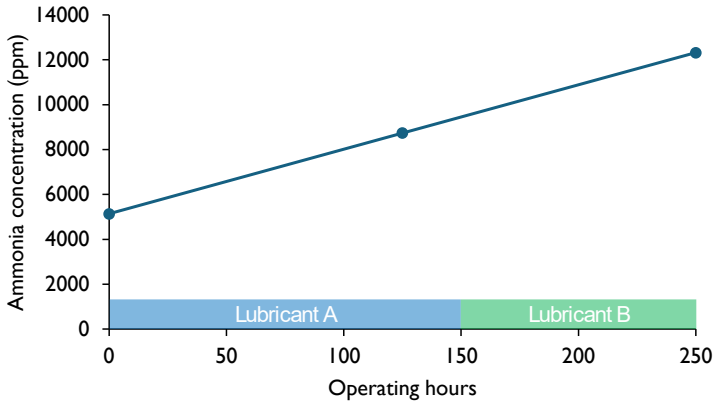

Figure 13: Ammonia concentration measurements in crankcase ventilation gases

The results show a clear increase in the NH_3 concentration throughout the endurance test. The concentration at the end of the test is consistent with the level measured during a study carried out in 2022 [1]. It is difficult to identify the reason for the concentration increase. However, this could be linked to the suggested wear phenomenon in the ring-liner- contact and therefore a degraded sealing of the combustion chamber. As a result, it is confirmed that the lubricant is exposed to high concentrations of ammonia around the liner and in the crankcase. These conditions will subsequently be reproduced in laboratories to study more closely any potential alteration of the lubricant

1.5. Aged lubricant composition analysis

In order to provide better insights on the structural degradation of the lubricant, used oils at 150 hours and after 100 hours for lubricants A and B respectively, were studied by mass spectroscopy at TotalEnergies R&D center. The mass measurements were obtained using an Orbitrap Qexactive plus instrument equipped with an electrospray ionization (ESI) source. Acquisitions were carried out on negative detection mode to have a selective ionization of detergent molecules. Prior to analysis, sample were solubilized in a toluene/methanol mixture (50/50, v/v) at 0.1 mg/mL with addition of 2% of ammonium hydroxide dopant to favorize ionization. Orbitrap and source parameters were set as follows: capillary voltage fixed to 3 kV, sheath gas flow rates equal to 10, capillary temperatures equal to 350 °C, AGC target at 1e6 ms with a maximum injection time of 50 ms, and S-lens Rf at the maximum of 100%.

The results are depicted in figures 14a, b, c and d through Kendrick mass defect plots, which serve as molecular maps to align molecular families differing only by alkylation levels on the same horizontal line. Both native lubricants exhibit three distinct families: 2 types of detergent additives, and dithiophosphate (DTP) antiwear additive. Post-aging, Lubricant A shows a complete absence of DTP, indicating their full consumption, aligning with the emergence of polyphosphates undetectable under the current conditions. Aging also reveals the presence of nitro-oxidation products in detergents, hinting at ammonia's impact on these additives. This is further evidenced in figures 15a and 15c with compound class distribution for Lubricant A, which compares the relative abundance of each class pre- and post-aging. The classes O3, O1, and O2P1S2 correspond to detergents, and DTP antiwears, respectively. The absence of native DTP (O2P1S2) post-aging confirms their total consumption. Nitro-oxidation is identifiable with the emergence of O3N1 and O5N1 (detergents nitro-oxidation) classes.

In contrast, Lubricant B Kendrick mass defect plots (Figures 18 and 20) show significant differences, notably the presence of monothiophosphate (MTP) and phosphate, which are consistent with degradation intermediates preceding polyphosphate formation. This suggests that Lubricant B anti-wear additives are less degraded than those in Lubricant A. Figures 16 and 17 underscores this with compound class distributions that show a decrease in native DTP (O2P1S2) and the appearance of MTP (O3P1S1) and phosphate (O4P1). The detergents in Lubricant B also undergo nitro-oxidation, but with a lower relative abundance than in Lubricant A.

Overall, these results strongly evidence that Lubricant B is less degraded than Lubricant A focusing on detergent and antiwear additives. This is corroborated by the lower wear metal content observed in the standard oil analysis discussed previously.

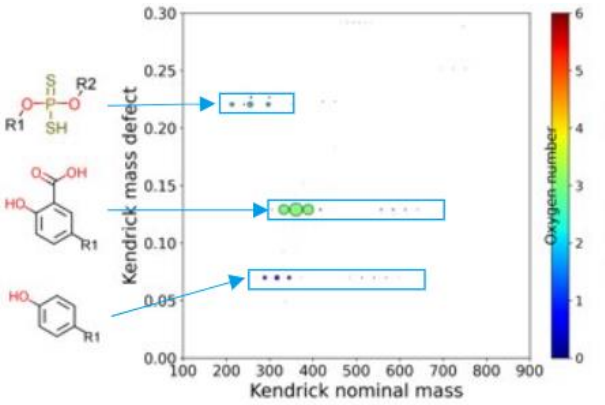

Figure 14a: Kendrick mass defect of ***Lubricant A - fresh***

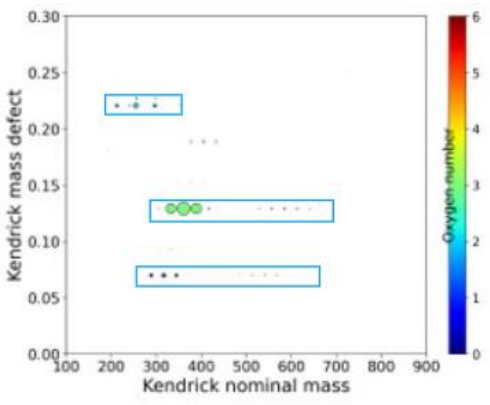

Figure 14b: Kendrick mass defect of ***Lubricant B – fresh***

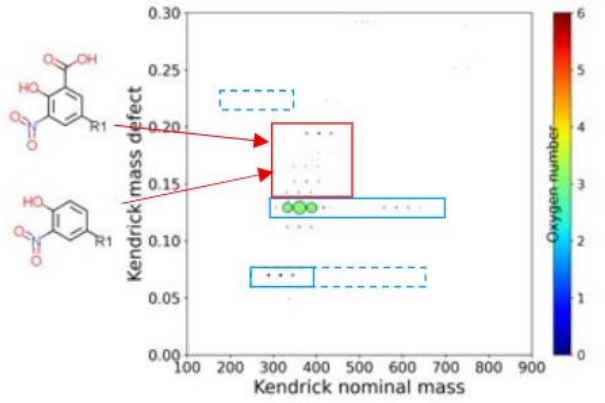

Figure 14c: Kendrick mass defect of ***Lubricant A - aged***

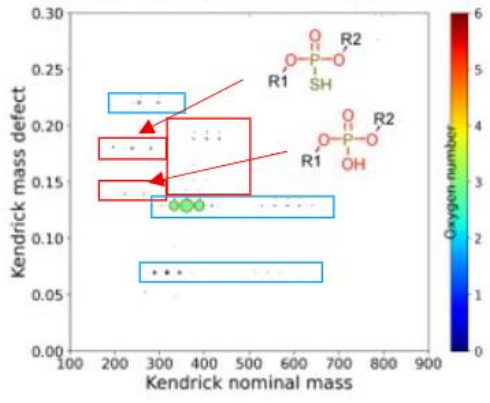

Figure 14d: Kendrick mass defect of ***Lubricant B – aged***

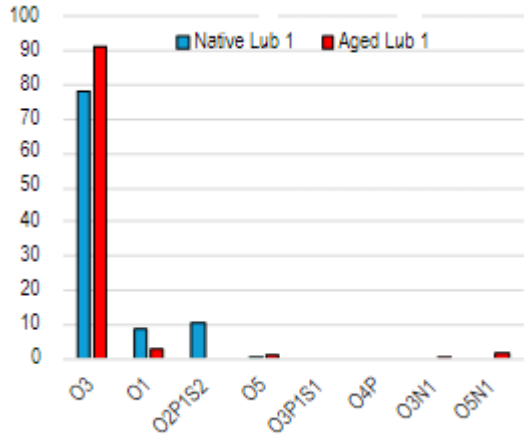

*Figure 15: Component class distribution for **Lubricant A***

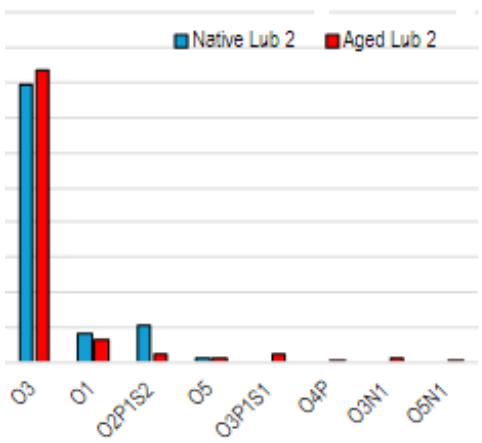

*Figure 16: Component class distribution for **Lubricant B***

1.6. Endurance engine inspection

Finally, at the end of the endurance test, the engine was disassembled by the Liebherr teams and the parts inspected one by one. As a reminder, on this test engine, almost all the components (except the ammonia injection system) come from a series production Diesel engine, both in terms of design and materials.

Regarding air path component, unlike the study carried out in 2022 [1], the turbocharger is in perfect condition. No clearance from the shaft suggests any wear of the bearing. The engine head does not show any particular deterioration with the exception of wear at the head of the valve stems. This can be explained by engine operation on a single point at low speed, on which the expected axial rotation of the valve is limited. Carbon deposits are also observed on the intake valves, most certainly from the lubricant. On base engine components, there is no particular trace of deterioration. The honing of the liners is still visible, without significant wear while the top of the liners shows a clear coloration potentially attributable to corrosion. Moving parts are more altered. The connecting rod small end and big end bearings show significant wear areas. The top rings show more wear than expected for this endurance period, as shown by the analysis results. Indeed, the polishing height of the top rings which corresponds to the worn surface exceeds half the height of the ring. The pistons do not show any carbon deposit as we could expect. However, the piston bottoms show a black deposit which suggests significant thermal stress.

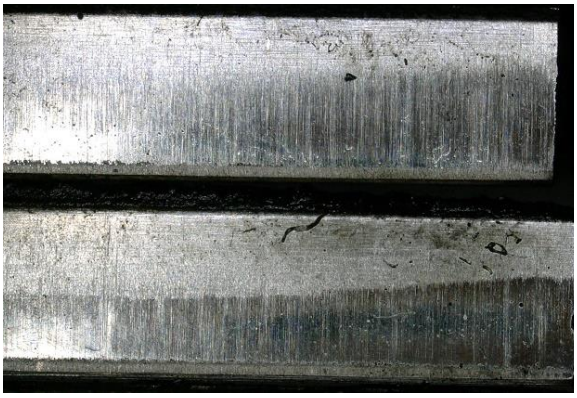

Figure 17a: Top rings from cylinders 1 and 2

Figure 17b: Piston bottom of cylinder 1

Figure 17c: Liner from cylinder 2

Overall, the engine components do not appear to have suffered any significant degradation with the exception of the connecting rod small end and big end bearings and the top rings. These degradations are correlated with the lubricant analyses. Based on the previous observations, it is likely that most of the degradations were performed during the first 150 h with Lubricant A.

2. Impact of ammonia on friction and tribolfilm performance

A first tribological study was therefore conducted by TotalEnergies to study the impact of a controlled ammonia atmosphere on lubricated contacts. The aim of this study is to understand whether the presence of ammonia impacts the friction performance and whether it can affect the tribofilm. A ball-on-disk tribometer was used to control precisely the contact speed and normal force applied on the lubricated contact. As depicted in figure 18, the tribometer is installed in a sealed chamber in order to control the atmosphere around the contact. For these first campaign, the same commercial lubricant is tested with a 100% air atmosphere and a 100% NH_3 atmosphere. These opposite conditions aim to study the impact of ammonia on the lubricated contact.

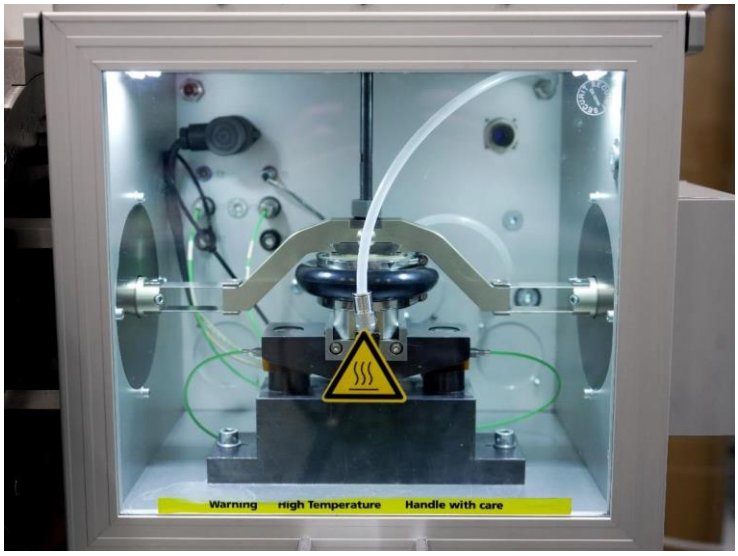

Figure 18: Tribometer with controlled atmosphere

The friction coefficient recordings along the two tests are shown in Figure 19. Figure 20 illustrates the average friction coefficient over each test. We observe a relatively flat evolution of the friction coefficient suggesting a limited evolution of the tribofilm during the test. The test performed under ammonia atmosphere leads to a 20% higher friction coefficient on average (running-in sequence excluded) compared to the test performed under air. This observation indicates that replacing air by ammonia, impacts the friction properties of a lubricated contact.

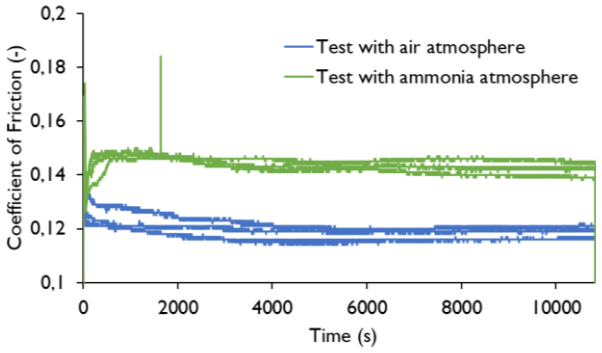

Figure 19: Friction coefficient calculation during the tests

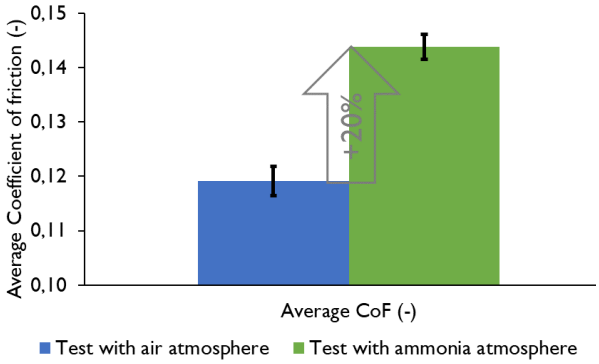

Figure 20: Averaged friction coefficient ; 600-10800 s of test sequence (without running-in)

At the end of the tests, the wear on the test parts is measured. The wear scar diameter is measured in 2 directions orthogonal to each other of the scar (diameter 1 and 2) for the 3 balls used in the tribometer. The results are presented in Figure 21a, b and c. All measurements (wear scar diameter, wear scar area and wear volume) are consistent with high wear in the presence of ammonia compared to the presence of air.

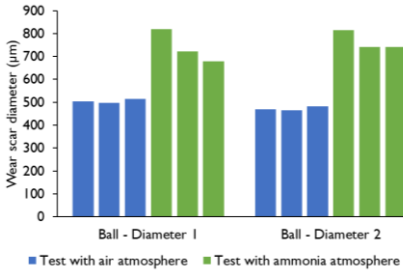

Figure 21a: Ball wear scar diameter measurements

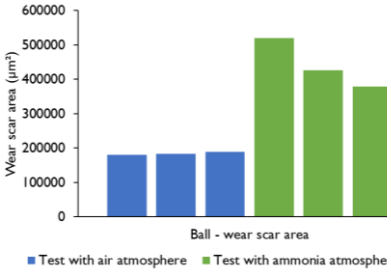

Figure 21b: Ball wear scar area measurements

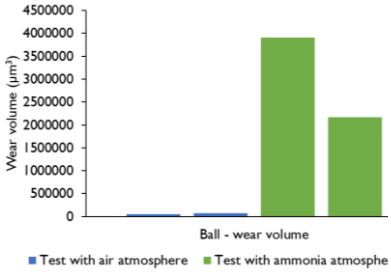

Figure 21c: Ball wear volume measurements

The disk is also analyzed after testing. The diameter of the wear scar, the surface and the wear volume are presented in Figures 22a,b and c. The differences in wear between the test parts in air atmosphere and in ammonia atmosphere are less significant but confirm greater wear in ammonia atmosphere.

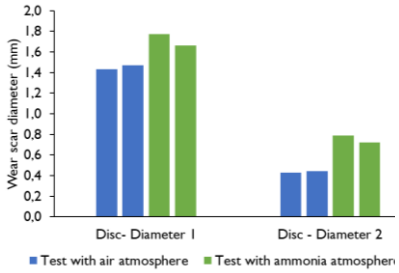

Figure 22a: Disk wear scar diameter measurements

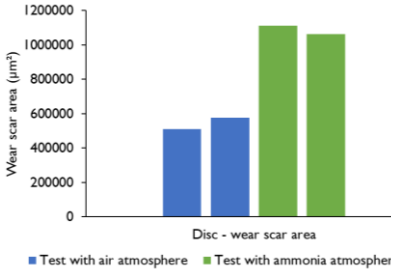

Figure 22b: Disk wear scar area measurements

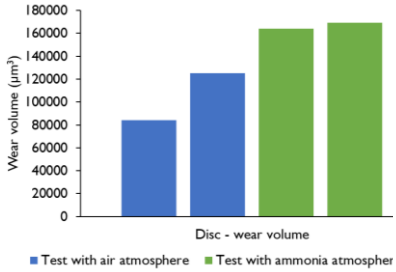

Figure 22c: Disk wear volume measurements

In order to better understand the behavior of the tribofilm for the two controlled atmospheres, the composition of the tribofilm was studied using the X-ray photoelectron spectroscopy technique (XPS). Figure 23 shows the comparison of the nitrogen concentration in the tribofilm for the two tests. Despite the high nitrogen content in the air, no nitrogen is absorbed in the tribofilm. On the contrary, in ammonia atmosphere, nitrogen atoms are detected, suggesting the absorption of ammonia in the tribofilm and a potential reaction with the lubricant constituents.

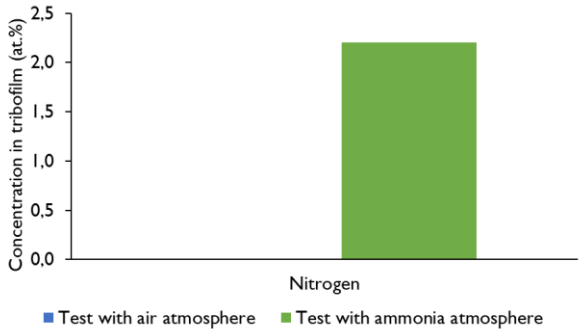

Figure 23: Nitrogen concentration in tribofilm measured with XPS

XPS analysis also makes it possible to measure the iron concentration at different depths. Thus, the thickness of the tribofilm can be estimated by identifying the depth at which the iron concentration stabilizes at a high concentration. In the case of the ammonia atmosphere test, the thickness of the

tribofilm is therefore estimated at approximately 30 µm, while for the air atmosphere test, the thickness of the tribofilm seems to exceed 70 µm as illustrated on Figure 24. Thus, ammonia seems to have a significant influence on the tribofilm thickness.

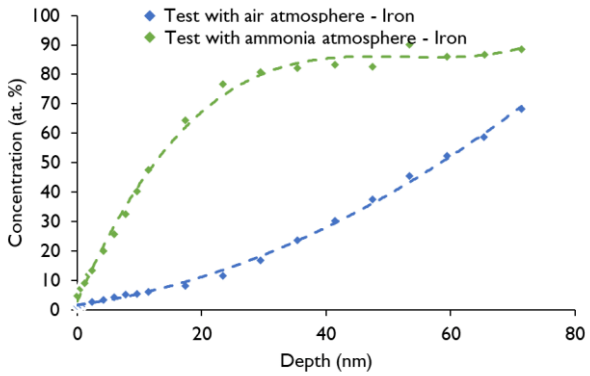

Figure 24: Iron concentration in tribofilm measured with XPS

Phosphorus and sulfur are constituents of the anti-wear additive that generally end up in the tribofilm. Figure 25 shows the phosphorus and sulfur concentrations for each tested atmosphere measured by XPS. In the case of the ammonia atmosphere, the concentration of phosphorus and sulfur decrease rapidly while the analysis is performed deeper. On the surface, the concentration can be higher compared to the reference test in air atmosphere. These results suggest an interaction of ammonia with the molecules present in the tribofilm.

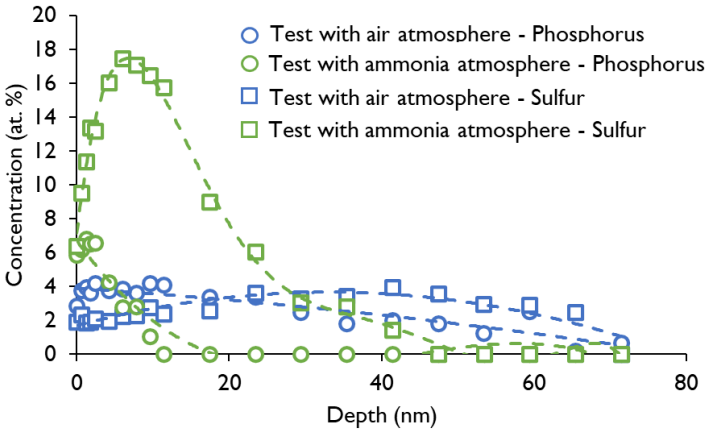

Figure 25: Phosphorus and sulfur concentrations in tribofilm measured with XPS

These results reveal an influence of ammonia on the wear sensitivity in the contacts of lubricated moving parts. The tribofilm seems to be altered, both in thickness and in its structure, suggesting a lower lubricating performance. As a consequence, engine wear protection in the presence of ammonia can set a challenge for the development of adequate ammonia engine lubricants.

3. Conclusions

The ageing of engine lubricant and engine wear protection performance were studied using a durability engine test, tribological testing and analytical techniques. A 250 h durability was developed on a 4-

cylinder Diesel engine retrofitted in dual fuel ammonia combustion mode. The use of 2 different engine lubricant technologies confirmed the possibility to mitigate wear phenomena through oil formulation. Standard oil analysis performed during the engine test did not reveal any significant ageing of the 2 lubricant technologies used. However, in-depth analytical techniques showed a total disappearance of the anti-wear additive and nitro-oxidation markers on the detergent molecules were observed. These phenomena are clearly limited with the lubricant B containing a new additive technology which also reduces wear and corrosion by more than 50% on the endurance test.

Furthermore, a new tribological test conducted under ammonia demonstrate the influence of ammonia on lubricated contacts, showing a degradation in the thickness and composition of the tribofilm.

Further studies will assess the degradation in composition and performance of the same lubricant when subjected to ammonia combustion as compared to Diesel combustion.

The new tribological test will be refined to consider atmospheres representative of the combustion gases and to evaluate molecules that enhance the tribofilm's resistance.

As experienced in this study, close collaborations between oil manufacturer and engine designer will allow concerted technical solutions to optimize the durability and performance of ammonia combustion engines.

Acknowledgement

The authors would like to thank their coworkers from Liebherr Machine Bulle, B. Seba for his expertise and great support in this collaboration, and their coworkers from TotalEnergies OneTech, C. Chalancon for the great support with samples preparation and laboratory testing, J. Crépier for the precious coordination of all analytical studies, as well as V. Doyen for her expertise and support.
Presented results were partially obtained in research projects with financial support from the participating project partners and the Austrian COMET program (Project InTribology, No. 872176 and No. 906860) at AC2T research GmbH. The authors wish to acknowledge the laboratory AC2T research GmbH for their contribution in the development of specific tribology tests, in particular, A. Agocs and C. Besser.

Literature

[1] Obrecht N., Griffaton G., Rappo M., "Lubricant Performance and Reliability of Ammonia Fueled Internal Combustion Engines", *2023 JSAE/SAE Powertrains, Energy and Lubricants International Meeting*, SAE 2023-32-0104.

[2] Machaj K., Kupecki J., Malecha Z., Morawski A.W., Skrzypkiewicz M., Stanclik M., Chorowski M., "Ammonia as a potential marine fuel: A review", *Energy Strategy Reviews, Volume 44, 2022*, 100926, ISSN 2211-467X

[3] Lhuillier C., Brequigny P., Contino F., and Rousselle C., "Combustion Characteristics of Ammonia in a Modern Spark-Ignition Engine," *SAE Technical Paper 2019-24-0237, 2019*, doi:10.4271/2019-24-0237

[4] MAN Energy Solutions, "MAN B&W two-stroke engine operating on ammonia", Nov 2020, On-line document (https://www.man-es.com/docs/default-source/document-sync/man-b-w-two-stroke-engine-operating-on-ammonia-eng.pdf?sfvrsn=c4bb6fea_2)

[5] Wartsila, "Wärtsilä launches new 4-stroke engine that can run on ammonia", September 9, 2022, F+L Daily, ISSN 2523-6539, on-line article

[6] Lhuillier C., Brequigny P., Contino F., Rousselle C. 2019. "Performance and emissions of an Ammonia-fueled SI engine with hydrogen enrichment", SAE Technical Paper 2019-24-0137

[7] Besser C, Agocs A, Ronai B, Ristic A, Repka M, Jankes E, McAleese C, Dörr N. 2019. "Generation of engine oils with defined degree of degradation by means of a large scale artificial alteration method." Tribol Int; 132: 39-49. https://doi.org/10.1016/j.triboint.2018.12.003.

[8] ASTM D7042–21. 2021. Standard Test Method for Dynamic Viscosity and Density of Liquids by Stabinger Viscometer (and the Calculation of Kinematic Viscosity). West Conshohocken: ASTM International

[9] ASTM D664-18e2. 2018. Standard Test Method for Acid Number of Petroleum Products by Potentiometric Titration. West Conshohocken: ASTM International

[10] ASTM D2896-21. 2021. Standard Test Method for Base Number of Petroleum Products by Potentiometric Perchloric Acid Titration. West Conshohocken: ASTM International.

Keywords: Ammonia, hydrogen, Dual Fuel combustion engine

Combustion concept for ammonia-fuelled cracker-engine-unit as propulsion system for inland waterway vessels

Annalena Braun[1], Torsten Baufeld[2], Dr. Sören Bernhardt[1], Dr. Heiko Kubach[1], Prof. Dr. Hinrich Mohr[3], Dr. Sascha Prehn[4]

(1) Karlsruhe Institute of Technology, (2) Liebherr Machines Bulle SA, (3) GasKraft Engineering, (4) University of Rostock

https://doi.org/10.18453/rosdok_id00004641

Abstract

The CAMPFIRE partner alliance is working intensively on the use of regeneratively produced ammonia as a maritime fuel and energy storage. In addition to topics relating to ammonia bunkering, refueling and storage for marine applications, one project proposal is the development of a pilot propulsion system for inland waterway vessels that operates exclusively on ammonia. The project consortium would like to present the potential but also the challenges of using ammonia in shipping based on the development of an innovative cracker-engine-unit with focus on the energy conversion of the internal combustion engine (ICE).

The paper and presentation will give an overview of the systematic combustion analysis on a SCE. The basis is a combustion concept with ammonia as the main fuel and hydrogen, cracked from Ammonia, as a pilot fuel. As a part of the experimental tests various fuel injection concepts (DI and PFI) for both fuels were investigated. For carrying out the tests the development of a new fuel injector concept was driven ahead. The experimental tests on the engines were supported by optical investigation on mixture formation with liquid ammonia as well 0D/1D and 3D simulation of the combustion chamber and SCE.

The various fuel injection configurations are evaluated for performance and emissions with the focus on maritime application. Resulting from the evaluation of the experimental data a preferred combustion concept was deduced for the planed multi-cylinder engine test at the Campfire Open Innovation Lab (COIL) near to Rostock.

1. Introduction

The goal of the CAMPFIRE[1] consortium is to research and develop new energy conversion and storage technologies based on green ammonia for the energy system of the future. A long-term objective is for small and medium-sized enterprises (SMEs) in the region of Northeast Germany to establish pathways for the utilisation of advanced technologies that can be exported to other areas. CAMPFIRE technologies produced in the Northeast will facilitate the development of an energy economy based on green ammonia and a carbon-free, secure energy supply in the Baltic Sea Region, in Europe, and abroad. In the long term, the consortium aims to develop effective and cost-efficient methods to reduce the global carbon dioxide levels in the Earth's atmosphere.

Maritime transport is an essential part of the global trading systems. Although it is the most efficient and climate friendliest transport method, worldwide shipping accounts for 3% of global CO_2 emissions. This demands a respective emissions reduction in parallel to all other polluters. For that reason, the IMO (International Maritime Organisation) has committed to achieve full climate neutrality for sea-going shipping until 2050. [1]

Due to the required operation ranges and limited volumetric and gravimetric storage capacity on board of vessels, pure electrification solution with batteries as energy storage are out of discussion for most shipping applications. As solution the use of alternative fuels based on renewable energies has highest priority. In this respect Ammonia is very interesting due to its possibility as Hydrogen carrier and CO_2-free local combustion.

The typical characteristic values of Ammonia compared to other fuels types are displayed in the following Table 1.

[1] https://wir-campfire.de/

Table 1: Fuel characteristics values

		Hydrogen	Methanol	Ammonia	eFuels (e-Diesel Fuel)	MDO	LNG
Molecular Formula		H_2	CH_3OH 	NH_3 	C_nH_{2n} n = 8 ... 20	C_nH_{2n} n = 8 ... 20	CH_4, C_3H_8 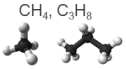
State of Aggregate @ 0°C, 1,013 bar	-	gaseous	liquid	gaseous	liquid	liquid	gaseous
Density @0°C, 1,013 bar	kg/m³	0,09 @ 15°C, 350 bar: 24 @ 15°C 700 bar: 40 Liquified -253°C: 71	792	0,73	approx. 890 (Diesel Fuel)	890 ... 900	0,72 Liquified -161 °C: 431 ... 464
Storage Conditions		Liquified: -245 ... -250 °C @13 bar Compressed: 350 bar / 700 bar @ ambient temp.	Ambient	Liquified: -34°C @ athm. pressure Gaseous: 10 ... 30 bar @ ambient temp.	ambient	ambient	Liquified: -161 ... -164 °C @ approx. athm. pressure
Boiling Point	°C	-253	64	-33	200	163 ... 399	-161
Lower Heating Value (gravimetric)	KWh/kg MJ/kg	33,3 120	5,5 20	5,2 19	11,9 43	11,8 approx. 42	13,9 50
Min. Ignition Energy	mJ	0,016	0,1	14	0,23	0,23	0,25 ... 0,28

In addition, the required gravimetric and volumetric storage density needs to be considered (see Figure 1). The figure shows that not only the fuel specifics are essential, but also the required containment technology.

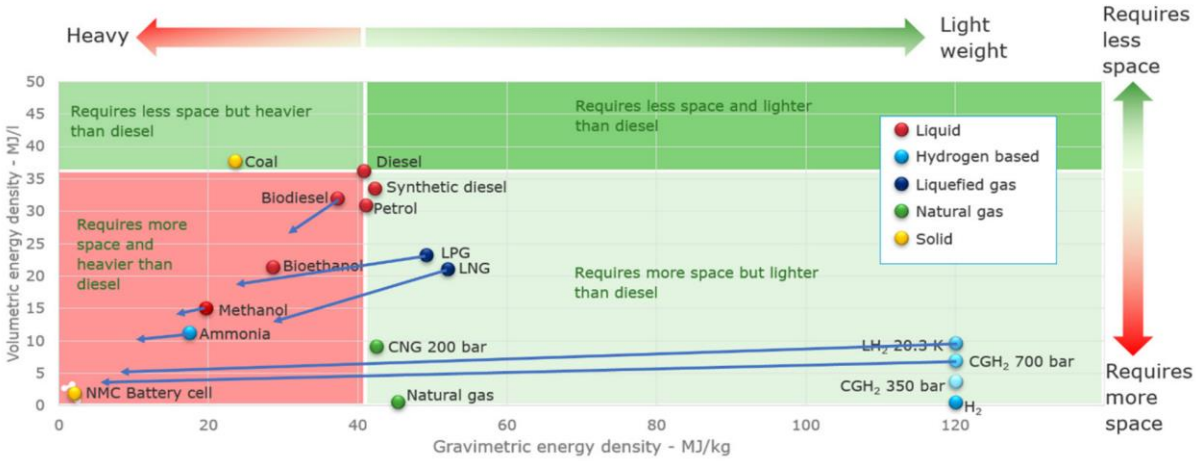

Figure 1: Energy densities for different energy carriers. The arrows represent the impact on density when considering the storage systems for different types of fuel (indicated values only) [2]

With this information plus the application type and operating profile as well as the intended operation range the configuration of a new built vessel fuelled by Ammonia can be executed. In case of a ship's retrofit to Ammonia operation the resulting restrictions can be defined accordingly.

The lower heating value of Ammonia is significantly reduced, compared to traditional fuels. But in comparison to Hydrogen, it offers the advantage that, depending on temperature, Ammonia is already present in liquid state at moderate pressures and temperatures (8,6 bar @ 20 °C). This results in a higher volumetric energy density compared to highly compressed or liquid Hydrogen. [3]

Other challenges with the use of Ammonia are related to material compatibility and interaction with lubrication oil, leading to further required investigation works. The safe handling of Ammonia during

bunkering, storage, and usage ashore and on board is another evident topic which needs high attention. This includes crew training concepts as well. [3]

Currently various developments for Ammonia-fuelled engines are ongoing. The first movers can be found in the slow-speed two-stroke segment as main propulsion for large seagoing vessels, followed by respective works on medium-speed four-stroke engines. In all that cases dual-fuel combustion concepts are utilized where the Ammonia is ignited by a Diesel pilot fuel spray and the Diesel operation mode is available as back-up option. The first and very few of these engines are expected to start field operation in 2025.

For high-speed four-stroke engines several developments are ongoing, e. g. for power generation purposes or inland waterway shipping within the CAMPFIRE alliance, but all far from end customer usage. Within these projects both dual-fuel and spark-ignited combustion concepts are under investigation.

Interestingly, recently a consortium in Japan and China claimed to finalize development of a car engine with Ammonia as fuel. [4]

The involvement in Ammonia-fuelled engine development showed, that a concentration on the engine development only is not sufficient. Due to the novelty the complete auxiliary systems around the engines and including the tank and fuelling infrastructure need engineering as this is not available as commodity. In this respect also, safety regulations must be developed and the respective processes need approval by the responsible authorities.

2. Application and Development Process

In this CAMPFIRE research and development project the focus is on inland waterway transport applications. An ammonia tanker (Figure 2) that mainly travels on the Rhine between Ludwigshafen and Rotterdam has been selected as the test vehicle for the field testing of the NH_3 cracker combustion engine.

Currently the ship is powered by an old diesel engine, which is now to be replaced by a hybrid drive consisting of the NH_3 engine, cracker, generator and electric motor connected to the propeller shaft (see Figure 2).

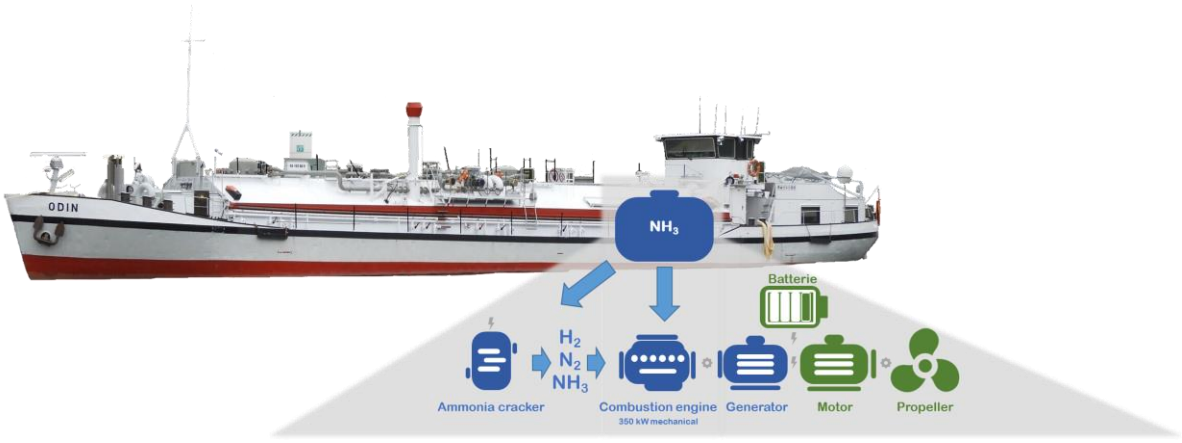

Figure 2: The hybrid drive, based on NH_3-engine, Cracker, generator, battery, e-motor and propeller that will be developed to integrate in inland water vessel MS ODIN.

The hybrid drive was chosen to enable redundancy in the drive and to obtain more flexibility of the drive. Legal safety requirements for an ammonia engine are not yet available. Nevertheless, measures have been defined in coordination with DNV to ensure the safety of the drive. This includes a separate room for the fuel tank and the battery unit and a ventilation concept for the entire area.

Currently, the operation and load profile of the ship is being recorded over a longer period of time using additional measuring technology. The recorded operating data is then used to examine and determine the efficient use of the hybrid drive. The characteristics of the combustion engine and the cracker must be considered, as well as features of the route (including the number of locks, water flow). The optimization of the hybrid drive should therefore contribute to a further increase in efficiency and a reduction in emissions.

However, before the engine is used in the ship, a number of development steps must be considered. A number of partners are involved in this CAMPFIRE research project, who contribute their specialist knowledge to the various tasks and enable the project to progress. In order to be able to evaluate different combustion concepts, determine their potential and test the necessary hardware, a methodology was defined that focuses on tests on the single-cylinder engine, which are accompanied by thermodynamic and CFD simulations (Figure 3).

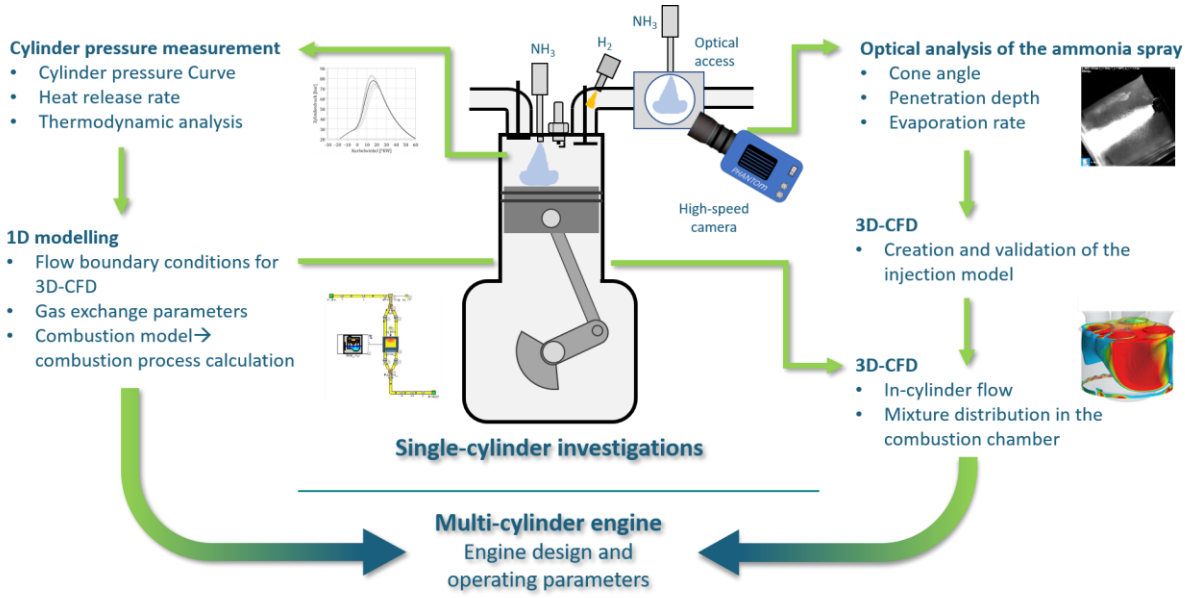

Figure 3: Development methodology for the combustion process

The single-cylinder engine (SCE), which runs on the test bench at KIT in Karlsruhe, was equipped with extensive measuring equipment. Since no knowledge of NH_3 injection was available, one of the first investigations was to visually examine the injection jet geometry and the evaporation of NH_3 with injection tests into the intake manifold. The results were important for the design and optimization of the NH_3 injectors and also for the design of the combustion concept.

Based on the experimental tests on the SCE models for the simulation of ammonia mixture formation and following combustion process are in development. These models represent the basis for setting up a multi-cylinder engine model that is used to derive basic requirements for the design of the full engine with regard to the turbocharger, the cooling system and the parameterization of the engine control unit.

3. Combustion Process Development

3.1. Testbed and Single Cylinder Engine

To allow proper single-cylinder engine monitoring and data acquisition of a wide range of relevant information for engine testing, the experimental activities were carried out in a fully instrumented testbench, as depicted in the scheme in Figure 4. The test engine is a single-cylinder unit based on the Liebherr D966 diesel engine. The cylinder head was modified so that a sleeve with spark plug can be fitted in place of the diesel injector. An injector for direct ammonia injection can be fitted in an additional bore in a lateral position. A specially manufactured intake manifold can accommodate both an injection valve for hydrogen and the ammonia injector. The relevant engine data are listed in Table 2.

The engine was coupled to a dynamometer to control load and speed. The in-cylinder pressure was measured by a Kistler 6045B piezoelectric pressure transducer in conjunction with a Kistler Piezo charge amplifier and referenced by an encoder with a resolution of 0.1 crank-angle degrees. A Kistler absolute pressure sensor was used to measure the intake pressure, exhaust pressure and fuel pressure of ammonia. The ignition settings were controlled by an SEM Multispark Control Unit (Default System). All the sensors above were connected to a Dewetron-800-CA high-speed data acquisition unit, allowing real-time combustion analysis using the Dewesoft software. Quantitative information about the combustion process and its cycle-to-cycle variability was obtained through a heat-release analysis from 100 consecutive cycles.

The fuel mass flow rate was measured through a Endress+Hauser coriolis flowmeter. The air mass was measured by a RMA rotary piston meter. A Bosch wide-band lambda sensor LSU 4.9, conditioned by an ETAS Lambda Meter LA4, determined the exhaust oxygen concentration. This allows the calculation of the air-fuel ratio. The concentration of HC, CO, CO_2, O_2 and NO_x on the exhaust were measured by an AVL AMA 4000. The concentration of NH_3, N_2O and NO_x on the exhaust were measured by a IAG FTIR and the H_2 in the exhaust was measured by a MS4 HSense.

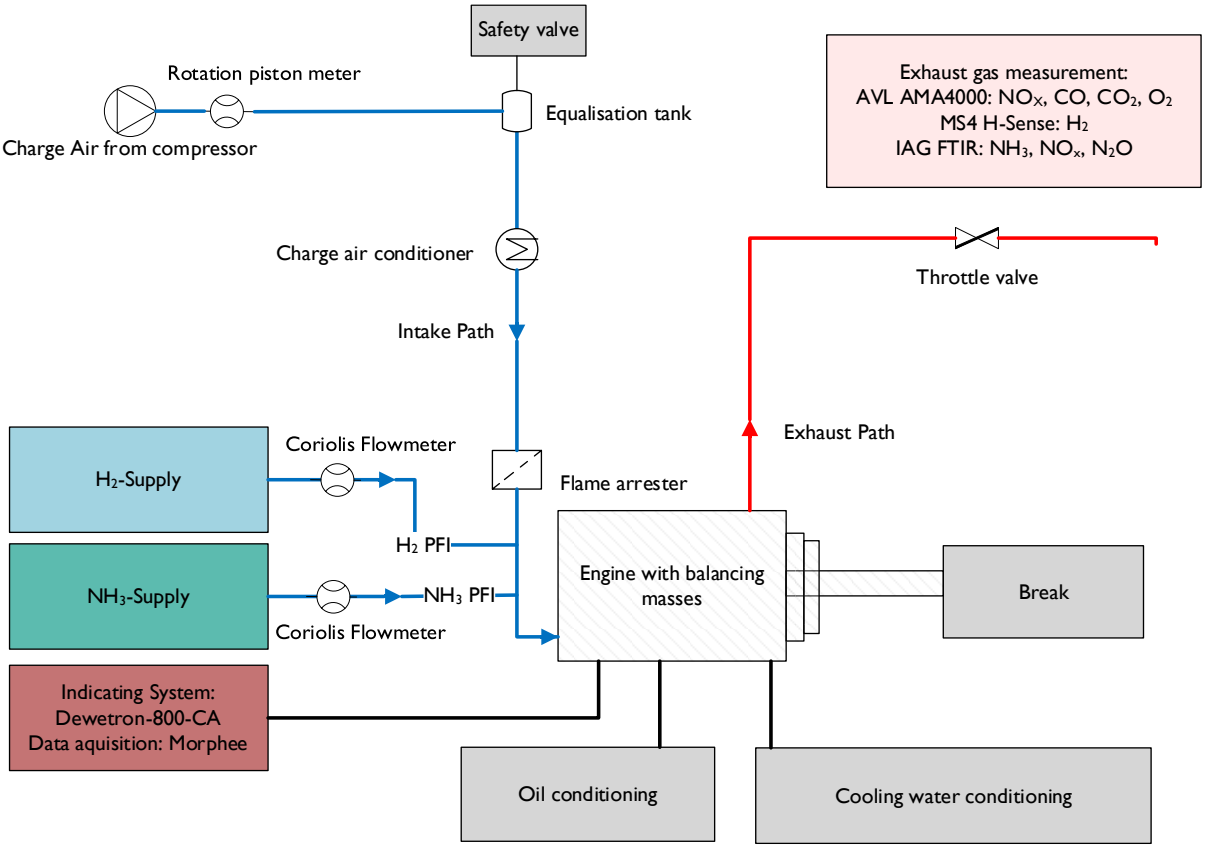

Figure 4: Scheme of the single-cylinder engine test bench

Table 2: Engine data

Cylinder	1
Stroke	157 mm
Bore	135 mm
Max. speed	1900 rpm
Operating principle	4-stroke SI
Displacement	2.24 l
Type	Modified Liebherr Diesel engine based on D966

3.2. Injection System Configuration

Ammonia and hydrogen were supplied from storage bottles. Hydrogen is supplied in gaseous form at a pressure of 300 bar at ambient temperature and can therefore be injected directly into the intake manifold via a pressure reducer using a hydrogen injector from Hörbiger. Most of the ammonia is in liquid form in the ammonia storage bottles. The pressure is a function of the ambient temperature via the vapour pressure in the bottles and is in the range of 2 to 8 bar. To achieve the desired injection pressure the ammonia must be compressed. For this purpose, a double-acting compressor station from Maximator was integrated, which can compress the ammonia up to 60 bar. The desired injection pressure is then set via a pressure reducer. The ammonia injector can be operated up to a pressure of 30 bar. In order to avoid pressure pulsations in the injection path, two Hydac membrane dampers

and two calming volumes were integrated into the injection pipes. The basic structure of the ammonia supply system is shown in Figure 5.

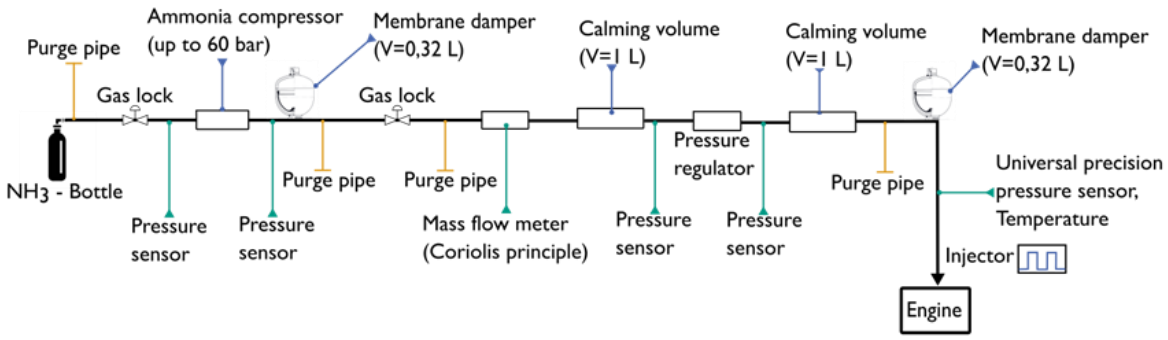

Figure 5: Ammonia infrastructure of the test bench

The DI injector from Liebherr can inject liquid and gaseous ammonia and gaseous hydrogen. The injection configurations shown in Figure 6 can be realised with the existing components. Hydrogen can be injected directly into the combustion chamber or into the intake manifold. In either case, the hydrogen is gaseous. Ammonia can be injected in liquid state into the intake manifold or directly into the combustion chamber by the Liebherr injector.

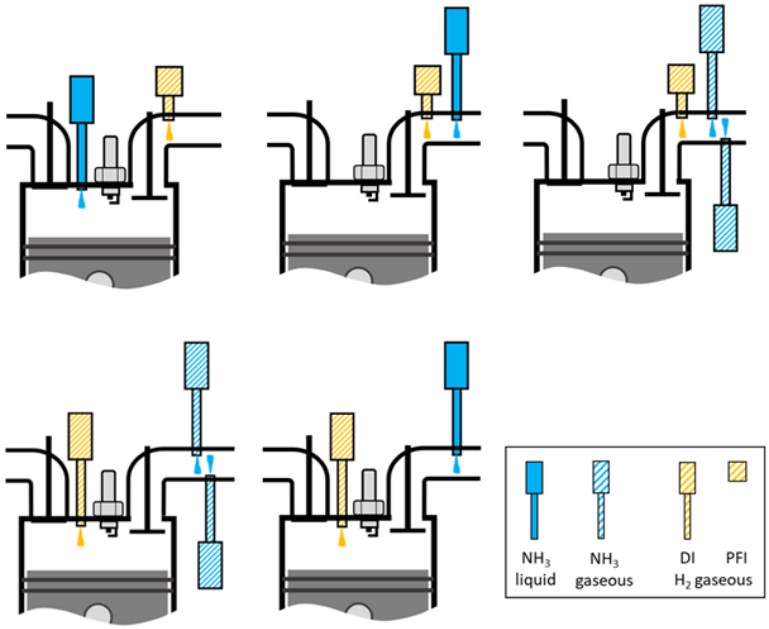

Figure 6: Injection configuration with J-Gap spark plug Combustion

The present study is divided in three sections: (I) the first one explores the behaviour of the combustion process and the emissions for different lambdas. The (II) second one shows a comparison between different compression ratios and the (III) last one shows the impact of a different ignition system.

(I) Lambda Variation

A lambda variation was carried out to determine the optimum operating conditions for the ammonia-hydrogen combustion. The combustion stability was limited to a COV of IMEP of 3%. The IMEP of this measurement was 17 bar at 88% energetic NH_3 share and 1500 rpm. Both fuels were injected in the intake path (PFI) of the single-cylinder engine. The objective during the operation was to find the lambda with the lowest COV of IMEP and the lowest emissions. Regarding a 100% hydrogen combustion a leaner lambda would be preferable because of lower NO_x emissions. In this combined NH_3-H_2-combustion process NO_x can be produced not only by the usual mechanisms such as Zeldovich mechanism but also from the ammonia fuel itself. This makes it important to know what influence lambda has on the generation of emissions during this combustion process.

Figure 7 shows the influence of the mixture composition on the combustion process. With a fuel air ratio of lambda higher than 1, the COV of IMEP increases. This means that the combustion stability decreases. This exacerbated cycle-to-cycle variability in reason of the mixture composition is caused by the deterioration of the flame development on its initial stages, leading to different combustion development, or in some cases, flame quenching. This is also the case when lambda is too rich. In terms of exhaust gas emissions, it is shown how the formation of nitrous oxide (NO_x) is greatly reduced as lambda is decreased, reaching the lowest emissions at lambda 0.9. With lambda smaller than lambda 1, the formation of NO_x decreases (logarithmic scale). The high vaporization enthalpy of ammonia leads to decreasing of the in-cylinder temperature and the lack of sufficient oxygen atoms below lambda 1 for the formation of NO_x lead to decreasing NO_x emissions. At the same time, hydrogen emissions increase, suggesting that ammonia decomposes into hydrogen in air-fuel-mixtures below lambda 1. Which is also shown by the decreasing NH_3 slip. The N_2O emissions decrease with decreasing lambda due to the lack of oxygen below lambda 1. In summary, it can be said that lambda has a major influence on emission formation and the combustion stability. The emissions can be controlled in a very targeted manner, also with regard to exhaust aftertreatment. Based on these results, lambda 1 operation was selected for further measurements. The trade-off between good combustion stability and low emissions is best here.

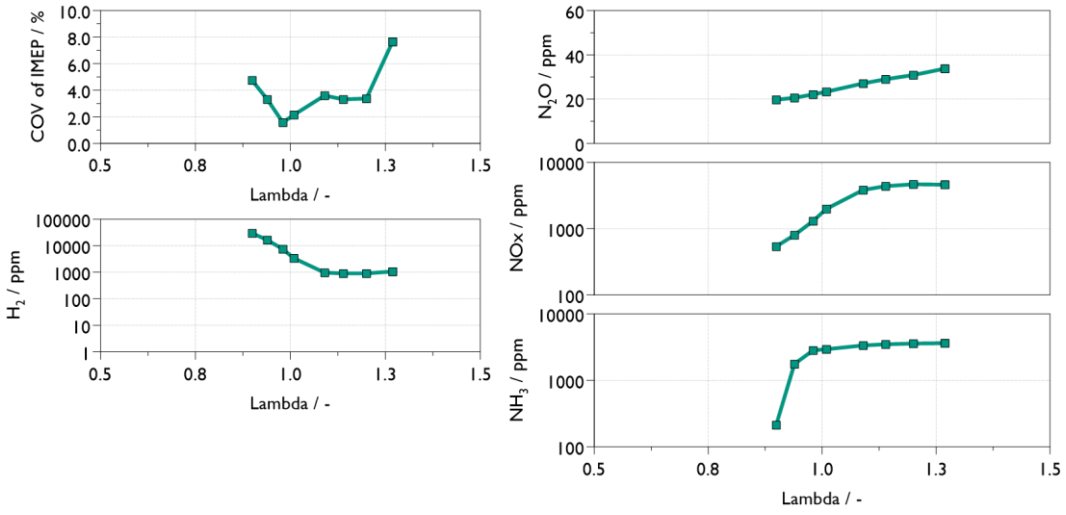

Figure 7: COV of IMEP and Emissions over Lambda at compression ratio 18.5 at 17 bar IMEP, 60 °C charge air temperature

(II) Compression ratio variation

The experiments were conducted by changing the compression ratio at lambda 1 in order to investigate the effect of a higher compression ratio on the maximum energetic NH_3 share. In this study knocking is characterized by a maximum knocking amplitude. The aim of the study was to get the maximum energetic NH_3 share.

In Figure 8 the impact of the COV of IMEP over the energetic NH_3 share for three different load points is shown. With increasing compression ratio, the energetic NH_3 share increases. The combustion process has two different limiting factors. The first limiting factor is the COV of IMEP it must not exceed 3 %. This criterion becomes critical if the ammonia content is too high. When the ammonia content of the mixture is too high it leads to an increase of the COV of IMEP resulting from a poor and late combustion. That means the combustion process gets unstable. The second limiting factor is the knocking criterion. This criterion is reached when too much hydrogen is injected. This behaviour is reinforced with increasing compression ratio.

For CR 14 to 18.5 the engine could be operated at all load points. The ignition timing was always set so that the mfb 50% is in the range 8±1° CA after TDC. A more precise adjustment of the mfb 50% during engine operation is not practicable, as the mfb 50% would be strongly influenced by slight deviations in the NH_3 share when readjusting the load and too many iterations would be necessary. Only at the operating point IMEP = 22 bar with a compression ratio of 18.5 did the mfb 50% have to be set to 12° CA after TDC in order to avoid exceeding the permissible peak pressure. With the highest CR of 22 it was not possible to reach fullload with 22 bar IMEP because the peak pressure was above the limit even with reasonable late adjustment of mfb 50%. The efficiency and energetic NH_3 share predominate for CR 17.

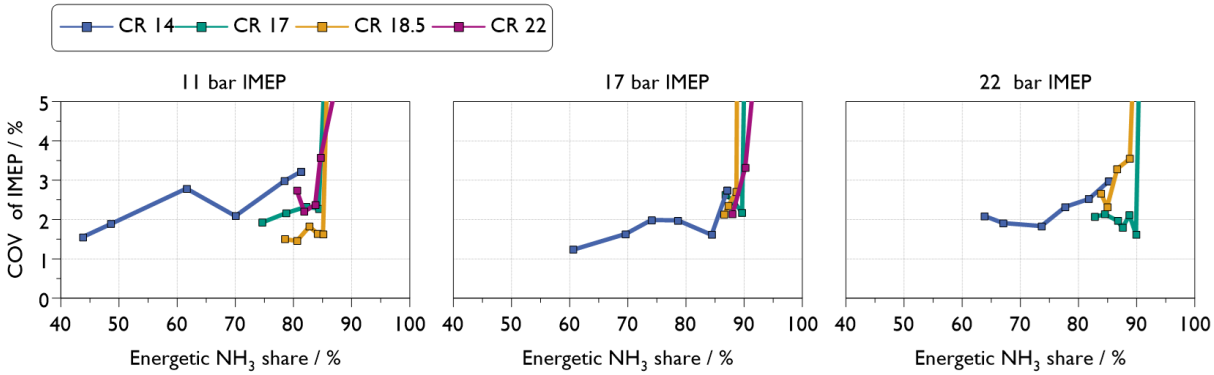

Figure 8: COV of IMEP over the energetic NH_3 share for different compression ratios at Lambda 1, 40 °C charge air temperature

Figure 8 shows cylinder pressure curves at IMEP of 17 bar for the variation of the compression ratios at maximum H_2 content, at maximum NH_3 content and in between at stable combustion behaviour with small COV of IMEP. Each curve is from a single combustion cycle. To illustrate the range of fluctuations, the dashed line shows the cycle with the lowest peak pressure and the solid line the cycle with the highest peak pressure from a measurement with 100 consecutive cycles.

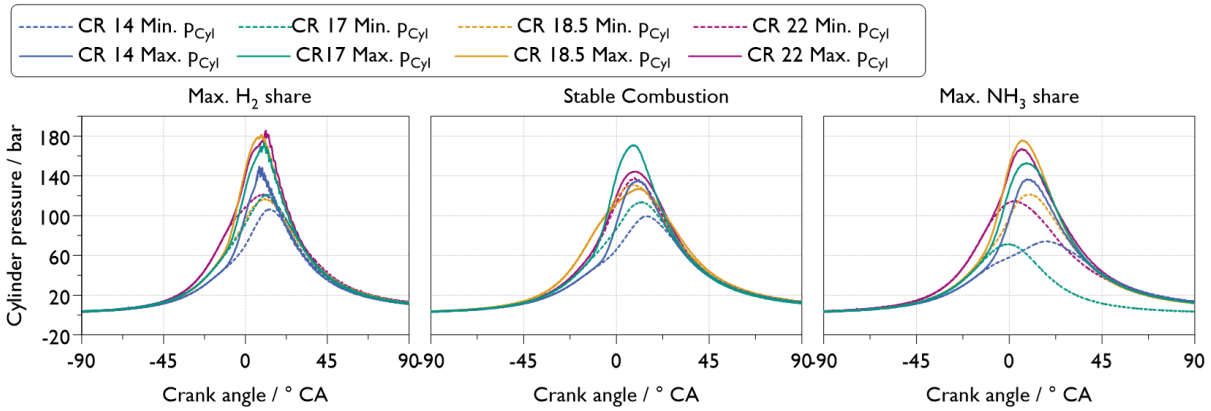

Figure 9: Cylinder pressure over crank angle for different compression ratios at 17 bar IMEP, Lambda 1, 40 °C charge air temperature

The left-hand diagram in Figure 9 shows that in all cases knocking combustion limits the maximum H_2 content. The permissible peak pressure of 220 bar is not reached. The maximum NH_3 content is limited by exceeding the COV of IMEP of 3%. In some cases, very late combustion phasing occurs, such as with CR = 14, or even misfiring, such as with CR = 17 and 22. This is related to the poor flammability and low laminar flame speed of ammonia. The "stable" range in between still has COV of IMEP values significantly greater than 1. For example, the fluctuation range of the peak pressure per cycle at CR = 17 is approx. 55 bar (corresponding to 32% of the maximum peak pressure). A further reduction in the COV of IMEP would be desirable for commercial applications.

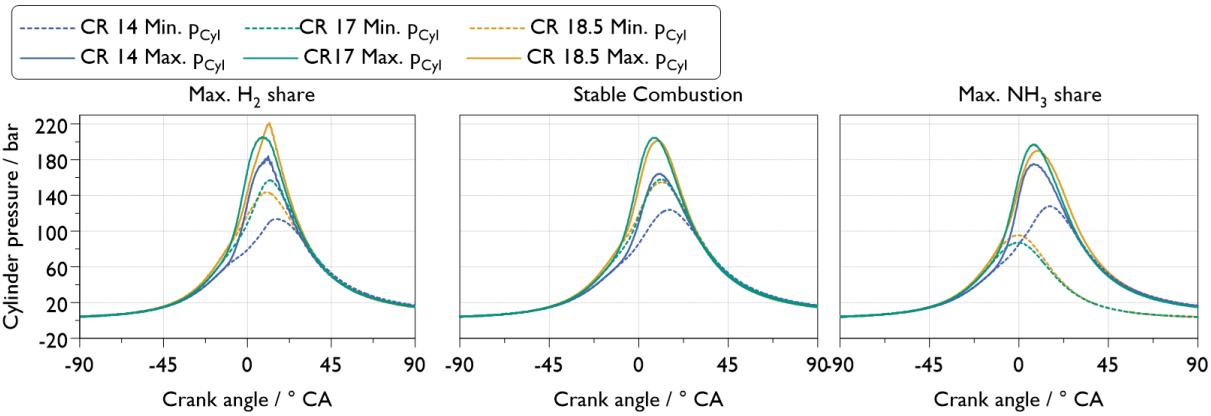

Figure 10: Cylinder pressure over Crank angle for different compression ratios at 22 bar IMEP, Lambda 1, 40 °C charge air temperature

Figure 10 shows the same as in Figure 9 but for the fullload conditions at 22 bar IMEP. There is no significant deviation in the behaviour in the stable range and at the limit of the maximum NH_3 content. With the latter, as with 17 bar IMEP, late combustion phasing and misfires occur, which prevent a further increase in the NH_3 content. At a compression ratio of CR = 14, the limiting factor is also the occurrence of knocking combustion, as in Figure 9. As Figure 11 shows, the maximum knocking amplitude reaches almost 5. At compression ratios 17 and 18.5, the permissible peak pressure of 220 bar is exceeded before knocking of a similar intensity to that at CR = 14 occurs, which is the limiting factor. It is not possible to operate the engine at the compression ratio CR = 22 at 22 bar IMEP due to peak pressures being exceeded in the entire NH_3 range.

The knocking in Figure 11 is calculated out of a high-pass filtered cylinder pressure signal. The software divides the high-pass filtered signal after combustion by the high-pass filtered signal before combustion. When there is no knocking the result of this equation is 1. When the combustion starts to knock the result of this equation increases. The limiting maximum knocking amplitude was set to 4. The limiting maximum knocking amplitude of 4 is not achieved for both CR 17 and CR 18.5. The peak pressure of the engine must not exceed 220 bar. The measurement has to be stopped because of the peak pressure for CR 17 und CR 18.5 which is shown in Figure 11 (right). CR 17 und CR 18 exceeded the peak pressure at around 82% energetic NH_3 share. The maximum knocking amplitude in this point is comparatively low, but it is still sufficient to exceed the peak pressure limit of the engine.

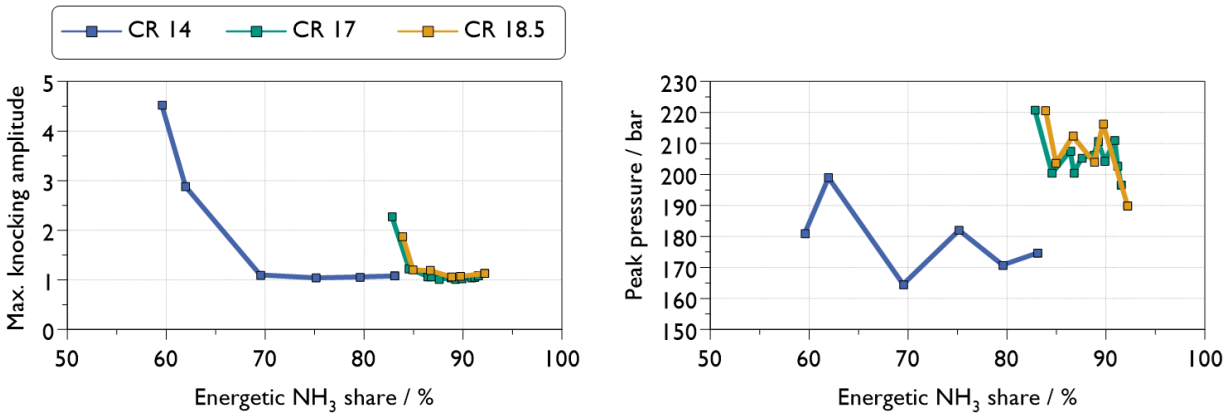

Figure 11: Left) Maximum knocking amplitude over the energetic NH_3 share at 22 bar IMEP, Lambda 1, 40 °C charge air temperature
right) Peak pressure over the energetic NH_3 share at 22 bar IMEP, Lambda 1, 40 °C charge air temperature

Figure 12 shows the total heating value and the net heat release rate for different compression ratios at 17 bar IMEP and 85% energetic NH_3 share. These are the mean values of each measurement with the lowest COV of IMEP to compare the velocity of the combustion. With the CR 18.5, a slightly faster burn-through can be recognised. However, the combustion processes differ only insignificantly. The compression ratio therefore has only a minor influence on combustion rate. The efficiency analysis in Figure 13 comes to the same conclusion, that on the one hand the increase in compression has only little effect on the efficiency and on the other hand the influence on the energetic NH_3 share is small. This means that by increasing the compression ratio not significantly more energetic NH_3 share can be driven. The negative part of CR 22 is a combination of increased wall heat losses and blowby.

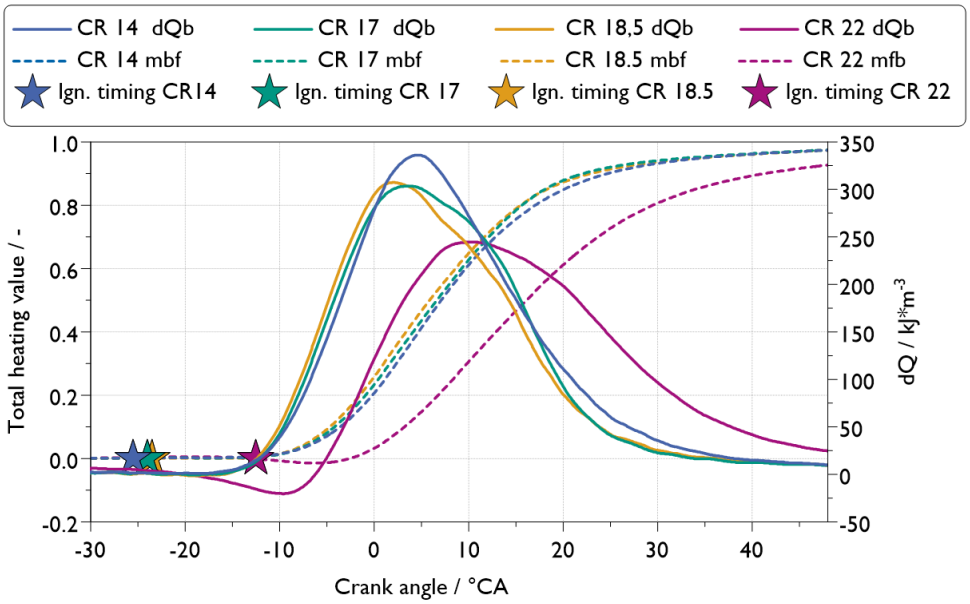

Figure 12: Total heating value, net heat release rate and ignition timing over crank angle for three different compression ratios at 17 bar IMEP, Lambda 1

If one first looks at the Figure 13 on the right, an increase in efficiency with load can be seen. At higher loads, significantly higher pressures and temperatures occur in the combustion chamber, which improve both the ignition and the decomposition of the ammonia and thus the burn-through behaviour. Both lead to the increase shown.

The dependence of the efficiency on the compression ratio is not uniform and not significant at higher loads. The diagram on the right-hand side shows values at maximum NH_3 share. The engine would not be operated directly at this limit. If looked at the full load point of 22 bar IMEP above the NH_3 share, the left-hand diagram is decisive. As shown in Figure 14, the possible NH_3 range at compression ratios 17 and 18.5 (22 is not possible here) is extremely narrow. The centre of the NH_3 range between the two limits is around 87% (red line). The difference in efficiency between the two compression ratios is in the range of the line thickness and can be neglected. As the pressure and temperature load on the engine are somewhat lower at CR = 17 (see Figure 15) and the knock susceptibility is also somewhat more moderate, the lower compression ratio would even be preferable.

As the right-hand side of the limit range is exceeded "more gently" with a compression ratio of 14 and the COV of IMEP does not rise as abruptly as with the higher compression ratios (see Figure 8), the engine could at least be operated very close to this limit. However, the efficiency would be one percentage point lower here and the running smoothness would be somewhat worse in principle. Overall, CR = 14 would therefore be unfavourable.

Somewhat surprisingly, the curve for CR = 22 is the lowest for the drivable load points, although mfb 50% and mfb 90% have the same values as at the other compression ratios. For a conclusive explanation, these operating points would have to be analysed in more detail. However, this was not done, as CR = 22 is out of the question for a real application due to the lack of full load capability.

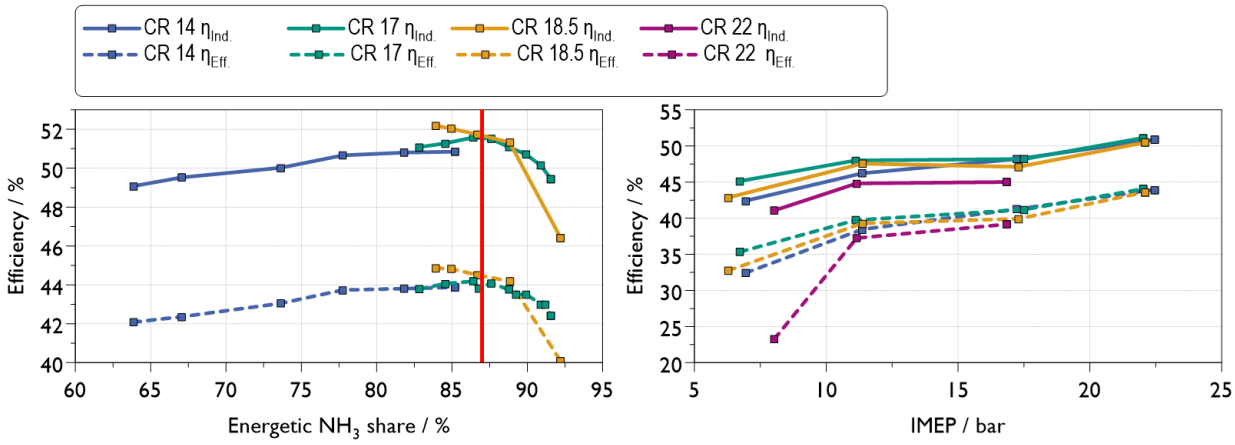

Figure 13: Indicated and effective efficiency a) over the energetic NH_3 share at 22 bar IMEP, Lambda 1 and 40 °C charge air temperature. b) over IMEP for the highest possible energetic ammonia share with a COV below 3%

Figure 13 shows the NH_3 range in which the engine can be operated for various loads and compression ratios. As mentioned, the limiting factors are a max. COV IMEP of 3%, a max. peak pressure of 220 bar, a max. exhaust gas temperature of 650 °C and a max. knock amplitude of 4 bar. The respective termination criteria are discussed in more detail in Figure 15. The basic aim is to operate the engine with the highest possible proportion of NH_3 - ideally without any addition of hydrogen.

The results show that pure ammonia operation is not possible, as the cyclical fluctuations increase sharply or combustion misfires also occur. The left-hand limit of the NH_3 range (max. possible H_2 share) should not actually be approached. However, it is important because it defines the width of the possible operating range. In the application presented in Chapter 2, the hydrogen mass flow is made available via a cracker unit. The actual mixing ratio of hydrogen and ammonia is therefore also dependent on the controllability of the cracker unit. A very narrow operating range with regard to the possible ammonia content places high demands here in order to avoid both misfiring and knocking in real operation at all times. In addition to the highest possible NH_3 content, the secondary objective is therefore also a sufficiently wide operating range.

A significant step in the right-hand limit of the operating range can only be observed for all loads when the compression ratio is increased from 14 to 17. This is most noticeable at the load of IMEP = 11 bar. From a compression ratio of 17, the trend is no longer clear. The shifts in the right-hand limit as a function of the compression ratio are marginal at 11 and 17 bar IMEP and almost within the range of measurement inaccuracy due to the determination of the relatively small hydrogen mass flow. For real operation and the design of the multi-cylinder engine, these dependencies are negligible. A preference as to whether CR = 17 or 18.5 should be selected cannot be derived from these measurements at these loads. At full load, however, the right-hand limit at CR = 17 is at a significantly higher NH_3 share. CR = 14 is unfavourable due to the significantly lower maximum NH_3 content and the lower efficiency. CR = 22 is unsuitable as full load operation is not possible. If looked at the width of the operating range, this is greater for CR = 17 at a load of IMEP = 11 for all loads, and even significantly greater at full load. At IMEP = 17 bar, the range is still larger but the difference is no longer as pronounced. From this point of view, a compression ratio of CR = 17 would therefore be the better choice.

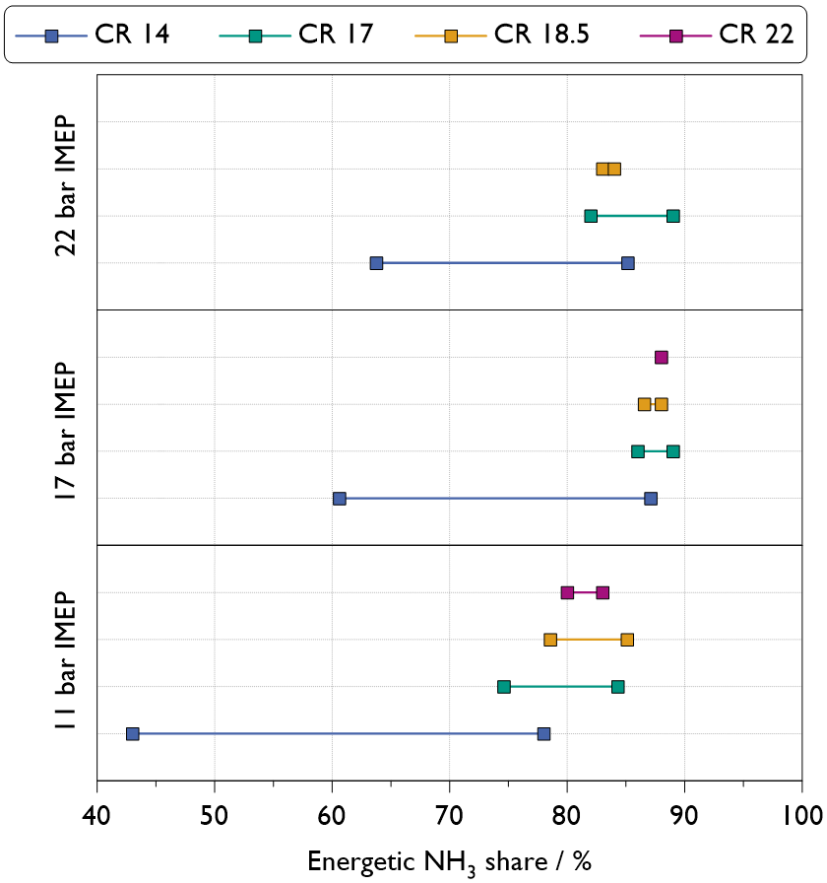

Figure 14: Possible energetic NH_3 range as a function of the compression ratio at different loads

Figure 15 shows the values of the termination criteria at full load relative to their upper limit ($T_{Ex.gas}$ = 650 °C, COV = 3% and Peak Pressure = 220 bar) and the target parameters (Max. NH_3 share = as high as possible, Achieved Load = 100%, Ind. Eff. = as high as possible) at the right operating range limit. It can be seen that the maximum exhaust gas temperature is never reached even at full load at all compression ratios and can therefore be categorised as uncritical. The peak pressure also has no limiting effect. In all cases, the maximum NH_3 content is defined by exceeding the limit value of 3% for the COV IMEP. The highest possible NH_3 content is reached at CR = 17 with 89%. At CR = 18.5, the indicated efficiency is one percentage point higher than with the two lower compression ratios. However, the better values with regard to the range of the possible NH_3 share at CR = 17 outweigh this efficiency advantage. The full load of 22 bar IMEP was also achieved for all compression ratios.

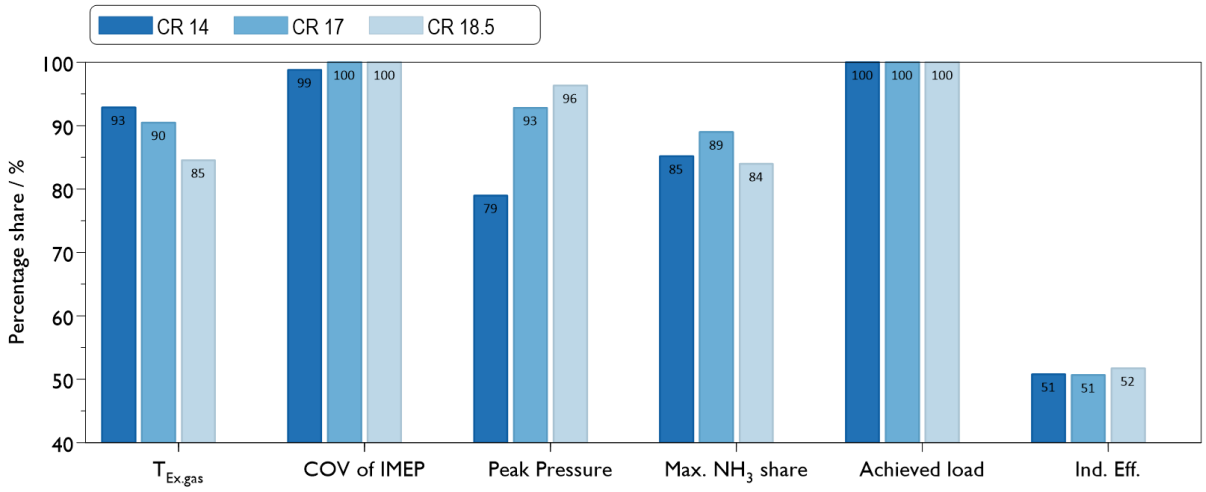

Figure 15: Termination criteria (relative to their limits: maximum exhaust gas temperature: 650 °C, maximum COV of IMEP: 3%, maximum peak pressure: 220 bar) and target parameters (max. NH_3 share and efficiency: as high as possible, load: 100% = 22 bar IMEP) for different compression ratios at 22 bar IMEP

In Figure 16, the emissions are plotted against the NH_3 share. The values for ammonia are at a relatively high level and initially increase significantly for CR = 14 from low to high NH_3 share in the fuel. In the possible operating range for CR = 17 of 82 to 89% NH_3 share determined according to Figure 14, the emissions are at an almost constant level of around 8 g/kWh. A drop in NH_3 slip immediately after exceeding the right-hand operating range limit must be assessed critically. If the sharp increase in cyclical fluctuations in reality leads to a sharp increase in NH_3 slip and the measuring device (FTIR) exceeds the measuring range limit, this measured value is taken into account in the internal averaging of the FTIR with zero and only leads to an apparent decrease in NH_3 slip. With the favoured compression ratio of CR = 17, the NO_x emissions are also at a similar level, albeit somewhat higher with values of 9 to 12 g/kWh. Exhaust gas aftertreatment to achieve permissible emission values is therefore essential.

However, the similar level of NH_3 and NO_x is an advantage. The ammonia contained in the exhaust gas can be used directly as a reducing agent in a SCR system. For a maximum conversion rate, a ratio of ammonia to nitrogen oxides of 1:1 should be aimed for [5]. The raw emissions are at least close to this ratio. In further planned tests with a real exhaust aftertreatment system, it is to be investigated whether and how much additional reducing agent must be injected in order to achieve the NO_x target values. Another open question is the cold-start efficiency of the exhaust gas aftertreatment system. Laughing gas is also clearly measurable as a raw emission in the exhaust gas with values of 0.07 to 0.15 g/kWh. These values can increase further in a downstream SCR system. This aspect must also be taken into account when designing the exhaust gas aftertreatment system. Hydrogen emissions are dependent on the compression ratio. Hydrogen in the exhaust gas is not only present as slip from the hydrogen share supplied, but also through the unburnt portion from the decomposition of ammonia. This takes place more efficiently at higher temperatures and therefore at higher compression ratios and leads to the observed increase with the compression ratio.

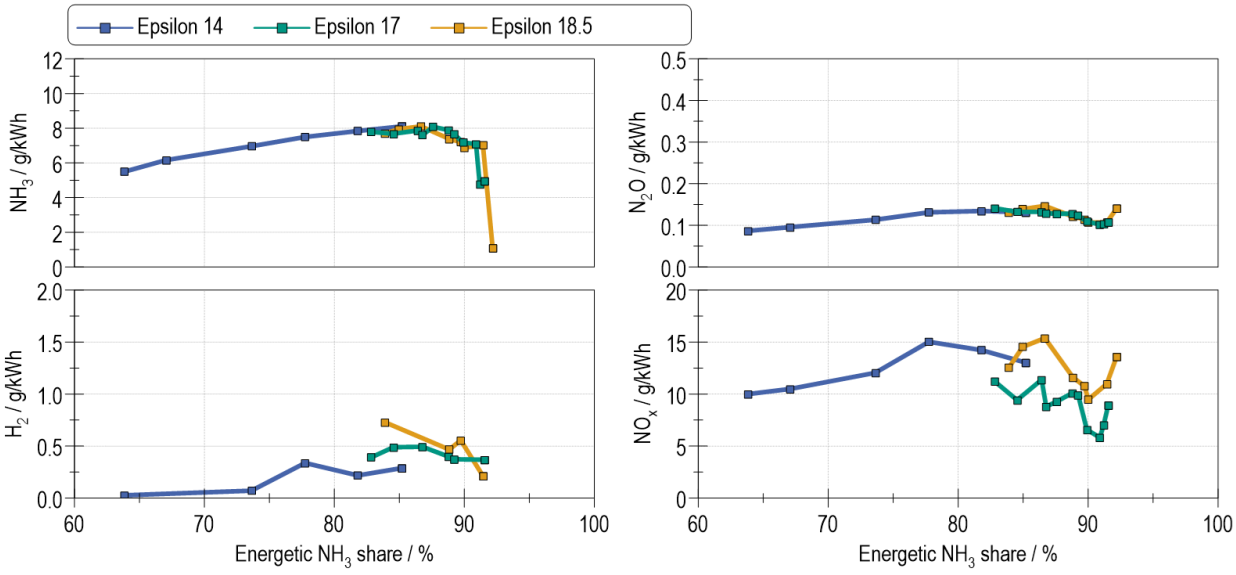

Figure 16: Emissions over the energetic NH_3 share for different compression ratios at 22 bar IMEP, Lambda 1 and 40 °C charge air temperature

(III) Variation of the ignition system

Another measure to increase the possible NH_3 content can be the selection of a suitable ignition system. The ignition energy and ignition phase are decisive factors for good combustion with low cyclical fluctuations. Independent of the ignition parameters themselves, combustion can be significantly improved by the mixture formation. Firstly, the correct local lambda must be present at the spark plug; this can be achieved either by good homogenization or targeted stratification. Secondly, cyclical fluctuations of the local lambda at the spark plug must be prevented. If a constant lambda cannot be guaranteed, then the ignition energy has to be further increased so that a reliable ignition occurs even in the worst case. The measurement presented in this chapter shows the influence of a higher ignition energy on the ammonia-hydrogen combustion process. A new ignition system from the company SEM was used for this purpose. This made it possible to adjust the spark duration and the spark current variably. The longer duration of the spark increases the probability that ignitable mixture will flow past the spark plug and ignite. The configuration of the engine for this measurement was ammonia and hydrogen via port fuel injection, ignited by a J-Gap spark plug at compression ratio 18.5.

The ignition current was measured on the primary side using a current clamp. The standard ignition system produces a single current peak for a single ignition spark (Figure 17 right). With the SEM Flexispark ignition system, it is possible to generate a longer ignition spark over several degrees of cranking angle (Figure 17 left). This increases the probability that an ignitable mixture comes close to the spark plug and can be ignited. With the capacitive Flexispark system, the ignition spark voltage, the ignition spark burning time and the ignition spark holding current can be variably adjusted. The Flexispark ignition system recognizes when a spark fails, then the capacitor discharge is switched off and the current is regulated by the plasma to a target value until it is switched off after a set time interval. This always triggers a spark and eliminates the excess current, which reduces spark plug wear [6]. The current is set in the closed control loop to values in 50 to 200 mA and the duration in 40 to 3000 μ s, which leads to spark energies in 2 to 150 mJ. This capacitive ignition system does not necessarily lead to increased wear of the spark plug. With a suitable choice of current and control duration, the ignition spark can be maintained in the low-wear glow discharge.

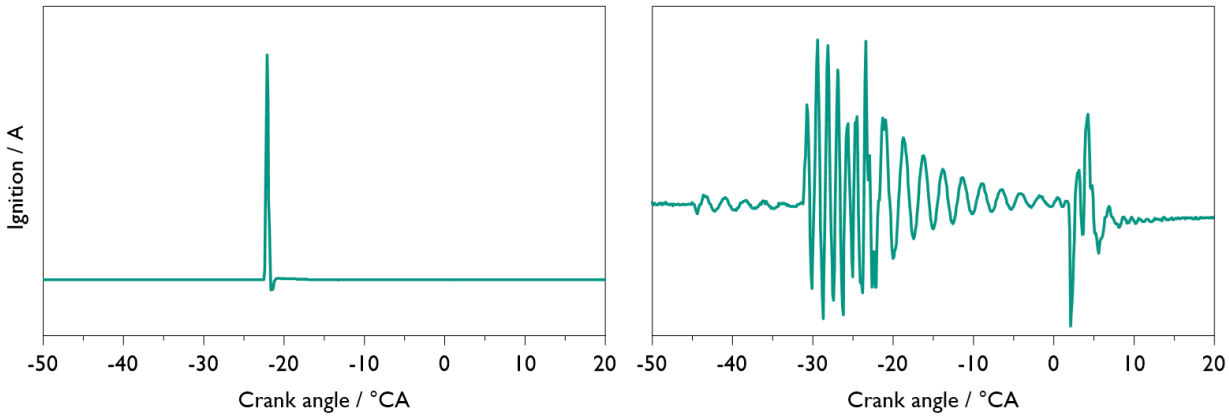

Figure 17: Ignition signal measured on the primary side with a current clamp.
left) Default inductive system with a single spark right) Capacitive Flexispark system with a multi spark ignition

At a compression ratio of 18.5, a full load point and a part load point were compared. The measurements were taken at Lambda 1 and an intake temperature of 40 °C. In Figure 17, top left, the COV of the IMEP is plotted against the energetic NH_3 share. At 11 bar IMEP, the limit was around 85% energetic NH_3 share; at 22 bar IMEP, 91% energetic NH_3 share could be realised. With the Flexispark ignition system, it was possible to completely eliminate the hydrogen and realise a 100% ammonia combustion process with a COV of IMEP below 3%. In general, combustion stability has been improved with the Flexispark ignition system.

Figure 18 shows the stabilization of combustion and its associated consequences. In the medium load range at 11 bar IMEP, the same COV of IMEP is achieved within the previously permissible range of the NH_3 share. However, there is no longer a limit on the maximum NH_3 share. Up to pure ammonia operation, the COV of IMEP only slightly increases from 1.6 to 2%. At full load at 22 bar, the COV of IMEP is even significantly better across the entire operating range compared to the previous ignition system. A 100% ammonia operation is also possible. The efficiency does not change at either load and continues to show a slight downward trend up to pure ammonia operation.

Initially, it may be surprising that at full load the efficiency does not increase despite the significant reduction in cyclic variations. The reason is evident from the diagrams on the ignition timing, the mfb50, and the maximum cylinder pressure (Figure 19). The improved combustion process would lead to an exceedance of the permissible peak pressure in at least some cycles if the mfb 50% remained the same. Therefore, for safety and comparability reasons, the peak pressure for both ignition systems were kept approximately constant. This required delaying the combustion timing. The center of combustion was shifted by about 2 to 3° CA, which is thermodynamically disadvantageous in principle. Thus, the efficiency remains "only" constant, even though the cyclic variations could be reduced.

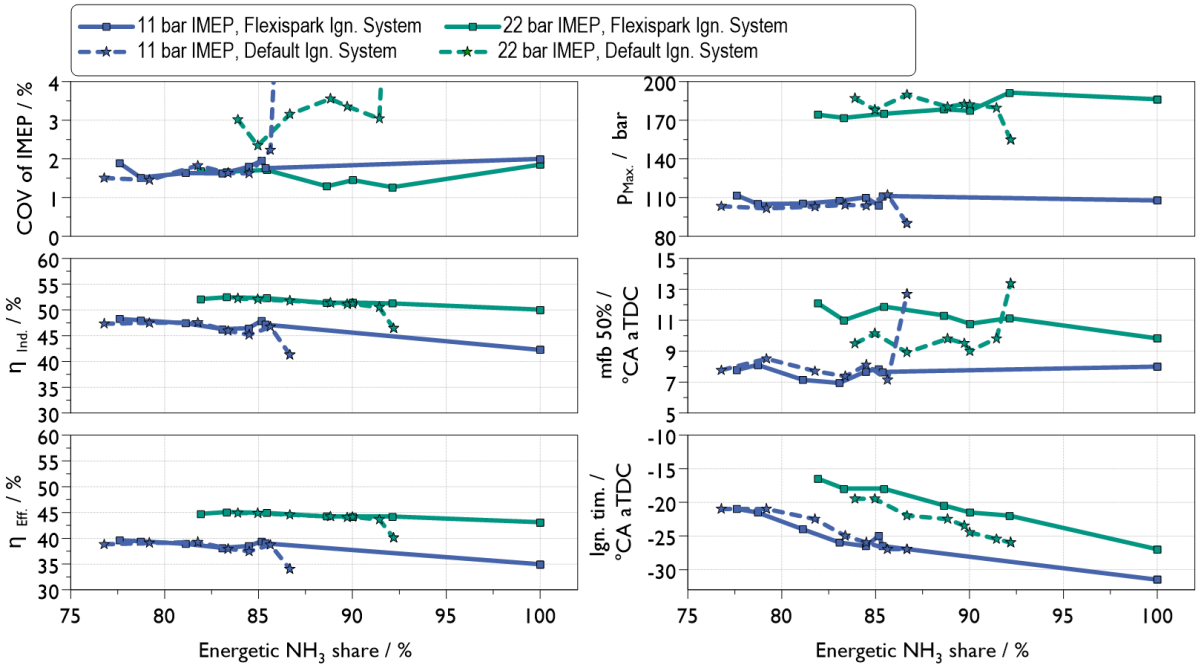

Figure 18: Comparison of the ignition systems. COV of IMEP, indicated efficiency, effective efficiency, peak pressure, mfb 50 % and ignition timing over the energetic NH_3 share for 50% and 100% load at CR 18,5, Lambda 1 and 40 °C charge air temperature

The following Figure 19 and Figure 20 describe the improvement in combustion behaviour. Figure 19 shows 100 consecutive combustion cycles for the original and the Flexispark ignition system vs. the load. Ignition timing and start of combustion (mfb 10%), center of combustion (mfb 50%) and end of combustion (mfb 90%) are shown. The ignition timing is constant for all 100 cycles. To demonstrate the advantage of the Flexispark ignition system, operating points were plotted with an NH_3 share at which significant cyclical fluctuations already occurred with the conventional ignition system.

The ignition points are set in such a way that, in the stable operating range, combustion centers of approx. 8° CA a. TDC occurred. With the Flexispark ignition system, the mfb 50 % could be kept constant. A significantly smaller combustion delay can also be recognised, which, with the exception of 22 bar IMEP, also exhibits smaller fluctuation ranges. This also applies to mfb 50% at all loads and in particular to the end of Combustion at mfb 90%. The difference in the fluctuation range is most pronounced here. The stabilisation of the ignition phase therefore has a positive influence on the entire combustion process and is ultimately responsible for the fact that operation with pure ammonia is possible.

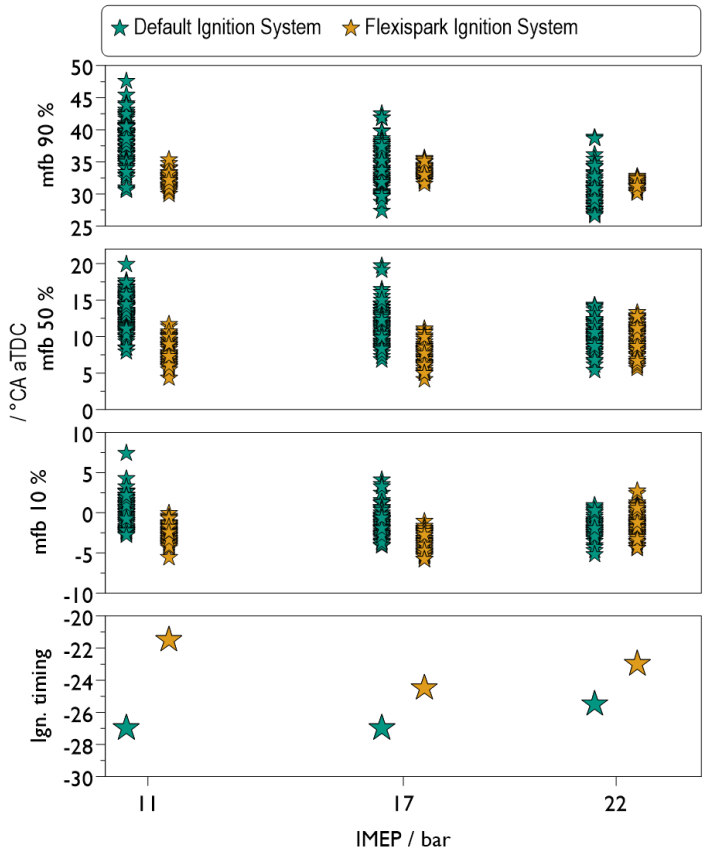

Figure 19: Comparison of the ignition timing, mfb 10%, mfb 50%, mfb 90% over the IMEP for the default und Flexispark ignition system at Lambda 1.

Figure 20 shows the operating point IMEP = 17 bar from Figure 19 in more detail. On the left, the mfb 90% is shown above the mfb 10%. As already described, the fluctuation range in both variables is generally smaller with the Flexispark system. However, a comparison of the two values also shows that with the Flexispark system, later mfb 10% does not lead to a later end of combustion to the same extent. Overall, the combustion process is much more stable and less subject to cyclical fluctuations. With the conventional ignition system, the green dots show a clear tendency for a late end of combustion to correlate with a large combustion delay. This means that difficulties with ignition continue throughout the entire combustion process. The combustion process has a stable overall shape, but shifts analogue to the start of combustion. The overall slower combustion process can be clearly seen in the right-hand diagram in Figure 20. The average value over all 100 cycles is shown here.

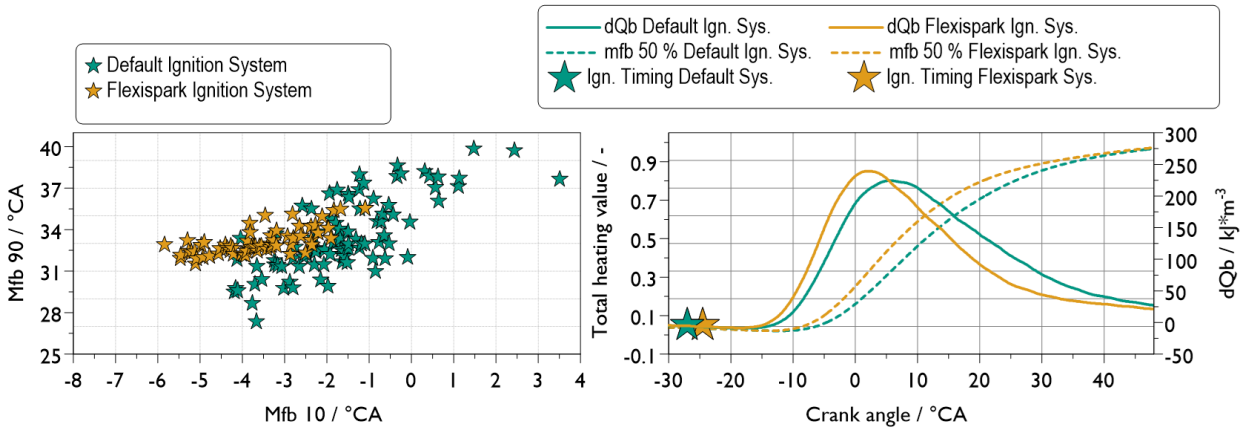

Figure 20: a) Comparison of mfb 90% over mfb 10% for the default and Flexispark ignition system at 17 bar IMEP, Lambda 1 and 92% energetic NH_3 share b) Total heating value and net heat release rate over crank angle for the default and Flexispark ignition system

4. Summary and outlook

The urgent evidence to reduce CO_2 emissions in all areas demand the quick realization of respective solutions for the worldwide shipping branch both for sea-going and inland waterway vessels. Therefore, several options are viable, most of them based on green e-fuels. Ammonia, produced on basis of renewable energies e. g. solar and wind power, looks as a promising candidate for shipping as worldwide trading and handling are already in place which eases the establishment of a fuel supply chain.

The presented project handles the development of a maritime propulsion system based on a cracker-engine-unit for inland waterway vessel application. Within this presentation the technological aspects for establishing such system concept were discussed. Special focus is set here on the combustion concept development on a single-cylinder research engine as basis for the upcoming multi-cylinder engine setup.

As ammonia requires a very high ignition energy compared to conventional fuels, which cannot be readily provided by most conventional ignition systems, measures to improve ignition are necessary. In this case, this is achieved by adding hydrogen to the ammonia. The hydrogen can be ignited with little energy, whereby the energy released from the hydrogen combustion leads to the decomposition of ammonia and its ignition. The supply of hydrogen via the aforementioned cracker unit costs money and energy. The primary aim of the investigations was therefore to define engine boundary conditions under which as little hydrogen as possible is required. Ideally, the combustion process should work with pure ammonia. The influence of injection timing, injection pressure, charge air temperature and direct injection of ammonia have already been investigated in initial studies [7]. The investigations in this paper focused on the variation of the air/fuel ratio, the compression ratio, and the ignition energy.

A lambda value of 1 proved to be the best solution for the air/fuel ratio. The combustion process reacts sensitively to lambda changes. A very slight deviation into the rich range could possibly stabilise the ignition behaviour somewhat, but the hydrogen emissions then increase exponentially. The nitrogen-based emissions could be reduced. Significant leaning beyond approx. lambda = 1.3 is not possible, as the cyclical fluctuations then increase abruptly. The resulting air thinning does not yet contribute to a reduction in nitrogen oxides.

The increase in the compression ratio was based on the idea that the higher pressures and temperatures have a positive effect on the ignition conditions and thus enable higher maximum ammonia contents. This showed that an increase does not always bring advantages. At CR = 22, full-load operation is not possible due to peak pressures being exceeded. This compression ratio can therefore be excluded. Compared to the basic compression ratio of CR = 14, the increases to 17 and 18.5 were able to achieve advantages in terms of both the maximum possible NH_3 content and efficiency. Significant in both cases, however, is the much higher susceptibility to knocking, which severely limits the range of possible NH_3 content in the fuel. However, the differences in emissions and efficiency between these two compression ratios are small. Based on these findings, CR = 17.5 is preferable.

Last but not Least, the conventional ignition system was replaced by a Flexispark ignition system from the company SEM. The system provides an extended ignition spark with increased ignition energy. Thanks to the improved ignition behaviour, the combustion was stabilised overall, i.e. the cyclical fluctuations were reduced. It was also possible to operate the engine with pure ammonia without adding any hydrogen. Here, too, the COV of the IMEP fell below the set limit value of 3% at all times. It remains to be investigated whether the new ignition system significantly reduces the service life of the spark plug. It also remains to be seen whether another ignition strategy, such as conventional spark ignition in a passive pre-chamber, could achieve a similar result. Both are already the subject of ongoing research.

In summary, it can be stated that a stable combustion process could be realised in a diesel-based engine with intake manifold injection of hydrogen and ammonia at a compression ratio of CR = 17. The required hydrogen admixture was low at approx. 10 to 15% and could even be completely avoided with a potent ignition system. The full load of the diesel engine could be achieved. The effective efficiency of approx. 44% is at a very good level. The raw nitrogen oxide emissions are high, as are the NH_3 emissions. However, due to the favourable concentration ratio of the latter two, even a passive SCR system could be sufficient to comply with existing limit values. This aspect is also the subject of future investigations.

After technology transfer from the single-cylinder engine, the multi-cylinder engine will be containerized and tested at the CAMPFIRE Open Innovation Lab (COIL) near to Rostock/Germany. There the marriage with the Ammonia cracker will happen as well, allowing the complete system to be initially tested and calibrated, followed by an endurance run under application typical conditions.

Acknowledgments

This work was carried out within the CAMPFIRE project of the Hydrogen Flagship Project TransHyDE and was funded by German Federal Ministry for Education and Research.

Literature

[1] International Maritime Organisation. (7th July of 2023). “International Maritime Organization (IMO) adopts revised strategy to reduce greenhouse gas emissions from international shipping” [Press release]. https://www.imo.org/en/MediaCentre/PressBriefings/pages/Revised-GHG-reduction-strategy-for-global-shipping-adopted-.aspx (Last accessed on 29.07.2024).

[2] DNV-GL. „Comparison of Alternative Marine fuels“. final report 2019-0567 Rev.3, Høvik (Norway) 2019, https://safety4sea.com/wp-content/uploads/2019/09/SEA-LNG-DNV-GL-Comparison-of-Alternative-Marine-Fuels-2019_09.pdf (Last accessed on 29.07.2024).

[3] Annalena Braun, Niklas Gierenz, Samuel Braun, Heiko Kubach, Sören Bernhardt, Sascha Prehn, Moritz Müller, Lena Engelmeier, Lukas Fehlemann, Michael Steffen, Torsten Baufeld, Günther Neuhaus, Karsten Müller, Hinrich Mohr. „Aspects of Ammonia as Green Fuel for Propulsion Systems of Inland Water Vessels“. *Energy Technology*, 2024; https://doi.org/10.1002/ente.202301648 (Last accessed on 29.07.2024).

[4] Julian Atchison. (July 3rd of 2023). “GAC Group: ammonia combustion engines in China” [Press release]. https://ammoniaenergy.org/articles/gac-group-ammonia-combustion-engines-in-china/ (Last accessed on 29.07.2024).

[5] Peter Balle, Bastian Geiger, Dirk Klukowski, Matias Pignatelli, Stefan Wohnrau, Michael Menzel, Ingo Zirkwa, Gunther Brunklaus, Sven Kureti. "Study of the selective catalytic reduction of NOx on an efficient Fe/HBEA zeolite catalyst for heavy duty diesel engines". Applied Catalysis B: Environmental, Volume 91, Issues 3–4, 2009, Pages 587-595, ISSN 0926-3373, https://doi.org/10.1016/j.apcatb.2009.06.031

[6] Jakob Ängeby, Bert Gustafsson, Anders Johnsson. „Zündsteuerungsmodul für Wasserstoffverbrennungsmotoren“. *MTZ Motortechnische Zeitschrift*. Vol. 84, Nr. 10, S. 48–53, 2023

[7] Annalena Braun, Samuel Braun, Heiko Kubach, Sören Bernhardt, Marcel Reinbold, Niklas Gierenz, Sascha Prehn, Bert Buchholz, Lena Engelmeier, Lukas Fehlemann, Jannik Plass, Michael Steffen, Torsten Baufeld, Hinrich Mohr: „Development of an Ammonia-fueled Cracker-Engine-Unit as Propulsion System for Inland Waterway Vessels“. *13th Dessau Gas Engine Conference*. May 15-16th 2024. Dessau-Roßlau

Anwendungszentrum Wasserstoff

FORSCHUNGSFABRIK WASSERSTOFF MV

Fraunhofer IGP

Fraunhofer Institute for Large Structures in Production Engineering IGP

Hydrogen Application Center

Green solutions for the maritime industry

- ✓ Test benches for energy converters up to 10 MW
- ✓ Evaluation of alternative fuels and lubricants
- ✓ Retrofit solutions for the existing fleet
- ✓ Production technologies for the H_2 ramp-up
- ✓ Development of H_2 based logistics chains

Contact:
Dr.-Ing. Benjamin Illgen
Fraunhofer IGP
Project supervisor
Hydrogen Application Center

Tel. +49 381 49682 - 230
benjamin.illgen@igp.fraunhofer.de

MV tut gut.

igp.fraunhofer.de

Keywords: ammonia combustion, high-pressure dual fuel,

Fundamental investigation of an ammonia HPDF combustion process on high-speed engines

M. Sc. Phillip Thorau[1], M. Sc. Karsten Stenzel[1], Dr.-Ing. Christian Reiser[1], Prof. Dr.-Ing. Bert Buchholz[2]

(1) WTZ Roßlau gGmbH, (2) LKV, University of Rostock

https://doi.org/10.18453/rosdok_id00004642

Abstract

In this current scientific article, the core principles of HPDF (High-Pressure Direct Fuel) ammonia combustion are explored, and an extensive analysis of the various factors influencing combustion and emissions formation is conducted through experimental engine studies. This comprehensive investigation includes the scrutiny of parameters such as engine speed, load, air-fuel ratio, and various injection strategies, encompassing timing, quantity, and frequency of injection. Against the backdrop of global environmental concerns, ammonia's potential as an alternative fuel source is of great interest. However, realizing this potential necessitates addressing emissions challenges, including ammonia raw emissions and the greenhouse gas nitrous oxide. Furthermore, the research contributes to a deeper comprehension of combustion characteristics and emission dynamics, thereby facilitating effective emissions management. By advancing the understanding of ammonia combustion, this study not only aids in overcoming technical hurdles but also supports the broader effort to transition towards more sustainable energy sources, aligning with global initiatives to mitigate environmental impact and reduce emissions.

1. Introduction

In view of climate change and the need to reduce greenhouse gas emissions, ammonia is becoming increasingly important as a carbon-free fuel for combustion engines. Ammonia offers several advantages: It has a high volumetric energy density, is easy to store and transport and uses existing infrastructure for production and distribution. Ammonia can be used in various engine technologies, including combustion engines and gas turbines. Especially in marine and heavy-duty applications, ammonia is seen as a promising fuel due to its high energy density and the need to reduce CO_2 emissions. However, there are technical challenges in the combustion of ammonia, such as high ignition temperatures, slow flame speeds and the formation of nitrogen oxides (NO_x) and nitrous oxide (N_2O), which are also harmful to the climate. To overcome these challenges, various strategies are being explored, such as the use of ammonia in dual-fuel systems, where ammonia is mixed with diesel to aid ignition and optimize emissions. Overall, ammonia represents a promising opportunity to reduce CO_2 emissions in the transportation and energy sectors. Ongoing research is focused on further improving the efficiency and environmental compatibility of ammonia combustion.

2. Fuel Properties

Table 1 compares ammonia and the fuels hydrogen and methanol. Taking into account the typical pressure and temperature conditions for storage, it can be seen that ammonia has good volumetric calorific values due to its liquid storage capability.

Table1: Characteristics of selected alternative fuels [1] [2] [3] [4]

	Unit	**Ammonia**	**Hydrogen**	**Methanol**
Vol. heating value [T=300 K]	MJ/l	11,9 (10 bar)	4,8 (700 bar)	15,8 (1 bar)
Stoichiometric air requirement	kg/kg	6,05	34,3	6,45
Auto-ignition temperature	°C	651	600	465
Enthalpy of vaporization	kJ/kg	1371	446	1173
Lam. flame speed (p = 1 bar, T=300 K, λ=1)	cm/s	6,5	290	55

The low flame speed leads to a slower combustion process compared to other fuels, which can reduce combustion efficiency. The high auto-ignition temperature and extreme heat of vaporization make liquid injection and diesel-like compression ignition more difficult. The high minimum ignition energy means that it is more difficult to safely ignite an ammonia-air mixture. The resulting increased resistance to knock allows ammonia-fueled engines to operate at higher compression ratios, offering efficiency benefits. Although ammonia has a much lower energy content per mass compared to standard carbon-based fuels, its low stoichiometric air-to-fuel ratio partially compensates for this in terms of in-cylinder energy content. [3] [5]

Volumetric storage density is the challenging factor for vehicles, even ammonia requires about three times the volume of carbon-based fuels (at identical efficiencies) for the same range. However, hydrogen requires even more storage volume, especially if the tank itself (for 70 MPa pressure or -253 °C temperature) is included. Furthermore, a transportation infrastructure for ammonia already

exists and its handling is not significantly different from that of LPG or propane. In ammonia combustion, the ammonia can be introduced via the intake manifold or directly into the combustion chamber and burned by an ignition jet, like known methane dual-fuel concepts. In addition, ammonia can be made to ignite itself using suitable measures and can be diffusively converted instead of premixed combustion, which leads to higher conversion rates. [6] [7]

2.1. Oxidation pathways of ammonia

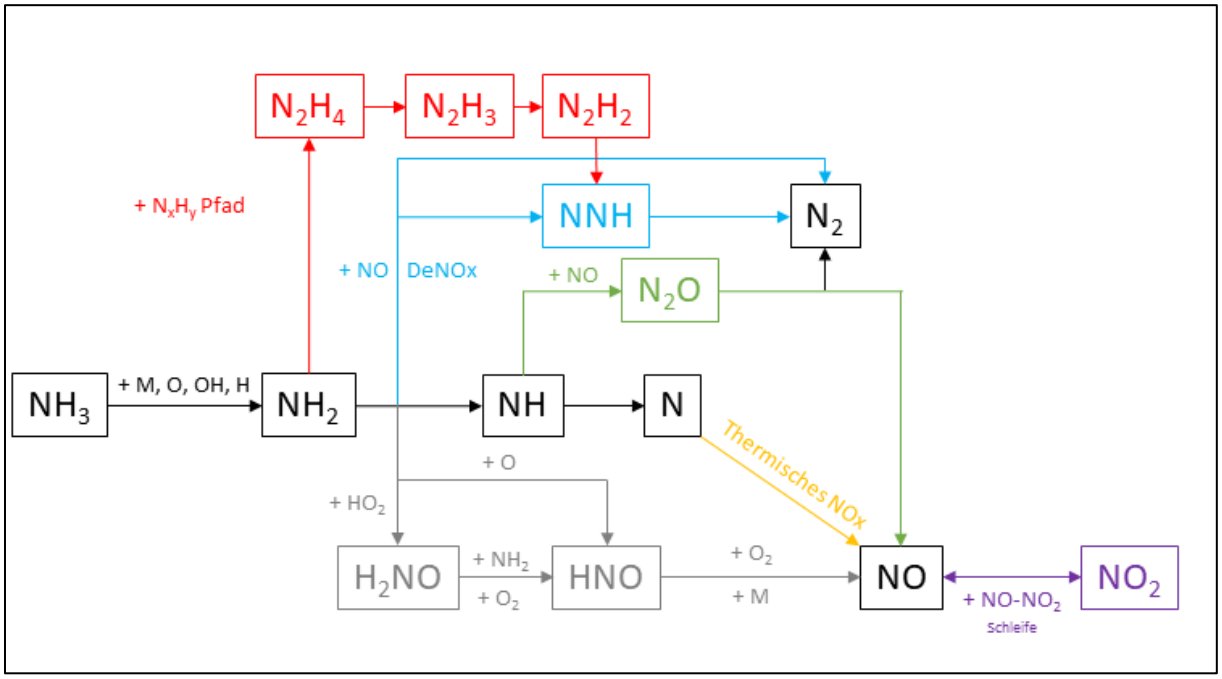

Figure 1: Schematic oxidation pathways of ammonia according to Tornatore et al. [8]

Ammonia is stable because the covalent bonds between the nitrogen atom and the three hydrogen atoms require a lot of energy to dissociate. The first step in ammonia oxidation is dehydrogenation to NH_2, which consumes highly reactive OH, O and H radicals. After dehydration to NH_2, there are several chemical reaction pathways that can now take place. Firstly, the NH_2 radicals can combine to form longer-chain N_xH_y compounds. This reaction is favoured by excess fuel and high pressure. [8]

Under fuel-rich conditions, the importance of O and OH as reaction partners in the radical pool decreases. The reactions of NH_2 with H and other NH_2 radicals increase, which leads to the considerable formation of H_2. A lack of oxygen suppresses the oxidation of NH_i, which means that less NO is produced, and more N atoms can be combined to form N_2 instead. [9] [10]

At high pressure and low temperature, the NH_2 radicals react with HO_2 to form H_2NO. The H_2NO molecule then oxidizes to HNO, which reacts further to form NO. This is the main route for the formation of fuel NO in ammonia flames, as HNO is subsequently oxidised to NO. This differs from hydrocarbon flames, where NO formation mainly occurs via the Zeldovich mechanism. [11] [12]

Another reaction pathway is through the oxidation of NH_2 with NO to molecular nitrogen and water or just NNH and hydroxide radicals. The NNH radical then reacts further to form molecular nitrogen and hydrogen radicals, which are now available for further reaction. The thermal $DeNO_x$ mechanism just described predominates between 1100 K and 1400 K and was first described by Miller and Glarborg and Bowmann. [13] [14]

If the NH_2 dehydrogenates further to NH at temperatures above 1400 K, it is possible that N_2O is formed by adding NO at low O_2 concentrations or by the reaction of NH_2 with NO_2 at high O_2 concentrations. On the one hand, N_2O can subsequently decompose by reaction with H radicals to form molecular nitrogen OH radicals at temperatures above 1600 K. Another reaction pathway is that the N_2O decomposes and then the reaction of molecular hydrogen with oxygen radicals leads to hydrogen or hydroxide radicals. However, under high pressure conditions or extremely lean fuel conditions, this reaction is reversed and forms a significant formation route for N_2O. [15] [16]

NO_2 is mainly formed by the oxidation of NO via the reaction $NO + HO_2 \rightarrow NO_2 + OH$. The NO_2 formed is returned to ammonia either directly or via intermediate products such as H_2NO ($NO\text{-}NO_2$ loop). The oxidation processes of ammonia, which favour the black and grey paths, lead to low NO_x and N_2O emissions and are particularly active under fuel-rich conditions. [8]

2.2. Classification of the HPDF Combustion

As early as the 1960s, ammonia was considered as a fuel in a compression-ignition engine by Gray et. al. Running a CI engine on pure ammonia is technically feasible but requires significant modifications to both the engine and the operating conditions. The main requirements are high compression ratios, increased temperatures in the intake manifold to improve ignitability. With high-speed four-stroke engines and today's performance requirements, the implementation of these measures is only possible at great expense, so that alternative methods must be used to utilise ammonia in combustion engines. The basics of the high-pressure dual-fuel combustion process with ammonia utilisation are described below. By using diesel as the ignition fuel to burn the ammonia, it is possible to reduce the compression ratio from 35:1 to 15.2:1. This is due to the increased ignition energy resulting from the addition of diesel. [17] [18]

The HPDF process (High-Pressure Dual-Fuel) combines the injection of two different fuels, a main fuel (e.g. methane or ammonia) and a pilot fuel (e.g. diesel). The main fuel is burnt in a diffusive flame, which is initiated by the ignition of the pilot fuel. Direct injection ensures that no unburnt fuel enters the exhaust gas during the charge change. Furthermore, no ammonia enters the intake duct, which could cause the corrosive properties of ammonia coupled with the humidity in the air to take effect. By injecting both fuels directly, compression ratios typical of diesel engines can be achieved, resulting in similar efficiencies to those of conventional diesel engines. HPDF combustion takes place in several phases: Firstly, the pilot fuel is injected and ignites. This is followed by the main injection, whereby the main fuel is injected and ignites when it meets the hot products of the pilot combustion. Part of the main fuel mixes with the combustion chamber air before ignition and burns suddenly, which leads to a local maximum in the heat release rate (premixed peak). The remaining main fuel burns diffusively until the end of injection and beyond in a pronounced burn-out phase. Ammonia dual-fuel combustion offers several advantages. Ammonia is carbon-free and therefore produces no direct CO_2 emissions during combustion. When stored in liquid form, ammonia has good volumetric calorific values and can be safely stored and transported at relatively low pressures and temperatures. [19] [20]

2.3. Experimental setup

The engine tests were carried out on the FM18 single-cylinder research engine at the WTZ Roßlau. The boundary conditions are shown in the following Table 2.

Table 2: FM18 Engine data

Parameter	Value	Unit
Bore x Stroke	175 x 215	mm
Displacement	5,17	l
Conrod length	457	mm
rated power	180	kW
Rated speed	1800	min^{-1}
Injection pressure NH_3	500	bar
Injection pressure Diesel	1000	bar

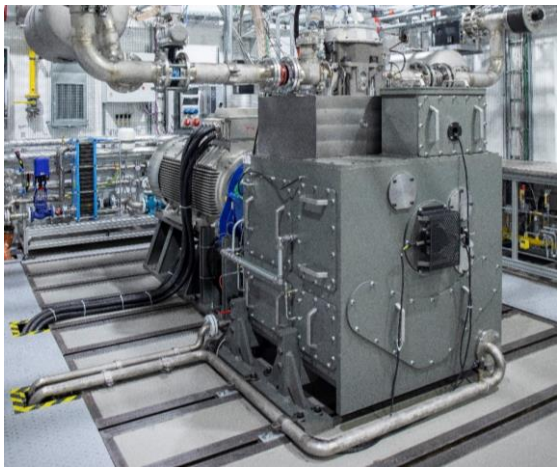

Figure 2: Single Cylinder Test Engine FM18

The ammonia supply system for the tests was designed and planned by project partner Neptun Ship Design (NSD). Due to the simplicity of the system, pressure-based storage of the ammonia was favoured. However, for future applications on ammonia carriers, liquefaction of the ammonia by lowering the temperature is being considered. The downstream high-pressure ammonia system enables injection pressures of up to 500 bar. In this context, reference is made to the work of Stenzel and Arndt et al [21] , in which the ammonia system is described in detail. A Fourier transform infrared spectrometer (FTIR), which can measure nitrous oxide, ammonia and all other emissions produced in conventional combustion engines, was used to record the exhaust emissions. This measuring device ensures a comprehensive characterization of exhaust emissions and thus enables a detailed analysis of ammonia combustion.

The injector used for the study was provided by Woodward L'Orange, another project partner. This injector has two separately controllable nozzles, allowing diesel and ammonia to be injected directly into the combustion chamber via two different channels.

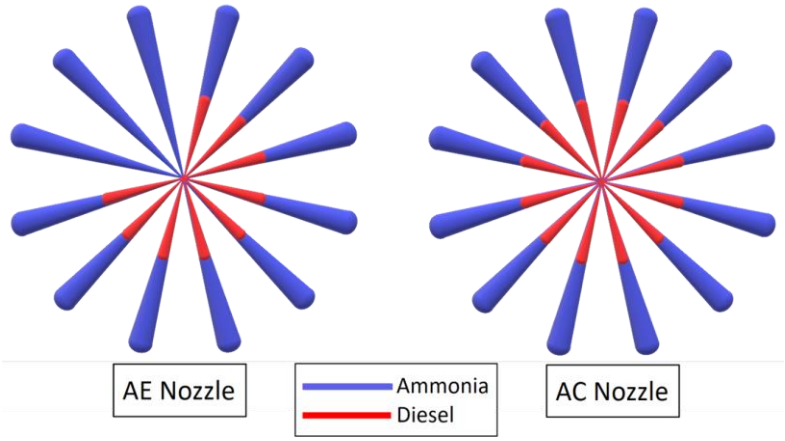

Figure 3: Schematic spray configurations of the investigated nozzles

Both injector sides are based on a servo-hydraulic principle. On the ammonia side it is necessary to use a separate control fluid circuit, which is also operated with diesel. Figure 3 shows the spray configurations of the investigated nozzle variants schematically.

Table 3: Investigated nozzle designs

	AC-Nozzle	**AE-Nozzle**
Number of nozzle holes for ammonia	12 (3x4)	12 (3x4)
Hydraulic flow rate of the ammonia side [l/min] @100 bar	22.8	22.8
Number of nozzle holes for diesel	12	9
Hydraulic flow rate of the diesel side [l/min]	3.0	2.25

3. Analysis of the combustion process investigations

This study analyzes the influence of the time offset between the injection of ammonia and diesel on combustion. Due to the servo-hydraulic principle of the HPDF injector, there is a time offset between the start of current (SOE) and the start of injection (SOI), which can be measured by a drop in pressure of the respective medium. In addition, the time delay of the pressure drop up to the measuring point was considered, considering the speed of sound.

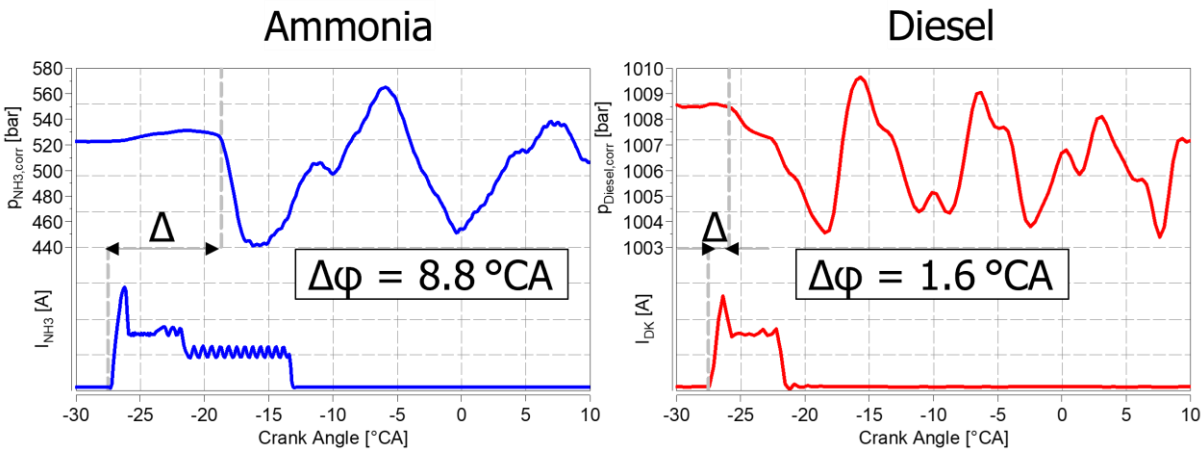

Figure 4: Description of the injection delay of the two fuel paths with corrected indicated pressure curve of both fuel lines

The difference in hydraulic injection time between the two fuels with simultaneous actuation is approximately 7.2° CA and can be considered constant throughout the measurement campaign since the engine speed and rail pressure were kept constant throughout the experiment. The setting values of the tests are shown in Table 4.

Table 4: Setpoints of the operation point

Parameter	**Definition**	**Value**	
pmi	Indicated mean effective pressure	17,2	bar
n_{MOT}	Engine speed	1800	min^{-1}
SOE_{DK}	Start of current diesel	-28	° CA ATDC
SOE_{NH3}	Start of current ammonia	-28	° CA ATDC
xq_{NH3}	Energetic ammonia share	> 90	%
p_{NH3}	Ammonia injection pressure	500	bar

Figure 5Figure 5 illustrates the pressure, heat release, and cumulative heat release curves of the two nozzles at the operating point. The left diagram illustrates the pressure curve p_{CYL} as a function of the crank angle. It can be observed that the AC nozzle exhibits a higher pressure peak than the AE nozzle. The two graphs below present the indicated injection pressure of ammonia and diesel. Both nozzles demonstrate comparable injection curves, with injection commencing at approximately -20° CA. The graphs on the right depict the heat release rate and the cumulative heat release, with the AC nozzle displaying an earlier heat release.

Looking at the current profiles, for the same indicated load on the motor at the AC nozzle, a significantly shorter start-up time is required on the ammonia side. Although the same hydraulic flow rate was defined through the nozzle, slight differences in the needle stroke setting led to changes in the flow rate. Additionally, it can be postulated that a reduction in the availability of diesel jets will precipitate a decline in the efficiency of ammonia conversion, necessitating a compensatory increase in fuel injection to maintain the indicated power output.

Moreover, an elevated pressure rise gradient and the heat release resulting from the higher ammonia mass flow can be discerned at the AC nozzle. A premix peak is observable at approximately -20° CA ATDC, which analogous for both nozzle variants. Based on the pressure curves of the two fuel paths (p_{NH3} & p_{Diesel}), it can be determined that this premix peak originates mainly from the diesel injection, but that a partially premixed portion of ammonia is already combusted at this point.

The main part of the ammonia then combusts at different rates depending on the nozzle variant. When comparing the cumulated heat release, the 10% conversion point is earlier with the AC Nozzle. This indicates a better oxidation of the ammonia due to higher penetration from the diesel spray.

The maximum heat release of the AC Nozzle already takes place in the TDC, where the AE Nozzle is delayed. This leads to an earlier center of combustion on the part of the AC nozzle and results in lower energy consumption and increased efficiency, as measured by the global maximum of the cumulated heat release curve at same indicated power. The reason for the earlier center of combustion of the AC-Nozzle is the improved penetration area of the spray lobes, which improves the mixture preparation and the resulting fuel conversion.

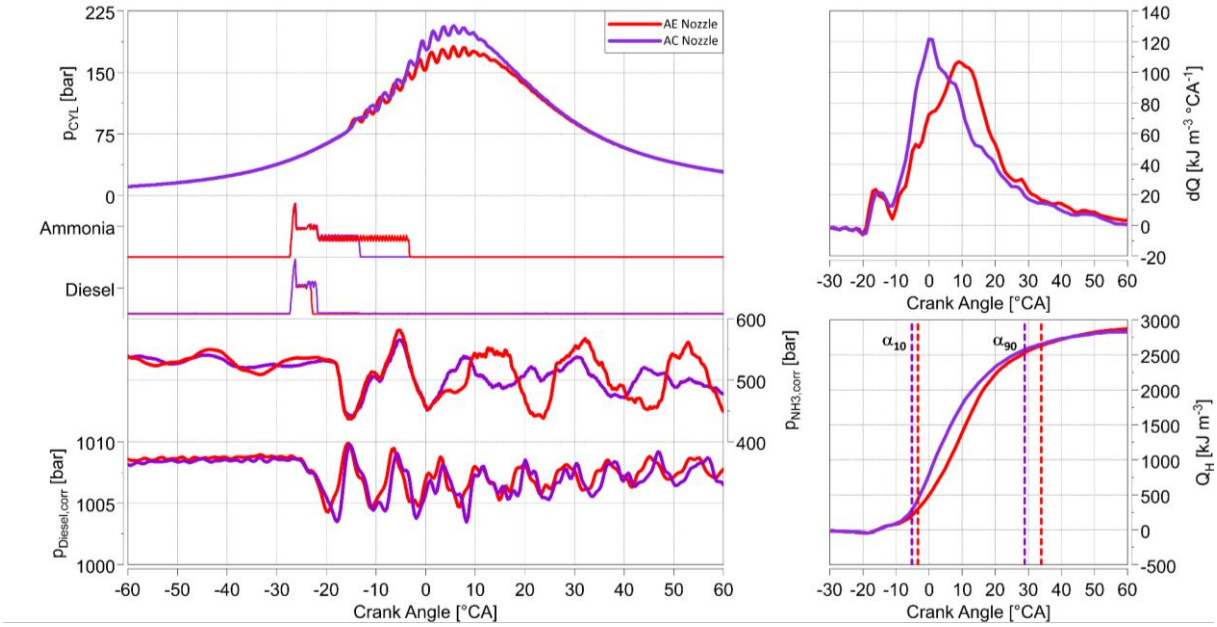

Figure 5: cylinder pressure, heat release and cumulated heat release of both nozzle variants at IMEP = 17 bar and simultaneal current

Based on the results of the simultaneous current injection of both fuel paths, the time difference of the current injections was then varied to evaluate the combustion process with earlier diesel or ammonia injection.

Figure 7 shows that a positive start of current difference corresponds to an earlier ammonia start of current. As already explained in Figure 6, a shortened duration of current on the ammonia side with the AC nozzle continues over the entire variation range. Furthermore, the shortest injection duration was set on the diesel side, which still ensures a clean opening of the injector without cycle fluctuations due to operation in the ballistic range. The injector of the AE-Nozzle requires a 100 µs longer energization time, whereupon the diesel mass flow in the diagram inevitably increases and leads to an increased diesel and a reduced ammonia content. The AC nozzle offers efficiency advantages over the entire variation range. This can be explained by the shorter burn duration. In addition, due to the higher mass flow on the ammonia side, the AC nozzle results in higher maximum pressures and higher maximum cylinder pressure gradients.

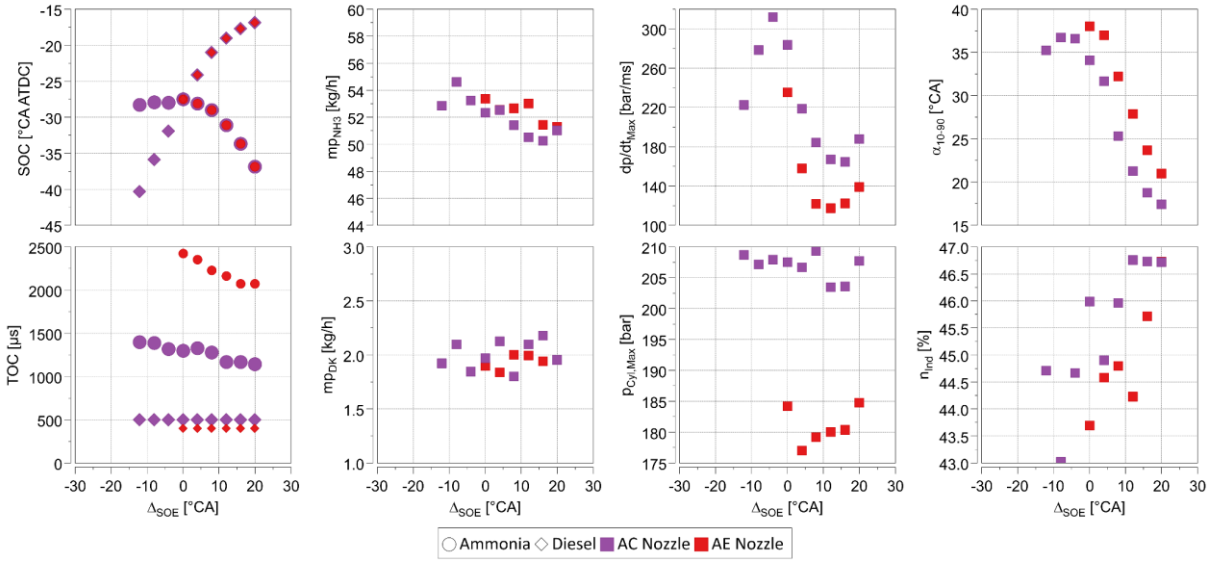

Figure 7: Setpoints values for the variation of the injection difference at IMEP = 17,2 bar

The diagrams in Figure 8 show the emission values of NH_3, NO_x, N_2O and CO_2 as a function of the time offset of the injection and illustrate the complex relationship between the injection timing and the resulting emissions. The variation range is limited on both sides by misfiring. The reason for this is that if diesel injection is too far upstream, diesel combustion starts too early and therefore ammonia combustion cannot be started. If the ammonia injection is also moved too far forward at the other limit of the variation range, this results in increased ammonia emissions due to wall deposits and misfiring due to a lack of jet interaction.

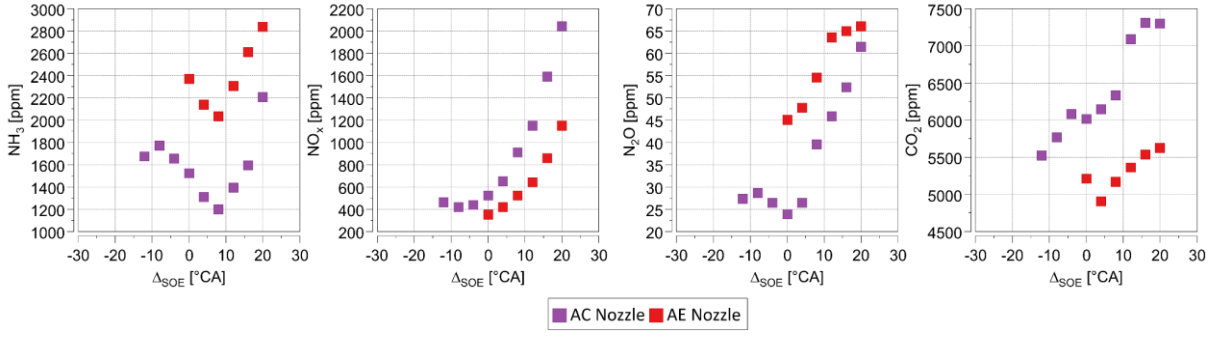

Figure 8: Reasonable emissions for the variation of the injection difference at IMEP = 17,2 bar

The NH_3 emissions reach their minimum at a Δ_{SOE} of 8° CA. This indicates that this injection point is particularly favorable for the reduction of NH_3 emissions. Considering the hydraulic delay of the separate fuel paths, it can be determined that according to Figure 4, a difference of the start of energization of Δ_{SOE} = 7.2° CA corresponds to simultaneous injection. Looking at a Δ_{SOE} = 8° CA the resulting ammonia emissions are lowest at this flow difference, regardless of the nozzle geometry.

In contrast, the emissions of NO_x and N_2O increase continuously with increasing Δ_{SOE} and reach their highest values at around 20° CA. The AE-Nozzle tends to have higher NH_3 emissions compared to the AC-Nozzle.

If ammonia injection is shifted increasingly earlier, the proportion of premixed ammonia increases and leads to an increase in Fuel-NO emissions due to higher cylinder pressure. It should also be noted that due to the increasing premixed combustion, the low flame speed of the ammonia leads to increased NH_3 emissions instead of combusting diffusive.

N_2O emissions follow a similar trend, with the AC nozzle reducing emissions by almost 50%, especially with upstream diesel injection. At negative Δ_{SOE} values, N_2O emissions are low, while at positive values they increase continuously and peak at around 20° CA. As already mentioned in Chapter 2.1, it arises as a product of incomplete combustion in locations with low temperature and is thus reduced as soon as combustion becomes hotter. If the AE nozzle has no diesel holes, ammonia can reach lean edge areas before it is ignited by neighbouring diesel jets, leading to increased N_2O emissions. A similar trend of increasing nitrous oxide emissions can also be observed with upstream ammonia injection.

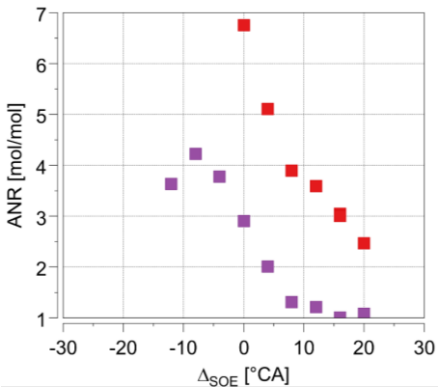

Figure 9: Ratio between ammonia and nitrous oxide emissions (ANR) at IMEP = 17.2 bar for various injection differences between both fuel paths

The ratio of NO_x to NH_3, shown in Figure 9, which provides a measure of the applicability of an SCR catalytic converter, shows that a ratio of one can already be achieved with an 8° CA upstream flow of the ammonia path from the AC nozzle. However, it must be considered that particularly high nitrous oxide emissions occur at precisely these operating points where the N_2O emissions are at the highest

point. As a result, a trade-off between the NH_3-NO_x ratio and laughing gas emissions must be found in the future.

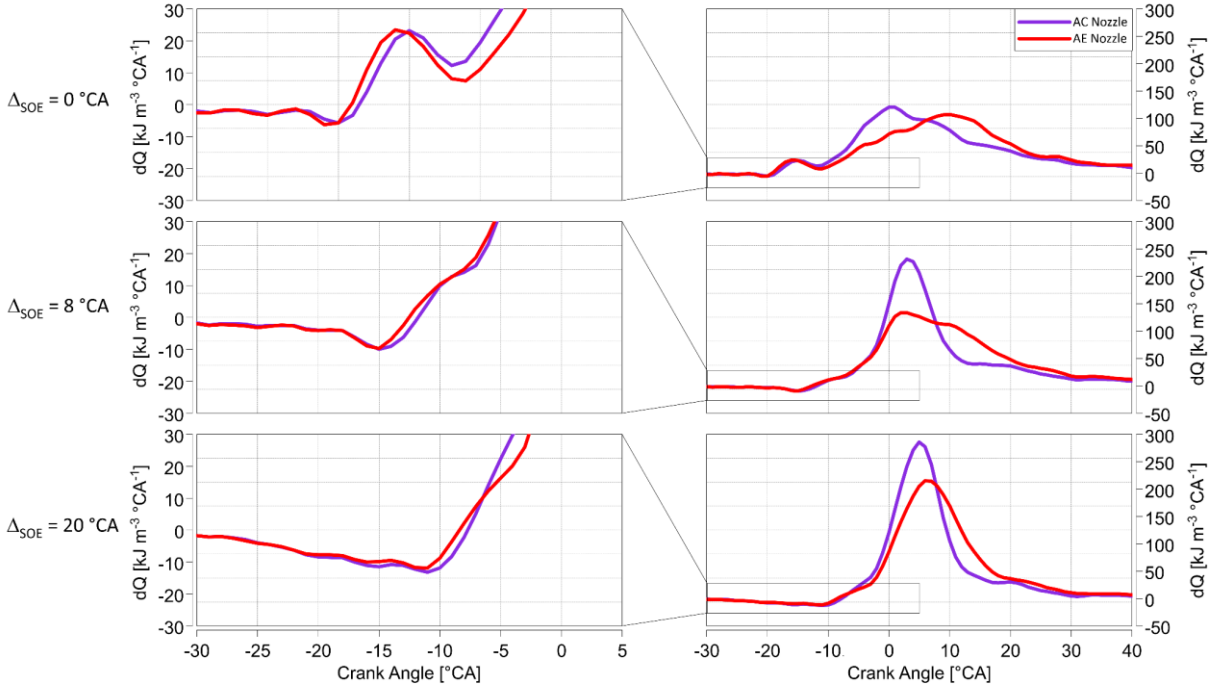

Figure 10: Heat release rates of different injection timings at IMEP=17.2 bar

The diagrams above show the heat release rate as a function of the crank angle. Each row contains diagrams for different current differences of 0° CA, 8° CA and 20° CA. The red line represents the heat release with the AE nozzle and the purple line the AC nozzle. Basically, it can be stated that the heat release of the diesel injection is almost identical under all the injection differences investigated and may be superimposed by the heat release of the ammonia.

When looking at the simultaneous flow, it can be seen in the left-hand column for Δ_{SOE} = 0° CA that the heat release rate for the AC nozzle shows an increase shortly before top dead center, followed by a peak shortly after TDC. The AE nozzle shows a similar curve, but with a slightly later heat release rate shortly after TDC. Simultaneous energizing shows that diesel (hydraulic delay + ignition delay) has a predominantly premixed combustion, followed by ammonia, which enters the combustion chamber about 9° CA after energization. It can also be assumed that the AC nozzle enables a more homogeneous mixture and temperature distribution in the combustion chamber, presumably due to the better distribution of the ammonia jets. This leads to a shorter ignition delay for ammonia, which is why the heat release with the AC nozzle always remains positive

At Δ_{SOE} = 8° CA, in the middle row of the graphs, the AC nozzle again shows an increase in heat release rate just before TDC, followed by a higher and shorter peak after TDC compared to 0° CA. The AE nozzle also shows an increase compared to simultaneous start of current, but with a higher peak and a slightly different shape. In the right column with the expanded scale, the differences between the two nozzles can be seen more clearly, with the AC nozzle achieving a higher and narrower peak than the AE nozzle.

At a flow rate difference Δ_{SOE} = 20° CA, the AE nozzle shows an even more pronounced increase in the heat release rate before TDC, followed by a very high peak after TDC. The AC nozzle also shows a very high peak in this case, but it is slightly before the peak of the AE nozzle and has a slightly different shape. The AC nozzle reaches a higher peak than the AE nozzle, but with a narrower curve. If the ammonia injection is brought earlier into the combustion, the high enthalpy of vaporization of the ammonia leads to a delay in the diesel combustion. The AC nozzle enables better mixing, which means that the premixed phase of combustion begins immediately after the evaporation, while the AE nozzle leads to a longer ammonia ignition delay due to poorer mixture preparation.

4. Conclusion

The investigation into the combustion process involving high pressure dual-fuel injection of ammonia and diesel reveals significant insights into the interaction between these two fuels and the impact of injection timing on combustion efficiency and emissions. The study highlights the critical role of the time offset between the ammonia and diesel injections, demonstrating that even small differences in timing can lead to notable changes in the combustion characteristics.

Key findings include the observation that the AC nozzle, with its better mixture preparation and shorter ignition delay for ammonia, consistently produced a more efficient combustion process compared to the AE nozzle. This is evident in the earlier heat release, higher peak pressures, and a more favorable center of combustion with the AC nozzle, leading to lower energy consumption and higher efficiency at the same indicated power output.

The emission analysis further underscores the complexity of optimizing the dual-fuel combustion process. While a timing offset of around 8° CA was found to minimize ammonia emissions and a ratio of NH_3 and NO_x (ANR), it simultaneously led to increased N_2O emissions, highlighting the trade-offs inherent in tuning the injection timing. The AC nozzle demonstrated better overall performance, particularly in reducing N_2O emissions, but the study suggests that further optimization is needed to balance emissions of NH_3, NO_x, and N_2O while maintaining efficient combustion.

In summary, the study provides a detailed understanding of how injection timing and nozzle configuration affect the combustion process and emissions in dual-fuel systems. These insights are crucial for developing more efficient and cleaner combustion strategies, particularly in applications where ammonia is used as a renewable fuel. Future research should focus on refining these findings to optimize the balance between combustion efficiency and emission control.

Abbreviations

SOC – start of current

TOC – time of current

dp/dt_{Max} – maximum gradient of cylinder pressure

p_CYL_{Max} – maximum cylinder pressure

η_i – indicated efficiency

$\alpha_{10\text{-}90}$ – burn duration between the 10% and 90% cumulated heat release point

ANR – ratio between unburned ammonia and nitrogen oxides

Δ_{SOE} – difference between both start of currents of both fuel paths

Literature

[1] F. Asinger, Chemie- und Energierohstoff, Berlin Heidelberg: Springer , 1986.

[2] M. C. u. S. Frigo, „Hydrogen generation system for ammonia–hydrogen fuelled internal combustion engines," *International Journal of Hydrogen Energy,* Bd. 40, Nr. 33, pp. 10673-10686, 2015.

[3] M. Aziz et al., „Ammonia as Effective Hydrogen Storage: A Review on Production, Storage and Utilization," *Energies,* Bd. 13, Nr. 12, p. 3062, 2020.

[4] K. P. Shrestha, Detailed kinetic modeling of ammonia combustion, BTU Cottbus - Senftenberg, 2021.

[5] M. Aziz et al., „Ammonia as Effective Hydrogen Storage: A Review on Production, Storage and Utilization," *Energies,* Bd. 13, Nr. 12, p. 3062, 2020.

[6] A. J. Reiter et al., „Combustion and emissions characteristics of compression-ignition engine," *Fuel,* Bd. 90, Nr. 1, pp. 87-97, 2011.

[7] V. Chintala et al., „A comprehensive review on utlization of hydrogen in a compression ignition engine under dual fuel mode," *Renewable and Sutainalbe Energiy Reviews,* Bd. 70, pp. 472-491, 2017.

[8] C. Tornatore, „Ammonia as Green Fuel in Internal Combustion Engines: State-of-the-Art and Future Perspectives," *Frontiers in Mechanical Engineering,* Bd. 8, Nr. 944201, 2022.

[9] H. Nakamura, „Combustuion and Ignition of Ammonia/air Mixtures in a Micro Flow Reactor with a Controlled Temperature Profile," *Proc. Combust. Inst. ,* Bd. 36, Nr. 3, pp. 4217 - 4226, 2017.

[10] E. Okafor, „Experimental and Numerical Study of the Laminar Burning Velocity of CH4-NH3 air Premixed Flames," *Combust flame ,* Bd. 187, pp. 185-198, 2018.

[11] I. Song, „Ammonia Oxidation at High Pressure and Intermediate Temperatures," *Fuel,* Bd. 181, pp. 358-365, 2016.

[12] A. Stagni, „An Experimental Theoretical and Kinetic-Modeling Study of the Gas-phase Oxidation of Ammonia," *React. Chem. Eng. ,* Bd. 5, Nr. 4, pp. 696-711, 2020.

[13] P. Glarborg, „Kinetic Modeling and Sensitivity Analysis of Nitrogen Oxide Formation in Well-Stirred Reactors," *Combust. flame ,* Bd. 65, Nr. 2, pp. 177-202, 1986.

[14] J. Miller, „Mechanism and Modeling of Nitrogen Chemistry in Combustion," *Prog. energy Combust. Sci. ,* Bd. 15, Nr. 4, pp. 287-338, 1989.

[15] S. J. Klippenstein, „The Role of NNH in NO Formation and Control," *Combust. Flame* , Bd. 158, Nr. 4, pp. 774-789, 2011.

[16] M. C. Drake et al, „Calculations of NOx Formations Pathways in Propagating Laminar, High Pressure Premixed CH4/air Flames," *Combust. Sci. Technol.,* Bd. 75, pp. 261-285, 1991.

[17] J. T. Gray, „Ammonia Fuel - Engine Compatibility and Combustion," in *Automotive Engineering Congress and Exposition*, 1966.

[18] N. Ebrahim et al., „Effects of ammonia on combustion, emissions, and performance of the ammonia/diesel dual-fuel compression ignition engine„" *Journal of the Energy Institute,,* Bd. Volume 107, 2023.

[19] D. Imhof, Visual Combustion Studies for Environmentally Friendly Marine Diesel and Gas Engines, Kyushu University, Japan, Kyushu: Kyushu University, 2023.

[20] S. G. Frankl, Numerische Simulation von kraftstoffflexiblen, direkteinspritzenden Schiffsmotoren, TU München, 2021.

[21] H. A. Karsten Stenzel, „AmmoniaMot - Experimental investigations of an ammonia dual-fuel combustion process for decarbonization of the maritime sector," *Rostocker Großmotoren Tagung* , 2022.

Keywords: alternative fuel, ammonia, spark-ignited, large engine

A spark ignited combustion concept for ammonia powered high-speed large engines – Test bed and 3D CFD simulation results

Dr. Shinsuke Murakami[1], Dr. Martin Kirsten[1], Thomas Kammerdiener[1], Andrej Poredos[1], Simon Bezensek[1], Dr. Günter Figer[1], Maria Segura[1], Dr. Maximilian Malin[2]

(1) AVL List GmbH, (2) LEC GmbH

https://doi.org/10.18453/rosdok_id00004643

Abstract

The ongoing energy transition and the global shift towards carbon-free fuels and e-fuels derived from renewable energy sources has sparked a significant interest in the application of ammonia. Ammonia, being a carbon free alternative fuel with some challenging attributes, shows great potential for marine propulsion systems and other high-power applications.

The paper explores two different ammonia combustion concepts for high-speed engines, as investigated by AVL. The first combustion concept involves a retrofittable approach of a premixed ammonia combustion with a Diesel pilot ignition, while the second concept pursues a pure zero-carbon fuel strategy by utilizing a mixture of ammonia and hydrogen ignited via a hydrogen-scavenged pre-chamber with a spark plug. Following a comprehensive comparison of these two concepts, the focus of the paper shifts to the analysis of the spark ignited ammonia engine.

The exploration commences with an introduction to AVL's single-cylinder high-speed engine featuring a 175 mm bore size and specific test configurations. Measurement results will be discussed regarding their impact on engine performance and emissions. Engine maps showing ammonia-nitrogen oxides ratio and excess air ratio values of NH_3-only consideration are presented, illustrating challenges associated with high levels of unburned ammonia and emissions of nitrous oxide (N_2O) as a by-product in the exhaust gas. Recognizing N_2O as a potent greenhouse gas, the paper underscores the necessity of minimizing those laughing gas emissions through combustion system development or by deploying exhaust gas aftertreatment systems with highest efficiencies, further illustrating N_2O emissions in CO_2 equivalent for emphasis.

In the subsequent section, the paper discusses simulation results of mixed hydrogen-ammonia fuel operation. Insights to mixture preparation and combustion are provided, with a specific focus on NO_x and N_2O emissions, along with unburned ammonia. The discussion focuses on the potential for enhancing air/fuel mixing and combustion based on simulation results, incorporating comparisons with experimentally obtained data whenever feasible.

As a conclusion, the paper finally summarizes key findings and is offering an outlook on future developments, encompassing ongoing work on combustion concepts like ammonia high-pressure direct injection, exhaust aftertreatment, and related simulation toolchain and its application. The seamless

integration of advanced 1D/3D CFD simulation methodology combined with the experimental results provides a holistic view of the ammonia combustion processes and sets the stage for further improvements for the development of ammonia powered combustion engines.

1. Introduction

Marine transportation is a critical facilitator of the global economy, but its contribution to total anthropogenic greenhouse gas (GHG) emissions has grown. This contribution increased from 2.76% in 2012 to 2.89% in 2018 [1]. In response, various initiatives have emerged to reduce shipping emissions, including the International Maritime Organization's (IMO) initial GHG strategy adopted in 2018. This strategy has spurred increased research and development of alternative fuels and hybrid propulsion systems for the maritime sector. Building on these efforts, the IMO's Marine Environment Protection Committee (MEPC 80) in July 2023 adopted a revised GHG Strategy with ambitious emissions reduction targets. These targets include a 20% reduction by 2030, a 70% reduction by 2040 (compared to 2008 levels), and ultimately, achieving net-zero emissions by 2050, as shown in Figure 1.

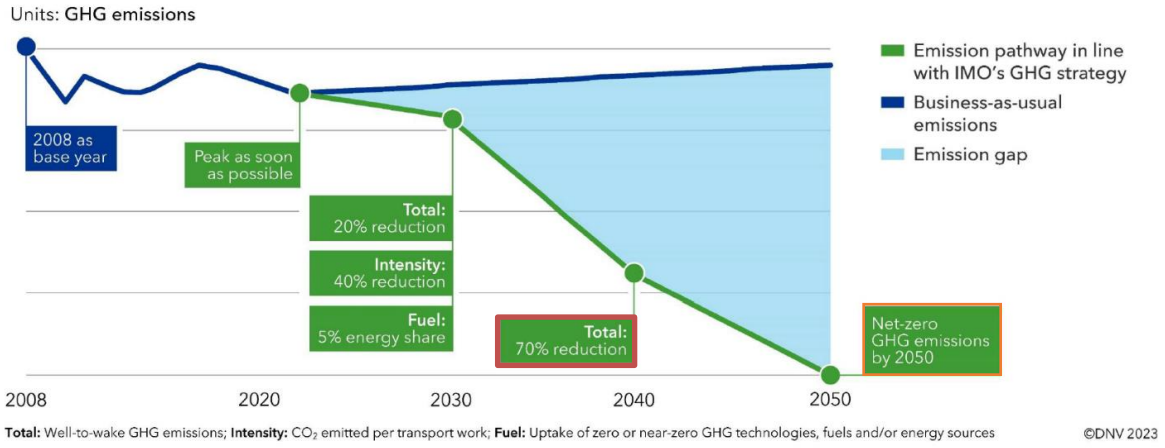

Figure 1: Revised IMO GHG strategy, Source DNV [3]

Ammonia is a zero-emission carbon free fuel and can be processed on board of vessels without producing any direct GHG emissions. If produced by electrolysis with renewable power sources, the well to wake emissions over the whole supply chain are on the same low level (100 gCO_2/kWh-GWP100) as e-Methane, e-Methanol and e-LH2 [3]. The attractiveness of ammonia for the maritime industry is not only based on the zero direct GHG emissions, but also on the already established infrastructure as ammonia is a commonly sea-traded good and many ports worldwide can provide ammonia infrastructure already today. This is however still limited to fossil ammonia requiring huge effort to transform to green ammonia. As a bridging solution, fossil ammonia will likely be used, and the green ammonia infrastructure build-up plans are readily accessible, and there is serious commitment to be observed from key stakeholders.

This paper explores two different ammonia combustion concepts for high-speed engines, investigated by AVL. The first combustion concept involves a retrofittable approach of a premixed ammonia combustion with a Diesel pilot ignition, while the second concept pursues a pure zero-carbon fuel strategy by utilizing a mixture of ammonia and hydrogen ignited via a hydrogen-scavenged pre-chamber with a spark plug. Following a comprehensive comparison of these two concepts, the focus of the paper shifts to the analysis of the spark ignited ammonia engine.

Measurement results of both combustion concepts will be discussed regarding their impact on engine performance and emissions. Engine maps showing ammonia-nitrogen oxides ratio and excess air ratio values of NH_3-only consideration are presented, illustrating challenges associated with high levels of

unburned ammonia and emissions of nitrous oxide (N_2O) as a by-product in the exhaust gas. Recognizing N_2O as a potent greenhouse gas, the paper underscores the necessity of minimizing those laughing gas emissions through combustion system development or by deploying exhaust gas aftertreatment systems with highest efficiencies, further illustrating N_2O emissions in CO_2 equivalent.

Additionally, the paper discusses simulation results of mixed hydrogen-ammonia fuel operation. Insights to mixture preparation and combustion are provided, with a specific focus on NO_x and N_2O emissions, along with unburned ammonia. The discussion focuses on the potential for enhancing air/fuel mixing and combustion based on simulation results, incorporating comparisons with experimentally obtained data whenever feasible.

The seamless integration of advanced 1D/3D CFD simulation methodology combined with the experimental results provides a holistic view of the ammonia combustion processes and sets the stage for further improvements for the development of ammonia powered combustion engines.

2. Assessment of Combustion Concept for Ammonia

The characteristics of different gas and dual fuel combustion concepts have already been discussed in previous papers [4], [5] and [6]. Their tolerance for the utilization of ammonia as alternative fuel are summarized in Table 1.

One possible and presumably simpler way is to employ a premixed combustion concept. The ammonia can be mixed with the air upfront of the combustion chamber, e.g. in the intake port via gas admission valves (port fuel injection, PFI). The pre-mixed air-fuel mixture will then be ignited either by a spark plug or by injecting diesel fuel. The spark ignition system or diesel injection system of the baseline engine can be carried over. This concept therefore allows a relatively simple conversion of an existing diesel or gas engine by simply applying an additional ammonia injection system, which would not only enable a quick introduction of ammonia-fueled engines into market but also a retrofit of already introduced engines whose lifetime exceeds the targeted timeframe for CO_2 reduction.

The other option is a diffusive combustion concept, in which ammonia is injected directly into the combustion chamber at high pressure of around 500 bar and higher. The injected ammonia will then be ignited by injecting the pilot diesel fuel. This concept generally offers an opportunity to solve the problems associated with premixed combustion, such as combustion anomaly or unburned ammonia emissions, but poses a challenge of engine complexity with two high-pressure fuel injection systems. Another challenge is the current availability of high-pressure pumps and fuel injection equipment for ammonia.

Table 1: Combustion Concepts for Ammonia

Strategy	Quick 'time-to-market'				Dedicated 'Flex Fuel'	
Mixture formation	Port gas admission				Direct injection	
Combustion & Ignition Concept	Pre-mixed combustion Spark ignition		Pre-mixed combustion Diesel pilot injection		Diffusive combustion Diesel pilot injection	
	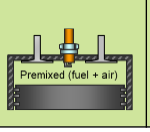	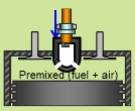	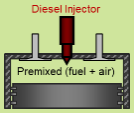	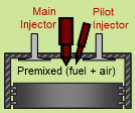	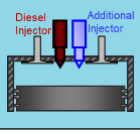	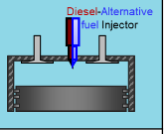
Substitution rate	100%		30 ~ 90%	> 95%	~95%	
Diesel back up capability	N.A.		100%		30 ~ 100%	

2.1. Pre- mixed combustion with spark ignition

The majority of large natural gas engines on the market employ spark-ignited pre-mixed combustion concept and apply either an open chamber concept or a pre-chamber combustion concept. These natural gas engines can be converted in a relatively simple way to carbon-neutral engines by adapting the relevant components such as gas supply system to those compatible to the selected alternative fuel.

Considering the lower heat value of ammonia compared to the natural gas, an appropriate sizing of gas admission valve is required. In addition, the ammonia compatibility of the materials used in the entire gas supply system as well as in the components that come in contact with ammonia (e.g. combustion chamber, exhaust system, crankcase and blowby system) must be carefully checked.

Both of the combustion concepts with or without pre-chamber can tolerate ammonia well to a certain extent. Open chamber spark-ignited (OCSI) concept, however, may suffer from the low reactivity characteristics of ammonia due to its limited ignition energy and a mixing of hydrogen to ammonia is necessary to assure a stable ignition and combustion.

The pre-chamber spark-ignited (PCSI) concept has a higher chance to realize a good ammonia combustion, but an admixing of hydrogen is still necessary at least at engine start and low load operation. Highlights from the measurement results on a single cylinder test engine will be given in a later section of the paper.

In both OCSI and PCSI, high levels of unburned ammonia emissions and nitrous oxide emissions as well as very high NO_x emissions are expected and thus, exhaust aftertreatment system is mandatory.

2.2. Pre- mixed combustion with diesel injection

By adding or adapting the gas supply system, it is feasible in a relatively simple manner to burn ammonia in diesel or dual fuel engines. One of the biggest advantages of such diesel substitution or dual fuel engines is the redundancy of engine operation in diesel mode. It is possible to continue the engine operation independently of the availability of the ammonia or even in case of troubles of ammonia-related subsystems.

Ammonia can be tolerated quite well by the diesel-ignited pre-mixed combustion concept. The strong ignition energy made available by the pilot diesel injection assures a stable ignition of the mixture.

Combined with a proper setting of the excess air ratio, 90 to 95% (energy based) substitution rate can be realized. Similar to the spark-ignited combustion, however, quite high unburned NH_3 emissions and very high NO_x emissions force an application of exhaust aftertreatment. Highlights from the measurement results on a single cylinder test engine will be given as a comparison basis to the spark-ignited pre-mixed combustion concept in a later section of the paper.

2.3. Diffusive combustion with diesel pilot injection

While the pre-mixed combustion concept could be realized in a relatively simple manner by adapting the gas supply system, the associated challenges such as combustion anomalies and exhaust gas emissions pose a limitation on the achievable substitution rate and potential reduction of GHG gas emissions. Diffusive combustion concept could offer a good solution to these known challenges of the pre-mixed combustions whereas the availability, reliability and durability of high-pressure injectors and high-pressure pumps that are compatible for the selected alternative fuel as well as the significantly increased complexity of the engine and subsystems are the main challenges.

From the diffusive combustions of ammonia, a significant reduction of unburned NH_3 emissions is expected compared to pre-mixed combustions. Injectors and high-pressure pumps for ammonia, however, are still at an early phase of the development and available to a limited extend.

3. Single Cylinder Engine Test Results

3.1. Test engine

The AVL high-speed single cylinder test engine SCE175 shown in Figure 2 was used for the investigations described in the following section of the paper. AVL designed a new clean sheet engine power cylinder unit to be used as a platform for the performance and mechanical development testing and successfully demonstrated a BMEP of 35 bar and a BSFC of 168 g/kWh at 1500 rpm in diesel engine version and a BMEP of 32.5 bar and a brake thermal efficiency of 50% at 1500 rpm with and engine-out emissions cap of 500 mg/Nm3 NO_x at 5% residual O_2 in gas engine version [7].

The engine is characterized by a high peak firing pressure capability of up to 330 bar while retaining state-of-the-art durability requirements. The engine can be operated as a diesel engine, gas engine or dual fuel engine with a common rail injection system for liquid fuel and with a port gas admission valve or venturi mixer for gaseous fuel. Each cam segment for intake and exhaust valves can be replaced or adjusted separately.

Figure 2: AVL High-Speed Single Cylinder Test Engine SCE175

For the present study, the engine was adapted to investigate the characteristics of pre-mixed ammonia combustion with two different ignition concepts. The schematic diagram of the engine configurations tested in the following measurements and their high-level specifications are given in Table 2. The gaseous fuel was mixed with the air by a venturi gas mixer and an air/fuel mixture was supplied to the engine. For the spark-ignited combustion concept, a mixture of hydrogen and ammonia was mixed with the air and additionally, a small quantity of pure hydrogen was supplied to the pre-chamber. For the diesel-ignited concept, only ammonia was mixed with the air by the venturi gas mixer.

Table 2: Schematic diagram and specifications of SCE175 used for testing in this study

NH_3 Gas Engine	
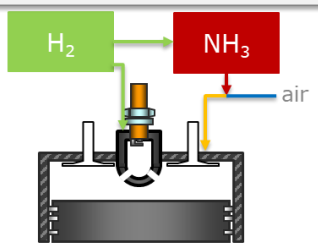	
Bore	175 mm
Stroke	215 mm
Displacement	5.2 l/cylinder
Rated speed	1500 rpm
BMEP NH3	25 bar
Rated power	162 kW
Compression ratio	13.5:1
Intake valve timing	Miller 490 °CRA
Combustion system	Quiescent

NH_3 Substitution Engine	
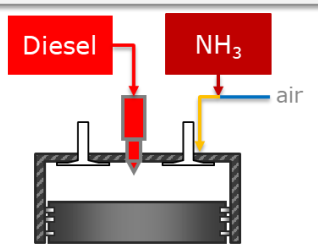	
Bore	175 mm
Stroke	215 mm
Displacement	5.2 l/cylinder
Rated speed	1350 / 1800 rpm
BMEP	25 bar
Rated power	195 kW
Compression ratio	16.5:1
Valve timings	Miller 490 °CRA
Combustion system	Quiescent

3.2. Diesel-ignited pre-mixed ammonia combustion test result

The ammonia air mixture supplied to the combustion chamber was then ignited by an injection of diesel fuel through a common rail diesel injector that is capable of the rated output in diesel operation mode i.e. 35 bar BMEP. While this concept has an advantage of being able to maintain the full load capability in diesel operation mode, the maximum possible substitution rate by ammonia is typically limited by the injection stability at low injection quantities.

Figure 3 shows the influences of diesel energy ratio and excess air ratio on unburned ammonia emission and nitrous oxide emission. The excess air ratio shown in the figure is a global excess air ratio considering both diesel and ammonia. The measurement was conducted within the shown operating area but the outer contour of the map is not necessarily the operational limit. Towards the lower excess air ratio and the higher diesel energy ratio (top left corner of the diagram), the operational limits typically are the exhaust gas temperature and CO emissions due to incomplete combustion of diesel fuel. Towards the higher excess air ratio and the lower diesel energy ratio (bottom right corner of the diagram), the operational limits typically are the high unburned ammonia emission and the low combustion stability.

At excess air ratio above 1.8 and diesel energy ratio above 50%, the unburned ammonia emission as well as nitrous oxide emission increases significantly when the diesel substitution rate is increased. In this area, the influence of the global excess air ratio is rather moderate because the excess air ratio of ammonia only is still quite high (3.5 to 5) and the very lean ammonia air mixture only vicinity of the diesel flame burns and a considerable portion of ammonia air mixture between the diesel flames remains unburned. Thus, a small variation in decimals of the global excess air ratio do not improve the ammonia combustion sufficiently.

As the excess air ratio and diesel energy ratio are further decreased, however, the unburned ammonia as well as nitrous oxide emission decreases significantly. In this area the excess air ratio of ammonia only becomes below 2.5 and it can be understood that the combustion of ammonia air mixture between the diesel flames also starts improving.

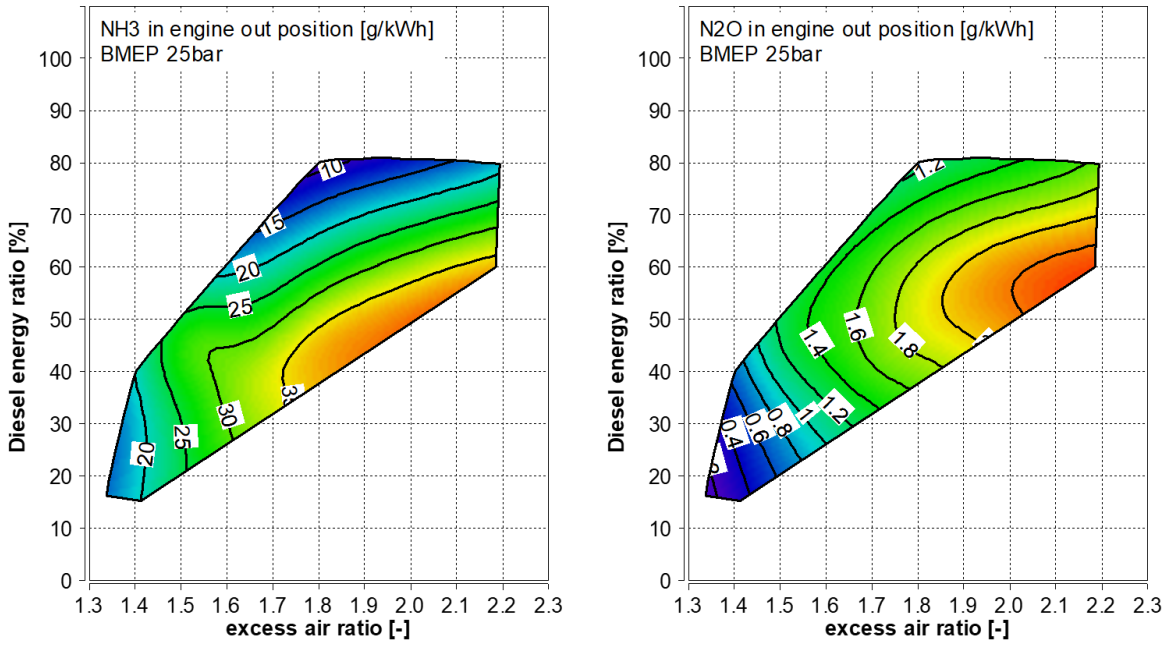

Figure 3: Unburned ammonia emission (left) and nitrous oxide emission (right) as a function of diesel energy ratio and excess air ratio measured at engine out at BMEP 25 bar and 1350 rpm

Figure 4 shows the effective engine efficiency of the single cylinder engine and the CO_2 equivalent emissions of the same measurement campaign. The values of the baseline diesel operation are indicated in the diagrams. Note that these values of diesel operation mode were measured with the same engine configuration as the ammonia substitution measurement and do not represent the optimum diesel performance measured on this engine platform.

The efficiency decreases as the ammonia energy ratio is increased mainly due to unburned ammonia emissions and slightly improves at the low excess air ratio and the low diesel energy ratio as the unburned ammonia emission decreases in this area.

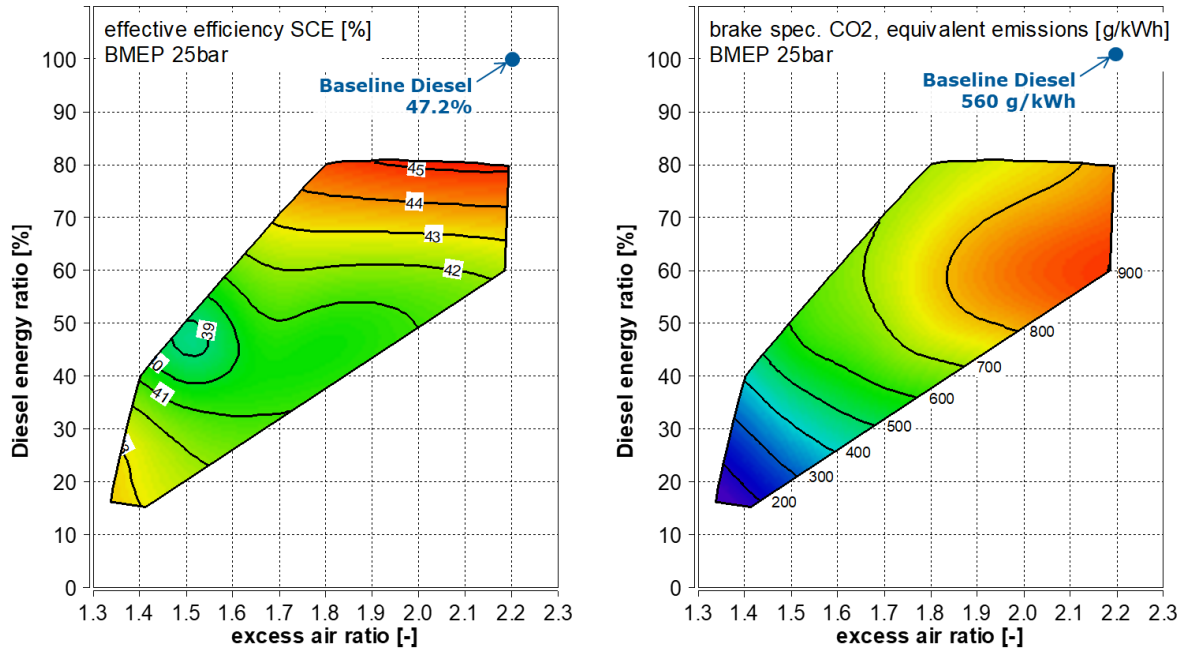

Figure 4: Brake thermal efficiency (left) and CO_2 equivalent emission (right) as a function of diesel energy ratio and excess air ratio measured at engine out at BMEP 25 bar and 1350 rpm

CO_2 equivalent emissions reflect the trend of the nitrous oxide emissions as the global warming potential of the nitrous oxide is 265 in 100 years scale according to the 5th assessment of the IPCC [8] and has a significant influence on the CO_2 equivalent emissions. Diesel energy ratio of above around 40% CO_2 equivalent emissions is even worse than the baseline diesel operation. The benefit can only be seen in the area of the low excess air ratio and the low diesel energy ratio where the nitrous oxide emissions can be decreased.

Therefore, it can be concluded that it is important for the pre-mixed ammonia combustion with diesel ignition to maximize the ammonia substitution rate and minimize the excess air ratio to optimize in order to realize a low unburned ammonia and a low nitrous oxide emission.

When the diesel injector with the full load capability is carried over, the injector capability for stable injections of small quantities is one of the key success factors for this combustion concept. In addition, the turbocharger layout including the air path control system to realize the low excess air ratio required for ammonia combustion and high excess air ratio in diesel operation mode is an important development topic. Furthermore, the optimizing the transition from diesel to ammonia operation is another development challenge, as the gradual increase in the ammonia ratio may fail due to excessive unburned ammonia and excessive nitrous oxide emissions.

3.3. Spark-ignited pre-mixed ammonia combustion test result

For the spark-ignited combustion concept, a mixture of hydrogen and ammonia was mixed with the air through a venturi mixer. The energy fraction of hydrogen mixed to ammonia was constant at 15% in the measurements discussed in this section. During the compression stroke, the ammonia-hydrogen-air mixture is forced into the pre-chamber and mixed with the pure hydrogen which is supplied

separately and directly into the pre-chamber. The quantity of the additional hydrogen to the pre-chamber was about 1% in energy fraction of the total fuel. This extra enrichment of the pre-chamber by the pure hydrogen is to ensure a stable start of combustion by a spark ignition.

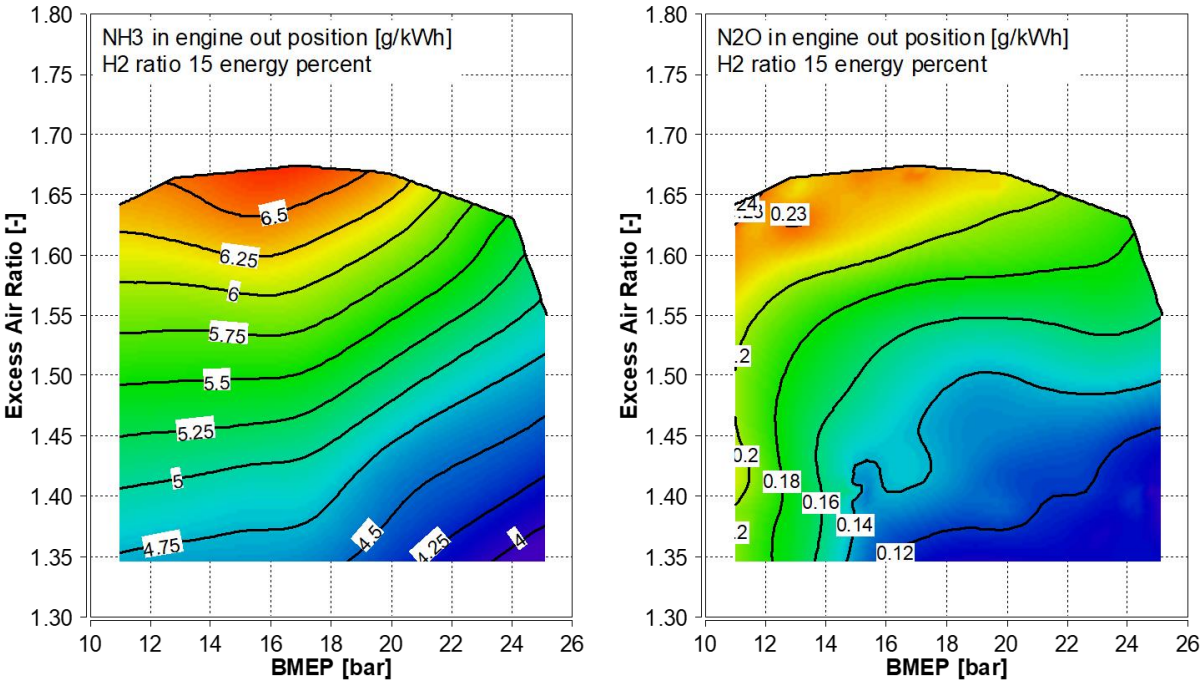

Figure 5: Unburned ammonia emission (left) and nitrous oxide emission (right) as a function of BMEP and excess air ratio measured at engine out at 1500 rpm with a constant hydrogen energy fraction of 15%

Figure 5 shows the unburned ammonia emission and nitrous oxide emission as function of the BMEP and the excess air ratio. The excess air ratio shown in the figures is a global excess air ratio considering ammonia and hydrogen. At first glance it can be noticed that the level of unburned ammonia emission and nitrous oxide emission is considerably lower than that of diesel-ignited combustion concept as shown in the Figure 3. Due to the absence of the diesel fuel, the excess air ratio of the spark-ignited concept can generally be set lower without suffering from the incomplete combustion and CO emissions. In addition, the mixing of hydrogen significantly supports the ammonia combustion and reduces the unburned emissions. Nevertheless, the trend itself is similar to the diesel-ignited combustion and the lower excess air ratio results in the reduction of the emissions.

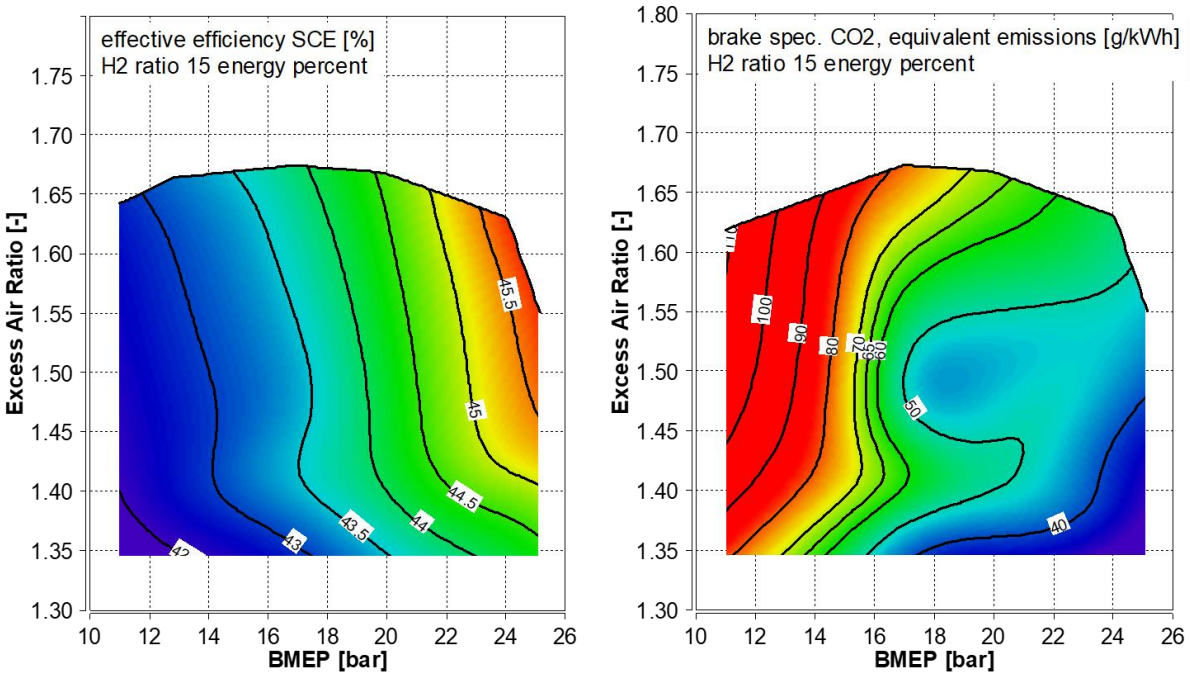

Figure 6: Unburned ammonia emission (left) and nitrous oxide emission (right) as a function of BMEP and excess air ratio measured at engine out at 1500 rpm with a constant hydrogen energy fraction of 15%

Figure 6 shows the effective engine efficiency of the single cylinder engine and the CO_2 equivalent emissions of the same measurement campaign. The efficiency is not significantly influenced by the excess air ratio but increases as the engine load is increased. The trend for the CO_2 equivalent emissions follows nitrous oxide emissions, but is at very low level compared to the diesel-ignited concept as shown in the Figure 4. The fuel is carbon free and thus, the CO_2 emission from the engine is at a quite low level and resulting from the combustion of the lubricating oil.

A drawback of the tested concept were the very high NO_x emissions, NO_x values above 35 g/kWh were measured, due to compact Rate of heat release as enabled by the hydrogen admixing and due to high temperature caused by the low excess air ratio. The level of NO_x emission is much higher than that of the unburned ammonia emission meaning that an additional urea injection would be required at SCR. Ideally, the levels of NO_x emission and NH_3 emission at engine out are balanced so that the additional urea injection at SCE can be avoided or minimized.

A reduction of hydrogen energy ratio and an optimization of the excess air ratio are further conceivable development steps to reduce the NO_x emissions at engine out. In addition, supplying the pre-chamber with the same fuel as the main chamber must be investigated. In this study, pure hydrogen was supplied to the pre-chamber for simplicity, and this must have had a certain influence on the resulting high NO_x emission. In the actual application, however, the partially cracked ammonia is likely to be supplied to both the main chamber and the pre-chamber to avoid installing an additional fuel tank for the pure hydrogen.

Figure 7 compares the engine performance and emissions of four different combustion concept, namely, diesel, natural gas, ammonia spark-ignited and ammonia diesel-ignited, at a BMEP of 25 bar. The engine configuration for the diesel engine is different from that of the ammonia diesel-ignited concept. The diesel engine is optimized for the single fuel operation, especially in terms of the

compression ratio. On the other hand, the engine configuration for the natural gas engine is the same as that of the ammonia spark-ignited concept.

The diesel engine has the highest brake thermal efficiency (BTE) of 48.6% but at the same time emits the highest CO_2 emission. The natural gas engine follows with the BTE of 47% measured at NO_x 500 mg/Nm³ at residual O_2 of 5%. The CO_2 emission from the gas engine is lower by more than 20% compared to the diesel engine. However, the benefit is partially compensated by the CH_4 emission, which has a global warming potential (GWP) of 28 according to the 5th assessment of the IPCC, resulting in 10% reduction in the CO_2 equivalent emission compared to the diesel engine.

The ammonia spark-ignited concept shows a remarkable potential for the reduction in the CO_2 equivalent emissions benefitting from the carbon free fuel and very low nitrous oxide emissions. It emits only 6 to 6.6% of CO_2 equivalent emissions compared to the diesel and gas engines, respectively. As discussed above, however, the excessive NO_x emission is the challenge of this combustion concept and further development steps are necessary.

It is clearly visible that the BTE of the ammonia diesel-ignited concept is remarkably lower than the others mainly due to the high unburned ammonia emission of around 20 g/kWh. While the CO_2 emission itself from this concept is about 20% compared to the diesel engine, the CO_2 equivalent emission counts for 36% of the diesel engine because of the nitrous oxide emission. Even though the nitrous oxide emission was reduced to a low level of about 0.3 g/kWh, the contribution to the CO_2 equivalent emission is still quite high due to its high GWP of 265. Further increase of the ammonia energy fraction and optimization of the excess air ratio to minimize the nitrous emission are the key development targets for this combustion concept.

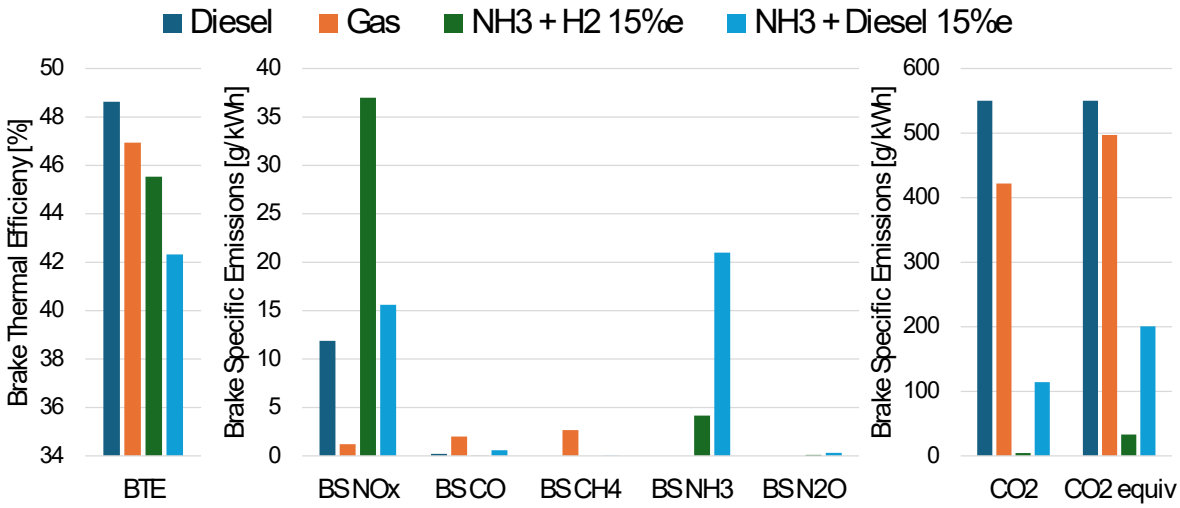

Figure 7: Comparison of brake thermal efficiency and emission performances among diesel, gas, NH_3 spark ignited and NH_3 diesel ignited at BMEP 25 bar

4. 3D CFD Simulation

For a better understanding of the physical phenomena and to potentially support further combustion concepts development, 1D thermodynamic and 3D CFD simulations of the diesel-ignited pre-mixed ammonia combustion and the spark ignited pre-mixed ammonia concept, were conducted. A computational model was setup for each concept separately and some selected operating conditions

were simulated by means of CFD, while 1D thermodynamic simulation was performed for the complete engine operating map using the AVL Simulation solutions FIRE™ M und CRUISE™ M respectively.

4.1. Diesel-ignited premixed ammonia combustion concept simulation

The computational model was setup for the operating point 25 bar BMEP at 1350 rpm. The simulations have been performed for two operating conditions – one for using pure diesel as a fuel and the other one using 20 energy percent of diesel and the rest ammonia. The given percentage describes the share in the total energy introduced in the combustion chamber. While the first operating condition reflects the standard diesel operating mode of the engine, the other one with 20% Diesel and 80% NH_3 represents conditions close to the limit where stable combustion still can be achieved. The computational model and the simulated operating conditions are presented in Figure 8.

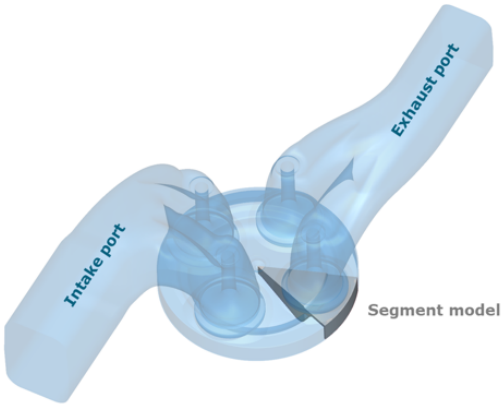

	100% Diesel	20% Diesel, 80% NH_3
Rotational speed [rpm]	1350	1350
IMEP [bar]	24.5	23.5
Diesel SOI BTDC [°CA]	4.8	13.3
Diesel DOI [°CA]	8.6	6.0
Rail pressure [bar]	2200	1400
Total air excess ratio [-]	2.22	1.47

Figure 8: Simulation model and simulated operating conditions

A mixture of ammonia and air is supplied to the intake port through a venturi mixer. This results in almost ideal homogeneity of the mixture. Therefore, homogeneous mixture was initialized in the intake ports at start of the simulation and the same mixture is supplied through the inlet boundary of the intake ports during the simulated cycles.

The engine utilizes an injector with nine injection holes. In order to minimize the required computational resources, only a cylinder segment of 40°, featuring one nozzle hole was simulated for the high-pressure cycle featuring compression, diesel injection and combustion as shown in Figure 8.

The combustion process was simulated deploying a general gas phase reaction solver. This requires the use of a chemical kinetic mechanism suitable for NH_3, H_2 and n-heptane combustion simulation [9]. The mechanism deployed in this study consists of 69 species and 389 chemical reactions. To speed up solving the chemical kinetics, an acceleration technique, called multi-zone model, was enabled. With this, cells having similar conditions (temperature and equivalence ratio) are grouped into zones for which the chemistry is solved at once rather than for each individual cell. The simulations performed in this study use a 5 K limit for temperature and 0.01 limit for the equivalence ratio to define the model zones. This specification enables a significant acceleration of the simulation while preventing a visible deterioration of the simulation result accuracy.

Simulations of both operating modes were conducted. Diesel injection and combustion were calibrated to the experimental data. Cylinder mean pressure and rate of heat release curves are presented in Figure 9.

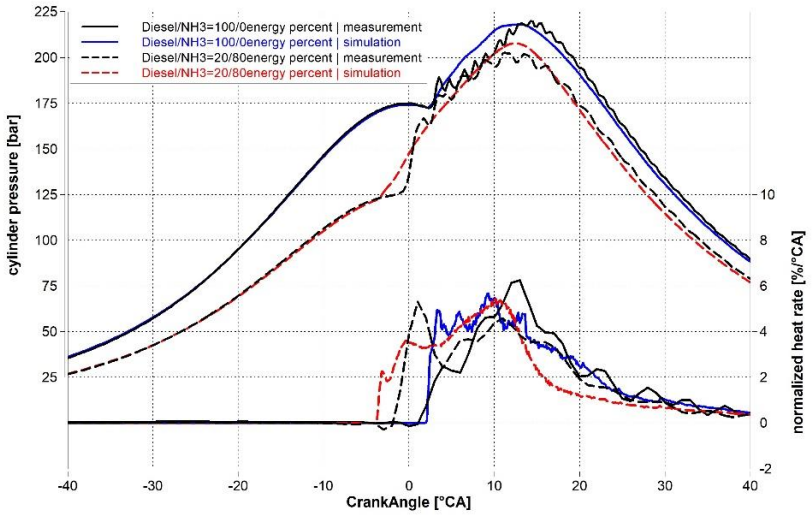

Figure 9: Simulated vs Experimental cylinder mean pressure and ROHR for two operating modes

A good agreement between simulated and experimental results can be observed, which indicates, the simulation realistically reflects related physical phenomena.

3D results obtained for fuel injection and combustion are presented in Figure 10. Diesel starts to evaporate earlier and more intense if it is injected into a pure air. In this particular case the rail pressure is significantly higher. Consequentially also the combustion starts earlier and a bit closer to the injection nozzle. The observed combustion progress is typical for a diesel diffusion flame, driven by the injection. Flow inertia from diesel injection and the aerodynamics of the piston bowl redirects the flame front from the piston bowl rim to the cylinder head.

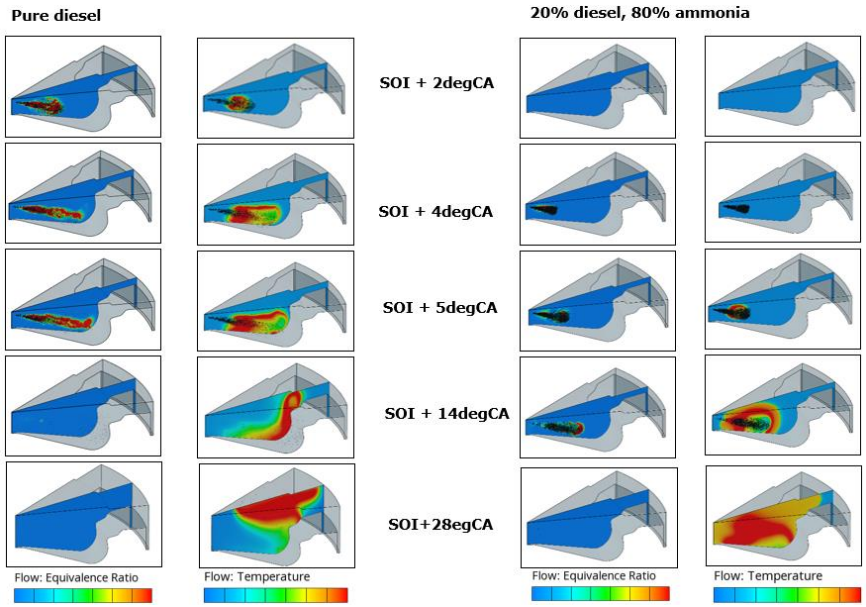

Figure 10: Comparison of fuel injection and combustion for both simulated operating modes

In the dual fuel case, the evaporation of the diesel starts later. Also, ignition is taking place significantly later compared to the pure diesel mode. There are several reasons for that. Injecting diesel into ammonia, means, there is less oxygen available for ignition and combustion. Due to the lower rail pressure and, consequently, the lower kinetic energy of the fuel jet, there is weaker jet breakup and evaporation is slower. The lower injection velocity also results in a weaker mixing process. Furthermore, the diesel-ammonia mix has elongated auto-ignition time, therefore ignition starts at a time, when the jet kinetic energy is almost neutralized. The ignition point is in a mixed fuel region. From this ignition kernel, the combustions spreads like from a fictitious spark plug, which is typical for pre-mixed cases. The aerodynamics of the bowl loses on importance. Once the flame reaches pure ammonia regions (this is when it moves into the squish area), the flame propagation slows down due to the low laminar flame speed of ammonia. This slow combustion is also a reason for the high ammonia slip related to this concept. Please refer to the Figure 11.

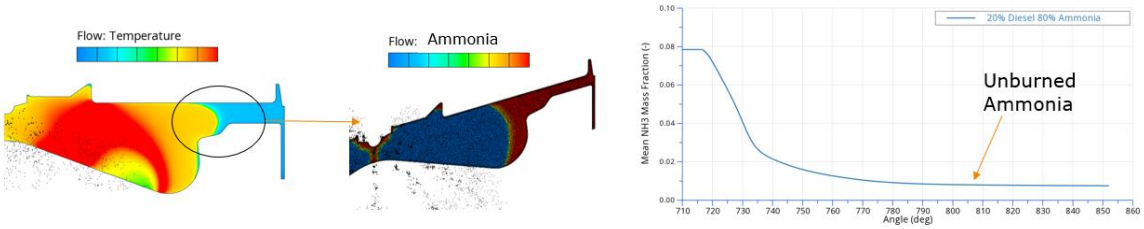

Figure 11: Slow combustion in pure ammonia region

4.2. Spark ignited premixed ammonia combustion concept simulation

The computational model was setup for three operating conditions. They represent load and an air excess ratio variation at constant engine speed, see Table 3.

Table 3: Simulated operating conditions

Operating condition	369	378	381
Rotational speed [rpm]	1500	1500	1500
IMEP [bar]	18.5	24.6	27.8
Air excess ratio	1.46	1.44	1.40

As written above, the mixture of ammonia and hydrogen is supplied to the intake port through a venturi mixer. This results in almost ideal homogeneity of the mixture. Therefore, homogeneous mixture was initialized in the intake ports at start of the simulation and is supplied through the inlet boundary of the intake ports during the simulation.

The energy share of the hydrogen was kept constant at 15%. An additional 1% energy share of pure Hydrogen is supplied into the pre-chamber to enrich the mixture in the spark plug area for stable ignition and fast propagation of the flame into the main chamber. The computational model including important geometry parts is presented in Figure 12. A key role at this combustion concepts plays the pre-chamber.

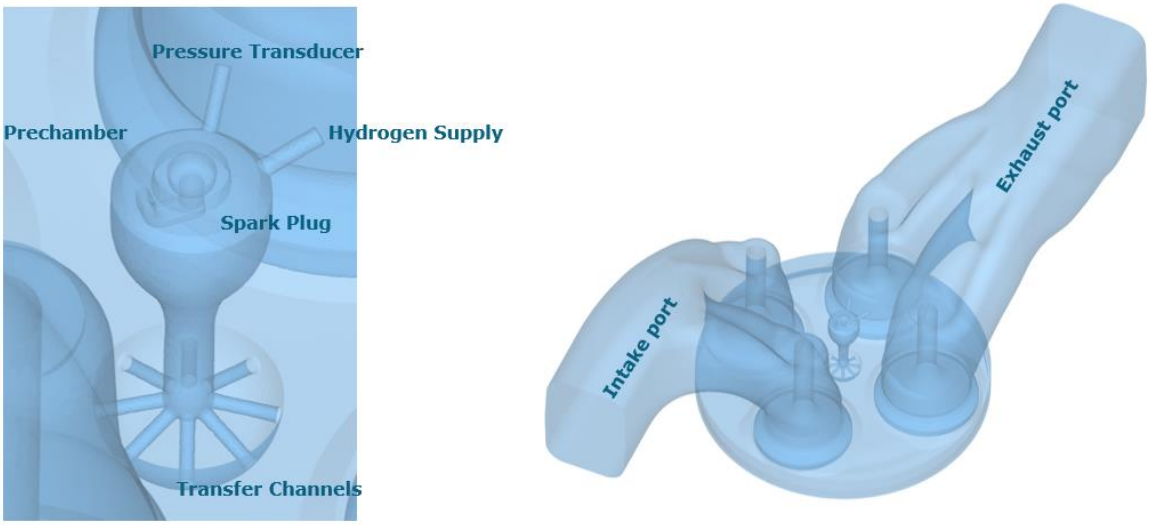

Figure 12: Simulation model (© AVL)

Simulating the combustion of the spark-ignition concept, the same models (general gas phase reaction kinetics and multi-zone accelerator) have been used as for the diesel-ignition concept.

CFD simulations of all selected operating conditions were conducted. Minor calibration of the combustion process was required in order to match mean cylinder pressure and rate of heat release curves from the experimental data. The calibration was done by means of variation of the combustion reaction rate. The mean cylinder pressure and the accumulated heat release curves for all simulated operating conditions are presented in Figure 13. Good agreement between simulated and the experimental results can be observed, which indicates that the simulation results realistically reflect the involved physical phenomena.

Slightly too fast reaction rates can be observed, which relates to the slightly overpredicted mean cylinder pressure for all simulated operating conditions. Simulated and experimental results are consistent for all modelled operating conditions, which indicates a high level of robustness of the simulation model and its potential to correctly predict in-cylinder flow conditions for a large variety of operating points.

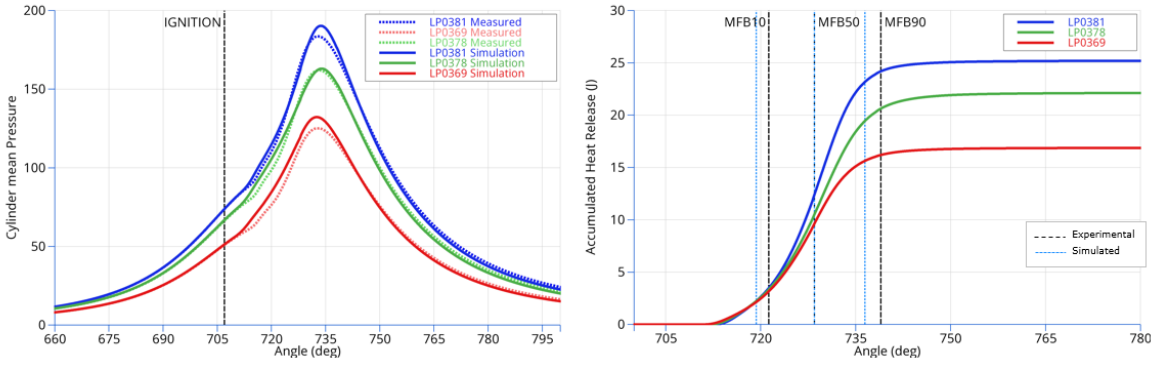

Figure 13: Simulated vs. experimental cylinder mean pressure and accumulated heat release

As already mentioned, the key role in this combustion concept plays the pre-chamber design and the enrichment of the pre-chamber mixture with additional hydrogen. For the hydrogen supply into the pre-chamber a non-return valve is used. It operates based on the pressure difference on both sides of the valve, which makes it a bit difficult to control the supplied mass. The dynamic of the hydrogen propagation into the pre-chamber and mass-fractions in the spark plug area are displayed in Figure 14. It can be observed, that the pre-chamber gets almost completely filed with hydrogen during the intake stroke and later a significant part of it propagates to the cylinder. However, a considerable mass-fraction of hydrogen remains within the pre-chamber and in the spark plug region thus helping to achieve stable ignition and combustion within the pre-chamber.

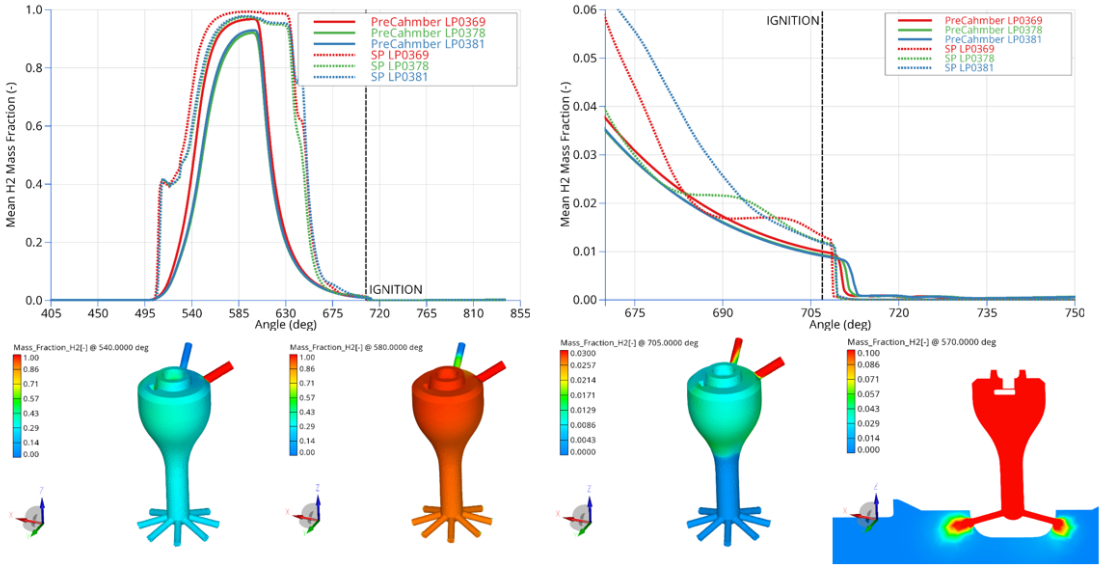

Figure 14: Hydrogen mass-fractions in the pre-chamber and spark plug area

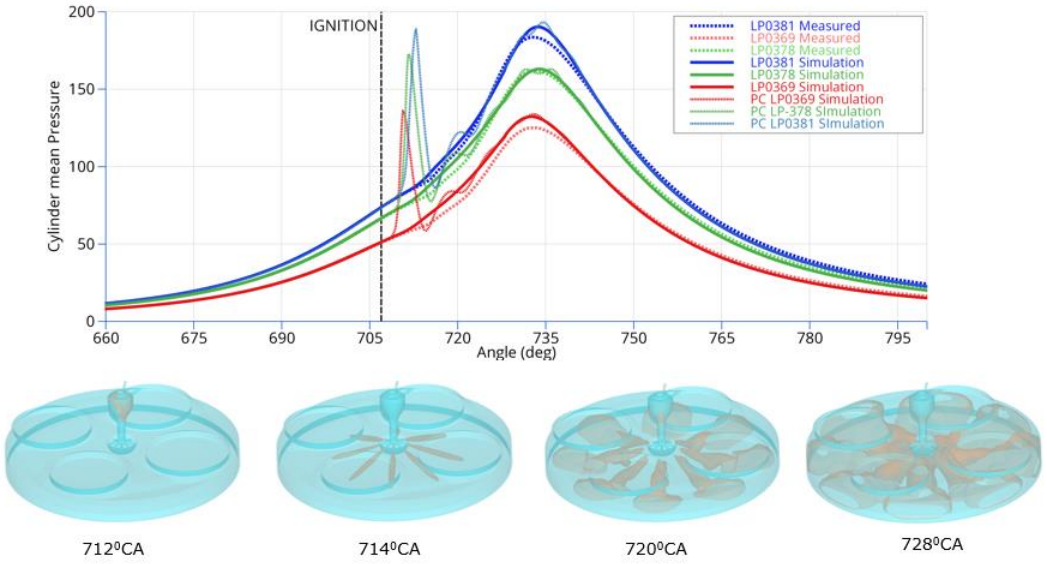

Figure 15: Pre-chamber pressure vs. cylinder mean pressure (top) and flame visualization (bottom)

In Figure 15 the combustion behaviour is shown. The flame front visualization nicely demonstrates the working engine concept. Ignition is initiated by the spark in the pre-chamber. Due to the relatively high

hydrogen concentration there, it is stable and reliable. High pressure appears in the pre-chamber after ignition (significantly higher than in a cylinder). Therefore, a strong flow and flame propagation from the pre-chamber to the main chamber through the transfer channels can be observed. The high-speed and energy intense jets entering the main chamber ensure ignition and combustion of the lean ammonia/hydrogen/air mixture in the cylinder volume.

5. Summary and Outlook

The paper described two different ammonia combustion concepts for high-speed engines, as investigated by AVL. The first combustion concept represented a retrofittable approach of a premixed ammonia combustion with a diesel pilot ignition, while the second concept pursued a pure zero-carbon fuel strategy by utilizing a mixture of ammonia and hydrogen ignited via a hydrogen-scavenged pre-chamber with a spark plug.

The measurements conducted on the AVL high-speed single cylinder test engine SCE175 with the new clean sheet engine power cylinder unit designed by AVL enabled a fair comparison of the engine performance and emissions from the different fuels and different combustion concepts revealing the potential and challenges of the ammonia combustions.

While the diesel-ignited ammonia combustion concept already showed a reasonable reduction in the CO_2 equivalent emissions by a relatively simple engine modification, there is still a good potential for the further optimization by a maximization of the ammonia energy ratio and a minimization of excess air ratio. A reduction in unburned ammonia emissions and nitrous oxide emissions are the key success factors.

The spark-ignited ammonia combustion concept showed an excellent potential for a reduction in the CO_2 equivalent emissions with low unburned ammonia emissions and low nitrous oxide emissions. However, an excessively high NO_x emission was measured and further optimizations of operational parameters, especially the energy ratio of the additional hydrogen, are required.

For specific applications, hydrogen is derived from Ammonia via an onboard cracking process. Further combustion development and optimizations will focus on the admission of N_2/H_2 mixtures to the pre- and main chamber.

For both - diesel and spark ignited - premixed NH_3 combustion, a trade - off is evident. A leaner mixture will increase unburnt NH_3 and N_2O (combustion byproduct) and reduce NO_x. On the contrary an enrichment of the mixture is limited. For the diesel ignited concept, the lower limit is the increase of CO, due the missing oxygen content for the combustion of Diesel.

For the spark ignited concept, the lower limit is the increased thermal load and the temperature limit of specific engine core components (fire deck, valves and seat rings, liner, piston). The trade off as described above is relevant for the layout of the aftertreatment system as determining the composition of the raw missions varying over speed and load of the engine.

As a next step, our developments are focused on substrate characterizations considering the low and high NH_3/NO_x ratio to cover diffusive and premixed ammonia combustion. The overall thermodynamic layout of the engine and aftertreatment is a key element enabling Ammonia engines to be a promising solution for the near future.

CFD simulations (in conjunction with other simulation models and disciplines) represents a suitable means of understanding and optimizing concepts for CO_2-neutral combustion engines. The ability to model complex physical and chemical processes and to simulate them predictively in a timely manner allows concepts and variations to be assessed efficiently and reliably. This is a decisive argument for the use of simulation, especially in the development of large engines, since the construction of components and system prototypes for physical testing is associated with immense costs and time expenditure.

Acknowledgements

For the ammonia test program, the authors would like to acknowledge the financial support of the "COMET - Competence Centers for Excellent Technologies" Program of the Austrian Federal Ministry for Climate Action, Environment, Energy, Mobility, Innovation and Technology (BMK) and the Federal Ministry for Digital and Economic Affairs (BMDW) and the Provinces of Styria, Tyrol and Vienna for the COMET Centre (K1) LEC EvoLET. The COMET Program is managed by the Austrian Research Promotion Agency (FFG).

Literature

[1] IMO, "Fourth IMO GHG Study 2020", https://wwwcdn.imo.org/localresources/en/OurWork/Environment/Documents/Fourth%20IMO%20GHG%20Study%202020%20-%20Full%20report%20and%20annexes.pdf

[2] Nyhus, E., Longva, T.: MEPC 80 - Increased emission reduction ambitions in revised IMO GHG strategy, DNV Webinar, July 11th, 2023, https://www.dnv.com/maritime/webinars-and-videos/on-demand-webinars/access/mepc-80-increased-emission-reduction-ambitions.html

[3] Figer, G., Mair C., Schubert, T., Macherhammer, J. (2023). Fuel Cells for Future Marine Propulsion Systems. 19th Symposium - Sustainable Mobility, Transport and Power Generation, 28.-29. September, Graz, Austria, 2023

[4] Murakami S, Segura M., Kammerdiener T., Kirsten M., Schlick H.: Diesel ignited combustion concepts for hydrogen, ammonia and methanol; 19th Symposium „Sustainable Mobility, Transport and Power Generation" 2023; Graz/Austria

[5] Murakami S., Kammerdiener Th., Strasser R., Zallinger M., Koops I., Ludu A.: Holistic Approach for Performance and Emission Development of High Speed Gas and Dual Fuel Engines; CIMAC World Congress 2016; Helsinki/Finland; paper No.273

[6] Murakami S., Baufeld T.: Current Status and Future Strategies of Gas Engine Development; CIMAC World Congress 2013; Shanghai/China; paper No.413

[7] Estebanez G., Kammerdiener T., Schmidleitner K., Rustler M., Malin M.: Greenhouse Gas Emissions Reduction on High-Speed large Engines; CIMAC World Congress 2023; Busan; paper No.652

[8] IPCC's Fifth Assessment Report (AR5) - Climate Change 2014: Synthesis Report. Contribution of Working Groups I, II and III to the Fifth Assessment Report of the Intergovernmental Panel on Climate Change, IPCC, Geneva, Switzerland, 151 pp.

[9] Leilei, X.; et al.: A skeletal chemical kinetic mechanism for ammonia/n-heptane Combustion. https://www.sciencedirect.com/science/article/pii/S0016236122026564?via%3Dihubaccess: July 27, 2023

SCHALLER AUTOMATION

GASMOS®

Gas monitoring system

Selective online measurement of gas concentrations in large engines

- Selective gas measurement
- Continuous online operation
- Automatic calibration
- Self-monitoring sensor system

IECEx

2020 | 2021 INNOVATIV DURCH FORSCHUNG Ausgezeichnet durch den Stifterverband SCH3544BLI

www.schaller-automation.com

Keywords: Methanol, E-fuel, VPD, S&FD, H22CDF-LM

HD Hyundai Heavy Industries Organizing Lineup of Medium-Speed Methanol Engine

Gwanghyeon Yu, Yongseok Lee, Kyungrock Lee, Wookhyeon Yoon, Sungchan An

Green Power & Engine System Research Department, Engine Research Institute, Engine & Machinery Business Unit, HD Hyundai Heavy Industries

https://doi.org/10.18453/rosdok_id00004644

Abstract

Over the years, the interest in carbon-neutrality is spreading throughout the industry as a whole. Especially, according to international marine organization (IMO), the international shipping should reduce total greenhouse gas (GHG) emissions, at least 100% (net-zero) by 2050 compared to 2008. To achieve carbon-neutrality, it is essential to transition ship fuels from fossil fuel to e-fuels. Representative e-fuels include methanol, ammonia and hydrogen, with methanol-powered engines already being commercially available. HD Hyundai Heavy Industries (HHI) successfully developed the world`s first 3.0~4.5 MW medium-speed methanol-powered engine, H32DF-LM, in 2022. This engine is now being supplied to methanol-powered ships worldwide. Furthermore, in March 2024, HHI successfully completed the type approval test for 1.3~2.0 MW medium-speed methanol engine, H22CDF-LM, thereby establishing the world`s first lineup of methanol engines. HHI is currently developing 2.0~3.0 MW methanol engine and also in the process of developing engines powered by ammonia and hydrogen. In addition, fuel supply system for each fuel type is being developed. Through these, we are doing our best as a total marine solution provider.

1. Introduction

Recently, various industries worldwide have been actively engaged in efforts to achieve carbon neutrality. Particularly, in the maritime transportation sector, shipowners, shipbuilders, and engine manufacturers are actively responding to carbon dioxide or greenhouse gas (GHG) reduction policies led by the International Maritime Organization (IMO). According to IMO regulations, a 50% reduction in GHG emissions compared to 2008 levels must be achieved by 2030, and a 100% reduction by 2050. [1] While achieving net zero is sufficient since emissions are considered from a life-cycle assessment (LCA), this remains a highly challenging goal. There are various methods to reduce GHG emissions from ships. As shown in the Figure 1, research is being conducted on a variety of technologies and methods, including energy management, ship coating, speed & voyage optimization, etc. However, there is no method as effective as switching from fossil fuels to eco-friendly fuels for ship propulsion. Therefore, there is a glowing global interest in and demand for e-fuels, such as methanol, ammonia, and hydrogen to replace conventional fossil fuels like diesel and LNG.

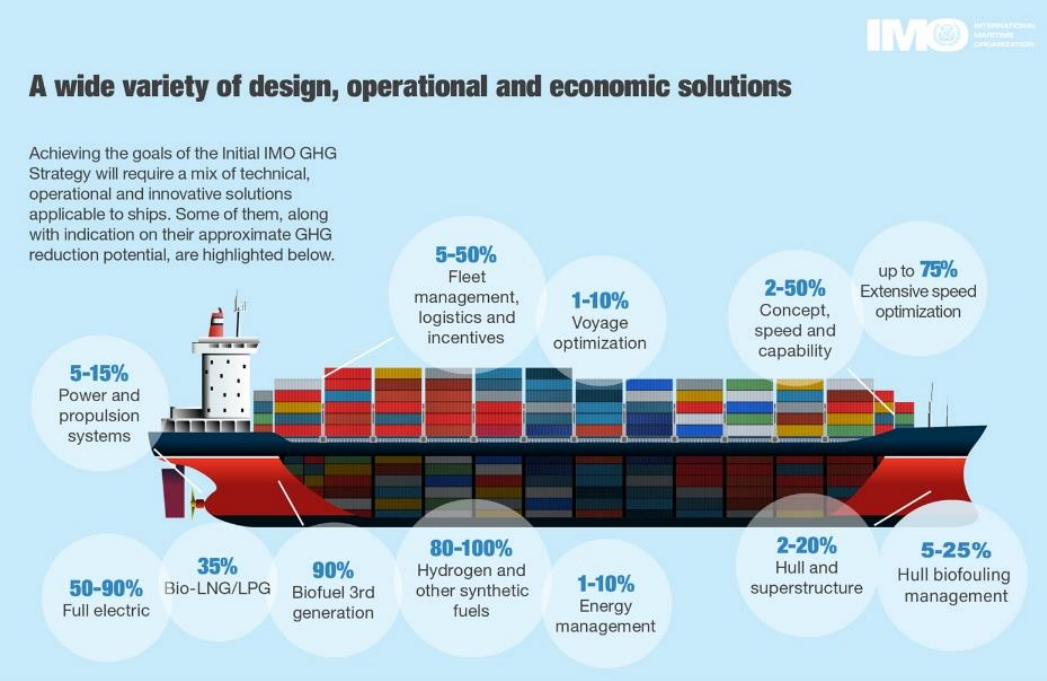

Figure 1: Strategies for reducing GHG emissions from ships [2]

E-fuel is a type of fuel synthesized by combining carbon dioxide captured from the atmosphere with green hydrogen produced though water electrolysis using electricity generated from renewable energy sources such as wind, hydro, and solar power. From a Tank-to-Wake (TTW) perspective, there are GHG emissions; however, from a LCA perspective, the amount of GHG emissions is reduced to nearly zero. [3] Therefore, the use of e-fuel can meet IMO regulations. However, due to limitation in production volume, high production costs, and the specific characteristics of the fuel, it is not easy to apply e-fuel to all ships immediately. To overcome these challenges, active research and development of related technologies are ongoing.

The Table 1 presents the fuel characteristics of diesel, methane, methanol, ammonia, and hydrogen fuels. As can be seen from the table, the characteristics of e-fuels differ significantly from those of

conventionally used diesel and methane. In the case of methanol, it has a high boiling point and low saturation vapor pressure, allowing it to remain in a liquid state at room temperature. Therefore, it is the most suitable fuel for utilizing existing fuel systems. However, due to its low heating value, more fuel is required to achieve the same power output, and its high latent heat of vaporization necessitates consideration of combustion stability. In the case of ammonia, although it has a low boiling point, it can remain in a liquid state under moderate pressure, making fuel storage and transportation easier compared to methane. However, issues related to its low combustion speed, toxicity, and corrosiveness need to be addressed.

Table 1: Fuel characteristics

	MDO	Methane	Methanol	Ammonia	Hydrogen
Boiling point (degC)	180-360	-161	64.7	-33.3	-252.9
Lower heating value (MJ/kg)	42.5	50	19.7	18.6	120.0
Latent heat of vaporization (kJ/kg)	250	510	1100	1369	446
Auto-ignition temperature (degC)	210	580	470	650	500
Laminar flame speed (cm/s)	30-40	37	37.6	6.8	265.0
Lower flammability limit (vol.%)	0.6	5.0	6.0	15.0	4.0
Energy density (MJ/L)	35.8	0.9	15.6	13.6	8.5
Saturation vapor pressure (kPa)	0.4-0.7	4600	13	857	2070

In the case of hydrogen, a significant advantage is that it only emits water upon complete combustion. However, despite its high heating value, it has a low energy density. Additionally, its extremely low boiling point presents technical challenges in storage and supply. Furthermore, due to its high combustion speed and low flammability limit, issues such as flashback and pre-ignition need to be addressed to ensure stability.

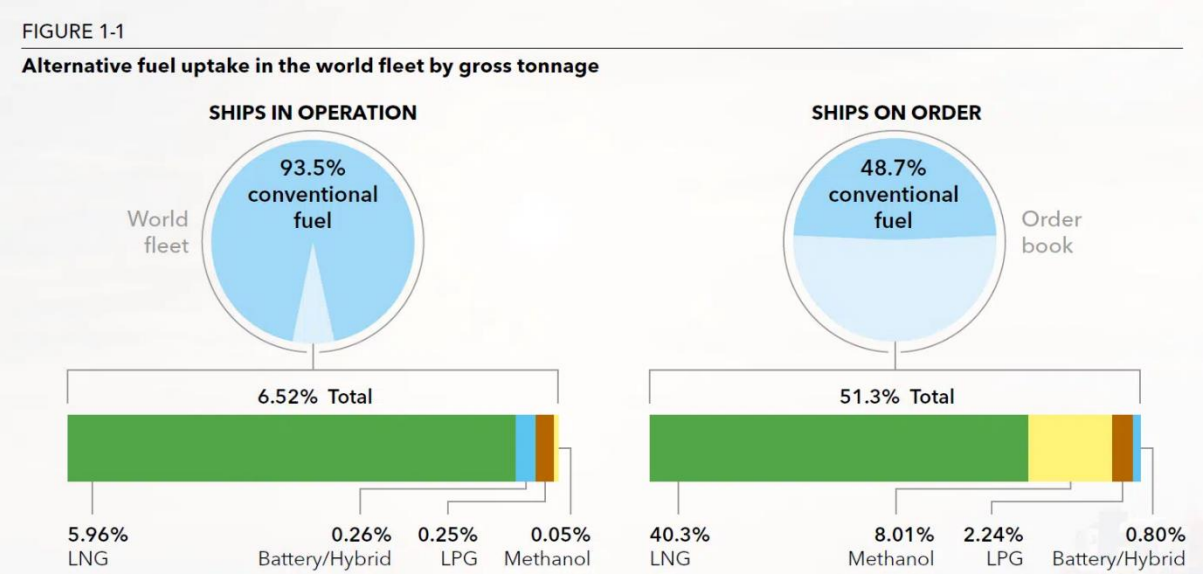

Figure 2: Alternative fuel uptake in the world fleet by gross tonnage [4]

As mentioned above, there are various technical challenges in applying e-fuels. However, numerous institutions worldwide are actively conducting related research, and it is expected that these issues will be resolved as the technology matures. Nevertheless, methanol is being utilized first during the fuel transition period because it can be directly applied using the existing fuel systems. Figure 2 shows the fuel type distribution of the entire fleet in operation and the fuel type distribution of newly ordered ships as of 2023. As shown in the figure, the majority of ships currently in operation are powered by diesel fuel. Only about 7% are powered by environmentally friendly fuels, with LNG accounting for the majority of this percentage. However, nearly half of the newly ordered ships are powered by environmentally friendly fuels. Notably, the proportion of methanol-powered ships has increased significantly. HD Hyundai Heavy Industries (HHI) is developing e-fuel engines, including those powered by methanol, to achieve carbon neutrality. Next, the history of engine development at HHI will be briefly outlined, and the virtual product development (VPD) technology utilized in this development will be introduced. Additionally, the development of HHI`s methanol engines, the H32DF-LM and H22CDF-LM, will be explained.

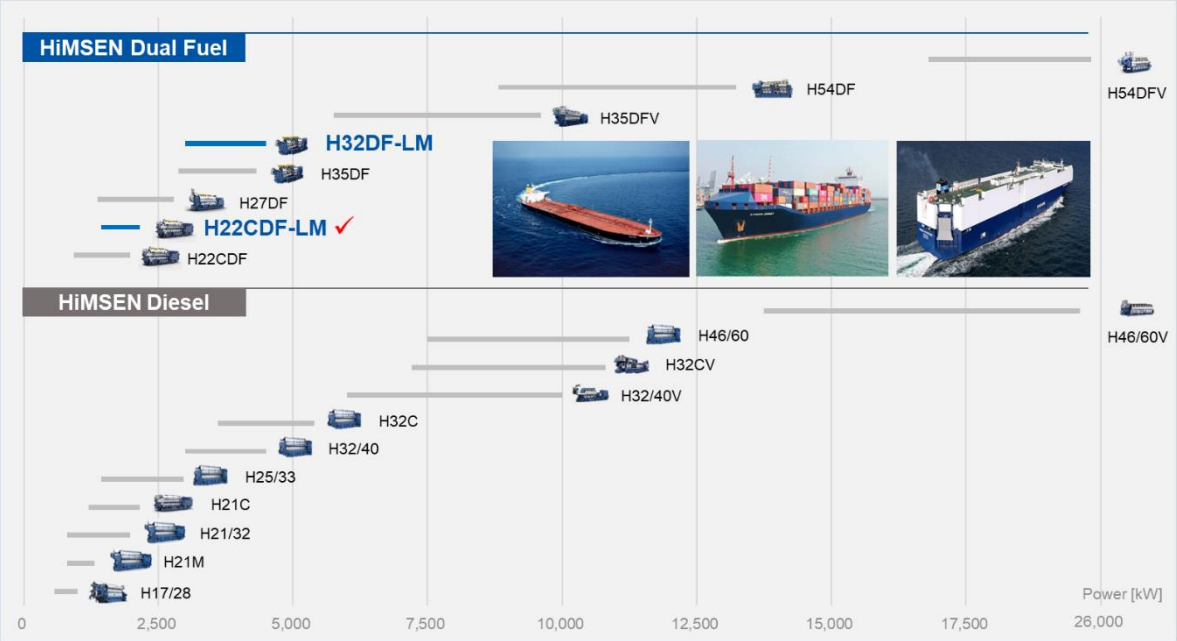

Figure 3: Lineup of HiMSEN

2. HiMSEN methanol engine development

2.1. Introduction to HiMSEN engine

HiMSEN is a brand of medium-speed engines developed by HHI, widely used for marine and power generation application. HiMSEN stands for Hi-Touch Marine and Stationary ENgine, and is designed with a focus on high efficiency, high performance, and low emissions, earning recognition for their reliability and economic benefits in various applications. In the early 2000s, HHI developed its first medium-sized diesel engine using proprietary technology. It took a long span of 12 years to establish an engine lineup ranging from 1MW to 22 MW. On average, developing a single engine took approximately two years. Additionally, in the early 2010s, the first medium-sized LNG dual-fuel engine was developed, and it took six years to establish the lineup. The development period was shortened

compared to the diesel engine development, which was due to the application of VPD technology. Meanwhile, in 2022, the world`s first methanol dual-fuel engine was successfully developed, and thanks to advancements in VPD technology, the time required to establish the lineup was further reduced. Through the development and utilization of VPD technology, HHI has been able to respond quickly and precisely to the diversification of fuels, the rapidly changing fuel market, and the needs of customers. Figure 3 shows the entire lineup of HiMSEN diesel, LNG dual-fuel, and methanol dual-fuel engines. Over the past 20 years, an engine lineup covering all power ranges from 1 MW to 26 MW has been established. Next, an introduction will be provided on the VPD technology developed and continuously advanced by HHI. Starting with methanol dual-fuel engines, the e-fuel engine lineup will continue to be expanded.

2.2. Introduction to VPD technology used in engine development

VPD stands for Virtual Product Development. It refers to be a comprehensive approach to product development that involves testing and validating product performance in a virtual environment through simulations, rather than creating prototypes for development. Unlike automobile engines, marine engines are larger in size and have higher power output. Consequently, the cost and time required for production prototype are substantial, and the manpower and expenses involving in testing are significantly higher. Therefore, a simulation-based development process is essential for the development of marine engine.

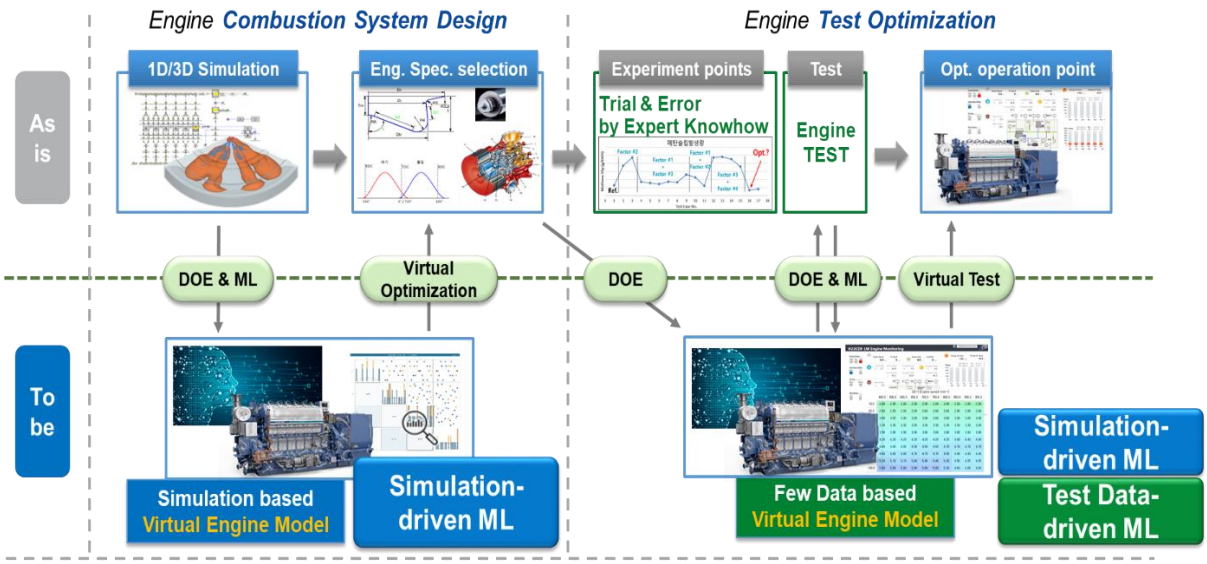

Figure 4: Utilization of virtual engine model in HiMSEN development

While simulation-based development offers many advantages over prototype-based development, the increasing variety of fuels, as well as the growing number and complexity of technologies and components applied to engines, have led to rising costs and time requirments for simulations. HHI has integrated various simulation techniques with artificial intelligent (AI) and machine learning (ML) technologies to create a virtual engine model. This model has been utilized in engine development to reduce the time required for simulation while ensuring high accuracy in the results. Figure 4 shows a schematic diagram of the virtual engine model utilized by HHI in engine development. For example, during the engine combustion system development stage, 1D and 3D simulations are conducted for

the basic and detailed design. Previously, it required changing many design variables one by one to investigate their impact on sensitivity and performance, resulting in significant time and effort needed for simulation and evaluation. Additionally, after prototype production, there are tests that need to be conducted to achieve stable engine operation and identify the optimal operating points. Previously, conducting all these tests consumed a significant amount of time and cost. However, recently, design of experiment (DOE) and ML have been utilized to build performance prediction models based on simulation and measurement data. By utilizing these models, virtual optimization was performed, enabling efficient development instead of numerous simulations and engine tests. Next, specific examples of the development and application of virtual engine models based on test and simulation data will be introduced.

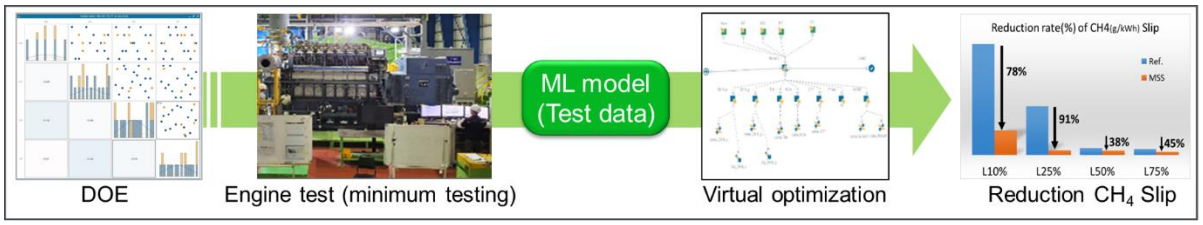

Figure 5: Utilization of a measurement data-based virtual engine model

First, the development of virtual engine model based on measurement data. HHI possesses a technology called Methane Slip Solution (MSS) to reduce methane slip in LNG dual-fuel engines. Among the MSS technologies, there is the Multi-Point Injection (MPI) technology, which was developed using a virtual engine model during the development process. [5] When operating with MPI, several new operating variables are introduced in addition to the existing variables of injection timing and injection duration. The optimal operating point, where methane slip is minimized, must be identified by combining various operating variables. Conducting actual tests would require performing tests on dozens of operating points, resulting in significant time and cost expenditures. Thus, virtual engine model based on measurement data was constructed to minimize the number of tests. Firstly, the number of test points required to create the virtual engine model was minimized using DOE, and a virtual engine model was generated using ML. After creating the model, virtual optimization was used to define the optimal points without conducting actual tests. The selected optimal points were then tested to validate the results. Through this process, the number of actual tests was minimized, and the optimal operating point where methane slip is minimized was identified.

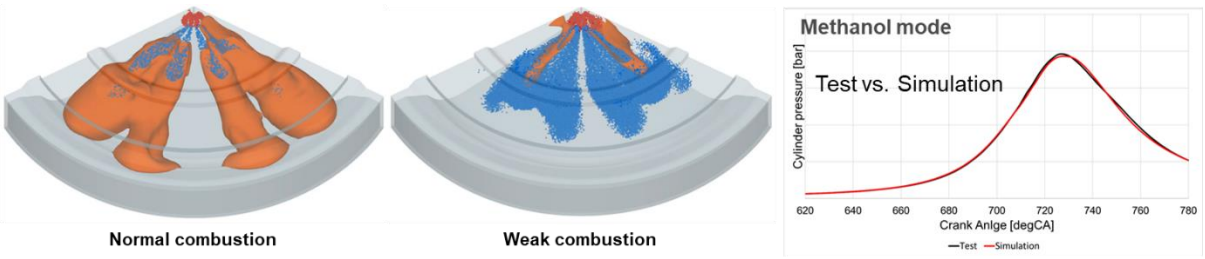

Figure 6: Utilization of a simulation data-based virtual engine model

Next, the development of virtual engine model based on simulation data. During the development of the methanol engine combustion system, a virtual engine model based on simulation data was

established and utilized in the basic and detailed design stage. In the basic design stage, fundamental specification of the combustion system, such as intake/exhaust valve timing, compression ratio, and turbocharger specification, are determined. In the detailed design stage, the specification of major combustion chamber components, such as the piston bowl shape and fuel injection valve shape, are determined. To fully consider various variables and constraints, DOE was used to understand the impact or sensitivity of all variables, while selecting the minimum number of simulation cases. And virtual engine model based on simulation data was constructed using ML. This model was utilized to design a combustion system that ensures optimal performance while considering engine operational stability and mechanical limit. Subsequently, the test conducted on the prototype engine exhibited performance consistent with the predictions, demonstrating excellent results.

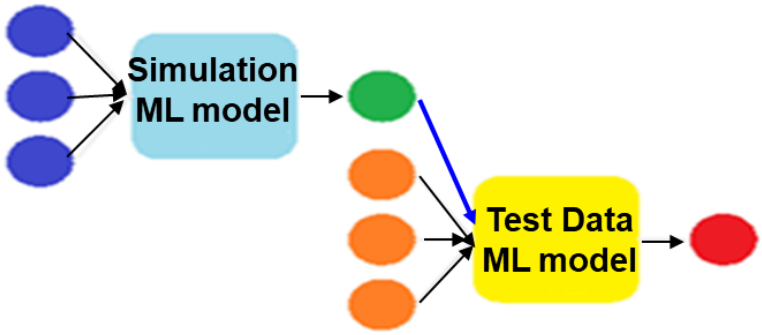

Figure 7: S&FD based PIML model

The last is the development of S&FD (simulation and few data) based Physics-informed machine learning (PIML) model using measurement and simulation data. PIML, which stands for Physics-informed Machine Learning, is a technique that incorporates physical information, such as governing equations, physical constraints, and actual measurement data, into the machine learning process. This approach enables more accurate and reliable predictions compared to purely data-driven methodologies. Additionally, PIML can effectively learn even in situations where data for building predictive models is insufficient. HHI has developed an engine performance prediction model by applying PILM to over 20 years of accumulated engine measurement data and simulation data obtained through advanced modeling. This has been termed the S&FD-based PIML model.

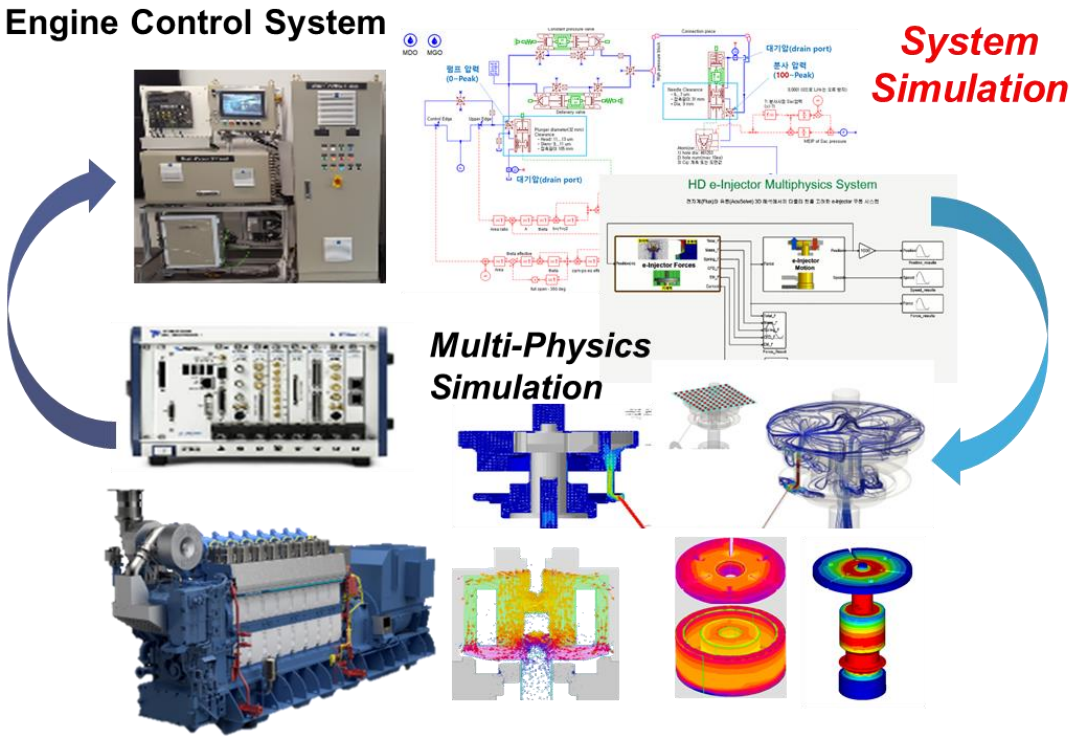

Figure 8: Integrated engine system simulation

There are broadly two types of data for machine learning: high-fidelity (HF) and low-fidelity (LF) data. High-fidelity data is highly reliable and accurate but expensive to produce. Consequently, high-fidelity data is typically scarce. In our context, this category includes measurement data or 3D simulation data. In contrast, low-fidelity data is less reliable and accurate, but it is inexpensive to produce and available in large quantities. Typically, simulation data, particularly 1D simulation data, falls into this category. Figure 7 shows a schematic of the S&FD-based PIML model. As shown in the figure, to construct the S&FD-based PIML model, prediction from the ML model built on low-fidelity data are utilized when developing the ML model based on high-fidelity data. Through this approach, better predictive accuracy was achieved compared to creating ML models using only high-fidelity or low-fidelity data.

HHI plans to continue developing VPD technology beyond this point. By utilizing AI, ML and reduced order model (ROM), HHI aims to develop 1D-3D coupled simulation technology that goes beyond single-dimensional simulation. Ultimately, this will lead to the development of integrated engine system simulation technology. Through this, we expect to perform rapid and accurate engine development in the diversifying fuel options and rapidly changing market trends.

2.3. Introduction to HHI's methanol dual-fuel engine

In September 2022, HHI developed the world's first 3.0-4.5 MW medium-speed methanol dual-fuel engine for marine applications. [6] The engine, named H32DF-LM, began development in 2019. The combustion simulation model was developed to observe the flame behavior during the combustion of diesel and methanol fuel within the combustion chamber. This model was utilized to determine the combustion concept for the methanol dual-fuel engine. In the diesel cycle, pilot diesel is pre-injected and ignited, followed by the injection of methanol. The simulation results confirmed that when

methanol is ignited with pilot diesel, the combustion and emission characteristics are similar to those of a diesel engine.

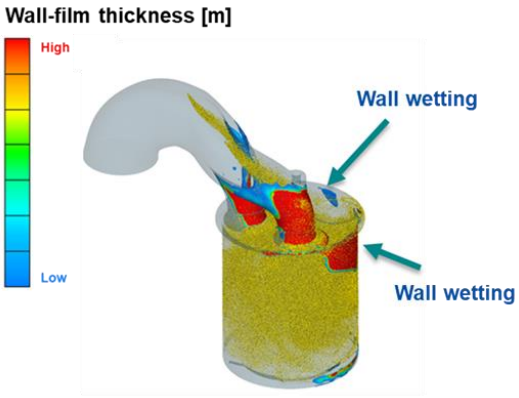

Wall-wetting in Otto-cycle

Concepts	Diesel-cycle	Otto-cycle
Power	◎	O
Fuel slip	◎	X
Efficiency	◎	O
NOx	O	◎

(◎: Good, O: Normal, X: Bad)

Figure 9: Simulation results of methanol Otto cycle and comparison between Diesel and Otto cycles

In the Otto cycle, methanol is injected at the port and ignited via pilot diesel. As shown in the figure 8, the simulation results identified wall wetting phenomena of methanol fuel and issues such as fuel slip. Therefore, the diesel cycle was selected as the combustion concept for the HiMSEN methanol dual-fuel engine.

The methanol engine development began based on the well-established HiMSEN H32 diesel engine, which has been previously developed and well-proven in the market. However, there were several technical challenges that needed to be addressed for the application of methanol fuel. A representative example of these challenges is the fuel injection system. Typically, a diesel engine requires only one fuel injection system. However, the methanol engine requires three separate fuel injection systems: one for main diesel, one for pilot diesel, and one for methanol.

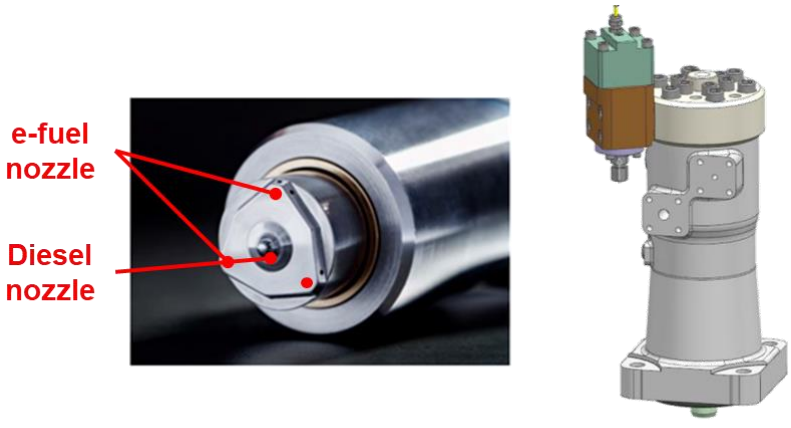

HPDF Injector e-FIP

Figure 10: HPDF injector(left) [7] and e-FIP(right)

To overcome this challenge, new designs and simulations were utilized. First, a high-pressure dual-fuel (HPDF) injector capable of performing three fuel injection functions within a single body was adopted.

Additionally, using virtual engine model based on simulation data, the detailed specifications of the diesel and methanol injector nozzles were optimized. Furthermore, a fuel injection pump named electronical-fuel injection pump (e-FIP), capable of electronically controlling the injection timing and fuel quantity for each cylinder was independently developed and implemented. This allows for the optimal operating point settings for specific engine loads to be adjusted according to customer needs. Additionally, many engine tests were replaced with engine simulations. The development tests confirmed very positive results, matching the expectations from the simulations.

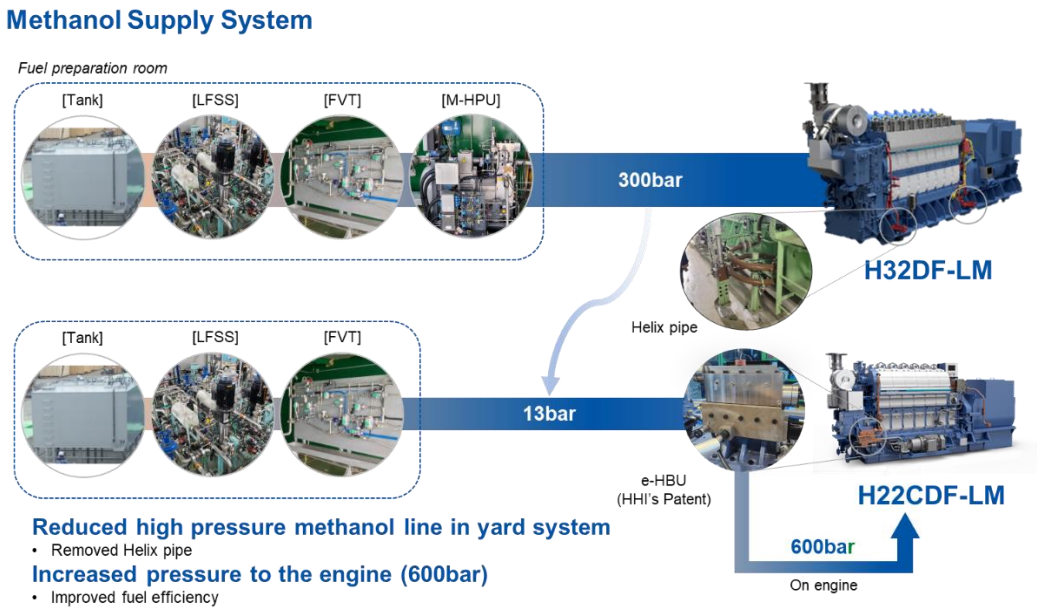

Figure 11: New fuel supply system: e-HBU

In March of this year, HHI leveraged the experience and expertise gained from the development of the H32DF-LM engine to develop a second methanol engine named H22CDF-LM. By developing the H22CDF-LM, a 1.4-2.2MW medium-speed methanol engine, HHI has begun to establish a lineup of methanol engines. This engine incorporates more advanced designs and technologies compared to the H32DF-LM. In the H32DF-LM, a high-pressure double-wall pipe was used to supply high-pressure methanol (300 bar) from the high-pressure methanol pump to the front end of the engine. To reduce the cost of the high-pressure double-wall pipe and to create a more stable engine system, the H22CDF-LM incorporated a newly developed fuel supply system named electronic-hydraulic boosting unit (e-HBU).

The innovation minimized the length of the high-pressure double-wall pipe, allowing for safer engine operation. Additionally, it enabled the pressurization and supply of methanol at over 600 bar, compared to the previous 300 bar, resulting in significantly improved thermal efficiency of engine. The new fuel supply system utilizing the e-HBU is planned to be applied across the entire HiMSEN methanol and ammonia engine product line, including H32DF-LM. The H22CDF-LM, developed in this manner, successfully completed the Type Approval Test (TAT) in March 2024, with the attendance of seven classification societies: ABS, BV, DNV, KR, LR, NK, and RINA. Additionally, as of July 2024, the first order for the H22CDF-LM is imminent.

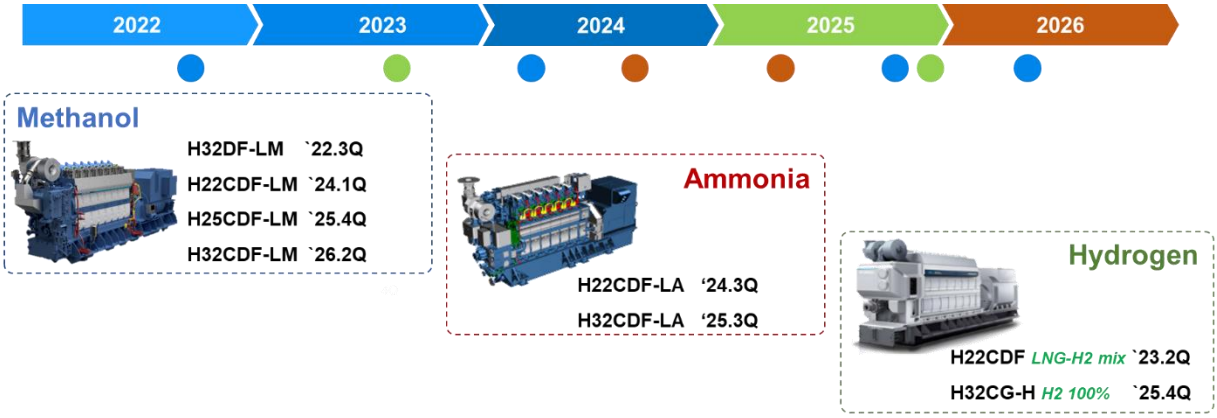

Figure 12: HHI's roadmap for the development of e-fuel engines

Figure 12 shows HHI's roadmap for the development of e-fuel engines. HHI plans to continue expanding its lineup of methanol engines to meet market conditions and customer demands. Furthermore, based on the experience gained from methanol engine development, HHI is also working on developing ammonia and hydrogen engines. The first ammonia engine, the H22CDF-LA, is nearing completion and is scheduled for TAT in September 2024. Additionally, the development of hydrogen engines is underway, taking into account market conditions and technological maturity.

3. Conclusions

HHI has developed its second methanol engine, the H22CDF-LM, and has begun establishing a methanol engine lineup.

1. By developing and utilizing VPD technology, reducing engine development time and advancing the development of high-performance engines.
2. AI and ML technologies are being used to build and utilize virtual engine model based on measurement and simulation data. This approach reduces the time and cost required for test and simulation while providing accurate results.
3. We plan to continuously develop VPD technology to secure integrated engine system simulation technology in the future
4. The development of H22CDF-LM methanol dual-fuel engine marks the beginning of the methanol engine lineup. This engine features a self-developed fuel supply system, enabling safer and more stable engine operation
5. HHI will continue to expand its methanol engine lineup based on market conditions and customer requirements. Additionally, the development of ammonia and hydrogen engines is underway and is expected to be completed in the near future.

Definitions, Acronyms, Abbreviations

GHG: Greenhouse gas

IMO: International maritime organization

LCA: Life-cycle assessment

LNG: Liquified natural gas

TTW: Tank-to-wake

MDO: Marine diesel oil

HHI: HD Hyundai heavy industries

HiMSEN: Hi-touch marine and stationery engine

VPD: Virtual product development

AI: Artificial intelligence

ML: Machine learning

DOE: Design of experiment

MSS: Methane slip solution

MPI: Multi-point injection

S&FD: Simulation and few data

PIML: Physics informed machine learning

HF: High fidelity

LF: Low fidelity

ROM: Reduced order model

HPDF: high-pressure dual-fuel

e-FIP: Electronic-fuel injection pump

e-HBU: Electronic-hydraulic boosting unit

TAT: Type approval test

Literature

[1] Marine environment protection committee (MEPC 80), 3-7 July 2023. [Web page] Available: https://www.imo.org/en/MediaCentre/MeetingSummaries/Pages/MEPC-80.aspx

[2] IMO's work to cut GHG emissions from ships. [Web page] Available: https://www.imo.org/en/MediaCentre/HotTopics/Pages/Cutting-GHG-emissions.aspx

[3] Elizabeth Lindstad et al, 2021. "Reduction of maritime GHG emissions and the potential role of E-fuels". Transportation Research Part D: Transport and Environmental Vol. 101

[4] DNV Energy Transition Outlook 2023, Maritime Forecast To 2050. [Web page] Available: https://afi.dnv.com

[5] Jonghwoo Park et al, 2023. "Performance prediction and optimization methodology based on a meta-model of HiMSEN engines". CIMAC Congress Busan.

[6] Yongseok Lee et al, 2023. "Development of carbon-neutral fuel engine: HiMSEN methanol engine". CIMAC Congress Busan.

[7] Clemens Senghaas, 2019. "New injector family for high-pressure gas and low-caloric liquid fuels". CIMAC Congress Vancouver.

Keywords: methanol, spark ignition, medium speed, simulation, knock

Simulation of large bore methanol-fuelled spark ignition engines

Prof. Dr. ir. Sebastian Verhelst, Dr. ir. Ward Suijs, Dr. ir. Yi-Hao Pu

Ghent University

https://doi.org/10.18453/rosdok_id00004645

Abstract

Methanol is an appealing low or net zero carbon fuel. For large bore engines, most commercially available engines or engines close to being introduced to the market employ a dual-fuel approach. While this is attractive for quickly introducing methanol-capable engines, this comes with some disadvantages too. Methanol is by its nature more suitable to spark ignition (SI), but the SI concept – relying on flame propagation – is not easily applied to large bores and low speeds. This explains the lack of experimental data on large bore methanol-fuelled SI engines. The high knock resistance enabled by methanol, due to its high autoignition temperature, high charge cooling and high laminar burning velocity, means bore sizes could potentially be larger than for current high octane fuels. Moreover, the SI concept is attractive for its power density, cost and low emissions potential. Assessing the actual potential of a large bore methanol SI engine is most easily done through simulation, avoiding high upfront costs. However, due to the lack of data, the validation of simulation results is not straightforward. The paper explains the sub-models that were selected and refined, and the approach taken to get to trustworthy results. It discusses a methanol evaporation model for port fuel injection, approaches to obtain the burn rate for methanol SI combustion, and predicting the occurrence of knocking combustion. Integrating these sub-models into overall engine cycle simulations finally leads to some case studies that are discussed.

1. Introduction

Renewable fuels complement electrification, particularly for the heavy duty applications with high demands on power and autonomy. Methanol is a particularly interesting option as it can be produced in different ways, both from biomass as through the e-fuel route [1], or hybrids thereof [2]. Its unique proposition is that of being the simplest hydrogen carrier that is liquid at atmospheric conditions.

So far, renewable methanol has primarily been demonstrated for marine applications, in bore sizes going from truck-derived marine engines to large bore two-stroke engines. With some exceptions, these employ the dual-fuel principle, with a pilot injection of a high reactivity fuel (mostly diesel). This is done for several reasons. The main technical reason is the high autoignition temperature of methanol, preventing easy compression ignition (CI). A practical reason is the relatively straightforward retrofit of a diesel engine, through adding a port fuel injection (PFI) system for methanol. The ability of a dual fuel engine to switch to full diesel operation is also a compelling reason, offering redundancy and reducing the risk of being able to secure renewable methanol as its production is only just getting started.

Such dual fuel engines are characterized by their methanol energy fraction (MEF). The MEF is never 100%, due to the need for pilot fuel, and can drop down to 0% for the lowest and highest loads. The actual MEF depends on the engine technology and the application. For a PFI conversion, methanol will primarily burn in a flame propagation mode, with misfires limiting the achievable MEF at the lowest loads (due to excessively lean mixtures) and end-gas autoignition limiting the MEF at the highest loads. If the methanol can be directly injected, it can burn in a mixing-controlled fashion after being ignited by the pilot fuel burning. The high heat of vaporization, which we will come back to later, is then a limitation to the MEF at the lowest loads.

In the long run, it would be very attractive to be able to run engines fully on methanol. This would do away with the complexity of needing to bunker and store two fuels onboard, and could take full benefit from the fuel properties of methanol, such as the ability to completely eliminate soot formation as the carbon atom in the methanol molecule is bonded to an oxygen atom [3]. Although compression ignition operation on neat methanol has been demonstrated [4-6], methanol is more suited for a spark ignition (SI) concept, because of its high autoignition temperature.

SI concepts have traditionally been limited to relatively small bore sizes, for several reasons. Larger bores are needed for applications requiring higher power outputs, and for those applications the fuel cost is a large part of the total cost of ownership. Thus, high engine efficiency is desired. SI engines have both lower peak and part load efficiency than CI engines, the first because of compression ratio limitations resulting from the need to avoid end-gas autoignition (“knock”), the latter because of the pumping losses when throttling at part load.

Methanol’s fuel properties offer pathways to increase part and peak load efficiency of SI engines however: it is much more knock-resistant than gasoline, owing to its higher autoignition temperature and its large cooling effect. Its heat of vaporization is roughly 3.5 times that of gasoline, and its heating value half that of gasoline (requiring larger fuel volumes to be injected), which results in a about a sevenfold increase in cooling effect [1]. As end-gas autoignition is primarily a temperature-driven phenomenon, this greatly reduces the knock propensity. This has been known for over a century, with methanol or fuel blends containing methanol being used as racing fuel or aircraft piston engines using methanol or methanol-water blends as anti-knock agent [7,8]. Thus, higher compression ratios can be

employed, and/or optimal spark timing at high loads, benefiting peak efficiency. Part load efficiency on the other hand can be increased primarily due to the higher dilution tolerance of methanol, linked to its higher laminar burning velocity. This allows reducing pumping losses through either increased lean operation or increased amounts of exhaust gas recirculation (EGR).

There is, however, very limited data available on the potential efficiency of methanol SI operation [9], particularly for larger bore sizes [10]. Before investing in the testing of large bore SI engines on methanol, assessing the actually achievable bore sizes, power densities and efficiencies through numerical simulation is desired, which is the topic of this paper. The desired applications of the engine models were on the one hand, assessing whether a medium speed methanol engine using conventional spark ignition is possible; and on the other hand, for energy system optimization models (ESOMs). Such ESOMs model entire energy systems, for example at the level of a country, to shed light on the best strategies to reduce greenhouse gas emissions. Energy converters are part of such models, including combustion engines, but need to be strongly simplified, to the level of an efficiency number, or a scaling law relating fuel conversion efficiency to engine power [11]. Hence, the chosen approach was a 0D/1D one, as a compromise between computational expense and accuracy.

The main focus here, is how to model methanol's injection, evaporation and combustion (normal as well as abnormal, namely end-gas autoignition); the integration of these sub-models and the applications of the resulting complete engine model.

2. Simulation framework

Combustion in SI engines is characterized by flame front propagation. This premixed type of combustion can be modelled via a two-zone framework, distinguishing a burned and an unburned zone that are separated by a propagating flame front. The basic equations are derived from the conservation of energy applied to these two zones as follows,

$$\frac{d(m_u u_u)}{dt} = -p\frac{dV_u}{dt} - \frac{dQ_u}{dt} - \left(\frac{dm_{f,b}}{dt}h_f + \frac{dm_{a,b}}{dt}h_a\right) + \frac{dm_{f,i}}{dt}h_{f,i} \quad (1)$$

$$\frac{d(m_b u_b)}{dt} = -p\frac{dV_b}{dt} - \frac{dQ_b}{dt} + \left(\frac{dm_{f,b}}{dt}h_f + \frac{dm_{a,b}}{dt}h_a\right) \quad (2)$$

Here m denotes mass, u denotes internal energy, V denotes volume, Q denotes heat loss to the wall, and h denotes enthalpy. Subscript u denotes parameters pertaining to the unburned zone, b those for the burned zone, f denotes fuel, a denotes air, and i denotes injection. Note that the blow-by is neglected in Eqs. (1) and (2).

Eqs. (1) and (2) contain a term describing the burn rate. Different approaches can be taken to close these equations: either this burn rate can be prescribed, or it can be modelled. Both approaches are discussed in subsequent sections. Before covering the treatment of combustion, however, it is important to ensure that the conditions at the start of compression are correctly estimated. With port fuel injection of methanol, having a strong cooling effect (as explained above), an accurate model of methanol evaporation is needed. This is treated first.

2.1. Methanol evaporation model

Previous experience of the authors has learned that the high heat of vaporization of methanol can lead to problems getting methanol evaporated at the right time and the right place, so substantial effort was put into how to model this evaporation in a way that can be integrated in 0D/1D tools.

First, a simple experiment was set up to collect data on the evaporation of methanol in the intake runner of an engine, to guide the development of a suitable model. These measurements have been reported elsewhere [12]. Figure 1 depicts the overall concept of the proposed methanol evaporation model. The methanol spray is assumed to leave the injector nozzle in droplet form and then puddle at the inside of the intake runner as a thin layer of liquid film. Both droplets and liquid film are assumed to have a uniform temperature, and the proposed modelling framework deals mainly with the mass flux, ϕm, and heat flux, ϕq, at the liquid-gas interface, namely the surface of the droplet and the surface of the liquid film.

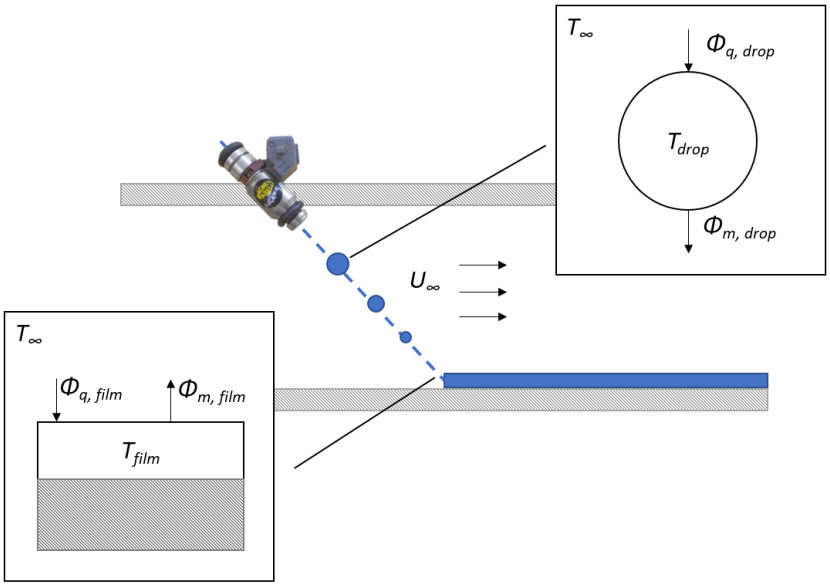

Figure 1: The schematic diagram of the proposed modelling framework in this research. Here, T is the temperature, U is the flow velocity, φ_m is the mass flux and φ_q is the heat flux. Subscripts 'drop' denotes the droplet, 'film' denotes the liquid film, and '∞' denotes the air flow.

For the droplet evaporation rate, the model proposed by Abramzon and Sirignano [13] is adopted due to its wide applicability and outstanding predictability compared to other models [14]. The instantaneous droplet evaporation rate is expressed in Eq. (3),

$$\dot{m}_{drop} = -2\pi R\rho D_{AB} Sh^* \ln(1 + B_M) \tag{3}$$

where R is the droplet radius, ρ is the air density, D_{AB} is the mass diffusivity of methanol vapour through air, Sh* is the modified Sherwood number that takes into account the Stefan flow and the thickness of a gas mixture film around each droplet.

The film evaporation rate is evaluated with Eq. (4) [15]

$$\dot{m}_{film} = A_{film}\phi_m = A_{film} M_{MeOH} k_c (c_{film} - c_\infty) \tag{4}$$

Where A_{film} is the surface area of the liquid film, k_c is the mass transfer coefficient, M_{MeOH} is the molar mass of the methanol, and c is the molar concentration of the methanol. Subscript *film* denotes the

concentration at the liquid film surface and ∞ denotes the concentration far away from the liquid film surface.

The temperature change of the air flow caused by both the droplet evaporation and the film evaporation can then be evaluated with Eq. (5)

$$\Delta T_{drop} = \frac{\dot{m}\Delta h_{vap}}{\dot{m}_{air} c_{p_{air}}} \tag{5}$$

Where $\dot{m}$ is the evaporation rate as either droplets or film, Δh_{vap} is the heat of vaporization of methanol, $\dot{m}_{air}$ is the air mass flow rate and $c_{p,air}$ is the specific heat capacity of air.

The thermophysical properties of air are referenced from [16] and the thermophysical properties of methanol are referenced from [17]. The viscosity and thermal conductivity of the mixture is calculated with the Wilke law [18].

The flow chart shown in Figure 2 summarizes the methodology for the proposed methanol evaporation modelling framework. To see the detailed calculation for each step, the readers are referred to [19].

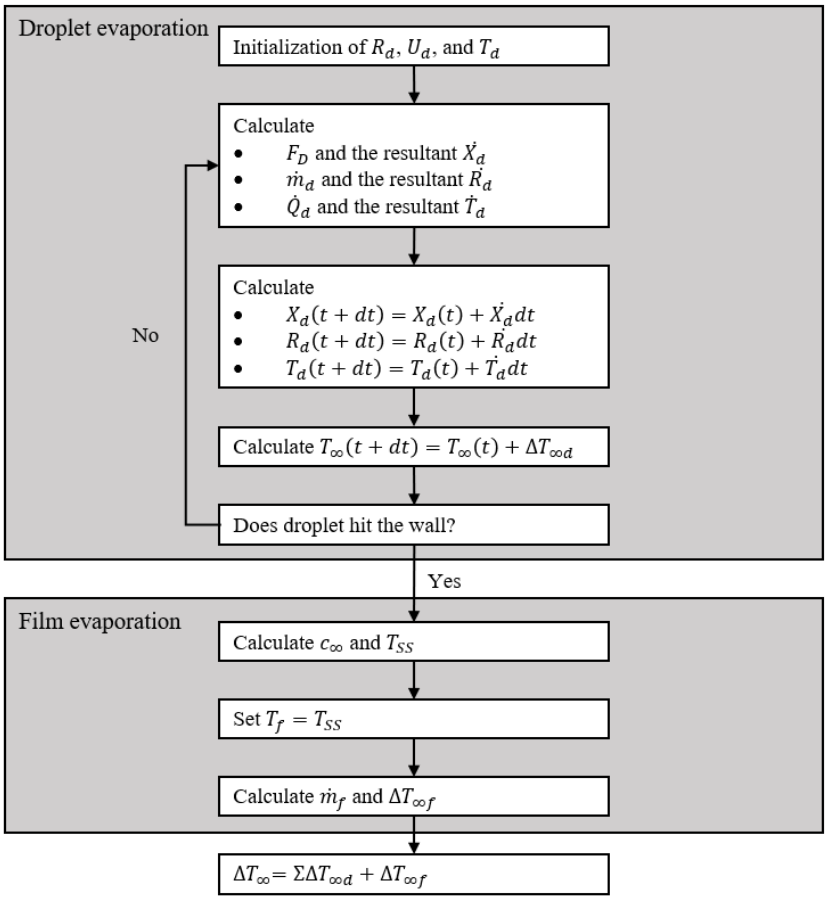

Figure 2: Flow chart of the proposed methodology to evaluate the temperature drop caused by methanol evaporation in the intake path.

One of the main conclusions of the model, that was validated using two sets of data from different engines employing port fuel injection [19], was that film evaporation is the dominant evaporation mode. Methanol droplets hardly get to evaporate before they impinge on the intake runner walls. On top of

this, if the intake is such that there is no room for a methanol film to form, only a very limited amount of methanol can evaporate before it enters the cylinders.

With the right conditions at the start of ignition, following the methanol evaporation, we now turn to the burn rate modelling.

2.2. Burn rate: prescribed

Two approaches were taken to determine the burn rate term, to close the two-zone pressure and temperature development equations. When studying the performance of end-gas autoignition prediction (Section 2.4), it was decided to impose a burn rate so as not to compound uncertainties in the burn rate prediction with those of the prediction of knocking combustion.

The available data on larger bore methanol SI engine operation was reviewed. The former combustion engine group at KTH Stockholm shared a comprehensive data set from a single cylinder version of a Scania D12 engine, converted to PFI SI operation with methanol, with a compression ratio of 13:1 [20]. The cylinder bore size was 127 mm, with a displacement of 1.95 liter. The dataset included sweeps of ignition timing, boost pressure and air-to-fuel equivalence ratios (lambda); all at 1200 rpm. A larger bore size and displacement volume was used at RWTH Aachen, with around 5 liter displacement, also using PFI [21].

From these data sets, Wiebe law parameters were extracted, as a function of lambda, see Table 1. These values were used in an initial estimation of the potential of a 256 mm bore PFI SI methanol-fuelled medium speed engine, see Section 3.1.

Table 1: Parameters of the Wiebe functions representing mass fraction burnt curves with different λ

Lambda	**1**	**1.5**	**2**
Combustion efficiency	98%	98%	98%
CA10-90 [°CA]	20	30	40
Wiebe exponent m	2	1	0.5

Rather than fixed values for certain lambdas, one can also try to capture the change in the burn rate curve in the form of a correlation. It was found that the KTH dataset could best be captured with a cosine law [22], where the combustion duration is predicted with the correlation of Alam et al. [23], which takes the compression ratio, spark timing, inlet pressure, lambda and engine speed into account. This approach was used for an assessment of the maximum bore of a methanol PFI SI engine, see Section 3.2.

2.3. Burn rate: predicted

The previous section used a data-driven approach, going from measured heat release profiles to burn rate profiles than can be imposed in a simulation. The section however also highlighted the lack of data on PFI SI methanol operation, particularly for larger bore sizes. An alternative approach is to predict the burn rate based on a turbulent burning velocity model, which typically requires the laminar burning velocity (LBV) as input. Specifically, the burn rate follows from the entrainment flame equations proposed by Blizard and Keck [24],

$$\frac{dm_e}{dt} = \rho_u A_e u_e \tag{6}$$

$$\frac{dm_b}{dt} = \frac{(m_e - m_b)}{\tau} \tag{7}$$

where me is the mass entrained by the flame front, ρ u is the density of the unburned mixture, A_e is the surface area of the flame front and u_e is the entrainment velocity. τ is a time constant that can be associated to λ_T, the Taylor length scale, and u_l, the laminar burning velocity (LBV), as expressed in Eq. (8):

$$\tau = \frac{\lambda_T}{S_l} \tag{8}$$

λ_T can then be associated to Λ, the integral length scale; Re_t the turbulent Reynolds number, and u′, the turbulent intensity as defined in Eqs. (9) and (10).

$$\lambda_T = C_{TLS} \frac{\Lambda}{\sqrt{R_{e_t}}} \tag{9}$$

$$R_{e_t} = \frac{\rho_u u' \Lambda}{\mu_u} \tag{10}$$

The form of the correlation that Metghalchi and Keck [25] originally proposed for the LBV was based on experimental data. This has been enhanced and modified by several other researchers. Vancoillie et al. [26] used a chemical kinetic code developed at Eindhoven University of Technology, CHEM1D [27], to compare different chemical kinetic mechanism of methanol oxidation against the published experimental data. Based on their studies, they selected the chemical reaction scheme of Li et al. [28] and calculated the LBV at different temperature (400-1000 K), pressure (5-105 bar), equivalence ratio (0.5-2) and EGR dilution ratio (0-50vol%). The calculation results were then used to establish an improved polynomial correlation. Mahendar and Erlandsson [29] have implemented this polynomial correlation in GT-POWER and demonstrated that it outperforms the default correlation within the software, especially when operating lean.

The major issue of the original correlation proposed by Vancoillie et al. [26] is that it is developed predominantly for automotive applications, hence the pressure range is not enough to cover the high in-cylinder pressure in HD engines. Similar to the method Suijs et al. [30] proposed for their knock/IDT model, Shahpouri et al. [31] calculated the LBV of methanol using the chemical reaction scheme from Pichler and Nilsson [32], with a much wider ranges of the input parameters compared to the work from Vancoillie et al., for example with the highest lambda going up to 4. All the dataset and codes from the work of Shahpouri et al. are made available online, including the artificial neural network (ANN) and support vector machine (SVM) models they trained for data retrieval. Since this research focuses on SI operation, the subset of the original dataset from Shahpouri et al. with excess air ratio up to 2 was extracted and used to train another ANN model with different hyperparameter as specified in Table 2. It can be noticed that with a much lower number of data points, the size of the trained ANN in this research can also be significantly smaller than the one from Shahpouri et al. Its predictions also agree better with the original calculation in terms of root mean square error (RMSE).

Table 2: Comparison of the hyperparameters and RMSE of ANN models from Shahpouri et al. and this research

	Shahpouri et al.	**This research**
Number of points	67518	23324
Number of hidden layers	2	4
Layer sizes	67, 266	10,10,10,5
Hidden Layer Transfer Function	Rectifier	tanh
Output Transfer Function	Rectifier	Sigmoid
RMSE [cm/s]	0.81	0.482

For the turbulent burning velocity (TBV), earlier work compared several models and concluded that the model proposed by Zimont fares well [33]. This was combined with a flame development model proposed by Lipatnikov and Chomiak [34]. A major concern after the attempt to calibrate the TBV models in the GT-Power environment is that it is unclear how thermophysical properties are evaluated within GT-POWER as the models fail to generate corresponding variations over a wide λ range. To avoid this issue, the thermophysical properties were estimated with data or correlations available in literature. However, the thermophysical properties of methanol in NIST [17] are only available up to 620 K. It was then decided to use the thermophysical properties of air to represent the air-methanol mixture in the cylinder. The term with the thermophysical properties that needs to be evaluated involves the Prandtl number and the mixture viscosity. This was found to be very close between air and air-methanol mixtures.

These two approaches: with a prescribed burn rate (with either a Wiebe or a cosine law, see Section 2.2) or a predictive burn rate model, were subsequently used together with a knock model, with the latter being the subject of the next section.

2.4. Knock model

With the equations listed above, a ”normal” premixed combustion event in SI engines can be modelled. SI engines can, however, also experience abnormal combustion. The specific abnormal combustion phenomenon that poses major operating constraints depends on multiple factors. End-gas autoignition, manifested as knock, is the largest concern for SI operation on methanol in large bore engines, thus it is important that the simulation tool is capable of predicting its occurrence. The phenomenological predictions of knock can be made based on the widely employed knock integral (KI) proposed by Livengood and Wu [35], as shown in Eq. (11),

$$KI = \int_{t_{IVC}}^{t_{KO}} \frac{dt}{\tau_{ID}(t)} = 1 \qquad (11)$$

where τ_{ID} is the instantaneous ignition delay time (IDT); t_{IVC} and t_{KO} are the time at the intake valve closure and knock onset respectively. The instantaneous IDT is defined as the delay from the moment an air-fuel mixture is exposed to certain conditions until it auto-ignites. The KI approach compares this characteristic time to the residence time of the unburned mixture in the cylinder to determine whether a knock event would occur or not. If KI reaches unity at a certain moment before exhaust valve open, knock is predicted to occur at that particular time. Otherwise, no knock is predicted.

By adopting this criterion, a knock model is in essence estimating the instantaneous IDT of various air-fuel mixtures exposed to various conditions. Suijs et al. [30] utilized a range of input parameters that are aligned with typical in-cylinder conditions of HD engines. The chemical kinetic software used was the open-source Cantera [36] and the reaction scheme used was also from Pichler and Nilsson [32] as it was found to give lower error under engine-like conditions. An ANN was trained with the tabulated IDT values for fast data retrieval.

3. Simulation results

The models described in the previous sections were used to investigate two research questions, linked to two research projects:

- Project FASTWATER [37] looked into, among many other things, whether a medium speed engine running spark ignition on port fuel injected methanol is feasible, i.e. what would be needed to ensure knock-free operation.
- Project BEST's [38] mission statement was to work out, for Belgium, the most economical electro- and synthetic energy carrier routes needed to face the climate change issues and ensure the stability of the grid and the security of supply in 2040 and beyond. As explained below, one of the pieces of the puzzle was to work out how large an engine running PFI SI on methanol can be, and how its power density and efficiency scales with engine size.

In order to do this, the models discussed previously were integrated either in a GT-Power environment, or in an in-house Matlab code (as specified below).

3.1. Case study: feasibility of knock-free operation of a PFI SI methanol-fuelled medium speed engine

First, a Wiebe law with the parameters as listed in Table 1 was used, along with a knock integral, to calculate to occurrence of knock on a medium speed engine with a 256 mm bore and 1000 rpm nominal speed. The results were reported elsewhere [39], and concluded that one needed to be able to ensure a 290 K intake temperature to allow the same power output as the baseline diesel engine, in order to avoid knocking operation.

The methanol evaporation model was used next to check the feasibility of attaining such an intake temperature. The temperature drop after introducing methanol in the intake path of the engine was evaluated using the methanol evaporation model. The injecting location was assumed to be the junction between the intake plenum and the individual runners that lead to the intake ports. The injection angle was assumed to be 45°. The geometries of the runner were referenced from the engine drawings.

The injector was assumed to be a commercially available product from Heinzmann GmbH, whose detailed information is published in [40]. According to it, the injection pressure was set to 10 bar and the initial droplet size is set to 0.175 mm.

Two different excess air ratios, corresponding to stoichiometric and lean operations, and 3 different boost levels, corresponding to 25%, 50%, and 75% of load on the original engine were used as the boundary conditions for the evaporation model. The results are detailed in Table 4.5. It can be seen that the lowest possible mixture temperature achieved is around 35.6 °C (= 308.8 K) which is far above the 290 K suggested by Pu et al. [39] to facilitate a knock-free operation with on-par output as the original diesel-fuelled DZC.

Table 3: The calculated temperature drops and methanol evaporated fractions under different operating conditions

Excess air ratio [λ]	**1**			**1.5**		
Boost pressure [abs. bar]	1.34	1.76	2.32	1.34	1.76	2.32
Intake air temperature	53.7	55.1	58.5	53.7	55.1	58.5
Evaporated fraction (Droplet)	1.3%	1.6%	2.1%	1.3%	1.6%	2.1%
Evaporated fraction (Film)	8.5%	7.5%	6.8%	12.9%	11.4%	10.4%
Evaporated fraction (Total)	9.8%	9.1%	8.8%	14.2%	13.0%	12.5%
Temperature drop (Droplet) [°C]	2.47	2.93	3.74	1.65	1.95	2.50
Temperature drop (Film) [°C]	15.61	13.72	12.40	15.81	13.93	12.68
Temperature drop (Total) [°C]	18.09	16.65	16.14	17.46	15.88	15.17
Mixture temperature [°C]	35.61	38.45	42.36	36.24	39.22	43.33

Further investigation reveals that a 290 K temperature after methanol injection is only possible if the initial droplet size (D_0) is reduced to 0.12 mm, which poses a significant challenge to the injector development under such a low injection pressure. Alternatively, the injection angle (θ inj) can be made smaller relative to the flow direction, which will ease the requirement of the D_0 to 0.145 mm.

The trajectories of the three different cases are illustrated in Figure 3, it can be seen that the high droplet evaporated fractions result from the extended airborne periods. However, if the intake runner is not long enough, eventually the droplets will land on the port walls or the back of the valve and the subsequent film evaporation will most likely not absorb heat from the air as these surfaces are hot.

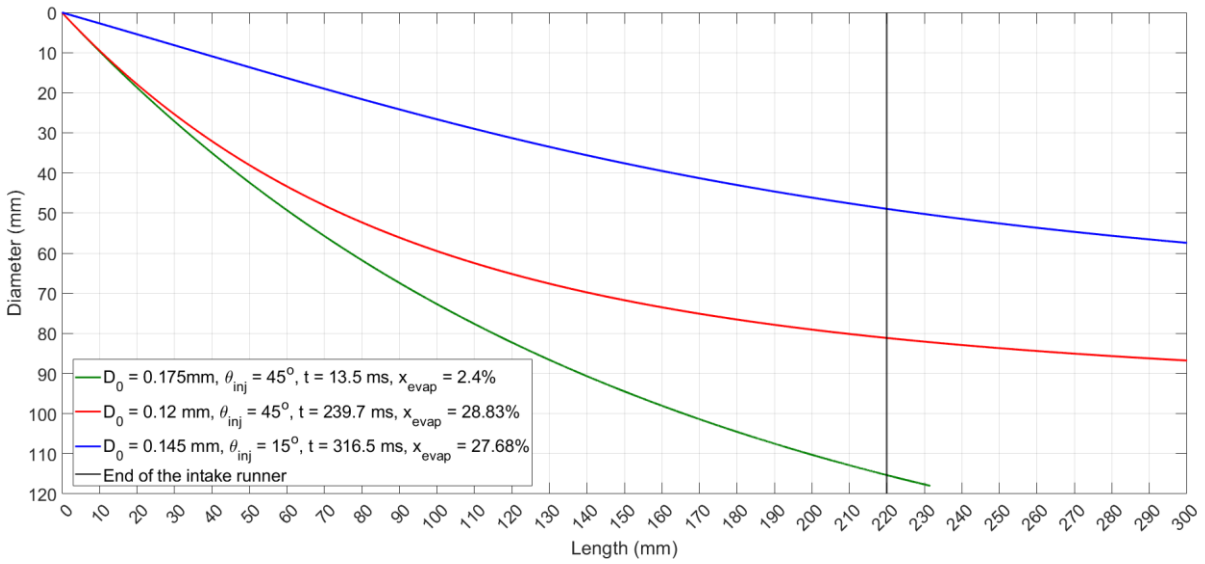

Figure 3: The droplet trajectories with different injection parameters. D_0 represents the initial droplet size, x_{evap} represents the evaporated fraction (as droplets), and ϑ_{inj} represents the injection angle relative to the intake air flow. The black line indicates the end of the intake runner, the droplets enter the cylinder head when they go beyond it.

The intake runner being too short is also the reason why film evaporation contributes so little to cooling down the mixture. There is simply not enough space in the intake runner to form a liquid film. Clearly, getting methanol evaporated in the intake is a challenging endeavour. The evaporation model is a helpful tool to explore potential solutions.

3.2. Scaling PFI SI methanol engines

With a predetermined and much-needed rise in renewable energy production, particularly solar and wind, a method of energy storage will be required to manage their intermittent nature. In addition, the applications that are difficult to electrify in the broad field of the mobility sector will have to part with their current use of fossil fuels. Within the BEST project, 'electrofuels' or 'e-fuels' are put forward as a possible solution to both issues. To create these fuels, renewable energy is combined with water to produce green hydrogen. This hydrogen can then be combined with nitrogen or carbon to produce a variety of fuels, which can be in either a liquid (e-methanol, e-gasoline, e-diesel) or gaseous (e-methane, e-ammonia) state at atmospheric conditions. Important questions that remain include how much e-fuels are needed to power the Belgian energy system and which technology is most efficient for converting these fuels back into final energy.

Given the variety of resources available, including nuclear, hydropower, wind and solar energy, as well as the existence of various conversion technologies, and the fluctuating demand and production, it is no longer feasible for an engineer to intuitively determine the optimal combination of these technologies for maximum economic efficiency. Therefore, multi-sector and whole-energy system optimisation models are being developed to assist in strategic energy planning of urban and regional energy systems. Due to the crucial role played by conversion technologies in these models, it is important to address their performance when running on the alternative e-fuels, particularly because these fuels can have significantly different properties than the conventional fossil fuels.

Here, the focus is on the internal combustion engine as energy converter. It is estimated that most of the light-duty applications where the ICE is currently used in, particularly passenger car applications, will be electrified as soon as possible and to the greatest extent possible. However, for heavy-duty applications such as long-haul trucks, marine propulsion, non-road mobile machinery, combined heat and power units and gensets, the low energy density of a battery electric drive will not be sufficient to meet autonomy requirements.

These applications are currently mainly powered by compression ignition diesel engines due to their high power output and efficiency. A research question here is if it would be possible to replace them with heavy-duty methanol-fuelled spark-ignition engines. As stated above, there are only a limited number of test cases to be found in the literature, which raises the question of what they are truly capable of. A two-zone semi-predictive zero-dimensional simulation model was developed within the commercial software MATLAB. The aim of this model is to predict the performance of methanol-fuelled port-fuel injected (PFI) SI engines as function of their size. A zero-dimensional approach was chosen over a quasi- or multidimensional approach due to the trade-off between accuracy and computational costs. The starting point for this model was a homogeneous two-zone finite heat release model featuring a constant combustion rate. It first did not include a heat transfer or knock model. Step by step, the complexity was increased by adding different sub-models to the simulation framework. To determine the optimal load point for each engine size, the burn rate had to respond to various imposed inlet operating conditions. As discussed in Section 2.2, burn rate parameters were experimentally derived from a heavy-duty Scania D12 PFI SI engine (B = 127 mm) and compared to

various correlations for the implementation of a semi-predictive combustion duration. Additionally, special attention has been given to the development of an improved Livengood & Wu knock model, as described in Section 2.4.

The two-zone model was subjected to an optimisation procedure to find the knock-limited operating load for each engine size. Different engine configurations were scaled based on the geometry of the Scania D12 engine (B = 127 mm), ranging from a bore size of 80 mm to 260 mm.

Each engine starts at low load and an optimisation process gradually increases the load until either the knock or peak pressure limit is reached. The following baseline starting conditions are set:

- An initial retarded spark timing of 10°ca aTDC
- In-cylinder pressure at IVC timing of 101.5 kPa (atmospheric conditions)
- n-cylinder temperature at IVC timing of 30 °C

The two-zone model then calculates the associated pressure and temperature trajectory of the burned and unburned gases and calculates the performance parameters, of which the achievable indicated mean effective pressure and indicated thermal efficiency are of main interest here. Simultaneously, the knock model evaluates the knock integral on a crank angle basis to check whether it exceeds one or not. From this point onwards, if knock is not occurring, spark timing is advanced by 1°ca increments until the CA50 reaches 10°ca aTDC or end-gas conditions increase to the point where knock occurs. Generally speaking, the spark timing where CA50 is between 8 - 10°ca aTDC is referred to as the minimum spark advance for maximum brake torque (MBT timing). This optimum timing is a compromise between starting combustion too early in the compression stroke and completing combustion too late in the expansion stroke [41]. If the spark timing can be advanced to this point without causing knock, it means that the engine load is below the maximum knock limit. Therefore, the charge density is then increased by increasing the intake pressure at IVC timing in 5 kPa increments. This step represents an increase in boost pressure to increase the load of the engine. To reduce the number of unknown variables, we furthermore assume that the in-cylinder temperature at IVC remains constant here regardless of the boost pressure.

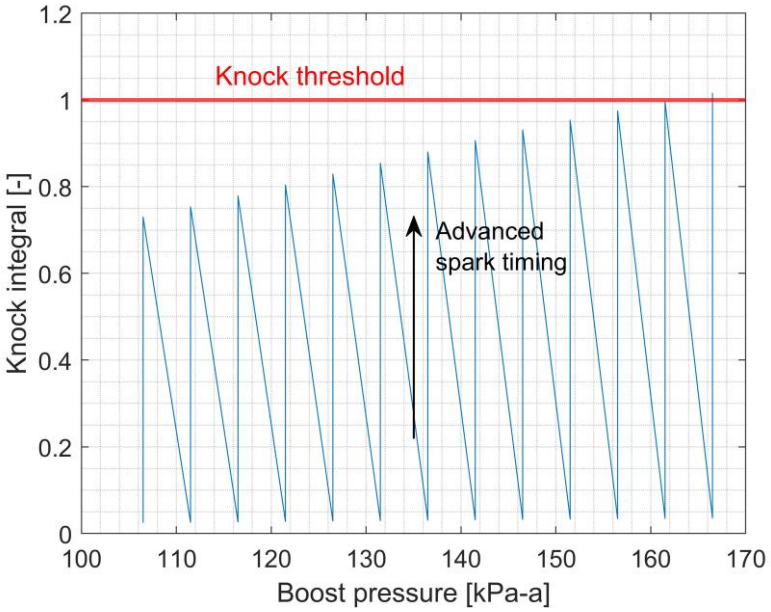

Figure 4: Illustration of the optimisation process for each engine configuration

Figure 4 illustrates the optimisation method. Starting from the left-hand corner, spark timing is advanced until CA50 reaches 10°ca aTDC. As the resulting knock integral value is less than one, the pressure can be increased to 105.5 kPa. This step is repeated until the knock integral reaches unity, in this example, at an inlet pressure of 165.5 kPa and a spark timing of -2°ca aTDC. The associated IMEP is called the knock-limited IMEP, and the parameter of interest for our upcoming scaling laws.

In addition, it is important to monitor the increase of load to ensure that it does not cause the peak pressure limit to be exceeded. At a constant inlet temperature, the higher intake pressure increases the charge density, causing the in-cylinder pressure to rise faster and to higher levels. Therefore, after each evaluation of the two-zone model, the optimisation procedure also compares the maximum in-cylinder pressure value with the defined limit.

An overview of the two-zone semi-predictive combustion model and its optimisation procedure is given in Figure 5. For each engine configuration, the initial operating conditions will be imposed, and the optimisation procedure will be executed to find the maximum indicated mean effective pressure and efficiency.

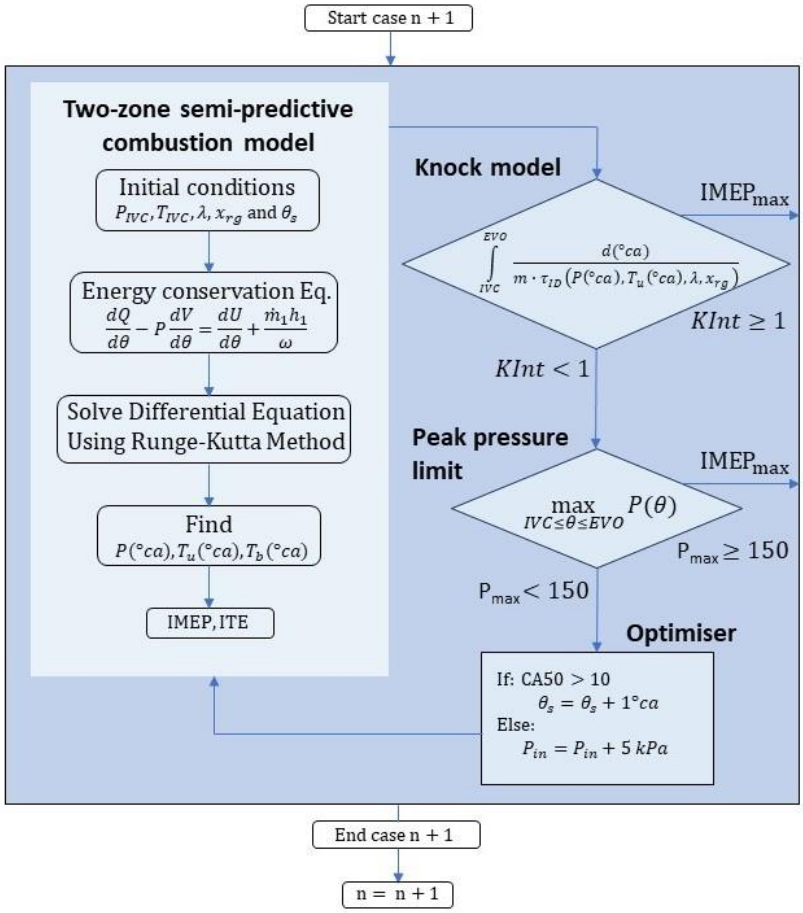

Figure 5: Flow chart of the optimisation procedure coupling a two-zone semi-predictive combustion model to a zero-dimensional knock model

The Scania D12 engine will be used as baseline engine for generating different (larger) engine geometries, as it is the only larger PFI SI methanol engine with a fairly comprehensive set of experimental data available [20].

To look at the performance of larger engines, the proportions of the combustion chamber are held constant; the stroke/bore ratio, connecting rod/stroke ratio and the compression ratio. However, engine rotational speed should not be considered as a constant. The speed of large-bore engines is limited by the inertial forces acting on the pistons. It was therefore decided to use a constant mean piston speed for each scaling law instead, as this parameter remains rather constant across different engine platforms. The engine's bore size was increased in increments of 10 mm, starting from 80 mm (automotive light-duty size) to 260 mm (medium speed engine size). Three mean piston speeds were investigated: the baseline value of 6.16 m/s (1200 rpm for the D12), as well as its double and triple values of 12.32 m/s and 18.54 m/s respectively. Starting with the lowest piston speed, engines up to a bore size of 110 mm are not limited by knock, but rather by the imposed peak in-cylinder pressure limit of the engine block. A near constant indicated mean effective pressure value of 29.6 bar corresponds to this pressure limit. For this range of engines, the thermodynamic limit has not yet been reached. Engine designers could therefore obtain even higher loads by investing in sturdier engine blocks. From 110 mm onwards, the IMEP becomes knock-limited. The main influence here will be the reduced rotational engine speed which decreases inversely with bore size for a constant stroke/bore ratio. The combustion duration (in seconds) will be increased, allowing the end-gases to have more

time to reach the conditions necessary to autoignite. For a bore size of 180 mm, the maximum IMEP will therefore only be 15 bar. For even bigger engine sizes, the trendline in Figure 6 stagnates. The reason for this is that boost pressure can no longer be applied without causing knock even for the latest spark timings, hence the model stops at ambient operating conditions and tries to advance the spark timing until the knock integral reaches unity.

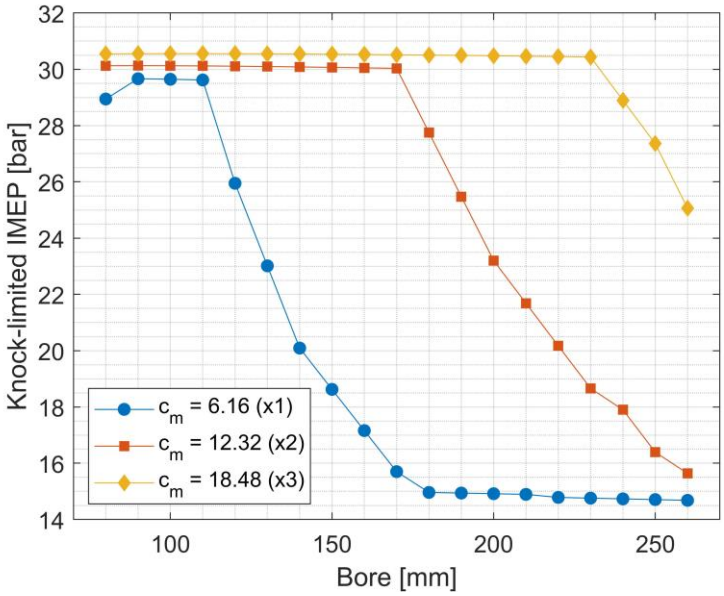

Figure 6: Knock-limited IMEP as function of bore size for different mean piston speeds and a fixed air-to-fuel ratio of lambda = 1

By doubling the mean piston speed (c_m = 12.32 m/s), the knock constraints are significantly lifted. Engines are now knock-free until a bore size of 170 mm. Using 25 bar IMEP as a target for heavy-duty diesel operation, PFI SI engines running on green methanol would therefore be a viable sustainable solution for engines up to 190 mm bore. For an even higher mean piston speed of 18.54 m/s, the engines are peak pressure limited up to 230 mm. Note however that such a mean piston speed value is already at the upper limit of what is possible in conventional spark-ignited engines [41]. Realistic performance values should therefore be sought between the first and second curve.

With respect to indicated thermal efficiency, the efficiency increases for higher mean piston speeds, see Figure 7. This is a result of the reduced residence time of the mixture in the cylinder, leaving less time for heat transfer to the surroundings. Note that if a friction model were added to predict the brake thermal efficiencies, the higher engine speed will have a detrimental effect due to the increased friction losses, hereby partially negating the previous effect. Looking at each curve individually, the efficiency for a c_m value of 6.16 m/s can be seen to drop in three stages. During the peak pressure limited stage, efficiency stays constant. The reduced surface area to volume ratio appears to have a negligible effect on efficiency improvement at larger bore sizes. After that stage, the IMEP becomes knock limited and efficiency reduces gradually together with the load. Once the inlet pressure reaches atmospheric conditions, the IMEP does not decrease significantly any more, however spark timing is retarded to remain below the knock limit. The efficiency therefore reduces as well. A similar behaviour can be seen for the higher mean piston speed curves, albeit to a much lesser extent due to the reduced occurrence of knock.

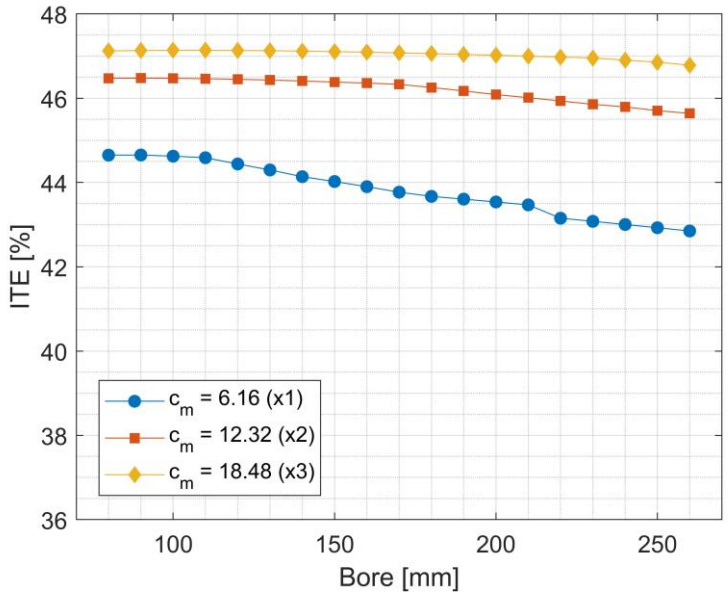

Figure 7: Indicated thermal efficiency as function of bore size for different mean piston speeds and a fixed air-to-fuel ratio of lambda = 1

The influence of the air-to-fuel ratio lambda on the knock-limited performance was investigated for the mean piston speed value of c_m = 12.32 m/s. Figure 8 shows the trend lines for lambda ranging from 1 to 1.6. For the same in-cylinder peak pressure limit of 150 bar, lower IMEP values are found in the pressure-limited zone. Due to the diluted mixture, a higher boost pressure is required to reach the same energy content in the cylinder. For lambda equal to 1.6, the maximum IMEP is 26 bar, while under stoichiometric conditions this could go up to 30 bar. On the other hand, the knock-limited zone is pushed further into larger bore engines. For lambda = 1.4, knock-limited operation only starts at 210 mm bore engines, while for lambda 1.6 it starts at 250 mm bore engines. At lean operating conditions, the ignition delay time becomes significantly larger, hereby postponing the moment of autoignition. In addition, because the loads are lower for the same boost pressure, the temperatures of the unburned gases are also reduced, which in turn increases again the ignition delay time. At the maximum bore size of 260 mm, the knock-limited IMEP is respectively 20.4 bar and 25.2 bar for lambda equal to 1.4 and 1.6. If an IMEP of 25 bar is targeted, PFI SI operation is possible up to 190 mm engines under stoichiometric operation. For leaner conditions, engines up to 230 mm and 260 mm are even feasible.

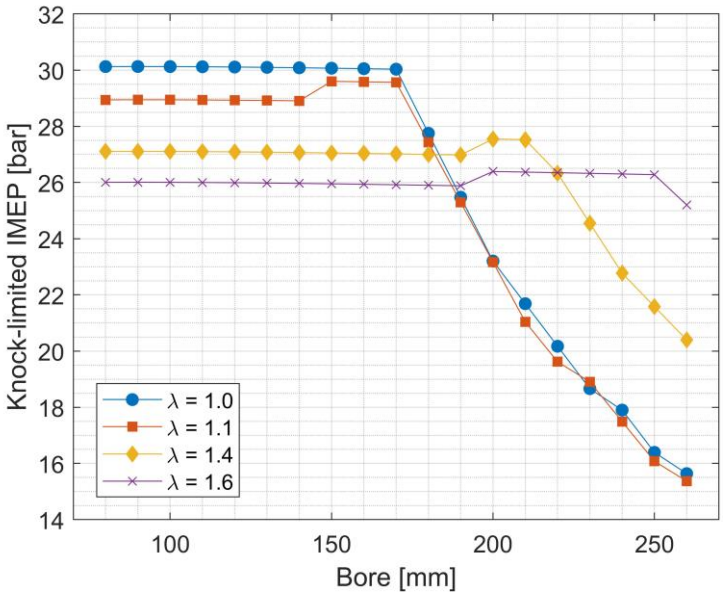

Figure 8: Knock-limited IMEP as function of bore size for different air-to-fuel ratios at a constant mean piston speed of c_m = 12.32 m/s

4. Conclusions

This paper reported work on important building blocks for 0D-1D simulation of PFI SI methanol engines:

- A methanol evaporation model, to allow the estimation of the evaporated fuel fraction in the intake. This is important to assess the temperature at the start of compression, which itself is crucial to determine the occurrence of end-gas autoignition and thus the achievable power density and efficiency of a methanol-fuelled PFI SI engine.
- The burn rate: data was extracted from the few reported measurements from literature, to fit either Wiebe law parameters or a cosine law, in order to be able to impose a burn rate in an engine simulation. Alternatively, one can opt for a predictive burn rate model, for which the laminar burning velocity (LBV) is an important input. A neural network was fitted to LBV calculations from chemical kinetics. The burn rate then results from an entrainment frame-work with appropriate models for the turbulent burning velocity and flame development.
- The occurrence of knock follows the Livengood-Wu approach using a knock integral. Another neural network was trained to produce the necessary autoignition delay time of methanol mixtures, as calculated from detailed chemical kinetics.

These building blocks were then applied on two cases, one to check the feasibility of a 256 mm bore medium speed PFI SI methanol engine. The difficulty in getting methanol evaporated in the intake air, so to make best use of its cooling potential, was shown to severely limit the achievable power density.

A second case was aimed at producing the power density and efficiency as a function of bore size, of PFI SI methanol engines. Such data can be used in Energy System Optimisation models, to check the role of methanol in power-to-methanol-to-power schemes.

An important takeaway for the modelling is that there is a strong need for more experimental data on larger bore methanol-fuelled SI engines.

Acknowledgements

This research received funding from FASTWATER, a project within Europe's Horizon 2020 Research and Innovation program (Contract No.: 860251), BEST (Belgian Energy System) – a project funded by the Belgian federal Energy Transition Fund, and CHyPS (Chean Hydrogen-based Propulsion for Ships), funded by the Flemish Agency for Innovation and Entrepreneurship (VLAIO).

Literature

[1] S Verhelst, JWG Turner, L Sileghem, J Vancoillie. Methanol as a fuel for internal combustion engines. Progress in Energy and Combustion Science 70(2019):43–88, https://doi.org/10.1016/j.pecs.2018.10.001

[2] E Anetjärvi, E Vakkilainen, K Melin. Benefits of hybrid production of e-methanol in connection with biomass gasification. Energy 276(2023):127202, https://doi.org/10.1016/j.energy.2023.127202

[3] PF Flynn et al. Diesel Combustion: An Integrated View Combining Laser Diagnostics, Chemical Kinetics, And Empirical Validation. SAE Technical paper nr. 1999-01-0509, https://doi.org/10.4271/1999-01-0509

[4] M Svensson, M Tuner, S Verhelst. Investigation of Combustion Characteristics of a Fuel Blend Consisting of Methanol and Ignition Improver, Compared to Diesel Fuel and Pure Methanol. SAE Technical Paper nr. 2024-01-2122, https://doi.org/10.4271/2024-01-2122

[5] M Svensson, M Tuner, S Verhelst. Experimental Investigation of Pilot Injection Strategies to Aid Low Load Compression Ignition of Neat Methanol. SAE Technical Paper nr. 2024-01-2119, https://doi.org/10.4271/2024-01-2119

[6] M Svensson. Assessing single-fuel solutions enabling compression ignition of renewable methanol. PhD thesis, Lund University, 2024, https://portal.research.lu.se/en/publications/assessing-single-fuel-solutions-enabling-compression-ignition-of-

[7] CE Douglas. The Secret Horsepower Race – Western Front Fighter Engine Development. Tempest Books, 2022.

[8] K Ludvigsen. Classic Racing Engines: Expert Technical Analysis of Fifty of the Greatest Motorsports Power Units: 1913-1994. Bentley Publishers, 2017.

[9] Annex Report Number 56 Methanol as Motor Fuel, Appendices. A Report from the Advanced Motor Fuels Technology Collaboration, International Energy Agency, https://www.iea-amf.org/app/webroot/files/file/Annex%20Reports/AMF_Annex_56_Appendices.pdf

[10] Y-H Pu, D Dejaegere, M Svensson, S Verhelst. Renewable methanol as a fuel for heavy-duty engines : a review of technologies enabling single-fuel solutions. ENERGIES 2024, 17(7):1719, https://doi.org/10.3390/en17071719

[11] W Suijs, S Verhelst S. Scaling performance parameters of reciprocating engines for sustainable energy system optimization modelling. ENERGIES 2023, 16(22):7497. https://doi.org/10.3390/en16227497

[12] Y-H Pu, T Larsson, T Robeyn, M De Paepe, S Verhelst. Methanol evaporation in an engine intake runner under various conditions. SAE Technical Paper nr. 2023-24-0018, https://doi.org/10.4271/2023-24-0018

[13] B Abramzon, WA Sirignano. Droplet vaporization model for spray combustion calculations. International Journal of Heat and Mass Transfer, 32(9):1605–1618, 1989, https://doi.org/10.1016/0017-9310(89)90043-4

[14] AP Pinheiro, JM Vedovoto. Evaluation of droplet evaporation models and the incorporation of natural convection effects. Flow, Turbulence and Combustion, 102:537–558, 2019, https://doi.org/10.1007/s10494-018-9973-8

[15] J Welty, GL Rorrer, DG Foster. Fundamentals of momentum, heat, and mass transfer. John Wiley & Sons, 4th edition, 2001.

[16] GM Harpole. Droplet evaporation in high temperature environments. J. Heat Transfer. Feb 1981, 103(1): 86-91, https://doi.org/10.1115/1.3244437

[17] P Linstrom, W Mallard, editors. NIST Chemistry WebBook, NIST Standard Reference Database Number 69. National Institute of Standards and Technology, Accessed: 2024-04-06.

[18] CR Wilke. A viscosity equation for gas mixtures. Journal of Chemical Physics, 18(4):517–519, 1950.

[19] Y-H Pu, J Dierickx, S Verhelst, Modelling the evaporative cooling effect from methanol injection in the intake of internal combustion engines. Fuel 372(2024):132131, https://doi.org/10.1016/j.fuel.2024.132131

[20] SK Mahendar, T Larsson, AC Erlandsson. Alcohol lean burn in heavy duty engines: Achieving 25 bar IMEP with high efficiency in spark ignited operation. International Journal of Engine Research. 2021;22(11):3313-3324. https://doi.org/10.1177/1468087420972897

[21] A Güdden, S Pischinger, J Geiger, B Heuser, M Müther. An experimental study on methanol as a fuel in large bore high speed engine applications—Port fuel injected spark ignited combustion. Fuel 303(2021):121292, https://doi.org/10.1016/j.fuel.2021.121292

[22] W Suijs, Scaling the performance of methanol-fuelled spark ignition engines, PhD thesis, Ghent University, 2024, http://hdl.handle.net/1854/LU-01J0TH1XXCRCRWGQ5WEV7FZ0XR

[23] SS Alam, SW Rosa, C Depcik, SP Burugupally, E McDaniel, JD Hobeck. Modification of the Wiebe function for methane-air and oxymethane-based spark-ignition engines. Fuel 303(2021):121218, https://doi.org/10.1016/j.fuel.2021.121218

[24] N Blizard, J Keck. Experimental and theoretical investigation of turbulent burning model for internal combustion engines. SAE Technical Paper nr. 740191, 1974.

[25] M Metghalchi, JC Keck. Burning velocities of mixtures of air with methanol, isooctane, and indolene at high pressure and temperature. Combustion and flame, 48:191–210, 1982.

[26] J Vancoillie, S Verhelst, J Demuynck. Laminar burning velocity correlations for methanol-air and ethanol-air mixtures valid at SI engine conditions. SAE Technical Paper 2011-01-0846, https://doi.org/10.4271/2011-01-0846

[27] Introduction to Chem1d. https://github.com/thijsa93400/TUe_chem1d/wiki. Accessed: 2024-05-03.

[28] J Li, Z Zhao, A Kazakov, M Chaos, FL Dryer, JJ Scire Jr. A comprehensive kinetic mechanism for CO, CH2O, and CH3OH combustion. International Journal of Chemical Kinetics, 39(3):109–136, 2007, https://doi.org/10.1002/kin.20218

[29] S. K. Mahendar, A. C. Erlandsson. Semi-predictive modeling of diluted ethanol and methanol combustion in conventional spark ignition operation. SAE Technical Paper 2021-01-0386, https://doi.org/10.4271/2021-01-0386

[30] W. Suijs, J. Dierickx, Y.-H. Pu, Y. Wang, S. Verhelst. Calibrating the Livengood-Wu integral knock model for differently sized methanol engines. Fuel Communications, page 100121, 2024, https://doi.org/10.1016/j.jfueco.2024.100121

[31] S Shahpouri, et al. Laminar Flame Speed modeling for Low Carbon Fuels using methods of Machine Learning. Fuel, 333:126187, 2023, https://doi.org/10.1016/j.fuel.2022.126187

[32] C Pichler, EJ Nilsson. Reduced kinetic mechanism for methanol combustion in spark-ignition engines. Energy & fuels, 32(12):12805–12813, 2018, https://doi.org/10.1021/acs.energyfuels.8b02136

[33] J Vancoillie, L Sileghem, S Verhelst. Development and validation of a quasi-dimensional model for methanol and ethanol fueled SI engines. Applied Energy, 132:412–425, 2014, https://doi.org/10.1016/j.apenergy.2014.07.046

[34] A Lipatnikov, J Chomiak. Turbulent flame speed and thickness: phenomenology, evaluation, and application in multi-dimensional simulations. Progress in Energy and Combustion Science, 28(1):1–74, 2002, https://doi.org/10.1016/S0360-1285(01)00007-7

[35] J Livengood, P Wu. Correlation of autoignition phenomena in internal combustion engines and rapid compression machines. Symposium (International) on Combustion, 5:347–356, 1955

[36] https://www.cantera.org/. Accessed: 2024-05-03.

[37] FASTWATER: FAST Track to Clean and Carbon-Neutral WATERborne Transport. EU H2020 project Contract Nr. 860251, https://fastwater.eu/

[38] BEST: Belgian Energy System project, https://uclouvain.be/en/research-institutes/immc/belgian-energy-system-%26ndash%3B-best-2020-2024.html

[39] Y-H Pu, W Suijs, R De Graeve, S Verhelst. Evaluation of a virtual medium-speed engine on methanol using spark-ignition. CIMAC 2023 : 30th CIMAC World Congress, Proceedings, paper 012.

[40] A. Sorrentino, V. Leytes, L. Mattheeuws, E. D. Wilde. Methanol port fuel injection for medium-speed application: injector development and engine design. In Proceedings of 30th CIMAC World Congress, 2023

[41] J. B. Heywood. Internal Combustion Engine Fundamentals, McGraw-Hill series in mechanical engineering. 1988.

Lubmarine

Supporting **Operational Excellence**

Together we go further

At Lubmarine, our commitment to customers runs deep. Our trusted experts are dedicated to delivering cutting-edge marine lubrication solutions and services that empower your fleet to navigate with confidence and optimize every voyage.

TotalEnergies

lubmarine.totalenergies.com

Keywords: Sustainable Fuels, Alternative Fuels, Future Fuels, Shipping Decarbonisation, Methanol, Marine engine retrofit technologies

Methanol retrofit technologies, from concept to engine operation: Performance and emissions evaluations on a large bore engine

Dr. Ludovico Viglione[1], Dr. Marios Ioannou[1], Alejandro Calvo Oliveira[1], Gennaro Caputo[2], Dr. Thorsen Sven Lauge[3], Placanica Michele[2]

[1]Wärtsilä Services Switzerland AG, [2]Wärtsilä Italia S.p.A., [3]Wärtsilä Danmark A/S

https://doi.org/10.18453/rosdok_id00004646

Abstract

IMO's Greenhouse Gas reduction strategy is one of the biggest challenges that the shipping industry faces. While intermediate measures of reducing emissions from ships are currently available, the reduction targets set by IMO for 2050 can only be met through the use of sustainable fuels that will gradually replace diesel. Methanol has been identified as one of the low carbon fuels that could decarbonise shipping, and results from recent investigations confirmed its strong potential in reducing GHG emissions if utilized as a marine fuel. This paper describes the approach that was adapted by Wärtsilä to retrofit a 2-stroke marine diesel research engine with existing systems and components to operate on Methanol. The workflow comprised of the development of a 3-D CFD model of the Wärtsilä 6RT-Flex50-B (RTX-5), which was calibrated with experimental data obtained from the combustion of methanol in a spray chamber. The outcomes from the numerical analysis were applied to define the nozzle tip configurations for the methanol injectors, and following an optimisation study, the best configurations were identified, designed and manufactured for use on the real engine. The conversion of the engine with the required hardware, and the development of the combustion system through numerical analysis, were executed in parallel. The main characteristics of the retrofit system are summarized, with focus on the key upgrades that were made to a high-pressure pump, a common rail system and fuel injectors, to achieve operation of the 6-cylinder 2-stroke marine engine on methanol. The study concludes with the results from the engine performance and emission measurements that were conducted on the engine, which was fully instrumented for the testing purposes. The analysis demonstrated that when the dual-fuel engine was operated on Methanol, it was considerably more efficient than when operated on conventional Diesel, with also significant reductions of NO_x emissions due to lower combustion temperatures, and of CO_2 emissions through reductions in fuel consumption.

1. Introduction

Methanol has been widely investigated as a potential fuel since the early stages of internal combustion engines. Its chemical and physical properties, industrial availability, and low carbon to hydrogen ratio, make this low-carbon alcohol attractive as an alternative to traditional fossil fuels. The use of light alcohols, such as methanol or ethanol, in spark-ignition engines seems relatively straightforward, and has been extensively analysed in the literature [1]. Methanol's high octane number and latent heat of evaporation, as well as its low air to fuel ratio (Table 1) enable this fuel to be particularly suitable in such applications, both as a standalone fuel, or as a blend with gasoline. On the contrary, the long ignition delay and the subcooling effect of methanol pose some challenges for its application in compression-ignition engines. Some examples of methanol direct injection as single fuel in heavy duty engines can be found in the literature where fuel autoignition is achieved by means of fuel additives [2] and increased compression ratios of up to 1:28 [3,4].

A more common approach is the adaptation of a dual fuel system, where methanol ignition is achieved through the use of a pilot fuel of higher reactivity, typically diesel. Two main strategies can be identified in the literature with regards to dual fuel operation: methanol port fuel injection, also referred as methanol "fumigation", or direct dual fuel injection, where both fuels are injected inside the cylinder (combustion chamber).

Focusing on the in-cylinder injection strategies, these can be distinguished as premixed combustion and diffusive combustion. The premixed combustion of methanol in a direct injection (DI) system was directly compared to a port-fuel injection (PFI) system [5], and the results did not reveal any significant benefits in the DI system. Instead, it was observed that for the DI system spray targeting, in relation to fuel mixing and wall wetting, had a strong impact in the emissions of HC, CO and Soot.

Direct injection with diffusive methanol combustion has been more recently applied to four-stroke engines and resulted in better combustion stability when compared to both, PFI and DI premixed strategies [6,7]. During this strategy, methanol is injected late in the compression stroke, near top dead center. Studies showed that increasing the level of methanol share led to reduced combustion duration with benefits on thermal efficiency, and therefore fuel consumption. Further application of the diffusive combustion system on marine engines [8] confirmed the combustion stability of the system and the strong importance of good spray targeting to maximize the interaction between the pilot and the main fuel across several engine loads.

The current paper discusses the methodology to design and develop a dual fuel retrofit concept of diffusive combustion on existing large bore 2-stroke low-speed marine engines. The study addresses the impact of different injector nozzle tip designs, which affect the spray pattern of methanol, the effect of different injection strategies and the overall engine tuning strategy by means of a numerical and experimental analysis.

Experimental activities were first carried out in a spray chamber that was optically accessible, and subsequently on a two-stroke 6-cylinder marine test engine (RTX5).

Table 1: Fuels properties [9]

	Methanol (CH_3OH)	Ethanol (C_2H_5OH)	LFO
Density [kg/m3]	792	785	835
Heat of Vaporization [MJ/kg]	1.168	0.919	0.270
Lower Heating Value [MJ/kg]	19.99	26.9	43.2
RON	109	109	n.d.
Stoichiometric A/F Ratio [kg/kg]	6.46	8.98	14.95

2. Methodology and tools

To define the computational methods the authors aimed for a good compromise between model accuracy and computational time, in consideration of the large engine size and the need of a robust tool to drive the design phase of a commercial retrofit kit. The computational models described in the next section were developed in OpenFoam environment with the additional use of a customized library "LibICE" developed by Politecnico di Milano [10]. The numerical model is based on RANS approach, the turbulence closure is addressed with the k-ϵ model, while the injection of both fuels is represented with a Lagrangian method and Reitz-Diwakar breakup model. The combustion is modelled with a perfectly stirred reactor model that accounts for both fuels. Two approaches were evaluated to solve the chemical reactions, the direct chemistry solution and a tabulated approach. The latter resulted to be equally accurate and faster than the former, and was therefore selected for the full engine model.

2.1. Optical combustion chamber and CFD model description

The combustion concept assessment and the initial validation of the numerical framework was performed in an optically accessible combustion chamber, where different spray orientations and injection strategies were tested, and subsequently utilized for the validation of the numerical models. The experimental chamber [11] developed by Wärtsilä Services Switzerland in collaboration with CNR STEMS, was specifically designed to replicate the geometry and the thermodynamic condition of a large bore marine engine (Figure 1). Two injectors, one acting as a pilot and the other as main injector, were fitted on the top end of the chamber, opposite to a sapphire window. To reproduce as close as possible the spray characteristics of the target engine, both the injectors were sized for 2-stroke marine applications, filling a gap in the available literature often oriented towards automotive size injectors. The injectors were located in eccentric position, at the same radial distance, in specially designed pockets that provided the option to freely rotate them along their respective axes, and therefore allow for the investigation of various spray interactions between the two fuels.

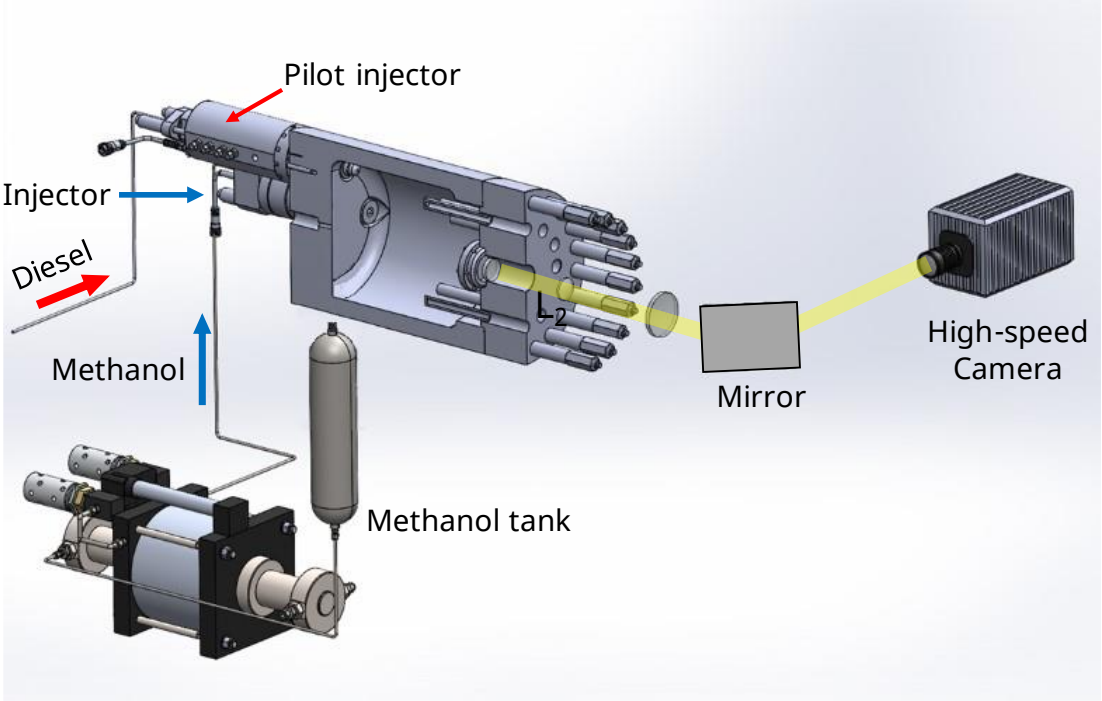

Figure 1: Optical accessible combustion chamber

Figure 2 depicts the meshes used to discretize the optical combustion chamber, where a hexahedral non-structured grid was applied with static local refinements in the combustion zone. A summary of the mesh characteristics with the respective computational times are reported in Table 2. The mesh independence check performed on the grids (Figure 3) demonstrated a small pressure sensitivity on the selected grid, and for this reason a medium grid was chosen for the tests to save computational time and maintain consistency with the grid structure utilized in the full engine tests.

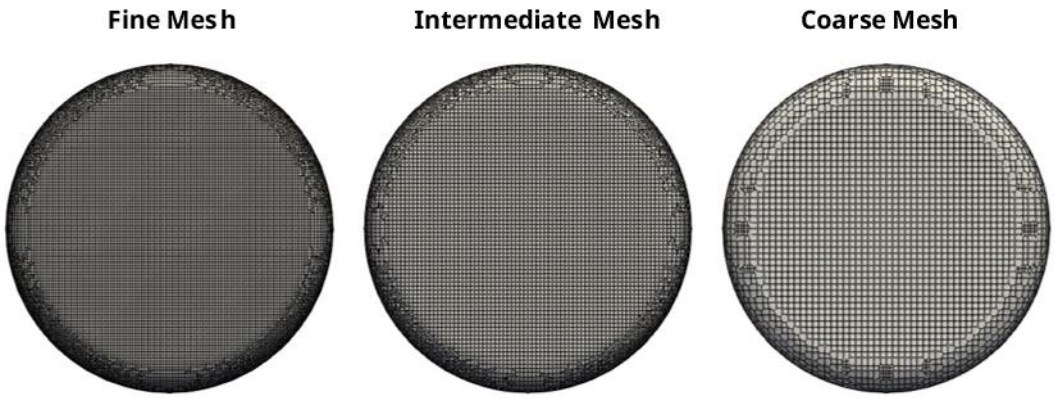

Figure 2: Mesh independence test - Hexaedral mesh for optical combustion chamber

Table 2: Mesh independence test - base cell sizes and computational time

Mesh size and computational time			
	Cell Count (x 10^3)	**base mesh [mm]**	**simulation time [h]**
Coarse	~ 109	6	~3
Medium	~ 323	4	~9
Refined	~ 745	3	~20

A well stirred reactor model was selected for the combustion simulation [12] and with this approach each cell is treated as a homogeneous reactor accounting for the dual fuel combustion. The chemical reaction rates were separately tabulated with two different chemical mechanisms, namely the NUIGMech1.0 [13] for n-heptane (used as diesel surrogate) and the CRECK DME model [14] for Methanol. The chemical decoupling of the two fuels was justified by the fact that the low quantity of the injected diesel was considered to not interact chemically with the main fuel. To assess the effectiveness of the double tabulation method, it was found necessary to compare it with the established direct chemistry integration method. While the reacting flow simulation with the direct chemical implementation method was time consuming (due to the extra computational overhead), a good computational improvement was implemented through use of the Dynamic Load Balancing method – DLBFoam [15].

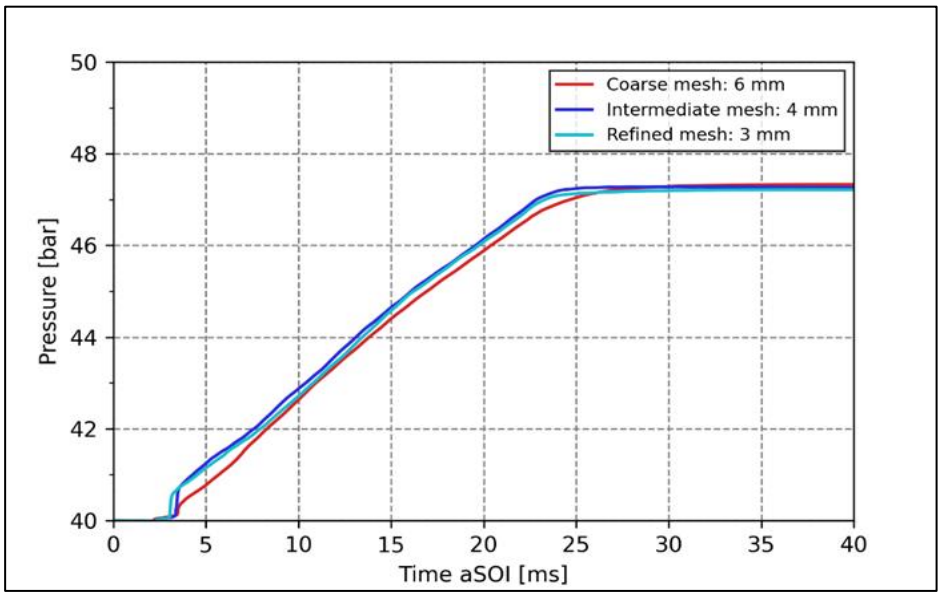

Figure 3: Optical combustion chamber mesh independence - CFD model pressure sensitivity

The comparison of the results between the two methods in Figure 4 show the satisfactory alignment between the tabulated and the direct kinetic approaches, where the pressure curves from both cases were very similar. The small differences identified at the early stages of combustion and in the evolution of the temperature contour had no significant impact on the overall measured quantity, therefore confirming the similarity of both methodologies.

The selected "intermediate mesh" and the tabulated chemistry approach were compared with the experimental data (Figures 4 and 5), and the pressure trace correlation was considered sufficient enough to justify the adaptation of these methodologies for the simulation of the full engine.

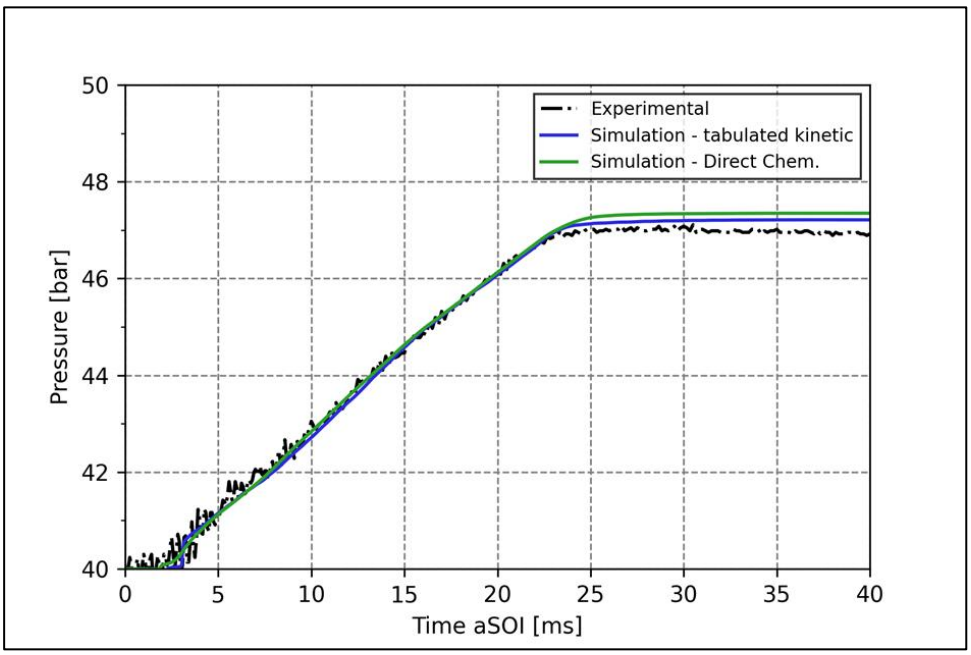

Figure 4: Combustion model validation - Experimental pressure measurement vs. Simulation results with tabulated kinetic and direct chemical integration model

2.2. Engine model

The numerical setup described for the optical combustion chamber was also applied to the R&D laboratory engine (RTX5), which is a Wärtsilä 6RT-Flex50-B 2-stroke uniflow scavenging marine engine, of 500 mm bore, 2050 mm stroke, and 6-cylinders in-line. Main engine parameters are reported in Table 3.

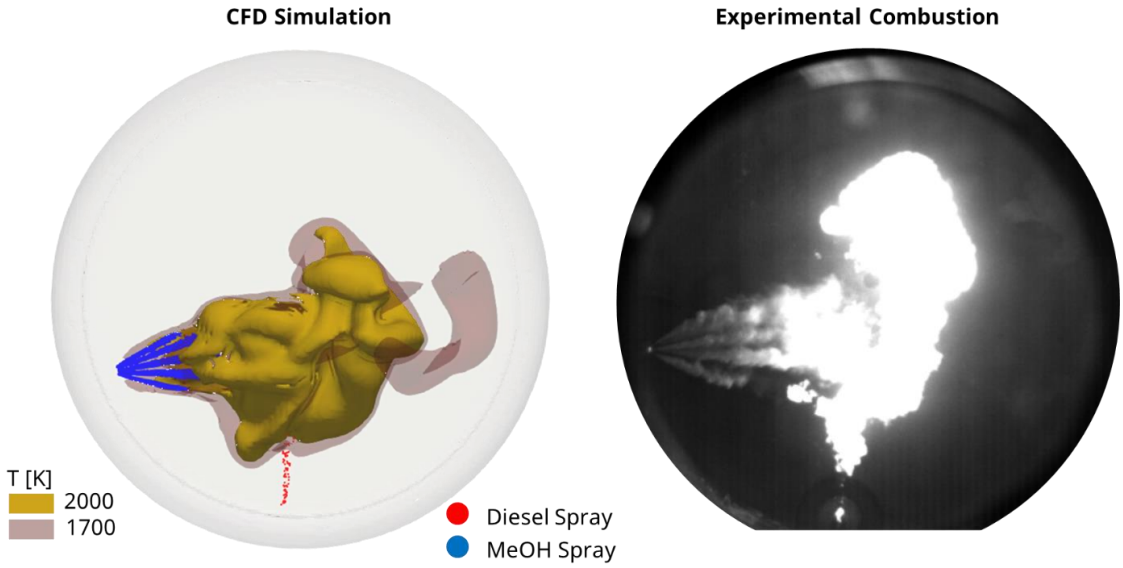

Figure 5: Optical combustion chamber test - CFD simulation results (temperatures iso-contours and lagrangian sprays) compared with experimental images of visible flame

To achieve a reasonable computational time for the complete engine simulation a base mesh size of 12 mm was applied to simulate the scavenging phase. Localized refinements were employed in the proximity of the intake ports and in the exhaust valve region to gain accuracy without compromising the total cell count. The injection and combustion phases were then computed with a more refined mesh, where the base size was set to 2.5 mm, and local conical refinement was applied in the vicinity of the nozzles during the injection process. A complete 1-D engine model was selected as the source to impose pressure and temperature values on the cylinder intake and exhaust boundaries, and a similar approach was applied to compute the injection mass flow rate for both fuels.

Table 3: Engine description

Engine Parameters	
Engine Type	Two-stroke RTX5
Number of Cylinders	6
Bore [cm]	50
Stroke [m]	2.05
Power [kW]	8040
MEP [bar]	21
Speed [rpm]	95

3. CFD simulation results

3.1. Design variables

The CFD model described in the previous section was utilised as a predictive tool to evaluate different design concepts of components that play a key role to the combustion process. The dual fuel combustion concept under consideration relies on the ignition of methanol after its interaction with

the pilot flame. Since the injector nozzle tip (Figure 6) determines the distribution of fuel inside the cylinder and the interaction of the main fuel with pilot flame, its impact on combustion is crucial.

The use of methanol as the main fuel for combustion leads to a significant increase of injected fuel quantity, when compared to standard diesel, due to its lower calorific value. The required higher fuel flow can be managed through increasing the rail pressure, increasing the nozzle holes diameter, or prolonging injection duration. Such strategies impact spray penetration and in case of nozzle hole diameter increase, the spray atomization. In this study the design of the nozzle tip, and specifically, the number of holes, size and characteristic angles were varied to evaluate their effect with respect to spray formation, heat release, and pollutant formation.

Figure 6: baseline injector nozzle tip

Figure 7 depicts two different nozzle tips where the characteristic angles of each hole where changed, while preserving the overall flow area, and therefore the injection duration and mass flowrate. The heat release rates resulting from the two different nozzle tip configurations, which were compared under the same engine operating conditions, are shown in Figure 8.

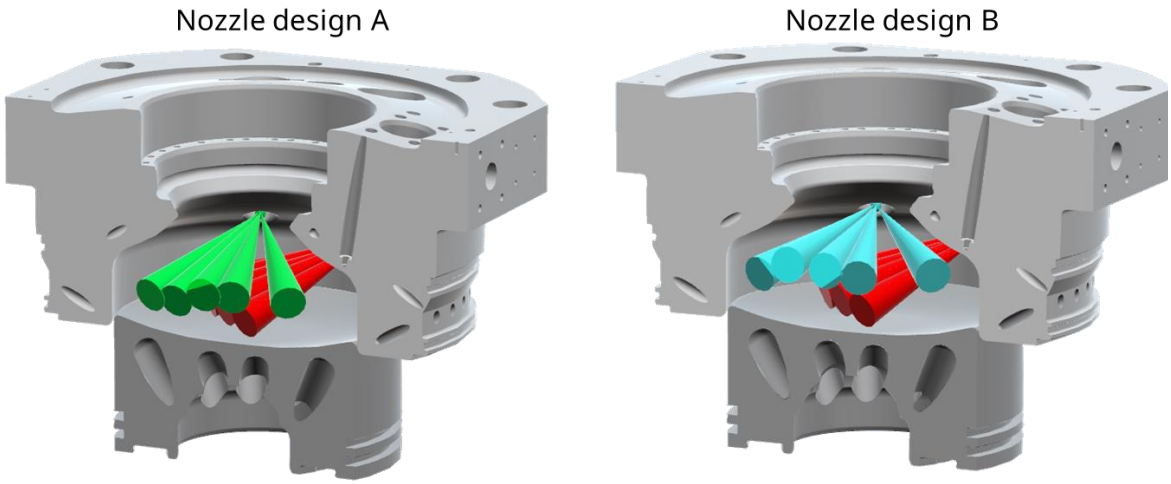

Figure 7: Comparison of methanol nozzle tip designs A and B

The heat release analysis shows a first energy spike, accounting for 5% of the total, due to the pilot fuel ignition, followed by the energy released from methanol combustion. Focusing on the methanol

combustion from the two nozzle tips, it is evident that a different heat release evolution takes place between nozzle design "A" and "B". The analysis showed that nozzle "A" provided a non-optimal spray interaction between the pilot and main fuels, which led to an initial premixed combustion phase and an abrupt heat release, whereas nozzle "B" showed a smoother ignition of methanol that resulted to a more controllable in-cylinder pressure rise and heat release.

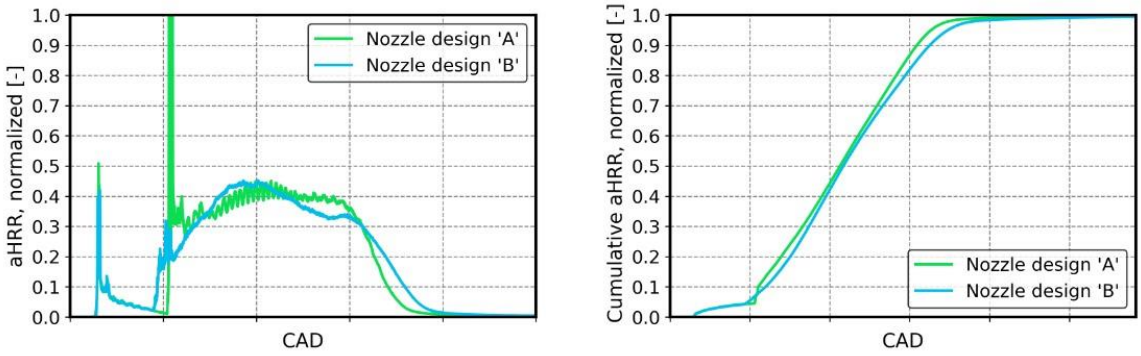

Figure 8: Nozzle tip design comparison (A vs B) with respect to heat release and cumulative heat release rate

The major impact from the nozzle tip design is clearly evident on the spray penetration and fuel mixing, as shown in figure 9 that compares nozzles "A" and "B". The blue colour contours represent the stochiometric iso-surfaces of methanol at same CAD. It can be seen that Nozzle "A" causes a narrow spray distribution, in relation to design "B", and creates a richer mixture plume in the earlier phases of combustion (5° after SOI). In the later stages of combustion, the more compact spray of Nozzle "A" had a strong impact on fuel penetration, with higher tendency to interact with the walls, increasing the risk of higher thermal stresses on components, and the formation of unburned hydrocarbons.

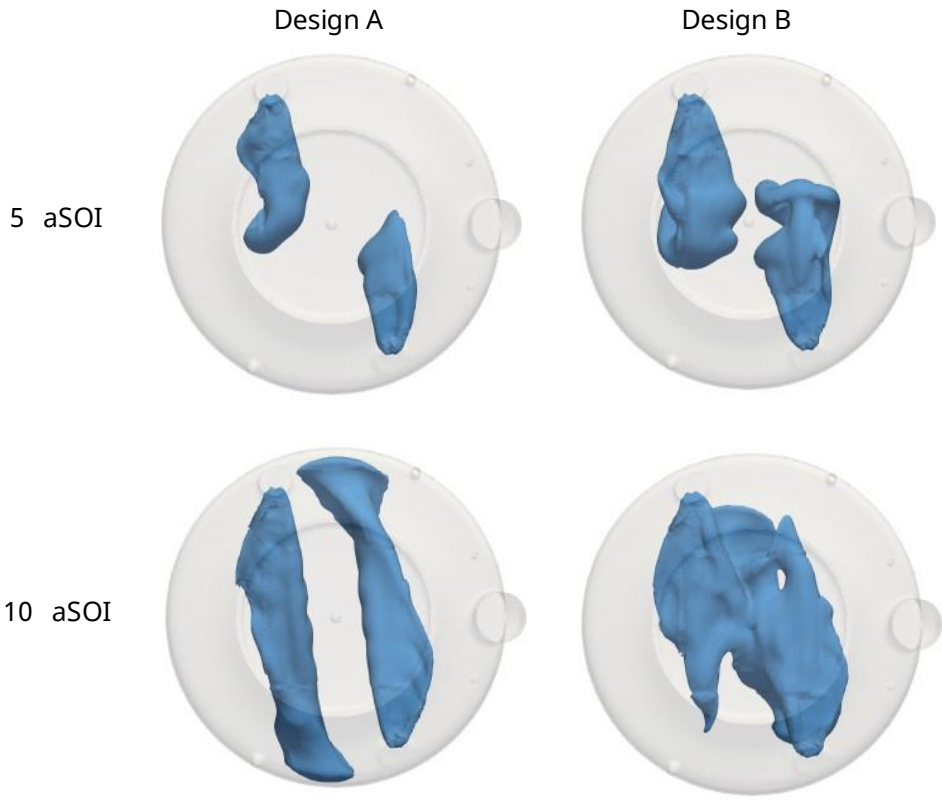

Figure 9: Comparison of Methanol stochiometric iso-contours from Nozzle tip designs A and B

The sensitivity analysis of the nozzle diameter involved scaling the dimension of each hole by ±30% with respect to the baseline design (Figure 10). The increase in flow area allowed for a shorter injection duration, and consequently faster combustion, but also led to higher combustion temperatures and longer spray penetrations. On the other hand, the reduction of the flow area was beneficial for spray penetration, but increased the combustion duration while decreasing the peak firing pressure and therefore deteriorating combustion efficiency.

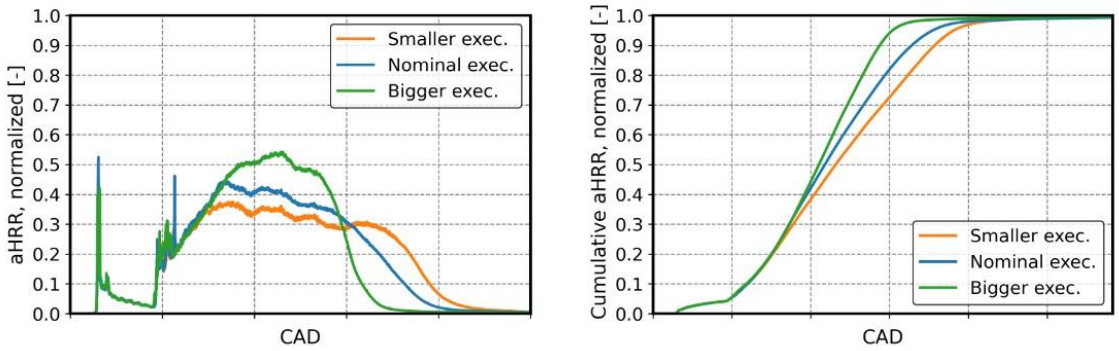

Figure 10: aHRR and cumulative aHRR trace effect on variation of nozzle hole diameters

A visualization of the in-cylinder flame development, represented by gas temperature iso-contour at 2300 K, is depicted in Figure 11. The results confirmed the different evolution of the flame between the two designs, showing that in the case of bigger hole diameters (Figure 11a) the spray penetrates

further into the combustion chamber, leading to a strong flame/liner interaction, whereas with the smaller hole sizes a significantly shorter flame depth was observed with negligible flame-wall contact (Figure 11b).

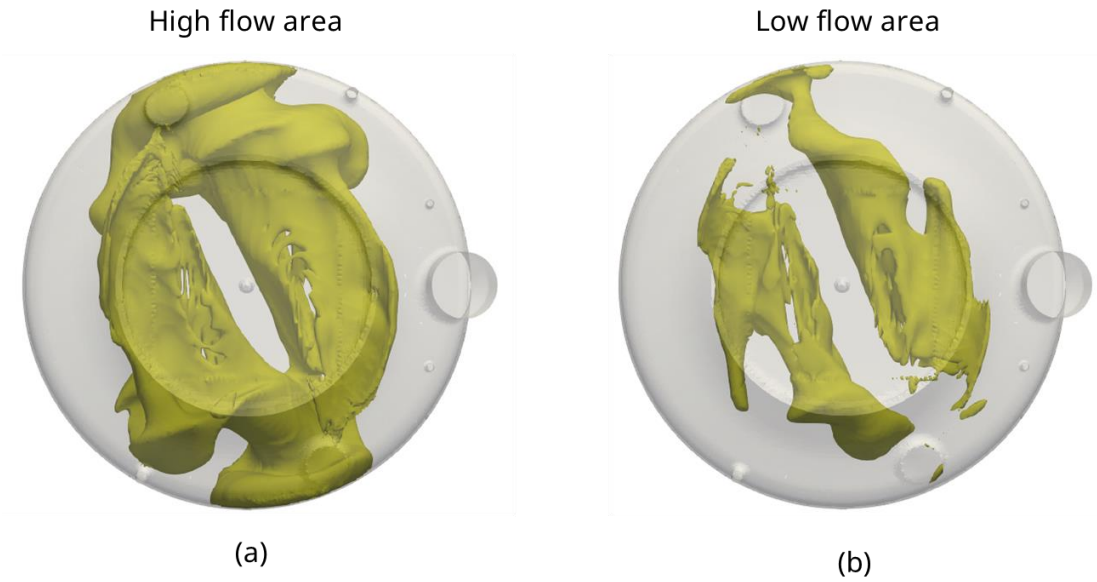

Figure 11: Flame temperature iso-contour visualization - (a): High flow area (1.3 x nominal Area) – (b) Low flow area (0.7 x Nominal)

Further investigation of the nozzle design characteristics involved a sensitivity analysis on the injection timing, and specifically the interval between the pilot fuel and main fuel injection events, hereafter referred as "dwell time". It was observed that dwell time, in combination to the nozzle tip geometry and engine load, had a strong impact on in-cylinder pressure. A sweep of the dwell time, with pilot SOI activated pre and post the main fuel SOI, and its effect on in-cylinder pressure is depicted in Figure 12. It can be seen that as the dwell time is reduced (i.e. shifted from after the main fuel SOI to before the main fuel SOI) an increase in firing pressure takes place. By starting the main fuel injection before the pilot fuel injection, methanol has sufficient time to vaporize and mix with air prior to the ignition of the pilot fuel. Consequently, when the pilot fuel ignites methanol initially burns in premixed combustion, followed by diffusive combustion as methanol injection continues to take place even after the pilot fuel injection terminates.

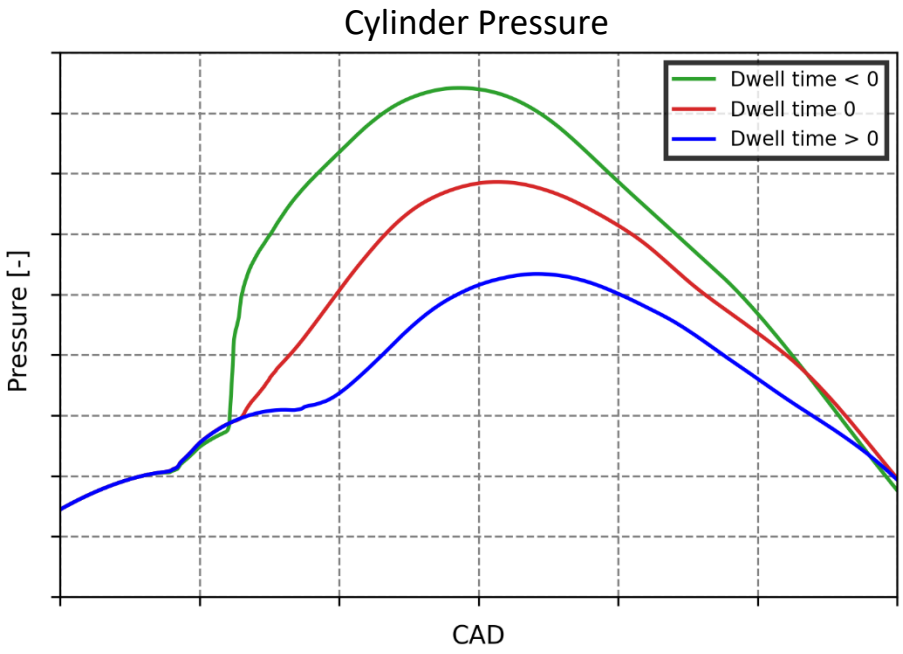

Figure 12: Effect of dwell time on in-cylinder pressure

All the above-mentioned parameters were considered for the selection of the Methanol and Diesel nozzle tip that were manufactured and subsequently tested on the RTX5 experimental engine.

4. Diesel engine conversion to Dual Fuel

To enable dual fuel operation, the engine was retrofitted with a methanol fuel injection system, while the original diesel fuel injection system was kept unchanged. As a result, in the event of failure of any of the methanol system components, the engine would switch automatically to Diesel mode operation, ensuring its continuous and safe operation.

4.1. Engine fuel components

The selected methanol fuel injection system consisted of a high-pressure reciprocating piston pump that was located inside the engine room, and a methanol dedicated fuel injection system that was located on the engine and consisted of a common rail that fed fuel to two injectors on each cylinder.

The high-pressure pump was equipped with flow control valves that ensured smooth operation throughout the full engine load range. Additionally, a drain valve was incorporated in the pump's skid to safely discharge methanol outside the engine room in case of an emergency.

The on-engine methanol fuel injection system was based on already existing Wärtsilä RT-Flex engine components, that were modified to accommodate methanol as the working fluid.

More specifically, the common rail was connected to high pressure pipes from the high-pressure pump and was large enough to account for the lower calorific value of methanol, compared to that of diesel, and ensured sufficient amount of fuel to the injectors and stable injection events. Six injection control units (ICUs), one for each cylinder, were installed on the methanol common rail, and through hydraulic -actuation these monitored and controlled the amount of fuel that was injected per cylinder. To

address the low lubricity of methanol, the reciprocating components inside the injection control unit were coated with a solid lubricant. Additionally, multiple sealing barriers, both solid and fluid, were installed to prevent possible fuel leaks into the hydraulic actuation system.

The injectors were symmetrically positioned on the cylinder cover, at a specified distance from the diesel injectors. As with the ICUs, the moving components of the methanol injection valves were coated with a solid lubricant to compensate for methanol's low lubricity. Furthermore, pressure sensors were installed at the inlet port of each injection valve for injection event and combustion diagnosis purposes.

4.2. Engine safety components

The methanol fuel supply and injection systems incorporated also a number of safety features to ensure a safe and reliable operation of the engine. With methanol being a low flash-point fuel the fuel supply pipes and all pipes operating at high pressures were required to have secondary barriers in order to collect possible fuel leakages caused by misalignments between the mating surfaces of pipe connections or pipe leakages. Additionally, the methanol common rail was equipped with an encapsulation and an air ventilation system to contain and remove possible fuel leakage during the engine operation. A series of gas detectors were also installed within the encapsulated volume to ensure the methanol concentration in the spaces monitored remained as low as possible, and within the 20% of the Lower Explosive Limit (LEL), in accordance with Classification Societies requirements (Figure 13).

A hydraulically-actuated safety valve, controlled via the engine control system, allowed for depressurisation of the methanol fuel system in case of engine failure. Nitrogen and drain valves were used to purge methanol from the fuel injection system in the event of a major failure or other hazardous events in the engine room.

To facilitate maintenance works and overhauls, additional safety measures were adapted to ensure that the fuel system could be effectively and completely purged from methanol. For this purpose, a parallel connection in the low-pressure piping system, upstream of the high-pressure pump, enabled diesel oil to be supplied into the methanol fuel system. A pair of shut-off valves were used to stop the low-pressure methanol supply and to start the diesel supply into the high-pressure pump. Any methanol trapped inside the fuel injection system was then gradually consumed by the engine, leaving only diesel oil inside the fuel pipes and components, therefore enabling the safe removal and maintenance of all methanol related components (Figure 14).

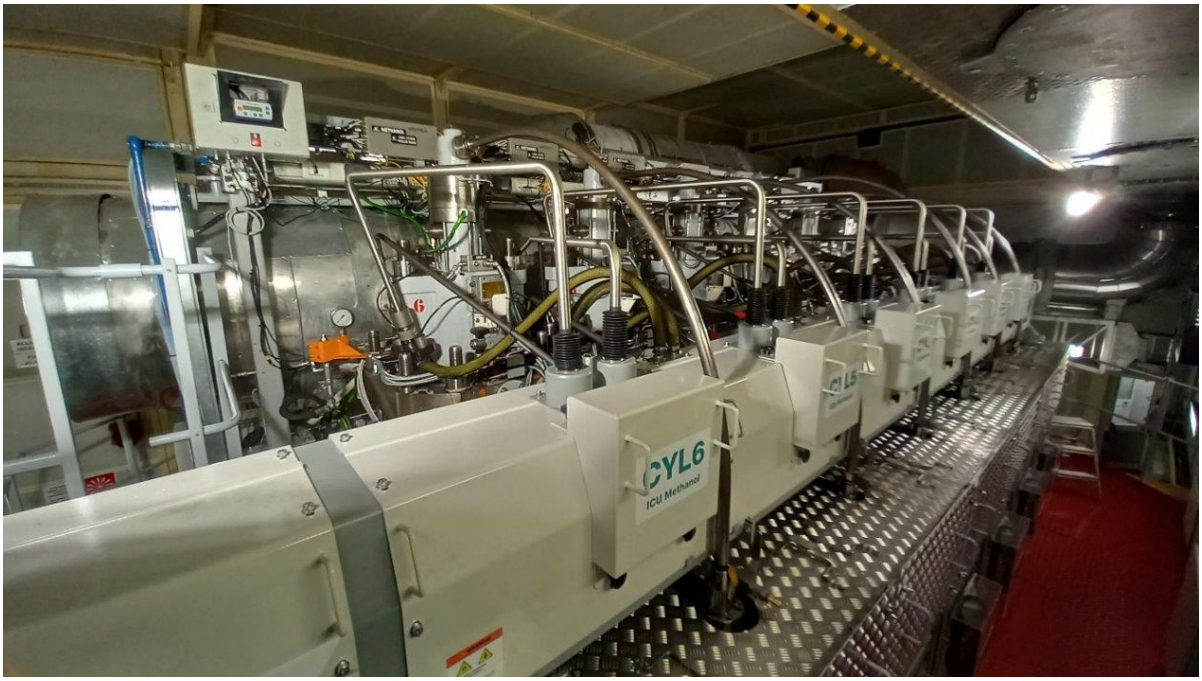

Figure 13: On-Engine methanol injection system: ventilated encapsulation of common rail and injection control units

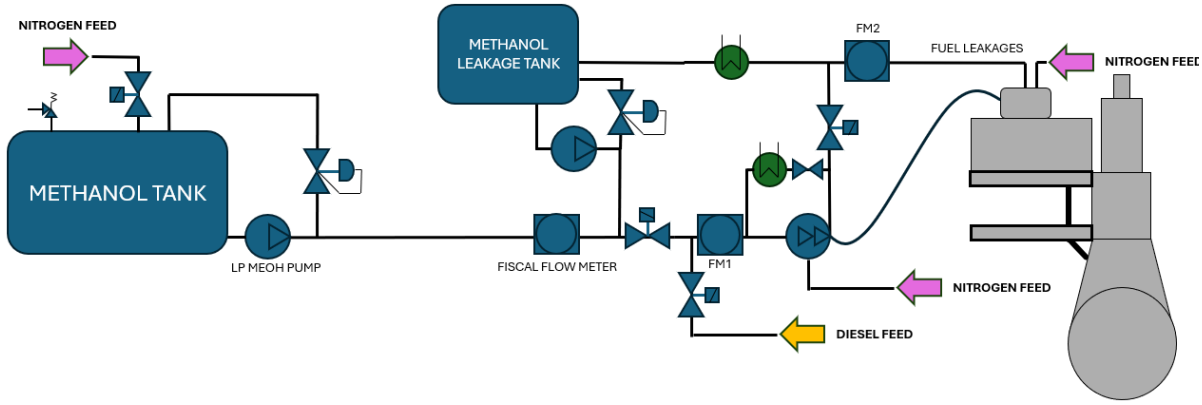

Figure 14: Schematic of the methanol fuel supply systems of 2-stroke R&D engine (RTX5)

5. Engine tests and Experimental results

RTX5 is an R&D engine that is used for investigation purposes of various technologies, prior to adaptation and implementation of these technologies on vessels. It is a fully instrumented engine with different types of sensors that can monitor and collect data about the performance of the engine and the condition of key components and systems. Measurements included the thermal load of components, pressures and temperatures in various locations such as the intake system, cylinder and exhaust system, and flows, such as fuel consumption. Furthermore, emission analysers were installed in the exhaust system of the engine that measured pollutants such as unburned hydrocarbons, CO, CO_2, NO_x, potential methanol slip and formaldehyde emissions.

The methanol combustion system, that was developed initially through CFD simulations, was further validated on RTX5 during the experimental campaign, where the engine was operated at different

ratings on both, Methanol and Diesel modes. For clarity purposes the work described in this study corresponds to one of the various ratings tested, the 21 bar MEP, at a power of 8040 kW and 95 rpm, which is representative of typical 2-stroke marine diesel engines.

As a first step, tests were conducted on diesel mode at four engine loads (25%, 50%, 75% and 100%) to create a baseline for the performance of the engine, while the NO_x emissions of the engine were kept within the Tier II limits. Subsequently, the engine was run in methanol mode at the same firing pressure as that of the diesel mode operation so that the two fuel modes could be directly compared on combustion efficiency. The results from the two sets of tests, at 75% engine load are depicted in Figures 15 and 16. Figure 15 shows that the fuel consumption in Methanol operation, which also includes the pilot fuel consumption, was reduced by about 5% compared to that of diesel mode. Furthermore, at the same engine load, figure 16 shows that NO_x emissions during methanol operation were 40% lower than those measured during diesel operation. Both, the improved fuel consumption and lower NO_x emissions were attributed to the improved thermal efficiency and lower combustion temperatures achieved during methanol operation. Figure 17 compares the in-cylinder pressure and heat release rate of the two fuel modes at 75% engine load, based on in-cylinder pressure trace data that was recorded and averaged over 300 engine cycles. The results show that the methanol and diesel heat release rates are very similar, but also demonstrate the relatively faster combustion of methanol compared to diesel, that explains the above observations about the improved fuel consumption.

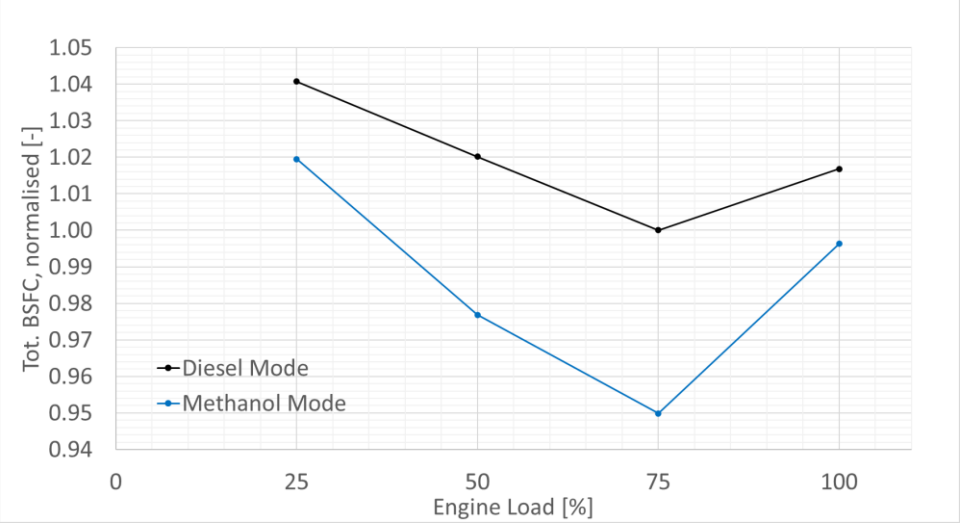

Figure 15: Brake-specific fuel consumption (BSFC) for operation on Methanol and Diesel Modes, at 75% engine load

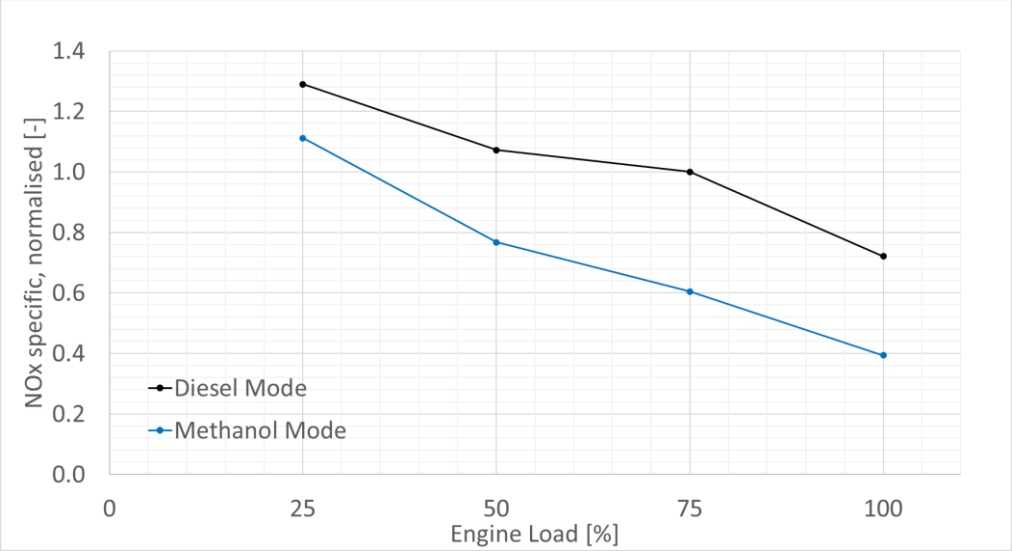

Figure 16: Specific NOx Emission on Diesel and Methanol modes, at 75% of engine load

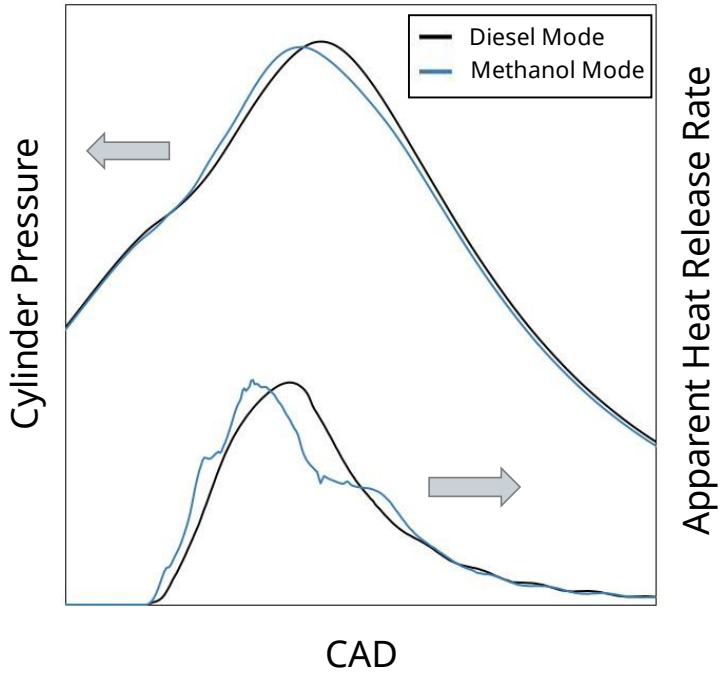

Figure 17: In-cylinder pressure and Heat release rate for operation on Methanol and Diesel modes, at 75% engine load (21bar MEP)

6. Engine Model Validation

The experimental tests on RTX5 engine provided a data base for the validation of the CFD simulations that were conducted prior to the tests to develop the methanol combustion system. The model validation was performed for selected cases of engine running, where a complete engine simulation was run to replicate the experimental boundaries.

For clarity, only two representative validation points are reported in Figure 18, where experimental data from operation in diesel and methanol modes are compared to the CFD simulation results. The plots show that the measured and simulated pressure curves and heat release are in good agreement for either fuel. Comparing the two fuel modes, both the experimental and simulated results capture the relatively longer combustion phase of diesel when compared to methanol, attributed to the faster burn of the latter.

Similar observations were made for all the other engine loads tested, the various engine tuning settings and the different nozzle tip designs that were evaluated on the engine. The good correlation between the experimental data and simulations demonstrated that the adopted CFD methodology can be successfully used as a predictive tool for the development of combustion systems of different fuels and the definition of nozzle tip designs, which can be applied as retrofit technology to existing 2-stroke marine diesel engines, and enable these to be converted to dual-fuel engines.

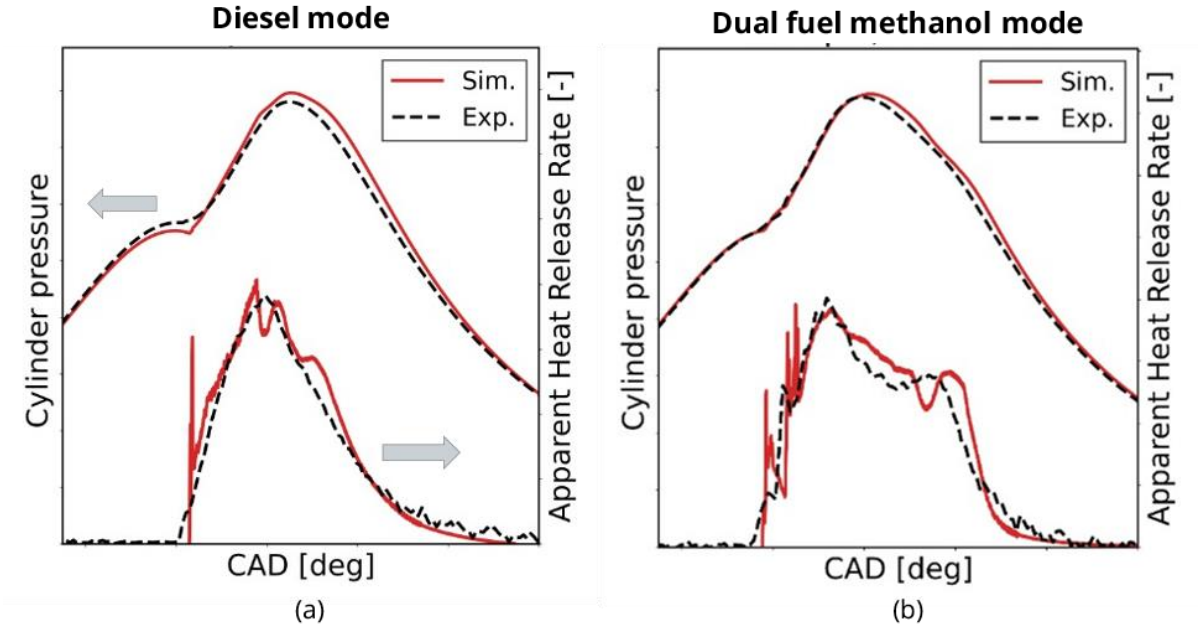

Figure 18: Comparison between Experimental data and CFD: In-cylinder pressure and Heat release rate for operation on (a) Diesel and (b) Methanol modes, at 75% engine load (21bar MEP)

7. Conclusions

This study described the different stages that were followed to conceptualise, design and develop a robust dual-fuel combustion system, which will be implemented to an innovative retrofit kit and enable existing marine diesel engine to be converted to dual-fuel engines and operate on sustainable fuels. The physical properties of methanol, such as its lower calorific value, its low lubricity and corrosive nature, were all considered in the design and sizing of the systems and components. The dual-fuel combustion concept was first analysed thoroughly by CFD simulations, focusing on the main parameters that characterize methanol combustion. The analysis was also used to design an important component for the combustion system, the injector nozzle tip. The analysis was followed by tests on an experimental engine, where the combustion system was validated and further developed. The results from the testing campaign demonstrated excellent engine running stability at different loads

and speeds with a minimum quantity of pilot fuel injected. At the end of the test campaign and after analysing the engine performance and emission results it was shown that the fuel consumption in methanol can be lower than that of diesel mode, as well as the NO_x emissions that were reduced significantly. The performance improvement and emission reductions can be explained by the lower combustion temperatures and the improvement on the thermodynamic efficiency achieved on methanol operation.

The study concluded that methanol as a main fuel for 2-stroke marine engines is a viable and promising solution in the decarbonisation of shipping.

Abbreviations

aHRR – Apparent heat release rate

aSOI – After start of Injection

BSFC – Brake specific fuel consumption

CAD – Crank angle degree

CFD – Computational fluid dynamics

CNR STEMS – Consiglio Nazionale delle Ricerche, Istituto di scienze e tecnologie per l'energia e la mobilità sostenibili

CO - Carbon monoxyde emission

DI - Direct injection

GHG – Green House Gas

HC – Unburned hydrocarbon emission

ICU – injection control units

MEP – Mean effective pressure

NO_x – Nitrogen oxides emission (NO, NO2)

PFI – Port fuel injection

RANS – Raynolds averaged Navier-Stokes equation

RON - Research Octane Number

RTX5 – Wärtsilä 6RT-Flex50-B – Test engine for R&D activities

Literature

[1] Verhelst, S., Turner, J., Sileghem, L., and Vancoillie, J.(2019) Methanol as a fuel for internal combustion engines, Progress in Energy and Combustion Science, Vol. 70, 2019, Pages 43-88, ISSN 0360-1285, https://doi.org/10.1016/j.pecs.2018.10.001.

[2] Cheng C., Faurskov Cordtz R., Dyhr Pedersen T., Winther K., Langballe Førby, N. & Schramm, J. (2023). Investigation of Combustion Characteristics, Physical and Chemical Ignition Delay of

Methanol Fuel in a Heavyduty Turbo-charged Compression Ignition Engine. Fuel, 348, Article 128536. https://doi.org/10.1016/j.fuel.2023.128536

[3] Nylund, N.-O., Murtonen, T., Westerholm, M., Söderström, C., Huhtisaari, T., & Singh, G. (2015). *Testing of various fuel and additive options in a compression-ignited heavy-duty alcohol engine*. ISAF-0056. Paper presented at 21st International Symposium on Alcohol Fuels, ISAF, Gwangju, Republic of Korea.

[4] Shamun S., Haşimoğlu C., Murcak A., Andersson ö , Tunér M., Tunestål P. (2017) Experimental investigation of methanol compression ignition in a high compression ratio HD engine using a Box-Behnken design, Fuel,Volume 209,2017, Pages 624-633, ISSN 0016-2361, https://doi.org/10.1016/j.fuel.2017.08.039.

[5] Jia Z., Denbratt I., (2018) Experimental investigation into the combustion characteristics of a methanol-Diesel heavy duty engine operated in RCCI mode, Fuel, Volume 226, 2018, ages 745-753, ISSN 0016-2361, https://doi.org/10.1016/j.fuel.2018.03.088.

[6] Repo J., Axelsson M., Heir V. (2023) Methanol combustion concept alternatives for new build and retrofit of 4-stroke medium speed engines, Paper presented at 30th CIMAC Congress 23, Busan, Korea

[7] Dong Y., Kaario O., Hassan G., Ranta O., Larmi M., Johansson B. (2020) High-pressure direct injection of methanol and pilot diesel: A non-premixed dual-fuel engine concept, Fuel, Volume 277,2020,117932, ISSN 0016 -2361, https://doi.org/10.1016/j.fuel.2020.117932.

[8] Coppo M., Negri C., Wermuth N., Garcia-Oliver J. M., Cao J. (2023) Powering a greener future: the OMT injector enables high-pressure injection of ammonia and methanol, Paper presented at 30th CIMAC Congress 23, Busan, Korea

[9] Sarathy S., Oßwald P., Hansen N., Kohse-Höinghaus K., (2014) Alcohol combustion chemistry, Progress in Energy and Combustion Science, Volume 44, 2014, Pages 40-102, ISSN 0360-1285, https://doi.org/10.1016/j.pecs.2014.04.003.

[10] Lucchini T., Della Torre A., D'Errico G., Onorati A. (2019) Modeling advanced combustion modes in compression ignition engines with tabulated kinetics, Applied Energy, Volume 247, 2019, Pages 537-548, ISSN 0306-2619, https://doi.org/10.1016/j.apenergy.2019.04.062.

[11] Sementa P., Lazzaro M., Tornatore C., Catapano F., Calvo Oliveira A., Thorsen L., Viglione L. (2024) Experimental Investigation of High-Pressure Ammonia Spray and Combustion under Marine Engine-Like Conditions Using Optical Diagnostics, THIESEL 2024 Conference on Thermo- and Fluid Dynamics of Clean Propulsion Powerplants

[12] Schirru, A., Hardy, G., Wright, Y.M., Lucchini, T. et al. (2023), "CFD Modeling of a DME CI Engine in Late-PCCI Operating Conditions," SAE Technical Paper 2023-01-0203, 2023, doi:10.4271/2023-01-0203

[13] Zhang K., Banyon C., Bugler J., Curran H. J., Rodriguez A, Herbinet O., Battin-Leclerc F., B'Chir C., Heufer K. A. (2016) An updated experimental and kinetic modeling study of n-heptane oxidation, Combustion and Flame, Volume 172, 2016, Pages 116-135, ISSN 0010-2180, https://doi.org/10.1016/j.combustflame.2016.06.028

[14] Pelucchi, M., Cavallotti, Faravelli, T., Klippenstein, S.J. (2018) H-Abstraction reactions by OH, HO2, O, O2 and benzyl radical addition to O2 and their implications for kinetic modelling of toluene oxidation, Physical Chemistry Chemical Physics, 20, pp. 10607-10627 (2018), DOI: 10.1039/C7CP07779C

[15] Tekgül B., Peltonen P., Kahila H., Kaario O., Vuorinen V. (2021) DLBFoam: An open-source dynamic load balancing model for fast reacting flow simulations in OpenFOAM, Computer Physics Communications, Volume 267, 10.1016/j.cpc.2021.108073 (2021).

Keywords: ammonia, ammonia-combustion, engine relevant conditions, pre-chamber, carbon free combustion, emissions, high IMEP, high BMEP, optical investigation

The GHG reduction potential of high-IMEP pure ammonia combustion

Silas Wüthrich, Patrick Albrecht, Patrick Cartier, Prof. Kai Herrmann

Institute of Thermal and Fluid Engineering (ITFE), University of Applied Sciences and Arts Northwestern Switzerland (FHNW)

https://doi.org/10.18453/rosdok_id00004647

Abstract

Ammonia as fuel has been widely discussed in the marine sector during the last years. Since ammonia as fuel poses major challenges in combustion, it is common to apply a dual-fuel combustion process, which requires a second fuel, typically diesel, to start the combustion. However, to further reduce greenhouse gas (GHG) emissions, the need for a carbon-based pilot fuel should be eliminated by applying a combustion scheme based on a single carbon-free fuel that maintains high engine efficiency and power output while keeping GHG-related emissions such as nitrous oxide (N_2O) low.

For ammonia, the most commonly used combustion process to date is based on a premixed charge of ammonia ignited by a pilot injection of a carbon-based fuel. This well controllable solution allows a wide range of ammonia / pilot fuel share ratios – such engines are even capable of running on 100% pilot (diesel) fuel only. This high fuel flexibility ensures a secure fuel supply from common suppliers around the world. A more sophisticated approach, in which directly injected ammonia is ignited by pilot injection of a carbon-based fuel, resulting in a diesel-like combustion process, is planned to be used in large-bore two-stroke engines. However, this approach also relies on a small quantity of carbon-based pilot fuel to ensure safe and stable ammonia combustion.

This paper presents research into an ammonia combustion process that does not require a pilot injection and therefore allows for 100% carbon-free operation of such combustion engines. Here, a small portion of an ammonia/air mixture at stoichiometric conditions is ignited in a pre-chamber. The resulting hot combustion gases then form a reactive jet, which enters the main chamber to ignite the premixed main charge at operating point specific air/ammonia equivalence ratios (λ). This combustion process has been applied over a wide range of air-fuel equivalence ratios (λ = 0.8 - 2.0) and different IMEP (up to 27 bar). The research was carried out using an optical engine test facility equipped with exhaust gas measurement. Simultaneously applied high-speed Schlieren and OH* chemiluminescence measurements allow the combustion process to be studied in terms of the (optical) start of ignition, the flame propagation speed, and other characteristics.

A high IMEP, completely carbon free combustion process has been realized, including characterization of heat release, ignition delay, start of combustion, flame propagation speed and pollutant emission

formation for marine engine relevant conditions. The effect of the very low laminar flame speed of ammonia is offset by the additional turbulence created by the reactive jet from the pre-chamber, suggesting that this carbon-free combustion process may be applicable to medium-speed engines as well. In addition, the experiments also provide some insight into the challenge of knocking cycles and lube oil induced pre-ignition events. On the emissions side, the critical formation of nitrous oxide (N_2O) has been studied and the overall GHG reduction potential for this type of combustion process has been assessed.

1. Introduction

The goal of a carbon-neutral society is set out in the Paris Agreement, a legally binding international treaty on climate change, which aims to keep the global average temperature increase well below 2 °C above pre-industrial levels and to step up efforts to limit the temperature increase to 1.5 °C [1]. While the Paris Agreement is mainly aimed at land-based applications, the International Maritime Organization (IMO) targets the greenhouse gas (GHG) reduction strategy for international shipping. Overall, it is imperative that both private and industrial sectors reduce their greenhouse gas emissions towards zero over the course of this century. Wherever possible, electrification based on renewable energies is the most efficient approach to achieve this goal.

On the other hand, due to the limited energy density of batteries, direct use of electricity is limited or not possible in certain applications within industrial sectors. This is particularly true for the marine sector, where – apart from certain niche applications such as ferries or short sea shipping – the switch from fossil to renewable fuels is the most promising options for decarbonization. Since large internal combustion engines (ICE) will continue to play a role for marine propulsion, the transition from fossil fuels to sustainable energy carriers is one of the necessities in view of reducing GHG emissions to keep global warming within tolerable limits.

Various technology paths for ICE and fuel systems for future propulsion of ships have been investigated. For the substitution of fossil fuels, ammonia or methanol were announced as potential candidates for an economically feasible route to decarbonization [2]. Of course, these fuels must be produced via renewable energy, and only ammonia can be considered as completely CO_2-free. Since methanol still contains carbon, the CO_2 needed for production must come from non-fossil sources (direct air capture) to be considered carbon-neutral. All possible options regarding non-fossil fuels – including "green" hydrogen for certain applications – have advantages and disadvantages in terms of scope, handling, efficiency, cost, environmental risks, etc. In particular, the use of ammonia has recently gained increasing attention and is being touted by various stakeholders as one of the most promising future fuels. Various studies have investigated the potential for application in marine shipping from a cost and production point of view [3-8]. Although ammonia is a well-known product since centuries, it has mainly been used to produce fertilizers. In terms of its use as an engine fuel, a transition phase up to 2050 is expected. In the current decade, the share of liquefied natural gas (LNG) will probably still increase before the desired transition to methanol or ammonia takes place. Even if the use of sustainable fuels produced by the synthesis of renewable energies (Power-to-X or synfuels) or from the processing of suitable biological wastes and residues (biofuels) is mandatory, the use of LNG as a marine fuel will probably still be a matter of course in a transition phase over the next decade and beyond.

Current concepts of gas engines are seen as good basis for future solutions designed for operation on such alternative fuels. Even though ammonia fuel application for IC engines is not new, the conversion still providing comparable efficiency and guaranteeing reliable operation, poses certain challenges in terms of ignition concepts and combustion properties. A range of involved complex processes such as flow field conditions, mixing properties, ignition, combustion onset, and flame propagation must be considered. Whereas the upcoming low-speed two-stroke ammonia engines will use a pilot fuel ignited direct injected ammonia combustion scheme (diesel-like) this work focusses on a 100% carbon free combustion without requiring a carbon-based pilot fuel. An optically accessible experimental test facility providing engine relevant operation conditions was used to fundamentally examine premixed

homogeneous combustion ignited by an actively filled pre-chamber. The investigations include typical operating conditions as well as very high engine loads for marine engines with compression temperatures around 950 K and peak pressures up to 300 bar and beyond. The influence of different operating parameters such as mixture charge composition or boost-pressure variations has been investigated. Insight into the thermo-chemical processes of combustion in terms of ignition delay, combustion onset, flame propagation speed, heat release, and exhaust gas composition will be provided.

2. Experimental setup, test execution and analysis

The optically accessible test facility *Flex-OeCoS* enables the examination of premixed pilot fuel ignited dual-fuel combustion processes in a range of IC engine relevant operational parameters [9]. Acquisition of crank-angle resolved operating conditions in terms of precise pressure as well as temperature measurements (by fine-wire thermocouples at different locations), and turbulent flow field determination (by means of high-speed PIV) has been established [10]. The adaptable setup with flexible operating modes has already been used for different dual-fuel combustion process investigations [11-14].

2.1. Test facility Flex-OeCoS

Figure 1 shows the working principle of the *Flex-OeCoS* test rig: One cylinder of a motor driven engine block feeds a mixture charge into an optical combustion chamber (Ø60 mm×20 mm), providing maximum optical access through rectangular and round sapphire windows at each side. Two intake valves (Ø16 mm) are located on the working cylinder, which is equipped with a flat-top piston. Two exhaust valves (Ø16 mm) are positioned on top of the combustion chamber, where a central bore at the top allows mounting of a pilot fuel injector, spark plug or pre-chamber. Various pressure sensors are implemented at different locations, and the entire head is thermally conditioned to achieve stable conditions during the aperiodic operation.

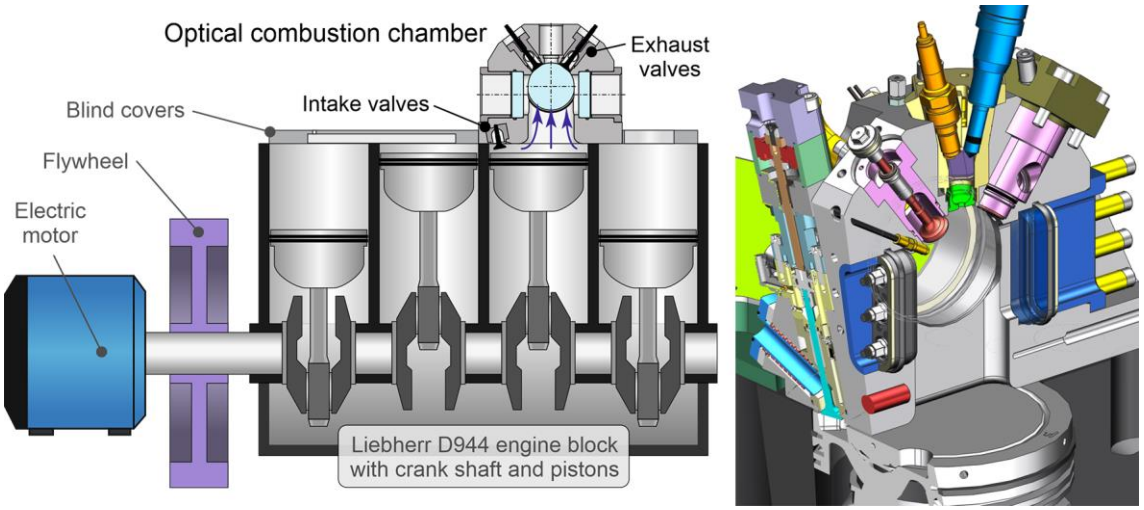

Figure 1: Concept of the Flex-OeCoS test facility (left), and cylinder head on the working cylinder with optical combustion chamber, intake/exhaust valves, and exchangeable design for different inserts on top (right). The optical accessible pre-chamber (yellow) is installed from the top between the exhaust valves (red) and features a sparkplug (orange), a direct injector (blue), a pressures sensor and an exchangeable nozzle (green).

The *Flex-OeCoS* test facility features adaptable operation at IC engine relevant conditions: Peak pressures in continuous operation of up to 260 bar (from boost-adjustable compression pressure (p_c) up to 160 bar), mixture charge temperatures (T) between 700 – 1050 K by inlet conditioning, and tunable flow (turbulence grades) depending on motor speed (n) of typically 300 – 1000 rpm. An overview of relevant test facility specifications is given in Table 1.

Table 1: Test facility specifications and parameter settings

Dimensions, Operating Parameter		
Working cylinder bore	Ø 130	[mm]
Stroke length	150	[mm]
Connecting rod length	237.1	[mm]
Displacement (working cylinder)	1990	[cm^3]
Compression ratio	13.02	[-]
Optical access main chamber diameter	Ø 60	[mm]
Optical access pre-chamber height / width	12.5 / 18	[mm]
Max. cylinder pressure	260	[bar]

Reference values (air charge)		
Intake boost pressure p_b	2.65 / 5.8 / 6 / 6.8	[bar]
Compression pressure p_c	70 / 130 / 145 / 160	[bar]
Intake temperature T_{in}	100 / 150	[°C]
Motor speed n	600	[rpm]
Turbulence intensity u'/C_m [9]	1.2	[-]

Independent pneumatic intake and exhaust valve actuators provide high variability. Moreover, pilot fuel injection settings (pressure, start, and duration) as well as mixture charge composition, by gas introduction in the air intake pipe close to the intake valve, can be freely adjusted by external supply units.

2.2. Optical setup, methodology and post-processing

As illustrated in Figure 2, simultaneous high-speed Schlieren/OH* chemiluminescence was applied to investigate prechamber combustion, combustion transition, ignition processes, turbulent flame front propagation, and abnormal combustion characteristics. Image acquisition was performed by means of three high-speed cameras: The chemiluminescence of the OH* radical as indicator of inflammation was acquired simultaneously with the Schlieren signal indicating vaporized and burned phases within the main chamber. A third Schlieren setup is focused on the optically accessible prechamber delivering insight into the ignition process around the sparkplug and flame evolution. The spatial resolution has been set to 60×60 mm (covering the entire main chamber) and 12.5x18 mm for the pre-chamber to achieve a temporal resolution of 0.1°CA, for the typical motor speed of n = 600 rpm, resulting in a frame rate of 36 kHz.

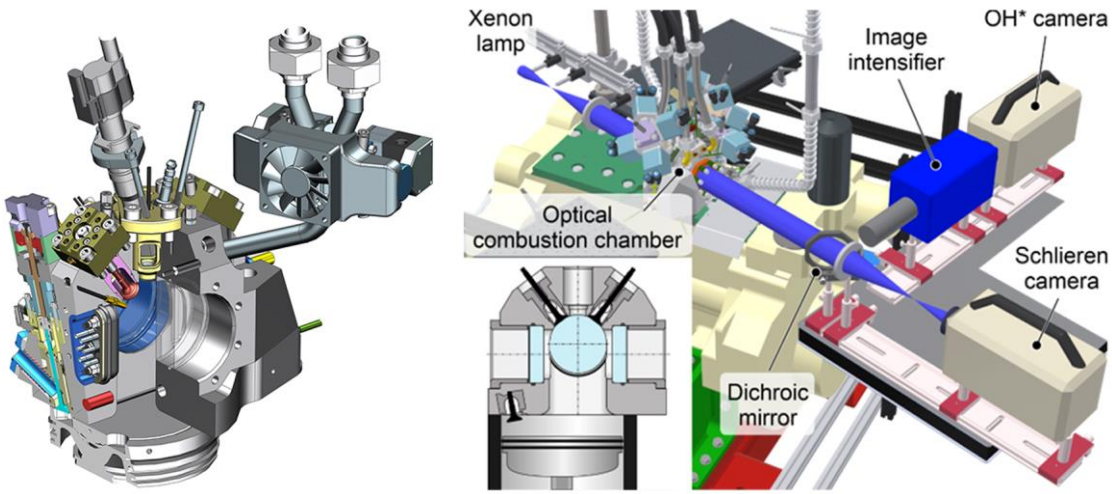

Figure 2: Optically accessible combustion chamber (left) and setup for simultaneous high-speed Schlieren and OH chemiluminescence measurements (right).*

The determination of the effective start of ignition (SOI) is based on the Schlieren signal deviation within the pre-chamber. Due to high turbulence levels, a detection of the flame with a threshold value only often leads to errors. Thus, detection is based on a predefined probability density function dependent on the image zone (background, high-temperature zone, flame) to assign pixel values to a specific location.

The OH* chemiluminescence corresponds to ignition and represents an integrated line-of-sight signal along the entire measurement volume. Even though other species (e.g. CO*), particularly under lean conditions at high pressures, may contribute considerably to the overall OH* signal at progressing combustion [15], the first OH* chemiluminescence emission appears at least simultaneously at ignition [16]. Moreover, also the interference of soot incandescence does not (yet) affect the ignition detection [17], especially since the chosen combustion strategy using pure ammonia should not produce any soot. The start of (high temperature) combustion therefore has been defined as the first OH* appearance, respectively the first image containing a "brighter spot" [18]. The automated optical ignition delay detection proved to be reliable, also compared to the corresponding ignition delay detection from the heat release analysis.

2.3. Exhaust gas extraction, conditioning and measurement

To achieve stable boundary conditions in an experiment, a sufficient number of preparation cycles are run first. This is followed by the actual combustion cycles relevant to the investigation, with further preparation and purge cycles before and after. Due to this process sequence, a fast-switching valve was developed for the exhaust gas analysis, which separates combustion cycles from preparation/purge cycles. Figure 3 shows the corresponding division of the exhaust gas channel by this valve, whereby the combustion cycles to be analyzed are routed into a conditioned system. The entire exhaust path system and sampling line is heated (200 °C) and the exhaust gas storage system has a sufficient volume of 5.1 liters. Moreover, the exhaust gas sampling point distance from the exhaust valve is ca. 500 mm.

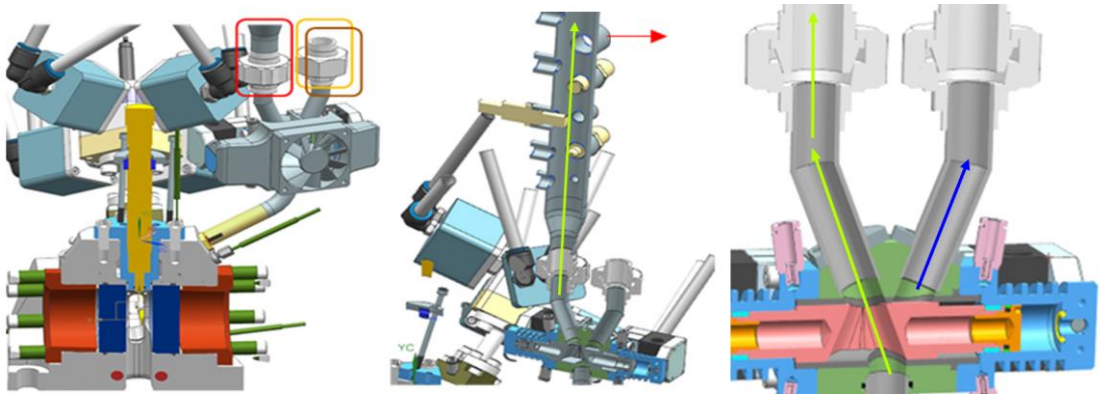

Figure 3: Exhaust gas path separation by a fast-switch valve (left + right), and conditioned exhaust gas sampling section (including sensors) in front of the exhaust gas storage system (center) with marked sampling point (red arrow).

The exhaust gases are then analyzed using a FTIR based measurement system (AVL SESAM i60 FT SII), which is equipped with a special evaluation method for ammonia combustion granting fast and exact exhaust gas evaluation in a wide range of NH_3 concentrations (up to 30'000 ppm NH_3 calibrated) and simultaneous detection of other species. The test bench is now capable to produce appropriate exhaust conditions, similar to those in a single-cylinder engine. It should be noted that the optical setup has an increased crevice volume which causes the exhaust gas composition regarding unburned fuel to be overestimated. The flexible combustion process variation and rapid fuel switching possibilities also allows efficient and comprehensive examinations of various exhaust gas measurement techniques.

2.4. Measurement procedure and analysis

The settings in Table 2 compression temperature (T_c), compression pressures (p_c) are based on pure air compression. These are denoted as reference values for all gas/air combustion investigations, where certain parameters, such as effective compression pressure and temperature, are dependent on the specific gas respectively mixture charge properties.

Table 2 gives an overview of performed measurements operation settings in terms of ammonia/air or methane/air mixture charge conditions such as air-fuel equivalence ratio (λ) and boost pressure variation. Gas admission pressure, start and duration (based on initially determined injection rate characteristics according to energizing time) can be set independently by a separate fuel supply unit to accommodate the boost pressure variation.

Table 2: Measurement conditions and pilot fuel injection parameter settings.

NH_3/air mixture charge		
Air-fuel equivalence ratio λ_{NH3}	2.0 / 1.75 / 1.5 / 1.25 / 1.0	
Start of gas admission	60 °CA before intake valve opens	[°CA]
Pre-chamber fuel	NH_3 ~ λ=1	[-]
Compression pressure p_c	*setting dependent* → see results	[bar]
Compression temperature T_c	*950*	[K]

Pre-chamber parameters		
Pre-chamber Injector	VDO 1353	
Pre-chamber Volume	3.49 / 2.1	[ml / %]
Nozzle diameter d_{nozzle}	Ø 4	[mm]
Start of ignition *SOI*	−10 / −7.5	[°CA]
Spark gap	0.25	[mm]
Coil load time *ET*	5.1	[ms]

Start of ignition, ignition delay (location), combustion onset, and flame propagation have been evaluated by post-processing procedures of the simultaneous high-speed Schlieren and OH* chemiluminescence measurements as well as the exhaust gas measurements. Combustion heat release rate has been analyzed by applying an in-house thermodynamic two-zone model that considers dissociation in the

burnt gas zone and accounts for losses by wall heat transfer, piston ring blow-by, and crevice volumes [19]. Due to the unique test facility layout (optical combustion chamber vs. working cylinder), significant efforts were made in terms of high precision pressure acquisition [10]. The wall heat losses were estimated using an adapted Woschni approach (inclusive extended heat transfer coefficient α_W based on flow measurements), piston-ring blow-by was measured, and the volume of crevices was determined from the drawings. However, since the wall-heat loss model had to be tuned by distinctive constants, the results are denoted as apparent heat release rate aHRR.

The ignition delay can be deduced from both optical data (OH* chemiluminescence) and from the calculated heat release rates. The heat release rate based ignition detection is well tuned and shows a very good agreement with the optical data (already presented in [318]). The ignition delay calculation method is very sensitive and therefore allows to detect ignition at about 0.35% - 0.5% of the total heat released.

An apparent flame propagation speed s_{aFP} can be determined by the Schlieren measurements, respectively the contour displacement representing the flame surface. The method applied here consists of a two-dimensional spatially averaged evaluation of reaction zone expansion based on the optical measurements. It resolves local behavior very well (i.e. large propagation speeds) but is also more prone to misidentification of burned zones since it still contains certain uncertainty in differentiation of the cause of refractive index variations. In addition, the effect of flame compression and expansion cannot be corrected for pressure variations, and the determined s_{aFP} always includes the effect of the expanding burned zone. Thus, higher pressure ratios are affecting the resulting s_{aFP} stronger for lower air-fuel equivalence ratios. However, the chosen approach can deal with (local) transport phenomena and leads to an accurate statement in terms of the early combustion phase. The designation "apparent" shall point out that the analyzed flame propagation speed must be interpreted as a qualitative value that nevertheless enables a comparison within operating parameter variations.

The properties of ammonia as fuel are compared to methane as standard fuel in Table 3 for visualization of the large discrepancies in terms of AFR, LHV and flame speed. The low flame speed of ammonia results in a slower combustion process, which can reduce the combustion efficiency. The high auto-ignition temperature and enormous heat of vaporization makes liquid injection and diesel-like compression ignition combustion more difficult – this is one of the reasons why a premixed combustion scheme is used. The high minimum ignition energy means that it is comparably more difficult to safely ignite an ammonia-air mixture. The high resistance to knocking (RON) allows to run ammonia fueled engines at higher compression ratios, which can be beneficial for efficiency. This should allow to run high IMEP despite the low reactivity by applying high compression temperatures, which results in a high specific cylinder load. Although ammonia has a much lower energy content per mass than carbon-based standard fuels, its low stoichiometric air-fuel ratio AFR partly compensates this regarding the in-cylinder energy content.

Table 3: Properties of ammonia and methane. Data collected for comparison only from [22-26].

	Storage conditions	Density @ storage conditions [kg/m³]	LHV @ storage conditions	Flammability limits in air [Vol-%]	Stoichiometric AFR (mass) [-]	LHV per Vol. @ stoichiometry (0.1 MPa, 373 K) [MJ/m³]	Auto-ignition temperature [K]	Minimum ignition energy [mJ]	Heat of vaporization [kJ/kg]	LBV @ stoichiometry (0.1 MPa, 300 K) [m/s]	RON [-]
Ammonia NH_3 (Liquid)	1.1 MPa 300 K	600	18.8 MJ/kg 11.3 GJ/m³	15 – 28	6.1 : 1	~ 2.23	930	8	1370	0.07	> 130
Methane CH_4 (Compressed)	25 MPa 300 K	187	50 MJ/kg 9.4 GJ/m³	5 – 15	17.2 : 1	~ 2.45	860	~ 0.21	–	0.38	120

3. Results

The results shown here are from a large measurement campaign and represent only a subset of all the measurement points carried out. They provide an insight into pure ammonia combustion using a pre-chamber in terms of pressure evolution, ignition delay, combustion onset, flame propagation, heat release and exhaust gas composition.

3.1. Combustion characterization varying the air-fuel equivalence ratio

Figure 4 shows a comparison of the pressure development for two different boost pressure levels consisting of an ammonia charge mixture variation with air-fuel equivalence ratio λ = 1.0 / 1.25 / 1.5 / 1.75 (/ 2.0) / inf. The spark timing within the prechamber is set to -10° CA corresponding to a pure air compression temperature of about 950 +/-5 K[14], [21], for both cases. Keeping the compression temperature nearly constant over a boost pressure variation is possible since the charge air is entering a separately pre-heated intake pipe to achieve individual pressure and temperature combinations. The pressure trace represents the median cycle value of fifteen combustion cycles and additionally the pressure trace of the pure air compression (idle, i.e. motored) is given in dashed line. The difference in pressure evolution between the two boost pressure levels is visible in two terms. Firstly, in maximum combustion pressure level, achieving 150 bar for the 70 bar compression pressure versus 280 bar for the 130 bar compression level regarding λ = 1.0 (and therefore exceeding the maximum allowed continuous operating pressure), secondly in terms of pressure gradient. The 70 bar compression level case thereby shows a decreasing pressure gradient with increasing λ, whereas in the high boost case the pressure gradient for λ = 1.0 to 1.5 remains nearly constant. For the low boost case, it is observable that the λ = 2.0 case has barely an increase in compression pressure, leading to the assumption that there is a high portion of unburned fuel exiting the combustion chamber.

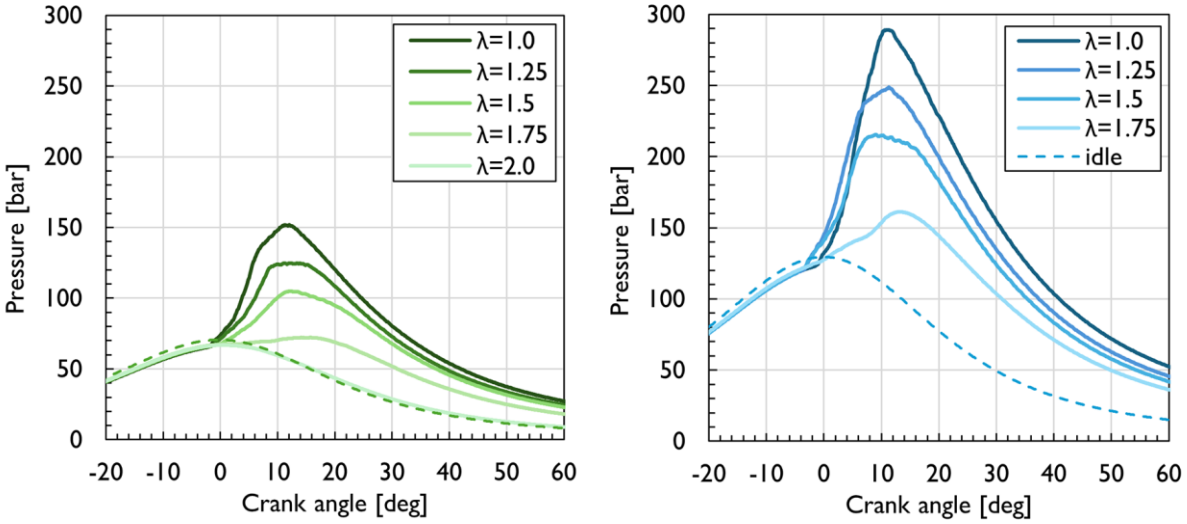

Figure 4: Comparison of the pressure development for two different boost pressures resulting in 70 bar (left) vs. 130 bar (right) compression pressure and a variation of λ. For the λ = 1.0 case at 130 bar, the SOI had to be retarded from -10 to -7.5° CA to avoid knocking.

The higher cylinder pressure at 130 bar compression pressure is on the one hand coupled to the already increased pressure before ignition, but on the other hand due to the increased air density allowing more fuel to be admitted to reach comparable air-fuel-equivalence ratios. Hence for the λ = 1.0 case for 70 bar 571 mg fuel was injected per cycle compared to 904 mg fuel for the 130 bar compression pressure case. Therefore, an increase of 58% in in-cylinder energy content can be expected. This increase in fuel energy is easily observable when comparing the heat release rate for both cases. Additionally, to the heat release rate the mass fraction burned is given for both cases and is represented in Figure 5. The heat release rate thereby represents the already observed discrepancy between the 70 bar case versus the 130 bar compression pressure, whereas the heat release increase in the early combustion phase is quite similar for λ = 1.0 to 1.5 for the 130 bar case. The main influence hereby is the higher integrated heat release before TDC, increasing the in-cylinder temperature before TDC and therefore stabilizes or even promotes the reaction rate for the leaner cases. This results in high combustion temperatures which allows the fuel oxidation in the phase after TDC to an acceptable level. This absolute fuel conversion level is then represented in terms of mass burned fuel fraction. The mass fraction burned is calculated based on the injected fuel mass and supported by the exhaust analysis giving the unburned fuel mass and side reactions which will be later represented in chapter 3.3. The high fuel conversion rates for the 130 bar case between 98.9% and 99.0% for the λ = 1.0 to 1.5 (98.7% for the λ = 1.75) cannot be reproduced at lower compression pressures. As already mentioned, the test-bench has large crevice volumes of about 1% of the TDC volume. Therefore, a fuel conversion rate of 99% represents nearly complete conversion in premixed cases.

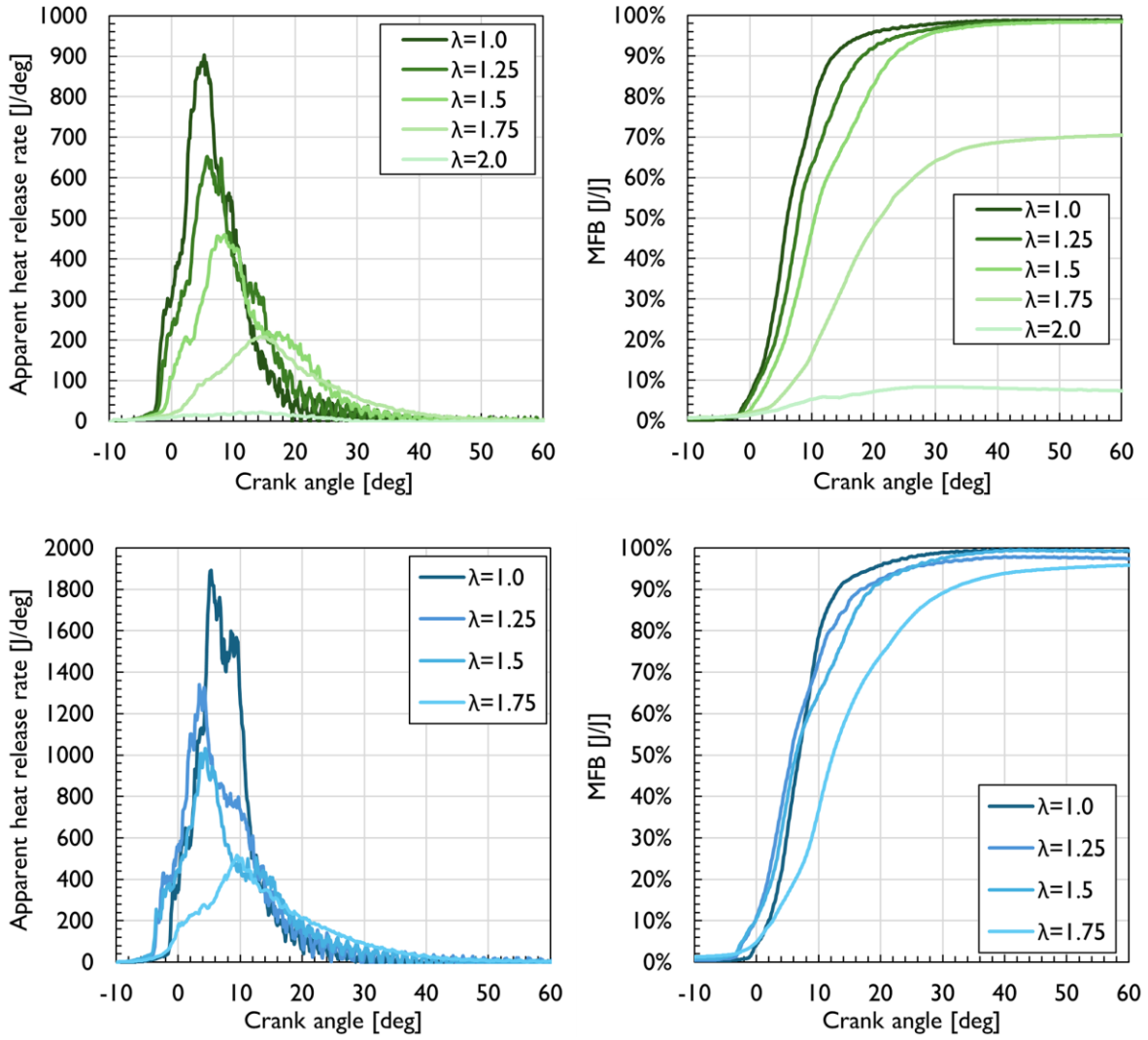

Figure 5: Apparent heat release rate (left) for 70 bar (top) and 130 bar (bottom) as well as mass fraction burned for both cases. All plots represent air-fuel-equivalence ratios between λ = 1.0 and λ = 1.75 (2.0). For the λ = 1.0 case at 130 bar, the SOI had to be retarded from -10 to -7.5° CA to avoid knocking.

The fuel conversion rates are in terms of mass fraction burned at 70 bar compression pressure is dropping earlier and faster to very low levels of 70% for λ = 1.75 resp. below 10% for λ = 2.0. Since these low fuel conversion rates are not acceptable in terms of fuel and cost effectiveness and emissions, such high air-fuel equivalence rates are only possible for full load operation of an engine at maximum boost pressure and compression temperature.

The optically accessible test bench has the benefit of an observable combustion process and therefore both Schlieren images and the superimposed OH* chemiluminscence images for the mainchamber are shown in Figure 6. These image series allow to evaluate the earlier stated assumptions based on the pressure signal acquisition. Wheras the pre-chamber is operated at nearly constant air-fuel equivalence ratio due to its separate ammonia injector (resulting in comparable ignition delays in the pre-chamber), the main chamber represents a λ-variation between λ = 1.0 to λ = 1.75 for 130 bar. The hot reactive jet enters the main chamber slightly before -1° CA in all cases, whereas the cold jet consisting of non-combusted fuel enriched gases enters the main chamber already around -4° CA. This fuel enriched zone is then ignited first by the hot jet, leading to a comparably higher heat release during flame onset

in the main chamber. This can be observed either in terms of the OH* signal (green) that rapidly increases between -1° CA and 0° CA, or in the Schlieren signal that shows a rapidly increasing surface area within the black border. The subsequent reaction rate can also be observed in terms of OH* chemiluminescence (green overlay intensity): Whereas the fuel rich cases show a strong color, the lean cases only show a relatively low OH* chemiluminescence intensity, leading to the assumption that the heat release rate must be low as well, which is confirmed by Figure 5.

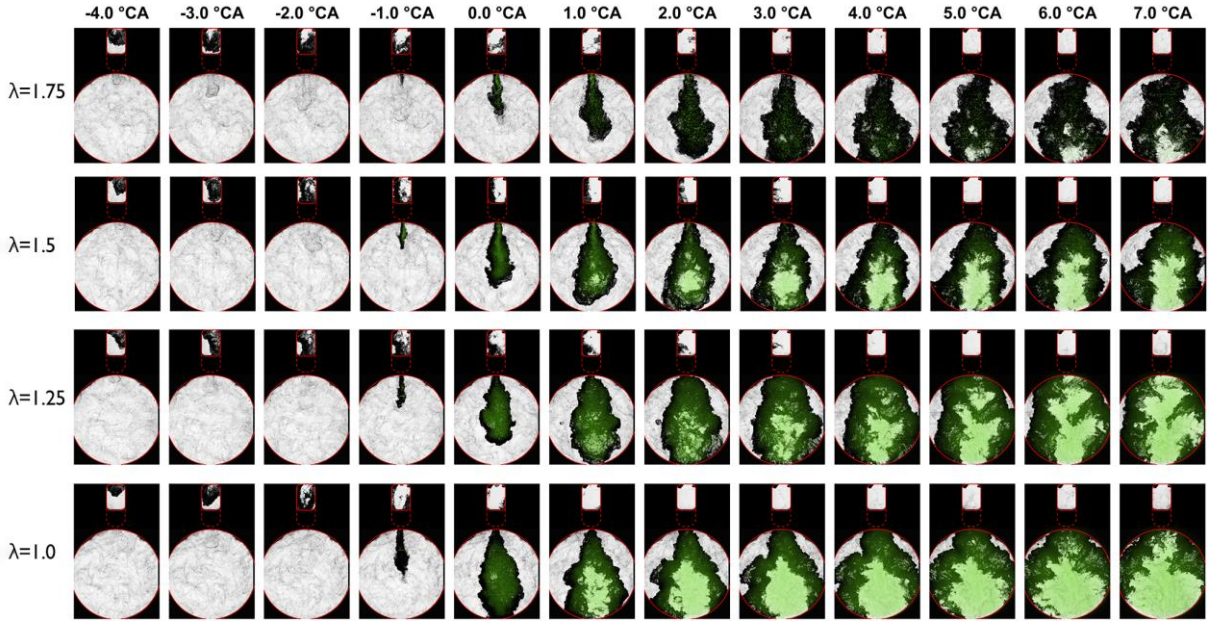

Figure 6: Image series with different air-fuel mixtures from λ = 1.0 to λ = 1.75 at 130 bar compression pressure and SOI = -10° CA showing superimposed high-speed OH-chemiluminescence and Schlieren images for both main and pre-chamber. The λ = 1.0 case shown here is a non-retarded cycle and features an SOI = -10° CA as well. Here pre-ignition can be observed at top left, knocking occurred later in the non-observable area.*

The directly observable phenomena were further evaluated using an in-house tool to calculate apparent flame speed s_{aFP} for both pre- and main chamber. Whereas the stoichiometric conditions within the pre-chamber are constant due to an increasing addition of NH_3 for the leaner cases, a variation in flame speed within the pre-chamber is nonetheless observable, especially for the two leaner cases. A lower flame speed is connected to either leaner or richer conditions than λ = 1.0, since the flame maximum speed must be near λ = 0.97 [28].

Since the air-fuel equivalence ratio in the pre-chamber cannot be measured directly, an alternative procedure was chosen to achieve stoichiometric conditions. Thereby, the energizing time (ET) of the pre-chamber injector was chosen iteratively by varying the ET until the highest possible flame speed with the lowest cyclic fluctuations (corresponding with λ = 1.0) was achieved. This was double checked using the static fuel flow rate for the pre-chamber injector and the theoretical fresh charge fill volume. The inflow of fresh charge leading to dilution is a factor that could not be fully considered within this project since detailed LES-Simulations would be needed to address this problem. For the lean cases, the fuel admission must be started very early (near BDC) and hence fuel loss out of the nozzle adds an additional uncertainty that results in a residual variation of λ within the pre-chamber. These two effects are more pronounced for the lean cases since escaped fuel, or entrained air, have a huge impact on the stoichiometry. The s_{aFP} within the main chamber then shows the typical decreasing flame speed for leaner cases, which can be expected for ammonia as well as methane and other fuels [20]. The fuel-

richer cases are showing a very high gradient in flame speed increase during flame onset within the main chamber. This can be seen in Figure 6 as well, where the flame front is propagating not only from top to bottom in front of the reactive jet, but also from the center towards the left and right side along the entrained jet, leading to a very large flame front and hence to a high flame front growth rate, resulting in the high gradient in s_{aFP}. At 130 bar compression pressure, the $\lambda = 1.0$ case shows a much lower flame speed (comparable to $\lambda = 1.75$ at 70 bar compression pressure) and a lower gradient. For this case the SOI within the pre-chamber had to be retarded from -10 to -7.5° CA to avoid knocking. The slower flame front increase is based on two main factors: the cylinder pressure and the turbulence level. Whereas the higher cylinder pressure leads to lower flame speeds, the turbulence level inside the main chamber drops as well, especially near TDC [9]. The start of jet entrainment is then further retarded due to a simultaneous drop in turbulence level within the pre-chamber. This effect is very pronounced towards TDC and already described in [20]. In Figure 7 bottom, left it is observable that the flame speed instantly increases after the spark at -10° CA for the corresponding cases, whereas the SOI of -7.5° CA leads to a slightly delayed increase in flame speed of around one degree since the already dropping turbulence reduces the reaction rate. In Figure 6 a non-retarded cycle of $\lambda = 1.0$ is compared with the other air-fuel equivalence ratios at 130 bar where it can be observed that the flame speed does not decrease to fuel leaner cases, rather it further increases, since the full burned zone reaches the walls earlier. This substantial higher flame speed within the main chamber is on the one hand coupled to the turbulence level before the jet penetration, and on the other hand coupled to the additional turbulence from the entraining reactive jet. The high velocity brings in a lot of turbulence and increases mixing and re-entrainment leading to elevated reaction rates.

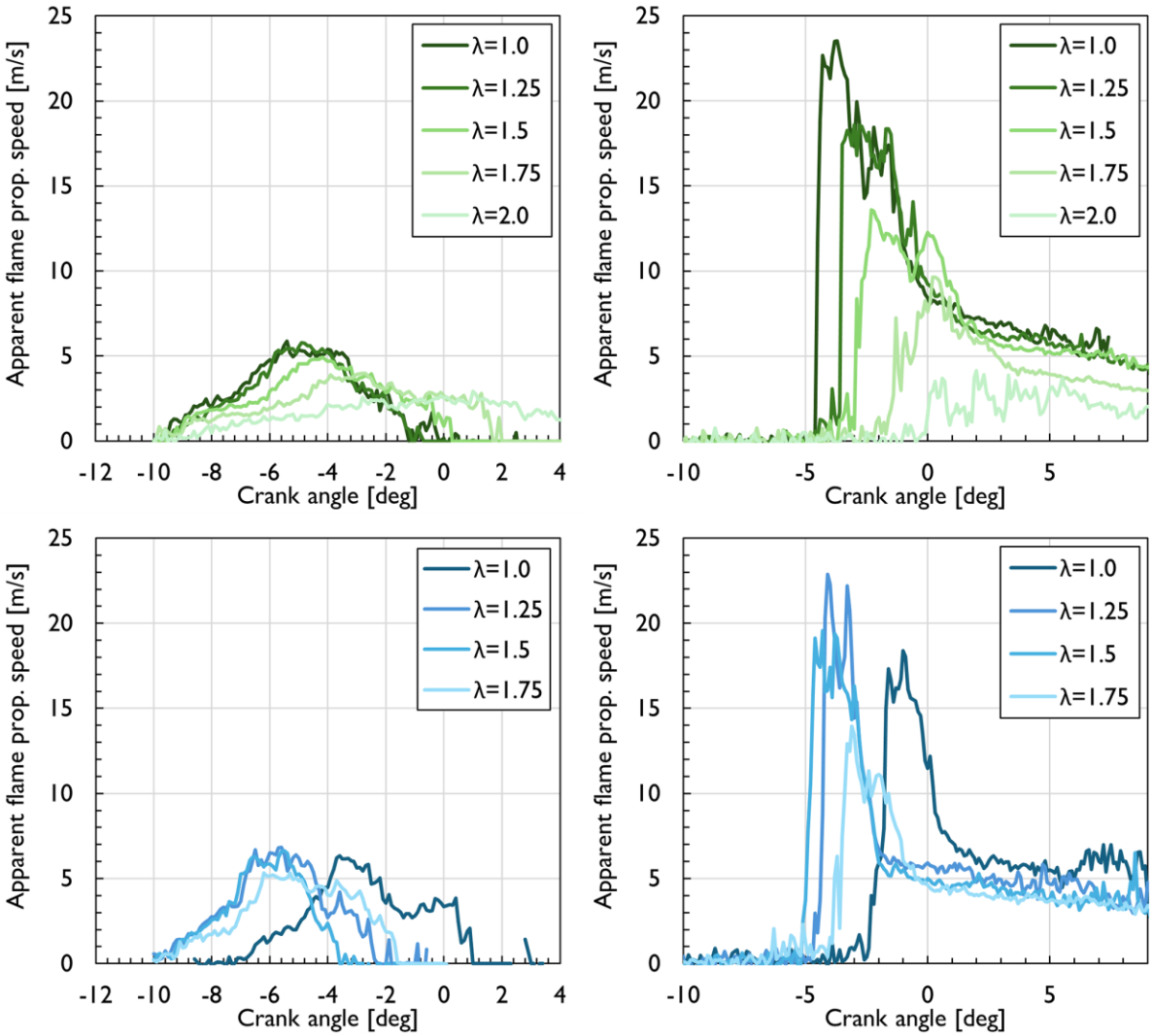

Figure 7: Apparent flame speed (s_{aFP}) based on high-speed Schlieren measurements for the pre-chamber (left) and main chamber (right) for two different boost pressures leading to a compression pressure of 70 bar (top) and 130 bar (bottom). For the case with λ = 1.0 at a compression pressure of 130 bar, the SOI had to be retarded from -10 to -7.5° CA to avoid knocking.

The differentiation between flame speed within the combustion chamber and effective heat release (resulting in an increasing cylinder pressure) is very important. Figure 8 shows the apparent flame speed on the y- axis vs. the apparent heat release rate on the x-axis and attempts to clarify this. If there would be a linear dependency, all the points would be on a diagonal from the bottom-left to the top-right corner. Nevertheless, the diagram shows another dependency: whereas the flame speed increases during the initial phase, the heat release rate does not increase in the same manner. In the beginning, the high flame speed due to jet turbulence is only present for a small proportion of the overall area. Therefore, the flame speed must be combined with the flame surface area to get a direct link to the

expected heat release rate. It is also very important to consider the combustion chamber shape as well as the position and number of the reactive jets from the pre-chamber to compare these results.

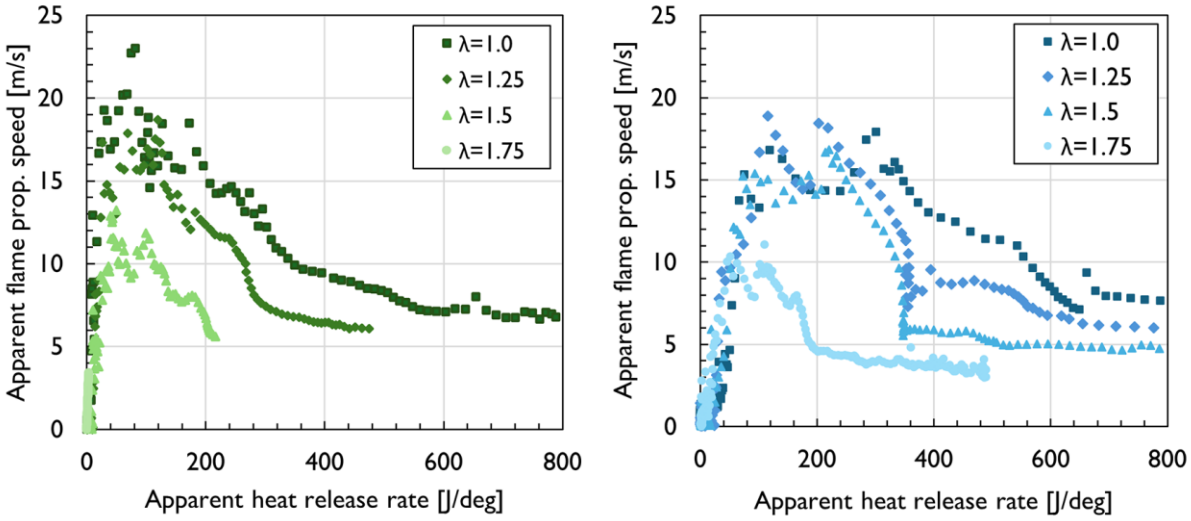

Figure 8: The apparent flame propagation speed in the main chamber vs. the apparent heat release rate shows the dependency between flame propagation and effective heat release during flame onset and initial flame propagation.

When looking at the 130 bar case for λ = 1.0 (Figure 8, right), three phases can be described. The first phase from 0 J/deg to 350 J/deg, the second phase from 350 J/deg to 460 J/deg and the third phase from 460 J/deg to the end. In the first phase, the initial flame front is initiated by the reactive jet (flame onset in the main chamber) and rapidly increases in size, then the flame speed remains at a certain level. The second phase is dominated by the flame traveling deeper in the combustion chamber, and since the turbulence level decreases around TDC, the flame speed decreases further. The third phase shows a second large decrease in flame speed. This happens when the reaction zones hit the walls, where the flame speed drops to zero, and the flame can only travel towards the remaining unburned zones. The end of the combustion cannot be observed within the optical accessible area due to the combustion chamber shape.

3.2. IMEP-variation by different cylinder charge conditions

In this section, results from an intake pressure variation, similar to a load variation in a real engine, are presented. The intake pressure influences both compression and combustion pressure and hence results in different IMEP and output power of the test bench. In addition to the pressure variation itself, a λ variation is also performed within the operating limits of the test bench.

In Figure 9 (left) cylinder pressure traces of a IMEP variation are shown at a constant λ for two high load points at IMEP = 26 bar and 20 bar, whereas a part load point with IMEP = 10 bar is shown as a comparison. All operating points have a similar compression end temperature and feature the same start of ignition at -10° CA. The high load point with 26 bar IMEP slightly exceeds the design pressure of the test bench (260 bar) but is still below the safety limit of 330 bar when the cylinder head lifts off due to the overpressure. Since the operation was very stable without any pre-ignition and abnormal combustion behavior, this high IMEP dataset has been considered as well.

The corresponding pre-chamber pressure and the difference between pre-chamber and main chamber pressure is illustrated in Figure 9 on the right. The pressure difference between pre-chamber and main

chamber is targeted to be in the range of 10 and 20 bar for full load – a 4 mm single hole was found to be suitable for all experiments carried out. Whereas the high load points have a similar maximum pressure difference in the order of 16 to 17 bar, the part load operation would benefit from a smaller nozzle size to reach the same pressure differences. The pressure difference between pre-chamber and main chamber is the main driver for the penetration length of the reactive jet and therefore important for increasing the turbulence within the main chamber.

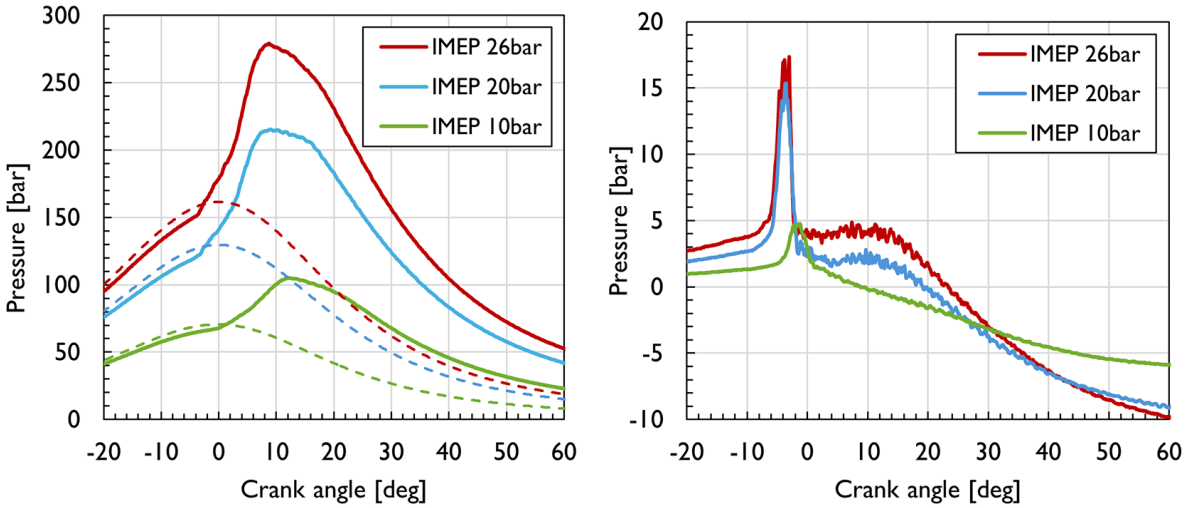

Figure 9: Left: cylinder pressure traces for three different IMEP at constant λ (λ = 1.5) including the idle cycle (dotted line). Right: pressure difference from pre-chamber to main chamber for those operating points.

The heat release rate for the 20 bar and the 26 bar IMEP load points are very similar in shape – only the level is slightly higher for the higher IMEP. This leads to a nearly identical shape of the mass fraction burned in Figure 10 (right). The fuel conversion rate is very high and in the range of 98.7 to 99.0% for all three experiments. The part load operating point with IMEP = 10 bar shows a slightly slower increase in heat release rate. The main reason is the reduced energy density, which results in colder in cylinder conditions during combustion and hence a reduced reaction rate. In addition, a smaller absolute heat release rate must be expected anyway since only about half the amount of fuel is contained in the cylinder at this load point. If the integrated heat release rate is normalized with the total fuel energy, then the result is quite comparable to the high load points – only a slight shift towards later crank angles can be observed.

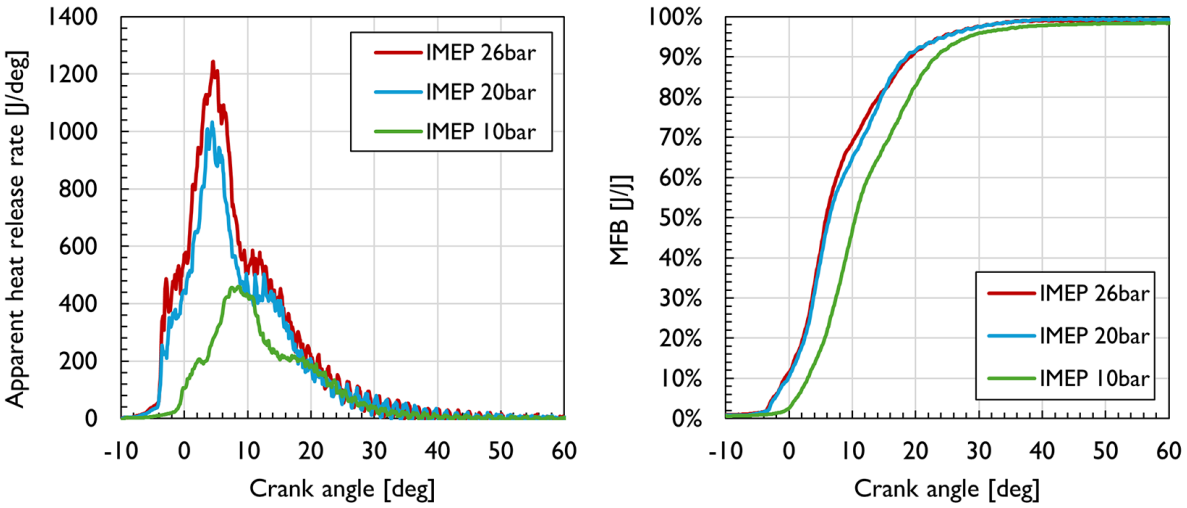

Figure 10: Heat release rate (left) and mass fraction burned (right) for three different IMEP at λ = 1.5.

In addition to the three already shown data sets for a constant λ of 1.5, the measurement matrix was extended to include a wider variation of boost pressures and λ. The results are summarized in characteristic combustion numbers in Figure 11 and Figure 12. The additional measurements resulted in IMEP between 5 bar and 30 bar (which is the highest IMEP achieved so far in the test bench). For each boost / compression pressure, λ was increased as long as the fuel conversion rate remained high (as discussed in 3.1). Consequently, at the λ resp. fuel conversion limit, a slightly decreased IMEP is observable for a compression pressure of 70 bar above λ = 1.5 and for 130 bar above λ = 1.7.

The ignition delay shown on the right side of Figure 11 is an important characteristic number for designing the combustion process in an engine and therefore important to know for different fuel-air ratios in the desired load range. The ignition delay shown here is the delay between start of discharge of the spark plug in the pre-chamber and start of combustion in the main chamber (i.e. a certain level of the heat release rate). The presented ignition delay for the higher load cases of around 1.2 ms is quite low for such a coupled combustion chamber, especially since pure ammonia is used as fuel. The nearly constant ignition delay behavior in a wide range of air-fuel equivalence ratios for the 130 bar case is beneficial for the combustion control strategy. When running part load, the ignition delay increases drastically and therefore would need additional measurement points to fully characterize this load regime. Otherwise, the spark discharge timing can be delayed to achieve full combustion resp. to get the desired torque. The highest boost pressure setpoints, leading to a compression pressure of 160 bar, have ignition delays below 1 ms. But, as already shown earlier, the ignition delay for the pre-chamber configuration is very sensitive regarding the chosen the spark discharge timing due to its strong dependence on the (decreasing) turbulence level around TDC.

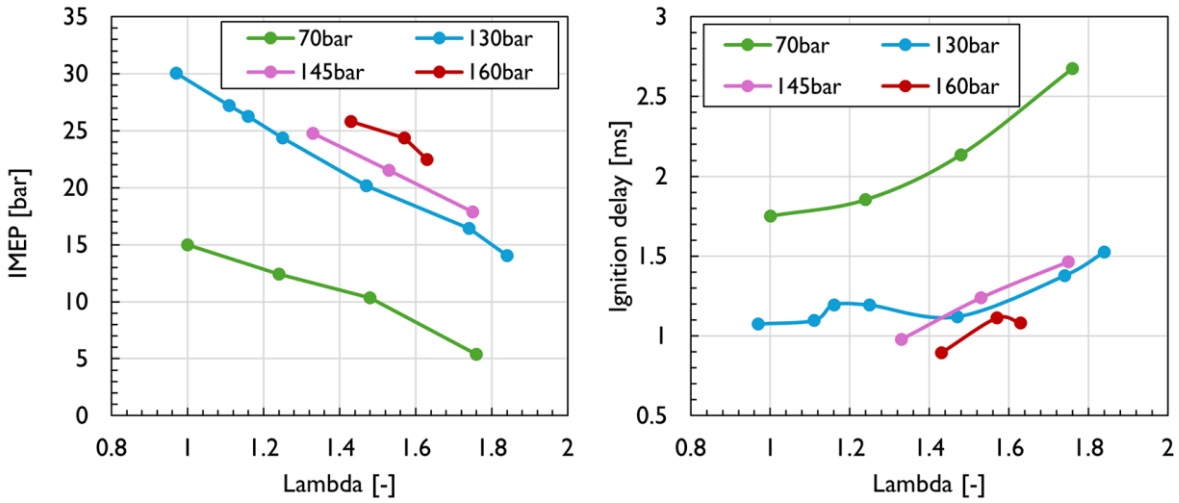

Figure 11: IMEP (left) and ignition delay of the main chamber charge (right) for a λ-variation at constant boost resp. compression pressure.

Figure 12 illustrates the stochastic phenomena of this type of combustion. Where diesel-like combustion schemes benefit from a very low coefficient of variation (COV), pure Otto-Cycles are well known to deliver higher COV. For pilot ignited dual-fuel combustion the COV mainly depends on the pilot fuel amount, which stabilizes the main combustion. Since the pre-chamber ignited combustion scheme is a combination of a spark plug initiated combustion followed by a reactive jet ignition it can be expected that it results in higher COV. For the λ = 1.0 case regarding 70 bar and 130 bar compression pressure, the COV is quite low at 1% resp. 2.5%. In general, for the 70 bar case the COV remains at very low values of around 2% which is very good for this type of combustion scheme, especially for ammonia combustion. Higher boost pressures lead to higher COV since the local transport phenomena have more influence within the main chamber. For the highest boost pressure of 160 bar, abnormal combustion behavior with pre-ignition further increases the COV. The plot in the center of Figure 12 represents the knock intensity (KRAT) according to Siemens-VDO (which is used in AVL indicating systems as well), where knock intensities above two are interpreted as knocking cycles. The knock intensities for all cases are non-critical, but nonetheless need certain attention. Leaner cases also show relatively high knock intensities, which is not expected. This is due to pressure fluctuations within the coupled combustion chambers that form a mass-spring oscillating system, which results in pressure oscillations even without knocking. Therefore, an in-house approach specifically designed for this test bench is used to evaluate the real knocking influence including min and max levels of all cycles and is shown in the plot on the right side of the Figure 12.

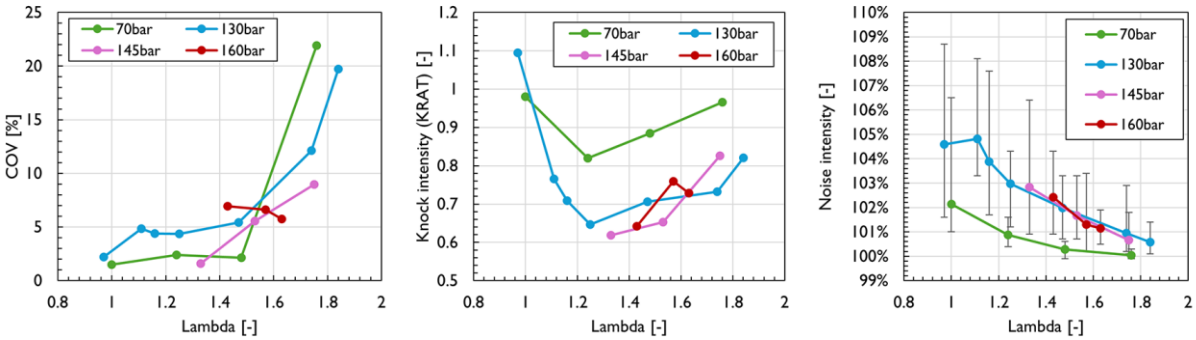

Figure 12: COV (left), knock intensity according to Siemens-VDO algorithm (center) and noise intensity according to the FHNW algorithm (right).

This so-called "noise intensity" calculates the intensity of stochastic noise above the normal noise level within the pre-chamber based on the pressure measurement. A reference window is used to characterize the amplitude of a pressure fluctuation from a non-knocking window, which is then compared to a pressure fluctuating coming from a higher-pressure gradient than during the initial flame propagation. This algorithm is very sensitive to knocking or hard combustion. A level of 100 % means that the combustion related pressure fluctuations correspond to a normal combustion. This algorithm shows the expected trend where fuel-air mixtures towards stoichiometric conditions should deliver the highest knock intensity levels. The maximum levels of the noise intensity was calculated to be 9% over standard pressure oscillation levels, leading to the assumption that only a very small share of the total fuel amount could have been combusted in a knocking manner.

3.3. Emission characterization for a wide range of IMEP

The emission characterization is an important task for all engine manufacturers to comply with current emission regulations. Since ammonia engines are intended to reduce the CO_2 based GHG emissions, it is very important to reduce nitrous oxide (N_2O) emissions to an absolute minimum level, since its GHG factor is nearly 300 times that of CO_2. Because ammonia contains nitrogen in its molecular structure, NO_x emissions are expected to be high as well. For an in-cylinder reduction of NO_x, a stoichiometric or even slightly rich combustion can probably reduce NO_x drastically since it provides a nearly identical pathway to reduce NO_x as in an SCR after treatment system using urea. The emission measurements are shown in Figure 13.

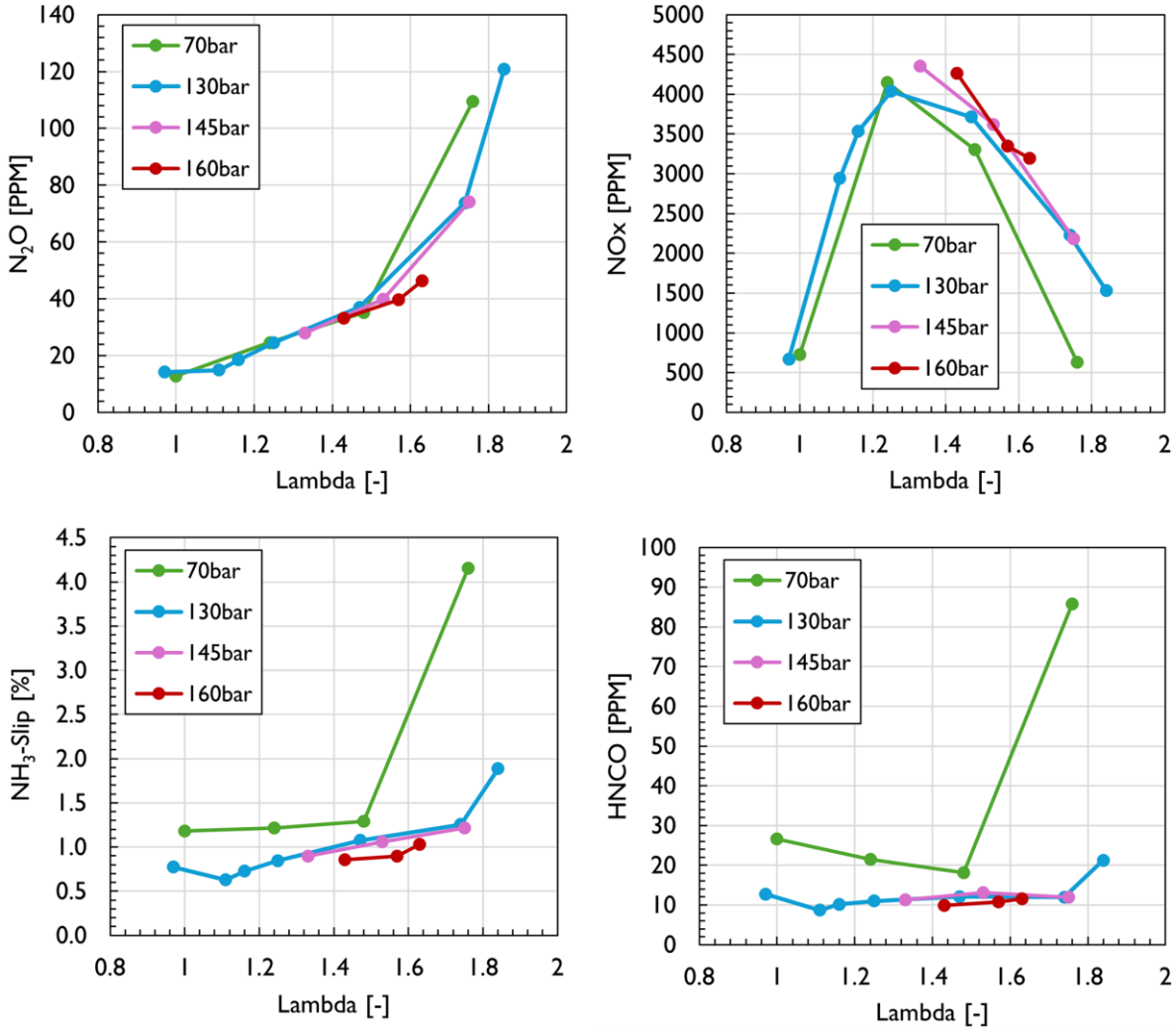

Figure 13: Emission characterization for all presented measurements with a λ-variation at different boost resp. compression pressures.

The measured N_2O levels are largely independent of the load point but depend on the fuel-air ratio. They are also very sensitive regarding incomplete combustion. To achieve low engine-out N_2O emissions therefore the engine should be designed to run at stoichiometric conditions, which is also favorable in terms of NO_x emissions as well. The maximum NO_x peak can be observed around $\lambda = 1.2$ for the different boost pressures – comparably low emission levels can only be achieved when the engine runs around $\lambda = 2.0$. However, such high air-fuel equivalence ratios can be problematic regarding the fuel conversion ratio as shown in the previous section. The NH_3-Slip, measured with the FTIR, supports this as well, shown in Figure 13 bottom left. NH_3 emissions are problematic due to its toxicity, in addition even very low concentrations far below the tolerable exposure limits can be detected by the human nose. Futher, NH_3 emissions directly increase the operating costs of the engine. Figure 13 bottom right represents the isocyanic acid (HNCO) emissions coming from the ammonia reacting with CO_2. HNCO has been identified as a concern for human health and therefore gains certain attention. The levels for the full load cases are generally very low. The high value of nearly 90 ppm for the 70 bar case at $\lambda = 1.7$ could be some misinterpretation from the FTIR since NH_3 has

exceeded the calibrated range at this point, and a strong interference between HNCO and NH_3 is evident.

Running a commercial heavy duty ammonia engine at $\lambda = 1.0$ is certainly not an easy task. High in cylinder energy contents lead to high mechanical and thermal stress on materials within the engine, and the turbocharging systems must deal with high exhaust gas temperatures. Therefore, the exhaust gas temperature of each cycle has been measured with a 0.25 mm thermocouple in the exhaust to resolve the exhaust gas temperature. The measured mean values as well as the cycle-based min and max values are shown in Figure 14. High exhaust gas temperatures above 500 °C were measured in the near stoichiometric case. Then the temperature drops in function of an increasing λ, nearly independent of the load condition, which is expected since the exhaust gas temperature at constant SOI is mainly influenced by the air-fuel equivalence ratio itself. The plot on the right-hand side in Figure 14 summarizes the dependency between NO_x and N_2O emissions but shows the emissions based on engine power in g/kWh. The best-case scenario for low NO_x and low N_2O emissions is still around $\lambda = 1.0$ or slightly below, whereas $\lambda = 1.6$ results in very high specific NO_x emissions while already increasing the N_2O levels to nearly 0.8 g/kWh.

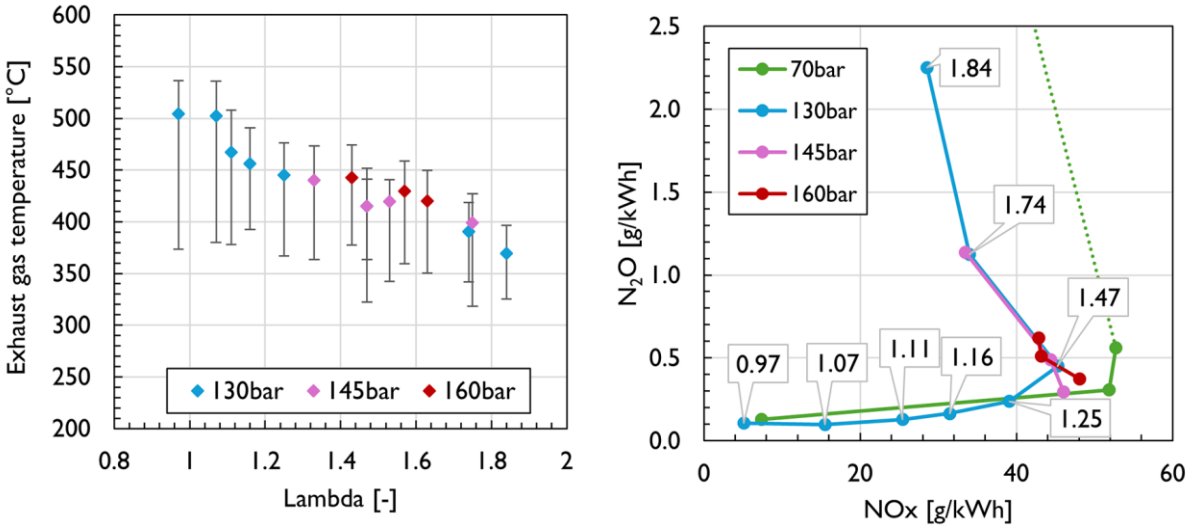

Figure 14: Exhaust gas temperature (left) for all presented measurement points, and the specific engine emissions N_2O versus NO_x for certain air-fuel equivalence ratios (right).

These high levels in specific emissions make a suitable exhaust gas aftertreatment system mandatory. Therefore, several companies are working on new deNO_x and deN_2O SCR-systems to be ready for the new ammonia engine families.

3.4. Abnormal combustion phenomena

In a premixed cylinder charge, the abnormal combustion phenomenon of pre-ignition due to the self-ignition of lubricating oil droplets intruding the combustion chamber and the resulting knocking is often encountered. This type of abnormal combustion phenomenon is characterized in particular by elevated peak combustion pressures, which results in exceptionally high mechanical and thermal loads on components. Another consequence of lubricating oil induced pre-ignition are increased emissions, especially of species exhibiting high temperature dependencies as it is the case with the formation of nitrogen oxides (NO_x).

Figure 15 shows pressure traces (left) of a motored cycle (Idle, dotted line), a normal cycle not affected by pre-ignition at all (Normal, blue line, lower image row) and a cycle affected by lubricating oil induced pre-ignition (Preignition, red line, upper image row).

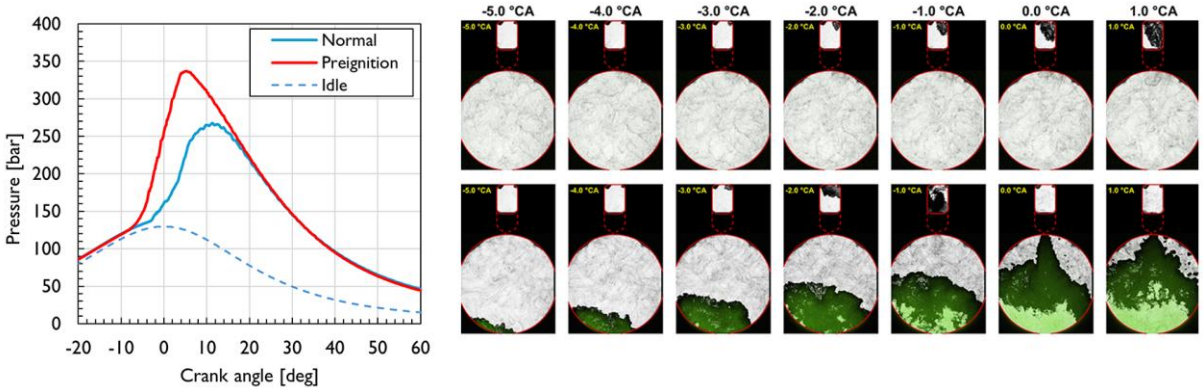

Figure 15: Comparison of pressure development (left) and the corresponding optical measurements (right) for a critical pre-ignited, knocking cycle (bottom images) vs. a normal cycle (top images) for a cylinder charge with λ = 1.0.

From the high-speed Schlieren recordings (right) it can be seen that a flame front originating from the self-ignition of lubricating oil already propagates from the bottom before the actual ignition in the pre-chamber – the reactive jet from the pre-chamber enters the main chamber when a large part of the fuel has already been converted by the pre-ignition. It is well observable that the ignition jet propagates partly through already burnt zones and is consequently disturbed. Later, more flame kernels form in the unburned zone near the combustion chamber wall. Even though more lubricating oil droplets in the combustion chamber could be the source of those additional flame kernels, the already advanced stage of combustion can result in self-ignition of the premixed cylinder charge itself, whereby initial knocking can be indicated based on the multiple ignition locations. During this time, the cumulative flame front surface area and thus fuel conversion increases very fast compared to the normal cycle, which is clearly shown in the elevated pressure rise rate (left). The peak combustion pressure is approx. 25% higher compared to normal cycles (at over 330 bar) due to the 5° CA earlier start of combustion in the case of pre-ignition. Such high combustion pressures can lead to severe damage and even failure of the engine under such operating conditions. Therefore, such pre-ignition events are considered critical and must be avoided.

Figure 16 shows another measurement where the strong influence of the location of pre-ignition in the combustion chamber on the further course of combustion can be seen. The slight shift of the initial flame kernel towards the combustion chamber wall causes the pre-chamber ignition jet to penetrate into a completely unburned zone and thus not showing any interaction with the propagating flame front originating from lubricating oil induced pre-ignition. Due to the over 8° CA earlier pre-ignition initiated start of combustion compared to the time when the ignition jet enters the main chamber, the corresponding pressure trace shows a steeper rise at the beginning. However, due to the high penetration depth and ignition energy of the ignition jet and the associated large initial flame front surface area, regular combustion dominates and is responsible for the main part of fuel conversion. Such pre-ignition events do not overload the engine and are therefore not considered to be critical.

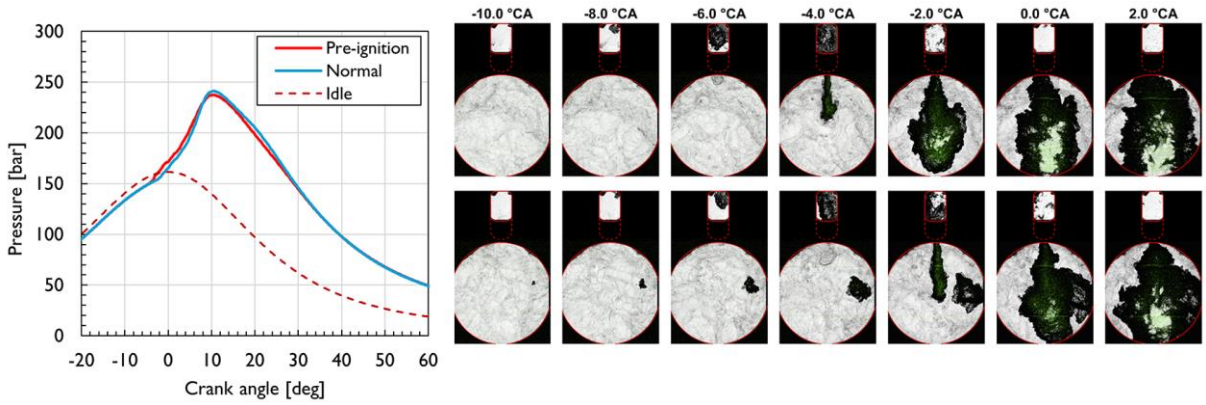

Figure 16: Comparison of the pressure development (left) and optical imaging (right) for a non-critical pre-ignited cycle vs. normal cycle for a cylinder charge with λ = 1.0.

Due to the high fluctuation of the occurrence as well as the influence of the phenomenon on the combustion process, it advantageous to completely suppress rather than minimize lubricating oil induced pre-ignition, especially under such operating conditions.

4. Conclusions

High IMEP combustion of pure ammonia initiated by a reactive jet from a pre-chamber has been successfully carried out in the optically accessible *Flex-OeCoS* test facility for a variation of air-fuel equivalence ratios, boost/compression pressures and loads (IMEP), including a characterization of the corresponding exhaust emissions. The well-known boundary conditions of the test rig allow precise acquisition of pressure and temperature to enable thermodynamic analysis in view of ignition delay, reactive jet transition, heat release, and IC engine characteristic numbers such as mass fraction burned. Moreover, the optical accessibility of the *Flex-OeCoS* test facility allows simultaneous high-speed Schlieren/OH* chemiluminescence recordings of the combustion processes in the pre-chamber and main chamber. Based on these images, an apparent flame propagation speed could be calculated for both the main chamber and the pre-chamber. In addition, qualitative statements could be made about the observed pre-ignition events in the main combustion chamber.

The variation of the air-fuel equivalence ratio between λ = 1.0 and λ = 2.0 gives a deeper insight into the λ-dependent amount of fuel mass burned, which for this combustion scheme is ideal in the range of λ = 1.0 to λ = 1.6 (slightly depending on engine load conditions), while higher loads allow a leaner combustion. Maximum fuel conversion rates of over 99% can be achieved, which is quite high for this particular test bench, which has a crevice volume in the order of 1% of the total combustion chamber volume.

The ignition delay, measured between spark ignition in the pre-chamber and the start of combustion in the main chamber, is between 1.1 and 1.4 ms for a range of air-fuel equivalence ratios at full load (high boost resp. compression pressures), while at part load (low boost resp. compression pressure) longer ignition delays of over 2 ms are observed. The ignition delay is very sensitive to the start of ignition / spark ignition time in the pre-chamber, as it is strongly dependent on the level of turbulence in the pre-chamber, which decays rapidly towards top dead center.

The apparent turbulent flame propagation speed s_{aFP}, calculated from optical high-speed recordings, increases to more than 23 m/s for λ = 1.0 in the early flame propagation phase, which is very high compared to the laminar flame speed of ammonia (~ 0.018 m/s).

The high-speed Schlieren/OH* chemiluminescence images optimally support the classical combustion characterization by pressure measurements and allow a spatially resolved, deeper insight into the ignition and combustion behavior. In addition, abnormal combustion behavior such as pre-ignition, misfiring and knocking can be directly observed and identified, which can be useful for improving engine designs or for the development of combustion models that can predict such behavior.

The accompanying exhaust gas measurement completes the characterization of the ammonia combustion of the pre-chamber initiated combustion process. Nitrous oxide (N_2O), a major pollutant in ammonia engine greenhouse gas emissions, must be closely monitored in the design of new engine families to fully realize the greenhouse gas reduction potential of ammonia engines against a methane burning engine. The N_2O based reduction potential of an ammonia combustion using a pre-chamber as ignition source, based on the measurements in this paper, is shown in Figure 17 (excluding a potential post-engine N_2O removal system).

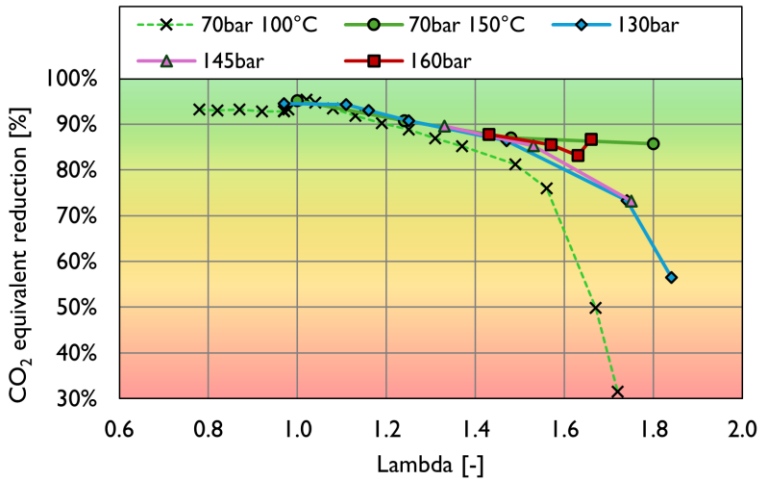

Figure 17: CO_2 reduction potential of a pre-chamber ignited ammonia engine without exhaust gas aftertreatment system based on N_2O emissions at different operating conditions.

However, the promising results of over 90% greenhouse gas emission reductions comparing to a methane burning engine for operating points with λ ≤ 1.2 support further investigations. Especially the possibility of N_2O catalyst systems should be considered. In addition, a diesel-like combustion scheme using a high-pressure direct ammonia injection in combination with a pilot injector is planned in comparison to the pre-chamber combustion concept presented here. Another study will investigate the addition of hydrogen to ammonia to facilitate the transition to completely carbon-free combustion.

Acknowledgments

Financial support from the Swiss Federal Office of Energy (SFOE, contract SI/502152-01) as well as funding by Winterthur Gas & Diesel (WinGD) is gratefully acknowledged.

Literature

[1] United Nations, "Paris Agreement", 2015, http://unfccc.int/files/essential_background/convention/application/pdf/english_paris_agreement.pdf.

[2] DNV Energy Transition Outlook 2020 (Det Norske Veritas), "*Maritime Forecast to 2050*".

[3] F. Abbasov, T. Earl; C. Calvo Ambel, B. Hemmings, L. Gilliam, "*Roadmap to decarbonising European shipping*". T&E - Transport & Environment, 2018.

[4] N. Ash, T. Scarbrough, "*Sailing on Solar – Could green ammonia decarbonise international shipping?*". Environmental Defense Fund, 2019.

[5] Lloyd's Register, UMAS (2019a), "*Fuel production cost estimates and assumptions*", Lloyd's Register; UMAS, 2019.

[6] Lloyd's Register, UMAS (2019b), "*Zero-Emission Vessels: Transition pathways*". Low Carbon Pathways 2050 series, Lloyd's Register; UMAS, 2019.

[7] Lloyd's Register; UMAS (2020), "*Techno-economic assessment of zero-carbon fuels*". Lloyd's Register; UMAS, 2020.

[8] P. Osterkamp, T. Smith, K. Søgaard, "*Five percent zero emission fuels by 2030 needed for Paris-aligned shipping decarbonization*", Global Maritime Forum. Getting to Zero Coalition (ed.), 2021.

[9] B. Schneider, C. Schürch, K. Boulouchos, S. Herzig, M. Hangartner, D. Humair, S. Wüthrich, C. Gossweiler, K. Herrmann, "*The Flex-OeCoS – a Novel Optically Accessible Test Rig for the Investigation of Advanced Combustion Processes under Engine-Like Conditions*", Energies 2020, 13(7), 1794; https://doi.org/10.3390/en13071794.

[10] S. Wüthrich, D. Humair, K. Herrmann, A. Bertola, "*Enhanced instrumentation of an optical research engine with unique combustion chamber*", 14th Int. AVL Symposium on Propulsion Diagnostics, June 23-24, 2020, Baden-Baden, Germany. ISBN 978-3-9816971-6-2.

[11] D. Humair, P. Cartier, P. Süess, S. Wüthrich, K. Herrmann, C. Barro, B. Schneider, C. Schürch, K. Boulouchos, "*Characterization of dual-fuel combustion processes*", Rostock 6th Large Engine Symposium, September 3-4, 2020, ISBN 978-3-941554-22-1.

[12] W. Vera-Tudela, B. Schneider, S. Wüthrich, K. Herrmann, "*Study on the ignitability of a high-pressure direct-injected methane jet using a diesel pilot, a glow-plug and a prechamber*", IJER-21-0139, 2021, https://doi.org/10.1177/14680874211048144.

[13] W. Vera-Tudela, B. Schneider, S. Wüthrich, K. Herrmann, "*Study on the ignitability of a high-pressure direct-injected methane jet using a scavenged pre-chamber under a wide range of conditions*", IJER-1-14, 2022, https://doi.org/10.1177/14680874221093144.

[14] S. Wüthrich, P. Cartier, P. Süess, B. Schneider, P. Obrecht, and K. Herrmann, "*Optical investigation and thermodynamic analysis of premixed ammonia dual-fuel combustion initiated by dodecane pilot fuel*", Fuel Communications 12 (2022) 100074, https://doi.org/10.1016/j.jfueco.2022.100074.

[15] J.M. Desantes, J.M. García-Oliver, W. Vera-Tudela, D. López-Pintor, B. Schneider, K. Boulouchos, "*Study of the auto-ignition phenomenon of PRFs under HCCI conditions in a RCEM by means of spectroscopy*", Applied Energy, Vol. 179, pp. 389-400, 2016, https://doi.org/10.1016/j.apenergy.2016.06.134.

[16] A. Srna, M. Bolla, Y.W. Wright, K. Herrmann, R. Bombach, S.S. Pandurangi, K. Boulouchos, G. Bruneaux, "*Ignition characteristics of n-dodecane pilot fuel spray in a premixed compressed methane/air charge*". Proceedings of the Combustion Institute 37 (2019) 4741–4749. https://doi.org/10.1016/j.proci.2018.06.177.

[17] J.M. Desantes, J.V. Pastor, J.M. García-Oliver, W. Vera-Tudela, "*An experimental study of the effects of fuel properties on reactive spray evolution using Primary Reference Fuels*", Fuel, Vol. 163, pp. 260-270, 2016, https://doi.org/10.1016/j.fuel.2015.09.064.

[18] A. Srna, R. Bombach, K. Herrmann, G. Bruneaux, "*Characterization of the spectral signature of dual-fuel combustion luminosity: implications for evaluation of natural luminosity imaging*", Applied Physics B (2019) 125:120, https://doi.org/10.1007/s00340-019-7222-z.

[19] P. Obrecht, "*WEG: calculation of the heat development law based on measured combustion chamber pressure traces*", in-house thermodynamic model, ETHZ-LAV & FHWN-ITFE, 2021.

[20] K. Herrmann, S. Wüthrich, P. Süess, P. Cartier, R. Moura, G. Weisser, "Initial investigations into ammonia combustion at conditions relevant for marine engines", CIMAC concress, June 12 – 16 2023, Busan

[21] S. Wüthrich, P. Albrecht, P. Cartier, and K. Herrmann, *„Comparison of Pilot Fuel Ignited Premixed Ammonia versus Methane Dual-Fuel Combustion",* 7th Large Engine Symposium, September 2022, Rostock, ISBN 978-3-941554-25-2

[22] J. Schramm, J. N. Klüssmann, L. R. Ekknud, A. Ivarsson, "*Ammonia Application in IC Engines*", 2020.

[23] C. Mounaïm-Rousselle, P. Bréquigny, C. Dumand, and S. Houillé, "*Operating Limits for Ammonia Fuel Spark-Ignition Engine*", Energies (14), 2021, https://doi.org/10.3390/en14144141.

[24] C. Lhuillier, P. Brequigny, F. Contino, and C. Mounaïm-Rousselle, "*Experimental study on ammonia/hydrogen/air combustion in spark ignition engine conditions*", Fuel (269), 2020, https://doi.org/10.1016/j.fuel.2020.117448.

[25] S. McAllister, J.-Y. Chen, and A. C. Fernandez-Pello, "*Fundamentals of Combustion Processes: Appendix*", New York, NY: Springer New York, 2011.

[26] S. Frankl, S. Gleis, S. Karmann, M. Prager, and G. Wachtmeister, "*Investigation of ammonia and hydrogen as CO2-free fuels for heavy duty engines using a high-pressure dual-fuel combustion process*", IJER, vol. 22, no. 10, pp. 3196–3208, Oct. 2021, https://doi.org/10.1177/1468087420967873.

[27] D. Han, Y. Liu, and Z. Huang, "*The Use of Ammonia as a Fuel for Combustion Engines*", Engines and Fuels for Future Transport, G. Kalghatgi, A. K. Agarwal, F. Leach, and K. Senecal, Eds. Singapore: Springer Singapore, 2022, pp. 233–256.

[28] R. Tanner, A. Guyer, W.D. Treadwell, "*Über die Verwendung von Ammoniak als Treibstoff*", *Eidgenössische technisch Hochschule in Zürich (ETHZ), Zürich 1945*

FVTR

Our Maritime Services

- Numerical simulation for combustion process development & analysis
- Engine test bench research for various liquid & gaseous fuels
- Injector & spray analysis for various fuels
- Exhaust gas treatment development from lab scale to full scale
- Studies & literature research

Whether it is natural gas, biofuel, methanol, hydrogen, ammonia, …
We support you in solving all your scientific & technical topics!

www.fvtr.de

Keywords: methanol, port fuel injection, spray, phase Doppler interferometry, medium speed engines.

Design and characterisation of a port fuel injector for high power medium speed engines

Dr. Marco Coppo[1], Dr. Marco Ferro[1], Dr. Claudio Negri[1], Dr.-Ing. Fabian Pinkert[2], Dr. Mathias Niendorf[3]

(1) OMT SpA, (2) FVTR GmbH, (3) University of Rostock

https://doi.org/10.18453/rosdok_id00004648

Abstract

The marine engine industry is betting heavily on the adoption of new fuels, such as methanol, to reach the decarbonisation targets recently made more ambitious by IMO. Direct injection of methanol is set to achieve the highest substitution rates, therefore minimising the amount of diesel needed to pilot the ignition of the main fuel and the associated emissions [1].

However, this requires the design of large and complex dual fuel injectors capable to integrate in the same package both the diesel (for pilot and full backup power) and the methanol injection stages, which, in turn, requires significant modifications to the cylinder head. Furthermore, the pressurisation of methanol to direct injection pressure levels (around 600-700 bar) requires costly equipment not currently available at scale nor fit for integration in the engine room. For all these reasons, direct injection of methanol is mostly planned for new engine designs.

On the other hand, if significant benefits in terms of reduction of utilisation of fossil fuels are to be reached quickly, port fuel injection of methanol at relatively low pressures (10-50 bar) promises to provide an easier, faster and more cost effective solution to convert the existing engine fleet.

The paper presents the port fuel injector developed by OMT to answer the need of powering large medium speed engines with unit power up to 1200 kW/cylinder, and the challenges addressed during development. The main issue that such injection technology needs to address is to achieve a fine atomisation of the fuel, so that it can be transported by the charge air into the cylinder without wetting the intake manifold walls, without having the possibility to rely on a high supply pressure. Furthermore, direct actuation is required due to the need to avoid a methanol return line, posing challenges in terms of actuation forces, which should contrast the spring force needed to ensure proper sealing in between injections. These challenges are discussed in the paper and the technical solution identified to address them is presented.

The article also presents the test setup devised to measure the spray characteristics and discusses the results of a Phase Doppler Interferometry (PDI) experimental campaign aimed at measuring spray parameters at different distances from the injector tip. Water spray data is provided in the present paper, and further tests are planned to characterise also the methanol spray with the aim of defining a correlation that could simplify further tests by running them with water only.

1. Introduction

In July 2023 IMO raised the bar for the whole marine industry by revising its strategy on reduction of greenhouse gas (GHG) emissions from ships [2], which led to the definition of more ambitious targets aimed at reaching net-zero emissions by 2050. Considering the typical vessel lifespan of 30 years, it follows that the global fleet that will have to achieve this target will largely consist of vessels built already in the next decade. This consideration forced ship owners to think carefully about their next investments, and resulted in an increased pressure on vessel and engine designers to provide, in the shortest possible time, commercially-ready solutions able to operate with synthetic renewable fuels such as methanol and ammonia [3].

However, in the same strategic document, IMO also set GHG reduction targets for 2030 (-30%) and 2040 (-80%), which are, in perspective, even more challenging to achieve as they can only be reached through a significant retrofitting of the existing fleet of vessels because the relative impact of newbuilds will be initially limited. It follows that the industry must support this additional market demand by providing cost effective and simple retrofit kits to rapidly scale up conversion projects, even if at the partial expense of maximum efficiency and GHG emission reduction.

According to [4], methanol obtained from renewable sources will be available sooner than ammonia and, in perspective, prices of the two fuels in the future will be comparable. Furthermore, methanol toxicity is lower than that of ammonia. This, coupled with the fact that it is easier to handle because it can be stored in liquid state at ambient pressure, makes methanol the current fuel choice for conversion projects.

Both lean-burn premixed combustion and diffusive combustion of methanol are technically possible. In the former, liquid fuel is introduced in the intake manifold through one or more port fuel injectors operating at fairly low pressure (10-30 bar) which are tasked with the atomization of the liquid jet so that the resulting droplets can be mixed with and transported by the air flow into the combustion chamber during the intake stroke. The air/fuel mixture is then ignited through a pilot injection of diesel fuel delivered by the standard injector used also for full diesel operation when methanol is not available.

On the other hand, direct injection of methanol in the combustion chamber requires the integration on the cylinder heads of dedicated injectors operating at high pressure (typically 600 800 bar), and the installation of an expensive pumping system to pressurize the fuel. As the space on the cylinder head is already limited, the integration of diesel and methanol injectors into one object is very challenging and leads to custom-made and fairly expensive solutions.

As reported in detail in [1] and [6], the direct injection technology is advantageous in terms of higher engine efficiency and fuel substitution ratio (i.e. smaller pilot injection quantities are required to ensure stable methanol combustion), when compared to port fuel injection. Additionally, the diffusive combustion approach limits the contact of unburnt fuel with cylinder liner walls, reducing issues related to engine oil contamination and piston/liner scuffing due to oil film breakup.
Conversely, a port fuel injection system is simpler in terms of number and complexity of components and in terms of installation constraints, which makes it cheaper than a direct injection one, and thus ideally suited to retrofitting existing diesel engines. In order to support its customers on their path to decarbonization, OMT developed a methanol port fuel injector suitable to power the largest medium speed marine engines. The paper presents the challenges faced during design and how they were

addressed, as well as reporting injector performance data both in terms of dynamics and of spray quality.

2. OMT Methanol Port Fuel Injector

2.1. Injector architecture

The injector is designed for a multi-point injection layout, i.e. with one injector for each cylinder, and for an engine power up to 1200 kW/cylinder. It is able to deliver the rated injected quantity of 29000 mm³/shot in 80° CA for an engine speed of 500 rpm with a methanol supply pressure of 30 bar. A section view of the injector and of its main component is shown in Figure 1. To limit the complexity of the engine interface, the injector is directly actuated by a solenoid, so that fuel return or control oil feeding and return lines are not needed. All potential leakages are directed towards a dedicated line with a low positive pressure of nitrogen or in vacuum, to avoid the possibility of formation of an explosive mixture, making the injector ATEX compliant. Finally, an inbuilt flow fuse limits the injected quantity in case of malfunctioning.
To maximize the atomization of the fuel with the limited differential pressure available, an outward-opening poppet valve architecture was chosen: given the same fluid characteristics, injection pressure and downstream conditions, the size of the droplets is proportional to the characteristic dimension of the liquid jet forming at the nozzle outlet (see [7] and [8]). Although the injection duration is approximately three times larger than for the case of direct injection, due to the much lower supply pressure, a much larger fuel passage section is required. Therefore, for this particular application, an implementation similar to that of high-pressure injectors, i.e. with holes open in a sac downstream of the needle seat, would require a very high number of holes to obtain a comparable thickness of the liquid film of the one that can be created at the exit of a poppet valve. As shown in Figure 2, thanks to a particularly narrow and long exit section of the poppet, it is possible to generate a liquid film with a thickness of less than 0.6 mm, which, in turn, is able to generate a spray with very fine droplets. Moreover, for this layout almost all the pressure available is used to generate fluid velocity, while in a traditional architecture some pressure is lost at the needle seat, especially considering that the maximum stroke of the needle is limited by the magnetic force available at the solenoid. Another advantage of the outward opening architecture is that it is possible to balance the fuel pressure forces on the needle, so that the actuator needs to counteract spring and inertia forces only, limiting the size and cost of the solenoid and, consequently, those of the injector. Moreover, in this configuration the intake manifold pressure acts in the direction of closing the needle, increasing the force on the seat and providing additional robustness against injector leakage.

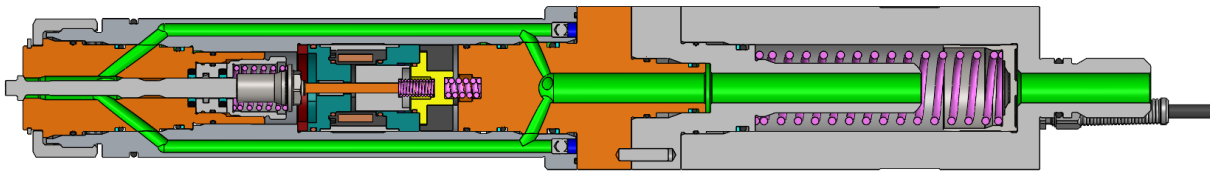

Figure 1: OMT PFI injector

A possible drawback of this architecture is that it is not possible to orient the spray with respect to the injector axis. However, the spray cone angle was chosen to be large enough (120°) to minimize

the risk of fuel impacting the manifold walls. By mounting the injector with its axis almost perpendicular to that of the intake manifold, the relative velocity of the spray with respect to the charge air flow is maximised for the portion of the spray propagating upstream in the intake manifold, consequently increasing the atomization of the droplets, while for the remaining part of the spray the droplets can proceed along the manifold for a long path and have therefore enough time to evaporate before encountering obstacles.

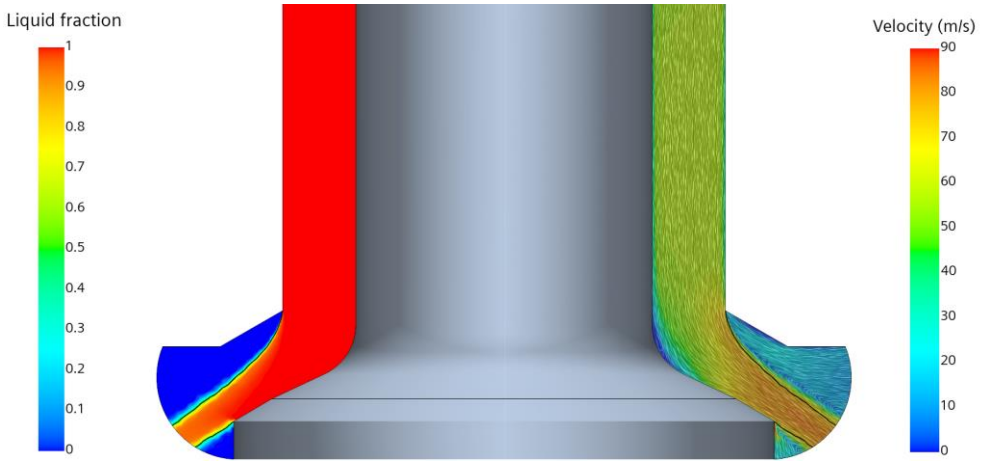

Figure 2: CFD simulation of the fuel motion at the injector exit in still air. Velocity field (right) and liquid fraction (left)

2.2. Injector Performance

A dedicated test bench (see Figure 3) was especially designed and procured to test and validate the PFI injectors. It allows injection of test oil or distilled water into a chamber filled with air at a configurable pressure, to simulate the actual injection condition of the engine intake manifold. Water temperature can be controlled up to 70 °C, to achieve conditions of similarity with methanol in terms of dynamic viscosity and vapour pressure, and hence properly validate injector operation in similar conditions of lubrication of the sliding components and cavitation onset as those in the field. Optical access to the spray chamber is allowed through a glass panel, so that investigation on the spray formation and evolution can be conducted in-house. The measurement is fully automated and it allows the acquisition of the mean injected mass and of the instantaneous needle lift, from which the injection rate shape of each shot can be reconstructed, allowing for the determination of the shot-to-shot dispersion of the injector.

Figure 3: PFI injector test bench (left), detailed view of the injection chamber (right)

Figure 4 and Figure 5 show a comparison between experimental results and data obtained from a lumped parameter simulation of the injector, performed with GT-Suite. Given the quite low operating pressure range, the behaviour of the injector is significantly affected by the geometrical characteristics of the upstream feeding line, hence they were considered and included into the model. It can be observed that very good agreement between simulated and tested injector lift is obtained both for a rated injection (see Figure 4) and for a smaller injection quantity (see Figure 5). Moreover, it can be observed that a small part-to-part variation of injection performance was obtained, with a dispersion for a rated injection limited to ±2% of injected mass.

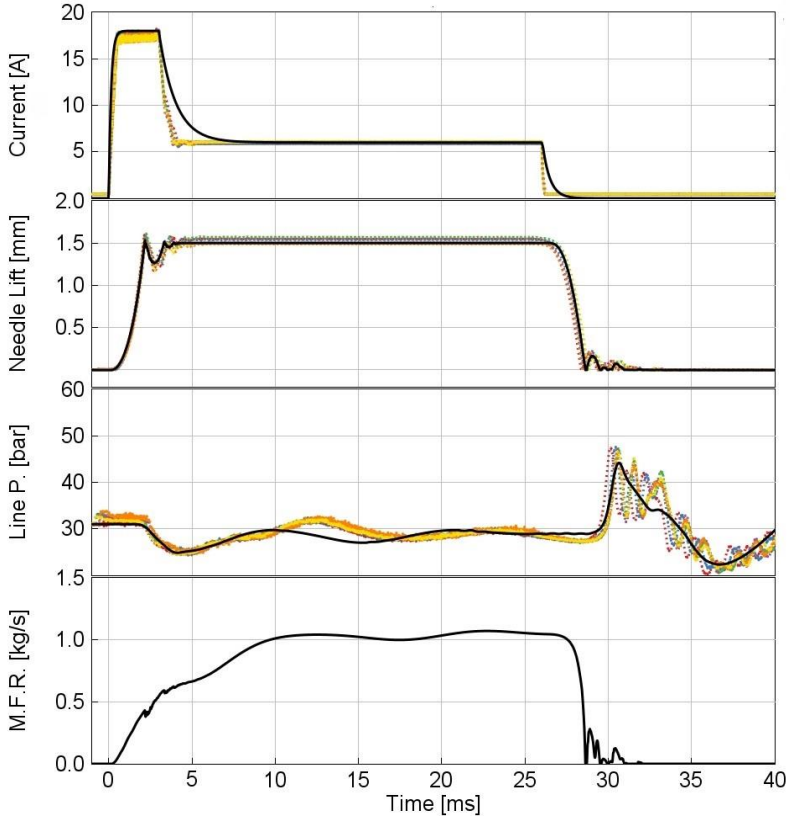

Figure 4: Comparison of simulation data (black solid line) with experimental results of 6 different injectors (dotted colored lines) for a rated injection

Once the lumped-parameter model is validated, it is possible to perform a simulation of the injector performance on the engine, to account for the actual geometry of the feeding line. Figure 6 shows a comparison between simulated injector operation on the test-bench and in the engine layout. It can be noticed how the difference in the pressure fluctuations in the upstream line considerably affects the injection rate shape and the total injected mass, highlighting the need for a differentiation of these two operation conditions when validating experimental data.

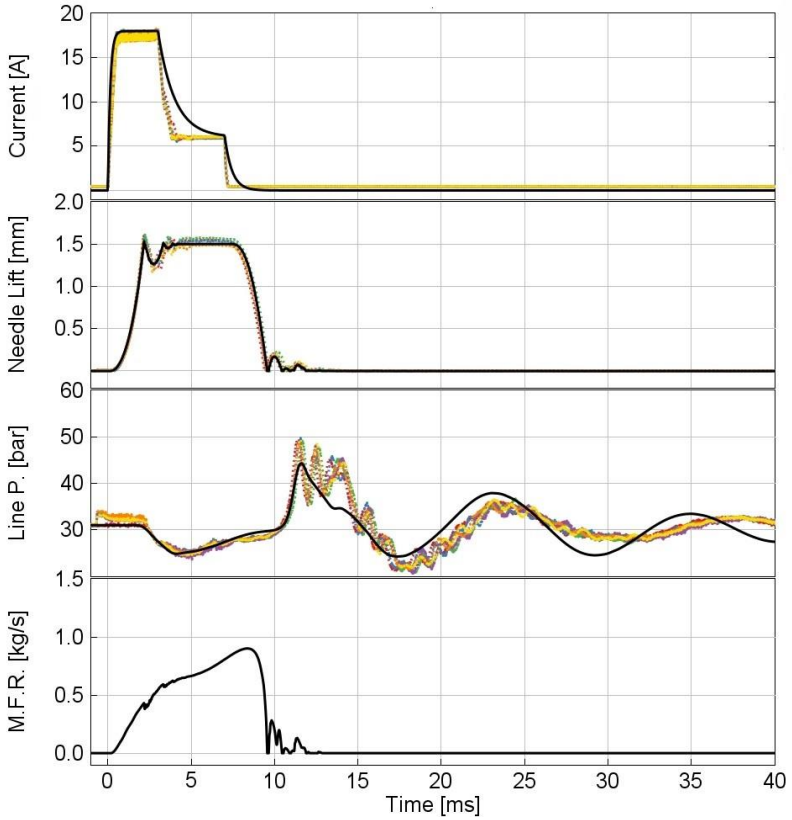

Figure 5: Comparison of simulation data (black line) with experimental results of 6 different injectors (dotted colored lines) for an injection equal to 30% of the rated injection

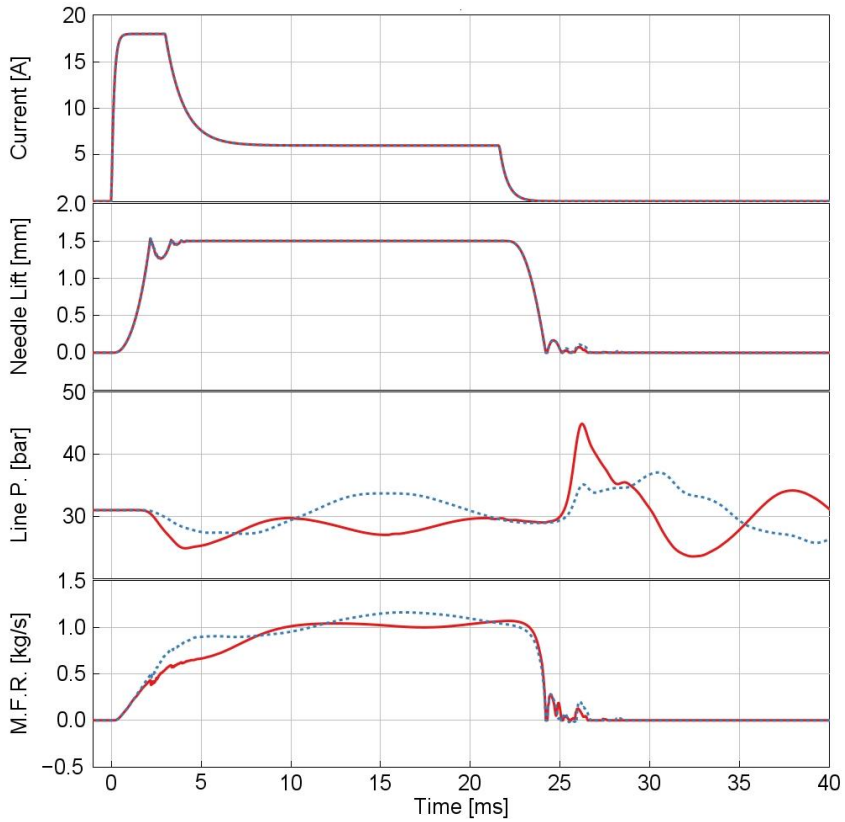

Figure 6: Simulation results considering the upstream feeding line of the test bench (solid line) vs. the actual engine layout (blue dotted line)

3. Spray Analysis

3.1. Experimental Setup and measurement procedures

The injector was tested in a newly developed test bench, designed for droplet sizing and spray visualization of methanol sprays. The sprays can be measured in quiescent air at ambient pressure and temperature. The test cell shown in figure 7 consists of a stainless-steel tank, fitted with multiple windows for the Phase Doppler Interferometry (PDI) system and for the high-speed camera. While the measurement system is fixed in space, the injector is positioned by a 2-axis traverse, allowing measurements from 120 to 370 mm nozzle distance.

Methanol or water is pressurized by an air-driven piston pump, allowing injection pressures of up to 1000 bar. In this test setup with injection pressures up to 25 bar the fluid is stored in a pneumatic accumulator close to the injector with a volume of 0,46 liters. A high-speed pressure transducer, mounted between the injector and the accumulator, shows the effectiveness of the accumulator in limiting the pressure loss during the injection to 11%.

After injection, the water or methanol mist is roughly separated from the scavenging air and then filtered using active carbon filters. The air scavenging flow in the test chamber is provided by a side channel blower situated behind the chamber. The test chamber pressure is kept very slightly below the atmospheric level as a part of the safety concept for confining the methanol vapors. The inside of the chamber is an explosion prevention zone.

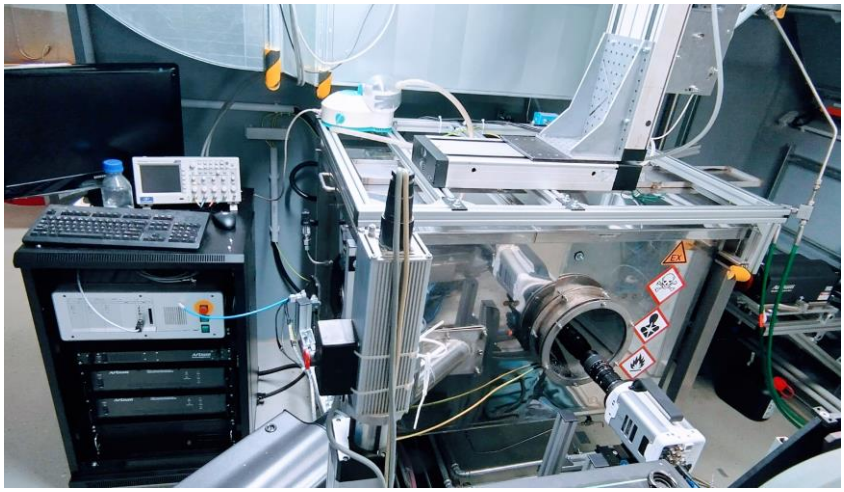

Figure 7: Particle Distribution and Spray test bench for analyzing methanol sprays

The droplet size measurements were carried out using an Artium Phase Doppler Interferometer. This system allows the measurement of velocity and diameter of droplets passing through the measurement volume. This volume of about 1mm³ is formed by the intersection of two laser beams. Droplets passing the measurement volume refract the fringe pattern of the laser beams into an array of three optical receivers. From the frequency of the signal and phase shift between the receivers, the velocity and diameter of the droplets can be calculated. [10]

The system was operated using two optical setups and, initially, operating the injector with water at room temperature. A receiver focal length of 1000 mm was found to disregard droplets above 500 µm. As larger droplets are believed to be important in the practical application of the spray within the intake manifold, a second focal length of 2000 mm was employed to capture droplets up to 1000 µm. Comparing the results obtained with the two measurement configurations, it was found that the second setup disregards droplets below 80 µm. The resulting droplet distribution histograms obtained with the two setups are compared in Figure 8 for one operating point, and the filtering effects at both ends of the particle diameter range are clearly visible. The results of both setups were combined with an overlap of the distributions between 100 and 300 µm to yield the most accurate results. In this way, the resulting measurable droplet range was between 40 and 1000 µm.

Finally, to gain a basic understanding of the spatial location and temporal evolution of the spray, high speed videos were captured of the entire spray cone and of the near nozzle region. For these measurements, a Photron Nova camera was used. The spray was illuminated from two sides by xenon light flashes.

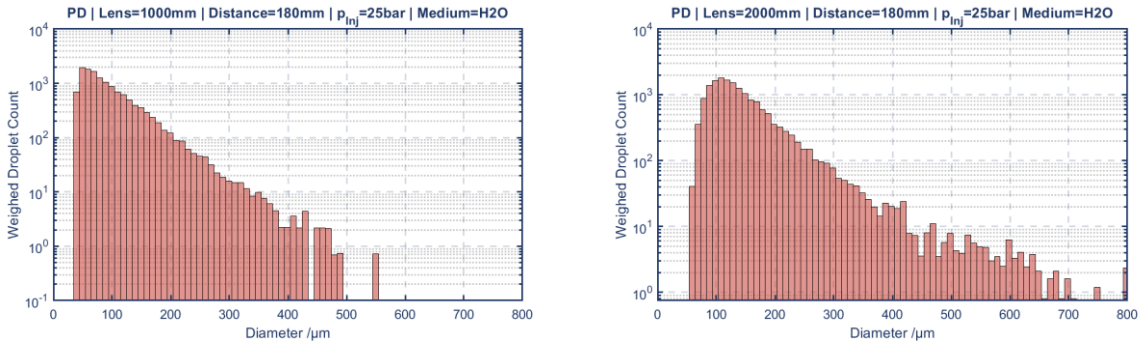

Figure 8: Comparison of the probability distribution (PD) histograms for two PDI Setups. The 1000 mm lens was found to disregard droplets above 500 µm while the 2000 mm lens was found to disregard droplets below 80 µm

3.2. Measurements results

The temporal evolution of the sprays in Figure 9 shows an opening phase of the needle between 1 and 3 ms after start of energization. In this phase a dominating instability frequency of the liquid sheet can be observed. At full needle lift water is injected with visibly stronger perturbations leading to a finer primary breakup. The cone half angle in the near nozzle region was measured to be 56,5°.

The PDI measurements were performed at injection pressures of 10 bar and 25 bar, to match the pressure differential of 15 and 30 bar injection pressure and 5 bar counter pressure in the intake manifold. The measurement locations were set in polar coordinates as the distance from the nozzle and the cone half angle. The nozzle distances chosen for this investigation were 180 and 340 mm. The spray was scanned in 1° intervals from 52° to 58° half cone angle. Most measurements were performed in the middle of the spray at about 55° to obtain a large data base for the probability distribution (PD) analysis. The average droplet diameters were calculated individually for all spray positions and averaged with weights corresponding to the total volume of liquid measured at each location.

The presented results are based on combined data from both focal lengths to provide good measurement accuracy at both ends of the size spectrum. Figure 10 visualizes the obtained particle distributions for all measurement locations across the spray in histograms. Three histograms appear to have an adequate resolution due to the large number of droplets measured. For the measurement point at 10 bar differential pressure and 340mm nozzle distance only a small number of droplet counts were obtained. It is likely that at this operating point the smallest droplets are underrepresented: the low spray velocity due to the low injection pressure combined with the large distance allows the smallest droplets to disperse over a large area and thus escape the measurement volume. For this reason, the results of this measurement point are not taken to be representative and are not further included in the comparison.

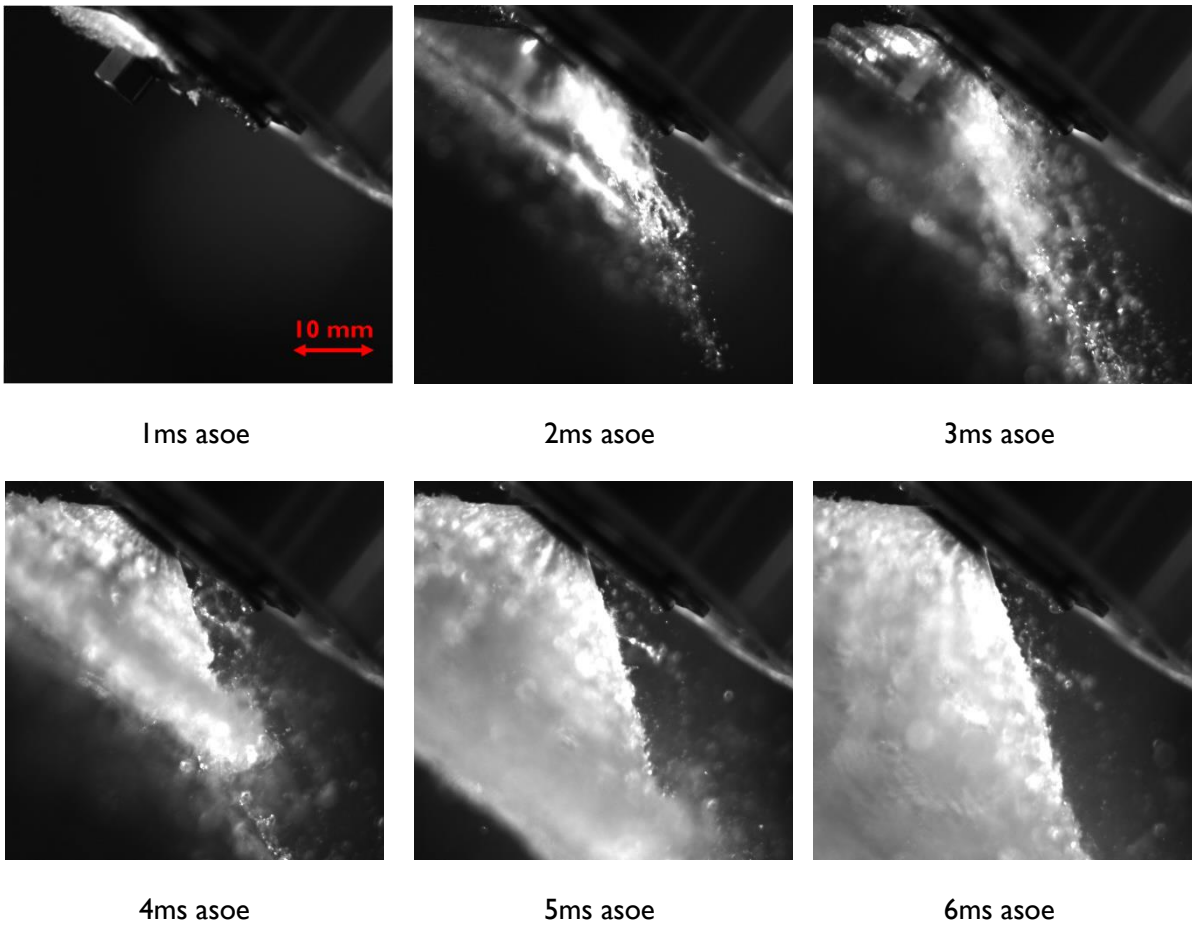

Figure 9: Spray evolution at 2 bar injection pressure in 1ms intervals after start of energization (asoe). Full lift of the poppet valve is reached after about 3 ms asoe. The measured cone half angle near the nozzle was 56,5°

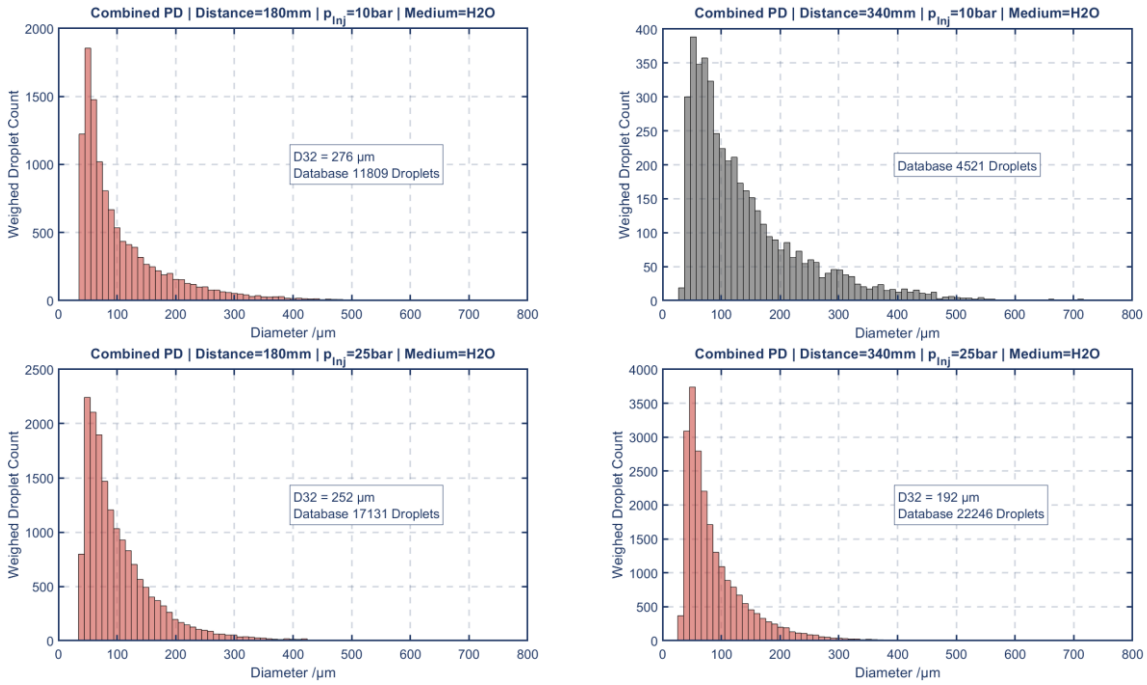

Figure 10: Particle Distributions at 180 and 340 mm distance from the nozzle at 10 and 25 bar injection pressure. A wider distribution at the low injection pressure can be observed. The histogram at 340 mm and 10 bar is believed to be unrepresentative of the spray because of the low number of droplets and the atypical histogram shape

A comparison of the mean diameters obtained is given in Figure 11. The Sauter mean diameter (SMD, D_{32}) was chosen as spray metrics, because of its extensive use in characterization of fuel sprays. For 25 bar of differential pressure, a distinct reduction in droplet diameter can be observed with further distance from the nozzle, and the SMD reaches a level of 192 µm at 340 mm from the nozzle. This can be explained by the droplet velocity: high droplet velocities lead to secondary breakup of larger droplets due to the aerodynamic forces. The driving non-dimensional parameter describing this instability is the Weber Number. As reported in [9], starting from a Weber number of about 12 bag breakup of droplets can occur, leading to a reduction of the mean diameter of a droplet ensemble.

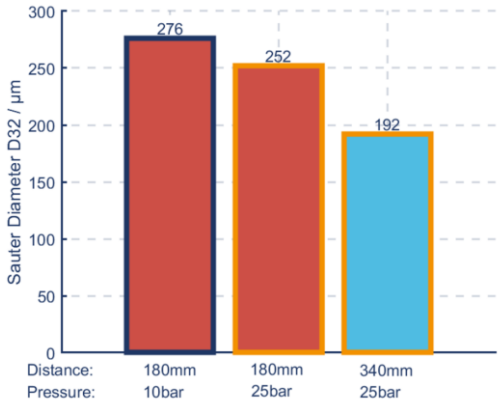

Figure 11: Resulting SMD for all operating points. The reduction of the diameter at 25 bar is likely due to secondary breakup.

To visualize the influence of the velocity on the evolution of the spray, 2D histograms of droplet diameter and velocity are shown in Figure 12. In the top row, at 10 bar injection differential pressure

the larger droplets have a velocity of up to 30 m/s and hardly any droplets have Weber Numbers above 12. On the contrary, as shown in the bottom left plot, at a differential pressure of 25 bar a significant number of droplets are in the region of secondary breakup. These break up and disappear going to 340mm distance (bottom right), thereby lowering the mean diameter. Furthermore, the whole of the ensemble gets slowed down. These findings not only serve to explain the experimental results but also give insight into the benefits of high injection velocities and into the effect of aerodynamic forces onto droplet distributions. Considering that in the intake manifold the air velocity reaches up to 100 m/s, we can expect that, given the larger relative velocity of the droplets in respect with the surrounding air flow, an even larger portion of droplets would undergo secondary breakup, thus lowering the effective mean diameter of the resulting spray. Moreover, the lower surface tension of methanol would increase even more the Weber number, further decreasing the SMD of the spray in real operating conditions.

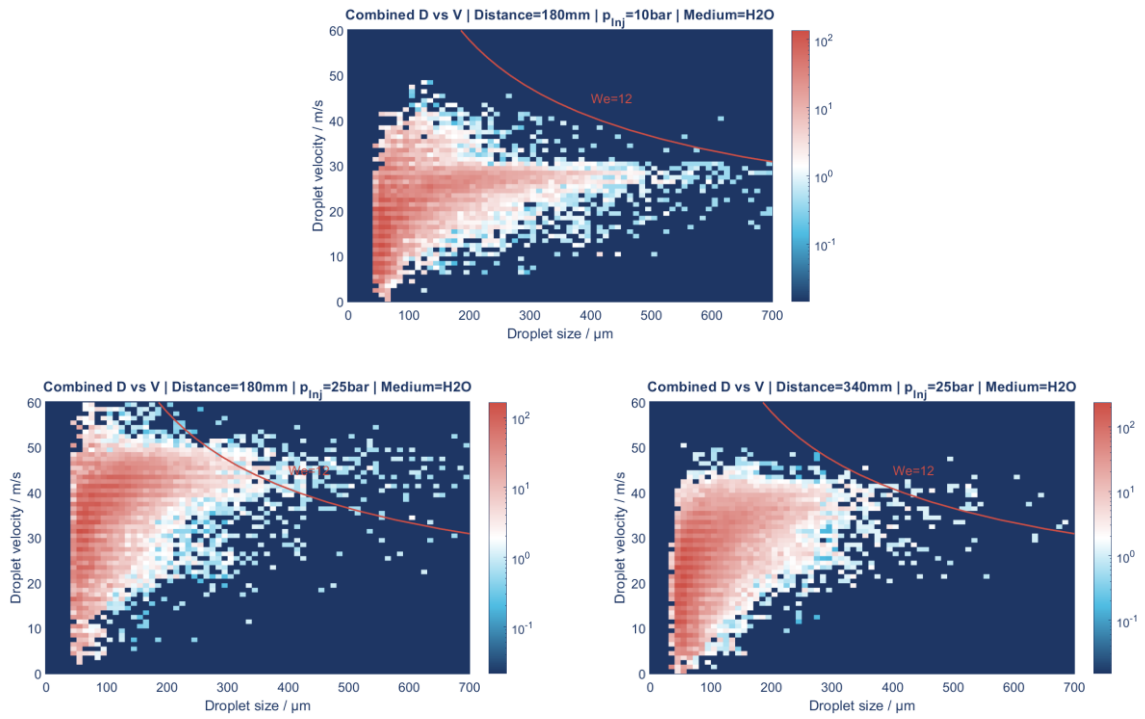

Figure 12: Two dimensional histograms of droplet velocity and droplet size for all operating points. The colormap is in logarithmic scale to allow visibility of the scarce occurrences of larger droplets. The critical Weber number of 12 is plotted in the diagrams to indicate regions of secondary breakup towards high diameters and high velocities.

4. Conclusions

In this paper the design of the OMT methanol port fuel injector for engines with power up to 1200 kW/cylinder has been presented and the main design choices illustrated. It was shown that, with an outward-opening poppet valve architecture, large volume flow rate can be achieved while keeping at a minimum the characteristic length scale of the injected fluid film, hence maximizing the quality of atomization. Measured injector performance matches well the simulated behaviour, and good injection repeatability was achieved.

To characterize the spray generated by the injector, a new test bench has been designed and built at FVTR, allowing to safely perform PDI and other measurements with low viscosity fuels such as

methanol. Measurement results showed that the OMT injector is capable of generating a fine spray, with a SMD of about 200 µm at a distance of 340 mm from the nozzle when water is used as fluid.

The next step is continuing the measurements across a larger number of operating points and locations, completing the characterization of the spray of the new injector and allowing to build a solid understanding of the atomization mechanism. Moreover, extending the measurement to the case of methanol injection will allow to understand the effect of the variation of fluid property on the spray particle distributions, to validate and tune existing correlation and scaling laws for this flow case, and to create a database for validating ongoing CFD simulations of the spray evolution.

Acknowledgments

The authors would like to acknowledge the colleagues at OMT their support in providing data and valuable input for writing this paper.

Literature

[1] Yin, X., et al., "In-depth comparison of methanol port and direct injection strategies in a methanol/diesel dual fuel engine", Fluid Processing Technology, Vol. 241, March 2023, 107607.

[2] International Maritime Organisation, "2023 IMO Strategy on Reduction of GHG Emissions from Ships", Resolution MEPC.377(80), 2023, London, United Kingdom.

[3] Coppo, M., et al., "Powering a greener future: the OMT injector enables high-pressure injection of ammonia and methanol", CIMAC Congress paper 139, 2023, Busan, South Korea.

[4] DNV, "Maritime Forecast to 2050 – Energy Transition Outlook 2023", 2023, Høvik, Norway.

[5] Dierickx, J. et al., "Retrofitting a high-speed marine engine to dual-fuel methanol-diesel operation: A comparison of multiple and single point methanol port injection", Fuel Communications, Vol. 7, June 2021, 100010.

[6] Altun, Ş. et al., "Comparison of direct and port injection of methanol in a RCCI engine using diesel and biodiesel as high reactivity fuels", Process Safety and Environmental Protection, Vol. 174, June 2023, pp. 681-693.

[7] Kooij S. et al. "What determines the drop size in sprays?" Physical review X, Vol. 8, July-September 2018, pp. 031019.

[8] Hiroyasu H. and Arai M. "Structures of Fuel Sprays in Diesel Engines." SAE Transactions, vol. 99, 1990, pp. 1050–61.

[9] Jain, Mohit, R. Surya Prakash, Gaurav Tomar, und R. V. Ravikrishna. "Secondary breakup of a drop at moderate Weber numbers". Proceedings of the Royal Society A: Mathematical, Physical and Engineering Sciences 471, Nr. 2177 (8. Mai 2015): 20140930.

[10] Ofner, B. (2001). Phase Doppler Anemometry (PDA). In: Mayinger, F., Feldmann, O. (eds) Optical Measurements. Heat and Mass Transfer. Springer, Berlin, Heidelberg.

Keywords: methane direct injection, gas injector, dual fuel engine, 3D-CFD, SOGAV, PFI, medium pressure direct injection, stratified charge, lambda distribution

3D – CFD Simulation of Direct Gaseous Injection for a Medium Speed Dual-Fuel Engine

Jules Christopher Dinwoodie[1], Sebastian Cepelak[1], Manuel Glauner[1], Pascal Seipel[1], Dr. -Ing. Karsten Schleef[1], Prof. Dr. -Ing. Bert Buchholz[1], Dr. -Ing Martin Theile[2]

[1]University of Rostock, [2]FVTR GmbH

https://doi.org/10.18453/rosdok_id00004649

Abstract

The use of Liquid Natural Gas (LNG) as a fuel theoretically results in around 25% less CO_2 emissions than a diesel engine equivalent. LNG can also be created from biological or synthetic sources as a carbon neutral fuel and there is a large existing onshore infrastructure, making LNG technologies in internal combustion engines a viable option for the road to carbon neutrality. The major problem with its use is methane slip – unburned fuel passing through the engine – as methane is also a greenhouse gas. Using direct injection prevents methane slip during valve overlap. In addition, direct injection can be used to target the fuel away from the cylinder walls and piston top land area, improving efficiency and reducing slip occurring due to incomplete combustion. Using a purely experimental approach it is nearly impossible to gain a thorough understanding of the mixture formation processes within the engine's cylinder. However, through the use of validated Computational Fluid Dynamics (CFD) models these processes can be calculated, analysed and assessed for efficacy.

A gas direct injector has been developed for use on a marine medium-speed dual-fuel methane/diesel engine. CFD was used to characterise the injector's behaviour. The developed CFD models were then applied to the 1/34 DF engine and the mixture formation processes analysed. The series produced low pressure port fuel injector was also modelled and compared with the newly developed medium pressure direct injector. Injection strategies using medium pressure direct injection (MPDI) are presented and conclusions drawn as to the efficacy of using MPDI on a dual-fuel marine engine to reduce harmful greenhouse gas emissions.

Direct gas injection on a four stroke engine of this size is very rare. Most manufacturers rely on low pressure port fuel injection, as high pressure direct injection (HPDI) is costly. Using medium pressure direct injection increases efficiency and power density at a lower price point than HPDI, offering a cost effective and advantageous solution to methane slip in the four stroke dual-fuel marine engine.

1. Introduction

Global shipping continues to grow and the need for low emissions shipping with it. One method of cutting CO_2 emissions by around 25% is the use of dual-fuel LNG/diesel engines, the benefit of LNG being the readily available on-shore infrastructure, the ability of adding drop in syn-LNG in any proportion and the unchallenging handling of the fuel.

The main obstacle to the use of these engines is the issue of methane slip, where unburned methane enters the atmosphere, as methane has a global warming potential of factor 28 over 100 years in comparison to CO_2. If this obstacle can be overcome, dual-fuel methane/diesel engines become a viable option for climate neutral shipping.

Methane slip occurs in turbocharged port fuel injection (PFI) gas engines due to injected methane remaining in the intake manifold and being pushed through the cylinder and out of the exhaust during valve overlap. This form of methane slip is known as shortcutting. Another source is methane slip due to incomplete combustion of methane residing in crevices in the cylinder or flame quenching in near-cylinder wall areas. Much effort has been spent on reducing these crevices to improve combustion efficiency, but the problem of methane shortcutting has not yet been properly addressed.

One method of eliminating methane slip due to shortcutting is by the use of a direct gas injector. Using this technology it is possible to inject methane into the cylinder after exhaust valve closing, effectively eliminating methane shortcutting. This method has not been serially implemented up to now due to the higher costs required for the gas compression. In a world where emissions regulations are becoming increasingly stringent, perhaps it is time to review this strategy as a viable option.

The TEME 2030+ project at the University of Rostock aims to show the potential of this technology using an experimental engine and a custom designed gas direct injector. 3D – CFD simulation supports the design of experiments and custom components for the engine.

In this paper, different operating strategies are presented for using a medium pressure direct injector. These strategies are analysed using 3D – CFD simulations and compared with the serial low pressure PFI injection commonly found in engines of this type.

The results of a cold flow simulation and low pressure PFI injection are fist presented. An approach for homogenous medium pressure direct injection is then examined before options for stratified charge operation are shown.

The simulations show promising results for a low-methane slip operation with improved engine performance, paving the way for the experimental results to follow.

2. Experimental Setup

The experimental engine, injector and optical spray chamber used for injector analysis are presented here, giving an overview of the technology available to the TEME 2030+ project team.

2.1. The Experimental Test Bed & Gas Direct Injectors

The University of Rostock operates one of the largest single cylinder research engines in Europe. This medium speed dual fuel methane / diesel marine engine has a 34 cm bore and a rated power output in excess of 500 kW running at a speed of 720 min^{-1} (generator mode). The engine specifications can be seen in table 1.

Table 1: Technical data of the 1/34 DF single cylinder research engine

Bore	340	mm
Stroke	460	mm
Displacement	41.76	l
Compression ratio	12.75	-
Rated speed	720	min^{-1}
Rated power	> 500	kW
Peak firing pressure	> 200	bar
Pilot fuel System	Decentralised DUAP MPI-CR diesel injector, tilted by 6.5°	-
Max. pilot fuel Pressure	2200	bar
Gas dosing system	Woodward SOGAV 105 / DUAP Gas Direct Injector	
Max. gas Pressure	10 / 600	bar abs
Max. charge air pressure	8.5	bar abs

Load Management

The engine's drive shaft is connected to a 1.2 MW dynamometer to simulate load. The engine is controlled by a freely programmable research engine control unit (ECU) based on the National Instruments PXI platform, allowing online pressure indication and next cycle control. A measurement frequency of 1 Hz is used, with some measurements, such as the in-cylinder pressure, being taken at a frequency of 0.1° CA (crank angle degrees) and synchronized with the crank angle movement. The engine is operated on the generator curve (720 min^{-1}) at different load points, this being the typical application for medium speed marine engines.

Air System

The experimental engine is supplied with compressed air at up to 8.5 bar which is regulated according to the load point of the engine based on the series engine's turbocharger map. Steam can be added to humidify the dry compressed air. To simulate the respective back pressure of a serially produced turbocharger, a system of valves in the exhaust system are opened or closed according to the load point. These technologies allow a great degree of freedom in engine testing, as different turbochargers can be simulated by setting the charge air and back pressures accordingly. An experimental exhaust gas recirculation system (EGR) has recently been installed, allowing EGR rates of up to 30% at 100% load to be realised. An experimental canning for a methane oxidation catalyser (MOC) has also been added, with exhaust gas analysis points before and after the catalyser enabling the performance testing of MOC's. The exhaust gas is analysed using a SESAM i60 Fourier transform infra-red (FTIR) spectrometer, whereby all relevant exhaust gas components can be measured.

Figure 1 represents the infrastructure of the engine test bed.

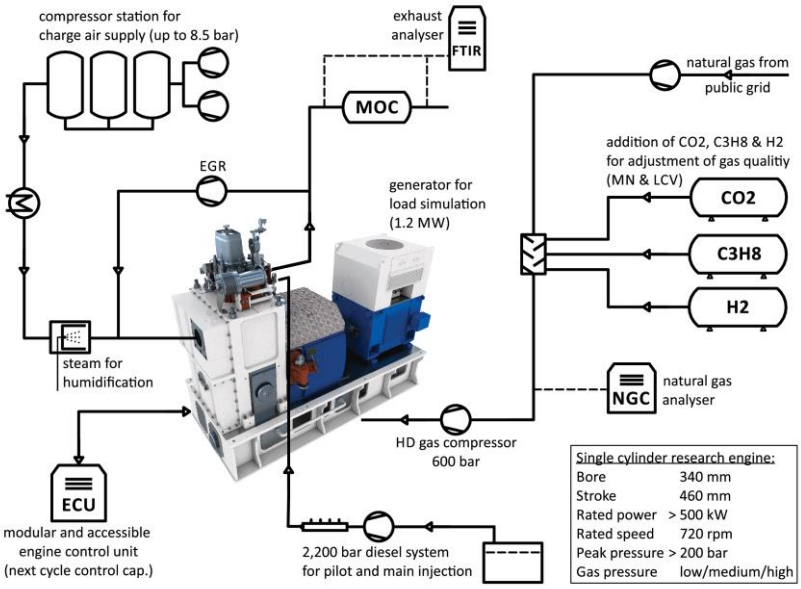

Figure 1: Engine test bed infrastructure

Fuel System

The engine is fitted with a DUAP pilot fuel injector which is decentralised and located between the intake and exhaust valves. The injector is tilted to an angle of 6.5° to compensate for the decentralised position. The four hole nozzle is adapted accordingly. The pilot injector is fed by a common rail system operating at up to 2200 bar. The series engine is fitted with a Woodward solenoid activated gas admission valve (SOGAV) which is located in the intake port and fed by a gas compressor, allowing a maximum gas pressure of 10 bar for port fuel injection (PFI). The natural gas used is taken from the national grid and fed into a mixing unit where propane (C_3H_7) and carbon dioxide (CO_2) can be added, changing the lower heating value and the methane number in order to simulate worldwide LNG qualities. It is also possible to mix in Hydrogen gas (H_2) and experiments have been carried out up to a substitution rate of 80vol%. A novel gas direct injector (DI) was developed within the TEME2030+ project and is mounted centrally in the cylinder head, seen next to the tilted diesel injector in figure 2.

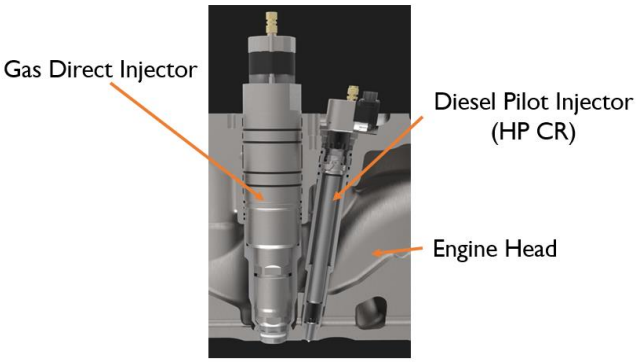

Figure 2: Gas direct injector & DUAP MPI-CR injector in cylinder head

The centrally mounted gas injector was designed by ITAZ GmbH on behalf of DUAP AG using gas simulation calculations over the entire scope of engine operation.

Table 2: Injector Parameters

Cylinder power	450	kW
Standard operating gas pressure range	50 - 80	bar
Maximum gas pressure limit	100	bar
Gas injected at 100 % engine load	4000	mg
Max. injection duration	80	° CA
Min. injection duration	7	° CA
Number of injections per combustion cycle	1 - 2	-
Outer diameter	75	mm
Valve diameter	25	mm
Total injector length	475	mm
Injector weight	22	kg

The gas direct injector is of an outward opening poppet valve type, producing a wide angled hollow cone jet. A jet-forming ring can additionally be installed which bundles the gas into a narrow angled jet. The operating parameters of the injector can be seen in table 2.

The injector is designed for methane or propane gas but addition of hydrogen up to 30vol% is also permissible. Up to 4 g of methane can be injected in up to 80° CA at a gas pressure of 50 to 80 bar at nominal engine speed. The minimum injection duration is 7° CA allowing 2 injections per combustion cycle, if required.

2.2. High Pressure High Temperature Optical Spray Chamber

The University of Rostock also operates a high pressure high temperature optical spray chamber. This consists of a heated and pressurized chamber with a large quartz window. Fuel Injectors are analysed using schlieren photography, whereby changes in the fluid's refractive index are made visible. As

changes to the density directly impact the refractive index of a fluid, this system is also suitable for analysing the flow emitting from a gas injector.

Collimated (laser) light is shone against a mirror at the back of the chamber, where it is reflected back. Changes in the density of the fluid in front of the mirror cause rays to be diffracted. A filter positioned at the reflected light's focal point is used to filter out the original collimated light, leaving the diffracted light to be photographed and hereby make the changes in density visible.

Figure 3 shows the University's optical spray analysis lab and the two measurement positions that will be used to analyse the newly developed gas injector.

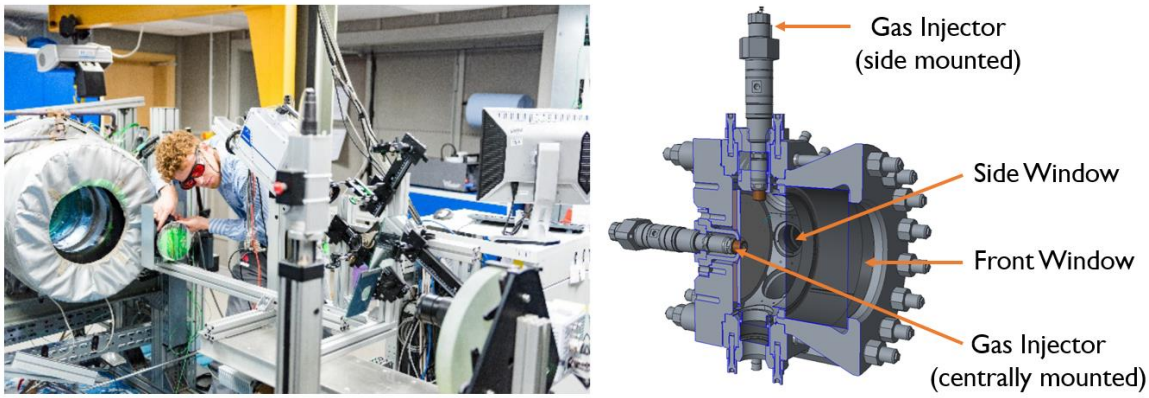

Figure 3: Optical spray analysis lab (left), high pressure high temperature optical spray chamber with gas injectors (right)

This spray chamber was also used for the optical measurement of the diesel pilot injector used in this project.

3. CFD Model

In order to predict the behaviour of the newly designed injector on the serial engine, a CFD model was developed in AVL Fire. Details of the cylinder mesh, system of equations and solver settings can be found in the following section.

3.1. Cylinder Mesh

Structured meshes of the engine's combustion chamber, including intake port, SOGAV, exhaust port and centrally mounted gas direct injector were created using AVL FAME software. The combustion chamber was modelled completely as the cylinder design does not allow for a symmetrical slice approach. The piston top land and threaded hole in the piston centre which is used for installing the piston crown were also modelled as these are recesses in which unburned methane could reside and escape from. Only the valve and nozzle region of the gas injector was modelled, as this has the most influence on the form of the gas injection. Local refinements were added to the near-valve area. The meshes were further refined to correctly resolve the piston top land area and using a time dependent refinement for the diesel spray. A sensitivity study was carried out to determine the most appropriate cell size.

Three cell sizes were chosen, 6 mm for coarse, 4 mm for medium and 3 mm for the fine mesh, resulting in maximum mesh sizes of approximately 1 million, 2 million and 4 million cells respectively. Choosing a smaller cell size results in higher accuracy but at the cost of computational speed, as more time is required to compute the conservation equations for every cell.

Comparison of the gaseous penetration length for the three cell sizes revealed 4 mm to be the most appropriate, as choosing a smaller size results in only a minor change in result, with 4 mm guaranteeing a high degree of accuracy with lower computational time requirements than the fine mesh.

A sample mesh can be seen in figure 4.

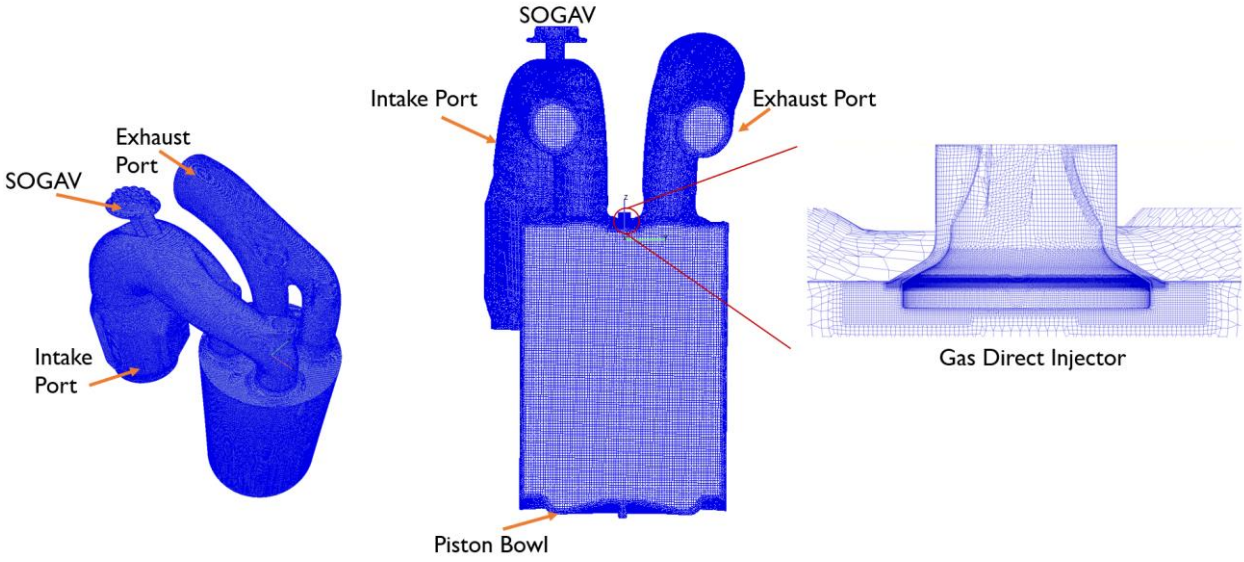

Figure 4: Mesh details showing a) complete mesh (left), b) central cut through mesh (centre) and c) detail of the gas direct injector (right)

As can be seen, the injector nozzle area is very highly refined in order to correctly resolve the sudden expansion of highly compressed gas in the combustion chamber. The resulting cell sizes are 0.25 mm around the injector and 0.0625 mm in a thin band at the exit from the valve seat gap.

3.2. System of equations

The AVL FIRE M solver was used to solve the Reynolds averaged Navier Stokes (RANS) conservation equations for mass, momentum, energy and concentration. Turbulence is modelled using the $k-\zeta-f$ model, a more computationally robust $\overline{v^2}-f$ model, according to Hanjalic, Popovac and Hadziabdic [1]. Due to the high pressures and temperatures within the combustion chamber, the ideal gas equation of state (EOS) has been replaced with the Peng Robinson EOS.

These equations are solved iteratively for every cell of the mesh at every time step to find an appropriate numerical solution and calculate the flow using RANS and the $k-\zeta-f$ modelled turbulence.

3.3. Solver settings and Parameters

The results presented in this paper arise from unsteady, variable time step simulations. The time step was set to 0.5° CA and reduced to 0.1° CA for the injection period using a ramp-up /ramp-down to retain stability. The lower time step was informed by a sensitivity study which was carried out to assess the effect of the time step on the penetration depth.

The calculations were started shortly after exhaust valve opening, allowing exhaust, intake, compression and power strokes to be simulated. The necessary boundary conditions such as wall temperatures and pressures in the inlet/outlet/cylinder were generated from experimental data and

0D/1D simulations. Wall temperatures were set as constant and the walls were treated as non-slip in nature.

The mesh size ranges from 603 000 to 4 million cells depending on the level of refinement (which increases during injections) and the simulated position of the piston. Two boundary layers of 0.2 mm thickness were used to correctly resolve the near wall flow field. During gaseous injection, three finer boundary layers of 0.05 mm thickness are employed due to the high velocity gradient in the wall layers in the direct vicinity of the gas injector.

The gas injection is calculated using a mass flow through the injector's boundary wall. The mass flow is ramped up and down to represent the opening and closing behaviour of the injector. In line with the injector's specifications, a 30° CA injection duration was chosen for the gaseous injection. The diesel pilot injection is treated as diesel EN590 while liquid, evaporating to n-heptane for the dual-fuel combustion model. The discrete droplet mechanism is used, solving differential equations for trajectory, momentum, heat and mass transfer of individual parcels of droplets entering the domain through the nozzle inlet. The droplets are tracked in the Lagrangian manner after an initial blob injection. The Schiller-Naumann [2] drag law has been applied and the Dukowicz evaporation model [3] is used. The initial droplet diameter is set as the diameter of the nozzle hole. Diesel parcels are set to stick to walls and follow a wave-tab secondary breakup scheme. The injected mass is divided into 100 000 parcels over the duration of injection. The diesel spray's breakup length was parametrized by the injector specific breakup time coefficient, based on measurements from previous testing in a high-pressure high-temperature spray chamber.

4. Results

4.1. Validation of the Diesel Spray Model

A separate mesh was created to represent the high-pressure high-temperature spray chamber in which the diesel injector was previously tested (see 2.2), using the same mesh generation parameters as for the cylinder mesh.

The chamber pressure and temperature used in the high-pressure high-temperature spray chamber represent those found in the real combustion chamber at 44° before top dead centre (b.TDC), the timing of the diesel pilot injection. The 75 mg diesel injection is equivalent to the amount used in engine testing at full load, ensuring that the results from the spray test and simulation are directly transferable to the full engine model. As the injector has an asymmetric spray, the entire spray chamber was modelled. The mesh size was 2.2 million cells. The injector specific breakup length parameter was varied in a series of simulations to fit with the experimental results. The best fit being found at a value of 260, as can be seen in figure 5.

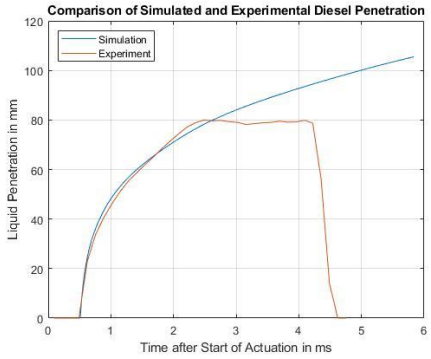

Figure 5: Comparison of Simulated and Experimental Diesel Penetration, liquid phase

The simulated diesel penetration follows the experimental well from the start of actuation, although there are anomalies in the experimental results due to the movement of the physical needle, meaning that the mass flow is not constant as in the simulated results. This explains the slight over- and under-shooting up to around 2.6 ms.

Following this initial period, the simulated results overshoot the experimental results. This is to be expected, as information about all injected parcels is stored and the maximum penetration calculated from this information. The optical measurement equipment, however, cannot track every single droplet, meaning that the simulated penetration length is expectedly higher than the experimental.

There is, however, a large discrepancy in the evaporation of the diesel, seen in the experiment at around 4.3 ms after the start of actuation. By 4.6 ms all the diesel has evaporated, seen in the fact that the liquid penetration length is zero. In the simulated result, a significant amount of the diesel remains liquid, evaporating much later than in the experiment.

The form of the diesel spray was also well reproduced by the simulation, as can be seen in figure 6.

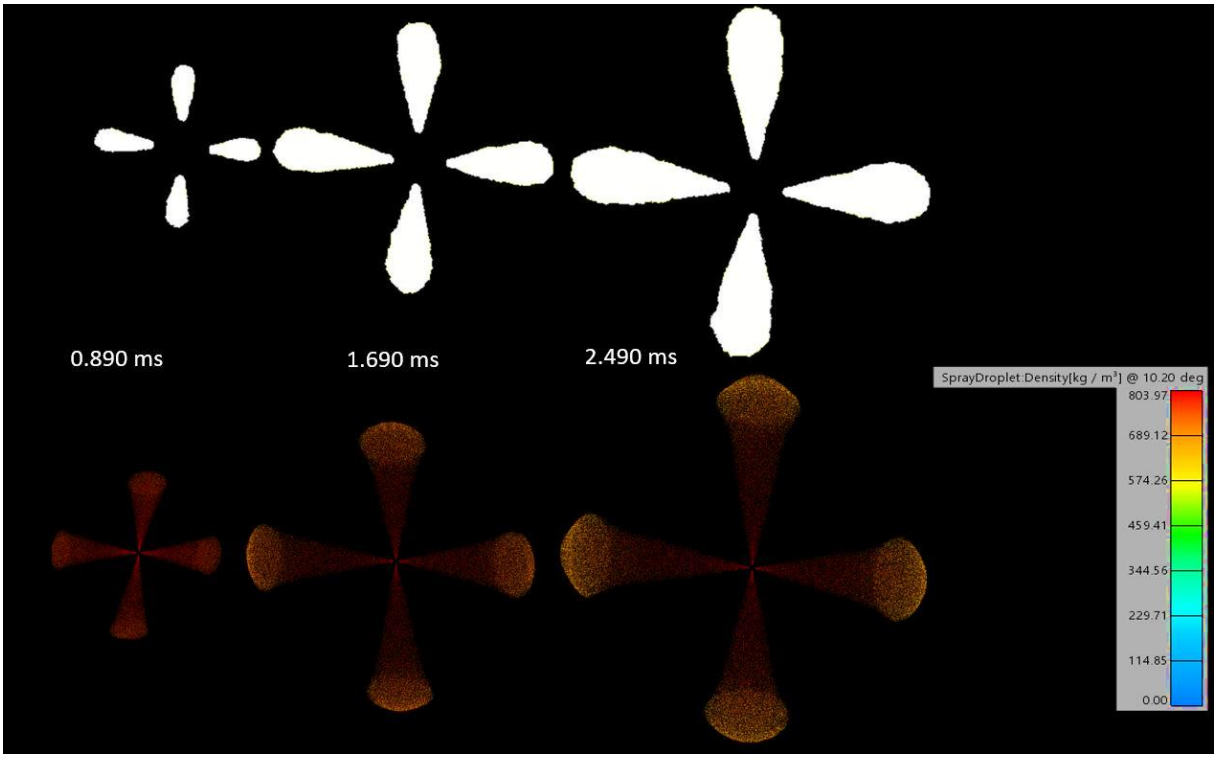

Figure 6: Comparison of experimental diesel sprays (shadowgraph, white, above) with simulated spray results, visualized using density (lower row)

There is more turbulence to be seen on the shadowgraph outline than is evident in the simulation, the reason being that the simulated results consist of droplets and not of a sheet-like diesel front which is perturbed by the surrounding air. The central portion of the diesel sprays are missing in the shadowgraphs as the mirror is obscured by the injector in this location.

The simulated results show good agreement with the measured ones, allowing the spray model to be successfully validated.

4.2. Validation of the CFD Engine Model by Cold Flow Simulation

A cold flow simulation consisting of exhaust, intake, and compression stroke was carried out and the resulting pressure trace compared with the measured pressure trace from the experimental engine. The results are shown in figure 7.

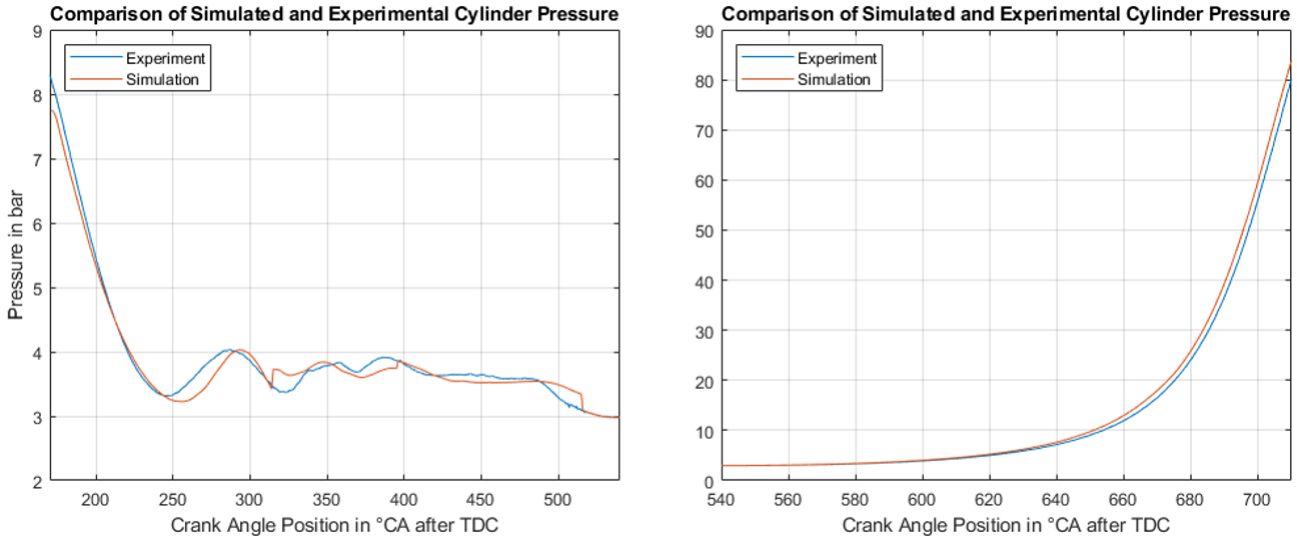

Figure 7: Comparison of experimental and simulated cylinder pressures

In general, the simulation produces good results and a very comparable pressure trace. The simulated results are not as highly refined as the experimental ones, resulting in the slightly more jagged appearance of the pressure oscillations between 170° CA and 540° CA after top dead centre (a.TDC). In the simulated result, pressure is lost more rapidly through the exhaust valve, as seen between 170° CA and approx. 240° CA. From around 640° CA, the simulated cylinder pressure is higher than the experimental results. A comparison of the mesh volume at bottom dead centre (BDC) and top dead centre (TDC) confirmed the accuracy of the mesh, giving a simulated compression ratio of 12.7495 in comparison with the experimental engine's 12.75.

At 710° CA a.TDC, the simulated cylinder pressure is 3.72 bar higher than the measured pressure. The simulation does not take blowby and leakage into account, however. An overall leakage of 3% cylinder mass would lead to a pressure drop of 3.3 bar. This leakage is high, but not impossible taking all the leakage sources into account. Another explanation for the discrepancy is the engine's compression ratio not being quite as stated in the specifications. A combination of these two factors and the low level of discrepancy accompanied by the comparability of the pressure traces make the simulated results feasible.

4.3. In Cylinder conditions

An understanding of the in cylinder conditions is essential in order to fully understand the mixing processes, as turbulence, tumble, swirl, and cylinder filling all have a role to play.

Analysis of Gas Exchange

The gas flow during the exhaust stroke, valve overlap and intake stroke is analysed using a series of plane cuts as shown in figure 8.

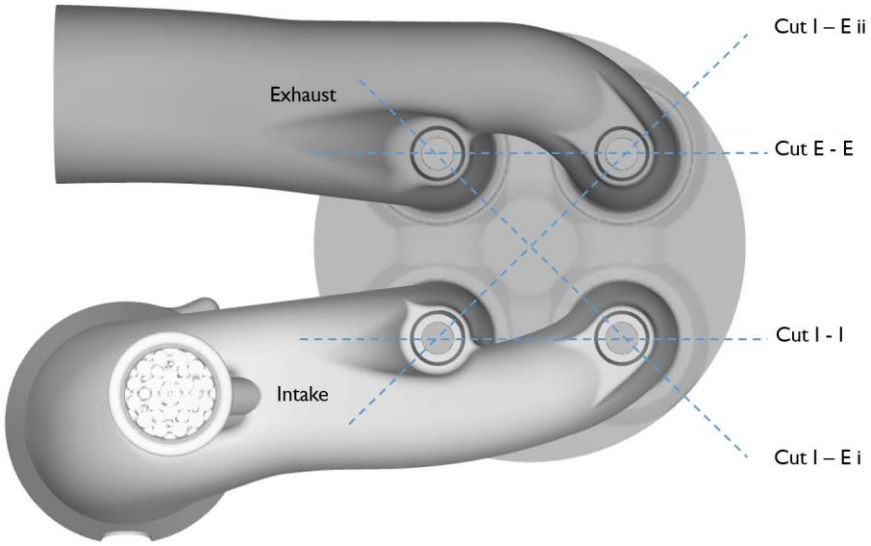

Figure 8: Position of cutplanes for analysis of gas exchange

A cutplane is laid through the centre plane of the two intake valves (cut I – I) and another through the central plane of the exhaust valves (cut E – E). Two further cuts are placed through the central plane of the cylinder, intake and outlet valves (cuts I – E i and I-E ii).

The simulation was started with a stationary flow field at 550° CA b.TDC, within the exhaust stroke. The upwards movement of the piston and the pressure difference between cylinder and exhaust manifold give the potential required to start the flow through the exhaust valves.

At this point the exhaust and cylinder are filled with exhaust gases. The mass fraction of CO_2 is 0.071, as expected for an air-fuel ratio (λ) of 2.2. The flow field demonstrates a relatively uniform character, the flow being oriented bottom to top and with a slight tilt towards the open exhaust valves.

These characteristics continue up the opening of the intake valves at 404° CA b.TDC. By this time, the exhaust valve is well opened, the intake valve is just opening. The flow field is still directed towards the exhaust as the intake valve opens. The highest velocities arise in the narrow intake valve seat gap. The fresh air entering the cylinder is entrained in the exhaust gas flow. In a turbocharged dual fuel engine with PFI, methane slip by shortcutting during valve overlap would occur here, as the fresh air and methane retained in the intake manifold is carried into the exhaust manifold. The exhaust valve closes at 326° CA b.TDC, shown in figure 9.

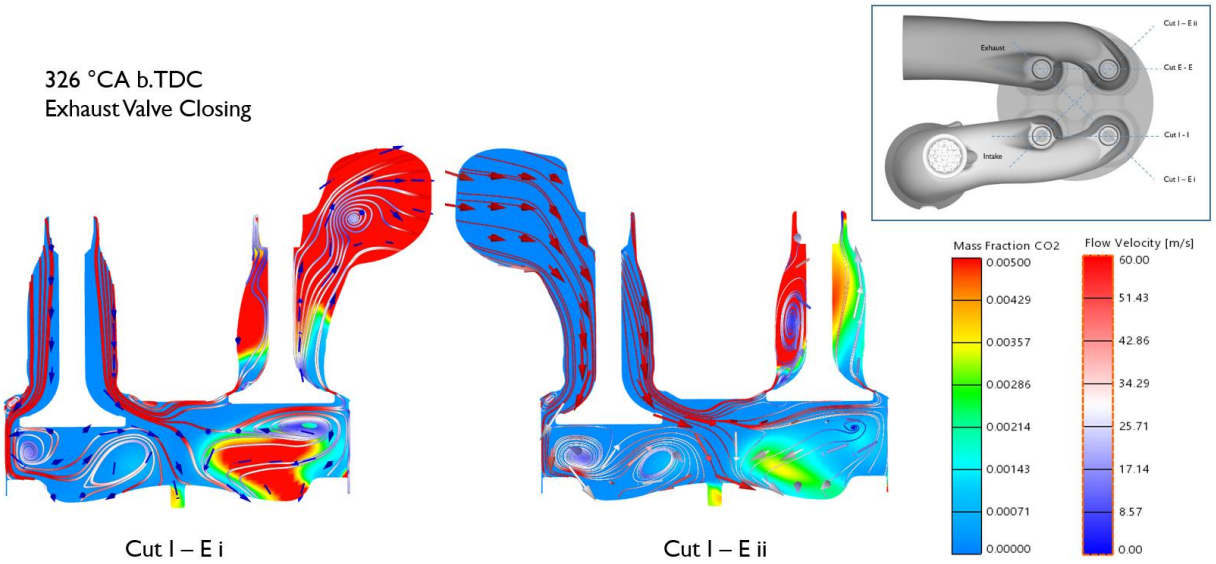

Figure 9: Flow field and CO_2 mass fraction at exhaust valve closing, cutplanes I – E

There is a small amount of exhaust gas that cannot escape the cylinder and is retained in the piston bowl below the exhaust valves. The red areas of the cutplanes indicate cells where the mass fraction of CO_2 is 0.005 (0.5%) or higher. This is caused by the flow emanating from the intake valves pushing the exhaust gas into this pocket while fresh air bypasses the cylinder. Vortices are also observed under both intake and exhaust valves. The flow field at intake valve closing is shown in figure 10.

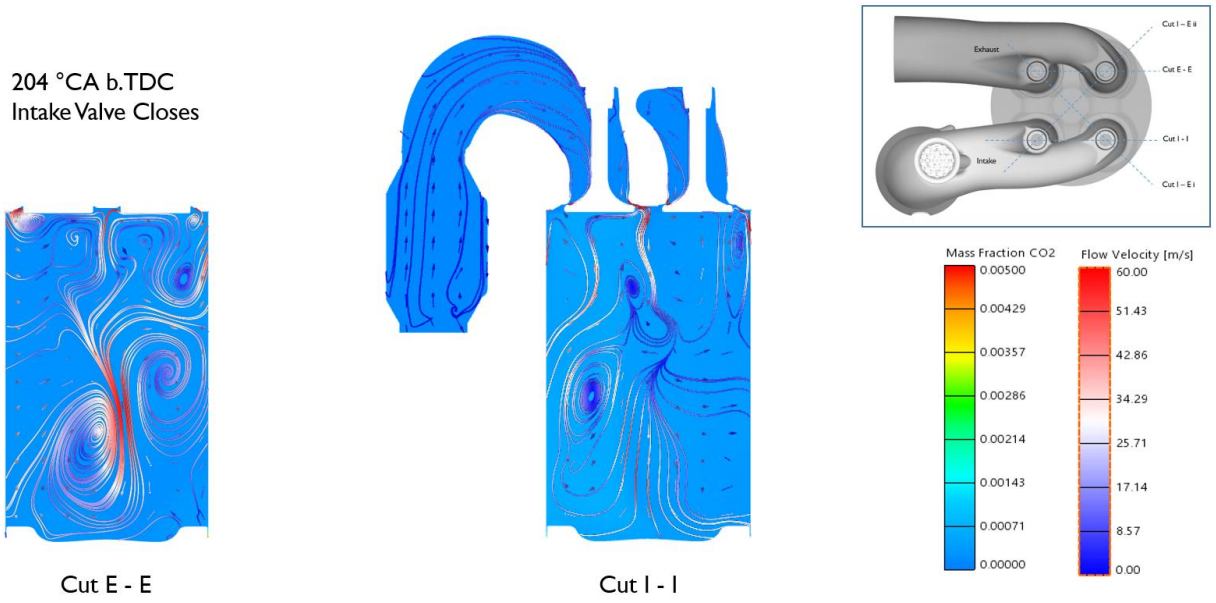

Figure 10: Flow field and CO_2 mass fraction at intake valve closing

The remaining exhaust gas is quite well dissipated by now, although the mix is not completely homogenous. As the intake valves close, the overall velocity of the incoming fresh charge is reduced, creating less dense and slower moving vortices. The highest velocities are found in the intake valve seat gaps and at the meeting of two downwards directed flows in cut E - E, creating two opposed spin vortices. The spin on the right hand side of cut E - E is largely counter clockwise, on the left hand side

mainly clockwise. This flow pattern is also represented on the intake side, as seen in cut I – I. This omega tumble can also be observed in the intake – exhaust cutplanes, not shown here.

Swirl

Cutplanes across the z-axis were also taken through the cylinder, 30 mm below the head. This position was chosen as it is within the engine's clearance volume, making it visible at any engine operation point. The results of the flow field and EGR mass fraction analysis can be seen in Figure 11.

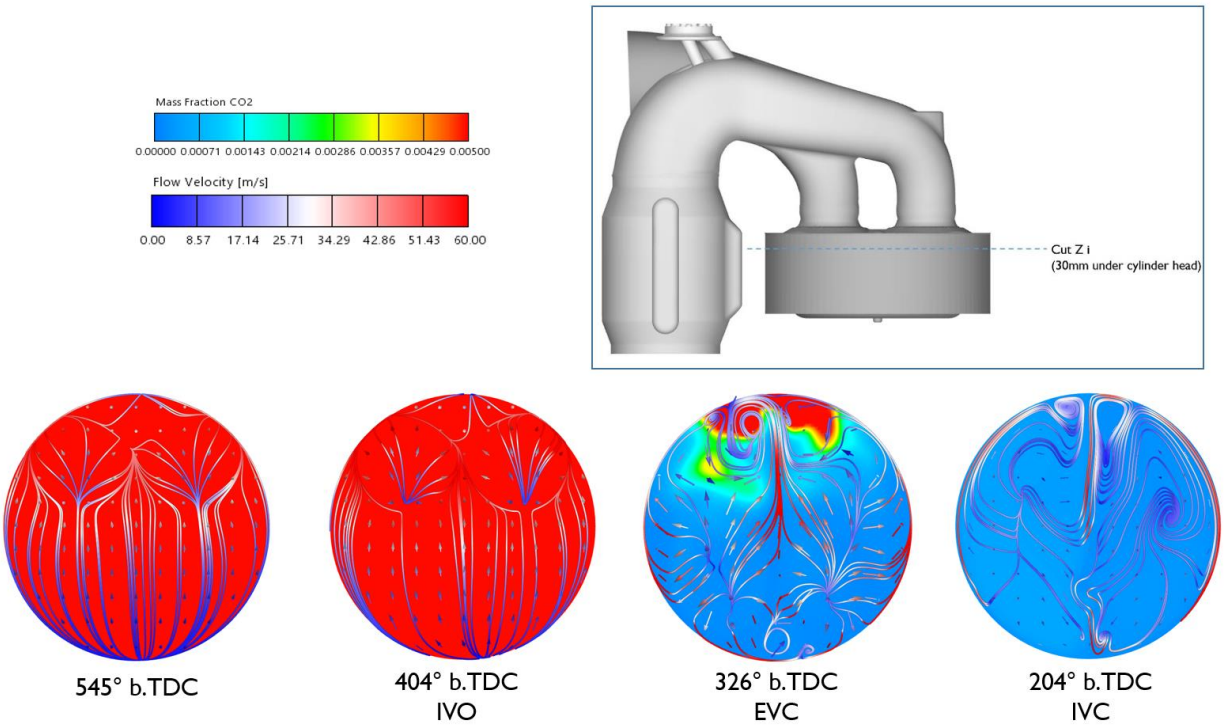

Figure 11: Cross-cylinder and swirl flow

Between 545° and 404° CA b.TDC cross flow from the intake side of the cylinder (bottom of circle) to the exhaust side (top) can be observed. This has a uniform direction, whereas the flow patterns shown from 326° b.TDC exhibit different behaviour. At exhaust valve closes (326° b.TDC) there is a central flow from intake to exhaust side, a counter clockwise flow on the right hand side and a clockwise flow on the left hand side which converge in the middle and slightly to the left of the mid-point of the two exhaust valves. At IVC (205° b.TDC) the flow seems to exhibit a low velocity omega swirl form, with the fresh air flowing along the sides of the chamber (right hand side: counter clockwise; left hand side clockwise) and returning in the middle (top to bottom).

Having now analysed the flow processes, the serial low pressure PFI operation is compared with alternative operation strategies using a medium pressure direct injector.

4.4. Low pressure PFI Operation

The serial low pressure PFI mixing process is examined here, allowing a comparison between conventional operation and operation with a medium pressure direct injector. The simulation was based on experimental results at 100% load. The mean indicated pressure was 20.4 bar, the charge air pressure 4.03 bar. The intake and exhaust pressure traces were used as boundary conditions for the inlet and outlet.

Figure 12 shows the location of the cutplane used for the examination of the PFI mixing process.

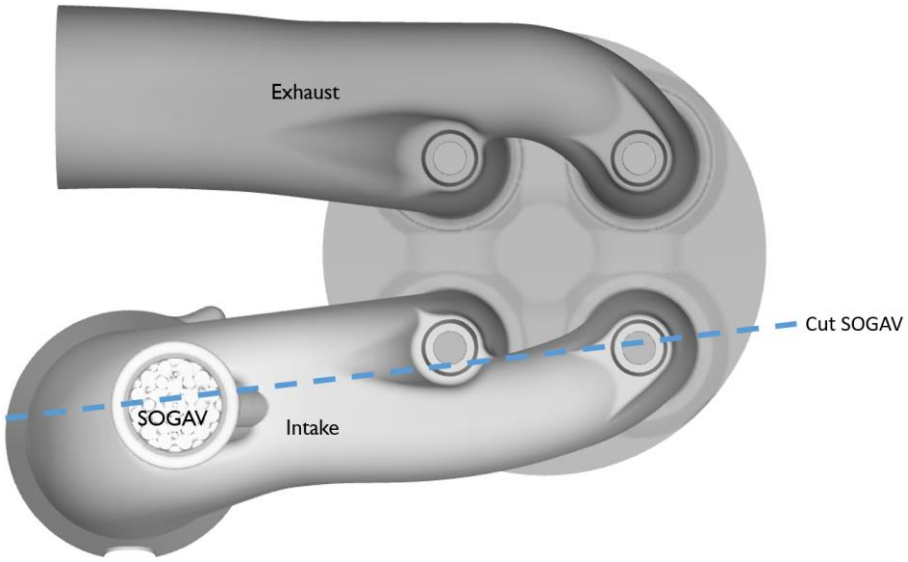

Figure 12: Location of cutplane for the examination of the low pressure process

A cutplane is taken across the two intake valves and the intake manifold including the SOGAV injector, showing the mixing of methane and air in the intake port and the admission of this mixture into the engine's cylinder.

In the low pressure process, methane is injected into the intake stroke between 361° b.TDC and 296° b.TDC, as seen in figure 13, visualised by the mass fraction of methane.

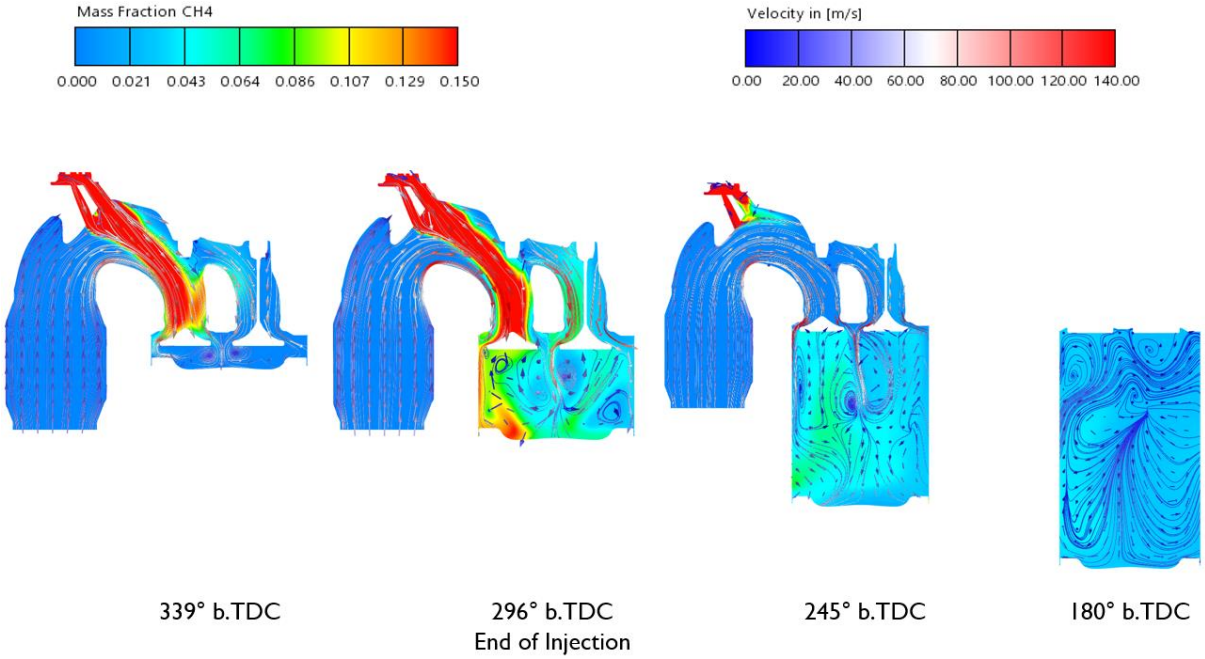

Figure 13: Injection of methane using a SOGAV injector at 100% load

At 361° b.TDC, the SOGAV injector is opened, admitting methane into the intake port. It takes around 20° CA for the methane to reach the left hand intake port, shown here at 339° b.TDC. The fuel travels through the intake manifold in a tight tube-like formation, primarily entering the combustion chamber

via the left hand intake valve, as shown at 296° b.TDC. The majority of methane is admitted via the intake valve closest to the intake manifold (left hand side). This behaviour is corroborated by independent simulations of the M34DF mixing process in [5], who found that 63% of fuel was admitted via the intake valve closest to the intake manifold – in figure 13 the left hand valve. Towards the end of injection, methane predominantly enters the cylinder on the left hand side of the left hand valve, travelling along the cylinder wall and into the piston bowl. Although the injection is completed at 296° b.TDC, methane from the intake port continues to enter the cylinder. This has largely ceased by 245° b.TDC. Fuel gas however still remains in the intake manifold and SOGAV bores until intake valve closing at 205° b.TDC. This methane will remain in the intake manifold until the next cycle, where it could be lost as methane slip though the exhaust valve during valve overlap. At 180° b.TDC, the mixture appears quite well homogenised, with a slightly richer area on the side of the cylinder closest to the intake manifold. Further homogenisation will take place in the compression stroke, as shown in figure 14.

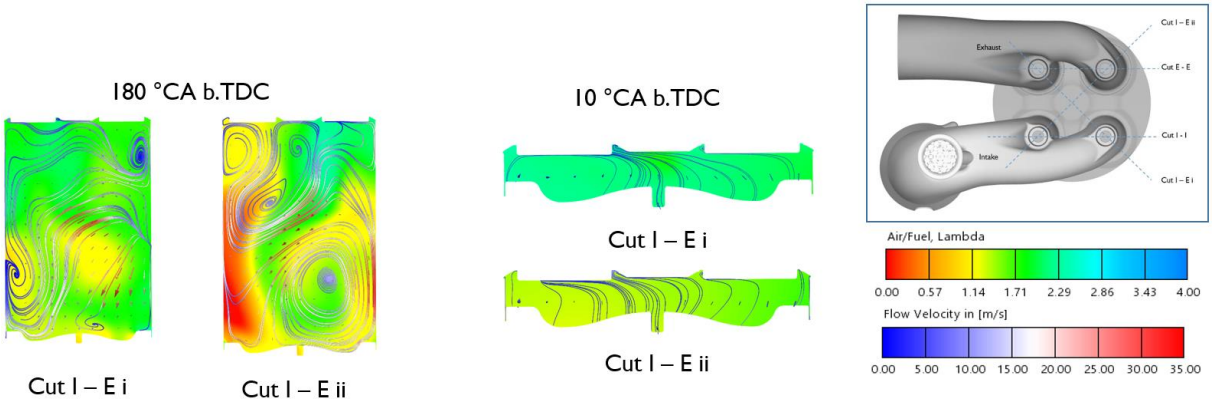

Figure 14: Homogenisation in the compression stroke, low pressure SOGAV operation

Here, cutplanes across the intake and exhaust are shown, revealing the air/fuel ratio (lambda) throughout the cylinder. At 180° b.TDC the mixture appears heterogeneous, especially in the cutplane I – E ii. The rich area shown on the left of the plane corresponds to the area of high methane concentration under the intake valve closest to the intake manifold as seen in figure 13. Both cutplanes exhibit a diagonal flow from top to bottom which develops into vortices that spin in differing directions, further homogenising the mixture. By 10° b.TDC, these vortices have disappeared and a more linear flow, normal to the piston bowl is observed, moving upwards to the cylinder head. The mixture is well homogenised, although a slightly richer area remains under the intake valve in cut I – E ii.

The homogenisation is made further visible in figure 15.

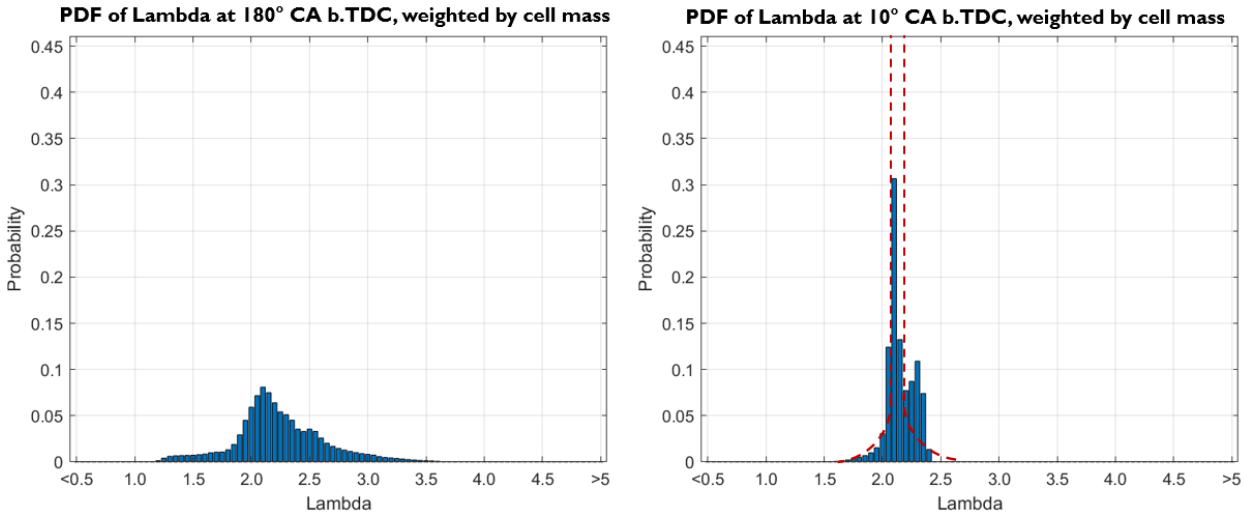

Figure 15: Lambda distribution at 180° and 10° b.TDC, low pressure SOGAV operation

These plots reveal the lambda value of each cell in the simulation. The cells were weighted by mass to counteract the effects of differing cell sizes in the domain and in the two different meshes show. From this information, the probability of lambda being a certain value can be ascertained, as is shown in figure 15. The red dashed line in the right hand plot indicates how a near - perfect homogenisation would appear, with nearly all cells having the global lambda value of 2.2. At 180° b.TDC, the lambda values range from 1.2 to 3.6. The distribution exhibits a peak at al lambda value of 2.1, with 8% of cells having this value. The results of the homogenisation processes during the compression stroke can clearly be seen at 10° b.TDC, where 31% of all cells in the domain are filled with a mixture of air and fuel at lambda 2.1. The span of lambda values has decreased, the lowest lambda value being 1.6, the highest being 2.4. The mixture is well, although not perfectly homogenised before the start of combustion which took place at 5° b.TDC in the experiment.

The following section examines if a similar level of homogeneity is possible using a medium pressure direct gas injector.

4.5. Homogenous Medium Pressure DI Operation

One of the main benefits of using direct injection is the possibility of eliminating methane slip resulting from methane residing in the intake manifold being lost through the exhaust valve during valve overlap. Using direct injection after exhaust valve closing results in extremely low levels of methane in the intake, as a minimal amount of the fuel adheres to the cylinder head due to the coandă effect and can enter the intake manifold towards the end of the intake stroke where the pressure difference between intake and cylinder is not so high.

If the injection window takes place after intake valve closing, methane in the intake manifold can be avoided altogether. This comes at the price of time available for homogenisation and the inability of using the turbulence in the intake stroke to homogenise the mixture.

In order to highlight the differences and benefits of medium pressure direct injection, simulations were carried out at 100% load, using the same boundary conditions as for low pressure SOGAV operation.

Table 3 shows the injection parameters used for the two simulations.

Table 3: Injection parameters for medium pressure direct injection

Parameter	Simulation 1	Simulation 2	Unit
Engine operating point	100	100	%
Start of injection	320	205	° b.TDC
Injection duration	30	30	° CA
Injected methane mass	3550	3550	mg

The start of injection in simulation 1 is 320° b.TDC, 5° CA after exhaust valve closing, ensuring no methane is lost through the exhaust valve.

The start of injection for the serial low pressure SOGAV operation is 361° b.TDC. For simulation one, this means that 41° CA are lost for homogenisation processes. However, the injection takes place more rapidly, ending only 5° CA after the SOGAV injection. The injected methane mass for SOGAV operation, simulation 1 and simulation 2 is identical.

In simulation 2, methane is first injected when the intake valve is closed, meaning a loss of 156° CA for homogenisation.

The direct injector is provided with a jet-forming ring. The following simulations were performed without this ring, allowing a higher homogenisation due to the wider spread of the hollow cone methane injection.

Figure 16 shows the injection of methane into the cylinder for both simulations.

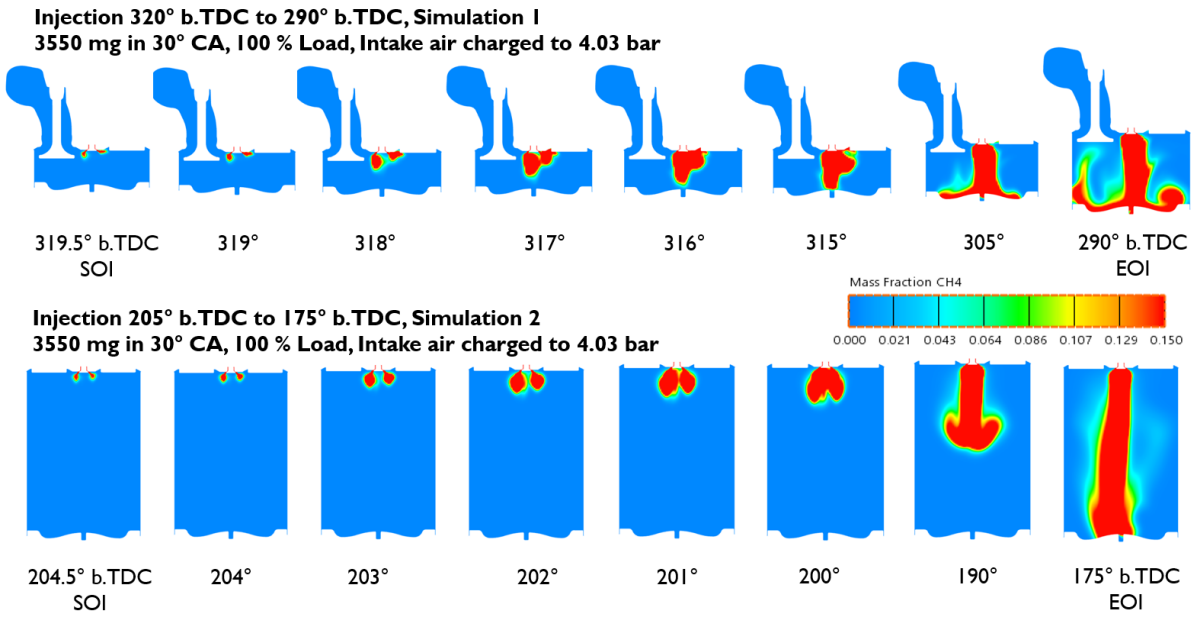

Figure 16: Direct injection of methane into the engine cylinder

In both scenarios, the fuel begins to propagate as a wide ring injection before collapsing to a narrow jet due to the area of low pressure underneath the poppet valve. This behaviour of gas injection from a poppet style valve is corroborated by [5]. The later injection (simulation 2) takes slightly longer to

collapse, in this case around 5° CA. In simulation one, the incoming stream of intake air deforms the jet, causing it to initially bend away from the intake valve. This also results in an earlier collapse, only 4° CA after SOI. Due to the piston position at the time of injection, the fuel hits the piston bowl earlier in simulation one, after which it follows the contour of the bowl towards the cylinder walls. The required injection pressure for both scenarios is 53 bar.

The benefit of fuel injection during the intake stroke (simulation 1) is that the turbulence created by the inflow of air through the intake valve can be utilised for the mixing of air and fuel. The disadvantage is the possibility of methane entering the intake manifold. The simulation revealed that a mere 9.14 $x10^{-12}$ mg of methane are present in the intake manifold at intake valve closing, a negligible amount, making this a viable injection strategy for medium pressure operation. Figure 17 shows the homogenisation during the compression stroke.

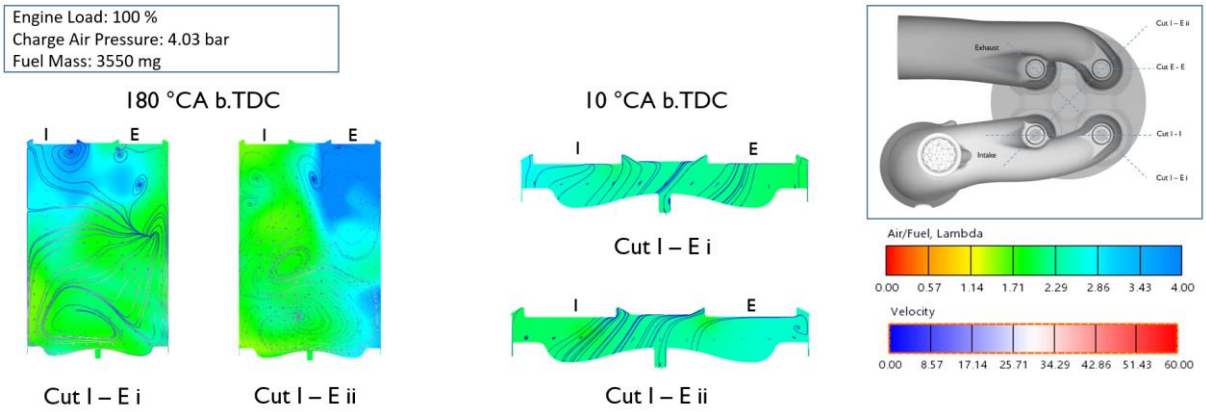

Figure 17: Cutplanes showing lambda during the compression stroke, Injection 320° - 290 °b.TDC

These cutplanes show the air/fuel ratio, lambda, at the start and end of compression. At 180° CA the mixture of gas and air is already well mixed due to the turbulence of the intake air flow. There are lean areas under the intake valve furthest from the intake manifold and under the exhaust valve furthest from the exhaust manifold. Although the mixture is well homogenised by 10° b.TDC, these areas remain slightly leaner. The flow patterns are similar to those found in the low pressure SOGAV operation, although not identical. The degree of homogenisation can be seen in figure 18.

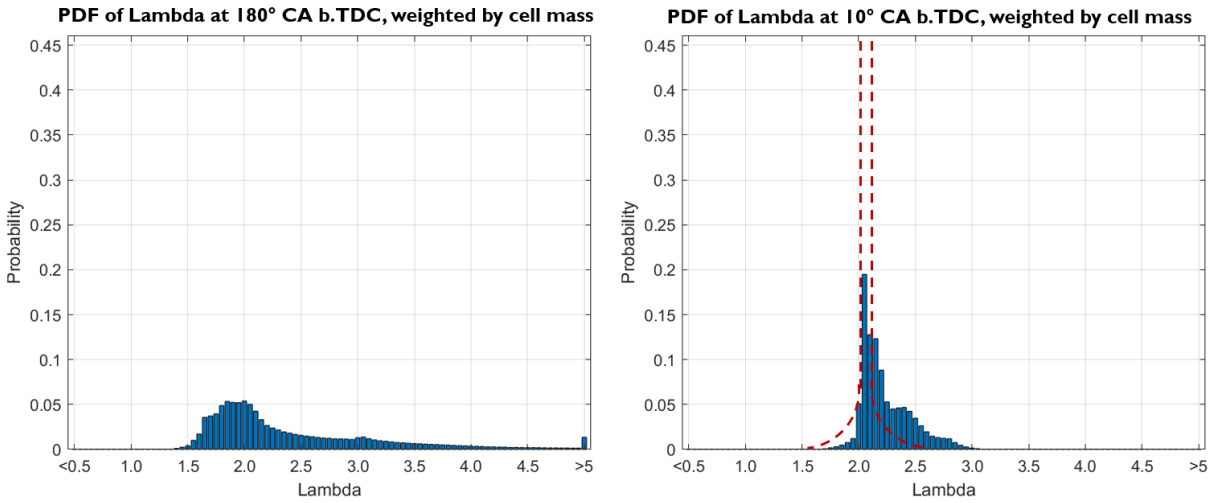

Figure 18: PDF of lambda at the start and end of compression, injection 320° - 290° b.TDC

Although homogenisation is evident, the mixture is more heterogeneous than with low pressure SOGAV operation due to the lesser time available. At 10° b.TDC, 19% of cells in the simulation have a lambda value of 2.1 in comparison to the 31% found in the simulation with SOGAV injection. Lambda ranges from 1.7 to 3.0, meaning that the mixture is easily combustible however.

In simulation 2, fuel was injected after intake valve closing in order to eliminate methane entering the intake manifold. This makes for a greater heterogeneity, as seen in figure 19.

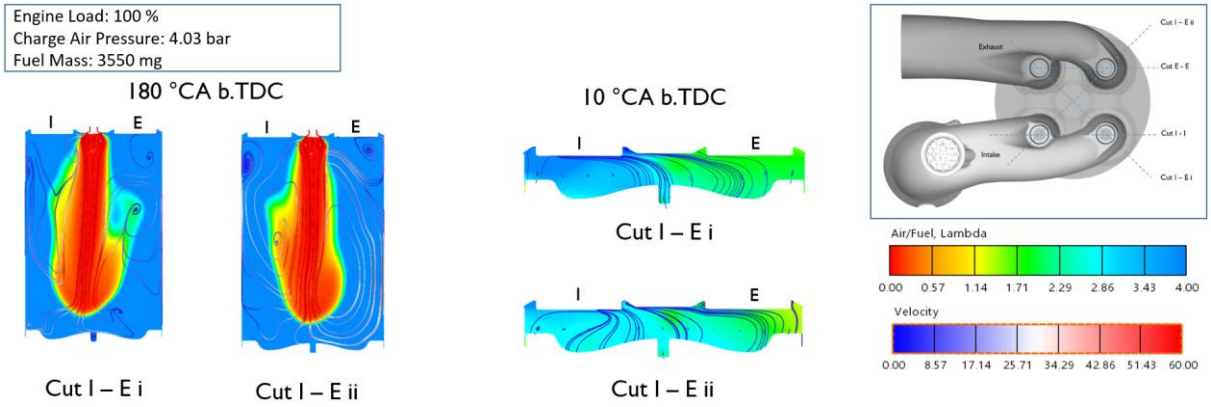

Figure 19: Cutplanes showing lambda during the compression stroke, Injection 205° - 175 °b.TDC

At 180° the gas injection is still taking place, shown by the incredibly rich area emanating from the centrally mounted gas injector. The downwards directed injection has a strong effect on the cylinder flow, making the flow field much different than previously observed. The gas and air mixture moves downwards until the piston bowl is hit, where it recirculates upwards before being re-entrained in the downwards flow. The mixture at 10° b.TDC is significantly more heterogeneous. The areas under the intake valves are leaner, whereas a richer mixture is found under the exhaust valves. These findings are reciprocated by the lambda distribution plots seen in figure 20.

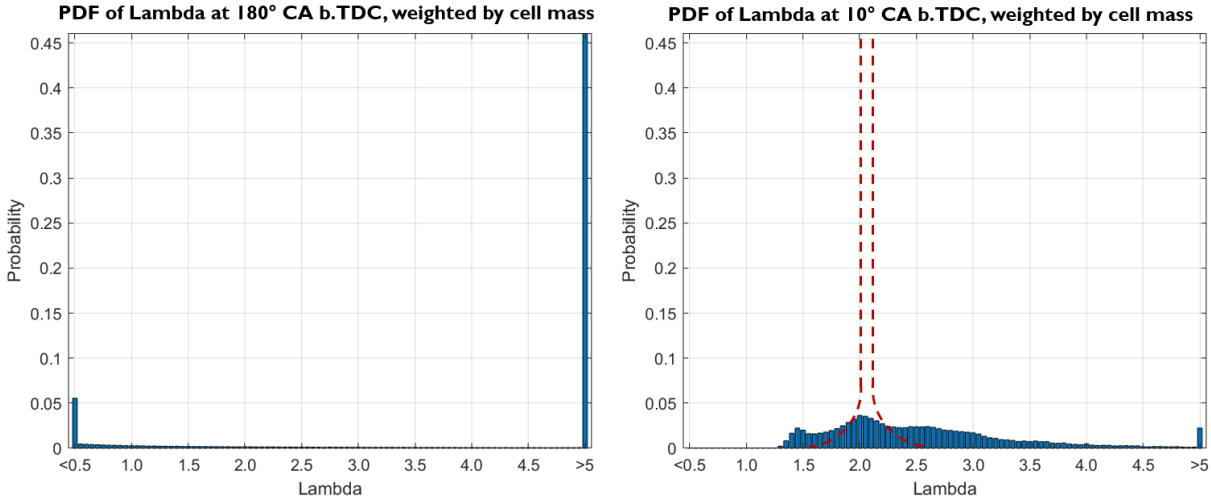

Figure 20: PDF of lambda at the start and end of compression, injection 205° - 175° b.TDC

The lambda distribution at 180° CA b.TDC reveals that no significant mixing has taken place during the injection. The cells are divided into extremely rich (5.5%) and extremely lean areas (80.5%). The remaining 14% represent cells where some mixing has occurred. The compression stroke is now the

only time available for mixing, resulting in a lower degree of homogenisation as seen at 10° b.TDC. Although there is a small peak (3.6% of all cells) at the lambda value 2.0, lambda is well distributed between 1.3 and >5. The lambda values are however generally within the combustibility limits for methane. Due to the increased number of rich cells and the heterogeneous mix, engine knock could become more prevalent using this injection strategy. A proved method for controlling engine knock is the use of stratified charge engine operation modes.

4.6. Stratified Charge Operation

Two stratified charge modes are presented here. The first, known from spark ignited engines to combat engine knock, consists of an early injection to create a lean homogenous mixture, followed by a late injection creating a rich area in the centre of the piston bowl. The homogenous mixture is too lean for knock to occur. Combustion speed is increased when burning from rich to lean areas ensuring the fuel-air mix burns throughout. It is beneficial that the fuel is more centred within the combustion chamber, meaning that less wall quenching occurs.

The second method consists of injecting the entire fuel in a late injection and trapping it within the piston bowl and centre of the cylinder.

Both methods are useful for reducing methane slip, as there is less wall quenching.

In order for these methods to work, a suitable piston crown must be chosen that is able to retain the fuel in the centre of the cylinder. One such piston geometry, an experimental high-squish piston available at the University of Rostock, is shown in figure 21, depicting lambda over the course of the two injections of method 1.

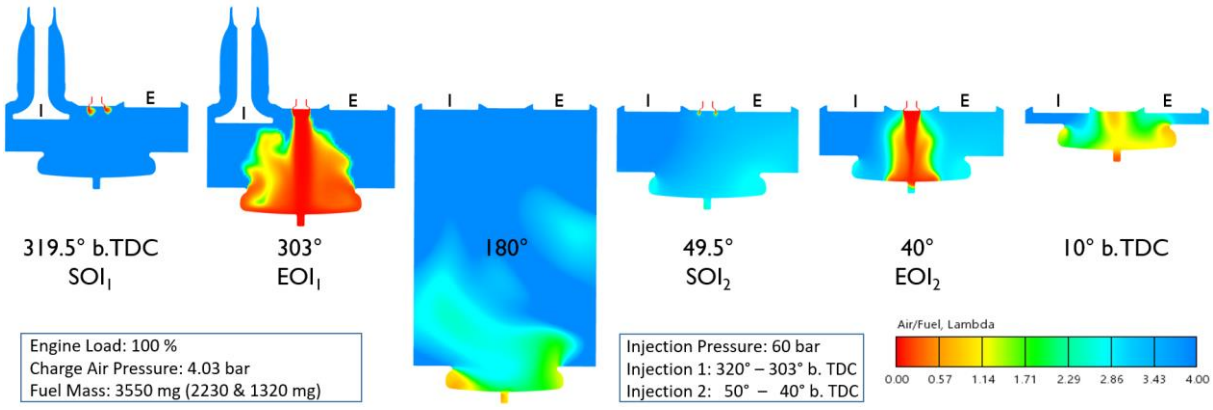

Figure 21: Stratified charge operation using two injections

The injector's jet-forming ring was installed for these simulations, creating a compact jet of fuel with rapid, targeted cylinder penetration. The fuel mass is divided into two shots, the first and larger delivering 2230 mg of methane in 17° CA starting at 320° b.TDC. This results in a global lambda of 3.5, a very lean mix that will not be prone to knocking. The second injection takes place at 50° b.TDC, delivering 1320 mg of fuel in 10° CA. The injection pressure is 60 bar and the injection is supercritical. The result can be seen at 10° b.TDC – a heterogeneous rich mix in the centre of the piston bowl and a lean mix at the piston walls. The global lambda value is now 2.2. The development of the lambda distribution is presented in figure 22.

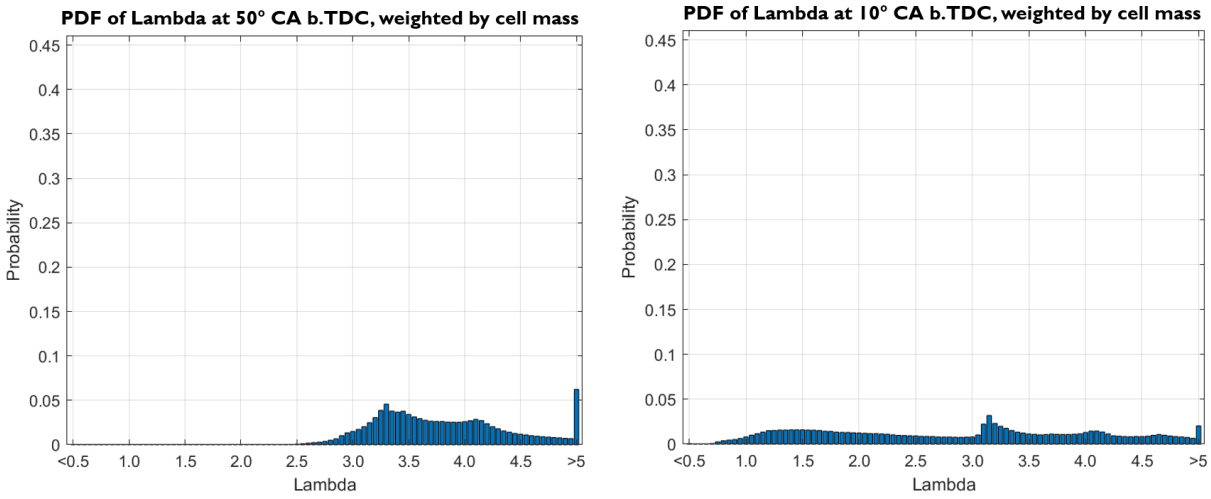

Figure 22: Development of lambda distribution between SOI_2 and 10° CA b.TDC

Although the first injection took place at the same time as simulation one in 4.5, the homogenisation is much lessened due to the geometry of the piston bowl, which tends to retain the gas and not recirculate it into the cylinder air. There is a peak (4.6%) at a lambda value of 3.35, and another (6%) at lambda greater than five. The richest lambda values represented occur at lambda 2.5. This lean mixture should guarantee an extremely low knock level. After the second injection from 50° - 40° b.TDC, mixing processes continue, producing a wide banded heterogeneous mix at 710° b.TDC, ranging from lambda values of 0.7 to greater than 5. This mixture should offer good combustion with low knock potential due to the decreased time in which rich mixtures are present in the cylinder and with the added advantage that less fuel is near the cylinder walls, increasing combustion efficiency and decreasing methane slip due to incomplete combustion.

Alternatively, a stratified charge can be achieved using a single late injection, as seen in figure 23.

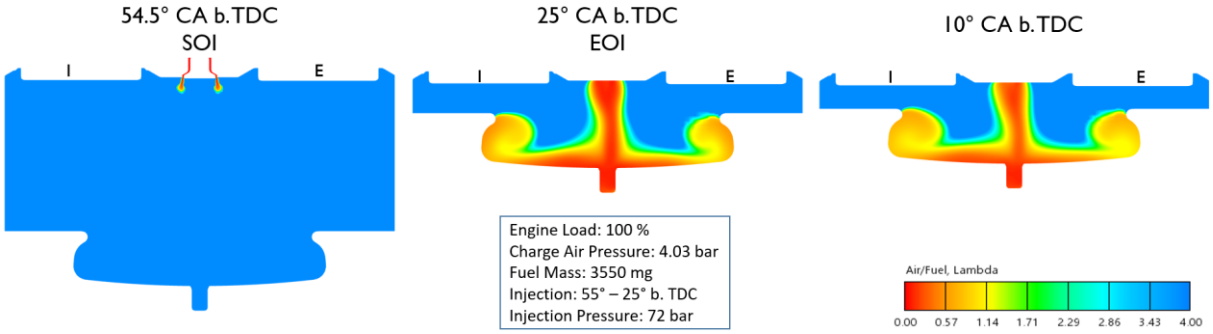

Figure 23: Stratified charge operation using a single injection

The jet-forming ring creates a rapid penetrating jet of methane which hits the piston crown and then follows its contour, creating a vortex around the outer edge of the piston bowl. The Coandă effect can be observed here, as the methane adheres to the engine head long after the end of injection at 25° CA b.TDC. At 10° CA b.TDC, a heterogeneous mix is present within the piston bowl, the richest areas being directly in contact with the piston. The bore used for mounting the piston (centre of piston bowl) is filled with methane. If the piston is not sufficiently warm, quenching effects could cause a rise in methane slip due to incomplete combustion in the proximity of the piston and within the piston mounting bore.

The lambda distribution for this operation mode is shown in figure 24.

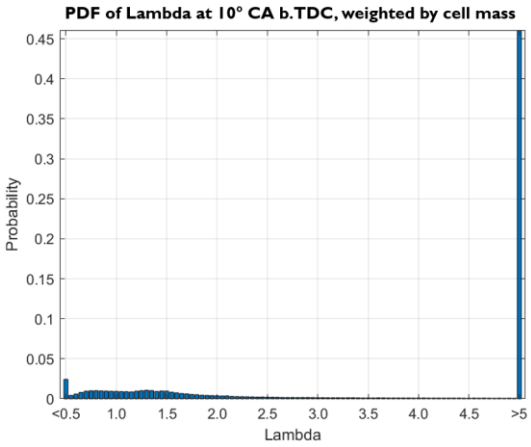

Figure 24: Lambda distribution at 10° CA b.TDC, single injection stratified charge

The distribution can be divided into a rich area with lambda values smaller than 0.5 up to lambda values around 2.5, and lean area in which little or no methane is present. The peak in the rich area occurs for lambda values smaller than 0.5 and speaks for 2.4% of the cells in the simulation. The major peak occurs in the lean area, with 65% of cells having a lambda value of five or greater.

Although the mixture is well positioned in the piston crown, the extremely rich lambda areas in close proximity to the piston could result in poor combustion behaviour.

To highlight the differences in these two approaches, the amount of fuel in different areas of the cylinder was calculated, as seen in figure 25.

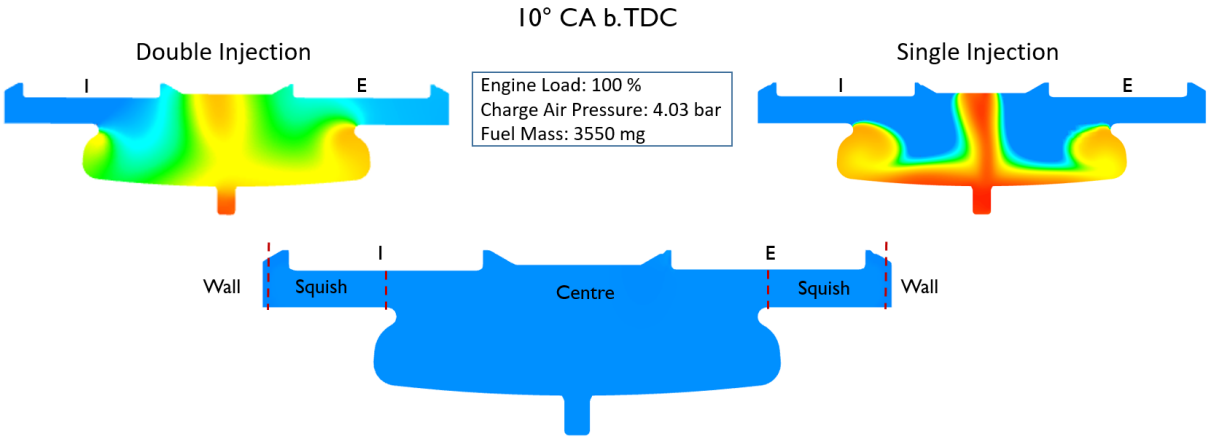

Figure 25: Comparison of methane distribution within the cylinder: double vs. single shot injection

The cylinder was divided into the central area above the piston bowl (radius, r < 104 mm), the squish area (104 mm< r < 166 mm), and a near-wall area (r > 166 mm). The piston has a diameter of 340 mm. The results of the methane distribution analysis are presented in table 4.

Table 4: Methane distribution in the engine cylinder

Operation Mode	**Double Injection Stratified**		**Single Injection Stratified**		**SOGAV Homogenous**	
	Mass CH4 in [mg]	%	**Mass CH4 in [mg]**	%	**Mass CH4 in [mg]**	%
Centre	2630.18	74.09	3315.88	93.4	2673.89	75.32
Squish	866.03	24.4	234.12	6.59	740.05	20.85
Wall	53.79	1.51	1.16×10^{-7}	3.26×10^{-9}	136.06	3.83
Total	3550	100	3550	100	3550	100

In comparison to homogenous operation with SOGAV injection, using a double shot stratified injection decreases the near-wall methane by 50%. Using a single shot injection as detailed eradicates near-wall methane.
The mass of methane in the centre of the piston bowl is very comparable for the double injection and homogenous operation. In the single injection simulation, this is almost 20% higher.

The mass of methane retained in the intake manifold was also calculated and is presented in the next section.

4.7. Comparison of Operation Modes: Methane Present in the Intake Manifold

A comparison of the methane present in the intake manifold at intake valve closing for the differing operation modes is presented in table 5.

Table 5: Methane present in the intake manifold at intake valve closing

Injection Strategy	Injector	CH4 in Intake Manifold at IVC	Unit
Low pressure PFI 100 %	SOGAV	376.1	mg
Low pressure PFI 50 %	SOGAV	183.5	mg
Medium pressure injection after EVC, 100 %	DI	9.14 e-12	mg
Medium pressure injection after EVC, 50 %	DI	5.57 e-13	mg
Medium pressure injection after IVC	DI	0	mg
Stratified charge methods	DI	0	mg

According to the simulation, 10.6% of the total fuel remains in the intake using the serial SOGAV injection strategy (10.3% at 50% load). This methane will enter the cylinder in the next cycle and either be lost via the exhaust valve or combusted with the fresh charge. Reducing the amount of methane in the intake will drastically reduce methane slip and could lead to better performance as cyclical fluctuations and knock potential will also be reduced. Using direct injection in the intake stroke after

exhaust valve closing reduces methane in the intake to negligible amounts. Injecting the methane into the cylinder after intake valve closing eliminates methane in the intake completely.

5. Conclusion and Outlook

The aim of this paper was to present ways in which using a methane direct injector could improve methane slip.

Using direct injection in the intake stroke after exhaust valve closing reduces methane in the intake to negligible amounts and provides a good level of homogenisation. The lambda values present in the cylinder range between 1.7 and 3.1 whereas the serial SOGAV strategy results in a lambda range from 1.7 to 2.4, showing that engine knock should not be significantly increased as richer areas are not prevalent in the more heterogeneous mixture produced by the DI strategy. There is also potential for performance increase using DI, as no air is displaced by the methane in the intake manifold. As methane is not lost to the exhaust, fuel economy is also increased.

Further retarding the injection timing to after IVC reduces methane in the intake to zero, but at the cost of a much more heterogeneous mixture due to not being able to utilise the turbulence caused by the intake air for mixing purposes. Richer areas are prevalent which could lead to higher knock levels.

As knock is a function of time, reducing the time in which the fuel is in the cylinder is one way of combatting knock, as seen in the stratified charge single injection strategy. Here the fuel was injected late in the compression stroke. Depending on the piston bowl geometry, this could lead to unburned methane due to very rich areas close to the piston surface. There will be no wall quenching along the cylinder wall, as next to no methane resides here.

Using a double injection strategy, the first injection to create a lean basic mixture and the second late in the compression stroke, a similar distribution of methane can be obtained as in homogenous SOGAV operation, but with 50% less methane in the near-wall area. The mixture is however much more heterogeneous.

The effect of these operation modes on combustion are yet to be analysed with the parameterisation of the combustion equations. This requires engine data which will be produced in the following months. Nevertheless, the simulated results show promise for eliminating methane slip by shortcutting and for decreasing the near-wall methane, leading to less wall-quenching.

If the costs of gas compression are outweighed by the benefits of low methane slip operation with improved combustion efficiency, medium pressure direct injection on dual-fuel marine engines could prove very effective at bridging the gap between the fuel market of today and tomorrow.

Acknowledgements

The authors would like to thank the Federal Ministry for Economic Affairs and Climate Action for funding the project 'TEME 2030+' (project number: 03SX537A). Furthermore, our thanks go to FVTR GmbH, Schaller Automation GmbH & Co. KG, KS Kolbenschmidt Large Bore Pistons GmbH, Kompressorenbau Bannewitz GmbH, M. Jürgensen GmbH und Co. KG, SICK AG und Umicore for supporting this project.

Supported by:

Federal Ministry for Economic Affairs and Climate Action

on the basis of a decision by the German Bundestag

Literature

[1] Hanjalic, K., Popovac, M., Hadziabdic, M. "A robust near-wall elliptic-relaxation eddy-viscosity turbulence model for CFD", Int. J. Heat Fluid Flow, 25, 1047–1051, 2004.

[2] Schiller, L. and Naumann, A. "A Drag Coefficient Correlation." Zeitschrift des Vereins Deutscher Ingenieure, 77, 318-320, 1935

[3] Dukowicz, J.K. "Quasi-steady droplet change in the presence of convection", informal report Los Alamos Scientific Laboratory, LA799MS, 1979

[4] Di Modica, D.V. "Numerische Untersuchung der Zylinderinnenströmung eines mittelschnelllaufenden Verbrennungsmotors", Masterthesis, TU Braunschweig, 2017

[5] Deshmukh et al. "Characterization of Hollow Cone Gas Jets in the Context of Direct Gas Injection in Internal Combustion Engines", SAE International, 2018, doi: 10.4271/2018-01-0296

List of the authors:

Patrick Albrecht	FHNW - University of Applied Sciences and Arts Northwestern Switzerland
Sungchan An	Hyundai Heavy Industries
Oscar Lacroix Andrivet	TotalEnergies OneTech
Dr. Matthias Auer	MAN Energy Solutions SE
Alberto Ballerini	Politecnico di Milano
Dr. Robert Bank	FVTR GmbH
Dr. Christophe Barro	WinGD
Torsten Baufeld	Liebherr Machines Bulle SA
Dr. Dirk Bergmann	Accelleron c/o Turbo Systems Switzerland Ltd
Dr. Sören Bernhardt	Karlsruher Institut für Technologie – Institut für Kolbenmaschinen
Simon Bezenšek	AVL List GmbH
Dr. Manickam Bhuvaneswaran	MAN Energy Solutions SE
Martin Bohnenblust	WinGD
Annalena Braun	Karlsruher Institut für Technologie – Institut für Kolbenmaschinen
Prof. Bert Buchholz	Rostock University, LKV
Gennaro Caputo	Wärtsilä Italia S.p.A.
Patrick Cartier	FHNW - University of Applied Sciences and Arts Northwestern Switzerland
Sebastian Cepelak	Rostock University, LKV
Dr. Marco Coppo	OMT SpA
Prof. Gianluca D'Errico	Politecnico di Milano
Dr. Athanasios Dimaratos	Laboratory of Applied Thermodynamics, Aristotle University of Thessaloniki
Jules Christopher Dinwoodie	Rostock University, LKV
Martin Drescher	FVTR GmbH
Koji Edo	Japan Engine Corporation
Dr. Marco Ferro	OMT SpA
Dr. Günter Figer	AVL List GmbH
Manuel Glauner	Rostock University, LKV
Bruno Griffaton	TotalEnergies OneTech

Dr. Troy Hawkins	Argonne National Laboratory
Prof. Kai Herrmann	FHNW - University of Applied Sciences and Arts Northwestern Switzerland
Peter Holand	MAN Energy Solutions SE
Antje Hoppe	FVTR GmbH
Dr. Yasuhisa Ichikawa	National Institute of Maritime, Port and Aviation Technology, National Maritime Research Institute
Dr. Marios Ioannou	Wärtsilä Services Switzerland
Thomas Kammerdiener	AVL List GmbH
Dr. Michael Kass	Oak Ridge National Laboratory
Dr. Brian Kaul	Oak Ridge National Laboratory
Dr. Chiharu Kawakita	New Energy and Industrial Technology Development Organization (NEDO)
Dr. Satoshi Kawauchi	National Institute of Maritime, Port and Aviation Technology, National Maritime Research Institute
Dr. Martin Kirsten	AVL List GmbH
Prof. Grigorios Koltsakis	Laboratory of Applied Thermodynamics, Aristotle University of Thessaloniki
Dominik Krnac	MAN Energy Solutions SE
Dr. Heiko Kubach	Karlsruher Institut für Technologie – Institut für Kolbenmaschinen
Dr. Fanny Langschwager	Rostock University, LKV
Dr. Eric Lauer	MAN Energy Solutions SE
Yongseok Lee	Hyundai Heavy Industries
Kyungrock Lee	Hyundai Heavy Industries
Dr. Maximilian Malin	Large Engines Competence Center
Herve Martin	Accelleron c/o Turbo Systems Switzerland Ltd
Juan Reina Martinez	WinGD
Josh Messner	U. S. Department of Energy
Akihiro Miyanagi	Japan Engine Corporation
Prof. Hinrich Mohr	GasKraft Engineering
Dr. Shinsuke Murakami	AVL List GmbH
Claudio Negri	OMT SpA
Dr. Mathias Niendorf	Rostock University, LKV

Dr. Yoichi Niki	National Institute of Maritime, Port and Aviation Technology, National Maritime Research Institute
Alix Noca	Liebherr Machine Bulle
Prof. Leonidas Ntziachristos	Laboratory of Applied Thermodynamics, Aristotle University of Thessaloniki
Nicolas Obrecht	TotalEnergies OneTech
Alejandro Calvo Oilveira	Wärtsilä Services Switzerland
Dr. Fabian Pinkert	FVTR GmbH
Michele Placanica	Wärtsilä Italia S.p.A.
Andrej Poredos	AVL List GmbH
Dr. Sascha Prehn	Rostock University, LKV
Yi-Hao Pu	Ghent University
Dr. Karthu Ramasamy	Pacific Northwest National Laboratory
Maria Rappo	TotalEnergies OneTech
Dr. Christian Reiser	WTZ Roßlau gGmbH
Markus Roßmann	Graz University of Technology - Institute of Thermodynamics and Sustainable Propulsion Systems
Dr. Andrea Schirru	WinGD
Dr. Karsten Schleef	Rostock University, LKV
Dr. Andreas Schmid	WinGD
Dr. Bruno Schneider	FHNW - University of Applied Sciences and Arts Northwestern Switzerland
Dr. Ulrike Schümann	Rostock University, LKV
Dr. Omar Seddik	WinGD
Maria Segura	AVL List GmbH
Pascal Seipel	Rostock University, LKV
Karsten Stenzel	WTZ Roßlau gGmbH
Elmar Strittmatter	Accelleron c/o Turbo Systems Switzerland Ltd
Pascal Süess	WinGD
Ward Suijs	Ghent University
Prof. Koji Takasaki	Kyushu Univ. & National Maritime Research Institute, Japan
Dr. Eric Tan	National Renewable Energy Laboratory
Dr. Martin Theile	FVTR GmbH
Timothy Theiss	Oak Ridge National Laboratory

Phillip Thorau	WTZ Roßlau gGmbH
Dr. Lauge Thorsen	Wärtsilä Danmark A/S
Dr. Muhammad Usman	Lloyds Register
Prof. Sebastian Verhelst	Ghent University, Lund University
Dr. Ludovico Viglione	Wärtsilä Services Switzerland
Dr. Beat von Rotz	WinGD
Georgia Voniati	Laboratory of Applied Thermodynamics, Aristotle University of Thessaloniki
Dr. Cornelius Wagner	MAN Energy Solutions SE
Dr. German Weisser	WinGD
Prof. Nicole Wermuth	Large Engines Competence Center
Prof. Andreas Wimmer	Graz University of Technology - Institute of Thermodynamics and Sustainable Propulsion Systems
Silas Wüthrich	FHNW - University of Applied Sciences and Arts Northwestern Switzerland
Wookhyeon Yoon	Hyundai Heavy Industries
GwangHyeon Yu	Hyundai Heavy Industries
Dr. Qiyan Zhou	Accelleron c/o Turbo Systems Switzerland Ltd

FVTR GmbH

Forschungszentrum für
Verbrennungsmotoren und
Thermodynamik Rostock GmbH

+49 381 4059 650
office@fvtr.de
www.fvtr.de

RGMT

**Rostock Large
Engine Symposium**

conference@fvtr.de
www.rgmt.de

LKV

Rostock University
Lehrstuhl für Kolbenmaschinen
und Verbrennungsmotoren

+49 381 498 9151
lkv.msf@uni-rostock.de
www.lkv.uni-rostock.de